ISSN 2312-4334

MINISTRY OF EDUCATION AND SCIENCE OF UKRAINE

East European Journal of Physics

No 2. 2023

2023

East European Journal of Physics

EEJP is an international peer-reviewed journal devoted to experimental and theoretical research on the nuclear physics, cosmic rays and particles, high-energy physics, solid state physics, plasma physics, physics of charged particle beams, plasma electronics, radiation materials science, physics of thin films, condensed matter physics, functional materials and coatings, medical physics and physical technologies in an interdisciplinary context.
Published quarterly in hard copy and online by V.N. Karazin Kharkiv National University Publishing
ISSN 2312-4334 (Print), ISSN 2312-4539 (Online)

The editorial policy is to maintain the quality of published papers at the highest level by strict peer review.
Approved for publication by the Academic Council of the V.N. Karazin Kharkiv National University (29.05.2023, Protocol no. 9).
EEJP registered by the order of Ministry of Education and Science of Ukraine No. 1643 of 28.12.2019, and included in the list of scientific professional editions of Ukraine (category "A", specialty: 104, 105), in which can be published results of dissertations for obtaining Ph.D. and Dr. Sci. degrees in physical and mathematical sciences.
The Journal is a part of the Web of Science Core Collection (ESCI) scientometric platform and indexed by SCOPUS.

Editorial office
Department of Physics and Technologies, V.N. Karazin Kharkiv National University
Kurchatov av., 31, office 402, Kharkiv, 61108, Ukraine
Tel: +38-057-335-18-33,
E-mail: eejp@karazin.ua,
Web-pages: http://periodicals.karazin.ua/eejp (Open Journal System)
Certificate of State registration No.20644-10464P, 21.02.2014

Східно-європейський фізичний журнал

Східно-європейський фізичний журнал – міжнародний рецензований журнал, присвячений експериментальним і теоретичним дослідженням ядерної фізики, космічних променів і частинок, фізики високих енергій, фізики твердого тіла, фізики плазми, фізики пучків заряджених частинок, плазмової електроніки, радіаційного матеріалознавства, фізики. тонких плівок, фізики конденсованої речовини, функціональних матеріалів та покриттів, медичної фізики та фізичних технологій у міждисциплінарному контексті.

Видається щоквартально в друкованому вигляді та в Інтернеті видавництвом Харківського національного університету імені В.Н. Каразіна
ISSN 2312-4334 (Друкована веерсія), ISSN 2312-4539 (Онлайн)
Редакційна політика полягає у підтримуванні якості опублікованих статей на найвищому рівні шляхом суворої експертної оцінки.
Схвалено до друку Вченою радою Харківський національний університет імені В.Н. Каразіна (29.05.2023 р., Протокол № 9).
Східно-європейський фізичний журнал зареєстровано наказом Міністерства освіти і науки України № 1643 від 28.12.2019 та включено до Переліку наукових фахових видань України (категорія «А», спеціальність: 104, 105), у яких може публікуватися результати дисертацій на здобуття ступенів кандидата та доктора фізико-математичних наук.
Журнал є частиною наукометричної платформи Web of Science Core Collection (ESCI) і індексується SCOPUS.

Редакція
Науково-навчальний інститут «ФТФ», Харківський національний університет імені В.Н. Каразіна
пр. Курчатова, 31, офіс 402, Харків, 61108, Україна
Тел: +38-057-335-18-33,
Електронна пошта: eejp@karazin.ua,
Веб-сторінка: http://periodicals.karazin.ua/eejp (система журналів з відкритим доступом)
Свідоцтво про державну реєстрацію №20644-10464П від 21.02.2014р.

East European Journal of Physics

No 2. 2023

East European Journal of Physics

No 2. 2023

East European Journal of Physics

No 2. 2023

East European Journal of Physics. **2.** 7-50 (2023)
DOI:10.26565/2312-4334-2023-2-01 ISSN 2312-4334

VORTEX DYNAMO IN ROTATING MEDIA[†]

Michael I. Kopp[a]*, Volodymyr V. Yanovsky[a,b]
[a]*Institute for Single Cristals, Nat. Academy of Science Ukraine, Nauky Ave. 60, Kharkiv 61072,Ukraine*
[b]*V.N. Karazin Kharkiv National University, 4, Svoboda Sq., Kharkiv, 61022, Ukraine*
**Corresponding Author e-mail: michaelkopp0165@gmail.com*
Received April 9, 2023; accepted April 24, 2023

The review highlights the main achievements in the theory of the vortex dynamo in rotating media. Various models of a vortex dynamo in rotating media are discussed: a homogeneous viscous fluid, a temperature-stratified fluid, a moist atmosphere, and a stratified nanofluid. The main analytical and numerical results for these models obtained by the method of multiscale asymptotic expansions are presented. The main attention is paid to models with a non-spiral external force. For a rotating moist atmosphere, characteristic estimates of the spatial and temporal scales of the generated vortex structures are obtained. New effects of the vortex dynamo in a rotating stratified nanofluid, which arise due to thermophoresis and Brownian motion of nanoparticles, are shown. The results of the analysis of the nonlinear equations of the vortex dynamo in the stationary regime are presented in the form of spiral kinks, periodic nonlinear waves, and solitons.
Keywords: *dynamo theory; large-scale instability; Coriolis force; multiscale asymptotic expansions; α - effect; solitons; kinks*
PACS: 47.32.C, 47.32.cd, 47.90.+a

1. INTRODUCTION

The review is devoted to modern problems with the vortex dynamo theory. This is an extensive area of research that includes the generation and nonlinear evolution of large-scale vortex structures. The focus of the review will be on the influence of the rotation of turbulent media on the generation of structures. The reason for the importance of this factor is both the widespread nature and the nontriviality of its influence. Rotation effects play an important role in many practical and theoretical applications of fluid mechanics [1] and are especially important in geophysics and astrophysics [2]-[5], where one has to deal with such rotating objects as the Earth, Jupiter, the Sun, etc. A variety of wave and vortex motions can be excited in rotating liquids. For example, gyroscopic waves, Rossby waves, internal waves, localized vortices, and coherent vortex structures. Large-scale vortex structures are of the greatest interest because they carry out efficient transfer of energy and momentum. Large-scale structures are understood to mean structures whose characteristic scale is much greater than the scale of turbulence or the scale of the external force that excites this turbulence. The study of the problem of generation of large-scale vortex structures (LSVS) is of great importance for a number of geophysical and astrophysical problems, such as the problem of the origin of Jupiter's Great Spot, Venus superrotation, vortex structures in solar prominences, the spiral structure of galaxies, etc. [6]-[7]. Geophysical problems include studies on the generation of LSVSs such as tropical cyclones (typhoons), tornadoes, etc. These LSVS play an important role in the global circulation of the atmosphere, which is very important for weather and climate [8]-[9] forecasts on our planet. The actual effect of LSVS generation in turbulence is called the vortex dynamo.

According to the Kolmogorov-Obukhov local theory of turbulence, large-scale violations of homogeneity and isotropy are restored on small scales of turbulent flow. In this regard, the question arises: can such turbulence enhance large-scale perturbations? In magnetohydrodynamics, the answer to this question was obtained earlier. It was shown in [10] that initially homogeneous, isotropic, and mirror-symmetric turbulence cannot enhance large-scale magnetic fields. However, if the mirror symmetry of turbulence is broken, then such a medium can enhance the large-scale magnetic field. The process of amplification of a large-scale field occurs under the action of a turbulent e.m.f. proportional to the average magnetic field $\vec{\mathcal{E}} = \alpha\overline{\vec{H}}$, and the coefficient α is proportional to the average helicity $\alpha \sim \overline{\vec{v}^t \mathrm{rot}\vec{v}^t}$ of the velocity field. The phenomenon of generation of large-scale magnetic fields by homogeneous isotropic but mirror-asymmetric (helical) turbulence discovered in [10] was called the α-effect. On the basis of this effect, the dynamo theory [11]-[12] was constructed by the efforts of many researchers and explains the origin of magnetic fields in various astrophysical objects: the Earth, planets, the Sun, galaxies, etc. Helical turbulence is characterized by a violation of the mirror symmetry of the turbulent velocity field, for which the correlation $\overline{\vec{v}^t \mathrm{rot}\vec{v}^t}$ is non-zero. Such a turbulent velocity field is characterized by the fact that right-handed and left-handed vortices are observed with different probabilities, i.e., there are more vortices of one sign than another.

The concept of a vortex dynamo was first developed in [13]–[14], where a hypothesis was put forward that helical turbulence is capable of generating large vortices. This hypothesis was based on the similarity of the equations of induction of a magnetic field and a vortex in hydrodynamics. It was hypothesized in [13] that helical turbulence is capable of generating large eddies similarly to a large-scale magnetic field in magnetohydrodynamics. The physical essence of this phenomenon lies in the inverse cascade of energy transfer from small vortices to larger ones. However, it

[†] ***Cite as:*** M.I. Kopp, and V.V. Yanovsky, East Eur. J. Phys. **2**, 7 (2023), https://doi.org/10.26565/2312-4334-2023-2-01

was shown in [15] that there is no effect on generating large-scale vortices by homogeneous isotropic helical turbulence in an incompressible fluid. The reason for the negative effect lies in the certain symmetry of the Reynolds stress tensor in the averaged Navier-Stokes equation. The Reynolds stresses are a linear functional of the mean velocity field (for weak fields), which can be represented as a series

$$\overline{v_k^t \nabla_k v_i^t} = \nabla_k \left(\overline{v_k^t v_i^t} \right) = T_i^{(0)} + T_{ik}^{(1)} V_k + T_{ikl}^{(2)} \nabla_k V_l + \cdots,$$

where the expansion coefficients of the tensors $T^{(n)}$ are expressed in terms of the moments of the turbulent fields. If the tensor $\overline{v_k^t v_i^t}$ is symmetric in indices, then the tensor $T_{ikl}^{(2)}$ must also be symmetric in indices i,k and not be expressed in terms of the antisymmetric tensor ε_{ikl}. The tensor of the third rank cannot be constructed only from Kronecker tensors δ_{ik}; therefore, the hydrodynamic α-effect is absent in the homogeneous isotropic turbulence of an incompressible fluid. However, a reverse energy cascade in helical turbulence is possible. This requires an additional symmetry break of the Reynolds stresses. The effect of generating large-scale eddies is associated with the appearance of the term $\alpha\vec{\Omega}$:

$$\frac{\partial \vec{\Omega}}{\partial t} + \alpha rot\vec{\Omega} = \nu \Delta \vec{\Omega},$$

where $\alpha \sim \overline{\vec{v}^T rot\vec{v}^T}$ is expressed in terms of the turbulence helicity, $\vec{\Omega} = rot\vec{V}$, $\vec{V}$ is a large-scale field of fluid velocity, ν is a turbulent kinematic viscosity. This effect is called the hydrodynamic alpha effect. The further development of the vortex dynamo theory was based on the search for additional factors that break the symmetry of the equations. These factors, in addition to the compressibility of the medium, are, for example, an inhomogeneous flow [16], a temperature gradient in a gravity field [17], and a specific water content and temperature gradient in a gravity field [18].

It should be noted that free convection, or heat and mass transfer of matter in the gravity field, plays a special role in the processes of LSVS generation in the atmosphere of the Earth and other planets. The occurrence of LSVS in convective systems was studied both within the laminar theory [19] and in the turbulent one [15]-[18]. The most developed is the turbulent theory (vortex dynamo), which shows the existence of large-scale instability in convective systems with small-scale helical turbulence [17]-[18], which results in the formation of one convective cell, which is interpreted as a huge tropical cyclone-type vortex. This theory was confirmed in a number of numerical and analytical calculations [20]. Large-scale vortex instability in rotating turbulent flows has been studied in many papers [21]-[24]. So, when considering rotating convective systems, attempts were made to apply the results obtained to the theory of the occurrence of tropical cyclones. The linear theory of the vortex dynamo [15]-[24] is best developed within the framework of the statistical approach, which also uses the second-order correlation approximation. Thus, the question arose about the mechanisms of saturation of large-scale instability and the emergence of stationary vortex structures. However, the construction of a nonlinear theory of the vortex dynamo within the framework of the statistical theory has great difficulties associated with the problem of closure of the averaged equations.

The nonlinear theory of the vortex dynamo was developed within the framework of a dynamic approach based on the method of multiscale asymptotic expansions. In [25], for the first time, the method of multiscale asymptotic expansions was applied to describe the generation of LSVSs in non-reflective, invariant turbulence. In this work, it was shown that parity violation in small-scale turbulence (external small-scale forces) leads to large-scale instability, the so-called anisotropic kinetic alpha effect (AKA effect). In another work [26], the inverse energy cascade and nonlinear saturation of the instability were studied. The instability of the hydrodynamic α-effect, obtained within the framework of the dynamic approach, can be interpreted as a new type of parametric instability arising from a special type of pumping (external force). Under the action of an external small-scale periodic force $\vec{F}_0$, fluctuations of the velocity field $\vec{v}_0$ arise, the nonlinear interaction of which affects large-scale velocity perturbations $\vec{W}$. The Reynolds stresses $R_{ij} = \overline{v_i v_j}$ (where averaged over the period) are modified by large-scale perturbations, and in the linear approximation, the gradient series can be expanded into a Taylor series [27]:

$$R_{ij} = -\alpha_{ijl} W_l - \nu_{ijlm} \nabla_l W_m + \ldots$$

The first term is known as the anisotropic kinetic α-effect (AKA) [25], which describes the generation of LSVSs. Thus, an external force that creates a small-scale parity violation can lead to non-trivial changes in the large-scale flow. In contrast to [25], in [27], a small-scale force was considered that creates a parity-invariant turbulent flow. In this case, the AKA effect is absent, and the dynamics of small large-scale perturbations $\vec{W}$ is determined by the turbulent viscosity. Although parity violation is a more general concept than helicity, it is helicity $\vec{v}rot\vec{v} \neq 0$ that is a widespread mechanism for parity violation in hydrodynamic flow. In [28]-[29], a nonlinear theory of the convective vortex dynamo was developed, where the method of multiscale asymptotic expansions was applied. Paper [28] is a more complete

version of [29], which presents the linear theory of LSVS generation in more detail. The small Reynolds number of small-scale motions is a parameter of the asymptotic expansions.

This method makes it possible to single out the main order of the emergence of instability from the entire hierarchy of perturbations. Nonlinear stabilization of large-scale convective instability, considered in [28]-[29], leads to the formation of helical vortex solitons or kinks of a new type in the fluid, despite stable stratification. The structure of the equations in [28]-[29] describing the instability in the linear approximation is similar to the AKA effect equation. But, unlike the AKA effect, α is a function of the Rayleigh number Ra. This means that in an unstratified fluid, $Ra = 0$, the instability disappears. In addition, in [28]-[29] helical turbulence was assumed to be given, in contrast to [25]-[26].

Using the method of multiscale asymptotic expansions, in [30], a large-scale vortex instability was obtained in a rotating viscous fluid under the action of an external small-scale helical force. In this work, the nonlinear stage of instability and the generation of vortex kinks of a new type were also investigated. The paper [30] was generalized to the case of a rotating moist atmosphere in [31], where it was shown that taking into account the effects of stratification in a rotating atmosphere, such as temperature heating and an additional source of condensation heat release, enhances large-scale vortex disturbances. It was shown in [31] that the helicity of the small-scale velocity field is due not only to the action of the Coriolis force, as in a homogeneous medium [30], but also to the stratification of the moist atmosphere. This circumstance leads to the appearance of a new instability of the α-effect type, as a result of which large-scale vortex structures are generated.

The origin of helical turbulence in natural conditions is usually associated with the influence of the Coriolis force on the turbulent motion of the medium [10], which was initially uniform, isotropic and mirror-symmetric. Thus, a problem arises in the origin of helicity itself. The natural hypothesis is that helicity itself arises as a result of the action of the Coriolis force on convective turbulence. In this case, large-scale instabilities in the atmosphere should appear self-consistently, without additional assumptions. For the first time, the question of the generation of large-scale vortex fields under the action of a small-scale force with zero helicity $\vec{F}_0 rot\vec{F}_0 = 0$ in a rotating homogeneous medium, i.e., without taking into account convective phenomena, was considered in [32]-[33], and taking into account convective phenomena in [34]-[36]. It was also demonstrated that nonlinear Beltrami waves and localised vortex structures such as kinks emerge as a result of the development of a large-scale instability in an obliquely rotating fluid.

The generation of the LSVS by a large-scale instability of the hydrodynamic α-effect has a threshold character and depends on the magnitude of the helicity. In this connection, the search for large-scale helical vortex instability based on atmospheric data was started in [37]. An extensive review of studies aimed at applying the theoretical hypothesis of a turbulent vortex dynamo to the study of tropical cyclogenesis is presented in [38]. The review presents the results of a numerical simulation of the spiral self-organization of humid-convective atmospheric turbulence during the formation of tropical cyclones. Particular attention is paid here to the influence of the initial conditions on the generation of helicity in the first hours of the experiments. These studies contributed to the application of the vortex dynamo theory for diagnosing the onset of cyclogenesis in a favorable tropical environment.

The question of the appearance of helicity, leading to the appearance of a LSVS, is central to any formalism. An important difference between these formalisms is that in statistical turbulence, it is difficult to correctly separate small-scale motions from large-scale ones, which leads to the problem of the influence of some scales on others and requires the use of additional hypotheses. However, this can be done consistently in the multiscale formalism. The difference in averaging over small-scale turbulent fluctuations (in the statistical theory) and small-scale motions (in the multiscale method) rather indicates the closeness of these theories. Therefore, it can be assumed that the average helicity arising in the statistical theory is quite similar to the average helicity in the multiscale method.

Next, we discuss in more detail the new types of large-scale instabilities and localized vortex structures in rotating turbulent media considered in our papers [30]-[36].

2. LARGE-SCALE INSTABILITY OF A ROTATING FLUID WITH A SMALL-SCALE FORCE

Let's start with a discussion of large-scale instability in a rotating viscous fluid under the action of a small-scale external force, which was first considered in [30]. The small-scale external force simulates the action of small-scale turbulence and maintains turbulent fluctuations at a certain stationary level. It was shown in [30] that, as a result of the development of a large-scale instability in a rotating fluid, nonlinear large-scale helical vortex structures such as Beltrami vortices or localized kinks with an internal helical structure arise.

2.1. Basic equations and statement of the problem

Consider the equations of motion of an incompressible rotating fluid with an external force in a rotating coordinate system

$$\frac{\partial \vec{V}}{\partial t} + (\vec{V}\nabla)\vec{V} = -\frac{1}{\rho_0}\nabla P + 2[\vec{V}\times\vec{\Omega}] + \nu\Delta\vec{V} + \vec{F}_0 \tag{1}$$

$$div\vec{V} = 0 \tag{2}$$

Here, $\vec{\Omega}$ is the constant angular velocity of rotation of the fluid, ν is the viscosity, and ρ_0 is the constant density of the fluid. The vector of angular velocity of rotation $\vec{\Omega}$ is directed along the axis OZ, and the external force $\vec{F}_0$ acts in a plane that is perpendicular to the axis of rotation (see Fig. 1).

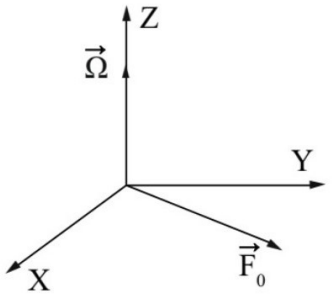

Figure 1. The angular velocity vector $\vec{\Omega}$ is directed perpendicular to the plane (X,Y) in which the external force $\vec{F}_0$ is located.

Let us denote the characteristic amplitude of the force f_0, and its characteristic spatial and temporal scales, respectively, as λ_0 and t_0. The external force has the following properties:

$$\vec{F}_0 = f_0 \vec{F}_0\left(\frac{\vec{x}}{\lambda_0}, \frac{t}{t_0}\right), div\vec{F}_0 = 0, \vec{F}_0 rot\vec{F}_0 \neq 0. \tag{3}$$

The main role of this force is the creation of small-scale helical fluctuations in the velocity field $\vec{v}_0$ with a small Reynolds number $R = \frac{v_0 t_0}{\lambda_0} \ll 1$, or, in other words, the maintenance of stationary small-scale helical turbulence. It is obvious that the characteristic speed caused by an external force has the same characteristic scales:

$$\vec{v}_0 = \vec{v}_0\left(\frac{\vec{x}}{\lambda_0}, \frac{t}{t_0}\right)$$

Let's maintain the old notation of variables but replace the dimensioned variables in the system of equations (1) and (2) with dimensionless variables for convenience:

$$\vec{x} \to \frac{\vec{x}}{\lambda_0}, \quad t \to \frac{t}{t_0}, \quad \vec{V} \to \frac{\vec{V}}{v_0}, \quad \vec{F}_0 \to \frac{\vec{F}_0}{f_0}, \quad P \to \frac{P}{\rho_0 P_0}, \quad t_0 = \frac{\lambda_0^2}{\nu}, \quad P_0 = \frac{v_0 \nu}{\lambda_0}, \quad f_0 = \frac{v_0 \nu}{\lambda_0^2}, \quad v_0 = \frac{f_0 \lambda_0^2}{\nu}.$$

Then, in dimensionless variables, equations (1)-(2) take the form:

$$\frac{\partial \vec{V}}{\partial t} + R(\vec{V}\cdot\nabla)\vec{V} = -\nabla P + [\vec{V}\times\vec{D}] + \Delta\vec{V} + \vec{F}_0, \tag{4}$$

$$div\vec{V} = 0. \tag{5}$$

Here, $R = \frac{\lambda_0 v_0}{\nu}$ is the Reynolds number of small-scale pulsations, $D_i = \frac{2\Omega_i \lambda_0^2}{\nu}$ is the dimensionless rotation parameter on the scale λ_0 ($i = 1,2,3$), associated with the Taylor number $Ta_i = D_i^2$, and which is a characteristic of the degree of influence of Coriolis forces over viscous forces.

In what follows, the Reynolds number $R \ll 1$ will be assumed to be small, and we will construct an asymptotic expansion from this small parameter. We consider the parameter D to be independent of the asymptotic expansion scheme. Of course, the Reynolds number on a large scale can be large. Consider the following formulation of the problem: we will consider the external force as small-scale and high-frequency. This force leads to small scale velocity fluctuations. After averaging, the rapidly oscillating fluctuations disappear. However, due to small non-linear interactions, non-zero terms may appear after averaging in some orders of perturbation theory. This means that these terms are not oscillatory, i.e., they are on a large scale. From a formal point of view, these members are secular. The difference from zero of such “constant” contributions leads to a rapid collapse of the asymptotic expansions. Therefore, the conditions for the conservation of the asymptotic expansion are based on the vanishing of the secular terms. This leads to conditions for the solvability of equations for large-scale perturbations. We discuss these equations below.

2.2. The method of multiscale asymptotic expansions and the equation for the large-scale velocity field

We denote the small-scale variables $x_0 = (\vec{x}_0, t_0)$, and the large-scale $X = (\vec{X}, T)$ ones. Denote the derivative $\frac{\partial}{\partial x_0^i}$ by ∂_i, and the derivative $\frac{\partial}{\partial t_0}$ by ∂_t. To designate large-scale spatial and temporal derivatives, the following notation will be used:

$$\frac{\partial}{\partial X_i} \equiv \nabla_i, \quad \frac{\partial}{\partial T} \equiv \partial_T$$

The spatial and temporal derivatives now turn into the corresponding derivatives with respect to both fast small-scale variables and slow large-scale variables. Therefore, we replace the spatial and temporal derivatives in equations (4)-(5) with operators of the form:

$$\frac{\partial}{\partial x_i} \to \partial_i + R^2 \nabla_i, \quad \frac{\partial}{\partial t} \to \partial_t + R^4 \partial_T \tag{6}$$

To construct a nonlinear theory, we represent the variables $\vec{V}, P$ in the form of asymptotic series:

$$\vec{V}(x,t) = \frac{1}{R}\vec{W}_{-1}(X) + \vec{v}_0(x_0) + R\vec{v}_1 + R^2\vec{v}_2 + R^3\vec{v}_3 + \cdots \tag{7}$$

$$P(x,t) = \frac{1}{R^3}P_{-3} + \frac{1}{R^2}P_{-2} + \frac{1}{R}P_{-1} + P_0 + R(P_1 + \overline{P}_1(X)) + R^2P_2 + R^3P_3 + \cdots$$

Substituting the expansions (6)-(7) into the system of equations (4)-(5) and collecting together the terms with R the same orders up to the power inclusive R^3, we obtain the equations of the multiscale asymptotic expansion. Let us pay attention to the analysis of rather deep orders of equations with respect to a small parameter, which is necessary to obtain equations for large-scale motions. This is typical for this method. There is only one equation in order R^{-3}:

$$\partial_i P_{-3} = 0 \quad \Rightarrow \quad P_{-3} = P_{-3}(X) \tag{8}$$

In order R^{-2}, we have the equation:

$$\partial_i P_{-2} = 0 \quad \Rightarrow \quad P_{-2} = P_{-2}(X) \tag{9}$$

In order R^{-1}, we get a system of equations:

$$\partial_t W_{-1}^i + W_{-1}^k \partial_k W_{-1}^i = -\partial_i P_{-1} - \nabla_i P_{-3} + \partial_k^2 W_{-1}^i + \varepsilon_{ijk} W_j D_k e_k, \quad \partial_i W_{-1}^i = 0 \tag{10}$$

Averaging equations (10) over fast variables gives the secular equation,

$$-\nabla_i P_{-3} + \varepsilon_{ijk} W_j D_k = 0, \tag{11}$$

which corresponds to the equation of geostrophic equilibrium.
In order zero R^0, we have the following system of equations:

$$\partial_t v_0^i + W_{-1}^k \partial_k v_0^i + v_0^k \partial_k W_{-1}^i = -\partial_i P_0 - \nabla_i P_{-2} + \partial_k^2 v_0^i + \varepsilon_{ijk} v_0^j D_k + F_0^i \tag{12}$$

$$\partial_i v_0^i = 0$$

These equations give one secular equation:

$$\nabla P_{-2} = 0 \quad \Rightarrow \quad P_{-2} = const \tag{13}$$

Consider a first-order R^1 approximation:

$$\partial_t v_1^i + W_{-1}^k \partial_k v_1^i + v_0^k \partial_k v_0^i + v_1^k \partial_k W_{-1}^i + W_{-1}^k \nabla_k W_{-1}^i = -\nabla_i P_{-1} - \partial_i \left(P_1 + \overline{P}_1\right) + \partial_k^2 v_1^i + 2\partial_k \nabla_k W_{-1}^i + \varepsilon_{ijk} v_1^j D_k, \tag{14}$$

$$\partial_i v_1^i + \nabla_i W_{-1}^i = 0$$

Secular equations follow from this system of equations:

$$W_{-1}^k \nabla_k W_{-1}^i = -\nabla_i P_{-1} \tag{15}$$

$$\nabla_i W_{-1}^i = 0 \tag{16}$$

Secular equations (15)-(16) satisfy the following field geometry:

$$\vec{W}_{-1} = \left(W_{-1}^x(Z), W_{-1}^y(Z), 0\right), \quad P_{-1} = const \tag{17}$$

For the second order R^2, we get the equations:

$$\partial_t v_2^i + W_{-1}^k \partial_k v_2^i + v_0^k \partial_k v_1^i + W_{-1}^k \nabla_k v_0^i + v_0^k \nabla_k W_{-1}^i + v_1^k \partial_k v_0^i + v_2^k \partial_k W_{-1}^i = -\nabla_i P_2 - \nabla_i P_0 + \partial_k^2 v_2^i + 2\partial_k \nabla_k v_0^i + \varepsilon_{ijk} v_2^j D_k, \tag{18}$$

$$\partial_i v_2^i + \nabla_i v_0^i = 0$$

It is easy to see that there are no secular terms in this order. Finally, we come to the most important order R^3. In this order, the equations are:

$$\partial_t v_3^i + \partial_T W_{-1}^i + W_{-1}^k \partial_k v_3^i + v_0^k \partial_k v_2^i + W_{-1}^k \nabla_k v_1^i + v_0^k \nabla_k v_0^i + v_1^k \partial_k v_1^i + v_1^k \nabla_k W_{-1}^i +$$

$$+ v_2^k \partial_k v_0^i + v_3^k \partial_k W_{-1}^i = -\partial_i P_3 - \nabla_i \left(P_1 + \overline{P}_1\right) + \partial_k^2 v_3^i + 2\partial_k \nabla_k v_1^i + \Delta W_{-1}^i + \varepsilon_{ijk} v_3^j D_k, \tag{19}$$

$$\partial_i v_3^i + \nabla_i v_1^i = 0$$

Averaging these equations over fast variables, we obtain the main secular equation describing the evolution of large-scale perturbations:

$$\partial_T W_{-1}^i - \Delta W_{-1}^i + \nabla_k \left(\overline{v_0^k v_0^i}\right) = -\nabla_i \overline{P}_1 \tag{20}$$

Equation (20) describes the evolution of a large-scale vortex field $\vec{W}$, but the final closure of equation (20) will be carried out after calculating the Reynolds stress $\nabla_k \left(\overline{v_0^k v_0^i}\right)$. To do this, it is necessary to find solutions for the small-scale velocity field $\vec{v}_0$.

2.3. Velocity field in zero approximation

Let us write the equation of the asymptotic expansion in the zeroth approximation (12) in the following form:

$$\widehat{D}_0 v_0^i = -\partial_i P_0 + \varepsilon_{ijk} v_0^j D_k + F_0^i, \tag{21}$$

where the operator $\widehat{D}_0$ is introduced

$$\widehat{D}_0 = \partial_t - \partial_k^2 + W_{-1}^k \partial_k.$$

The pressure P_0 is found in the condition $\partial_i v_0^i = 0$:

$$P_0 = \widehat{P}_1 u_0 + \widehat{P}_2 v_0 + \widehat{P}_3 w_0 \tag{22}$$

Here we introduced the notation for the operators

$$\widehat{P}_1 = \frac{D_2 \partial_z - D_3 \partial_y}{\partial^2}, \quad \widehat{P}_2 = \frac{D_3 \partial_x - D_1 \partial_z}{\partial^2}, \quad \widehat{P}_3 = \frac{D_1 \partial_y - D_2 \partial_x}{\partial^2},$$

and velocities $v_0^x = u_0$, $v_0^y = v_0$, $v_0^z = w_0$. Then, excluding the pressure from (21), we obtain a system of equations for finding the zero-order velocity field:

$$\begin{aligned}
\left(\widehat{D}_0 + \widehat{p}_{1x}\right) u_0 + \left(\widehat{p}_{2x} - D_3\right) v_0 + \left(\widehat{p}_{3x} + D_2\right) w_0 &= F_0^x \\
\left(D_3 + \widehat{p}_{1y}\right) u_0 + \left(\widehat{D}_0 + \widehat{p}_{2y}\right) v_0 + \left(\widehat{p}_{3y} - D_1\right) w_0 &= F_0^y \\
\left(\widehat{p}_{1z} - D_2\right) u_0 + \left(\widehat{p}_{2z} + D_1\right) v_0 + \left(\widehat{D}_0 + \widehat{p}_{3z}\right) w_0 &= F_0^z
\end{aligned} \tag{23}$$

The tensor components $\widehat{p}_{ij}$ are as follows:

$$\hat{p}_{1x}=\frac{D_2\partial_x\partial_z-D_3\partial_x\partial_y}{\partial^2},\ \hat{p}_{2x}=\frac{D_3\partial_x^2-D_1\partial_x\partial_z}{\partial^2},\ \hat{p}_{3x}=\frac{D_1\partial_x\partial_y-D_2\partial_x^2}{\partial^2},$$

$$\hat{p}_{1y}=\frac{D_2\partial_y\partial_z-D_3\partial_y^2}{\partial^2},\ \hat{p}_{2y}=\frac{D_3\partial_y\partial_x-D_1\partial_y\partial_z}{\partial^2},\ \hat{p}_{3y}=\frac{D_1\partial_y^2-D_2\partial_y\partial_x}{\partial^2},\tag{24}$$

$$\hat{p}_{1z}=\frac{D_2\partial_z^2-D_3\partial_z\partial_y}{\partial^2},\ \hat{p}_{2z}=\frac{D_3\partial_z\partial_x-D_1\partial_z^2}{\partial^2},\ \hat{p}_{3z}=\frac{D_1\partial_z\partial_y-D_2\partial_z\partial_x}{\partial^2}.$$

In accordance with the problem statement, we choose the coordinate system so that the axis OZ coincides with the direction of the angular velocity of rotation. Then the components of the rotation parameter are $D_1=D_2=0, D_3=D$. To solve the system of equations (23), it is necessary to specify the force $\vec{F}_0$ explicitly. Taking into account condition (3), we choose an external force in a rotating coordinate system in the following form:

$$\vec{F}_0=f_0\left(\vec{i}\cos\phi_2+\vec{j}\cos\phi_1\right),\quad F_0^z=0,\tag{25}$$

where f_0 is the amplitude of the external force,

$$\phi_1=\vec{k}_1\vec{x}-\omega_0 t,\quad \phi_2=\vec{k}_2\vec{x}-\omega_0 t,\quad \vec{k}_1=\vec{k}_0\left(1,0,1\right),\quad \vec{k}_2=\vec{k}_0\left(0,1,1\right).$$

Thus, the external force is given in the plane (X,Y) orthogonal to the axis of rotation, and the divergence of this force is zero. We seek the solution of the system of equations (23) according to the Cramer rule:

$$u_0=\frac{1}{\Delta}\left\{\left[\left(\hat{D}_0+\hat{p}_{2y}\right)\left(\hat{D}_0+\hat{p}_{3z}\right)-\left(\hat{p}_{2z}+D_1\right)\left(\hat{p}_{3y}-D_1\right)\right]F_0^x+\left[\left(\hat{p}_{3x}+D_2\right)\left(\hat{p}_{2z}+D_1\right)-\left(\hat{p}_{2x}-D_3\right)\left(\hat{D}_0+\hat{p}_{3z}\right)\right]F_0^y\right\}\tag{26}$$

$$v_0=\frac{1}{\Delta}\left\{\left[\left(\hat{D}_0+\hat{p}_{1x}\right)\left(\hat{D}_0+\hat{p}_{3z}\right)-\left(\hat{p}_{3x}+D_2\right)\left(\hat{p}_{1z}-D_2\right)\right]F_0^y+\left[\left(\hat{p}_{3y}-D_1\right)\left(\hat{p}_{1z}-D_2\right)-\left(D_3+\hat{p}_{1y}\right)\left(\hat{D}_0+\hat{p}_{3z}\right)\right]F_0^x\right\}\tag{27}$$

$$w_0=\frac{1}{\Delta}\left\{\left[\left(D_3+\hat{p}_{1y}\right)\left(\hat{p}_{2z}+D_1\right)-\left(\hat{D}_0+\hat{p}_{2y}\right)\left(\hat{p}_{1z}-D_2\right)\right]F_0^x+\left[\left(\hat{p}_{2x}-D_3\right)\left(\hat{p}_{1z}-D_2\right)-\left(\hat{D}_0+\hat{p}_{1x}\right)\left(\hat{p}_{2z}+D_1\right)\right]F_0^y\right\}\tag{28}$$

Here Δ is the determinant of the system of equations (23), which in its expanded form has the form:

$$\Delta=\left(\hat{D}_0+\hat{p}_{1x}\right)\left(\hat{D}_0+\hat{p}_{2y}\right)\left(\hat{D}_0+\hat{p}_{3z}\right)+\left(D_3+\hat{p}_{1y}\right)\left(\hat{p}_{2z}+D_1\right)\left(\hat{p}_{3x}+D_2\right)+\left(\hat{p}_{2x}-D_3\right)\left(\hat{p}_{3y}-D_1\right)\left(\hat{p}_{1z}-D_2\right)-$$

$$-\left(\hat{p}_{3x}+D_2\right)\left(\hat{D}_0+\hat{p}_{2y}\right)\left(\hat{p}_{1z}-D_2\right)-\left(\hat{p}_{2z}+D_1\right)\left(\hat{p}_{3y}-D_1\right)\left(\hat{D}_0+\hat{p}_{1x}\right)-\left(D_3+\hat{p}_{1y}\right)\left(\hat{p}_{2x}-D_3\right)\left(\hat{D}_0+\hat{p}_{3z}\right)\tag{29}$$

To calculate expressions (26)-(29), we write the external force (25) in complex form:

$$\vec{F}_0=\vec{i}\,\frac{f_0}{2}e^{i\phi_2}+\vec{j}\,\frac{f_0}{2}e^{i\phi_1}+c.c.\tag{30}$$

Then all operators in formulas (26)-(29) act from the left on eigenfunctions:

$$\hat{D}_0e^{i\phi_1}=e^{i\phi_1}\hat{D}_0\left(k_1,-\omega_0\right),\quad \hat{D}_0e^{i\phi_2}=e^{i\phi_2}\hat{D}_0\left(k_2,-\omega_0\right),\ \Delta e^{i\phi_1}=e^{i\phi_1}\Delta\left(k_1,-\omega_0\right),\quad \Delta e^{i\phi_2}=e^{i\phi_2}\Delta\left(k_2,-\omega_0\right)\tag{31}$$

To simplify the formulas, we set $\omega_0=1$, $k_0=1$ and introduce new notation:

$$\hat{D}_0\left(k_1,-\omega_0\right)=\hat{A}_1^*=2-i\left(1-W_1\right),\quad \hat{D}_0\left(k_2,-\omega_0\right)=\hat{A}_2^*=2-i\left(1-W_2\right)\tag{32}$$

Here and below, complex conjugate quantities will be denoted by an asterisk. When performing further calculations, parts of the components in the tensors $\hat{p}_{ij}\left(k_1\right)$ and $\hat{p}_{ij}\left(k_2\right)$ vanish, so we write out only the non-zero components:

$$\hat{p}_{11}\left(k_1\right)=\hat{A}_1^*,\ \hat{p}_{12}\left(k_1\right)=-\frac{D}{2},\ \hat{p}_{32}\left(k_1\right)=\frac{D}{2},\ \hat{p}_{22}\left(k_1\right)=\hat{D}_1^*,\ \hat{p}_{33}\left(k_1\right)=\hat{A}_1^*,\tag{33}$$

$$\hat{p}_{11}\left(k_2\right)=\hat{A}_2^*,\ \hat{p}_{12}\left(k_2\right)=-D,\ \hat{p}_{21}\left(k_2\right)=\frac{D}{2},\ \hat{p}_{22}\left(k_2\right)=\hat{A}_2^*,\ \hat{p}_{31}\left(k_2\right)=-\frac{D}{2},\ \hat{p}_{33}\left(k_2\right)=\hat{A}_2^*.$$

Taking into account formulas (31)-(33), we find the determinant:

$$\Delta(k_1) = \hat{A}_1^* \left(\hat{A}_1^{*2} + \frac{D^2}{2} \right), \quad \Delta(k_2) = \hat{A}_2^* \left(\hat{A}_2^{*2} + \frac{D^2}{2} \right) \tag{34}$$

In a similar way, we find the velocity field of the zero approximation:

$$u_0 = \frac{f_0}{2} \frac{\hat{A}_2^* e^{i\phi_2}}{\hat{A}_2^{*2} + \frac{D^2}{2}} + \frac{f_0}{4} \frac{De^{i\phi_1}}{\hat{A}_1^{*2} + \frac{D^2}{2}} + c.c., \tag{35}$$

$$v_0 = -\frac{f_0}{4} \frac{De^{i\phi_2}}{\hat{A}_2^{*2} + \frac{D^2}{2}} + \frac{f_0}{2} \frac{\hat{A}_1^* e^{i\phi_1}}{\hat{A}_2^{*2} + \frac{D^2}{2}} + c.c., \tag{36}$$

$$w_0 = \frac{f_0}{4} \frac{De^{i\phi_2}}{\hat{A}_2^{*2} + \frac{D^2}{2}} - \frac{f_0}{4} \frac{De^{i\phi_1}}{\hat{A}_1^{*2} + \frac{D^2}{2}} + c.c. \tag{37}$$

The relations obtained for the velocity field in the zeroth approximation make it possible to find the Reynolds stresses necessary to close the equation.

2.4. Reynolds stresses and large-scale instability

Consider large-scale fields that satisfy the geometry of the problem within the framework of the "quasi-two-dimensional" model (17). Large-scale derivatives with respect to Z are then preferred.

$$\nabla_Z \equiv \frac{\partial}{\partial Z} \gg \frac{\partial}{\partial X}, \frac{\partial}{\partial Y}.$$

In this case, equation (20) can be written in the coordinate form:

$$\partial_T W_1 - \nabla_Z^2 W_1 + \nabla_Z \left(\overline{v_0^z v_0^x} \right) = 0, \quad W_1 \equiv W_{-1}^x \tag{38}$$

$$\partial_T W_2 - \nabla_Z^2 W_2 + \nabla_Z \left(\overline{v_0^z v_0^y} \right) = 0, \quad W_2 \equiv W_{-1}^y \tag{39}$$

To close the equations (38)-(39) it is necessary to calculate the Reynolds stresses $\overline{w_0 u_0}$ and $\overline{w_0 v_0}$. These terms are easily calculated using formulas (35)-(37). As a result, we get:

$$\begin{aligned} \overline{w_0 u_0} &= -\frac{f_0^2}{8} \frac{D^2}{16(1-W_1)^2 + \left[\frac{D^2}{2} + 4 - (1-W_1)^2 \right]^2} + \frac{f_0^2}{2} \frac{D}{16(1-W_2)^2 + \left[\frac{D^2}{2} + 4 - (1-W_2)^2 \right]^2} \\ \overline{w_0 v_0} &= -\frac{f_0^2}{8} \frac{D^2}{16(1-W_2)^2 + \left[\frac{D^2}{2} + 4 - (1-W_2)^2 \right]^2} - \frac{f_0^2}{2} \frac{D}{16(1-W_1)^2 + \left[\frac{D^2}{2} + 4 - (1-W_1)^2 \right]^2} \end{aligned} \tag{40}$$

Now equations (38)-(39) have a closed form:

$$\partial_T W_1 - \Delta W_1 + \frac{\partial}{\partial Z} \overline{w_0 u_0} = 0, \quad \partial_T W_2 - \Delta W_2 - \frac{\partial}{\partial Z} \overline{w_0 v_0} = 0. \tag{41}$$

For small values of $W_{1,2}$ the Reynolds stress (40) can be expanded into a series in $W_{1,2}$. As a result, we obtain the following linearized equations (41):

$$\partial_T W_1 - \nabla_Z^2 W_1 = \alpha_1 \nabla_Z W_1 - \alpha_2 \nabla_Z W_2 \tag{42}$$

$$\partial_T W_2 - \nabla_Z^2 W_2 = \alpha_1 \nabla_Z W_2 + \alpha_2 \nabla_Z W_1 \tag{43}$$

where

$$\alpha_1 = \frac{f_0^2}{8} D^2 \alpha, \quad \alpha_2 = \frac{f_0^2}{2} D\alpha, \quad \alpha = \frac{32D^2\left(10 - D^2\right)}{\left(\left(D^2+6\right)^2 + 64\right)^2}.$$

The solution of the linear system of equations (42)-(43) will be found in the form of plane waves with the wave vector $\vec{K} \parallel OZ$, i.e.

$$W_{1,2} = A_{W_{1,2}} \exp\left(-i\omega T + iKZ\right) \tag{44}$$

Substituting (44) into the system of equations (42)-(43), we obtain the dispersion equation:

$$\left(-i\omega + K^2 - i\alpha_1 K\right)^2 - \alpha_2^2 K^2 = 0 \tag{45}$$

Dispersion equation (45) shows the existence of unstable oscillatory solutions with the oscillation frequency

$$\omega = \frac{f_0^2}{8} D^2 \alpha K$$

and instability increment

$$\gamma = \frac{f_0^2}{2} D\alpha K - K^2$$

The instability is large-scale because the unstable term dominates the damping at large scales: $\frac{f_0^2}{2} D\alpha > K$. The maximum instability increment is $\gamma_{\max} = \alpha^2 f_0^4 D^2 / 16$ and is achieved on the wave vector $K_{\max} = \alpha f_0^2 D / 4$.

Thus, in the considered stationary small-scale "turbulent" medium, large-scale motions arise and grow exponentially. It can be expected that stabilization of this instability will occur at the nonlinear stage. We show below that, as a result of the development of instability in the system, large-scale spiraling, circularly polarized vortices of the Beltrami type are generated.

2.5. Stationary nonlinear vortex structures

Obviously, as the amplitude increases, the nonlinear terms decrease and the instability saturates. As a result, stationary, nonlinear vortex structures are formed. To find them, we put in equations (41) $\partial_T = 0$ and integrate the equations once over Z. We obtain the following system of equations:

$$\begin{aligned} \frac{d}{dZ} W_1 &= \overline{w_0 u_0} + C_1 \\ \frac{d}{dZ} W_2 &= \overline{w_0 v_0} + C_2 \end{aligned} \tag{46}$$

From equations (46), follow:

$$\frac{dW_1}{dW_2} = \frac{\overline{w_0 u_0} + C_1}{\overline{w_0 v_0} + C_2} \tag{47}$$

Integrating the system of equations (47), we get:

$$\int \overline{w_0 v_0} dW_1 + C_2 W_1 = \int \overline{w_0 u_0} dW_2 + C_1 W_2 \tag{48}$$

The integrals in expression (48) are calculated through elementary functions, which give the expression for the first integral of motion J of equations (47):

$$J = \frac{D^2}{8} \frac{W_1}{\left[4 + \frac{1}{2} D^2 - \left(W_2 - 1\right)^2\right]^2 + 16\left(W_2 - 1\right)^2} + \frac{1}{2^{5/2}\left(D^2+8\right)} \ln \frac{\left(W_1-1\right)^2 + D\sqrt{2}\left(W_1 - 1\right) + 4 + \frac{D^2}{2}}{\left(W_1-1\right)^2 - D\sqrt{2}\left(W_1 - 1\right) + 4 + \frac{D^2}{2}} +$$

$$+ \frac{D}{8\left(D^2+8\right)} \frac{\left(W_1-1\right)^2 - 4 - \frac{D^2}{2}}{4\left(W_1 - 1\right)} - \frac{D^2}{8} \frac{W_2}{\left[4 + \frac{D^2}{2} - \left(W_1 - 1\right)^2\right]^2 + 16\left(W_1 - 1\right)^2} +$$

$$+\frac{1}{2^{5/2}(D^2+8)}\ln\frac{(W_2-1)^2+(W_2-1)D\sqrt{2}+4+\frac{D^2}{2}}{(W_2-1)^2-D\sqrt{2}(W_2-1)+4+\frac{D^2}{2}}+\frac{D}{8(D^2+8)}\frac{(W_2-1)^2-4-\frac{D^2}{2}}{4(W_2-1)}+C_1W_2+C_2W_1$$

It is clear that system (46) is analogous to a dynamical system in which the coordinate Z plays the role of time. As a result, the standard methods for studying dynamical systems apply. A phase portrait of a dynamic system is thus used to gain a qualitative understanding of all possible modes implemented in it. The phase portrait of the system (46) is depicted in Fig. 2. From which the most interesting modes of behaviour are easily noticeable. Such regimes correspond to trajectories in the phase portrait connecting hyperbolic points with stable and unstable foci.

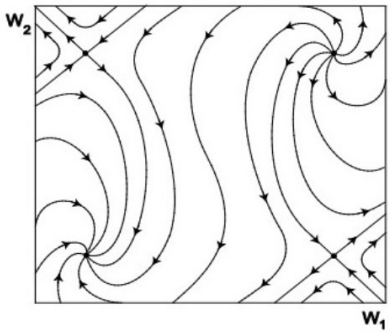

Figure 2. Phase portrait of a dynamical system (46) with parameters $D=1, C_1=-0.03, C_2=0.03$. One can see two hyperbolic singular points, as well as stable and unstable nodes.

On the left side of Fig. 3, we see the solution corresponding to the trajectory connecting the hyperbolic singular point with the stable node. On the right in Fig. 3, the solution corresponds to the trajectory connecting the unstable and stable foci. All these solutions correspond to large-scale localized vortex structures, such as kinks with rotation, which are generated by the instability considered here. The kink connecting a hyperbolic point to a stable knot contains rotations around the stable knot, as shown on the left in Fig. 3. In the kink that connects the unstable and stable foci, the velocity vector field W rotates around both singular points, as can be seen from the right side of Fig. 3. Note that, in contrast to previous works on the hydrodynamic α-effect in a rotating fluid, the method of asymptotic expansion makes it possible to construct a nonlinear theory in a natural way and study stationary nonlinear vortex kinks.

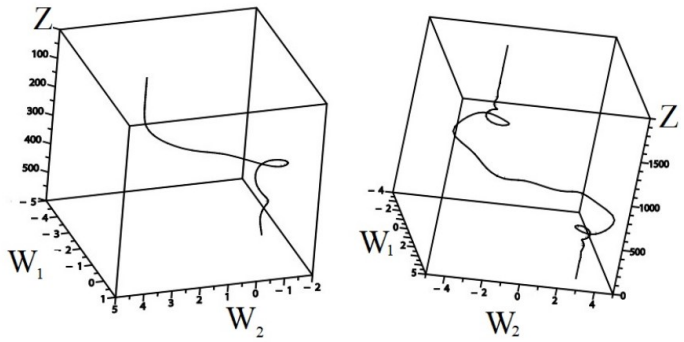

Figure 3. On the left, a kink is shown connecting a hyperbolic point to a stable knot with parameters $D=1, C_1=0.04, C_2=0.04$. When approaching a stable node, the rotation of the velocity field is observed. On the right, a kink is shown connecting the unstable and stable foci with the $D=1, C_1=0.04, C_2=0.04$ parameters. Here you can see the internal helical structure of the kink

3. NONLINEAR LARGE-SCALE VORTEX STRUCTURES IN AN OBLIQUELY ROTATING FLUID

This section presents the results of works [32]-[33], where a large-scale instability was studied that occurs in an obliquely rotating viscous fluid with small-scale turbulence. In [32]-[33], turbulence is modelled by an external small-scale and high-frequency force with a small Reynolds number. However, the main difference from the results of [30], which were presented in the previous section, is that the external force has no helicity. Therefore, the instability discussed above should be absent. The mathematical aspects of the theory [32]-[33] are based on a rigorous multiscale asymptotic expansion method. In the third order of perturbation theory, nonlinear equations were obtained for a large-scale velocity field. A study was also carried out of the linear and nonlinear stages of instability, and in the stationary mode, nonlinear periodic waves and vortex kinks were found [32]-[33].

3.1 Statement of the problem and equation for a large-scale velocity field

Let us consider a turbulent flow in an obliquely rotating viscous fluid whose axis of rotation does not coincide with the OZ axis. We will model turbulence with an external small-scale and high-frequency force $\vec{F}_0$ located in the plane (X,Y) (see Fig. 4). This force is not random and is set in a deterministic way in the following way:

$$F_0^z = 0,\ \vec{F}_{0\perp} = f_0\left(\vec{i}\cos\phi_2 + \vec{j}\cos\phi_1\right),$$
$$\phi_1 = \vec{k}_1\vec{x} - \omega_0 t,\quad \phi_2 = \vec{k}_2\vec{x} - \omega_0 t,\quad \vec{k}_1 = \vec{k}_0(1,0,0),\quad \vec{k}_2 = \vec{k}_0(0,1,0) \tag{49}$$

Obviously, the non-helical external force (49) satisfies the following properties:

$$div\vec{F}_0 = 0,\quad \vec{F}_0 rot\vec{F}_0 = 0,\quad rot\vec{F}_0 \neq 0,\quad \vec{F}_0 = f_0\vec{F}_0\left(\frac{\vec{x}}{\lambda_0};\frac{t}{t_0}\right) \tag{50}$$

In addition, the external force (49) is invariant with respect to the parity transformation $\vec{F}_0(\vec{x},t) = \vec{F}_0(-\vec{x},-t)$.

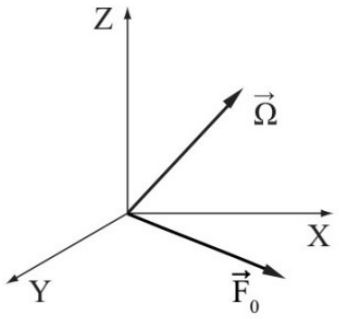

Figure 4. The angular velocity $\vec{\Omega}$ is inclined with respect to the plane (X,Y) in which the external force $\vec{F}_{0\perp}$ is located.

In the absence of rotation $\Omega = 0$, an external force $\vec{F}_0$ excites a small-scale flow $\vec{v}_0$ with a small Reynolds number $R = \frac{v_0 t_0}{\lambda_0} \ll 1$ and zero helicity $\overline{\vec{v}_0 rot\vec{v}_0} = 0$. To describe a turbulent flow in an obliquely rotating viscous incompressible fluid, we use the Navier-Stokes equations in a rotating coordinate system (1)-(2), which in a dimensionless form have the form (4)-(5). Further, the problem is to find an equation for a large-scale, slow velocity field $\vec{W}$. To do this, we also apply the method of multiscale asymptotic expansion with a small parameter R. Then, already in the third order of the perturbation theory, we obtain nonlinear equations for the large-scale components of the velocity field (W_1, W_2) in the framework of the "quasi-two-dimensional" model (17):

$$\partial_T W_1 - \nabla_Z^2 W_1 + \nabla_Z\left(\overline{v_0^z v_0^x}\right) = 0,\quad W_1 \equiv W_{-1}^x \tag{51}$$

$$\partial_T W_2 - \nabla_Z^2 W_2 + \nabla_Z\left(\overline{v_0^z v_0^y}\right) = 0,\quad W_2 \equiv W_{-1}^y \tag{52}$$

These equations are supplemented by the secular equations (11), (15), and (16). The fundamental difference between equations (51)-(52) and (38)-(39) is the Reynolds stresses, since the small-scale velocity fields v_0 included in them will be different. Naturally, to close equations (51)-(52), it is necessary to find solutions for the small-scale velocity field v_0.

3.2. Small-scale velocity field in the zeroth approximation in R

Using the results of Section 2.2, we calculate the zero-approximation velocity field, considering the geometry of the problem (see Fig. 4) and the selection of external force (49). We find expressions for the operator $\hat{D}_0$ by representing (49) in complex form (30):

$$\hat{D}_0(k_1,-\omega_0) = \hat{A}_1^* = 1 - i(1 - W_1),\quad \hat{D}_0(k_2,-\omega_0) = \hat{A}_2^* = 1 - i(1 - W_2) \tag{53}$$

and non-zero components of the tensors $\hat{p}_{ij}(k_1)$ and $\hat{p}_{ij}(k_2)$:

$$\hat{p}_{21}(k_1) = D_3,\quad \hat{p}_{31}(k_1) = -D_2,\quad \hat{p}_{12}(k_2) = -D_3,\quad \hat{p}_{32}(k_2) = D_1. \tag{54}$$

Here, to simplify the formulas, it was assumed that $k_0 = 1, \omega_0 = 1, f_0 = 1$. Taking into account formulas (53)-(54), we find the determinant:

$$\Delta(k_1)=\hat{A}_1^*\left(\hat{A}_1^{*2}+D_1^2\right),\quad \Delta(k_2)=\hat{A}_2^*\left(\hat{A}_2^{*2}+D_2^2\right) \tag{55}$$

Using formulas (26)-(29) and (53)-(55) it is easy to find the zero approximation velocity field:

$$u_0=\frac{1}{2}\frac{e^{i\phi_2}\hat{A}_2^*}{\hat{A}_2^{*2}+D_2^2}+c.c. \tag{56}$$

$$v_0=\frac{1}{2}\frac{e^{i\phi_1}\hat{A}_1^*}{\hat{A}_1^{*2}+D_1^2}+c.c. \tag{57}$$

$$w_0=\frac{1}{2}\frac{e^{i\phi_2}D_2}{\hat{A}_2^{*2}+D_2^2}-\frac{1}{2}\frac{e^{i\phi_1}D_1}{\hat{A}_1^{*2}+D_1^2}+c.c. \tag{58}$$

Note that the angular velocity component D_3 has dropped out of the expressions for the zero-approximation velocity, which is a consequence of the choice of an external force.

3.3. Reynolds stresses and large-scale instability

To close equations (51)-(52), we need to calculate the Reynolds stresses $\overline{w_0u_0}$ and $\overline{w_0v_0}$. These terms are easily calculated using formulas (56)-(58). As a result, we get:

$$\overline{w_0u_0}=\frac{1}{2}\frac{D_2}{\left|A_2^2+D_2^2\right|^2},\quad \overline{w_0v_0}=-\frac{1}{2}\frac{D_1}{\left|A_1^2+D_1^2\right|^2}. \tag{59}$$

Now equations (51)-(52) are closed and take the form:

$$\begin{aligned}
&\partial_T W_1-\Delta W_1+\frac{1}{2}\frac{\partial}{\partial Z}\frac{D_2}{4\left(1-W_2\right)^2+\left[D_2^2+W_2\left(2-W_2\right)\right]^2}=0,\\
&\partial_T W_2-\Delta W_2-\frac{1}{2}\frac{\partial}{\partial Z}\frac{D_1}{4\left(1-W_1\right)^2+\left[D_1^2+W_1\left(2-W_1\right)\right]^2}=0
\end{aligned} \tag{60}$$

For small values W_1, W_2, equation (60) can be linearized, which gives:

$$\begin{aligned}
&\partial_T W_1-\Delta W_1-\alpha_2\frac{\partial}{\partial Z}W_2=0\\
&\partial_T W_2-\Delta W_2+\alpha_1\frac{\partial}{\partial Z}W_1=0,
\end{aligned} \tag{61}$$

System (61) describes the positive feedback between the velocity components W_1, W_2, which is carried out by projections of the Coriolis force through the coefficients $\alpha_{1,2}$:

$$\alpha_1=2\frac{D_1\left(D_1^2-2\right)}{\left(4+D_1^2\right)^2},\quad \alpha_2=2\frac{D_2\left(D_2^2-2\right)}{\left(4+D_2^2\right)^2}$$

The solution to the linear system (61) will be sought in the form:

$$W_1, W_2 \sim \exp\left(\gamma T+iKZ\right) \tag{62}$$

Substituting equation (62) into equation (61), we obtain the dispersion equation:

$$\gamma=\pm\sqrt{\alpha_1\alpha_2}K-K^2 \tag{63}$$

Dispersion equation (63) shows the existence of a large-scale instability $\alpha_1\alpha_2>0$ with a maximum increment $\gamma_{\max}=\frac{\alpha_1\alpha_2}{4}$, with a wave vector $K_{\max}=\frac{1}{2}\sqrt{\alpha_1\alpha_2}$.

As a result of the development of instability in the system, large-scale helical vortices of the Beltrami type are generated. At $\alpha_1\alpha_2<0$, damped oscillations with frequency $\omega_0=\sqrt{\alpha_1\alpha_2}K$ appear instead of instability. As can be

seen from (63), the increment of large-scale instability γ depends on the values of D_1, D_2, i.e., on how the external forces F_0^x, F_0^y are located with respect to the perpendicular projection of the angular velocity of rotation. If one of the components D_1, D_2 vanishes or is equal to $\sqrt{2}$, then there is no instability. Instability exists in the following cases:

- $D_1 > \sqrt{2}, D_2 > \sqrt{2}$,
- $D_1, D_2 > 0, D_1 < \sqrt{2}, D_2 < \sqrt{2}$,
- $D_1 > 0, D_2 > 0, D_1^2 < 2, D_2^2 < 2$,
- $D_1 > 0, D_2 > 0, D_1^2 < 2, D_2^2 < 2$,
- $D_1 < 0, D_2 < 0, D_2^2 > 2, D_1^2 < 2$, или $D_2^2 < 2, D_1^2 < 2$,
- $D_1 > 0, D_2 < 0, D_2^2 > 2, D_1^2 < 2$, или $D_2^2 < 2, D_1^2 > 2$.

Of course, the instability should stabilise at the nonlinear stage, which we discuss below.

3.4. Stationary solutions of the nonlinear equation for a large-scale velocity field

As the perturbation amplitude W_1, W_2 increases, the nonlinear terms in (60) decrease, and the instability saturates. As a result, stationary, nonlinear vortex structures are formed. To find them in equation (63), we set $\frac{\partial}{\partial T} = 0$ and integrate the equations once with respect to Z. As a result, we obtain the following system of equations:

$$\frac{dW_1}{dZ} = \frac{1}{2}\frac{D_2}{4(1-W_2)^2 + \left[D_2^2 + W_2(2-W_2)\right]^2} + C_1, \qquad \frac{dW_2}{dZ} = -\frac{1}{2}\frac{D_1}{4(1-W_1)^2 + \left[D_1^2 + W_1(2-W_1)\right]^2} + C_2 \tag{64}$$

Let's move on to some convenient variables in this system: $1 - W_1 = \widetilde{W}_1, 1 - W_2 = \widetilde{W}_2$. Then we get

$$\begin{aligned} \frac{d\widetilde{W}_1}{dZ} &= -\frac{1}{2}\frac{D_2}{\left(D_2^2+1\right)^2 + 2\left(1-D_2^2\right)W_2^2 + \widetilde{W}_2^4} + C_1 \\ \frac{d\widetilde{W}_2}{dZ} &= \frac{1}{2}\frac{D_1}{\left(D_1^2+1\right)^2 + 2\left(1-D_1^2\right)\widetilde{W}_1^2 + \widetilde{W}_1^4} + C_2 \end{aligned} \tag{65}$$

Again, considering Z as a variable analogous to time, we can use the usual methods of dynamical systems. So the system of equations (65) can be written in the Hamiltonian form:

$$\frac{d\widetilde{W}_1}{dZ} = -\frac{\partial \mathcal{H}}{\partial \widetilde{W}_2}, \quad \frac{d\widetilde{W}_2}{dZ} = \frac{\partial \mathcal{H}}{\partial \widetilde{W}_1}$$

where the Hamiltonian $\mathcal{H}$ has the form:

$$\mathcal{H} = \mathcal{H}_1\left(D_1, \widetilde{W}_1\right) + \mathcal{H}_2\left(D_2, \widetilde{W}_2\right) \tag{66}$$

The function $\mathcal{H}\left(D, \widetilde{W}\right)$ is

$$\mathcal{H}\left(D, \tilde{W}\right) = \frac{D}{2}\int \frac{d\tilde{W}}{\left(D^2+1\right)^2 + 2\left(1-D^2\right)\tilde{W}^2 + \tilde{W}^4} + C\tilde{W} \tag{67}$$

The integral in formula (67) is calculated using elementary functions. Let's put it simply: $D_1 = D_2 = D = 1$. Then function (67) is

$$\mathcal{H}\left(\widetilde{W}\right) = \frac{1}{16}\left\{\ln\frac{\widetilde{W}^2 + 2\widetilde{W} + 2}{\widetilde{W}^2 - 2\widetilde{W} + 2} + arctg\frac{2\widetilde{W}}{2-\widetilde{W}^2}\right\} + C\widetilde{W} \tag{68}$$

The amounts $\mathcal{H}_1\left(\widetilde{W}_1\right) + \mathcal{H}_2\left(\widetilde{W}_2\right)$ can be combined into one formula. Then the Hamiltonian is

$$\mathcal{H} = \frac{1}{16}\ln\frac{\left(\widetilde{W}_1^2 + 2\widetilde{W}_1 + 2\right)\left(\widetilde{W}_2^2 + 2\widetilde{W}_2 + 2\right)}{\left(\widetilde{W}_1^2 - 2\widetilde{W}_1 + 2\right)\left(\widetilde{W}_2^2 - 2\widetilde{W}_2 + 2\right)} + \frac{1}{16}arctg\frac{2\widetilde{W}_2\left(\widetilde{W}_1^2 - 2\right) + 2\widetilde{W}_1\left(\widetilde{W}_2^2 - 2\right)}{2\left(\widetilde{W}_1 + \widetilde{W}_2\right)^2 - \widetilde{W}_1^2\widetilde{W}_2^2 - 4} + C_1\widetilde{W}_1 + C_2\widetilde{W}_2 \tag{69}$$

For Hamiltonians (69), it is easy to construct a phase portrait (Fig. 5), where for constant parameters $C_1 = 0.1$, $C_2 = 0.1$. The phase portrait shows the presence of closed trajectories on the phase plane around elliptical points and separatrices that connect hyperbolic points. Obviously, closed trajectories correspond to nonlinear periodic solutions (see the left side of Fig. 6), and localized solutions, such as kinks, correspond to separatrices (see the right side of Fig. 6).

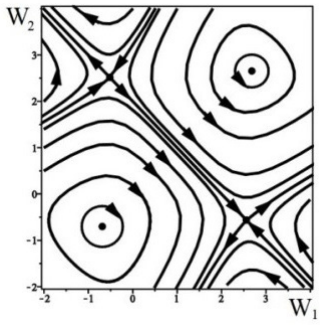

Figure. 5. The phase plane for the Hamiltonian (69) for constants $(C_1 = 0.1, C_2 = 0.1)$ is shown. One can see the presence of closed trajectories around the elliptic points and separatrices that connect the hyperbolic points.

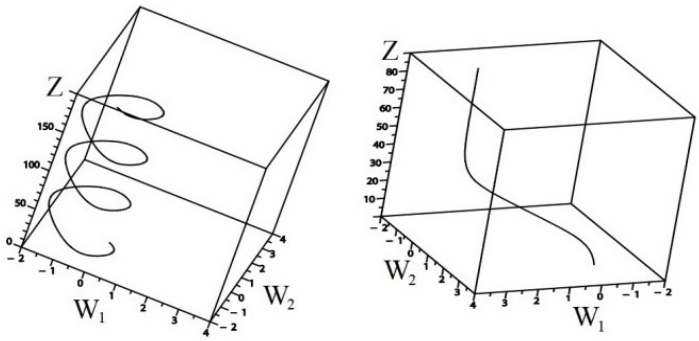

Figure. 6. The non-linear helical beltrami wave is shown on the left, which corresponds to a closed trajectory on the phase plane. The spiral is oriented along the axis Z and inclined with respect to the axis of rotation. On the right is a localized solution (kink) that corresponds to a separatrix on the phase plane. Solutions are obtained with parameters $(C_1 = 0.1, C_2 = 0.1)$.

4. NONLINEAR LARGE-SCALE VORTEX STRUCTURES IN AN OBLIQUELY ROTATING STRATIFIED FLUID

In this section, we discuss the nonlinear theory of generation of large-scale vortex structures (LSVS) in an obliquely rotating stratified medium with small-scale non-spiral turbulence, which was developed in [34]. Here turbulence was modeled by an external small-scale force with zero helicity, which creates small-scale flows with a small Reynolds number. Analytical results were obtained based on the method of multiscale asymptotic expansions. Nonlinear equations were found to describe the evolution of large-scale motions in the third order of perturbation theory. Linear instability and stationary nonlinear regimes were studied, and stationary solutions were obtained in the form of nonlinear Beltrami waves and localized vortex structures-kinks of a new type [34].

When temperature stratification is present, there are significant differences from the findings presented in works [32]-[33]. Firstly, the physical state changes completely. Accounting for temperature stratification in a gravitational field leads to free convection, resulting in the creation of vortex convective cells. The outcomes of [32]-[33] are not applicable in this scenario. Secondly, the mechanism of helicity generation is different here. Initially, non-helical external forces and the Coriolis force excite mirror-symmetric turbulence that organizes convective cells in such a way that the average helicity of small-scale motions is not zero (α -effect). Thirdly, the regime of large-scale instability is significantly altered. The increment of instability becomes much greater in the presence of convection $Ra \neq 0$.

4.1. Equations for Large Scale Fields

The Boussinesq-Oberbeck approximation describes the perturbations of velocity, temperature, and pressure in a rotating coordinate system with a constant temperature gradient. The system of equations is as follows:

Momentum equation:

$$\frac{\partial V_i}{\partial t} + V_k \frac{\partial V_i}{\partial x_k} = \nu \Delta V_i - \frac{1}{=\rho} \frac{\partial P}{\partial x_i} + 2\varepsilon_{ijk} V_j \Omega_k + g e_i \beta T + F_0^i \tag{70}$$

Energy equation:

$$\frac{\partial T}{\partial t}+V_k\frac{\partial T}{\partial x_k}-Ae_kV_k=\chi\Delta T \tag{71}$$

Continuity equation:

$$\frac{\partial V_i}{\partial x_i}=0 \tag{72}$$

The system of equations (70)-(73) describes the evolution of perturbations against the background of the main equilibrium state, set by a constant temperature gradient $\nabla\overline{T}=-A\vec{e}$ (heating from below $A>0$) and hydrostatic pressure: $\nabla\overline{P}=\overline{\rho}\vec{g}-\overline{\rho}\left[\vec{\Omega}\times\left[\vec{\Omega}\times\vec{r}\right]\right]$, where $\vec{r}$ is the radius vector of the fluid element. The vector of the angular velocity of rotation $\vec{\Omega}$ is considered constant (solid-body rotation) and inclined with respect to the plane (X,Y), as shown in Fig. 7, i.e., for the Cartesian geometry of the problem: $\vec{\Omega}=(\Omega_1,\Omega_2,\Omega_3)$; $\vec{e}=(0,0,1)$ is a unit vector in the direction of the Z axis; gravity is directed vertically downwards $\vec{g}=(0,0,-g)$; β is the coefficient of thermal expansion. Equation (70) includes an external force $\vec{F}_0$, which simulates an excitation source in the medium of small-scale and high-frequency fluctuations of the velocity field $\vec{v}_0$ with a small Reynolds number $R=\frac{v_0t_0}{\lambda_0}\ll 1$.

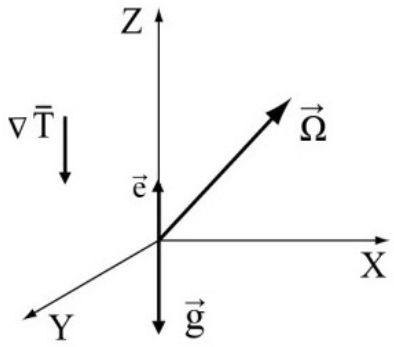

Figure 7. The angular velocity of rotation $\vec{\Omega}$ is not perpendicular to the plane (X,Y) in which the external force $\vec{F}_{0\perp}$ is located, but inclined at an angle with respect to it.

In this context, we employ an external non-helical force in the form of equation (49) and with properties (50). To simplify notation, we switch to dimensionless variables in equations (70)-(72), while retaining the notation for the dimensional variables

$$x\to\frac{x}{\lambda_0},\quad t\to\frac{t}{t_0},\quad \vec{V}\to\frac{\vec{V}}{v_0},\quad \vec{F}_0\to\frac{\vec{F}_0}{f_0},\quad P\to\frac{P}{\rho p_0},\quad t_0=\frac{\lambda_0^2}{\nu},\quad p_0=\frac{v_0\nu}{\lambda_0},\quad f_0=\frac{v_0\nu}{\lambda_0^2},\quad T\to\frac{T}{\lambda_0 A}.$$

In dimensionless variables, equations (70)-(72) take the form:

$$\frac{\partial V_i}{\partial t}+RV_k\frac{\partial V_i}{\partial x_k}=\Delta V_i-\frac{\partial P}{\partial x_i}+\varepsilon_{ijk}V_jD_k+e_i\widetilde{Ra}T+F_0^i \tag{73}$$

$$\frac{\partial T}{\partial t}+RV_k\frac{\partial T}{\partial x_k}-e_kV_k=Pr^{-1}\Delta T \tag{74}$$

$$\frac{\partial V_i}{\partial x_i}=0 \tag{75}$$

New dimensionless parameters have appeared here: $\widetilde{Ra}=\frac{Ra}{Pr}$, $Ra=\frac{g\beta A\lambda_0^2}{\nu\chi}$ is the Rayleigh number on the scale λ_0, $Pr=\frac{\nu}{\chi}$ is the Prandtl number. We consider the Reynolds number $R=\frac{v_0t_0}{\lambda_0}\ll 1$ to be a small parameter of the asymptotic expansion, and the parameters D_i and $\widetilde{Ra}$ are arbitrary and do not affect the expansion scheme. The

primary objective of this section is to obtain the solvability equations for the multiscale asymptotic expansion, which involves finding equations for large-scale perturbations. As in the previous sections, we express the spatial and temporal derivatives in equations (73)-(75) using an asymptotic expansion (6). In constructing the nonlinear theory, we represent the variables $\vec{V}$, P as an asymptotic series (7), and the temperature perturbations T as the following series:

$$T(x,t) = \frac{1}{R} T_{-1}\left(X\right) + T_0\left(x_0\right) + RT_1 + R^2 T_2 + R^3 T_3 + \cdots \tag{76}$$

To obtain the equations of the multiscale asymptotic expansion, we substitute the expansions (6)-(7), (76) into the system of equations (73)-(75) and group together the terms with the same orders in R up to the power of R^3 . The algebraic structure of the asymptotic expansion in equations (73)-(75) differs from the asymptotic expansion presented in Section 2.2 due to the presence of terms related to the expansion of temperature perturbations. The fundamental secular equations, or equations for large-scale fields, are derived at the third order in R :

$$\partial_T W_{-1}^i - \Delta W_{-1}^i + \nabla_k \left(\overline{v_0^k v_0^i}\right) = -\nabla_i \overline{P}_1 \tag{77}$$

$$\partial_T T_{-1} - Pr^{-1} \Delta T_{-1} = -\nabla_k \left(\overline{v_0^k T_0}\right) \tag{78}$$

Equations (77)-(78) are supplemented by secular equations:

$$-\nabla_i P_{-3} + \widetilde{Rae}_i T_{-1} + \varepsilon_{ijk} W_j D_k = 0\,,\ W_{-1}^k \nabla_k W_{-1}^i = -\nabla_i P_{-1}$$

$$W_{-1}^k \nabla_k T_{-1} = 0\,,\ \nabla_i W_{-1}^i = 0\,, W_{-1}^z = 0\,.$$

These equations are satisfied by choosing the following geometry for the velocity field:

$$\vec{W}_{-1} = \left(W_{-1}^x\left(Z\right),\quad W_{-1}^y\left(Z\right), 0\right),\quad T_{-1} = T_{-1}\left(Z\right),\quad P_{-1} = const \tag{79}$$

In the framework of a quasi-two-dimensional problem, when large-scale derivatives with respect to Z are preferable, i.e.

$$\nabla_Z \equiv \frac{\partial}{\partial Z} \gg \frac{\partial}{\partial X}, \frac{\partial}{\partial Y}$$

Then the system of equations (77)-(78) is simplified and takes the following form:

$$\partial_T W_1 - \nabla_Z^2 W_1 + \nabla_Z \left(\overline{v_0^z v_0^x}\right) = 0, \quad W_{-1}^x = W_1 \tag{80}$$

$$\partial_T W_2 - \nabla_Z^2 W_2 + \nabla_Z \left(\overline{v_0^z v_0^y}\right) = 0, \quad W_{-1}^y = W_2 \tag{81}$$

$$\partial_T T_{-1} - Pr^{-1} \Delta T_{-1} + \nabla_Z \left(\overline{v_0^z T_0}\right) = 0 \tag{82}$$

Equations (80)-(82) describe the evolution of large-scale vortex fields $\vec{W}$, but the final closure of these equations is achieved after calculating the Reynolds stresses $\nabla_k \left(\overline{v_0^k v_0^i}\right)$. This shows that we need to find solutions for the small-scale velocity field $\vec{v}_0$.

4.2. Solving Equations for Small-Scale Fields and Calculating Reynolds Stresses

We write the asymptotic expansion equations in the zeroth approximation in the following form:

$$\widehat{D}_W v_0^i = -\partial_i P_0 + \widetilde{Rae}_i T_0 + \varepsilon_{ijk} v_0^j D_k + F_0^i \tag{83}$$

$$\widehat{D}_\theta T_0 = e_k v_0^k \tag{84}$$

$$\partial_i v_0^i = 0 \tag{85}$$

where the notation for the operators is introduced:

$$\widehat{D}_W = \partial_t - \partial_k^2 + W_{-1}^k \partial_k\,, \widehat{D}_\theta = \partial_t - Pr^{-1}\partial^2 + W_{-1}^k \partial_k$$

Small-scale temperature oscillations are easily found from equation (84):

$$T_0 = \frac{v_0^z}{\widehat{D}_\theta} \tag{86}$$

Substituting (86) into (83), and using the condition of solenoidality of the fields $\vec{v}_0$ and $\vec{F}_0$, we find the pressure P_0 :

$$P_0 = \widehat{P}_1 u_0 + \widehat{P}_2 v_0 + \widehat{P}_3 w_0 \tag{87}$$

Here we introduce the notation for the operators

$$\widehat{P}_1 = \frac{D_2\partial_z - D_3\partial_y}{\partial^2}, \quad \widehat{P}_2 = \frac{D_3\partial_x - D_1\partial_z}{\partial^2}, \quad \widehat{P}_3 = \frac{D_1\partial_y - D_2\partial_x}{\partial^2} + \widetilde{Ra}\frac{\partial_z}{\widehat{D}_\theta\partial^2}$$

and velocities: $v_0^x = u_0$, $v_0^y = v_0$, $v_0^z = w_0$. Using expression (87), we can eliminate the pressure from equation (83) and, as a result, obtain a system of equations for finding the zero-order velocity field:

$$\begin{gathered}
\left(\widehat{D}_W + \widehat{p}_{1x}\right)u_0 + \left(\widehat{p}_{2x} - D_3\right)v_0 + \left(\widehat{p}_{3x} + D_2\right)w_0 = F_0^x \\
\left(D_3 + \widehat{p}_{1y}\right)u_0 + \left(\widehat{D}_W + \widehat{p}_{2y}\right)v_0 + \left(\widehat{p}_{3y} - D_1\right)w_0 = F_0^y \\
\left(\widehat{p}_{1z} - D_2\right)u_0 + \left(\widehat{p}_{2z} + D_1\right)v_0 + \left(\widehat{D}_W - \frac{\widetilde{Ra}}{\widehat{D}_\theta} + \widehat{p}_{3z}\right)w_0 = 0
\end{gathered} \tag{88}$$

The components of the tensor $\widehat{p}_{ij}$ have the following form:

$$\begin{gathered}
\widehat{p}_{1x} = \frac{D_2\partial_x\partial_z - D_3\partial_x\partial_y}{\partial^2}, \widehat{p}_{2x} = \frac{D_3\partial_x^2 - D_1\partial_x\partial_z}{\partial^2}, \widehat{p}_{3x} = \frac{D_1\partial_x\partial_y - D_2\partial_x^2}{\partial^2} + \widetilde{Ra}\frac{\partial_x\partial_z}{\hat{D}_\theta\partial^2}, \\
\widehat{p}_{1y} = \frac{D_2\partial_y\partial_z - D_3\partial_y^2}{\partial^2}, \widehat{p}_{2y} = \frac{D_3\partial_y\partial_x - D_1\partial_y\partial_z}{\partial^2}, \widehat{p}_{3y} = \frac{D_1\partial_y^2 - D_2\partial_y\partial_x}{\partial^2} + \widetilde{Ra}\frac{\partial_y\partial_z}{\hat{D}_\theta\partial^2}, \\
\widehat{p}_{1z} = \frac{D_2\partial_z^2 - D_3\partial_z\partial_y}{\partial^2}, \widehat{p}_{2z} = \frac{D_3\partial_z\partial_x - D_1\partial_z^2}{\partial^2}, \widehat{p}_{3z} = \frac{D_1\partial_z\partial_y - D_2\partial_z\partial_x}{\partial^2} + \widetilde{Ra}\frac{\partial_z^2}{\hat{D}_\theta\partial^2}
\end{gathered} \tag{89}$$

The solution to the system of equations (88) is easily found according to Cramer's rules (26)-(28). Then, using the complex form of the external force (49), we find the zero approximation velocity field:

$$u_0 = \frac{f_0}{2}\frac{\widehat{\mathcal{A}}_2^*}{\widehat{\mathcal{A}}_2^*\widehat{D}_{W_2}^* + D_2^2}e^{i\phi_2} + c.c. = u_{03} + u_{04} \tag{90}$$

$$v_0 = \frac{f_0}{2}\frac{\widehat{\mathcal{A}}_1^*}{\widehat{\mathcal{A}}_1^*\widehat{D}_{W_1}^* + D_1^2}e^{i\phi_1} + c.c. = v_{01} + v_{02} \tag{91}$$

$$w_0 = -\frac{f_0}{2}\frac{D_1}{\widehat{\mathcal{A}}_1^*\widehat{D}_{W_1}^* + D_1^2}e^{i\phi_1} + \frac{f_0}{2}\frac{D_2}{\widehat{\mathcal{A}}_2^*\widehat{D}_{W_2}^* + D_2^2}e^{i\phi_2} + c.c. = w_{01} + w_{02} + w_{03} + w_{04}, \tag{92}$$

where

$$\widehat{\mathcal{A}}_{1,2}^* = \widehat{D}_{W_{1,2}}^* - \frac{\widetilde{Ra}}{\widehat{D}_{\theta_{1,2}}^*}.$$

This indicates that the zero-order velocity field is not influenced by the angular velocity component D_3 , as a result of the chosen external force (49). It is worth noting that the velocity components follow the subsequent relationships:

$$w_{02} = \left(w_{01}\right)^*, \ w_{04} = \left(w_{03}\right)^*, \ v_{02} = \left(v_{01}\right)^*, v_{04} = \left(v_{03}\right)^*, \ u_{02} = \left(u_{01}\right)^*, \ u_{04} = \left(u_{03}\right)^*.$$

In order to solve equations (80)-(81), which portray the development of large-scale vortex fields, it is crucial to compute the Reynolds stress $T^{ik} = \overline{v_0^i v_0^k}$, specifically its components:

$$T^{31} = \overline{w_0 u_0} = \overline{w_{01}\left(u_{01}\right)^*} + \overline{\left(w_{01}\right)^* u_{01}} + \overline{w_{03}\left(u_{03}\right)^*} + \overline{\left(w_{03}\right)^* u_{03}} \tag{93}$$

$$T^{32} = \overline{w_0 v_0} = \overline{w_{01}\left(v_{01}\right)^*} + \overline{\left(w_{01}\right)^* v_{01}} + \overline{w_{03}\left(v_{03}\right)^*} + \overline{\left(w_{03}\right)^* v_{03}} \tag{94}$$

By substituting the solutions for the small-scale velocity field (90)-(92) into formulas (93)-(94), we can obtain the following expressions for the correlators:

$$T^{31} = \frac{f_0^2}{4}\frac{D_2(\widehat{\mathcal{A}}_2 + \widehat{\mathcal{A}}_2^*)}{\left|\widehat{\mathcal{A}}_2\,\widehat{D}_{W_2} + D_2^2\right|^2}, \qquad T^{32} = -\frac{f_0^2}{4}\frac{D_1(\widehat{\mathcal{A}}_1 + \widehat{\mathcal{A}}_1^*)}{\left|\widehat{\mathcal{A}}_1\,\widehat{D}_{W_1} + D_1^2\right|^2} \tag{95}$$

If we assume the medium is the atmosphere, the Prandtl number is approximately equal to one $Pr = 1$. In this case, the expressions for the Reynolds stress components become simplified:

$$T^{31} = \frac{f_0^2}{2} D_2 \frac{(1+\tilde{W}_2^2 - Ra)}{(1+\tilde{W}_2^2)((1+\tilde{W}_2^2)^2 + 2(D_2^2 - Ra)(1-\tilde{W}_2^2) + (D_2^2 - Ra)^2)} \tag{96}$$

$$T^{32} = -\frac{f_0^2}{2} D_1 \frac{(1+\tilde{W}_1^2 - Ra)}{(1+\tilde{W}_1^2)((1+\tilde{W}_1^2)^2 + 2(D_1^2 - Ra)(1-\tilde{W}_1^2) + (D_1^2 - Ra)^2)} \tag{97}$$

By substituting (96)-(97) into (80)-(81), we can obtain closed equations for the evolution of large-scale vortex fields $\vec{W}$:

$$(\partial_T - \nabla_Z^2)\tilde{W}_1 = \frac{f_0^2}{2} D_2 \nabla_Z \left[\frac{1+\tilde{W}_2^2 - Ra}{(1+\tilde{W}_2^2)((1+\tilde{W}_2^2)^2 + 2(D_2^2 - Ra)(1-\tilde{W}_2^2) + (D_2^2 - Ra)^2)}\right] \tag{98}$$

$$(\partial_T - \nabla_Z^2)\tilde{W}_2 = -\frac{f_0^2}{2} D_1 \nabla_Z \left[\frac{1+\tilde{W}_1^2 - Ra}{(1+\tilde{W}_1^2)((1+\tilde{W}_1^2)^2 + 2(D_1^2 - Ra)(1-\tilde{W}_1^2) + (D_1^2 - Ra)^2)}\right] \tag{99}$$

These closed equations (98)-(99) can be considered as the equations of a nonlinear vortex dynamo in a stratified fluid that is rotating obliquely with a non-spiral force acting on the small-scale. If the rotation effect disappears ($\Omega = 0$) or the rotation axis coincides with the OZ axis ($\vec{\Omega} \,||\, OZ$), the usual diffusion spreading of large-scale fields will occur. In the limit of a homogeneous fluid $Ra = 0$, equations (98)-(99) are completely equivalent to equations (60) when $f_0 = 1$.

4.3. Large scale instability

Equations (98)-(99) are used to describe the nonlinear behavior of large-scale perturbations in the vortex field. Consequently, it is important to investigate the stability of small perturbations in the field $\vec{W}$. For small values of $\vec{W} = (W_1, W_2)$, equations (98)-(99) can be simplified to a system of linear equations:

$$\begin{aligned} &\partial_T W_1 - \nabla_Z^2 W_1 - \alpha_2 \nabla_Z W_2 = 0 \\ &\partial_T W_2 - \nabla_Z^2 W_2 + \alpha_1 \nabla_Z W_1 = 0 \end{aligned} \tag{100}$$

where the following notation for the coefficients is introduced:

$$\alpha_1 = f_0^2 D_1 \left[\frac{(D_1^2 - Ra - 2)(2 - Ra) + Ra(4 + (D_1^2 - Ra)^2)}{(4 + (D_1^2 - Ra)^2)^2}\right],$$

$$\alpha_2 = f_0^2 D_2 \left[\frac{(D_2^2 - Ra - 2)(2 - Ra) + Ra(4 + (D_2^2 - Ra)^2)}{(4 + (D_2^2 - Ra)^2)^2}\right]. \tag{101}$$

This shows that equations (100) are similar to the equations for a vortex dynamo or hydrodynamic α-effect. To study the large-scale instability described by equation (100), we choose perturbations in the form of plane waves with the wave vector $\vec{K} \,||\, OZ$. As a result, we find the dispersion equation:

$$\left(-i\omega + K^2\right)^2 - \alpha_1 \alpha_2 K^2 = 0 \tag{102}$$

Representing $\omega = \omega_0 + i\Gamma$, from equation (102) we find:

$$\Gamma = Im\omega = \pm\sqrt{\alpha_1\alpha_2}K - K^2 \tag{103}$$

Solutions (103) show the existence of instability at $\alpha_1\alpha_2 > 0$ for large-scale vortex disturbances. If $\alpha_1\alpha_2 < 0$, then instead of instabilities, damped oscillations occur, respectively, with frequency $\omega_0 = \sqrt{\alpha_1\alpha_2}K$. By means of the coefficients α_1, α_2 a positive feedback is established between the velocity components, which is carried out by projections of the Coriolis force. Note that in the linear theory considered here, the coefficients α_1, α_2 do not depend on the field amplitudes but only on the rotation parameters $D_{1,2}$, the Rayleigh number Ra, and the amplitude of the external force f_0. Let us analyze the dependence of these coefficients on dimensionless parameters, assuming the dimensionless amplitude of the external force to be equal to $f_0 = 10$. Fixing the level of the dimensionless force means choosing a certain level of the stationary background of small-scale and fast oscillations. In the coefficients α_1, α_2 instead of the Cartesian projections D_1 and D_2, it is convenient to pass to their projections in the spherical coordinate system (D, ϕ, θ) (see Fig. 8).

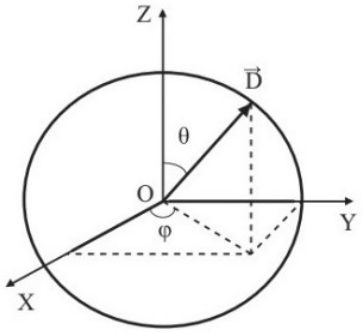

Figure 8. The conversion between the Cartesian projections of the rotation parameter D (or the rotation angular velocity vector Ω) and their projections in a spherical coordinate system is demonstrated.

The coordinate surface represented by $D = const$ forms a sphere, where θ stands for latitude ($\theta \in [0, \pi]$) and ϕ denotes longitude ($\phi \in [0, 2\pi]$). To investigate the impact of rotation and stratification on the gains α_1, α_2, we assume that D_1 and D_2 are equal, corresponding to a fixed longitude value of $\phi = \pi/4 + \pi n$, where $n = 0, 1, 2...k$, k is an integer. Under this assumption, the amplification factors for vortex disturbances are given by:

$$\alpha = \alpha_1 = \alpha_2 = f_0^2\sqrt{2}D\sin\theta\left[\frac{4(D^2\sin^2\theta - 2Ra - 4)(2 - Ra) + 2Ra(16 + (D^2\sin^2\theta - 2Ra)^2)}{(16 + (D^2\sin^2\theta - 2Ra)^2)^2}\right]$$

This implies that generating vortex disturbances at the poles $(\theta = 0, \theta = \pi)$ is not efficient since $\alpha \to 0$. The left side of Fig. 9 illustrates the dependence of the coefficient α on the fluid stratification parameter (Rayleigh number Ra) at a fixed value of latitude $\theta = \pi/2$ and number $D = 2$.

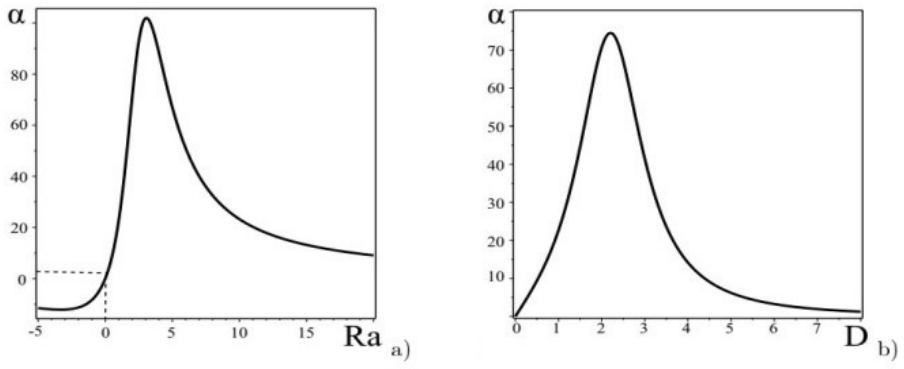

Figure 9. a) Plot of the dependence of the α-effect on the medium stratification parameter Ra (Rayleigh number); b) plot of the dependence of the α-effect on the medium rotation parameter D.

It also shows the case of a homogeneous medium, where large-scale vortex disturbances are generated by the external small-scale non-spiral force and the Coriolis force. Fig. 9 indicates that temperature stratification ($Ra \neq 0$) can result in a significant increase in the coefficient α , leading to faster generation of large-scale vortex disturbances than in a homogeneous medium. This effect is particularly significant at higher numbers. Moreover, an increase in Rayleigh numbers leads to a decrease in the values of the coefficient. We are also interested in exploring the impact of the medium rotation effect on the amplification factor or the process of generating large-scale disturbances. Therefore, we set the Rayleigh number to $Ra = 2$ at $\theta = \pi / 2$. On the right-hand side of Fig. 9, the functional relationship $\alpha(D)$ is presented. It is evident from the graph that the coefficient attains its maximum value $\alpha_{\max}$ at a specific rotation parameter D after which it gradually diminishes with an increase in D . This implies that the α -effect is suppressed. Similar behavior was observed in the magnetohydrodynamic α -effect [39]. On the left side of Fig. 10, the combined impact of rotation and stratification on the (D, Ra) plane is depicted. The gray shaded region indicates the $\alpha > 0$ instability area. The maximum instability increment $\Gamma_{max} = \dfrac{\alpha_1 \alpha_2}{4}$ is achieved for wave numbers $K_{max} = \dfrac{\sqrt{\alpha_1 \alpha_2}}{2}$. The graph on the right-hand side of Fig. 10 shows the dependence of the instability increment Γ on the wave numbers K , which has a conventional pattern similar to the α -effect. Consequently, a rotating stratified atmosphere experiences the generation of large-scale helical circularly polarized vortices of the Beltrami type due to the development of a large-scale instability.

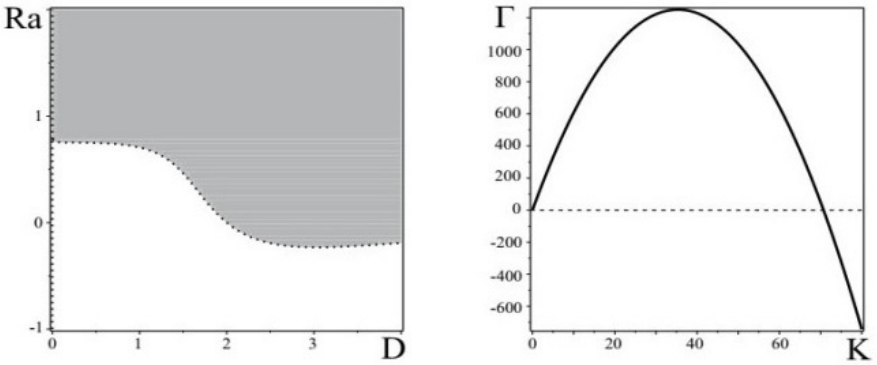

Figure 10. The image on the left displays a graph representing the (D, Ra) plane. The region indicating positive values of α (representing unstable solutions) is shaded in gray, while the region indicating negative values of α is shown in white. On the right-hand side, there is a plot showing the relationship between the increment of instability and the wave numbers K , with $D = 2$ and $Ra = 2$ as the parameters.

4.4. Stationary nonlinear vortex structures

Obviously, with an increase in the amplitude of perturbations, the nonlinear terms decrease and the instability saturates. As a result, nonlinear vortex structures are formed. To find them, we put in equations (98)-(99) $\partial_T = 0$ and integrate the equations once over Z. Furthermore, we make the assumption that the projections D_1 and D_2 hold identical values. To simplify the calculations, we assign the latitudinal angle a value of $\theta = \pi / 2$. Consequently, we derive a set of nonlinear equations in the following format:

$$\frac{d\tilde{W}_1}{dZ} = -f_0^2 D\sqrt{2}\,\frac{1+\tilde{W}_2^2 - Ra}{(1+\tilde{W}_2^2)(4(1+\tilde{W}_2^2)^2 + 4(D^2-2Ra)(1-\tilde{W}_2^2) + (D^2-2Ra)^2)} + C_1 \tag{104}$$

$$\frac{d\tilde{W}_2}{dZ} = f_0^2 D\sqrt{2}\,\frac{1+\tilde{W}_1^2 - Ra}{(1+\tilde{W}_1^2)(4(1+\tilde{W}_1^2)^2 + 4(D^2-2Ra)(1-\tilde{W}_1^2) + (D^2-2Ra)^2)} + C_2 \tag{105}$$

C_1, C_2 are integration constants that can take any value. It is important to note that the system of dynamic equations (104)-(105) is conservative, meaning it possesses a Hamiltonian. To obtain the Hamiltonian, we can express equations (104)-(105) in the Hamiltonian form.

$$\frac{d\widetilde{W}_1}{dZ} = -\frac{\partial \mathcal{H}}{\partial \widetilde{W}_2}, \quad \frac{d\widetilde{W}_2}{dZ} = \frac{\partial \mathcal{H}}{\partial \widetilde{W}_1}$$

where the Hamiltonian $\mathcal{H}$ has the form:

$$\mathcal{H} = \mathcal{H}_1(\widetilde{W}_1) + \mathcal{H}_2(\widetilde{W}_2) + C_2\widetilde{W}_1 - C_1\widetilde{W}_2 \tag{106}$$

and functions $\mathcal{H}_{1,2}$ are

$$\mathcal{H}_{1,2} = f_0^2 D\sqrt{2}\int \frac{(1+\tilde{W}_{1,2}^2 - Ra)d\tilde{W}_{1,2}}{(1+\tilde{W}_{1,2}^2)(4(1+\tilde{W}_{1,2}^2)^2 + 4(D^2-2Ra)(1-\tilde{W}_{1,2}^2) + (D^2-2Ra)^2)}$$

Assuming $D = Ra = 2$ and $f_0 = 10$ one can easily calculate the Hamiltonian (106):

$$\mathcal{H} = -\frac{25}{2}\sqrt{2}\left(\frac{\widetilde{W}_1(\widetilde{W}_1^2+3)}{(\widetilde{W}_1^2+1)^2} + \frac{\widetilde{W}_2(\widetilde{W}_2^2+3)}{(\widetilde{W}_2^2+1)^2} + arctg\widetilde{W}_1 + arctg\widetilde{W}_2\right) + C_2\widetilde{W}_1 - C_1\widetilde{W}_2$$

Equations (104)-(105) being Hamiltonian implies that the phase space can only have two types of fixed points: elliptic and hyperbolic fixed points. This can be observed through a qualitative analysis of the system by linearizing the right-hand sides of equations (104)-(105) near fixed points, determining their type, and constructing a phase portrait. Through this analysis, we have identified four fixed points, two of which are hyperbolic and two of which are elliptic. The phase portrait of the dynamic system of equations (104)-(105) with parameters $C_1 = -1$, $C_2 = 1$, $D = Ra = 2$ and $f_0 = 10$ is shown in Fig. 11, which allows us to qualitatively describe possible stationary solutions. The phase portrait also reveals the presence of closed trajectories around elliptic points and separatrices connecting hyperbolic points. Closed trajectories correspond to nonlinear periodic solutions or nonlinear waves (see Fig. 12a), while separatrices correspond to localized kink-type vortex structures (see Fig. 12b), which are the most interesting localized solutions.

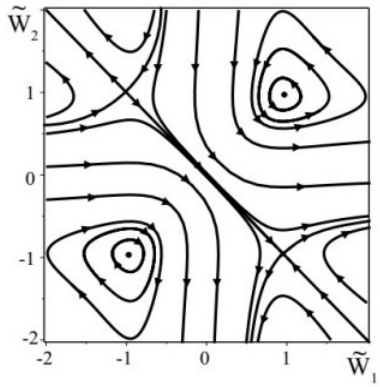

Figure 11. The phase plane for the dynamic system of equations (104)-(105) under the condition $C_1 = -1$ and $C_2 = 1$. Here you can see the presence of closed trajectories around elliptical points and separatrices that connect hyperbolic points.

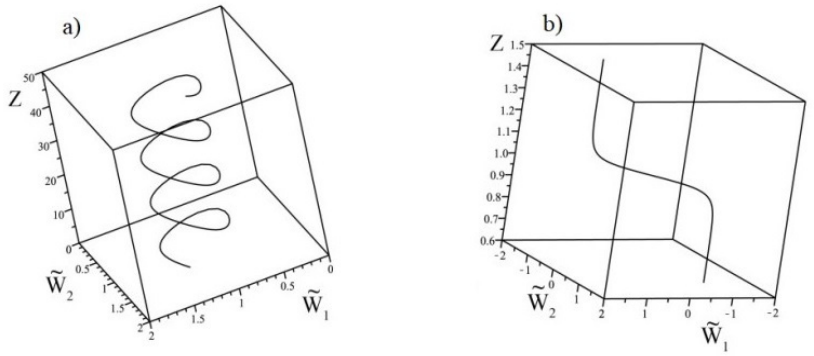

Figure 12. a) The phase plane displays a non-linear helical wave, which corresponds to a closed trajectory. b) Localized nonlinear vortex structure (kink), which corresponds to the separatrix on the phase plane ($C_1 = -1$, $C_2 = 1$, $D = Ra = 2$).

5. NONLINEAR VORTEX DYNAMO IN A ROTATING STRATIFIED MOIST ATMOSPHERE

A moist atmosphere is composed of dry air, water vapor, and fluid water droplets. If the specific humidity value is below saturation, the atmosphere behaves like a binary mixture of dry air and water vapor, following the usual

hydrodynamic equations. However, when the specific humidity reaches saturation, excess water vapor condenses and forms a new substance called water content. This process releases a large amount of energy, although we only consider its energy effect here as describing a phase transition is a difficult task. This section presents the results of large-scale instability in a rotating stratified moist atmosphere with small-scale helicity at low Reynolds numbers, as described in [31]. The small-scale helicity is induced by an external force that considers the influence of Coriolis force and stratification in a moist atmosphere. The method of multiscale asymptotic expansions was applied in [31], resulting in averaged nonlinear equations for large-scale fields in the third order of Reynolds number in a rotating moist atmosphere. The instability of the hydrodynamic α-effect was obtained for small amplitudes of large-scale velocity perturbations, and the criteria for the development of this instability were determined based on the rotation and stratification of the medium. The numerical estimates of the characteristic times and scales of instability given in [31] may explain the origin of the large-scale spiral structure of cloud mesovortices and typhoons at the initial stage of their development. Furthermore, a numerical analysis of the nonlinear equations in the stationary regime was conducted in [31], which revealed the existence of localized helical vortex structures of the kink type.

5.1. Statement of the problem and basic equations for large-scale vortex fields

The problem statement is as follows: Consider a layer of the atmosphere where the specific humidity is equal to the saturated humidity. The negative gradient of the saturated value of specific humidity in the atmosphere is determined by the stationary vertical gradients of temperature and pressure. When ascending air flows, twisted by the Coriolis force, condense water vapor and release latent thermal energy. In this medium, small-scale non-spiral turbulence is present, which is modeled by an external small-scale force. The main objective of this section is to understand how moisture phase transitions affect the dynamics of large-scale or averaged fields. To describe the process of wet convection, we use the well-known Boussinesq approximation to write hydrodynamic equations for perturbations of velocity V, temperature T, pressure P, and specific water content m in a rotating coordinate system.

$$\frac{\partial V_i}{\partial t}+V_k\frac{\partial V_i}{\partial x_k}=\nu\Delta V_i-\frac{1}{\overline{\rho}}\frac{\partial P}{\partial x_i}+2\varepsilon_{ijk}V_j\mathrm{W}_k+ge_i\left(\beta T+\beta_1 m\right)+F_0^i \tag{107}$$

$$\frac{\partial T}{\partial t}+V_k\frac{\partial T}{\partial x_k}-Ae_kV_k=\chi\Delta T+\frac{L}{c_p}K \tag{108}$$

$$\frac{\partial m}{\partial t}+V_k\frac{\partial m}{\partial x_k}-Be_kV_k=d\Delta m+K \tag{109}$$

$$\frac{\partial V_i}{\partial x_i}=0 \tag{110}$$

The system of equations (107)-(110) describes the evolution of disturbances against the background of the main equilibrium state $\overline{T}(z)$, $\overline{\rho}(z)$, $\overline{m}(z)$, specified by a constant temperature gradient $\nabla\overline{T}=-A\vec{e}$ $(A>0)$ (heating from below), an equilibrium gradient of specific water content $\nabla\overline{m}=-B\vec{e}$ $(B<0)$, and hydrostatic pressure: $\nabla\overline{P}=\overline{\rho}\vec{g}-\left[\vec{\Omega}\times\left[\vec{\Omega}\times\vec{r}\right]\right]$, where $\vec{r}$ is the radius vector of the fluid element. Here $\vec{g}=(0,0,-g)$ is the gravitational acceleration vector directed along the OZ axis. The angular velocity vector $\vec{\Omega}$ is constant, which means that the medium is rotating as a solid body around the OZ axis. The direction of the vector is also along the OZ axis, which means that the rotation is around a vertical axis. The constant rotation is an assumption of the problem, which simplifies the analysis of the equations and allows us to study the effects of moisture phase transitions on the large-scale dynamics. The heat balance equation (108) includes the source of latent heat release from saturated air condensation [18]:

$$Q=\frac{L}{c_p}K=\frac{L}{c_p}cAe_kv_k,\ c=\frac{dq_n}{d\overline{T}}, \tag{111}$$

where L is the specific heat of condensation of water vapor, c_p is the heat capacity of dry air at constant pressure, K is the rate of condensation, and q_n is the specific saturated humidity or mass fraction of saturated steam. $e=(0,0,1)$ is a unit vector in the direction of the Z axis directed vertically upwards, β is the coefficient of thermal expansion, $\beta_1=-\frac{1}{\overline{\rho}}\left(\frac{\partial\rho}{\partial m}\right)_{T,P}$ and d is the diffusion coefficient.

The Navier-Stokes equation (107) includes an external small-scale force F_0, which models the excitation source in the medium of small-scale and high-frequency pulsations of the velocity field v_0 with a small Reynolds number

$R = \frac{v_0 t_0}{\lambda_0} \ll 1$. The main role of this force is to maintain a small level of small-scale motions in the presence of dissipation. Here we consider a small-scale external force of the form (25) with properties (3). Applying the usual dimensionless procedure to the variables x, t, V, P, F_0, T as well as to perturbations of the specific water content $m \to m / \lambda_0 B$, we write equations (107)-(110) in a dimensionless form:

$$\frac{\partial V_i}{\partial t} + RV_k \frac{\partial V_i}{\partial x_k} = \Delta V_i - \frac{\partial P}{\partial x_i} + D\varepsilon_{ijk} V_j + e_i \left(\widetilde{Ra} T + \widetilde{R}_m m \right) + F_0^i \tag{112}$$

$$\frac{\partial T}{\partial t} + RV_k \frac{\partial T}{\partial x_k} - ae_k V_k = Pr^{-1} \Delta T \tag{113}$$

$$\frac{\partial m}{\partial t} + RV_k \frac{\partial m}{\partial x_k} - be_k V_k = S^{-1} \Delta m \tag{114}$$

$$\frac{\partial V_i}{\partial x_i} = 0 \tag{115}$$

Here, new dimensionless parameters have appeared that are characteristic of a moist atmosphere: $\widetilde{R}_m = \frac{R_m}{S}$, $R_m = \frac{g\beta_1 B \lambda_0^4}{\nu d}$ is the diffusion analogue of the Rayleigh number on the scale λ_0; $S = \frac{\nu}{d}$ is the Schmidt number, $a = 1 + \frac{c}{c_p} L, b = 1 + \frac{cA}{B}$. The small parameter of the asymptotic expansion will be the Reynolds number R of small-scale motions, and the parameters Ra, R_m and D will be considered arbitrary, not affecting the expansion scheme.

Consider the problem statement below. Moist air found in certain parts of the atmosphere is made up of dry air, water vapor, and fluid water droplets. This environment experiences small-scale, high-frequency movements supported by an external force. The Coriolis force twists ascending airflows, leading to the condensation of water vapor into water and the release of latent thermal energy. The negative gradient of the saturated value of specific humidity in the atmosphere is determined by stationary vertical gradients of temperature and pressure. The impact of moisture phase transitions can significantly affect the dynamics of large-scale or averaged fields. To obtain equations for large-scale fields, the multiscale asymptotic expansion method is used. This method identifies the equations for large-scale perturbations by separating them from the hierarchy of perturbations. By using the technique described in the previous sections, the spatial and temporal derivatives in the system (112)-(115) are represented as an expansion (6). The variables $\vec{V}, P, T$ are represented as an asymptotic series (7) and (76). In constructing a nonlinear theory, perturbations of specific water content m are also represented as an asymptotic series.

$$m(x,t) = \frac{1}{R} M_{-1}(X) + m_0(x_0) + Rm_1 + R^2 m_2 + R^3 m_3 + \cdots \tag{116}$$

The algebraic structure of the asymptotic expansion of equations (112)–(115) in various orders R is given in [31]. It is also shown that it is in order R^3 that the main secular equations, or equations for large-scale fields in a moist atmosphere, are obtained:

$$\partial_T W_{-1}^i - \Delta W_{-1}^i + \nabla_k \left(\overline{v_0^k v_0^i} \right) = -\nabla_i \overline{P}_1 \tag{117}$$

$$\partial_T T_{-1} - Pr^{-1} \Delta T_{-1} = -\nabla_k \left(\overline{v_0^k T_0} \right) \tag{118}$$

$$\partial_T M_{-1} - S^{-1} \Delta M_{-1} = -\nabla_k \left(\overline{v_0^k m_0} \right) \tag{119}$$

Equations (117)-(119) are supplemented by the following secular equations:

$$-\nabla_i P_{-3} + \widetilde{Ra} e_i T_{-1} + e_i \widetilde{R}_m M + D\varepsilon_{ijk} W_{-1}^k = 0,\ W_{-1}^k \nabla_k W_{-1}^i = -\nabla_i P_{-1},\ W_{-1}^k \nabla_k T_{-1} = 0$$

$$W_{-1}^k \nabla_k M_{-1} = 0,\ \nabla_i W_{-1}^i = 0,\ W_{-1}^z = 0.$$

These equations are satisfied by large-scale fields of the Beltrami type:

$$\vec{W}_{-1} = \left(W_{-1}^x(Z), W_{-1}^y(Z), 0\right), M_{-1} = M_{-1}(Z), T_{-1} = T_{-1}(Z), P_{-1} = const \tag{120}$$

In the framework of the "quasi-two-dimensional" problem, when large-scale derivatives with Z are preferable

$$\nabla_Z \equiv \frac{\partial}{\partial Z} \gg \frac{\partial}{\partial X}, \frac{\partial}{\partial Y}$$

the system of equations (117)-(119) is simplified and takes the following form:

$$\partial_T W_1 - \nabla_Z^2 W_1 + \nabla_Z \left(\overline{v_0^z v_0^x}\right) = 0, \quad W_1 \equiv W_{-1}^x \tag{121}$$

$$\partial_T W_2 - \nabla_Z^2 W_2 + \nabla_Z \left(\overline{v_0^z v_0^y}\right) = 0, \quad W_2 \equiv W_{-1}^y \tag{122}$$

$$\partial_T T_{-1} - Pr^{-1} \Delta T_{-1} + \nabla_Z \left(\overline{v_0^z T_0}\right) = 0 \tag{123}$$

$$\partial_T M_{-1} - S^{-1} \Delta M_{-1} + \nabla_Z \left(\overline{v_0^z m_0}\right) = 0 \tag{124}$$

The system of equations (121)-(124) describes the evolution of large-scale disturbances in a rotating moist atmosphere within the framework of the condensation heat release model. To study the dynamics of a large-scale vortex field, it is necessary to obtain equations (121)–(122) in a closed form, i.e., to calculate the Reynolds stresses $\nabla_k \left(\overline{v_0^k v_0^i}\right)$. It is clear that in order to solve this problem, it is necessary to find solutions for a small-scale velocity field $\vec{v}_0$.

5.2. Small-scale fields in zero order by R

Let us consider the equations for zero order in R equations (112)-(115)

$$\widehat{D}_0 v_0^i = -\partial_i P_0 + D\varepsilon_{ijk} v_0^j e_k + \widetilde{Ra} e_i T_0 + \widetilde{R}_m e_i m_0 + F_0^i \tag{125}$$

$$\widehat{D}_m m_0 = b e_k v_0^k \tag{126}$$

$$\widehat{D}_\theta T_0 = a e_k v_0^k \tag{127}$$

where the notation for the operators is introduced

$$\widehat{D}_0 = \partial_t - \partial^2 + W_{-1}^k \partial_k, \widehat{D}_m = \partial_t - S^{-1}\partial^2 + W_{-1}^k \partial_k, \widehat{D}_\theta = \partial_t - Pr^{-1}\partial^2 + W_{-1}^k \partial_k.$$

Using the condition of solenoidality of the fields $\vec{v}_0$ and $\vec{F}_0$, we exclude from equation (125) the pressure P_0

$$P_0 = \frac{D\left(\partial_x v_0^y - \partial_y v_0^x\right)}{\partial^2} + \frac{\widetilde{Ra}\partial_z T_0}{\partial^2} + \frac{\widetilde{R}_m \partial_z m_0}{\partial^2} \tag{128}$$

From equations (126)-(127) we find expressions for small-scale temperature T_0 and specific water content m_0:

$$T_0 = \frac{a v_0^z}{\widehat{D}_\theta}, \quad m_0 = \frac{b v_0^z}{\widehat{D}_m}. \tag{129}$$

Putting (129) into (128), we get

$$P_0 = \frac{D\left(\partial_x v_0^y - \partial_y v_0^x\right)}{\partial^2} + \left(\frac{a\widetilde{Ra}}{\partial^2 \widehat{D}_\theta} + \frac{b\widetilde{R}_m}{\partial^2 \widehat{D}_m}\right)\partial_z v_0^z. \tag{130}$$

As a result of substituting (130) into (125), we obtain a system of equations for finding the velocity field of the zero approximation:

$$\begin{cases} \hat{p}_{11}v_0^x + \hat{p}_{12}v_0^y + \hat{p}_{13}v_0^z = F_0^x \\ \hat{p}_{21}v_0^x + \hat{p}_{22}v_0^y + \hat{p}_{23}v_0^z = F_0^y \\ \hat{p}_{31}v_0^x + \hat{p}_{32}v_0^y + \hat{p}_{33}v_0^z = F_0^z \end{cases} \tag{131}$$

The tensor components $\hat{p}_{ij}$ are as follows:

$$\hat{p}_{11} = \hat{D}_0 - D\frac{\partial_x\partial_y}{\partial^2},\ \hat{p}_{12} = D\frac{\partial_x^2}{\partial^2} - D,\ \hat{p}_{13} = \left(\frac{a\widetilde{Ra}}{\hat{D}_\theta} + \frac{b\tilde{R}_m}{\hat{D}_m}\right)\frac{\partial_x\partial_z}{\partial^2},$$

$$\hat{p}_{22} = \hat{D}_0 + D\frac{\partial_x\partial_y}{\partial^2},\ \hat{p}_{23} = \left(\frac{a\widetilde{Ra}}{\hat{D}_\theta} + \frac{b\tilde{R}_m}{\hat{D}_m}\right)\frac{\partial_y\partial_z}{\partial^2},\ \hat{p}_{31} = -D\frac{\partial_z\partial_y}{\partial^2},$$

$$\hat{p}_{21} = -\left(D\frac{\partial_y^2}{\partial^2} - D\right),\ \hat{p}_{32} = D\frac{\partial_z\partial_x}{\partial^2},\ \hat{p}_{33} = \hat{D}_0 + \left(\frac{a\widetilde{Ra}}{\hat{D}_\theta} + \frac{b\tilde{R}_m}{\hat{D}_m}\right)\left(\frac{\partial_z^2}{\partial^2} - 1\right)$$

In equation system (131), we utilize the explicit form of the external helical force F_0, which is determined by expression (25). The small-scale velocity fields (v_0^x, v_0^y, v_0^z) are obtained by applying Cramer's rule to the components of the external helical force, as described in equations (26)-(28). Following similar procedures as in section 2.3, we determine the zero-approximation velocity field in R:

$$u_0 = C_1 e^{i\phi_1} + A_2 e^{i\phi_2} + c.c. = u_{01} + u_{02} + u_{03} + u_{04} \tag{132}$$

$$v_0 = A_1 e^{i\phi_1} - C_2 e^{i\phi_2} + c.c. = v_{01} + v_{02} + v_{03} + v_{04} \tag{133}$$

$$w_0 = -C_1 e^{i\phi_1} + C_2 e^{i\phi_2} + c.c. = w_{01} + w_{02} + w_{03} + w_{04} \tag{134}$$

Here $w_{02} = (w_{01})^*$, $w_{04} = (w_{03})^*$, $v_{02} = (v_{01})^*$, $v_{04} = (v_{03})^*$, $u_{02} = (u_{01})^*$, and new designations are introduced:

$$A_{1,2} = \frac{f_0}{2}\frac{\hat{D}_{1,2}^* - \frac{1}{2}\left(\frac{a\widetilde{Ra}}{\hat{D}_{\theta_{1,2}}^*} + \frac{b\tilde{R}_m}{\hat{D}_{m_{1,2}}^*}\right)}{\hat{D}_{1,2}^*\left(\hat{D}_{1,2}^* - \frac{1}{2}\left(\frac{a\widetilde{Ra}}{\hat{D}_{\theta_{1,2}}^*} + \frac{b\widetilde{R}_m}{\hat{D}_{m_{1,2}}^*}\right)\right) + \frac{D^2}{2}},\ C_{1,2} = \frac{f_0}{4}\frac{D}{\hat{D}_{1,2}^*\left(\hat{D}_{1,2}^* - \frac{1}{2}\left(\frac{a\widetilde{Ra}}{\hat{D}_{\theta_{1,2}}^*} + \frac{b\tilde{R}_m}{\hat{D}_{m_{1,2}}^*}\right)\right) + \frac{D^2}{2}} \tag{135}$$

In contrast to the case of a homogeneous medium examined in Section 2, the small-scale velocity field (132)-(134) is influenced by the temperature gradient, specific water content gradient, and processes related to heat release during vapor condensation. This matter will be further addressed when analyzing the stability of small perturbations of a large-scale velocity field $\vec{W}$.

5.3. Nonlinear vortex dynamo equations and large-scale instability

To close the system of equations (121)-(122) describing the evolution of large-scale velocity fields $\vec{W}$, it is necessary to calculate the correlators of the following form:

$$T^{31} = \overline{w_0 u_0} = \overline{w_{01}(u_{01})^*} + \overline{(w_{01})^* u_{01}} + \overline{w_{03}(u_{03})^*} + \overline{(w_{03})^* u_{03}} \tag{136}$$

$$T^{32} = \overline{w_0 v_0} = \overline{w_{01}(v_{01})^*} + \overline{(w_{01})^* v_{01}} + \overline{w_{03}(v_{03})^*} + \overline{(w_{03})^* v_{03}} \tag{137}$$

Formulas (136), (137) determine the Reynolds stresses, for which we need expressions for small-scale velocity fields (132)-(134). After substituting these expressions into formulas (136)-(137), we find:

$$T^{31} = -2|C_1|^2 + C_2 A_2^* + C_2^* A_2, \qquad T^{32} = -2|C_2|^2 - \left(C_1 A_1^* + C_1^* A_1\right) \tag{138}$$

Substituting expressions (135) into formulas (138), we find expressions for the Reynolds stresses:

$$T^{31}=-\frac{f_0^2}{8}\frac{D^2}{\left|\widehat{D}_1^2+\frac{D^2}{2}-\left(\widetilde{Ra}\frac{a}{2}\frac{\widehat{D}_1}{\widehat{D}_{\theta_1}}+\widetilde{R}_m\frac{b}{2}\frac{\widehat{D}_1}{\widehat{D}_{m_1}}\right)\right|^2}+\frac{f_0^2}{2}D\frac{\left(1-\widetilde{Ra}\frac{a}{2}\frac{Pr^{-1}}{\left|\widehat{D}_{\theta_2}\right|^2}-\widetilde{R}_m\frac{b}{2}\frac{S^{-1}}{\left|\widehat{D}_{m_2}\right|^2}\right)}{\left|\widehat{D}_2^2+\frac{D^2}{2}-\left(\widetilde{Ra}\frac{a}{2}\frac{\widehat{D}_2}{\widehat{D}_{\theta_2}}+\widetilde{R}_m\frac{b}{2}\frac{\widehat{D}_2}{\widehat{D}_{m_2}}\right)\right|^2} \tag{139}$$

$$T^{32}=-\frac{f_0^2}{8}\frac{D^2}{\left|\widehat{D}_2^2+\frac{D^2}{2}-\left(\widetilde{Ra}\frac{a}{2}\frac{\widehat{D}_2}{\widehat{D}_{\theta_2}}+\widetilde{R}_m\frac{b}{2}\frac{\widehat{D}_2}{\widehat{D}_{m_2}}\right)\right|^2}-\frac{f_0^2}{2}D\frac{\left(1-\widetilde{Ra}\frac{a}{2}\frac{Pr^{-1}}{\left|\widehat{D}_{\theta_1}\right|^2}-\widetilde{R}_m\frac{b}{2}\frac{S^{-1}}{\left|\widehat{D}_{m_1}\right|^2}\right)}{\left|\widehat{D}_1^2+\frac{D^2}{2}-\left(\widetilde{Ra}\frac{a}{2}\frac{\widehat{D}_1}{\widehat{D}_{\theta_1}}+\widetilde{R}_m\frac{b}{2}\frac{\widehat{D}_1}{\widehat{D}_{m_1}}\right)\right|^2} \tag{140}$$

As a result, equations (121)-(122) take a closed form. If the properties of the medium are such that the Prandtl $Pr=\frac{\nu}{\chi}$ and Schmidt $S=\frac{\nu}{d}$ numbers are equal to one, we find

$$T^{31}=-\frac{f_0^2}{8}\frac{D^2\left(4+\tilde{W}_1^2\right)}{\left(4+\tilde{W}_1^2\right)\left[16\tilde{W}_1^2+\left[\frac{D^2}{2}+4-\tilde{W}_1^2\right]^2+\frac{\widetilde{R}^2}{4}\right]-\widetilde{R}\left(16-\tilde{W}_1^4\right)-D^2\frac{\widetilde{R}}{2}\left(4-\tilde{W}_1^2\right)}+$$
$$+\frac{f_0^2}{2}\frac{D\left(4+\tilde{W}_2^2-\frac{\widetilde{R}}{2}\right)}{\left(4+\tilde{W}_2^2\right)\left[16\tilde{W}_2^2+\left[\frac{D^2}{2}+4-\tilde{W}_2^2\right]^2+\frac{\widetilde{R}^2}{4}\right]-\widetilde{R}\left(16-\tilde{W}_2^4\right)-D^2\frac{\widetilde{R}}{2}\left(4-\tilde{W}_2^2\right)} \tag{141}$$

$$T^{32}=-\frac{f_0^2}{8}\frac{D^2\left(4+\tilde{W}_2^2\right)}{\left(4+\tilde{W}_2^2\right)\left[16\tilde{W}_2^2+\left[\frac{D^2}{2}+4-\tilde{W}_2^2\right]^2+\frac{\widetilde{R}^2}{4}\right]-\widetilde{R}\left(16-\tilde{W}_2^4\right)-D^2\frac{\widetilde{R}}{2}\left(4-\tilde{W}_2^2\right)}-$$
$$-\frac{f_0^2}{2}\frac{D\left(4+\tilde{W}_1^2-\frac{\widetilde{R}}{2}\right)}{\left(4+\tilde{W}_1^2\right)\left[16\tilde{W}_1^2+\left[\frac{D^2}{2}+4-\tilde{W}_1^2\right]^2+\frac{\widetilde{R}^2}{4}\right]-\widetilde{R}\left(16-\tilde{W}_1^4\right)-D^2\frac{\widetilde{R}}{2}\left(4-\tilde{W}_1^2\right)} \tag{142}$$

In formulas (141)-(142), the following designation is adopted: $\widetilde{R}=aRa+bR_m$. As a rule, in atmospheric convection, the equilibrium gradient of specific water content is small $|B|\ll c|A|$ and taking into account that the expression $\left|\frac{L}{c_p}\right|\gg\left|\frac{\beta_1}{\beta}\right|$ for $\widetilde{R}$ can be represented as a sum $\widetilde{R}=\left(1+L\frac{c}{c_p}\right)Ra=Ra+R_q$, where $Ra=\frac{g\beta A\lambda_0^4}{\nu^2}$ is the Rayleigh number for "dry" convection at $\nu=\chi=d$, $R_q=\frac{g\beta(\gamma_m-\gamma_a)}{\nu^2}$ is a number characterizing the intensity of condensation heat release, and γ_m is a wet adiabatic and $\gamma_a=\frac{g}{c_p}$ is a dry adiabatic gradient related by the relation [19]:

$$\gamma_m=\gamma_a+\frac{L}{c_p}\frac{dq_n}{dz} \tag{143}$$

Please note that when the medium is homogeneous ($\widetilde{Ra}=\widetilde{R}_m=0$), equations (141)-(142) are equivalent to the findings presented in reference [30]. Equations (121)-(122) describe the nonlinear vortex dynamo equations in a humid,

rotating atmosphere with a small external force on a small scale. In case of the disappearance of the rotational effect ($\Omega = 0$) or the external force's amplitude is zero ($f_0 = 0$), the large-scale fields will undergo conventional diffusion spreading.

Initially, we examine the stability of small perturbations, followed by investigating the likelihood of stationary structures. When the $W_{1,2}$ values are small, the Reynolds stresses (141)-(142) can be expanded into a series in $W_{1,2}$, resulting in linearized equations (121)-(122).

$$\partial_T W_1 - \nabla_Z^2 W_1 = \alpha_1 \nabla_Z W_1 - \alpha_2 \nabla_Z W_2 \quad (144)$$

$$\partial_T W_2 - \nabla_Z^2 W_2 = \alpha_1 \nabla_Z W_2 + \alpha_2 \nabla_Z W_1 \quad (145)$$

Here

$$\alpha_1 = \frac{f_0^2}{8} D^2 \alpha \ , \ \alpha_2 = \frac{f_0^2}{2} D \left(\alpha \left(1 - \frac{\widetilde{R}}{10} \right) - \alpha_0 \frac{\widetilde{R}}{25} \right), \quad (146)$$

$$\alpha_0 = \frac{4}{\left(D^2+6\right)^2 + 64 + \widetilde{R}^2 - 12\widetilde{R}\left(1+\frac{D^2}{10}\right)}, \qquad \alpha = \frac{32D^2\left(10 - D^2 + \widetilde{R}\left(1+\frac{D^2}{10}\right) + \frac{3}{50}\widetilde{R}D^2\right)}{\left(\left(D^2+6\right)^2 + 64 + \widetilde{R}^2 - 12\widetilde{R}\left(1+\frac{D^2}{10}\right)\right)^2}.$$

We seek a solution to the linear system of equations (144)-(145) in the form of plane waves with wave vector $\vec{K} \parallel OZ$. This results in a dispersion equation of the form (45). The solutions of this equation demonstrate the existence of unstable oscillatory solutions for large-scale vortex disturbances. It is important to note that the gain α_2 for small amplitudes of large-scale disturbances depends on the amplitude of the external force f_0 (turbulence intensity), the rotation parameter D, and the stratification parameter $\widetilde{R}$, which takes into account the characteristics of Ra "dry" and R_q "wet" convection. To start, we examine how the values of coefficient α_2 change with the parameter $\widetilde{R}$, for a fixed rotation parameter $D = 1$ and external force amplitude $f_0 = 10$. The functional dependence $\alpha_2(\widetilde{R})$ is illustrated in Fig. 13a. The coefficient α_2 value at $\widetilde{R} = 0$ corresponds to a homogeneous medium where the generation of large-scale vortex disturbances is caused by the Coriolis force and the action of an external small-scale force [30]. Fig. 13a illustrates that the presence of temperature stratification ($Ra \neq 0$) and an additional source of condensation heat release ($R_q \neq 0$) can increase the coefficient α_2, resulting in faster generation of large-scale vortex disturbances than in a homogeneous medium. At a critical value of the stratification parameter $\widetilde{R} = \widetilde{R}_0$, the generation of perturbations ceases because $\alpha_2 = 0$. Beyond this point, for $\widetilde{R} > \widetilde{R}_0$, the sign of the gain α_2 changes. The rising mode becomes damped, and vice versa. Additionally, we examine the influence of the medium's rotational effect on the gain or the process of generating large-scale disturbances by fixing the value of parameter $\widetilde{R} = 2$ and the external force amplitude $f_0 = 10$. The functional dependence $\alpha_2(D)$ is illustrated on the right side of Fig. 13. An analysis of the dependence on the rotation parameter $\alpha_2(D)$ reveals that the coefficient $\alpha_2 \to 0$ decreases with "fast" rotation $D \to \infty$, implying that the α -effect is suppressed.

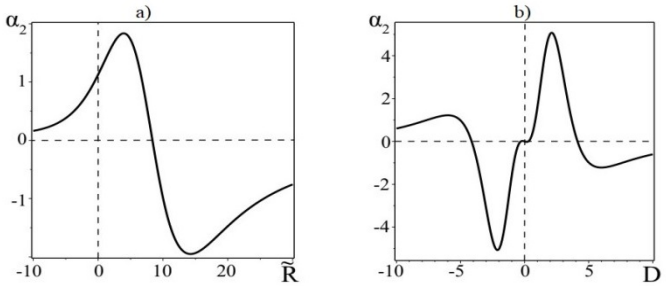

Figure 13. a) Plot of dependence of α - effect on medium stratification parameter $\widetilde{R}$. b) Plot of dependence of α - effect on medium rotation parameter D.

The graph depicting the dependency $\alpha_2(D)$ shows that there are certain parameter D values at which the generation of vortex disturbances ceases ($\alpha_2 = 0$). Fig. 14a illustrates a graphic representation of the combined

influence of rotation and stratification in the plane $(D, \widetilde{R})$, highlighting the region of instability $\alpha_2 > 0$ in gray. The maximum instability increment $\Gamma_{max} = \dfrac{\alpha_2^2}{4}$ is attained at the wavenumbers $K_{max} = \dfrac{\alpha_2}{2}$. The dependence graph (Fig. 14b) of the instability increment Γ on the wavenumbers K has a standard form, typical of the α-effect. As a consequence of the development of large-scale instability in a rotating humid atmosphere, large-scale spiral circularly polarized vortices of the Beltrami type are generated.

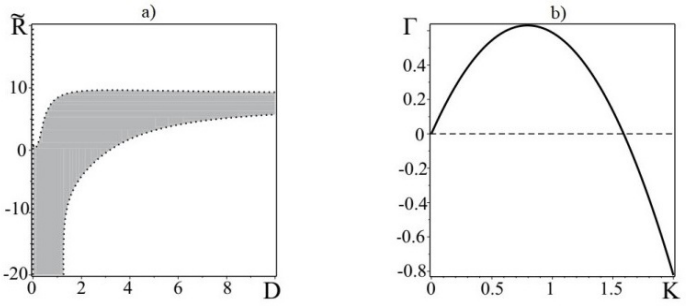

Figure 14. a) The plot illustrates the values of coefficient α_2 in the $(D, \widetilde{R})$ plane, where the area corresponding to unstable solutions (positive values of α_2) is shaded in gray, and the area corresponding to stable solutions (negative values of α_2) is shown in white. b) The plot shows the dependence of instability increment on wavenumbers K for parameters $D = 1$, $\widetilde{R} = 2$ and $f_0 = 10$.

In conclusion to this section, we can estimate the typical spatial $L_{max} \sim 1/\alpha_2$ and time $T_{max} \sim 1/\alpha_2^2$ scales of the unstable mode and its growth under the conditions of the hydrodynamic α-effect in a rotating moist atmosphere. To achieve this, we calculate the coefficient α_2 using the standard characteristics of atmospheric turbulence, such as the characteristic velocity $v_0 \approx 0.1$ in m/s, the scale of fluctuations $\lambda_0 \approx 10^3$ in meters, and the turbulent viscosity $\nu \approx 10^5$ in m/s, as described in references [5] and [18].

Hence the characteristic time of turbulent pulsations $t_0 = \lambda_0^2/\nu \approx 10$ s and the value of the rotation parameter $D = 2\Omega\lambda_0^2/\nu \approx 1.4 \cdot 10^{-3}$ (the angular velocity of the Earth's rotation $\Omega \approx 7 \cdot 10^{-5}$ s^{-1}) and the Reynolds number $R = v_0\lambda_0/\nu \approx 10^{-3}$. Let's compare the dimensionless parameters D, Ra, R_m with respect to the Reynolds number R:

$$D/R > 1, Ra/R = \beta A \cdot 10^6 > 1, R_m/R = \beta_1 B \cdot 10^6 > 1,$$

which is consistent with the asymptotic expansion scheme used here. The smallness of the rotation parameter D makes it possible to neglect the terms of order D^2 when estimating the coefficient α_2

$$\alpha_2 = \frac{f_0^2}{2} D\kappa, \tag{147}$$

where the value of $\kappa \approx 4.5 \cdot 10^{-2}$ is calculated according to formulas (146) for the stratification parameter $\widetilde{R} = 5$.

Let us express the hydrodynamic helicity $\alpha_v = (t_0/3)\overline{v_0 rot v_0}$ (see, for example, [11]) in terms of the dimensionless source amplitude:

$$\alpha_v = \frac{t_0 v_0^2}{3\lambda_0} f_0^2, \tag{148}$$

Here f_0 is the dimensionless amplitude of the external force included in formula (147). When deriving this formula, it is assumed that there is a balance between the source and dissipation, which corresponds to the stationary case. Substituting (148) into (147), we find expressions for the characteristic spatial and temporal scales:

$$\begin{aligned} L_{max} &\approx \frac{2}{3}\frac{\alpha_v D\kappa}{v_0 R} = 106 \text{ km}, \\ T_{max} &\approx \frac{4}{9}\frac{t_0 v_0^2 R^2}{\alpha_v^2 D^2 \kappa^2} = 1.3 \text{ days}. \end{aligned} \tag{149}$$

Here, the hydrodynamic helicity coefficient $\alpha_v \approx 10^{-2}$ m/s was considered [5]. Thus, quite acceptable estimates (149) of the characteristic scales of instability have been obtained, which can explain the origin of the large-scale spiral structure of cloudy mesovortices and typhoons at the initial stage of development.

5.4. Stationary nonlinear vortex structures

Clearly, with an increase in the amplitude of perturbations $W_{1,2}$, the nonlinear terms decrease and the instability saturates. As a result, nonlinear vortex structures are formed. Next, we put $\partial_T = 0$ in equations (121)-(122) and integrate the equations once over Z, and we get a system of nonlinear equations of the following form:

$$\frac{d\tilde{W}_1}{dZ} = -\frac{D^2\frac{f_0^2}{8}\left(4+\tilde{W}_1^2\right)}{\left(4+\tilde{W}_1^2\right)\left[16\tilde{W}_1^2+\left[\frac{D^2}{2}+4-\tilde{W}_1^2\right]^2+\frac{\tilde{R}^2}{4}\right]-\tilde{R}\left(16-\tilde{W}_1^4\right)-D^2\frac{\tilde{R}}{2}\left(4-\tilde{W}_1^2\right)}+$$
$$+\frac{D\frac{f_0^2}{2}\left(4+\tilde{W}_2^2-\frac{\tilde{R}}{2}\right)}{\left(4+\tilde{W}_2^2\right)\left[16\tilde{W}_2^2+\left[\frac{D^2}{2}+4-\tilde{W}_2^2\right]^2+\frac{\tilde{R}^2}{4}\right]-\tilde{R}\left(16-\tilde{W}_2^4\right)-D^2\frac{\tilde{R}}{2}\left(4-\tilde{W}_2^2\right)}+C_1 \quad (150)$$

$$\frac{d\tilde{W}_2}{dZ} = -\frac{D^2\frac{f_0^2}{8}\left(4+\tilde{W}_2^2\right)}{\left(4+\tilde{W}_2^2\right)\left[16\left(1-\tilde{W}_2\right)^2+\left[\frac{D^2}{2}+4-\tilde{W}_2^2\right]^2+\frac{\tilde{R}^2}{4}\right]-\tilde{R}\left(16-\tilde{W}_2^4\right)-D^2\frac{\tilde{R}}{2}\left(4-\tilde{W}_2^2\right)}-$$
$$-\frac{D\frac{f_0^2}{2}\left(4+\tilde{W}_1^2-\frac{\tilde{R}}{2}\right)}{\left(4+\tilde{W}_1^2\right)\left[16\tilde{W}_1^2+\left[\frac{D^2}{2}+4-\tilde{W}_1^2\right]^2+\frac{\tilde{R}^2}{4}\right]-\tilde{R}\left(16-\tilde{W}_1^4\right)-D^2\frac{\tilde{R}}{2}\left(4-\tilde{W}_1^2\right)}+C_2 \quad (151)$$

Here, C_1, C_2 are arbitrary constants of integration. Let us now find out what types of stationary vortex structures are described by the system of equations (150)-(151). Let's start a qualitative analysis of the system of equations (150)-(151), assuming for simplicity of calculations that the dimensionless parameters are $f_0 = D = 1$, $\tilde{R} = 2$.

For a given set of values of the parameters, the phase portrait of equations (150)-(151) can be determined based on the constants C_1 and C_2. It has been established using standard methods that the system of equations has four fixed points in the region shown in Fig. 15. No fixed points exist outside of this region, and degenerate cases are observed on the boundary, resulting in two fixed points. When the parameter values D are slightly modified, the region of existence of four fixed points is slightly deformed, altering its size and shape. Linearizing the vector field (150)-(151) in the neighborhood of the fixed points for the values of constants C_1 and C_2 (as shown in Fig. 15) where there are four fixed points, we can determine the type of fixed points. For four fixed points, two are hyperbolic, and the remaining two are stable and unstable focus. The position and type of the fixed points are used to construct the phase portrait of the system (150)-(151). The phase portrait enables us to describe all possible stationary vortex solutions qualitatively. Fig. 16 illustrates the phase portrait of the system of equations (150)-(151). The most interesting localized solutions are those that correspond to the phase portrait trajectories connecting fixed points on the phase plane. For instance, a separatrix linking a hyperbolic singular point with a stable focus corresponds to a solution for a localized kink-type vortex structure with rotation.

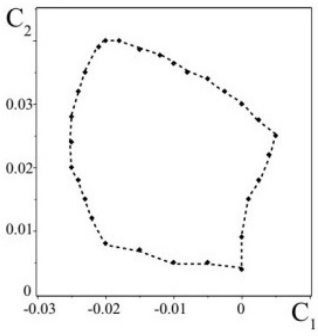

Figure 15. The boundary of the parameter region (C_1, C_2) in the phase portrait is marked by the dashed line. Within this region, there are two hyperbolic fixed points, as well as a stable and an unstable focus. Outside of this region, there are no fixed points. This area was constructed numerically for a value of $f_0 = D = 1$, $\tilde{R} = 2$.

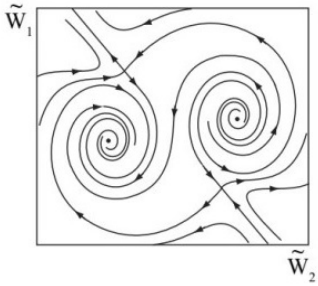

Figure 16. Phase portrait of the system of equations (150)-(151) at $f_0 = D = 1$, $\tilde{R} = 2$, $C_1 = -0.01$ and $C_2 = 0.01$. One can see the presence of two hyperbolic singular points and stable and unstable foci.

Fig. 17a illustrates the solution obtained through numerical integration. It corresponds to a spiral kink of one type. Another type of spiral kink is represented by the solution in Fig. 17b, for which the separatrix on the phase plane connects the unstable and stable focus. These solutions result in large-scale localized vortex structures, including kinks with rotation, which are produced by the instability of the α -effect.

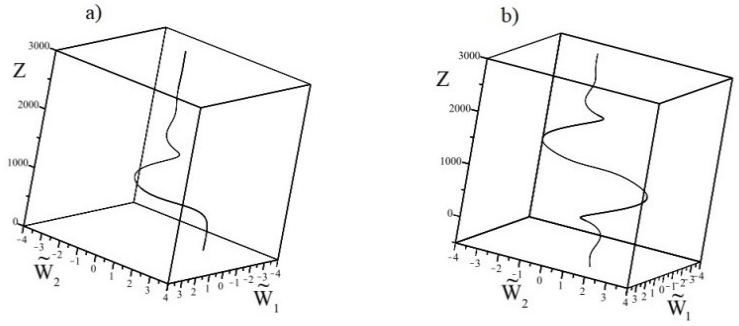

Figure 17. a) The image displays a kink that connects a hyperbolic point with a stable focus. As the stable focus is approached, the velocity field exhibits rotations. b) The picture illustrates the kink connecting the unstable and stable focus. It shows the internal helical structure of the kink. These solutions were obtained using the parameters: $f_0 = D = 1$, $\tilde{R} = 2$ and $C_1 = -0.01$, $C_2 = 0.01$.

6. VORTEX DYNAMO IN A ROTATING MOIST ATMOSPHERE WITH A SMALL-SCALE NON-HELICAL FORCE

This section presents the findings of a study conducted in [35] on a large-scale instability in a rotating stratified humid atmosphere subjected to a small-scale non-helical force. The previous section explored helical turbulence. Helical turbulence in natural conditions is typically attributed to the influence of the Coriolis force on the previously uniform, isotropic, and mirror-symmetric (non-spiral) turbulent motion of the medium. This raises a question about the origin of helicity itself. The natural hypothesis is that helicity arises due to the Coriolis force acting on convective turbulence. In this scenario, large-scale instabilities in the atmosphere should emerge self-consistently, without additional assumptions.

The turbulence in reference [35] was simulated by utilizing an external small-scale force that had no helicity $\vec{F}_0 rot\vec{F}_0 = 0$ and induced velocity fluctuations with a low Reynolds number $R = \dfrac{v_0 t_0}{\lambda_0} \ll 1$. Additionally, the medium's rotation axis was assumed to deviate from the vertical direction. The authors employed the method of multiscale asymptotic expansions and derived the equations of a nonlinear vortex dynamo. The study investigated linear instability and stationary nonlinear regimes and resulted in the discovery of localized vortex structures, namely nonlinear Beltrami waves and kinks.

6.1. Closed equations for large-scale vortex fields

We utilize equations (112)-(115) in the Boussinesq approximation with an external non-helical force $\vec{F}_0$ to describe the generation of large-scale vortex structures, such as tropical cyclones. This approach differs from the method used in Section 5, which involved a helical force as the source of turbulence for a vortex dynamo in a moist atmosphere (see Fig. 18).

Instead, we use an external non-helical force of the form (49) with properties (50). To understand how the small-scale motions created by this non-helical force influence the dynamics of large-scale perturbations, we apply the method of multiscale asymptotic expansion. The algebraic structure of the asymptotic expansion of equations (112)-(115) in different orders in is presented in [35]. By considering the third order of the asymptotic expansion in the Reynolds number R, we obtain the basic equations for the evolution of the vortex field in “quasi-two-dimensional” geometry, which take the form (121)-(124).

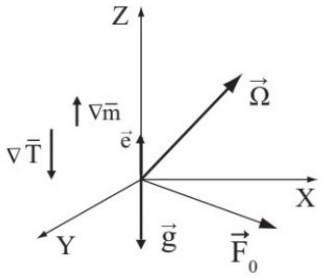

Figure 18. The angular velocity $\vec{\Omega}$ is inclined with respect to the plane (X,Y) in which the external force $\vec{F}_0$ is located.

To derive these equations in a closed form, it is necessary to calculate the Reynolds stresses $\nabla_k\left(\overline{v_0^k v_0^i}\right)$ by first obtaining solutions for a small-scale velocity field $\vec{v}_0$. It is important to note that this velocity field will differ from the one found in Section 5.2 for two reasons. Firstly, because a non-helical external force is being considered, and secondly, because all projections of the Coriolis force (oblique rotation) are taken into account. To reflect this difference, the term $D\varepsilon_{ijk}v_0^j e_k$ in equation (125) is replaced with $\varepsilon_{ijk}v_0^j D_k$. By performing the same mathematical operations as in Section 5.2, we obtain the zero approximation velocity field:

$$u_0 = \frac{f_0}{2}\frac{\widehat{A}_2^*}{\widehat{A}_2^*\widehat{D}_2^* + D_2^2}e^{i\phi_2} + c.c. = u_{03} + u_{04} \tag{152}$$

$$v_0 = \frac{f_0}{2}\frac{\widehat{A}_1^*}{\widehat{A}_1^*\widehat{D}_1^* + D_1^2}e^{i\phi_1} + c.c. = v_{01} + v_{02} \tag{153}$$

$$w_0 = -\frac{f_0}{2}\frac{D_1}{\widehat{A}_1^*\widehat{D}_1^* + D_1^2}e^{i\phi_1} + \frac{f_0}{2}\frac{D_2}{\widehat{A}_2^*\widehat{D}_2^* + D_2^2}e^{i\phi_2} + c.c. = w_{01} + w_{02} + w_{03} + w_{04} \tag{154}$$

where

$$\widehat{A}_{1,2}^* = \widehat{D}_{1,2}^* - \frac{a\widetilde{Ra}}{\widehat{D}_{\theta_{1,2}}^*} - \frac{b\widetilde{R}_m}{\widehat{D}_{m_{1,2}}^*} \tag{155}$$

This indicates that the component of the rotation parameter D_3 is eliminated due to the choice of an external force of the form (49). The resulting small-scale velocity field $\vec{v}_0$ (152)-(154) has a non-trivial topology due to the rotation of the medium, which gives rise to the topological characteristic of helicity $\mathrm{H} = \overline{\vec{v}_0 rot\vec{v}_0}$. Helicity is a measure of the "knotting" of the field lines of force [5]. We will now demonstrate that an external force without helicity $\vec{F}_0 rot\vec{F}_0 = 0$, when combined with the Coriolis force, generates an average helicity $\mathrm{H} \neq 0$. In coordinate representation, the average helicity is defined as follows:

$$\mathrm{H} = \overline{u_0\frac{\partial w_0}{\partial y}} - \overline{w_0\frac{\partial u_0}{\partial y}} + \overline{w_0\frac{\partial v_0}{\partial x}} - \overline{v_0\frac{\partial w_0}{\partial x}},$$

or after substituting formulas (152)-(154)

$$\mathrm{H} = 2i(u_{04}w_{03} - u_{03}w_{04} + w_{02}v_{01} - v_{02}w_{01}) = \frac{if_0^2}{2}\cdot\left(\frac{D_2(\widehat{A}_2 - \widehat{A}_2^*)}{\left|\widehat{A}_2\widehat{D}_2 + D_2^2\right|^2} + \frac{D_1(\widehat{A}_1 - \widehat{A}_1^*)}{\left|\widehat{A}_1\widehat{D}_1 + D_1^2\right|^2}\right).$$

For the Prandtl and Schmidt numbers $\mathrm{Pr} = S = 1$, the average helicity H takes the form:

$$\mathrm{H} = -f_0^2\cdot\left(\frac{D_1(1+\tilde{W}_1^2+\widetilde{R})}{(1+\tilde{W}_1^2)\left((1+\tilde{W}_1^2)^2 + 2(D_1^2-\widetilde{R})(1-\tilde{W}_1^2) + (D_1^2-\widetilde{R})^2\right)} + \right.$$

$$\left. + \frac{D_2(1+\tilde{W}_2^2+\widetilde{R})}{(1+\tilde{W}_2^2)\left((1+\tilde{W}_2^2)^2 + 2(D_2^2-\widetilde{R})(1-\tilde{W}_2^2) + (D_2^2-\widetilde{R})^2\right)}\right) \tag{156}$$

Reynolds stresses are calculated by formulas (136)-(137), using expressions (152)-(155) we obtain

$$T^{31} = \frac{f_0^2}{4}\frac{D_2(\hat{A}_2 + \hat{A}_2^*)}{\left|\hat{A}_2\hat{D}_2 + D_2^2\right|^2}, \qquad T^{32} = -\frac{f_0^2}{4}\frac{D_1(\hat{A}_1 + \hat{A}_1^*)}{\left|\hat{A}_1\hat{D}_1 + D_1^2\right|^2} \tag{157}$$

If the properties of the medium are such that the Prandtl number Pr and the Schmidt number S are equal to one, then the expressions for the Reynolds stress components will be simplified:

$$T^{31} = \frac{f_0^2}{2}D_2\frac{(1+\tilde{W}_2^2-\widetilde{R})}{(1+\tilde{W}_2^2)((1+\tilde{W}_2^2)^2+2(D_2^2-\widetilde{R})(1-\tilde{W}_2^2)+(D_2^2-\widetilde{R})^2)} \tag{158}$$

$$T^{32} = -\frac{f_0^2}{2}D_1\frac{(1+\tilde{W}_1^2-\widetilde{R})}{(1+\tilde{W}_1^2)((1+\tilde{W}_1^2)^2+2(D_1^2-\widetilde{R})(1-\tilde{W}_1^2)+(D_1^2-\widetilde{R})^2)}, \tag{159}$$

where $\widetilde{R} = aRa + bR_m$.

As a result, the equations for the components of the large-scale velocity field $\vec{W}$ take a closed form:

$$(\partial_T - \nabla_Z^2)\tilde{W}_1 = \frac{f_0^2}{2}D_2\nabla_Z\left[\frac{1+\tilde{W}_2^2-\widetilde{R}}{(1+\tilde{W}_2^2)((1+\tilde{W}_2^2)^2+2(D_2^2-\widetilde{R})(1-\tilde{W}_2^2)+(D_2^2-\widetilde{R})^2)}\right] \tag{160}$$

$$(\partial_T - \nabla_Z^2)\tilde{W}_2 = -\frac{f_0^2}{2}D_1\nabla_Z\left[\frac{1+\tilde{W}_1^2-\widetilde{R}}{(1+\tilde{W}_1^2)((1+\tilde{W}_1^2)^2+2(D_1^2-\widetilde{R})(1-\tilde{W}_1^2)+(D_1^2-\widetilde{R})^2)}\right] \tag{161}$$

Equations (160)-(161) represent the equations of a nonlinear vortex dynamo in a rotating stratified moist atmosphere with a small-scale non-helical force. It is important to note that this vortex dynamo effect occurs only in a turbulent medium that is undergoing rotation. Equations (160)-(161) have a similar form to equations (98)-(99), except that the stratification parameter in equations (160)-(161) contains the parameters of both dry and wet convection: $\widetilde{R} = \left(1 + L\frac{c}{c_p}\right)Ra = Ra + R_q$. When there is no rotation ($\Omega = 0$) or external force ($F_0 = 0$), the large-scale fields are dampened by viscous dissipation. In the limit of a dry atmosphere $R_q = 0$, equations (160)-(161) are identical to equations (98)-(99), and in the limit of a homogeneous fluid $\widetilde{R} = 0$, equations (160)-(161) are identical to equations (60) when $f_0 = 1$.

6.2. Large scale instability

Let us consider the initial stage of the evolution of vortex disturbances $W_{1,2}$. Then, for small perturbations (W_1, W_2), expression (156) can be linearized:

$$H = H_{01} + H_{02} - f_0^2 2D_1 \cdot \frac{(-D_1^2 + \widetilde{R} + 2)(\widetilde{R}+2) + \frac{\widetilde{R}}{4}(4 + (D_1^2 - \widetilde{R})^2)}{(4 + (D_1^2 - \widetilde{R})^2)^2} \cdot W_1 -$$

$$-f_0^2 2D_2 \cdot \frac{(-D_2^2 + \widetilde{R} + 2)(\widetilde{R}+2) + \frac{\widetilde{R}}{4}(4 + (D_2^2 - \widetilde{R})^2)}{(4 + (D_2^2 - \widetilde{R})^2)^2} \cdot W_2,$$

where $H_{01} + H_{02}$ is the constant average helicity of the small-scale field for very small perturbations $(W_1, W_2) \to 0$:

$$H_{01} + H_{02} = -\frac{f_0^2}{2}\left(D_1 \cdot \frac{\widetilde{R}+2}{4 + (D_1^2 - \widetilde{R})^2} + D_2 \cdot \frac{\widetilde{R}+2}{4 + (D_2^2 - \widetilde{R})^2}\right) \tag{162}$$

This indicates that the helicity of a velocity field on a small scale in a moist atmosphere that is rotating is influenced by both the Coriolis force and an external force that lacks helicity. As a result, the rotation of the medium produces helicity and suggests the emergence of a hydrodynamic α-effect, which is responsible for creating large-scale vortices. When the values are small $W_{1,2}$, equations (160)-(161) become linearized, reducing to the following set of linear equations:

$$\begin{cases} \partial_T W_1 - \nabla_Z^2 W_1 - \alpha_2 \nabla_Z W_2 = 0 \\ \partial_T W_2 - \nabla_Z^2 W_2 + \alpha_1 \nabla_Z W_1 = 0 \end{cases} \tag{163}$$

where the following notation is introduced for the coefficients

$$\alpha_1 = -2H_{01}\left[\frac{(D_1^2 - \widetilde{R} - 2)(2 - \widetilde{R}) + \frac{\widetilde{R}}{4}(4 + (D_1^2 - \widetilde{R})^2)}{(\widetilde{R} + 2)(4 + (D_1^2 - \widetilde{R})^2)}\right],\ \alpha_2 = -2H_{02}\left[\frac{(D_2^2 - \widetilde{R} - 2)(2 - \widetilde{R}) + \frac{\widetilde{R}}{4}(4 + (D_2^2 - \widetilde{R})^2)}{(\widetilde{R} + 2)(4 + (D_2^2 - \widetilde{R})^2)}\right] \tag{164}$$

The above statement suggests that the amplification coefficients $\alpha_{1,2}$ consist of a fixed average helicity $H_{01,02}$. Equations (163) bear a resemblance to the equations used to describe vortex dynamos in media that have helical turbulence [5]. In order to analyze the large-scale instability that is described by the system of equations (163), we opt to use perturbations in the form of plane waves that have a wave vector $\vec{K} \| OZ$, which can be represented as $W_{1,2} \sim \exp(-i\omega t + iKZ)$. By applying this approach to the system of equations (163), we derive the dispersion equation.

$$\left(-i\omega + K^2\right)^2 - \alpha_1 \alpha_2 K^2 = 0 \tag{165}$$

Representing $\omega = \omega_0 + i\Gamma$, from equation (165) we find

$$\Gamma = Im\omega = \pm\sqrt{\alpha_1 \alpha_2}\, K - K^2 \tag{166}$$

The solutions presented in (166) demonstrate that large-scale vortex disturbances exhibit instability when $\alpha_1 \alpha_2 > 0$. On the other hand, if $\alpha_1 \alpha_2 < 0$, damped oscillations with frequency $\omega_0 = \sqrt{\alpha_1 \alpha_2}\, K$ are observed instead of instabilities. Positive feedback between the velocity components is established through the projections of the Coriolis force, facilitated by the coefficients α_1 and α_2. It is worth noting that in the linear theory being discussed here, the coefficients α_1 and α_2 are independent of the field amplitudes but rather depend on the rotation parameters $D_{1,2}$, the total Rayleigh number $\widetilde{R}$, and the amplitude of the external force f_0. When examining the coefficients α_1 and α_2, it is convenient to switch from Cartesian projections to their projections in the spherical coordinate system (D, φ, θ), where the coordinate surface $D = const$ represents a sphere, with θ representing latitude ($\theta \in [0, \pi]$) and φ representing longitude ($\phi \in [0, 2\pi]$). In this case, the rotation parameters D_1 and D_2 in the amplification coefficients of vortex disturbances α_1 and α_2 are

$$D_1 = D\sin\theta\cos\varphi, \quad D_2 = D\sin\theta\sin\varphi.$$

By setting the rotation parameter D, the stratification parameter $\widetilde{R}$, and the amplitude of the external force f_0 to fixed values, we can determine the relationship between the gain and the latitude θ and longitude φ (as shown in Figure 19).

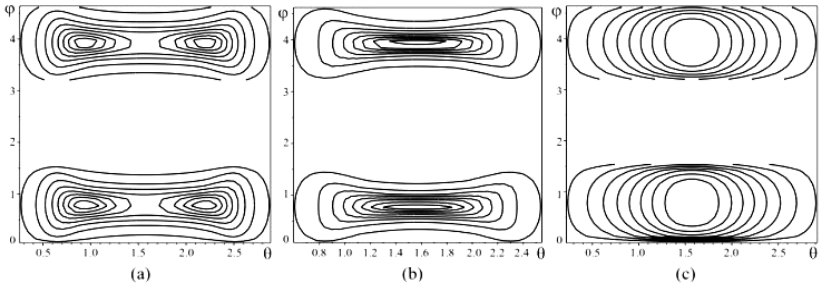

Figure 19. Contour plot for gain α versus longitude φ and latitude θ with increasing stratification parameters: *a*) $\widetilde{R} = 3$; *b*) $\widetilde{R} = 5$; *c*) $\widetilde{R} = 15$. The calculations were carried out for $D = 2$ and $f_0 = 10$.

Figure 19 indicates that as the stratification parameter $\widetilde{R}$ increases, the maximum gain α shifts towards the equator (latitude $\theta = \pi/2$) and longitude $\varphi = \pi/4$. It is less effective to generate large-scale vortex disturbances at the poles ($\theta = 0, \theta = \pi$) (where $\alpha \to 0$), which is consistent with meteorological observations [4], [8] that indicate the absence of large-scale cyclones at the Earth's poles. Subsequent calculations will focus on latitude $\theta = \pi/2$ and

longitude $\varphi = \pi/4$ Next, we will examine the impact of the medium rotation D on the gain α or the process of generating large-scale perturbations by setting the value of the number $\widetilde{R} = 5$.

On the left side of Fig. 20a it is shown that at a certain value of the rotation parameter D, the coefficient α reaches its maximum value $\alpha_{\max}$. Further, as the number D increases, the coefficient α gradually tends to zero, i.e., the α-effect is suppressed. The dependence of the coefficient α on the medium stratification parameter $\widetilde{R}$ at a fixed value of the number $D = 3$ is also shown in Fig. 20. The case of a homogeneous medium $\widetilde{R} = 0$ is shown in Fig. 20b, where the generation of large-scale vortex disturbances is due to the action of an external small-scale non-helical force and the Coriolis force [32]. From Fig. 20c we see that the presence of stratification for "dry" and "wet" convection ($\widetilde{R} \neq 0$) can lead to a significant increase in the coefficient α and, as a result, faster generation of large-scale vortex disturbances than in a homogeneous medium. Further, with an increase in the Rayleigh numbers $\widetilde{R}$, a decrease in the values of the coefficient α is observed. Fig. 21 is a graph showing the combined effect of rotation and stratification in the $(D, \widetilde{R})$ plane. Here, the region of instability $\alpha > 0$ is highlighted in grey. The graph of the dependence (see the right side of Fig. 21) of the instability increment Γ on the wave numbers K has a standard form, typical for the α-effect.

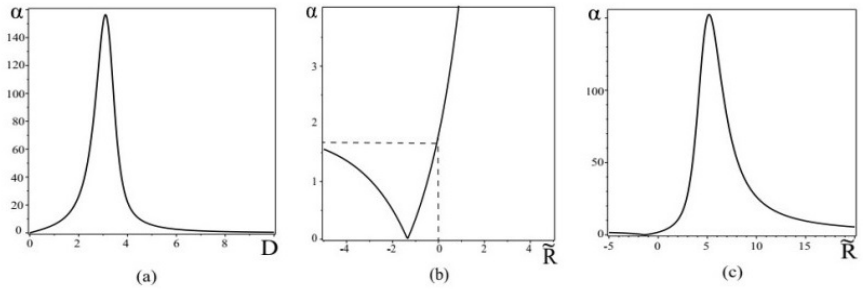

Figure 20. a) plot of the dependence of the α-effect on medium rotation parameter D; b) the graph shows the value in the case of a homogeneous medium $\widetilde{R} = 0$; c) plot of the α-effect versus the medium stratification parameter $\widetilde{R}$. The calculations were carried out for $f_0 = 10$.

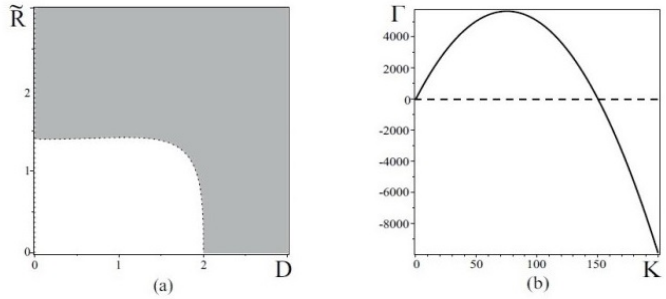

Figure 21. On the left is a graph for α in the $(D, \widetilde{R})$ plane, where the area corresponding to positive values of α (unstable solutions) is shown in grey and the area corresponding to negative values of α is shown in white; on the right is a graph of the dependence of the instability increment Γ on the wave numbers K for the parameters $D = 3$, $\widetilde{R} = 5$.

6.3. Stationary nonlinear vortex structures

It is evident that the exponential growth of small perturbations $W_{1,2}$ resulting from the development of large-scale instability eventually saturates. This is attributed to the emergence of nonlinear effects, which weaken the coefficient of the nonlinear α-effect ($\alpha \sim 1/W_{1,2}^4$) and increase the amplitude of perturbations. Consequently, nonlinear vortex structures are formed. To search for stationary structures, we substitute into equations (160)-(161) $\partial_T = 0$ and integrate these equations once over Z. We focus on the case of the maximum value of α_{max}, where latitude $\theta = \pi/2$ and longitude $\varphi = \pi/4$ This results in a system of nonlinear equations in the following form:

$$\frac{d\tilde{W}_1}{dZ} = -f_0^2 D\sqrt{2}\,\frac{1+\tilde{W}_2^2-\widetilde{R}}{(1+\tilde{W}_2^2)(4(1+\tilde{W}_2^2)^2+4(D^2-2\widetilde{R})(1-\tilde{W}_2^2)+(D^2-2\widetilde{R})^2)} + C_1 \tag{167}$$

$$\frac{d\tilde{W}_2}{dZ} = f_0^2 D\sqrt{2}\,\frac{1+\tilde{W}_1^2-\widetilde{R}}{(1+\tilde{W}_1^2)(4(1+\tilde{W}_1^2)^2+4(D^2-2\widetilde{R})(1-\tilde{W}_1^2)+(D^2-2\widetilde{R})^2)} + C_2 \tag{168}$$

Here C_1, C_2 are arbitrary constants of integration. Note that the dynamic system of equations (167)-(168) is conservative and therefore Hamiltonian. It is easy to find it by writing equations (167)-(168) in the Hamiltonian form:

$$\frac{\mathrm{d}\widetilde{W}_1}{\mathrm{d}Z} = -\frac{\mathrm{d}H}{\mathrm{d}\widetilde{W}_2}, \quad \frac{\mathrm{d}\widetilde{W}_2}{\mathrm{d}Z} = \frac{\mathrm{d}H}{\mathrm{d}\widetilde{W}_1}$$

where the Hamiltonian H has the form:

$$\mathrm{H} = H_1(\widetilde{W}_1) + H_2(\widetilde{W}_2) + C_2\widetilde{W}_1 - C_1\widetilde{W}_2 \tag{169}$$

the functions $\mathrm{H}_{1,2}$ are

$$\mathrm{H}_{1,2} = f_0^2 D\sqrt{2}\int \frac{(1+\tilde{W}_{1,2}^2 - \tilde{R})\mathrm{d}\tilde{\mathrm{W}}_{1,2}}{(1+\tilde{W}_{1,2}^2)(4(1+\tilde{W}_{1,2}^2)^2 + 4(D^2-2\tilde{R})(1-\tilde{W}_{1,2}^2) + (D^2-2\tilde{R})^2)}$$

The integral in the Hamiltonian $\mathrm{H}_{1,2}$ is not calculated exactly in quadratures, so we calculate it for fixed rotation parameters $D = \sqrt{10}$ and stratification $\widetilde{R} = 5$, which were used in the linear theory. Under these conditions, Hamiltonian (169) takes the form:

$$\mathrm{H} = -\frac{25}{4}\sqrt{5}\left(\frac{\widetilde{W}_1(11\widetilde{W}_1^2+21)}{(\widetilde{W}_1^2+1)^2} + \frac{\widetilde{W}_2(11\widetilde{W}_2^2+21)}{(\widetilde{W}_2^2+1)^2} + 11(arctg\widetilde{W}_1 + arctg\widetilde{W}_2)\right) + C_2\widetilde{W}_1 - C_1\widetilde{W}_2$$

After performing a qualitative analysis of the system of equations (167)-(168), we found that only two types of fixed points can be observed in the phase space: elliptic and hyperbolic fixed points. By linearizing the right-hand side of equations (167)-(168) in the vicinity of fixed points, we determined their type and constructed a phase portrait. Through this analysis, we identified the presence of four fixed points, two of which are hyperbolic and two are elliptic. The phase portrait of the dynamic system of equations (167)-(168) for constants $C_1 = -0.05$, $C_2 = 0.05$ and parameters $D = \sqrt{10}$, $\widetilde{R} = 5$ and $f_0 = 10$ is displayed in Fig. 22. This figure shows the existence of closed trajectories on the phase plane around elliptic points and separatrices that link hyperbolic points. The closed trajectories correspond to nonlinear periodic solutions or nonlinear waves, while the separatrices correspond to localized kink-type vortex structures (as depicted in Fig. 23).

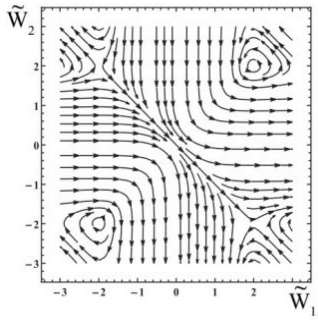

Figure 22. Phase plane for the dynamic system of equations (167)-(168) under the conditions $C_1 = -0.05$ and $C_2 = 0.05$. Here you can see the presence of closed trajectories around elliptical points and separatrices that connect hyperbolic points.

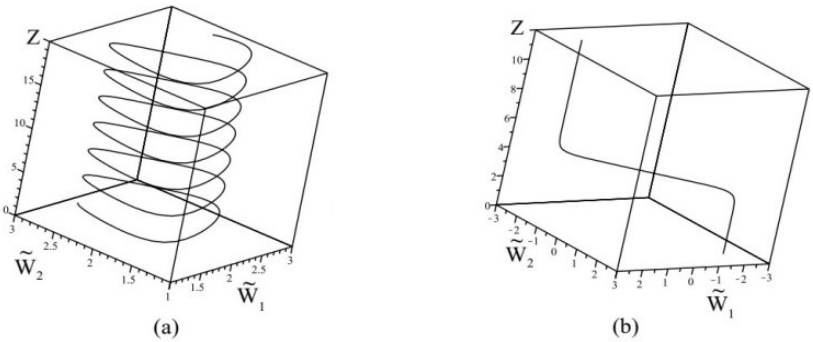

Figure 23. On the left is a non-linear spiral wave that corresponds to a closed trajectory on the phase plane; on the right is a localized non-linear vortex structure (kink), which corresponds to a separatrix on the phase plane.

7. VORTEX DYNAMO IN AN OBLIQUELY ROTATING STRATIFIED NANOFLUID WITH A SMALL-SCALE NON-HELICAL FORCE

An important factor to consider is the impact of small particles present in the hydrodynamic medium, which is of interest due to its prevalence in both technological and natural environments. The presence of nanoparticles in the medium results in what is commonly referred to as a nanofluid. One issue that arises with nanofluids is the generation of large-scale structures, which is discussed in this section based on the results of a study (reference [36]). The study revealed the occurrence of a large-scale instability in an obliquely rotating stratified nanofluid, caused by an external small-scale non-helical force. Nonlinear equations for large-scale motions were obtained using a method of multiscale asymptotic expansions, and a linear large-scale instability was examined as a function of rotation parameters D, temperature stratification $\widetilde{Ra}$, and nanoparticle concentration $\widetilde{R}_n$. The study also discovered a new effect of LSVS generation in a nanofluid associated with an increase in nanoparticle concentration. This effect resulted in the formation of circularly polarized Beltrami vortices. The saturation mode of the large-scale instability was studied, and a dynamic system of equations for large-scale perturbations of the velocity field was obtained in the stationary regime. Numerical solutions of this system of equations were found, which showed the existence of localized vortex structures in the form of nonlinear Beltrami waves and kinks.

7.1. Equations and Statement of the Problem

The system being considered is an infinite horizontal layer of an incompressible nanofluid that undergoes constant rotation at a fixed angular velocity $\vec{\Omega} = (\Omega_1, \Omega_2, \Omega_3)$, with inclination in relation to the (X, Y) plane, as illustrated in Fig. 24.

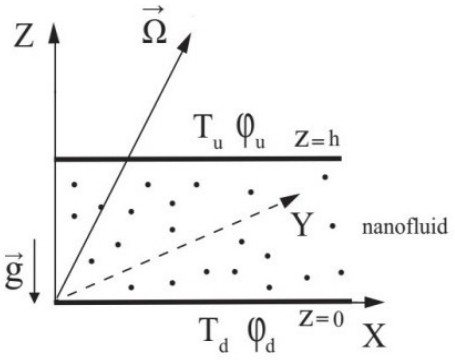

Figure 24. The angular velocity $\vec{\Omega}$ is inclined with respect to the plane (X, Y) in which the external force $\vec{F}_{0\perp}$ is located.

The nanofluid is contained between two parallel planes, $z = 0$ and $z = h$, where the temperature and volume fraction of nanoparticles remain constant:

$$\begin{aligned} T = T_d, \phi = \phi_d \quad &\text{при} \quad z = 0, \\ T = T_u, \phi = \phi_u \quad &\text{при} \quad z = h, \end{aligned} \tag{170}$$

at $T_d > T_u, \phi_u > \phi_d$. Both boundary surfaces are assumed to be free. The hydrodynamic equations governing the behavior of a viscous, incompressible, rotating nanofluid under the Boussinesq approximation are given by the following expressions (as seen, for instance, in references [40]-[41]):

$$\rho_{00}\left(\frac{\partial \vec{V}}{\partial t} + \vec{V}\cdot\nabla\vec{V}\right) = -\nabla P + \mu\nabla^2\vec{V} + [\phi\rho_p + (1-\phi)\rho_{00}(1-\beta(T-T_u))]\vec{g} + 2\rho_{00}\vec{V}\times\vec{\Omega} + \vec{F}_0 \tag{171}$$

$$(\rho c)_f\left(\frac{\partial T}{\partial t} + \vec{V}\cdot\nabla T\right) = k_f\nabla^2 T + (\rho c)_p\left(D_B\nabla\phi\cdot\nabla T + D_T\frac{\nabla T\cdot\nabla T}{T_u}\right) \tag{172}$$

$$\frac{\partial \phi}{\partial t} + \vec{V}\cdot\nabla\phi = D_B\nabla^2\phi + \frac{D_T}{T_u}\nabla^2 T \tag{173}$$

$$\nabla\vec{V} = 0 \tag{174}$$

Equations (171)-(174) are accompanied by boundary conditions for the velocity of the nanofluid. The vertical impermeability condition of the layer boundaries and the absence of tangential stresses at these boundaries result in the following boundary conditions for the velocity:

$$V_z = 0, \quad \frac{\partial^2 V_z}{dz^2} = 0, \quad \text{при} \quad z = 0, h \tag{175}$$

Here, $\rho_{00} = \phi\rho_p + (1-\phi)\rho_f$ is the density of the nanofluid at the control temperature T_u, ρ_p is the density of the nanoparticles, ρ_f is the density of the base fluid at the temperature T_u, ϕ is the volume fraction of the nanoparticles, and β is the coefficient of thermal expansion. The unit vector $\vec{e} = (0,0,1)$ is directed towards the positive Z axis. Gravity is directed vertically downwards $\vec{g} = (0,0,-g)$; $(\rho c)_f, (\rho c)_p$ is the effective heat capacity of the base fluid and nanoparticles; D_B - Brownian diffusion coefficient, D_T - thermophoretic diffusion coefficient. The signs of the coefficients and are positive, and they are respectively equal:

$$D_B = \frac{k_B T}{3\pi\mu d_p}, \quad D_T = \left(\frac{\mu_f}{\rho_f}\right)\left(\frac{0.26k_f}{2k_f + k_p}\right),$$

where d_p is the diameter of the nanoparticles, k_B is the Boltzmann constant, k_f, k_p is the thermal conductivity of the base fluid and nanoparticles, and μ_f is the viscosity of the base fluid. Equation (171) includes an external force $\vec{F}_0$, which simulates an excitation source in the medium of small-scale and high-frequency fluctuations of the velocity field with a small Reynolds number $R = \frac{v_0 t_0}{\lambda_0} \ll 1$, where λ_0 is the characteristic scale, t_0 is the characteristic time. Let us pass in equations (171)-(174) and boundary conditions (170), (175) to dimensionless variables, which we denote by an asterisk (*):

$$(x^*, y^*, z^*) = \frac{(x,y,z)}{h}, \vec{V} = (V_x^*, V_y^*, V_z^*) = (V_x, V_y, V_z)\frac{h}{\chi_f}, t^* = \frac{t \cdot \chi_f}{h^2}, P^* = \frac{P \cdot h^2}{\chi_f \mu},$$

$$\vec{\Omega}^* = \frac{\vec{\Omega}}{\Omega_0}, \phi^* = \frac{\phi - \phi_d}{\phi_u - \phi_d}, T^* = \frac{T - T_u}{T_d - T_u}, F_0^* = F_0 \frac{h^3}{\chi_f \mu}, \chi_f = \frac{k_f}{(\rho c)_f}.$$

Omitting the asterisk (*) in the system of dimensionless equations (176)-(179) and boundary conditions (180), we get

$$\frac{1}{\mathrm{Pr}}\left(\frac{\partial \vec{V}}{\partial t} + \vec{V}\cdot\nabla\vec{V}\right) = -\nabla P + \nabla^2\vec{V} - \vec{e}R_n\phi - \vec{e}R_m + \vec{e}RaT + \sqrt{Ta}(\vec{V}\times\vec{\Omega}) + \vec{F}_0 \tag{176}$$

$$\frac{\partial T}{\partial t} + \vec{V}\cdot\nabla T = \nabla^2 T + \frac{N_B}{L_e}(\nabla\phi\cdot\nabla T) + \frac{N_A N_B}{L_e}(\nabla T\cdot\nabla T) \tag{177}$$

$$\frac{\partial \phi}{\partial t} + \vec{V}\cdot\nabla\phi = \frac{1}{L_e}\nabla^2\phi + \frac{N_A}{L_e}\nabla^2 T \tag{178}$$

$$\nabla\cdot\vec{V} = 0 \tag{179}$$

$$\begin{aligned} &T_d = 1, \phi_d = 0, V_z = \frac{\partial^2 V_z}{\partial z^2} = 0 \quad \text{при} \quad z = 0, \\ &T_u = 0, \phi_u = 1, V_z = \frac{\partial^2 V_z}{\partial z^2} = 0 \quad \text{при} \quad z = 1, \end{aligned} \tag{180}$$

where $\mathrm{Pr} = \mu/\rho_{00}\chi_f$ is the Prandtl number, $R_n = (\rho_p - \rho_f)(\phi_u - \phi_d)gh^3/\mu\chi_f$ is the concentration Rayleigh number, $R_m = (\rho_p\phi_d + \rho_f(1-\phi_d)gh^3/\mu\chi_f$ is the Rayleigh number of the base density, $Ra = (T_d - T_u)\rho_{00}g\beta h^3/\mu\chi_f$ is the Rayleigh number, $Ta = 4\Omega_0^2 h^4\rho_{00}^2/\mu^2$ is the Taylor number, $L_e = \chi_f/D_B$ is the Lewis number, $N_B = (\phi_u - \phi_d)\cdot\frac{(\rho c)_p}{(\rho c)_f}$ is the coefficient characterizing the increase in the density of nanoparticles, and $N_A = D_T(T_d - T_u)/D_B T_u(\phi_u - \phi_d)$ is the modified diffusion coefficient. Let us represent all the quantities in equations (176)-(179) as the sum of the ground (stationary) state and the perturbed one:

$$\vec{V} = \vec{V}', T = T_b(z) + T', \phi = \phi_b(z) + \phi', P = P_b(z) + P'. \tag{181}$$

After substituting (181) into equations (176)-(179), we find the evolution equations for the perturbed quantities $\vec{V}', T', \phi'$:

$$\frac{1}{\mathrm{Pr}}\left(\frac{\partial \vec{V}'}{\partial t} + \vec{V}'\cdot\nabla\vec{V}'\right) = -\nabla P' + \nabla^2\vec{V}' - \vec{e}R_n\phi' + \vec{e}RaT' + \sqrt{Ta}(\vec{V}'\times\vec{\Omega}) + \vec{F}_0$$

$$\frac{\partial T^{'}}{\partial t}+\vec{V}^{'}\cdot\nabla T^{'}+V_z^{'}\frac{dT_b}{dz}=\nabla^2 T^{'}+\frac{N_B}{L_e}(\nabla\phi^{'}\cdot\nabla T^{'})+\frac{N_B}{L_e}\left(\frac{d\phi_b}{dz}\frac{dT^{'}}{dz}+\frac{d\phi^{'}}{dz}\frac{dT_b}{dz}\right)+$$
$$+\frac{N_A N_B}{L_e}(\nabla T^{'}\cdot\nabla T^{'})+\frac{2N_A N_B}{L_e}\frac{dT^{'}}{dz}\frac{dT_b}{dz} \tag{182}$$
$$\frac{\partial\phi^{'}}{\partial t}+\vec{V}^{'}\cdot\nabla\phi^{'}+V_z^{'}\frac{d\phi_b}{dz}=\frac{1}{L_e}\nabla^2\phi^{'}+\frac{N_A}{L_e}\nabla^2 T^{'}$$

against the background of the main equilibrium state, set by constant gradients of temperature and volume fraction of nanoparticles:

$$0=-\frac{dP_b}{dz}-R_m-R_n\phi_b+RaT_b$$
$$0=\frac{d^2T_b}{dz^2}+\frac{N_B}{L_e}\left(\frac{d\phi_b}{dz}\frac{dT_b}{dz}\right)+\frac{N_A N_B}{L_e}\left(\frac{dT_b}{dz}\right)^2 \tag{183}$$
$$0=\frac{d^2\phi_b}{dz^2}+N_A\frac{d^2T_b}{dz^2}.$$

Using boundary conditions (180), from equations (183) we find solutions for $T_b=1-z$ and $\phi_b=z$, which have a linear dependence on z.

Let the external force $\vec{F}_0$ have the form (49) and satisfy the properties (50). The simple physical form of the external force (49) can be easily implemented in laboratory experiments. Let us rescale the variables in the equations for perturbations (182):

$$\vec{x}\to\frac{\vec{x}}{\lambda_0},\ t\to\frac{t}{t_0},\ \vec{V}\to\frac{\vec{V}^{'}}{v_0},\ P\to\frac{P^{'}}{p_0},\ F_0\to\frac{F_0}{f_0},\ T\to\frac{T^{'}}{R},\ \phi\to\frac{\phi^{'}}{R},\ \frac{p_0t_0}{\lambda_0 v_0}=\frac{f_0t_0}{v_0}=\frac{t_0}{\lambda_0^2}=1.$$

As a result, we obtain the following system of equations for perturbations:

$$\frac{1}{\mathrm{Pr}}\left(\frac{\partial\vec{V}}{\partial t}+R\vec{V}\cdot\nabla\vec{V}\right)=-\nabla P+\nabla^2\vec{V}-\vec{e}\,\widetilde{R}_n\phi+\vec{e}\,\widetilde{Ra}T+\vec{V}\times\vec{D}+\vec{F}_0 \tag{184}$$

$$\frac{\partial T}{\partial t}+R\vec{V}\cdot\nabla T-V_z=\nabla^2 T+R\frac{N_B}{L_e}(\nabla\phi\cdot\nabla T)+\frac{N_B}{L_e}\left(\frac{dT}{dz}-\frac{d\phi}{dz}\right)+ \tag{185}$$

$$+R\frac{N_A N_B}{L_e}(\nabla T\cdot\nabla T)-\frac{2N_A N_B}{L_e}\frac{dT}{dz}$$

$$\frac{\partial\phi}{\partial t}+R\vec{V}\cdot\nabla\phi+V_z=\frac{1}{L_e}\nabla^2\phi+\frac{N_A}{L_e}\nabla^2 T \tag{186}$$

where new designations are introduced

$$D=\frac{2h^2}{\mu}\rho_{00}\lambda_0^2\Omega,\quad \widetilde{R}_n=R_n\cdot\lambda_0^3,\quad \widetilde{Ra}=Ra\cdot\lambda_0^3.$$

In equations (184)-(186), we treat the Reynolds number $R=\frac{v_0t_0}{\lambda_0}\ll 1$ as a small parameter for the purpose of asymptotic expansion, while considering the other parameters $D,\widetilde{R}_n,\widetilde{Ra}$ as arbitrary and not impacting the expansion scheme. An external force acting on the equilibrium state results in small-scale and high-frequency velocity oscillations. Although the average values of these oscillations are zero, nonlinear interactions generate terms in certain orders of the perturbation theory that do not cancel out upon averaging.

7.2. Large scale instability

By employing the method of multiscale asymptotic expansions in the context of the "quasi-two-dimensional" problem, we derived a closed system of equations for the large-scale velocity field $\vec{W}$. This system has the form of equations (80)-(81), and the expressions for the Reynolds stress components at $Pr=1$ are given by:

$$T^{31}=\frac{f_0^2 D_2 k_0^2 (k_0^4+\widetilde{\omega}_2^2-\widetilde{Ra}-l_{n_2})}{2(k_0^4+\widetilde{\omega}_2^2)((k_0^4+\widetilde{\omega}_2^2)^2+2(D_2^2-\widetilde{Ra})(k_0^4-\widetilde{\omega}_2^2)+(D_2^2-\widetilde{Ra})^2+r_{n_2}(k_0^4+\widetilde{\omega}_2^2)+2p_{n_2}D_2^2)},$$

$$T^{32}=-\frac{f_0^2 D_1 k_0^2 (k_0^4+\widetilde{\omega}_1^2-\widetilde{Ra}-l_{n_1})}{2(k_0^4+\widetilde{\omega}_1^2)((k_0^4+\widetilde{\omega}_1^2)^2+2(D_1^2-\widetilde{Ra})(k_0^4-\widetilde{\omega}_1^2)+(D_1^2-\widetilde{Ra})^2+r_{n_1}(k_0^4+\widetilde{\omega}_1^2)+2p_{n_1}D_1^2)}, \quad (187)$$

where $\widetilde{\omega}_{1,2}=\omega_0-k_0W_{1,2}$. The expressions for the coefficients $l_{n_{1,2}}$, $p_{n_{1,2}}$, $r_{n_{1,2}}$ have a very cumbersome form and are given in [36].

When the amplitude (W_1,W_2) is small, the nonlinear equations for $\vec{W}$ can be approximated by linear vortex dynamo equations similar to system (100). The solutions of this linear system describe circularly polarized plane waves, known as Beltrami waves. The amplitude of these waves grows exponentially over time. The large-scale velocity field satisfies the Beltrami flow, which satisfies the following condition:

$$\vec{W}\times rot\vec{W}=0$$

To determine the conditions under which a large-scale vortex instability occurs, we first examine the dependence of the amplification α_{nf} on the angle θ of inclination of the axis of rotation of the nanofluid. The solid line in Fig. 25 represents this dependence for fixed values of

$$D=2,\widetilde{Ra}=2,k_0=\omega_0=1,\mathrm{Pr}=5,\widetilde{R}_n=0.122,N_A=5,L_e=5000.$$

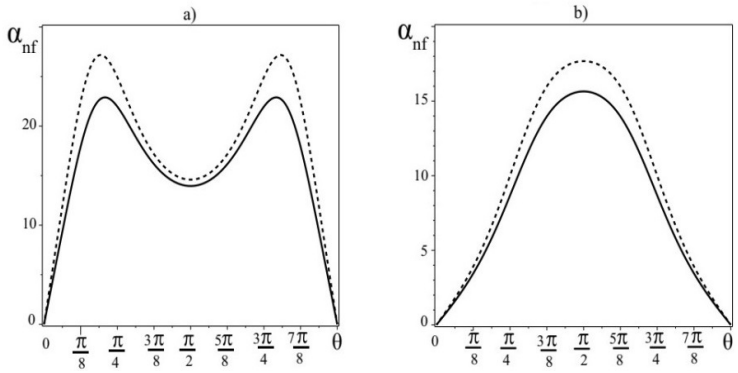

Figure 25. The solid line shows the dependence of the gain α_{nf} for a nanofluid on the angle of inclination θ, and the dashed line shows the dependence of the gain α_b for a pure fluid on the angle of inclination θ. Graphs a) are built for the Prandtl number $\mathrm{Pr}=5$, and graphs b) for $\mathrm{Pr}=1$.

The values of the nanofluid parameters $\mathrm{Pr},\widetilde{R}_n,N_A,L_e$ (Al_2O_3-water) are taken from [40]. As can be seen from Fig. 25a, the maximum value α_{nf} for a nanofluid is the angle of inclination $\theta_{max}\approx\pi/5+\pi n$, and the minimum value is $\theta_{min}\approx\pi/2+\pi n$. The dashed line in Fig. 25a corresponds to the dependence $\alpha_b(\theta)$ in the case of a "pure" fluid with the Prandtl number $\mathrm{Pr}=5$. The graphs in Fig. 25a show that the maximum amplification coefficient $\alpha_b=(\alpha_{nf})_{\widetilde{R}_n=0}$ for a "pure" fluid is greater than that for a nanofluid. The same conclusion remains valid for the Prandtl numbers $\mathrm{Pr}=1$. In this case, the maximum gains in nano- and "pure" fluids are at the deflection angles $\theta\approx\pi/2+\pi n$ (see Fig. 25b). Hence, it follows that the characteristic time T_{nf} and characteristic scale L_{nf} of large-scale vortices generated in a nanofluid exceed the corresponding scales T_b,L_b in a "pure" fluid:

$$T_{nf}\gg T_b,\quad L_{nf}\gg L_b,T_{nf}\approx(\alpha_{nf}^2/4)^{-1},L_{nf}\approx(\alpha_{nf}/2)^{-1},T_b\approx(\alpha_b^2/4)^{-1},L_b\approx(\alpha_b/2)^{-1}$$

Let us consider the influence of the nanofluid rotation effect on the amplification factor α_{nf} or the process of large-scale vortex generation. For these purposes, we fix the nanofluid parameters $\mathrm{Pr},\widetilde{R}_n,N_A,L_e$, and the Rayleigh number $\widetilde{Ra}=2$.

The incline angle chosen is $\theta_{max}\approx0.645\sim\pi/5$, which corresponds to the maximum values of the gain (see Fig. 26a). As can be seen from Fig. 26a, at a certain value of the rotation parameter D, the coefficient $\alpha_{nf}(\alpha_b)$

reaches its maximum value $\alpha_{\max}^{(nf,b)}$. Further, as the number D increases, the gains gradually tend to zero, i.e., the α -effect is suppressed.

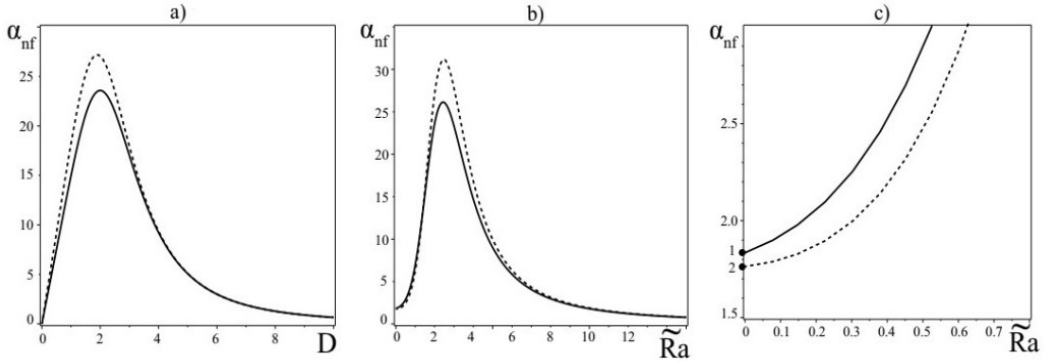

Figure 26. a) The solid line shows the dependence of the gain α_{nf} for a nanofluid on the rotation parameter D, and the dashed line shows the dependence of the gain α_b for a pure fluid on the rotation parameter D; b) The solid line shows the dependence of the gain α_{nf} for a nanofluid on the Rayleigh number $\widetilde{Ra}$, and the dashed line shows the dependence of the gain α_b for a "pure" fluid on the Rayleigh number $\widetilde{Ra}$; c) Point 1 corresponds to the value α_{nf} (nanofluid) at $\widetilde{Ra} = 0$, and Point 2 corresponds to the value α_b ("pure" fluid) at $\widetilde{Ra} = 0$.

Further, fixing the nanofluid parameters $\mathrm{Pr}, \widetilde{R}_n, N_A, L_e$, rotation $D = 2$ and tilt angle $\theta_{max} \approx 0.645$, we determine the dependence of the coefficient α_{nf} on the Rayleigh number $\widetilde{Ra}$. It can be seen from Fig. 26b that the maximum value of the gain $\alpha_{nf}(\alpha_b)$ corresponds to small Rayleigh numbers $\widetilde{Ra}$. Large-scale vortices are efficiently generated in the range of Rayleigh numbers $\widetilde{Ra} \in [0,3]$; this means that at high Rayleigh numbers $\widetilde{Ra}$, large-scale instability does not occur in nano- and ordinary fluids, but ordinary convective instability arises. Under the condition when there is no heating $\widetilde{Ra} = 0$, the amplification factor in pure fluid α_b (point 2 in Fig. 26c) is less than that in nanofluid α_{nf} (point 1 in Fig. 26c): $\alpha_{nf} > \alpha_b$. On Figs. 26a-26b it is also observed that the maximum gain $\alpha_b = (\alpha_{nf})_{\widetilde{R}_n=0}$ for a "pure" liquid is greater than that for a nanofluid. On Fig. 27a is a graph showing the combined effect of rotation and temperature stratification in the $(D, \widetilde{Ra})$ plane. Here, the region of instability $\alpha_{nf} > 0$ is highlighted in grey. Curve 1 corresponds to the instability boundary for a nanofluid ($\widetilde{R}_n = 0.122$), and curve 2 corresponds to the instability boundary for a pure fluid ($\widetilde{R}_n = 0$).

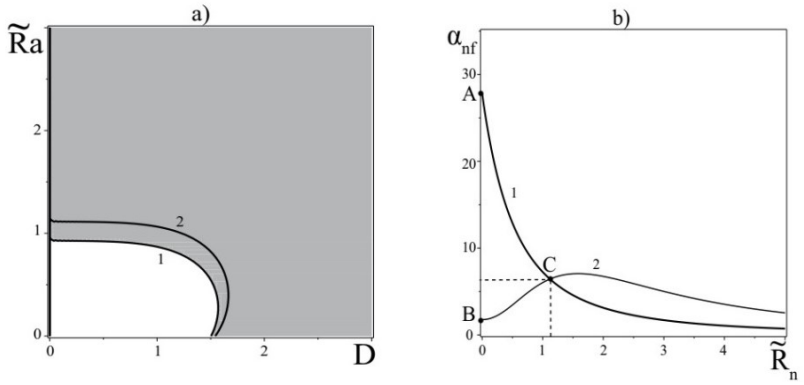

Figure 27. a) Plot α_{nf} in the plane $(D, \widetilde{Ra})$, where the area corresponding to positive values α_{nf} (unstable solutions) is shown in grey and negative values are shown in white. Curve 1 corresponds to the instability boundary for a nanofluid ($\widetilde{R}_n = 0.122$), and curve 2 corresponds to the instability boundary for a pure fluid ($\widetilde{R}_n = 0$). b) A graph of the α_{nf}-effect versus the Rayleigh concentration number $\widetilde{R}_n$.

Now let's analyze the influence of the Rayleigh concentration number $\widetilde{R}_n$ on the gain or generation of the LSVS for the following fixed parameters: $D = 2, \widetilde{Ra} = 3, k_0 = \omega_0 = 1, \mathrm{Pr} = 5, N_A = 5, L_e = 5000, \theta \approx 0.645$. On Fig. 27b, the intersection of the graphs (curve 1 and curve 2) is at point $C(\widetilde{R}_n^{(0)}, \alpha_{nf}^{(0)})$. Curve 1 is constructed for the case when there

is a temperature gradient $\widetilde{Ra} = 3$. At $\widetilde{R}_n = 0$, curve 1 shows the maximum value α_b^{st} (point A) which corresponds to a "pure" stratified fluid. A further increase in the concentration of nanoparticles leads to a decrease in α_{nf}. Curve 2 is plotted for the case when there is no temperature gradient. It can be seen from the behaviour of curve 2 that an increase in the concentration of nanoparticles first leads to an increase α_{nf} and then to a decrease. At $\widetilde{R}_n = 0$, curve 2 shows the maximum value α_b^h (point B) corresponding to the amplification factor for a homogeneous fluid [32]. Here we see that in a "pure" stratified fluid, the generation of LSVSs is more efficient than in a homogeneous fluid, which is consistent with the conclusions of [34]. Thus, at a certain value of the number $\widetilde{R}_n^{(0)}$ (the concentration of nanoparticles), we obtain equal rates of LSVS generation (point C in Fig. 27b) in the nanofluid both with $\widetilde{Ra} \neq 0$ and without a temperature gradient $\widetilde{Ra} = 0$. Physically, this process can be explained as follows. An increase in the concentration of nanoparticles on the upper surface layer leads to the appearance of a flow due to the gravitational segregation of nanoparticles on the lower surface. In turn, in the presence of a temperature gradient, a heat flux $\vec{q} \sim \vec{e}(T_d - T_u)/h$ arises that prevents the nanoparticles from settling on the lower surface layer. With an increase in the concentration of nanoparticles $\widetilde{R}_n$, a decrease in the proportion of heat flux occurs and, as a result, a decrease in the gain α_{nf}. On the charts in Fig. 28, the dependence of the instability increment Γ on the wave numbers K for the hydrodynamic α_{nf}-effect in a nanofluid at constant parameters $D = 2, \widetilde{Ra} = 2, \mathrm{Pr} = 5, \widetilde{R}_n = 0.122, N_A = 5, L_e = 5000, \theta \approx 0.645$ is shown.

As can be seen from Fig. 28a, with an increase in the frequency ω_0 of the external force F_0 at $k_0 = 1$, the maximum growth rate Γ_{max} of large-scale vortex disturbances decreases. Fixing the frequency of the external force at $\omega_0 = 1$, we plot the growth rate (see Fig. 28b) as the small-scale wavenumber k_0 changes. For numbers $k_0 < 1$, one can observe both an increase in the maximum growth rate Γ_{max} of large-scale vortex disturbances ($k_0 = 0.8$) relative to the level Γ_{max} at $k_0 = 1$, and a decrease in the maximum growth rate of large-scale vortex disturbances at $k_0 = 0.5$. This behavior is due to the structural dependence of the coefficient α_{nf} on small-scale parameters of the external force (ω_0, k_0).

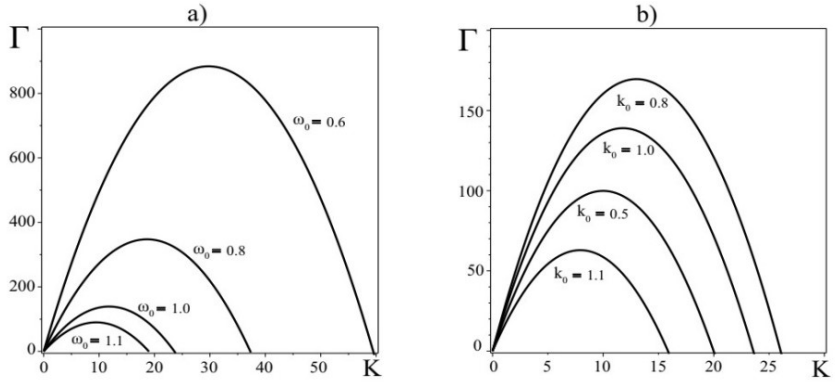

Figure 28. a) Plot of the dependence of the instability increment Γ on the wave numbers for different frequencies ω_0 of the external force $\vec{F}_0$ at $k_0 = 1$. b) Plot of the dependence of the instability increment Γ on the wave numbers K for different wave numbers k_0 of the external force $\vec{F}_0$ at $\omega_0 = 1$.

7.3. Instability saturation and nonlinear structures

An increase in W_1 and W_2 leads to saturation of the instability. As a result of the development and stabilization of the instability, nonlinear structures arise. In the stationary case, these structures are described by nonlinear equations in the Hamiltonian form

$$\frac{\mathrm{d}W_1}{\mathrm{d}Z} = \frac{\mathrm{d}H}{\mathrm{d}W_2}, \quad \frac{\mathrm{d}W_2}{\mathrm{d}Z} = -\frac{\mathrm{d}H}{\mathrm{d}W_1} \tag{188}$$

where the Hamiltonian H has the form:

$$H = H_1(W_1) + H_2(W_2) + C_2 W_1 - C_1 W_2$$

and the functions $H_{1,2}$ are

$$H_{1,2} = \frac{f_0^2\sqrt{2}}{4} D\sin\theta \int \frac{k_0^2(k_0^4 + \widetilde{\omega}_{1,2}^2 - \widetilde{Ra} - l_{n_{1,2}})\mathrm{d}W_{1,2}}{2\,\mathrm{Pr}(k_0^4 + \widetilde{\omega}_2^2)\Lambda_{1,2}}. \tag{189}$$

The integral in the Hamiltonian $H_{1,2}$ is not calculated exactly in quadratures. We used the values of nanofluid parameters $\mathrm{Pr} = 1, \widetilde{R}_n = 0.122, N_A = 5, L_e = 5000$ (Al_2O_3-water) [40]. As a result of the analysis of nonlinear equations, four fixed points were found, two of which are of the hyperbolic type and two of the elliptic type.

The figure in Fig. 29 depicts the phase portrait of a dynamic system of equations, which bears resemblance to equations (104)-(105), given certain constants $C_1 = -0.005$ and $C_2 = 0.005$ parameters $D = \widetilde{Ra} = 2$, $k_0 = \omega_0 = 1$, $f_0 = 10$. Through the phase portrait, we can qualitatively describe potential stationary solutions. Of particular interest are localized solutions that can be found in the phase portrait trajectories connecting fixed (singular) points on the phase plane. As shown in Fig. 29, closed trajectories are present on the phase plane surrounding elliptical points and separatrices that link hyperbolic points. Nonlinear periodic solutions, such as nonlinear waves, correspond to closed trajectories, while localized kink-type vortex structures (as seen in Fig. 30) correspond to separatrices.

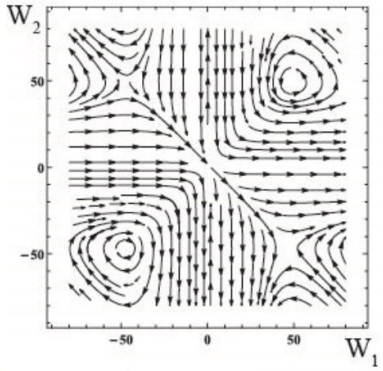

Figure 29. Phase plane of the dynamic system of equations (188) for constants $C_1 = -0.05$ and $C_2 = 0.05$. Here you can see the presence of closed trajectories around elliptical points and separatrices that connect hyperbolic points.

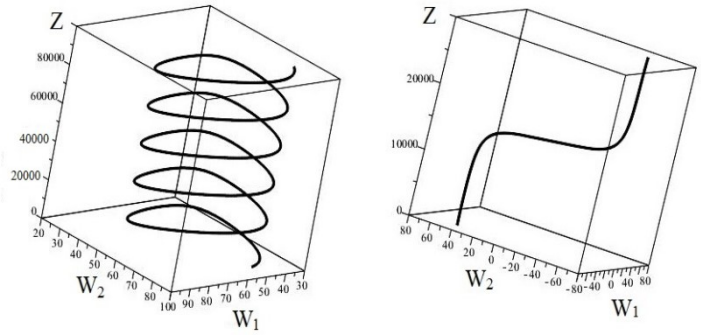

Figure 30. On the left is a non-linear spiral wave that corresponds to a closed trajectory on the phase plane; on the right is a localized non-linear vortex structure (kink), which corresponds to a separatrix on the phase plane.

8. CONCLUSIONS

The review paper presents the theoretical findings of the authors [30]-[36] in the area of vortex dynamo in rotating media. The focus is on the mechanisms behind the generation of large-scale vortex structures resulting from both non-helical external forces and the Coriolis force. A comprehensive analysis of closed systems of nonlinear equations describing the linear and nonlinear stages of the growth of large-scale vortex flows in rotating turbulent media has been conducted. The authors have obtained reasonable estimates of the characteristic scales of instability in a rotating moist atmosphere, which can explain the formation of the large-scale spiral structure of cloudy mesovortices and typhoons at the initial stage of their development. A promising direction in the development of the vortex dynamo theory for rotating nanofluid media containing floating microorganisms. For these media, the theory of large-scale instability can also be developed using the asymptotic method of multiscale expansions. We can anticipate the discovery of new large-scale stationary vortex structures in rotating porous media saturated with nanofluids. The investigation of these structures is not only useful for geophysical applications but also for a variety of technological problems.

ORCID IDs
Michael I. Kopp, https://orcid.org/0000-0001-7457-3272, **Volodymyr V. Yanovsky,** https://orcid.org/0000-0003-0461-749X

REFERENCES

[1] H. P. Greenspan, *The Theory of Rotating Fluids* (Cambridge University Press, 1968).
[2] V.I. Petviashvili, and O.A. Pohkotelov, *Solitary Waves in Plasmas and in the Atmosphere* (London, 1992). https://doi.org/10.4324/9781315075556
[3] M.Ya. Marov, and A.V. Kolesnichenko, *Turbulence and Self-Organization. Modeling Astrophysical Objects* (Springer, New York, 2013). https://doi.org/10.1007/978-1-4614-5155-6
[4] A.S. Monin, *Theoretical Geophysical Fluid Dynamics* (Springer Dordrecht, 1990). https://doi.org/10.1007/978-94-009-1880-1
[5] Anatoli Tur, and Vladimir Yanovsky, *Coherent Vortex Structures in Fluids and Plasmas* (Springer, 2017). https://doi.org/10.1007/978-3-319-52733-8
[6] M.V. Nezlin, and E.N. Snezhkin, *Rossby Vortices, Spiral Structures, Solitons* (Springer Series in Nonlinear Dynamics, 1993).
[7] A.M. Fridman, and A.V. Khoperskov, *Physics of Galactic Disks* (Cambridge International Science Publishing, 2013).
[8] A.S. Monin, *An Introduction to the Theory of Climate* (Springer Dordrecht, 1986). https://doi.org/10.1007/978-94-009-4506-7
[9] O. Onishchenko, V. Fedun, W. Horton et al., "The stationary concentrated vortex model", Climate, **9**, 39-52 (2021). https://doi.org/10.3390/cli9030039
[10] M. Steenbeck, F. Krause, and K.H. Rädler, "Berechnung der mittleren Lorentz Feldstärke $\overline{\vec{v}\times\vec{b}}$ für ein elektrisch leitendes Medium in turbulenter, durch Coriolis-Kräfte beeinfluß ter Bewegung", Z. Naturforsch **21**, 369-376 (1966). https://doi.org/10.1515/zna-1966-0401
[11] S.M. Tobias, "The turbulent dynamo", J. Fluid Mech. **912**, P1 (2021). https://doi.org/10.1017/jfm.2020.1055
[12] F. Rincon, "Dynamo theories", J. Plasma Phys. **85**, 205850401 (2019) https://doi.org/10.1017/S0022377819000539
[13] S.S. Moiseev, R.Z. Sagdeev, A.V. Tur, G.A. Khomenko, and V.V. Yanovsky, "A theory of large-scale structure origination in hydrodynamic turbulence", Sov. Phys. JETP, **58**, 1144 (1983).
[14] G. Khomenko, S. Moiseev, & A. Tur, The hydrodynamical alpha-effect in a compressible medium, J. Fluid Mech. **225**, 355-369 (1991). https://doi.org/10.1017/S0022112091002082
[15] F. Krause, and G. Rüdiger, "On the Reynolds stresses in mean-field hydrodynamics. I. Incompressible homogeneous isotropic turbulence", Astron. Nachr. **295**, 93-99 (1974). https://doi.org/10.1002/asna.19742950205
[16] V.V. Gvaramadze, G.A. Khomenko, and A.V. Tur, "Large-scale vortices in helical turbulence of incompressible fluid", Geophys. Astrophys. Fluid Dyn. **46**, 53-69 (1989). https://doi.org/10.1080/03091928908208904
[17] S.S. Moiseev, P.B. Rutkevich, A.V. Tur, and V.V. Yanovsky, "Vortex dynamos in a helical turbulent convection", Sov. Phys. JETP, **67**, 294-299 (1988).
[18] S.S. Moiseev, K.R. Oganyan, P.B. Rutkevich et al., "An eddy dynamo and spiral turbulence", in: *Integrability and Kinetic Equations for Solitons*, edited by V.G. Bar'yachtar, (Naukova Dumka, Kiev, 1990), pp. 280-332.
[19] B.Ya. Shmerlin, and M.V. Kalashnik, "Rayleigh convective instability in the presence of phase transitions of water vapor. The formation of large-scale eddies and cloud structures", Phys. Usp. **56**, 473-485 (2013). https://doi.org/10.3367/UFNe.0183.201305d.0497
[20] G.V. Levina, S.S. Moiseev, and P.B. Rutkevich, "Hydrodynamic alpha-effect in a convective system," in: *Nonlinear Instability, Chaos and Turbulence, Adv. Fluid Mech. Series*, edited by L. Debnath, D.N. Riahi, (WIT Press, Southampton, Boston, UK, USA, 2000), Vol. 2, pp. 111-161 (2000).
[21] P.B. Rutkevich, "Equation for vortex instability caused by convective turbulence and coriolis force", JETF **77**, 933-938 (1993).
[22] L.L. Kitchatinov, G. Rüdiger, and G. Khomenko, "Large-scale vortices in rotating stratified disks", Astron. Astrophys. **287**, 320-324 (1994). https://adsabs.harvard.edu/full/1994A%26A...287..320K
[23] L.M. Smith, and F. Waleffe, "Generation of slow large scales in forced rotating stratified turbulence", J. Fluid Mech. **451**, 145-168 (2002). https://doi.org/10.1017/S0022112001006309
[24] N. Kleeorin, and I. Rogachevskii, "Generation of large-scale vorticity in rotating stratified turbulence with inhomogeneous helicity: mean-field theory", J. Plasma Phys. **84**, 735840303 (2018). https://doi.org/10.1017/S0022377818000417
[25] U. Frisch, Z.S. She, and P.L. Sulem, "Large scale flow driven by the anisotropic kinetic alpha effect", Physica D, **28**, 382-392 (1987). https://doi.org/10.1016/0167-2789(87)90026-1
[26] P.L. Sulem, Z.S. She, H. Scholl, and U. Frisch, "Generation of Large-Scale Structures in Three-Dimensional Flow Lacking Parity-Invariance. Journal of Fluid Mechanics", J. Fluid Mech. **205**, 341-358 (1989). https://doi.org/10.1017/S0022112089002065
[27] B. Dubrulle, and U. Frisch, "Eddy viscosity of parity-invariant flow", Phys. Rev. A **43**, 5355-5364 (1991). https://doi.org/10.1103/physreva.43.5355
[28] A.V. Tur, and V.V. Yanovsky, "Large-scale instability in hydrodynamics with stable temperature stratification driven by small-scale helical force," (2012). https://doi.org/10.48550/arXiv.1204.5024
[29] A.V. Tur, and V.V. Yanovsky, "Non-Linear Vortex Structure in Stratified Fluid Driven by Small-scale Helical Force", Open J. Fluid Dyn. **3**, 64-74 (2013). https://doi.org/10.4236/ojfd.2013.32009
[30] M.I. Kopp, A.V. Tur, and V.V. Yanovsky, "The Large-scale instability in rotating fluid with small scale force", Open J. Fluid Dyn. **5**, 128-138 (2015). https://doi.org/10.4236/ojfd.2015.52015.
[31] M.I. Kopp, A.V. Tur, and V.V. Yanovsky, "Nonlinear vortex dynamo in a rotating stratified moist atmosphere", J. Exp. Theor. Phys. **124**, 1010-1022 (2017). https://doi.org/10.1134/S1063776117060127
[32] M.I. Kopp, A.V. Tur, and V.V. Yanovsky, "Nonlinear Vortex Structures in Obliquely Rotating Fluid", Open J. Fluid Dyn. **5**, 311-321 (2015). https://doi.org/10.4236/ojfd.2015.54032
[33] M.I. Kopp, A.V. Tur, and V.V. Yanovsky, "The large-scale instability and nonlinear vortex structures in obliquely rotating fluid with small scale non spiral force", VANT, **4**, 264-269 (2015).
[34] M.I. Kopp, A.V. Tur, and V.V. Yanovsky, "Nonlinear vortex structures in obliquely rotating stratified fluids driven by small scale non helical forces", Ukr. J. Phys. **66**, 478-488 (2021). https://doi.org/10.15407/ujpe66.6.478
[35] M.I. Kopp, A.V. Tur, and V.V. Yanovsky, "Vortex Dynamo in a Rotating Stratified Moist Atmosphere driven by Small-scale Non-helical Forces", Geophys. Astrophys. Fluid Dyn. **115**, 551-576 (2021). https://doi.org/10.1080/03091929.2021.1946802

[36] M.I. Kopp, A.V. Tur, and V.V. Yanovsky, "Vortex Dynamo in an obliquely rotating stratified nanofluid by small-scale non-helical forces," East Eur. J. Phys. **2**, 51-72 (2021). https://doi.org/10.26565/2312-4334-2021-2-02
[37] G.V. Levina, and M.T. Montgomeri, "The first examination of the helical nature of tropical cyclogenesis", Doklady Earth Sciences, **434**, 1285-1289 (2010). https://doi.org/10.1134/S1028334X1009031X
[38] G.V. Levina, "On the Path from the Turbulent Vortex Dynamo Theory to Diagnosis of Tropical Cyclogenesis", Open J. Fluid Dyn. **8**, 86-114 (2018). https://doi.org/10.4236/ojfd.2018.81008.
[39] G. Rüdiger, "On the α-Effect for Slow and Fast Rotation", Astron. Nachr. **299**, 217-222 (1978). https://doi.org/10.1002/asna.19782990408
[40] D. Yadav, G.S. Agrawal, and R. Bhargava, "Thermal instability of rotating nanofluid layer", Int. J. Eng. Sci. **49**, 1171-1184 (2011). https://doi.org/10.1016/j.ijengsci.2011.07.002
[41] S. Agarwal, and B.S. Bhadauria, "Unsteady heat and mass transfer in a rotating nanofluid layer", Continuum Mech. Thermodyn. **26**, 437-445 (2014). https://doi.org/10.1007/s00161-013-0309-6

ВИХРОВЕ ДИНАМО У СЕРЕДОВИЩАХ, ЩО ОБЕРТАЮТЬСЯ

Михайло Й. Копп[a], Володимир В. Яновський[a,b]

[a]*Інститут монокристалів, Національна Академія Наук України, пр. Леніна 60, 61072 Харків, Україна*
[b]*Харківський національний університет імені В.Н. Каразіна, майдан Свободи, 4, 61022, Харків, Україна*

В огляді висвітлено основні досягнення теорії вихрового динамо в середовищах, що обертаються. Обговорюються різні моделі вихрового динамо в таких середовищах: однорідна в'язка рідина, температурно-стратифікована рідина, волога атмосфера і стратифікована нанорідина. Наведено основні аналітичні та чисельні результати для цих моделей, що отримані методом багатомасштабних асимптотичних розкладів. Головна увага приділяється моделям із неспіральною зовнішньою силою. Для вологої атмосфери, що обертається, отримані характерні оцінки просторового і часового масштабів вихрових структур. Виявлено нові ефекти вихрового динамо у стратифікованій нанорідині, що обертається, які виникають за рахунок термофорезу та броунівського руху наночастинок. Результати аналізу нелінійних рівнянь вихрового динамо у стаціонарному режимі приводять до існування спіральних кінків, періодичних нелінійних хвиль та солітонів.

Ключові слова: *теорія динамо; великомасштабна нестійкість; сила Коріоліса; багатомасштабні асимптотичні розкладання; α-ефект; солітони; кінки*

East European Journal of Physics. **2.** 51-62 (2023)
DOI:10.26565/2312-4334-2023-2-02 ISSN 2312-4334

NUMERICAL ANALYSIS ON MHD MIXED CONVECTION FLOW OF Al_2O_3/H_2O (ALUMINUM-WATER) NANOFLUIDS IN A VERTICAL SQUARE DUCT[†]

Bishnu Ram Das[‡], P.N. Deka[§], Shiva Rao*
Department of Mathematics, Dibrugarh University, Dibrugarh-786004, Assam, India
[‡]e-mail: bishnuram.das84@gmail.com, [§]e-mail: pndeka@dibru.ac.in
**Corresponding Author e-mail: shivarao374@gmail.com*
Received February 9, 2023; revised March 6, 2023; accepted March 9, 2023

In this work, we have considered steady laminar magnetohydrodynamics (MHD) mixed convection flow of an electrically conducting fluid in presence of Al_2O_3 nanoparticle while water is the base fluid in a vertical square duct. The walls of the duct are thermally insulated. In the energy equation, the effect of viscous dissipation and Joule heat are also considered. In this case, the walls of the duct are kept at a constant temperature. By using dimensionless quantities, the governing equations of momentum, induction, and energy are first transformed into dimensionless equations and then the reduced equations are solved using an explicit finite difference approach. The velocity, temperature, and induced magnetic field profiles are plotted graphically to analyze the effect of different flow parameters. It is observed that the nanofluid motion expedites with the increase of the value of the magnetic parameter, Reynolds number, and Prandtl number. The current research may find its application in the numerous industrial as well as cooling sectors. This study observed its importance with the view to increasing the heat transfer efficiency for practical applications relevant to industry and engineering issues. The issues discussed in this study have not been included in the earlier investigation for steady nanofluid flow due to a square duct.
Keywords: *Nanofluids; Explicit finite-difference numerical method (EFDM); MHD flow; Buoyancy force; Mixed convection; square duct; Heat transfer; Magnetic field*
PACS: 44.20.+b, 44.40.+a, 44.30.+v, 47.11.-j, 47.11.Bc

1. INTRODUCTION

Nanofluids which have a wide range of applications in industry are defined as suspensions of solid nanoparticles in some form of organic or inorganic materials in basic fluids which are mainly utilized for heat transfer applications. These nanoparticles improve the heat transfer performance by raising conduction and convection coefficients which enables them to be more effective in various applications. The currently available heat transfer fluids which are used for these purposes including water, ethylene glycol mixture, engine oil, etc., possess poor heat transfer capability. In recent times, the consideration of nanofluids in engineering and industrial applications has drawn a lot of attention from scientists due to their improved thermal properties and advantageous heat transfer characteristics without any pressure drop. As a result of their large thermal conductivity, nanofluids are used in place of base fluids as working fluids nowadays. Mixed convection flow is the combination of forced and natural convection flows. Further, mixed convection flow in a channel or duct is encountered in the Dual-Coolant Lead-Lithium (DDCL) flow for fusion power as a tritium breeder and many industrial applications and engineering devices such as a cooling systems for electronic components and reactors. Choi and Eastman [1] introduced the concept of nanofluids and presented impressive results with many possibilities for usage. Nanofluids are new classes of nano-technology-based materials concerning nanoparticles (1nm to 100 nm) dispersed in base fluids. These heat transfer fluids have promoted great interest among researchers in the last few years, mainly due to their potential applications. The nanofluids have higher thermal conductivities in comparison to the base fluids, which could result in higher heat transfer rates.

Convection process in a square duct is relevant to certain heat transfer engineering applications acting as electronic equipment, food drying, heat exchangers, cooling, and nuclear reactors. Experimentally and numerically in recent years, many researchers have studied natural convection and mixed convection in a square duct under a wide range. The mixed convection of $\mathbf{Al_2O_3/water}$ nano fluid interior of a square duct accommodates boiling quadrilaterals obstacles on its bottom wall considered by Doustdar and Yekani [2]. Mixed convection flows in a square duct partially heated from below using nanofluid were studied by Mansour et al. [3]. The results of a numerical study on the mixed convection in a square duct filled with a $\mathbf{Al_2O_3/water}$ nanofluid was investigated by Ghasemi and Aminossadati [4]. They concluded that the heat transfer rate can be reduced by adding a considerable amount of nanoparticles into the distilled water cases of upward and downward sliding walls. Abu-Nada and Oztop [5] investigated the effect in natural convection processes with nanofluid which are enclosed in containers. Hemmat Esfe et al. [6] studied the heat transfer and Mixed-convection fluid flow of an $\mathbf{Al_2O_3/water}$ nanofluid with effective thermal conductivity and viscosity is dependent on temperature and nanoparticle concentration core of a square duct. Their results stipulated that adding $\mathbf{Al_2O_3}$ nanoparticle produces an extraordinary enhancement of heat transfer concerning that of the unmixed fluid. The effect of the Prandtl number and Reynolds number for laminar mixed convection in a top wall moving, the bottom heated square duct was discussed by Moallemi and Jang [7]. They investigated that when Reynolds number and Grashof numbers were kept constant, increment of Prandtl number enhanced the heat transfer rate. The mixed convection in a square duct having a side wall

[†] ***Cite as:*** B.R. Das, P.N. Deka, and Shiva Rao, East Eur. J. Phys. **2**, 51 (2023), https://doi.org/10.26565/2312-4334-2023-2-02

moving and a local heat source at the bottom wall was investigated by Yang and Aydin [8]. Analyzed mixed convection for a square duct with both side walls moving by Dagtekin and Oztop [9]. They conducted the study for three different configurations based on the direction of moving walls. Wong and De Leon [10] carried out a review paper detailing the current and future applications of nanofluids. Li et al. [11] investigated the forced convective heat transfer of nanofluids in solar collectors during the day and night, with distilled water and nanoparticles of $\mathbf{Al_2O_3}$, $\mathbf{ZnO}$, and $\mathbf{MgO}$. The nanofluid achieved a $\mathbf{3}$℃ temperature difference during the daytime peak solar radiation compared with the base fluids. With a concentration of $\mathbf{0.2\%\ ZnO}$, a temperature difference of $\mathbf{2.55}$℃ for daytime and $\mathbf{1}$℃ for nighttime was reached, and this was determined to be the most attractive option for solar energy utilization. Tooraj et al. [12] witnessed a 28% performance improvement in a flat plate collector when it was operated with $\mathbf{Al_2O_3/water}$ nanofluids. Otanicar [13] studied the economic and environmental influences of using nanofluids to enhance solar collector efficiency with conventional solar collectors. The thermophysical properties of the nanofluid are calculated density by Pak and Cho [14], and thermal conductivity by Yu and Choi [15]. The specific heat of the nanofluid is calculated by Xuan and Roetzel [16]. The 3D flow of MHD nanofluid with varied nanoparticles including $\mathbf{Fe_3O_4}$, $\mathbf{Cu}$, $\mathbf{Al_2O_3}$ and $\mathbf{TiO_2}$ and water as the base fluid past an exponentially stretched surface was discussed by Jusoh et al. [17]. Hung et al. [18] indicated that $\mathbf{Al_2O_3/Water}$ nanofluids require less pumping power, followed by $\mathbf{CuO/Water}$ nanofluid and $\mathbf{TiO_2/Water}$ nanofluid for 1% nanoparticle volume concentration. The computed numerical results are presented graphically for velocity, temperature, and induced magnetic field for different flow parameters.

Sheikhpour et al. [19] examined the role of nanofluids in drug delivery and biomedical technology. Majumder and Das [20] presented a short review of organic nanofluids preparation, surfactants, and applications. Dehaj et al. [21] observed the efficiency of the parabolic solar collector using $NiFe_2O_4$/water nanofluid and U-tube. Sivaraj and Banerjee [22] studied the transport properties of non-Newtonian nanofluids and applications, and Thumma et al. [23] examined that generalized differential quadrature analysis of unsteady three-dimensional MHD radiating dissipative Casson fluid conveying tiny particles. Lahmar et al. [24] analyzed heat transfer by squeezing unsteady nanofluid flow under the effects of an inclined magnetic field and variable thermal conductivity. Rosca and Pop [25] studied hybrid nanofluid flows determined by a permeable power-Law stretching/shrinking sheet modulated by orthogonal surface shear. Selimefendigil and Oztop [26] examined thermal management and modeling of forced convection and entropy generation in a vented cavity by simultaneous use of a curved porous layer and magnetic field. Jamshed studied [27] the numerical investigation of MHD impact on Maxwell nanofluid. Jamshed et al. [28] observed the computational framework of Cattaneo-Chritov heat flux effects on Engine Oil-based Williamson hybrid nanofluids. Jamshed studied [29] that thermal augmentation in solar aircraft using tangent hyperbolic hybrid nanofluid: a solar energy application. Rao and Deka [30] took the Buongiorno model to analyze the heat and mass transfer phenomena of Williamson nanofluid past a moving cylinder. Recently, Rao and Deka [31] made a numerical investigation on the unsteady MHD Casson nanofluid flow caused due to a porous stretching sheet and found that thermal radiation played a very important role in the heat transfer character of the fluid.

Yusuf et al. [32] investigated entropy generation on flow and heat transfer of a reactive MHD Sisko fluid through inclined walls with a porous medium. Hamzah et al. [33] studied MHD mixed convection and entropy generation of CNT-water nanofluid in a wavy lid-driven porous enclosure at different boundary conditions. Khan et al [34] analyzed the analytical assessment of (Al_2O_3-Ag/H_2O) hybrid nanofluid influenced by induced magnetic field for second law analysis with mixed convection, viscous dissipation, and heat generation. Ahmed and Pop [35] investigated mixed convection boundary layer flow from a vertical flat plate embedded in a porous medium filled with nano-fluids. Malvandi and Ganji [36] studied the mixed convection of alumina-water nanofluid inside a concentric annulus considering nanoparticle migration. Tayebi et al. [37] studied the Magnetohydrodynamic natural convection heat transfer of a hybrid nanofluid in a square enclosure in the presence of a wavy circular conductive cylinder. Shah et al. [38] examined radiative MHD Casson nanofluid flow with activation energy and chemical reaction over past nonlinearly stretching surfaces through entropy generation. Rajesh et al. [39] observed that hydromagnetic effects on hybrid nanofluid $Cu-Al_2O_3$/water flow with convective heat transfer due to a stretching sheet. Molli and Naikoti [40] studied the MHD natural convective flow of $Cu/water$ nanofluid over a past infinite vertical plate with the presence of time-dependent boundary conditions. Khashi [41] concludes that flow and heat transfer of hybrid nanofluid over a permeable shrinking cylinder with Joule heating. Alighamdi [42] studied the boundary layer stagnation point flow of the Casson hybrid nanofluid over an unsteady stretching surface. Shahzad et al. [43] observed computational investigation of magneto-cross fluid flow with multiple slips along wedge and chemically reactive species, and Ibrar et al. [44] discovered the interaction of single and multi-walls carbon nanotubes in magnetized-nano Casson fluid over radiated horizontal needle. Lund et al. [45] analyzed the effects of Stefan blowing and slip conditions on unsteady MHD Casson nanofluid flow over an unsteady shrinking sheet. Recently, Rao and Deka [46] studied the numerical investigation of transport phenomena in a nanofluid under the transverse magnetic field over a stretching plate associated with solar radiation. Rao and Deka [47] investigated numerical solution using EFDM for unsteady MHD radiative Casson nanofluid flow over a porous stretching sheet with stability analysis.

The present paper aims to investigate the laminar steady MHD mixed convection flow of an electrically conducting fluid in a vertical square duct in the presence of a strong transverse magnetic field using a finite difference scheme. The walls of the duct are assumed as thermally insulating and walls have a constant temperature. The local balance equations

of momentum, magnetic induction, and energy are solved numerically by the finite difference method using the Hartmann number (Ha), Grashof number (G_r), Reynolds number (R_e), Prandtl number (P_r), and magnetic Reynolds number (R_m) as the parameters. The computed numerical results are presented graphically for velocity, temperature, and induced magnetic field for flow parameters.

- To consider a suitable mathematical model involving governing equations and boundary conditions for the nanofluid MHD flow across the square duct.
- Nondimensionalization of the governing equations and performance of the explicit finite difference method.
- Plotting graph for the velocity, temperature, and induced magnetic field distribution for different physical parameters.
- We will compare the obtained results with previous work to validate the efficiency of the numerical approach.

Table 1. Thermo-physical numerical values of water (H_2O) and aluminum (Al_2O_3)

	Density (ρ)	**Specific heat capacity (C_p)**	**Thermal conductivity (k)**	**Electrical conductivity (σ)**
Al_2O_3	3970	765	40	35×10^6
H_2O	997.1	4179	0.613	0.05

2. MATHEMATICAL FORMULATION AND SOLUTIONS

Description of geometry

The steady laminar flow of a Newtonian fluid in a vertical square duct with a uniform horizontal magnetic field of constant intensity B_o applied transverse to the duct walls is considered.

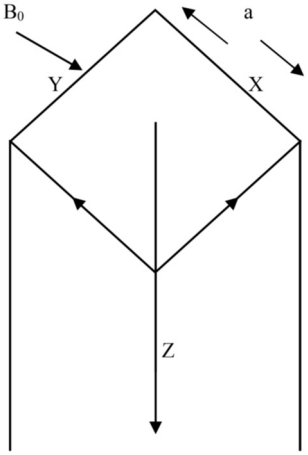

Figure 1. Physical model and the coordinate system

Let a be the length of the cross-section of the duct. It is assumed that the fluid occupies an area between $x = 0,\ x = a;$ and $y = 0,\ y = a.$ The flow is to be consumed by a constant pressure slop $\frac{\partial p}{\partial z}$ and is constrained to proceed in the z-direction. T_o is a uniform temperature at the walls of the duct is simulate. By the axiom of fully developed flow, the velocity and temperature fields are side by side, and the only non-vanishing fundamental of velocity and temperature $V_z(x,y)\ and\ T(x,y)$ are side by side to the duct axis and independent of the perpendicular coordinate. The uniform horizontal applied magnetic field of force B_o acts along the y-direction and it induces a magnetic field $B_z(x,y)$ in the flow direction. In this study, an electrically conducting fluid flows along the axis of the duct under the influence of an externally imposed driving pressure gradient and the Lorentz forces caused by the interaction of the flow with the uniform magnetic field, directed along y. Buoyancy forces, caused by density changes that result from temperature variation, can easily be included thus giving rise to mixed MHD convection.

The following assumptions are made in this study:

- The flow is steady, fully developed and fluid is Newtonian.
- The duct is considered to be infinite so that all the fluid properties except the pressure gradient are independent of the variable z.

The velocity $\vec{V}$, magnetic field $\vec{B}$ and temperature T shall be the ensuing form

$$\vec{V} = \{0,0,V_z(x,y)\},\ \overrightarrow{B} = \{0,B_o,B_z(x,y)\},\ \ T = T(x,y)$$

3. GOVERNING EQUATIONS

The equation of continuity is

$$\left(\nabla.\vec{V}\right) = 0. \tag{1}$$

The Momentum equation is

$$\rho_{nf}\left[\frac{\partial \vec{V}}{\partial t}+\left(\vec{V}.\nabla\right)\vec{V}\right]=-\nabla p+\mu_{nf}\nabla^2\vec{V}+\left(\vec{J}\times\vec{B}\right)+g(\rho\beta)_{nf}(T-T_o). \tag{2}$$

Maxwell's equation is

$$\nabla.\vec{B}=0, \tag{3}$$

$$\nabla\times\vec{B}=(\mu_e)_{nf}\vec{J}. \tag{4}$$

Ohm's law:

$$\vec{J}=\sigma_{nf}\left(\vec{E}+\vec{V}\times\vec{B}\right). \tag{5}$$

The magnetic induction equation is given by

$$\frac{\partial \vec{B}}{\partial t}=\nabla\times\left(\vec{V}\times\vec{B}\right)+\lambda_{nf}\nabla^2\vec{B}. \tag{6}$$

Now using equations (1) and (3) in (6) we have

$$\frac{\partial \vec{B}}{\partial t}+\left(\vec{V}.\nabla\right)\vec{B}=\left(\vec{B}.\nabla\right)\vec{V}+\lambda_{nf}\nabla^2\vec{B}. \tag{7}$$

The energy equation or temperature equation:

$$\left(\rho C_p\right)_{nf}\left[\frac{\partial T}{\partial t}+\left(\vec{V}.\nabla\right)T\right]=k_{nf}\nabla^2T+\mu_{nf}\phi+\frac{J^2}{\sigma_{nf}}, \tag{8}$$

where

$$\nu_{nf}=\frac{\mu_{nf}}{\rho_{nf}}, \tag{9}$$

$$\lambda_{nf}=\frac{1}{\sigma_{nf}(\mu_e)_{nf}}. \tag{10}$$

Brinkman's [48] model for the dynamic viscosity of nanofluid is

$$\mu_{nf}=\frac{\mu_f}{(1-\phi)^{2.5}}. \tag{11}$$

Following Khan [49], the effective density of nanofluid is considered as

$$\rho_{nf}=\left[1-\phi+\phi\frac{\rho_s}{\rho_f}\right]\rho_f. \tag{12}$$

The effective magnetic permeability of nanofluid is given by

$$(\mu_e)_{nf}=\left[1-\phi+\phi\frac{(\mu_e)_s}{(\mu_e)_f}\right](\mu_e)_f. \tag{13}$$

Maxwell [50] gives the electrical conductivity of nanofluid

$$\sigma_{nf}=\left[1+\frac{3(\sigma-1)\phi}{(\sigma+2)-(\sigma-1)\phi}\right]\sigma_f. \tag{14}$$

The heat capacitance of the nanofluid is given [51] by Khanafer

$$\left(\rho C_p\right)_{nf}=\left[1-\phi+\phi\frac{(\rho C_p)_s}{(\rho C_p)_f}\right]\left(\rho C_p\right)_f. \tag{15}$$

The thermal expansion coefficient of nanofluid is

$$(\rho\beta)_{nf}=(1-\phi)(\rho\beta)_f+\phi(\rho\beta)_s. \tag{16}$$

Maxwell-Garnet determined the thermal conductivity of nanofluid

$$k_{nf}=\left[\frac{k_s+2k_f-2\phi(k_f-k_s)}{k_s+2k_f+\phi(k_f-k_s)}\right]k_f, \tag{17}$$

where k_s and k_f are solid and fluid thermal conductivity respectively.

Using velocity, temperature, and current density distribution stated above for steady case, equations (2), (7), and (8) give

$$\frac{1}{(1-\phi)^{2.5}}\ \mu_f\left[\frac{\partial^2 V}{\partial x^2}+\frac{\partial^2 V}{\partial y^2}\right]+\frac{B_o}{\left[1-\phi+\phi\frac{(\mu_e)_s}{(\mu_e)_f}\right](\mu_e)_f}\frac{\partial B}{\partial y}+\left[1-\phi+\phi\frac{\rho_s}{\rho_f}\right]\rho_f\ g\beta_f(T-T_o)\ -\frac{\partial p}{\partial z}=0, \tag{18}$$

$$\frac{1}{\left[1-\phi+\phi\frac{(\mu_e)_s}{(\mu_e)_f}\right](\mu_e)_f\left[1+\frac{3(\sigma-1)\phi}{(\sigma+2)-(\sigma-1)\phi}\right]\sigma_f}\left[\frac{\partial^2 B}{\partial x^2}+\frac{\partial^2 B}{\partial y^2}\right]+B_o\frac{\partial V}{\partial y}=0, \tag{19}$$

$$\begin{aligned}&\left[\frac{k_s+2k_f-2\phi(k_f-k_s)}{k_s+2k_f+\phi(k_f-k_s)}\right]k_f\left[\frac{\partial^2 T}{\partial x^2}+\frac{\partial^2 T}{\partial y^2}\right]+\frac{1}{(1-\phi)^{2.5}}\ \mu_f\left[\left(\frac{\partial V}{\partial x}\right)^2+\left(\frac{\partial V}{\partial y}\right)^2\right]+\\&\frac{1}{((\mu_e)_f)^2\left[1-\phi+\phi\frac{(\mu_e)_s}{(\mu_e)_f}\right]^2\left[1+\frac{3(\sigma-1)\phi}{(\sigma+2)-(\sigma-1)\phi}\right]\sigma_f}\left[\left(\frac{\partial B}{\partial x}\right)^2+\left(\frac{\partial B}{\partial y}\right)^2\right]=0.\end{aligned} \tag{20}$$

The corresponding boundary conditions are:

$$\begin{aligned}&V_z=0,\quad B_z=0,\quad T=T_o,\quad at\ y=0,\\&V_z=0,\quad B_z=0,\quad T=T_o\quad at\ \ y=a, for\ 0\le x\le b,\\&V_z=0,\quad B_z=0,\quad T=T_o,\quad at\ x=0,\\&V_z=0,\quad B_z=0,\quad T=T_o,\quad at\ x=a,\ for\ 0\le y\le b.\end{aligned} \tag{21}$$

The above equations (18), (19), and (20) can be transformed into dimensionless parameters that are defined

$$\bar{x}=\frac{x}{a}\ ,\bar{y}=\frac{y}{a}\ ,\bar{V}=\frac{V}{V_o}\ ,\bar{B}=\frac{B}{B_o}\ ,\bar{T}=\frac{T-T_o}{\Delta T}. \tag{22}$$

Where $B_o=-a^2(\mu_e)_{nf}\sqrt{\frac{\sigma_{nf}}{\rho_{nf}\nu_{nf}}}\frac{\partial p}{\partial z}, V_o=-\frac{a^2}{\rho_{nf}\nu_{nf}}\frac{\partial p}{\partial z}, \Delta T=\frac{V_o^2}{C_p}$,

Using dimensionless quantities (22) in equations (18), (19), and (20) and release bullet, become

$$\frac{\partial^2 V}{\partial x^2}+\frac{\partial^2 V}{\partial y^2}+\frac{B_o^2a^2\left[1+\frac{3(\sigma-1)\phi}{(\sigma+2)-(\sigma-1)\phi}\right]\frac{\sigma_f}{\mu_f}(1-\phi)^{\cdot 5}}{V_oa\left[1-\phi+\phi\frac{(\mu_e)_s}{(\mu_e)_f}\right](\mu_e)_f\left[1+\frac{3(\sigma-1)\phi}{(\sigma+2)-(\sigma-1)\phi}\right]\sigma_f}\frac{\partial B}{\partial y}+\frac{g\beta_f a^3(T-T_o)}{\nu_f^2}\cdot\frac{\nu_f}{V_oa}\ +1=0, \tag{23}$$

$$\frac{\partial^2 B}{\partial x^2}+\frac{\partial^2 B}{\partial y^2}+V_oa\left[1-\phi+\phi\frac{(\mu_e)_s}{(\mu_e)_f}\right](\mu_e)_f\left[1+\frac{3(\sigma-1)\phi}{(\sigma+2)-(\sigma-1)\phi}\right]\sigma_f\ \frac{\partial V}{\partial y}=0, \tag{24}$$

$$\begin{aligned}&\frac{\partial^2 T}{\partial x^2}+\frac{\partial^2 T}{\partial y^2}+\frac{\mu_f C_p}{(1-\phi)^{2.5}k_f\left[\frac{k_s+2k_f-2\phi(k_f-k_s)}{k_s+2k_f+\phi(k_f-k_s)}\right]}\cdot\frac{V_o^2}{C_p\Delta T}\left[\left(\frac{\partial V}{\partial x}\right)^2+\left(\frac{\partial V}{\partial y}\right)^2\right]\ +\\&\frac{B_o^2a^2\left[1+\frac{3(\sigma-1)\phi}{(\sigma+2)-(\sigma-1)\phi}\right]\frac{\sigma_f}{\mu_f}}{V_o^2a^2\left[1-\phi+\phi\frac{(\mu_e)_s}{(\mu_e)_f}\right]^2\left[1+\frac{3(\sigma-1)\phi}{(\sigma+2)-(\sigma-1)\phi}\right]^2\sigma_f^2(\mu_e)_f^2\left[\frac{k_s+2k_f-2\phi(k_f-k_s)}{k_s+2k_f+\phi(k_f-k_s)}\right]}\cdot\frac{\mu_f C_p}{k_f}\cdot\frac{V_o^2}{C_p\Delta T}\left[\left(\frac{\partial B}{\partial x}\right)^2+\left(\frac{\partial B}{\partial y}\right)^2\right]=0.\end{aligned} \tag{25}$$

Let

$E_1=\frac{1}{(1-\phi)^{2.5}}, E_2=\left[1-\phi+\phi\frac{\rho_s}{\rho_f}\right], E_3=\left[1-\phi+\phi\frac{(\mu_e)_s}{(\mu_e)_f}\right], E_4=\left[1+\frac{3(\sigma-1)\phi}{(\sigma+2)-(\sigma-1)\phi}\right], E_5=\left[1-\phi+\phi\frac{(\rho C_p)_s}{(\rho C_p)_f}\right], E_6=\left[\frac{k_s+2k_f-2\phi(k_f-k_s)}{k_s+2k_f+\phi(k_f-k_s)}\right]$.

Therefore, the equations (23), (24), and (25) in terms of $E_1,\ E_2,\ E_3,\ E_4,\ E_5,\ E_6$ are

$$\frac{\partial^2 V}{\partial x^2}+\frac{\partial^2 V}{\partial y^2}+\ \frac{Ha^2}{R_m}\frac{E_4}{E_1E_3E_4}\frac{\partial B}{\partial y}+\frac{G_r}{R_e}T+1=0, \tag{26}$$

$$\frac{\partial^2 B}{\partial x^2}+\frac{\partial^2 B}{\partial y^2}+\ R_mE_3E_4\frac{\partial V}{\partial y}\ =0, \tag{27}$$

$$\frac{\partial^2 T}{\partial x^2}+\frac{\partial^2 T}{\partial y^2}+\frac{E_1}{E_6}P_r\left[\left(\frac{\partial V}{\partial x}\right)^2+\left(\frac{\partial V}{\partial y}\right)^2\right]+\frac{Ha^2P_r}{R_m^2}\frac{E_4}{E_3^2E_4^2E_6}\left[\left(\frac{\partial B}{\partial x}\right)^2+\left(\frac{\partial B}{\partial y}\right)^2\right]=0, \tag{28}$$

where

$Ha = B_o a \sqrt{\frac{\sigma_f}{\mu_f}}$, is the Hartmann number,

$G_r = \frac{g\beta_f(T-T_o)a^3}{\nu_f^2}$, is the thermal Grashof number,

$P_r = \frac{\mu_f C_p}{k_f}$, is the Prandtl number,

$R_e = \frac{V_o a}{\nu_f}$, is the Reynolds number,

and

$R_m = V_o a(\mu_e)_f \sigma_f$, is the magnetic Reynolds number.

The corresponding boundary conditions (21) gives

$$\begin{aligned} &V = 0, \quad B = 0, \quad T = 0, \quad when\ y = 0, \\ &V = 0, \quad B = 0, \quad T = 0, \quad when\ y = 1, \\ &V = 0, \quad B = 0, \quad T = 0, \quad when\ x = 0, \\ &V = 0, \quad B = 0, \quad T = 0, \quad when\ x = 1. \end{aligned} \tag{29}$$

4. NUMERICAL TECHNIQUE AND GRID INDEPENDENCE STUDY

The dimensionless governing equations (26), (27), and (28) along with the boundary conditions (29) were discretized using the finite difference technique. In this numerical procedure, the computational domain is divided into a uniform grid system. Both the second-derivative and the squared first-derivative terms are discretized using the central difference of second-order accuracy. The finite difference form of $\partial^2 V/\partial x^2$ and $\partial V/\partial x$, for example, were discretized as $\frac{\partial^2 V}{\partial x^2} = \frac{V_{i+1,j}-2V_{i,j}+V_{i-1,j}}{\Delta x^2} + O(\Delta x^2)$ and $\frac{\partial V}{\partial x} = \frac{V_{i+1,j}-V_{i-1,j}}{2\Delta x} + O(\Delta x^2)$, respectively. Therefore, the resultant difference equations become

$$V_{i,j} = A_3\left(V_{i+1,j} + V_{i-1,j}\right) + A_4\left(V_{i,j_{+1}} + V_{i,j_{-1}}\right) + A_5\left(B_{i,j_{+1}} - B_{i,j_{-1}}\right) + A_6\left(T_{i,j}\right) + A_7 \tag{31}$$

$$\begin{aligned} T_{i,j} = {} & A_3\left(T_{i+1,j} + T_{i-1,j}\right) + A_4\left(T_{i,j_{+1}} + T_{i,j_{-1}}\right) + A_{12}\left(V_{i+1,j} - V_{i-1,j}\right)^2 + \\ & A_{13}\left(V_{i,j_{+1}} - V_{i,j_{-1}}\right)^2 + A_{14}\left(B_{i+1,j} - B_{i-1,j}\right)^2 + A_{15}\left(B_{i,j_{+1}} - B_{i,j_{-1}}\right)^2. \end{aligned} \tag{32}$$

$A_1 = \frac{Ha^2}{R_m}\frac{E_4}{E_1E_3E_4}$, $A_2 = \frac{G_r}{R_e}$, $A_3 = \frac{k^2}{2(h^2+k^2)}$, $A_4 = \frac{h^2}{2(h^2+k^2)}$, $A_5 = \frac{A_1h^2k}{2(h^2+k^2)}$, $A_6 = \frac{A_2h^2k^2}{(h^2+k^2)}$,
$A_7 = \frac{h^2k^2}{h^2+k^2}$, $A_8 = R_mE_3E$, $A_9 = \frac{A_8h^2k}{2(h^2+k^2)}$, $A_{10} = \frac{E_1}{E_6}P_r$, $A_{11} = \frac{Ha^2P_r}{R_m^2}\frac{E_4}{E_3^2E_4^2E_6}$, $A_{12} = \frac{A_{10}k^2}{4(h^2+k^2)}$,
$A_{13} = \frac{A_{10}h^2}{4(h^2+k^2)}$, $A_{14} = \frac{A_{11}k^2}{4(h^2+k^2)}$, $A_{15} = \frac{A_{11}h^2}{4(h^2+k^2)}$

are constants, $\Delta x = h\ and\ \Delta y = k$.

The corresponding discretized boundary conditions are:

$$\begin{aligned} &V_{i,1} = 0, \quad B_{i,1} = 0, \quad T_{i,1} = 0, \quad when\ j = 1, \\ &V_{i,n_{+1}} = 0, \quad B_{i,n_{+1}} = 0, \quad T_{i,n_{+1}} = 0, \quad when\ j = n+1, \quad for\ 1 \le i \le m+1, \\ &V_{1,j} = 0, \quad B_{1,j} = 0, \quad T_{1,j} = 0, \quad when\ i = 1, \\ &V_{m_{+1},j} = 0, \quad B_{1,m_{+1}} = 0, \quad T_{1,m_{+1}} = 0, \quad when\ i = m+1, \quad for\ 1 \le j \le n+1\ . \end{aligned} \tag{33}$$

Using boundary conditions (32) the values $V_{i,j}$, $B_{i,j}$ and $T_{i,j}$ in the equations (30), (31), and (32) with the parameters (Ha), (R_m), (P_r), (R_e), (G_r) have been iterated. We have repeated the process, till the converged solution for $V_{i,j}$, $B_{i,j}$ and $T_{i,j}$ in the grid system are obtained.

5. RESULTS AND DISCUSSION

To obtain some physical insight into the problem, a numerical simulation has been constructed to justify the effect of various physical parameters that governed are by the system with the inclusion of various physical situations, on the

fluid variables, such as velocity, temperature, and induced magnetic field. The effect Hartmann number (Ha), Thermal Grashof number (G_r), Reynolds number (R_e), Prandtl number (P_r) and magnetic Reynolds number (R_m) on the velocity, temperature, and induced magnetic field profiles are shown graphically.

The velocity profile of $Al_2O_3/Water$ nanofluid for different values of Hartmann number (Ha) is shown in Figure 2. It is observed that a rise in the Hartmann number causes a decrease in the velocity profile. This is due to the fact that when a magnetic field is applied to an electrically conducting fluid a Lorentz force is produced. This force retards the fluid velocity in the boundary layer region as the magnetic field opposes the transport phenomena.

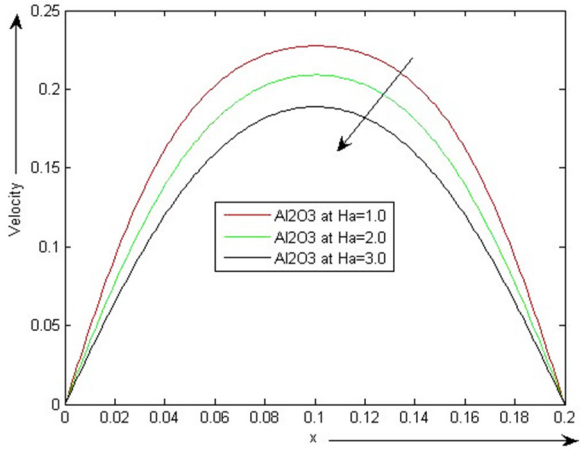

Figure 2. Effect of Hartmann number (Ha) on the velocity profile, when $Ha = 2, P_r = 0.71, R_m = 10, G_r = 2, R_e = 10, h = k = 0.001, m = n = 200, \phi = 0.02, k_f = 40, k_s = 0.613$

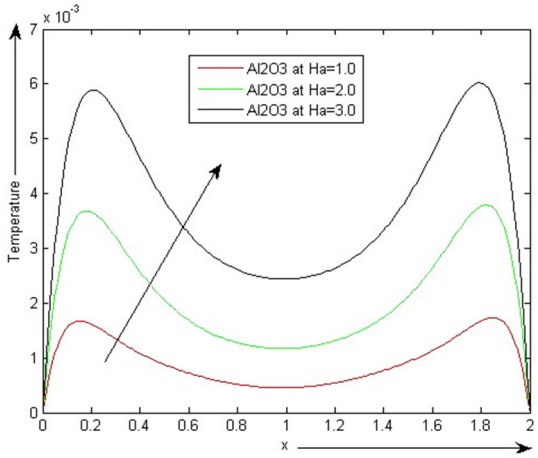

Figure 3. Effect of Hartmann number (Ha) on the temperature profile, when $Ha = 2, P_r = 0.71, R_m = 10, G_r = 2, R_e = 10, h = k = 0.01, m = n = 200, \phi = 0.02, k_f = 40, k_s = 0.613$

On the other hand, in Figure 3, it is observed that the temperature distribution in the boundary layer region increases with the increase in Hartmann number (Ha). According to the Lorentz force effect, the flow encounters frictional resistance, which causes the boundary layer to heat up. In consequence, the temperature profile increases as (Ha) increase. The effect of magnetic fields on nanofluid has many industrial applications in the cooling sector also.

The effect of thermal Grashof number (Gr) on the velocity profile of $Al_2O_3/Water$ nanofluid is shown in Figure (4). Thermal Grashof number can be defined as the ratio of thermal buoyancy force to the viscous force in the boundary layer regime. With large values of this parameter, buoyancy dominates, and for small values viscosity dominates. In the above figure the velocity of $Al_2O_3/Water$ nanofluid is found to increase with the increase in thermal Grashof number (G_r). This means that the buoyancy force accelerates the velocity field. An increase in the value of the thermal Grashof number tends to induce much flow in the boundary layer due to the effect of thermal buoyancy. Again, it is found in Figure 5 that, the temperature of $Al_2O_3/Water$ nanofluid decreases with the increase in thermal Grashof number (G_r). This means that buoyancy force reduces the temperature field.

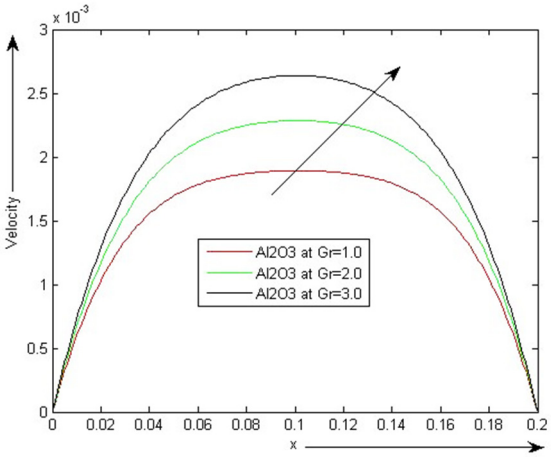

Figure 4. Effect Thermal Grashof number (G_r) on the velocity profile, when $Ha = 2,\ P_r = 0.71,\ R_m = 1,\ G_r = 6,\ R_e = 1.5, h = k = 0.01, m = n = 200, \phi = 0.02,\ k_f = 40, k_s = 0.613$

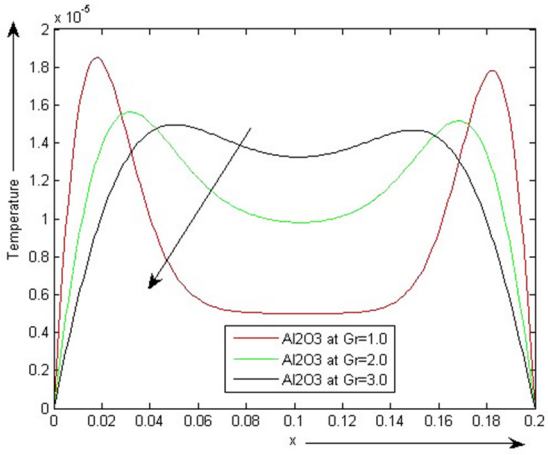

Figure 5. Effect Thermal Grashof number (G_r) on the temperature profile, when $Ha = 100, P_r = 1.0, R_m = 10, G_r = 2,\ R_e = 1.5, h = k = 0.001, m = n = 200, \phi = 0.02, k_f = 40,\ k_s = 0.613$

Figure 6 shows the variation of the velocity field of Al_2O_3/Water nanofluid for various values of Reynolds number (R_e). It is defined as the ratio of inertia force to viscous force. The Reynolds number depends on the relative internal movement due to different fluid velocities. For fluid flow analysis, the Reynolds number is considered to be a prerequisite. When viscous force dominates over the inertia force, the flow is smooth and at low velocities, the Reynolds number value is comparatively less, therefore velocity with Al_2O_3/Water nanofluid decreases as Reynolds number increases. Again Figure 7 shows the variation of the temperature field of Al_2O_3/Water nanofluid for various values of Reynolds number (R_e). It is seen that the temperature field increases as the (R_e) increases, and thus the rate of heat transfer is enhanced. However, the Reynolds number starts to decrease with temperature when the temperature exceeds the critical value depending on the corresponding concentration.

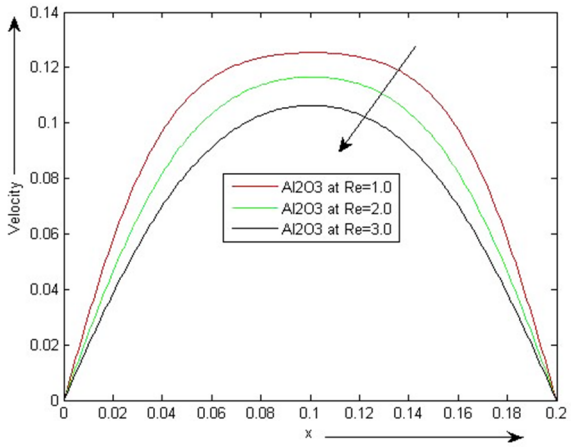

Figure 6. Effect Reynolds number (R_e) on the velocity profile, when $Ha = 5,\ P_r = 0.71,\ R_m = 5,\ G_r = 2,\ R_e = 10,\ h = k = 0.001,\ m = n = 200, \phi = 0.02, k_f = 40, k_s = 0.613$

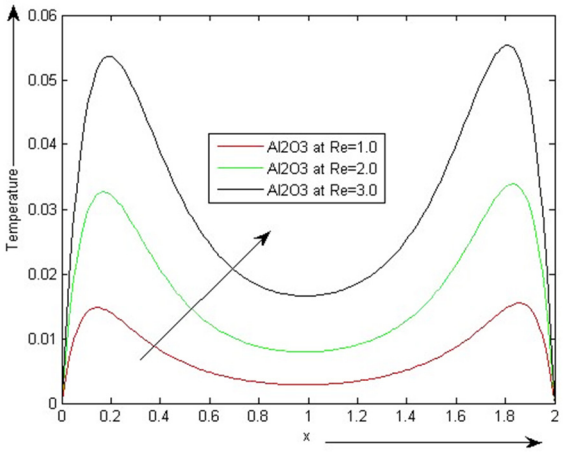

Figure 7. Effect Reynolds number (R_e) on the temperature profile, when $Ha = 2,\ P_r = 6.93,\ R_m = 10,\ G_r = 2, R_e = 10,\ h = k = 0.01,\ m = n = 200, \phi = 0.02, k_f = 40, k_s = 0.613.$

The effect of Prandtl number (P_r) on velocity and temperature profiles is demonstrated graphically in Figures 8 and 9, respectively. It can be observed that the velocity of the nanofluid flow inside the boundary layer region increases whereas the temperature profile decreases due to an increase in Prandtl number (P_r). Prandtl number is the ratio of momentum diffusivity to thermal diffusivity. With a higher value of the Prandtl number, the momentum diffuses more rapidly than the heat, indicating that fluids with a higher Prandtl number have low thermal conductivity and a thinner thermal layer structure. This results in the temperature in the boundary layer region to decreases with the increase in the Prandtl number owing to the increase in the heat transfer rate of the fluid.

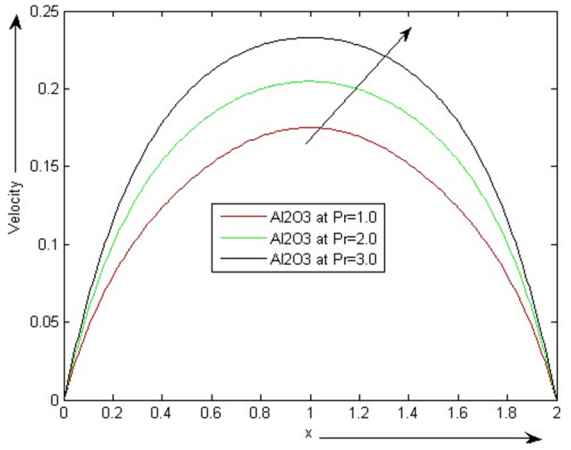

Figure 8. Effect Prandtl number (P_r) on the velocity profile, when $Ha = 2,\ P_r = 6.93,\ R_m = 5,\ G_r = 2,\ R_e = 1,\ h = k = 0.01,\ m = n = 200,\ \phi = 0.02,\ k_f = 40,\ k_s = 0.613$

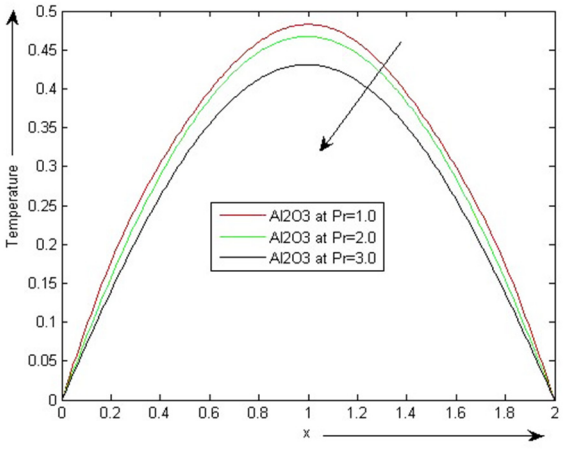

Figure 9. Effect Prandtl number (P_r) on the temperature profile, when $Ha = 100,\ P_r = 0.71,\ R_m = 10, G_r = 2,\ R_e = 1,\ h = k = 0.01, m = n = 200, \phi = 0.02, k_f = 40, k_s = 0.613$

Figure 10 shows the variation of the velocity field of Al_2O_3/Water nanofluid at various values of magnetic Reynolds number (R_m). It can be seen that the velocity profile rises with the increase in magnetic Reynolds number.

Again, Figure 11 shows the variation in the temperature profile of Al_2O_3/Water nanofluid at various values of Magnetic Reynolds number (R_m). The magnetic Reynolds number is the magnetic analog of the Reynolds number, which is a fundamental dimensionless group that occurs in magnetohydrodynamics (MHD). It gives an estimate of the relative

effects of the advection or induction of a magnetic field by the motion of a conducting medium, often a fluid, to magnetic diffusion. Therefore, the temperature profile decreases as the value of (R_m) increases.

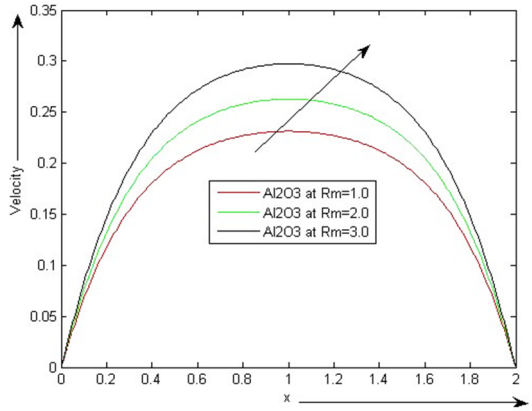

Figure 10. Effect Magnetic Reynolds number (R_m) on the velocity profile, when $Ha = 2, P_r = 6.93, R_m = 5,\ G_r = 2,\ R_e = 1, h = k = 0.001, m = n = 200, \phi = 0.02, k_f = 40,\ k_s = 0.613$

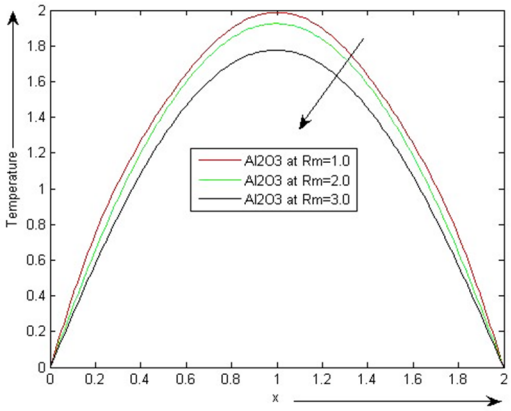

Figure 11. Effect Magnetic Reynolds number (R_m) on the temperature profile, when $Ha = 100, P_r = 0.71,\ R_m = 1,\ G_r = 4,\ R_e = 10, h = k = 0.01, m = n = 200, \phi = 0.02,\ k_f = 40, k_s = 0.613$

In Figures 12 (A), 12 (B), 12 (C), and 12 (D), the distribution of induced magnetic field B for mixed convection with the transverse magnetic field are plotted for $Ha = 100,\ G_r = 100;\ Ha = 200,\ G_r = 100,\ Ha = 300,\ G_r = 100;\ Ha = 400,\ G_r = 100$ and other parameters are fixed. It is observed that B becomes flattened for increasing values of Hartmann number Ha. Moreover, current lines and magnetic fields are almost orthogonal in almost all the duct cross-sections.

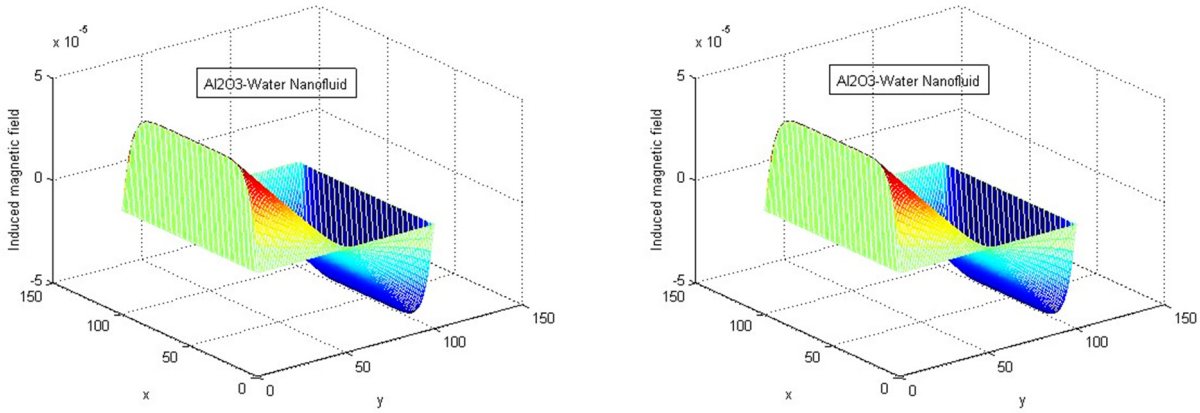

A B

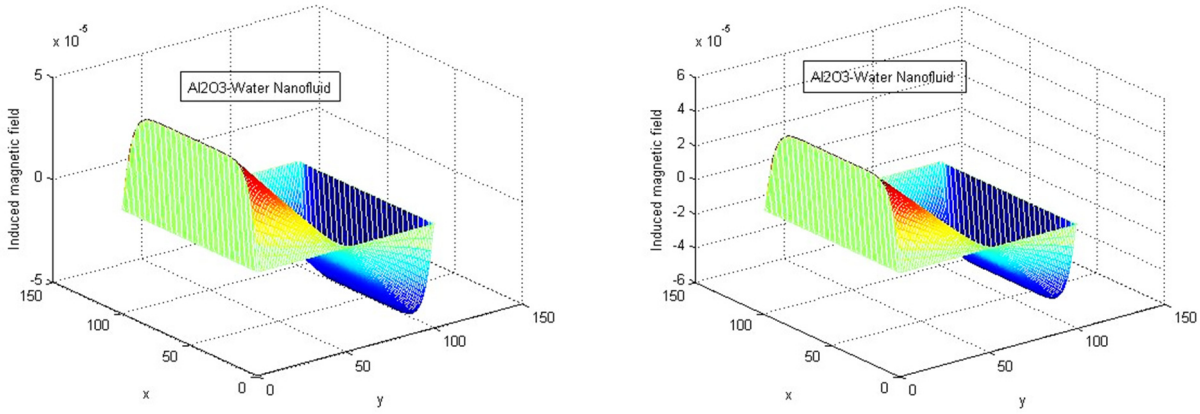

C D

Figure 12. (A) Induced magnetic field for $Ha = 100$ and $G_r = 100$; (B) Induced magnetic field for $Ha = 100$ and $G_r = 200$; (C) Induced magnetic field for $Ha = 100$ and $G_r = 300$; (D) Induced magnetic field for $Ha = 100$ and $G_r = 400$

6. CONCLUSIONS

In the present exploration, we have made an investigation over the nanofluid flow (with base fluid water and nanoparticles as aluminum) through a square duct under the action of the strong transverse magnetic field. The numerical results are obtained by implementing the finite difference scheme coded in MATLAB software. The findings are summarized below:

- The velocity profile of the nanofluid declines with the increase in the value of the Hartmann number, whereas it increases with the increase in the value of the Prandtl number.
- The temperature profile of the nanofluid increase with the increase in Hartmann number and Reynolds number.
- The temperature profile of the nanofluid decelerates with the increase in the Prandtl number and Magnetic Reynolds number.
- The velocity profile of the nanofluid increase with the increase in the Prandtl number and Magnetic Reynolds number.
- The present study provides a model for enhanced heat transfer phenomena and hence finds its application in the cooling sector in industries, post-accidental heat removal in nuclear reactors, and heat exchangers. Besides these, some other important scientific applications of this study may be relevant to manufacturing industries, solar collectors, and so on.

Nomenclature

a	length of the cross-section of the square duct
$\bar{B}$	magnetic field
B_o	applied magnetic field
C_p	specific heat at constant pressure
Ha	Hartmann number
G_r	Grashof number
R_e	Reynolds number
P_r	Prandtl number
R_m	Magnetic Reynolds number
g	acceleration due to gravity
p	Pressure force
T	fluid temperature
T_o	wall temperature
V	velocity in the z-direction
x, y, z	Cartesian coordinates
β	coefficient of thermal expansion
ρ_{nf}	density of nanofluid
σ_{nf}	electrical conductivity of nanofluid
μ_{nf}	dynamic viscosity of nanofluid

Subscripts

nf	nanofluids
f	Base Fluid
s	Solid particles of nanofluid

ORCID IDs

Bishnu Ram Das, https://orcid.org/0000-0002-9760-098X; **P.N. Deka,** https://orcid.org/0000-0001-9485-9294
Shiva Rao, https://orcid.org/0000-0003-2055-4441

REFERENCES

[1] S.U.S. Choi, and J.A. Eastman, *Enhancing Thermal Conductivity of Fluids with Nanoparticles, in Developments and Applications of Non-Newtonian Flows*, edited by. D.A. Singer, and H.P. Wang, Vol. FED 231, (American Society of Mechanical Engineers, New York, 1995), pp. 99-105.

[2] M.M. Doustdar, and M.K. Yekani, "Numerical study of mixed convection of nanofluid in a square duct containing hot obstacles," Aerospace Mechanics Journal, **12**, 67-78 (2016).

[3] M.A. Mansour, R.A. Mohamed, M.M. Abd-Elaziz, and S.E. Ahmed, "Numerical simulation of mixed convection flows in a square duct partially heated from below using nanofluid," International Communication Heat Mass Transfer, **37**, 1504-1512 (2010), https://doi.org/10.1016/j.icheatmasstransfer.2010.09.004

[4] B. Ghasemi, and S.M. Aminossadati, "Mixed convection in a square duct filled with nanofluids," International Commun. Heat Mass Transfer, **37**, 1142-1148 (2010), https://doi.org/10.1016/j.icheatmasstransfer.2010.06.020

[5] E. Abu-Nada, and H.F. Oztop, "Effects of inclination angle on natural convection in enclosures filled with Cu/water nanofluid", International Journal Heat Fluid Flow, **30**, 669-678 (2009), https://doi.org/10.1016/j.ijheatfluidflow.2009.02.001

[6] E.M. Hemmat, M. Akbari, and A. Karimipour, "Mixed convection in a square duct with an inside hot obstacle filled by an Al_2O_3/water nanofluid," Journal Applied Mechanics Technology Physics, **56**, 443-453 (2015), https://doi.org/10.1134/S0021894415030141

[7] M.K. Moallemi, and K.S. Jang, "Prandtl number effects on laminar mixed convection heat transfer in a lid-driven cavity," International Journal of Heat Mass Transfer, **35**, 1881-1892 (1992), https://doi.org/10.1016/0017-9310(92)90191-T

[8] O. Aydin, and W.J. Yang, "Mixed convection in cavities with a locally heated lower wall and moving sidewalls," Numerical Heat Transfer: Part A: Applications, **37**, 695-710 (2000), https://doi.org/10.1080/104077800274037

[9] H.F. Oztop, and I. Dagtekin, "Mixed convection in square duct differentially heated square cavity," International Journal of Heat and Mass Transfer, **47**, 1761-1769 (2004), https://doi.org/10.1016/j.ijheatmasstransfer.2003.10.016

[10] K.V. Wong, and O. De Leon, "Applications of Nanofluids: Current and Future," Advances in Mechanical Engineering, Article ID 519659, (2010), https://doi.org/10.1155/2010/519659

[11] Y. Li, H.-Q. Xie, W. Yu, and J. Li, "Investigation on Heat Transfer Performances of Nanofluids in Solar Collector," Materials Science Forum, **694**, 33-36 (2011). https://doi.org/10.4028/www.scientific.net/MSF.694.33

[12] T. Yousefi, F. Veysi, E. Shojaeizadeh, and S. Zinadini, "An experimental investigation on the effect of $Al_2O_3/Water$ nanofluid on the efficiency of solar flat plate collectors," Renewable Energy, **39**(1), 293-298 (2011), https://doi.org/10.1016/j.renene.2011.08.056

[13] R.A. Taylor, P.E. Phelan, T. Otanicar, C.A. Walker, M. Nguyen, S. Trimble, and R. Prasher, "Applicability of Nanofluids in High Flux Solar Collectors," Journal of Renewable and Sustainable Energy, **3**(2), 023104 (2011), http://dx.doi.org/10.1063/1.3571565
[14] B.C. Pak, and Y.I. Cho, "Hyrodynamic and heat transfer study of dispersed fluids with submicron metallic oxide particle," Exp. Heat Transfer, **11**, 151 (1998), https://doi.org/10.1080/08916159808946559
[15] W. Yu, and S.U.S. Choi, "The role of interfacial layers in the enhanced thermal conductivity of nanofluids; a renovated Maxwell model," Journal Nanoparticles Res. **5**, 167-171 (2003), https://doi.org/10.1023/A:1024438603801
[16] Y. Xuan, and W. Roetzel, "Conceptions for heat transfer correlation of nanofluids," International Journal Heat Mass Transfer, **43**, 3701-3707 (2000), http://dx.doi.org/10.1016/S0017-9310(99)00369-5
[17] J. Rahimah, R. Nazar, and I. Pop, "Magnetohydrodynamic boundary layer flow and heat transfer of nanofluids past a bidirectional exponential permeable stretching/shrinking sheet with viscous dissipation effect," Journal Heat Transfer, **141**, 012406 (2019), https://doi.org/10.1115/1.4041800
[18] T.-C. Hung, and W.-M. Yan, "Enhancement of thermal performance in double-layered microchannel heat sink with nanofluids," International Journal Heat Mass Transfer, **55**, 3225-3238 (2012), https://doi.org/10.1016/j.ijheatmasstransfer.2012.02.057
[19] M. Sheikhpour, M. Arabi, A. Kasaeian, A.R. Rabei, and Z. Taherian, "Role of nanofluids in drug delivery and biomedical technology: methods and applications," Nanotechnol. Sci. Appl. **13**, 47 (2020), https://doi.org/10.2147%2FNSA.S260374
[20] S.D. Majumder, and A. Das, "A short review of organic nanofluids: preparation, surfactants, and applications," Front. Mater. **8**, 630182 (2021), https://doi.org/10.3389/fmats.2021.630182
[21] M.S. Dehaj, M. Rezaeian, and D. Mousavi, S. Shamsi, and M. Salarmofrad, "Efficiency of the parabolic through solar collector using $NiFe_2O_4/water$ nanofluid and U-tube," Journal Taiwan Inst. Chem. Eng. **120**, 136-149 (2021), https://doi.org/10.1016/j.jtice.2021.02.029
[22] R. Sivaraj, and S. Banerjee, "Transport properties of non-Newtonian nanofluids and applications," The European Physical Journal Special Topics, **230**, 1167-1171 (2021), https://doi.org/10.1140/epjs/s11734-021-00031-1
[23] T. Thumma, A. Wakif, and I.L. Animasaun, "Generalized differential quadrature analysis of unsteady three-dimensional MHD radiating dissipative Casson fluid conveying tiny particles," Heat Transfer, **49**(5), 2595-2626 (2020), https://doi.org/10.1002/htj.21736
[24] S. Lahmar, M. Kezzar, M.R. Eid, and M.R. Sari, "Heat transfer of squeezing unsteady nanofluid flow under the effects of an inclined magnetic field and variable thermal conductivity," Physica A, **540**, 123-138 (2020), https://doi.org/10.1016/j.physa.2019.123138
[25] N.C. Roşca, and I. Pop, "Hybrid nanofluids flows determined by a permeable power-Law stretching/shrinking sheet modulated by orthogonal surface shear," Entropy, **23**(7), 813 (2021), https://doi.org/10.3390/e23070813
[26] F. Selimefendigil, and H.F. Oztop, "Thermal management and modeling of forced convection and entropy generation in a vented cavity by simultaneous use of a curved porous layer and magnetic field," Entropy, **23**(2), 152 (2021), https://doi.org/10.3390/e23020152
[27] W. Jamshed, "Numerical investigation of MHD impact on Maxwell nanofluid," International Commun. Hear. Mass Transfer, **120**, 104973 (2021), https://doi.org/10.1016/j.icheatmasstransfer.2020.104973
[28] W. Jamshed, K.S. Nisar, and R.W. Ibrahim, "Computational frame work of Cattaneo-Chritov heat flux effects on Engine Oil based Williamson hybrid nanofluids: a thermal case study," Case Stud. Therm. Eng. **26**, 101179 (2021), https://doi.org/10.1016/j.csite.2021.101179
[29] W. Jamshed, "Thermal augmentation in solar aircraft using tangent hyperbolic hybrid nanofluid: a solar energy application," Energy Environ. **33**(6), 1-44 (2021), https://doi.org/10.1177/0958305X211036671
[30] S. Rao, and P. Deka, "A Numerical Study on Unsteady MHD Williamson Nanofluid Flow past a Permeable Moving Cylinder in the presence of Thermal Radiation and Chemical Reaction," Biointerface Research in Applied Chemistry, **13**(5), 1-19 (2023), https://biointerfaceresearch.com/wp-content/uploads/2023/01/BRIAC135.436.pdf
[31] S. Rao, and P. Deka, "A Numerical Study on Heat Transfer for MHD Flow of Radiative Casson Nanofluid Over a Porous Stretching Sheet," Latin American Applied Research – an International Journal, **53**(2), 129-136 (2023), https://doi.org/10.52292/j.laar.2023.950
[32] T.A. Yusuf, R.N. Kumar, R.J.P. Gowda, and U.D. Akpan, "Entropy generation on flow and heat transfer of a reactive MHD Sisko fluid through inclined walls with porous medium," Int. J. Ambient Energy, **43**(1), 6307-6316 (2022), https://doi.org/10.1080/01430750.2021.2013941
[33] H.K. Hamzah, F.H. Ali, and M. Hatami, "MHD mixed convection and entropy generation of CNT-water nanofluid in a wavy lid-driven porous enclosure at different boundary conditions." Sci. Rep. **12**, 2881 (2022), https://doi.org/10.1038/s41598-022-06957-3
[34] W.U. Khan, M. Awais, N. Parveen, A. Ali, S.E. Awan, M.Y. Malik, and Y. He, "Analytical Assessment of (Al_2O_3-Ag/H_2O) Hybrid Nanofluid Influenced by Induced Magnetic Field for Second Law Analysis with Mixed Convection," Viscous Dissipation and Heat Generation, Coatings, **11**, 498 (2021), https://doi.org/10.1038/s41598-022-06957-3
[35] S. Ahmed, and I. Pop, "Mixed convection boundary layer flow from a vertical flat plate embedded in a porous medium filled with nano-fluids," Int. Commun. Heat Mass Transf. **37**, 987-999 (2010), https://doi.org/10.1016/j.icheatmasstransfer.2010.06.004
[36] A. Malvandi, and D.D. Ganji, "Mixed convection of alumina-water nanofluid inside a concentric annulus considering nanoparticle migration," Particulogy, **24**, 113-122 (2016), https://doi.org/10.18869/acadpub.jafm.68.236.25641
[37] T. Tayebi, and A.J. Chamkha, "Magnetohydrodynamic Natural Convection Heat Transfer of Hybrid Nanofluid in a Square Enclosure in the Presence of a Wavy Circular Conductive Cylinder," Journal Therm. Sci. Eng. Appl. **12**(3), 031009 (2020), https://doi.org/10.1115/1.4044857
[38] Z. Shah, P. Kumam, and W. Deebani, "Radiative MHD Casson Nanofluid Flow with Activation energy and chemical reaction over past nonlinearly stretching surface through Entropy generation," Sci. **10**(1), 1-14 (2020), https://doi.org/10.1038/s41598-020-61125-9
[39] V. Rajesh, M. Srilatha, and A.J. Chamkha, "Hydromagnetic effects on hybrid nanofluid Cu-Al2O3/Water flow with convective heat transfer due to a stretching sheet," Journal Nanofluids, **9**(4), 293-301 (2020), https://doi.org/10.1166/jon.2020.1755
[40] S. Molli, and K. Naikoti, "MHD Natural Convective Flow of Cu-Water Nanofluid over a Past Infinite Vertical Plate with the Presence of Time Dependent Boundary Condition," International Journal Thermofluid Sci. Technol. **7**(4), 1-15 (2020), https://doi.org/10.36963/IJTST.2020070404

[41] N.S. Khashi'ie, N.M. Arifin, I. Pop, and N.S. Wahid, "Flow and heat transfer of hybrid nanofluid over a permeable shrinking cylinder with Joule heating: A comparative analysis," Alexandria Eng. Journal, **59**(3), 1787-1798 (2020), https://doi.org/10.1016/j.aej.2020.04.048
[42] W. Alghamdi, T. Gul, M. Nullah, A. Rehman, S. Nasir, A. Saeed, and E. Bonyah, "Boundary layer stagnation point flow of the Casson hybrid nanofluid over an unsteady stretching surface," AIP Adv. **11**(1), 015016 (2021), https://doi.org/10.1063/5.0036232
[43] M. Shahzad, M. Ali, F. Sultan, WA. Khan, and Z. Hussain, "Computational investigation of magneto-cross fluid flow with multiple slip along wedge and chemically reactive species", Results Phys. **16**, 102972 (2020), https://doi.org/10.1016/j.rinp
[44] N. Ibrar, M.G. Reddy, S.A. Shehzad, P. Sreenivasulu, and T. Poornima, "Interaction of single and multi-walls carbon nanotubes in magnetized-nano casson fluid over radiated horizontal needle," SN Appl. Sci. **2**, 677 (2020), https://doi.org/10.1007/s42452-020-2523-8
[45] L.A. Lund, Z. Omar, J. Raja, I. Khan, and E.M. Sherif, "Effects of Stefan blowing and slip conditions on unsteady MHD casson nanofluid flow over an unsteady shrinking sheet: dual solutions," Symmetry, **12**, 487 (2020), https://doi.org/10.3390/sym12030487
[46] S. Rao, and P. Deka, A Numerical investigation on Transport Phenomena in a Nanofluid Under the Transverse Magnetic Field Over a Stretching Plate Associated with Solar Radiation. Nonlinear Dynamics and Applications, **2022,** 473-492, https://doi.org/10.1007/978-3-030-99792-2_39
[47] S. Rao, and P. Deka, "A numerical solution using EFDM for unsteady MHD radiative Casson nanofluid flow over a porous stretching sheet with stability analysis," Heat Transfer, **51**(8), 8020-8042 (2022), https://doi.org/10.1002/htj.22679
[48] H.C. Brinkman, "The viscosity of concentrated suspensions and solutions," J. Chem. Phys. **20**, 571-581 (1952), https://doi.org/10.1063/1.1700493
[49] W.A. Khan, M. Ali, F. Sultan, M. Shahzad, M. Khan, and M. Irfan, "Numerical interpretation of autocatalysis chemical reaction for nonlinear radiative 3D flow of Cross magnetofluid," Pramana J. Phys. **92**, 16 (2019), https://doi.org/10.1007/s12043-018-1678-y
[50] J.A. Maxwell, *Treatise on Electricity and Magnetism*, second ed. (Oxford University Press, Cambridge, 2010).
[51] K. Khanafer, K. Vafai, and M. Lightsone, "Buoyancy-driven heat transfer enhancement in a two-dimensional enclosure utilizing nanofluids," Int. J. Heat Mass. Transf. **46**, 3639-3653 (2003), https://doi.org/10.1016/S0017-9310(03)00156-X

ЧИСЛОВИЙ АНАЛІЗ МГД ЗМІШАНОГО КОНВЕКЦІЙНОГО ПОТОКУ НАНОРІДИН Al_2O_3/H_2O (АЛЮМІНІЙ-ВОДА) У ВЕРТИКАЛЬНОМУ КВАДРАТНОМУ КАНАЛІ

Бішну Рам Дас, П.Н. Дека, Шива Рао
Факультет математики, Університет Дібругарх, Дібругарх-786004, Ассам, Індія

У цій роботі ми розглянули стаціонарну ламінарну магнітогідродинамічну (МГД) змішану конвекцію електропровідної рідини в присутності наночастинок Al_2O_3, тоді як вода є основною рідиною у вертикальному квадратному каналі. Стінки воздуховода утеплені. У рівнянні енергії також враховується ефект в'язкої дисипації та джоулева теплота. У цьому випадку на стінках каналу підтримується постійна температура. Використовуючи безрозмірні величини, керівні рівняння імпульсу, індукції та енергії спочатку перетворюються на безрозмірні рівняння, а потім скорочені рівняння розв'язуються за допомогою явного методу кінцевих різниць. Профілі швидкості, температури та індукованого магнітного поля будуються графічно для аналізу впливу різних параметрів потоку. Помічено, що рух нанофлюїду прискорюється зі збільшенням значення магнітного параметра, числа Рейнольдса та числа Прандтля. Сучасні дослідження можуть знайти застосування в багатьох галузях промисловості та охолодження. У цьому дослідженні відзначено його важливість для підвищення ефективності теплопередачі для практичних застосувань, пов'язаних із промисловістю та технікою. Проблеми, які обговорюються в цьому дослідженні, не були включені в попередні дослідження сталого потоку нанофлюїдів через квадратну трубу.

Ключові слова: *нанофлюїди; явний чисельний метод кінцевих різниць (EFDM); МГД потік; сила виштовхування; змішана конвекція; квадратний повітропровід; теплопередача; магнітне поле*

EAST EUROPEAN JOURNAL OF PHYSICS. **2.** 63-68 (2023)
DOI:10.26565/2312-4334-2023-2-03 ISSN 2312-4334

COMPOSITE FERMIONS QED LAGRANGIAN DENSITY IN FRACTIONAL FORMULATION[†]

Amer D. Al-Oqali
Department of Physics, Mutah University, Al-Karak, Jordan
E-mail: aoqali@mutah.edu.jo
Received February 13, 2023; revised March 10, 2023; accepted March 12, 2023

Quantum electrodynamics (QED) is a highly precise and successful theory that describes the interaction between electrically charged particles and electromagnetic radiation. It is an integral part of the Standard Model of particle physics and provides a theoretical basis for explaining a wide range of physical phenomena, including the behavior of atoms, molecules, and materials. In this work, the Lagrangian density of Composite Fermions in QED has been expressed in a fractional form using the Riemann-Liouville fractional derivative. The fractional Euler-Lagrange and fractional Hamiltonian equations, derived from the fractional form of the Lagrangian density, were also obtained. When α is set to 1, the conventional mathematical equations are restored.
Keywords: *Quantum Electrodynamics; Composite Fermions; Fractional derivative; Lagrangian density; Euler-Lagrange equations*
PACS: 31.30.J, 71.10.Pm, 45.10.Hj, 45.20.Jj, 11.10.Ef

1. INTRODUCTION

Composite Fermions are a theoretical concept in condensed matter physics that explains the behavior of electrons when subjected to a strong magnetic field [1-4]. These electrons can form composite particles with unique physical properties, such as those seen in fractional quantum Hall states [5-7]. Understanding composite fermions provides insights into the behavior of electrons in high magnetic fields and has applications in various fields, from technology development to the discovery of basic physical principles.

Fractional derivatives [8-12] have become a valuable tool in various fields because they provide the ability to accurately model physical phenomena that cannot be captured by ordinary derivatives. There has been a surge of research in fractional calculus, leading to its application in physics, engineering, and related areas [13-16]. The Maxwell equations have been expressed in fractional form [17-19], as have those in quantum mechanics, including the fractional Schrödinger equation [20, 21] and the fractional Dirac equation [22]. These advancements demonstrate the versatility of fractional calculus in describing a wide range of physical systems.

The main goal of this work is to examine the composite Fermions QED Lagrangian density and transform it into a fractional form using the Riemann-Liouville (RL) fractional derivative. The ultimate purpose is to derive the fractional Hamilton's equations and fractional Euler-Lagrange (EL) equations from this reformulation, thereby providing a fresh perspective on the dynamics of composite Fermions within a QED framework.

The structure of the paper is as follows: In Sec. 2, a brief explanation of RL fractional derivative is provided. The topic of the QED Lagrangian density is discussed in Sec. 3. In Sec. 4, the fractional form of the Lagrangian density and the fractional Euler-Lagrange equations are presented. The focus of Sec. 5 is on the Hamiltonian equations derived from the Lagrangian density. The paper concludes with a concise summary of the key points in Sec. 6.

2. PRELIMINARIES

This section provides essential definitions used in this study. For a more comprehensive understanding, readers can refer to reference [23]. The following are the definitions of the left and right RL fractional derivative.
The Left RL fractional derivative

$$ {}_aD_x^{\alpha}\, f(x) = \frac{1}{\Gamma(n-\alpha)} \left(\frac{d}{dx}\right)^n \int_a^x (x-\tau)^{n-\alpha-1}\, f(\tau)\, d\tau. \tag{1}$$

The right RL fractional derivative

$$ {}_xD_b^{\alpha}\, f(x) = \frac{1}{\Gamma(n-\alpha)} \left(-\frac{d}{dx}\right)^n \int_x^b (\tau-x)^{n-\alpha-1}\, f(\tau)\, d\tau. \tag{2}$$

The value of α signifies the order of differentiation, where $n-1 \le \alpha < n$, with Γ symbolizing the gamma function. In cases where α is an integer, the derivative is calculated using the conventional definition.

$$ \begin{cases} {}_aD_x^{\alpha}\, f(x) = \left(\frac{d}{dx}\right)^n f(x) \\ {}_aD_t^{\alpha}\, f(x) = \left(\frac{d}{dx}\right)^n f(t) \end{cases}, \quad \alpha = 1,2,\ldots \tag{3}$$

[†] ***Cite as:*** A.D. Al-Oqali, East Eur. J. Phys. **2**, 63 (2023), https://doi.org/10.26565/2312-4334-2023-2-03

3. COMPOSITE FERMIONS QED LAGRANGIAN DENSITY

The Lagrangian density for composite fermions in QED, with the speed of light set to 1, has the following mathematical form [1]:

$$\mathcal{L} = \overline{\psi}\left(i\gamma^{\mu}\partial_{\mu} - m\right)\psi - \tfrac{1}{4}F_{\mu\nu}F^{\mu\nu} + \frac{e\pi\, v^2{}_{eff}}{2\theta\phi_0}\varepsilon^{\mu\nu\rho}A_{\mu}\ \partial_{\nu}A_{\rho} - \left(1 + v_{eff}\right)e\overline{\psi}\,\gamma^{\mu}\psi\, A_{\mu}\,. \tag{4}$$

This equation involves the Levi-Civita symbol $\varepsilon^{\mu\nu\rho}$, which is an antisymmetric tensor, as well as ψ which is a Dirac's spinor and made up of four complex parts, $\overline{\psi} = \psi^{+}\gamma^{0}$, γ^{μ} is Dirac matrix, e is the charge of an electron, ϕ_0 is a unit of magnetic flux, it also includes a gauge parameter, θ, for the Chern-Simons fields. $F_{\mu\nu}$ is the electromagnetic field tensor and the A_{μ} are electromagnetic fields. The first term represents the fields that are associated with spinors, while the second term represents fields related to electromagnetism. The third term involves gauge Chern-Simons fields, and the final two terms describe the coupling of the spinor fields to both the electromagnetic fields and the Chern-Simons fields.

4. FRACTIONAL FORM OF COMPOSITE FERMIONS QED LAGRANGIAN DENSITY

The fractional Lagrangian density of (4) can be written as:

$$\mathcal{L} = \overline{\psi}\left(i\gamma^{\mu}\,{}_{a}^{c}D_{x_{\mu}}^{\alpha} - m\right)\psi - \tfrac{1}{4}F_{\mu\nu}F^{\mu\nu} + \frac{e\pi\, v^2{}_{eff}}{2\theta\phi_0}\varepsilon^{\mu\nu\rho}A_{\mu}\ {}_{a}D_{x_{\nu}}^{\alpha}A_{\rho} - \left(1 + v_{eff}\right)e\overline{\psi}\,\gamma^{\mu}\psi\, A_{\mu}\,. \tag{5}$$

Begin by expanding the second term in the Lagrangian:

$$F_{\mu\nu}F^{\mu\nu} = g^{\mu\rho}g^{\nu\lambda}\left({}_{a}D_{x_{\mu}}^{\alpha}A_{\nu} - {}_{a}D_{x_{\nu}}^{\alpha}A_{\mu}\right)\left({}_{a}D_{x_{\rho}}^{\alpha}A_{\lambda} - {}_{a}D_{x_{\lambda}}^{\alpha}A_{\rho}\right)$$

Hence, we have

$$\mathcal{L} = \overline{\psi}\left(i\gamma^{\mu}\,{}_{a}^{c}D_{x_{\mu}}^{\alpha} - m\right)\psi - \frac{1}{4}\,g^{\mu\rho}g^{\nu\lambda}\left({}_{a}D_{x_{\mu}}^{\alpha}A_{\nu} - {}_{a}D_{x_{\nu}}^{\alpha}A_{\mu}\right)\left({}_{a}D_{x_{\rho}}^{\alpha}A_{\lambda} - {}_{a}D_{x_{\lambda}}^{\alpha}A_{\rho}\right) + \\ + \frac{e\pi\, v^2{}_{eff}}{2\theta\phi_0}\varepsilon^{\mu\nu\rho}A_{\mu}\ {}_{a}D_{x_{\nu}}^{\alpha}A_{\rho} - \left(1 + v_{eff}\right)e\overline{\psi}\,\gamma^{\mu}\psi\, A_{\mu} \tag{6}$$

In the case of a Lagrangian involving multiple fields, there will be a separate equation for each field. The EL equation for the field A_{β} is expressed as follows:

$$\frac{\partial\mathcal{L}}{\partial A_{\beta}} - {}_{a}D_{x_{\sigma}}^{\alpha}\left[\frac{\partial\mathcal{L}}{\partial\left({}_{a}D_{x_{\sigma}}^{\alpha}A_{\beta}\right)}\right] = 0. \tag{7}$$

Thus, the equation of motion is expressed as

$$\frac{e\pi\, v^2{}_{eff}}{2\theta\phi_0}\varepsilon^{\mu\nu\rho}\delta_{\mu}^{\beta}\ {}_{a}D_{x_{\nu}}^{\alpha}A_{\rho} - \left(1 + v_{eff}\right)e\overline{\psi}\,\gamma^{\mu}\psi\, A_{\mu}\,\delta_{\mu}^{\beta} - {}_{a}D_{x_{\sigma}}^{\alpha}\left[-\tfrac{1}{4}\,g^{\mu\rho}g^{\nu\lambda}\left(\delta_{\mu}^{\sigma}\delta_{\nu}^{\beta} - \delta_{\nu}^{\sigma}\delta_{\mu}^{\beta}\right)\left({}_{a}D_{x_{\rho}}^{\alpha}A_{\lambda} - {}_{a}D_{x_{\lambda}}^{\alpha}A_{\rho}\right) - -\tfrac{1}{4}\,g^{\mu\rho}g^{\nu\lambda}\left(\delta_{\rho}^{\sigma}\delta_{\lambda}^{\beta} - \delta_{\lambda}^{\sigma}\delta_{\rho}^{\beta}\right)\left({}_{a}D_{x_{\mu}}^{\alpha}A_{\nu} - {}_{a}D_{x_{\nu}}^{\alpha}A_{\mu}\right) + \frac{e\pi\, v^2{}_{eff}}{2\theta\phi_0}\varepsilon^{\mu\nu\rho}A_{\mu}\,\delta_{\nu}^{\sigma}\,\delta_{\rho}^{\beta}\right] = 0$$

$$\frac{e\pi\, v^2{}_{eff}}{2\theta\phi_0}\varepsilon^{\beta\nu\rho}\ {}_{a}D_{x_{\nu}}^{\alpha}A_{\rho} - \left(1 + v_{eff}\right)e\overline{\psi}\,\gamma^{\beta}\psi\, A_{\mu} - {}_{a}D_{x_{\sigma}}^{\alpha}\left[-\tfrac{1}{4}\left(g^{\sigma\rho}g^{\beta\lambda} - g^{\beta\rho}g^{\sigma\lambda}\right)\left({}_{a}D_{x_{\rho}}^{\alpha}A_{\lambda} - {}_{a}D_{x_{\lambda}}^{\alpha}A_{\rho}\right) - -\tfrac{1}{4}\left(g^{\mu\sigma}g^{\nu\beta} - g^{\mu\beta}g^{\nu\sigma}\right)\left({}_{a}D_{x_{\mu}}^{\alpha}A_{\nu} - {}_{a}D_{x_{\nu}}^{\alpha}A_{\mu}\right) + \frac{e\pi\, v^2{}_{eff}}{2\theta\phi_0}\varepsilon^{\mu\sigma\beta}\ {}_{a}D_{x_{\sigma}}^{\alpha}A_{\mu}\right] = 0$$

$$\frac{e\pi\, v^2{}_{eff}}{2\theta\phi_0}\varepsilon^{\beta\nu\rho}\ {}_{a}D_{x_{\nu}}^{\alpha}A_{\rho} - \left(1 + v_{eff}\right)e\overline{\psi}\,\gamma^{\beta}\psi - {}_{a}D_{x_{\sigma}}^{\alpha}\left[-\tfrac{1}{4}\left({}_{a}D_{x^{\sigma}}^{\alpha}A^{\beta} - {}_{a}D_{x^{\beta}}^{\alpha}A^{\sigma} - {}_{a}D_{x^{\beta}}^{\alpha}A^{\sigma} + {}_{a}D_{x^{\sigma}}^{\alpha}A^{\beta}\right) - -\tfrac{1}{4}\left({}_{a}D_{x^{\sigma}}^{\alpha}A^{\beta} - {}_{a}D_{x^{\beta}}^{\alpha}A^{\sigma} - {}_{a}D_{x^{\beta}}^{\alpha}A^{\sigma} + {}_{a}D_{x^{\sigma}}^{\alpha}A^{\beta}\right) + \frac{e\pi\, v^2{}_{eff}}{2\theta\phi_0}\varepsilon^{\mu\sigma\beta}\ {}_{a}D_{x_{\sigma}}^{\alpha}A_{\mu}\right] = 0$$

or alternatively,

$$\frac{e\pi\, v^2{}_{eff}}{2\theta\phi_0}\left(\varepsilon^{\beta\nu\rho}\ {}_{a}D_{x_{\nu}}^{\alpha}A_{\rho} - \varepsilon^{\mu\sigma\beta}\ {}_{a}D_{x_{\sigma}}^{\alpha}A_{\mu}\right) - \left(1 + v_{eff}\right)e\overline{\psi}\,\gamma^{\beta}\psi - {}_{a}D_{x_{\sigma}}^{\alpha}\left({}_{a}D_{x^{\sigma}}^{\alpha}A^{\beta} - {}_{a}D_{x^{\beta}}^{\alpha}A^{\sigma}\right) = 0$$

using $F^{\sigma\beta} = \left({}_{a}D_{x^{\sigma}}^{\alpha}A^{\beta} - {}_{a}D_{x^{\beta}}^{\alpha}A^{\sigma}\right)$, as a result of this

$$\frac{e\pi\, v^2{}_{eff}}{2\theta\phi_0}\left(\varepsilon^{\beta\nu\rho}\ {}_{a}D_{x_{\nu}}^{\alpha}A_{\rho} - \varepsilon^{\beta\sigma\mu}\ {}_{a}D_{x_{\sigma}}^{\alpha}A_{\mu}\right) - \left(1 + v_{eff}\right)e\overline{\psi}\,\gamma^{\beta}\psi - {}_{a}D_{x_{\sigma}}^{\alpha}\,F^{\sigma\beta} = 0$$

By replacing the dummy indices ν with μ and ρ with σ in the first term on the left-hand side, we obtain

$$\frac{e\pi\, v^2{}_{eff}}{\theta\phi_0}\varepsilon^{\beta\mu\sigma}\ {}_{a}D_{x_{\sigma}}^{\alpha}A_{\mu} - \left(1 + v_{eff}\right)e\overline{\psi}\,\gamma^{\beta}\psi - {}_{a}D_{x_{\sigma}}^{\alpha}\,F^{\sigma\beta} = 0, \tag{8}$$

on the other hand, the EL equation for $\overline{\psi}$ reads as

$$\frac{\partial \mathcal{L}}{\partial \overline{\psi}} - \ {}_aD^{\alpha}_{x_\sigma}\left[\frac{\partial \mathcal{L}}{\partial\left({}_aD^{\alpha}_{x_\sigma}\overline{\psi}\right)}\right] = 0, \tag{9}$$

which becomes

$$\left(i\gamma^{\mu}\ {}_aD^{\alpha}_{x_\mu} - m\right)\psi - \left(1 + v_{eff}\right)e\ \gamma^{\mu}\psi\ A_{\mu} = 0, \tag{10}$$

finally, the EL equation of the field ψ is presented as follows:

$$\frac{\partial \mathcal{L}}{\partial \psi} - \ {}_aD^{\alpha}_{x_\sigma}\left[\frac{\partial \mathcal{L}}{\partial\left({}_aD^{\alpha}_{x_\sigma}\psi\right)}\right] = 0, \tag{11}$$

which can be written as

$$-m\overline{\psi} - \left(1 + v_{eff}\right)e\ \gamma^{\mu}\overline{\psi}\ A_{\mu} - \ {}_aD^{\alpha}_{x_\sigma}\left(\overline{\psi}\ i\gamma^{\mu}\ \delta^{\sigma}_{\mu}\right) = 0$$

$$m\overline{\psi} + \left(1 + v_{eff}\right)e\ \gamma^{\mu}\overline{\psi}\ A_{\mu} = -i\gamma^{\sigma}\ {}_aD^{\alpha}_{x_\sigma}\overline{\psi}\,. \tag{12}$$

5. FRACTIONAL HAMILTONIAN FORMULATION

In the following section, we will derive the fractional Hamiltonian equations using the RL fractional derivative approach, based on the fractional Lagrangian density. Let us consider the fractional Hamiltonian density as

$$\mathcal{H} = \left(\overline{\psi}, \psi,\ {}_aD^{\alpha}_{x_j}\psi, A_{\mu},\ {}_aD^{\alpha}_{x_j}A_{\mu}, \bar{\pi}, \pi,\ \pi_{\mu}\right). \tag{13}$$

Now, taking the total differential of $\mathcal{H}$, we get:

$$d\mathcal{H} = \frac{\partial \mathcal{H}}{\partial \overline{\psi}}d\overline{\psi} + \frac{\partial \mathcal{H}}{\partial \psi}d\psi + \frac{\partial \mathcal{H}}{\partial A_{\mu}}dA_{\mu} + \frac{\partial \mathcal{H}}{\partial\left({}_aD^{\alpha}_{x_j}\psi\right)}d\left({}_aD^{\alpha}_{x_j}\psi\right) + \frac{\partial \mathcal{H}}{\partial\left({}_aD^{\alpha}_{x_j}A_{\mu}\right)}d\left({}_aD^{\alpha}_{x_j}A_{\mu}\right) + \frac{\partial \mathcal{H}}{\partial \bar{\pi}}d\bar{\pi} + \frac{\partial \mathcal{H}}{\partial \pi}d\pi + \frac{\partial \mathcal{H}}{\partial\ \pi_{\mu}}d\ \pi_{\mu} \tag{14}$$

The canonical momenta $\bar{\pi}, \pi,\ \pi_{\mu}$ are given as follows:

$$\pi = \frac{\partial \mathcal{L}}{\partial\left({}_aD^{\alpha}_{t}\Psi\right)}; \qquad \bar{\pi} = \frac{\partial \mathcal{L}}{\partial\left({}_aD^{\alpha}_{t}\overline{\psi}\right)}; \qquad \pi_{\mu} = \frac{\partial \mathcal{L}}{\partial\left({}_aD^{\alpha}_{t}A_{\mu}\right)}; \tag{15}$$

In order to construct $\mathcal{H}$, we start by defining it in its general form as follows:

$$\mathcal{H} = \bar{\pi}\ {}_aD^{\alpha}_{t}\overline{\psi} + \pi\ {}_aD^{\alpha}_{t}\psi \pm \pi_{\mu}\ {}_aD^{\alpha}_{t}A_{\mu} - \mathcal{L}\left(\psi, \overline{\psi},\ {}_aD^{\alpha}_{x_\sigma}\psi, A_{\beta},\ {}_aD^{\alpha}_{x_\sigma}A_{\beta}\ \right). \tag{16}$$

The total differential of $\mathcal{H}$ can also be defined as:

$$d\mathcal{H} = \bar{\pi}\ d\left({}_aD^{\alpha}_{t}\overline{\psi}\right) + \ {}_aD^{\alpha}_{t}\overline{\psi}\ d\bar{\pi} + \pi\ d\left({}_aD^{\alpha}_{t}\psi\right) + \ {}_aD^{\alpha}_{t}\psi\ d\pi + \ \pi_{\mu}\ d\left({}_aD^{\alpha}_{t}A_{\mu}\right) + \ {}_aD^{\alpha}_{t}A_{\mu}d\ \pi_{\mu} - \frac{\partial \mathcal{L}}{\partial \psi}d\psi -$$
$$- \frac{\partial \mathcal{L}}{\partial \overline{\psi}}d\overline{\psi} - \frac{\partial \mathcal{L}}{\partial\left({}_aD^{\alpha}_{x_\sigma}\psi\right)}d\left({}_aD^{\alpha}_{x_\sigma}\psi\right) - \frac{\partial \mathcal{L}}{\partial A_{\beta}}dA_{\beta} + \frac{\partial \mathcal{L}}{\partial\left({}_aD^{\alpha}_{x_\sigma}A_{\beta}\right)}d\left({}_aD^{\alpha}_{x_\sigma}A_{\beta}\right), \tag{17}$$

but

$$\frac{\partial \mathcal{L}}{\partial \psi} = \ {}_aD^{\alpha}_{t}\pi + \ {}_aD^{\alpha}_{x_j}\left(\frac{\partial \mathcal{L}}{\partial\left({}_aD^{\alpha}_{x_j}\psi\right)}\right), \tag{18}$$

$$\frac{\partial \mathcal{L}}{\partial \overline{\psi}} = \ {}_aD^{\alpha}_{t}\bar{\pi} + \ {}_aD^{\alpha}_{x_j}\left(\frac{\partial \mathcal{L}}{\partial\left({}_aD^{\alpha}_{x_j}\overline{\psi}\right)}\right), \tag{19}$$

and

$$\frac{\partial \mathcal{L}}{\partial A_{\mu}} = \ {}_aD^{\alpha}_{t}\ \pi_{\mu} + \ {}_aD^{\alpha}_{x_j}\left(\frac{\partial \mathcal{L}}{\partial\left({}_aD^{\alpha}_{x_j}A_{\mu}\right)}\right). \tag{20}$$

Using Eqs. (18), (19), and (20) Eq. (17) can be written as

$$d\mathcal{H} = \bar{\pi}\, d\left({}_aD_t^{\alpha}\overline{\psi}\right) + {}_aD_t^{\alpha}\overline{\psi}\; d\bar{\pi} + \pi\, d\left({}_aD_t^{\alpha}\psi\right) + {}_aD_t^{\alpha}\psi\; d\pi + \pi_\mu\, d\left({}_aD_t^{\alpha}A_\mu\right) + {}_aD_t^{\alpha}A_\mu d\,\pi_\mu - {}_aD_t^{\alpha}(\pi)d\psi - {}_aD_{x_j}^{\alpha}\left(\frac{\partial\mathcal{L}}{\partial\left({}_aD_{x_j}^{\alpha}\psi\right)}\right)d\psi - {}_aD_t^{\alpha}(\bar{\pi})d\overline{\psi} - {}_aD_{x_j}^{\alpha}\left(\frac{\partial\mathcal{L}}{\partial\left({}_aD_{x_j}^{\alpha}\overline{\psi}\right)}\right)d\overline{\psi} - \frac{\partial\mathcal{L}}{\partial\left({}_aD_{x_\sigma}^{\alpha}\psi\right)}d\left({}_aD_{x_\sigma}^{\alpha}\psi\right) - {}_aD_t^{\alpha}\left(\pi_\mu\right)dA_\beta - {}_aD_{x_j}^{\alpha}\left(\frac{\partial\mathcal{L}}{\partial\left({}_aD_{x_j}^{\alpha}A_\beta\right)}\right)dA_\beta - \frac{\partial\mathcal{L}}{\partial\left({}_aD_{x_\sigma}^{\alpha}A_\beta\right)}d\left({}_aD_{x_\sigma}^{\alpha}A_\beta\right), \tag{21}$$

or

$$d\mathcal{H} = {}_aD_t^{\alpha}\overline{\psi}\; d\bar{\pi} + {}_aD_t^{\alpha}\psi\; d\pi + {}_aD_t^{\alpha}A_\mu\, d\,\pi_\mu - {}_aD_t^{\alpha}(\pi)d\psi - {}_aD_{x_j}^{\alpha}\left(\frac{\partial\mathcal{L}}{\partial\left({}_aD_{x_j}^{\alpha}\psi\right)}\right)d\psi - {}_aD_t^{\alpha}(\bar{\pi})d\overline{\psi} - {}_aD_{x_j}^{\alpha}\left(\frac{\partial\mathcal{L}}{\partial\left({}_aD_{x_j}^{\alpha}\overline{\psi}\right)}\right)d\overline{\psi} - \frac{\partial\mathcal{L}}{\partial\left({}_aD_{x_i}^{\alpha}\psi\right)}d\left({}_aD_{x_i}^{\alpha}\psi\right) - {}_aD_t^{\alpha}\left(\pi_\beta\right)dA_\beta - {}_aD_{x_j}^{\alpha}\left(\frac{\partial\mathcal{L}}{\partial\left({}_aD_{x_j}^{\alpha}A_\beta\right)}\right)dA_\beta - \frac{\partial\mathcal{L}}{\partial\left({}_aD_{x_i}^{\alpha}A_\beta\right)}d\left({}_aD_{x_i}^{\alpha}A_\beta\right) \tag{22}$$

By comparing Eqs. (14) and (22), we obtain Hamilton's equation of motion

$$\frac{\partial\mathcal{H}}{\partial A_\mu} = -\,{}_aD_t^{\alpha}\left(\pi_\mu\right) - {}_aD_{x_j}^{\alpha}\left(\frac{\partial\mathcal{L}}{\partial\left({}_aD_{x_j}^{\alpha}A_\mu\right)}\right), \tag{23}$$

$$\frac{\partial\mathcal{H}}{\partial\psi} = -\,{}_aD_t^{\alpha}\pi - {}_aD_{x_j}^{\alpha}\left(\frac{\partial\mathcal{L}}{\partial\left({}_aD_{x_j}^{\alpha}\psi\right)}\right), \tag{24}$$

$$\frac{\partial\mathcal{H}}{\partial\overline{\psi}} = -\,{}_aD_t^{\alpha}(\bar{\pi}) - {}_aD_{x_j}^{\alpha}\left(\frac{\partial\mathcal{L}}{\partial\left({}_aD_{x_j}^{\alpha}\overline{\psi}\right)}\right), \tag{25}$$

$${}_aD_t^{\alpha}A_\mu = \frac{\partial\mathcal{H}}{\partial\pi_\mu}, \quad {}_aD_t^{\alpha}\psi = \frac{\partial\mathcal{H}}{\partial\pi}, \quad {}_aD_t^{\alpha}\overline{\psi} = \frac{\partial\mathcal{H}}{\partial\bar{\pi}}, \tag{26}$$

$$\frac{\partial\mathcal{L}}{\partial\left({}_aD_{x_j}^{\alpha}\psi\right)} = -\frac{\partial\mathcal{H}}{\partial\left({}_aD_{x_j}^{\alpha}\psi\right)}, \quad \frac{\partial\mathcal{L}}{\partial\left({}_aD_{x_j}^{\alpha}A_\beta\right)} = -\frac{\partial\mathcal{H}}{\partial\left({}_aD_{x_j}^{\alpha}A_\mu\right)}. \tag{27}$$

Consider the Lagrangian density given in Eq. (5)

$$\mathcal{L} = \overline{\psi}\left(i\gamma^\mu\, {}_aD_{x_\mu}^{\alpha} - m\right)\psi - \frac{1}{4}F_{\mu\nu}F^{\mu\nu} + \frac{e\pi\, v^2{}_{eff}}{2\theta\phi_0}\varepsilon^{\mu\nu\rho}A_\mu\;\; {}_aD_{x_\nu}^{\alpha}A_\rho - \left(1 + v_{eff}\right)e\overline{\psi}\,\gamma^\mu\psi\, A_\mu$$

We can determine $\bar{\pi}$, π and π_i such that:

$$\bar{\pi} = \frac{\partial\mathcal{L}}{\partial\left({}_aD_t^{\alpha}\overline{\psi}\right)} = 0, \tag{28a}$$

$$\pi == \frac{\partial\mathcal{L}}{\partial\left({}_aD_t^{\alpha}\Psi\right)} = i\gamma^0\overline{\psi}, \tag{28b}$$

$$\begin{cases} \pi_i = \dfrac{\partial\mathcal{L}}{\partial\left({}_aD_t^{\alpha}A_i\right)} = -F^{oi} + \dfrac{e\pi\, v^2{}_{eff}}{2\theta\phi_0}\varepsilon^{ij}A_j \\ \pi_0 = \dfrac{\partial\mathcal{L}}{\partial\left({}_aD_t^{\alpha}A_0\right)} = 0 \end{cases}. \tag{28c}$$

Then we can write the fractional Hamiltonian density of the system as follows:

$$\mathcal{H} = \mathcal{H} = \bar{\pi}\;\, {}_aD_t^{\alpha}\overline{\psi} + \pi\, {}_aD_t^{\alpha}\psi + \pi_\mu\;\, {}_aD_t^{\alpha}A_\mu - \mathcal{L}\left(\psi, \overline{\psi},\, {}_aD_{x_\sigma}^{\alpha}\psi, A_\beta,\, {}_aD_{x_\sigma}^{\alpha}A_\beta\;\right). \tag{29}$$

By inserting Eqs. (5) and (28) into Eq. (29), we obtain

$$\mathcal{H} = i\gamma^0\overline{\psi}\; {}_aD_t^{\alpha}\psi + \pi_i\left(-\pi_i + \frac{e\pi\, v^2{}_{eff}}{2\theta\phi_0}\varepsilon^{ij}A_j \;+\; {}_aD_{x^i}^{\alpha}A_0\right) - i\gamma^0\overline{\psi}\;\, {}_aD_t^{\alpha}\psi - \overline{\psi}\left(i\gamma^\mu\, {}_a^cD_{x_j}^{\alpha} - m\right)\psi + \frac{1}{2}F_{0i}F^{0i} + \frac{1}{4}F_{ij}F^{ij} - \frac{e\pi\, v^2{}_{eff}}{2\theta\phi_0}\varepsilon^{\mu 0i}A_\mu\left(-\pi_i + \frac{e\pi\, v^2{}_{eff}}{2\theta\phi_0}\varepsilon^{ij}A_j \;+\; {}_aD_{x_i}^{\alpha}A_0\right) - \frac{e\pi\, v^2{}_{eff}}{2\theta\phi_0}\varepsilon^{\mu i\rho}\, A_\mu\;\, {}_aD_{x_i}^{\alpha}A_\rho + \left(1 + v_{eff}\right)e\overline{\psi}\,\gamma^\mu\psi\, A_\mu$$

Substituting for F^{0i} from equation (28c), we get

$$\mathcal{H} = -\frac{1}{2}\pi_i^{\,2} + \pi_i\ {}_aD^{\alpha}_{x^i} A_0 - \overline{\psi}\left(i\gamma^j\ {}_aD^{\alpha}_{x_j} - m\right)\psi - \frac{1}{2}\left(\frac{e\pi\, v^2{}_{eff}}{2\theta\phi_0}\varepsilon^{ij}\right)^2 A_j{}^2 + \frac{1}{4}F_{ij}F^{ij} - \frac{e\pi\, v^2{}_{eff}}{2\theta\phi_0}\varepsilon^{\mu 0i}A_\mu\left(-\pi_i - {}_aD^{\alpha}_{x_i}A_0\right) - \frac{e\pi\, v^2{}_{eff}}{2\theta\phi_0}\varepsilon^{\mu i\rho}A_\mu\ {}_aD^{\alpha}_{x_i}A_\rho\ + \left(1+v_{eff}\right)e\overline{\psi}\,\gamma^\mu\psi\,A_\mu\,. \tag{30}$$

Now we will find the Hamiltonian equations of motion for the same system. Initially, the equation of motion for A_μ

$$\frac{\partial\mathcal{H}}{\partial A_\mu} = -\ {}_aD^{\alpha}_{t}\left(\pi_\mu\right) - {}_aD^{\alpha}_{x_j}\left(\frac{\partial\mathcal{L}}{\partial\left({}_aD^{\alpha}_{x_j}A_\mu\right)}\right) - \left(\frac{e\pi\, v^2{}_{eff}}{2\theta\phi_0}\varepsilon^{i\mu}\right)^2 A_\mu - \frac{e\pi\, v^2{}_{eff}}{2\theta\phi_0}\varepsilon^{k0\mu}\left(-\pi_\mu + {}_aD^{\alpha}_{x_\mu}A_0\right) - \frac{e\pi\, v^2{}_{eff}}{2\theta\phi_0}\varepsilon^{\mu i\rho}\ {}_aD^{\alpha}_{x_j}A_\rho + \left(1+v_{eff}\right)e\overline{\psi}\,\gamma^\mu\psi = {}_aD^{\alpha}_{t}F^{0j} - \frac{e\pi\, v^2{}_{eff}}{2\theta\phi_0}\varepsilon^{i\mu 0}\ {}_aD^{\alpha}_{t}A_\mu - {}_aD^{\alpha}_{x_j}(-F^{jk}) + + {}_aD^{\alpha}_{x_j}(-F^{0j}) - \frac{e\pi\, v^2{}_{eff}}{2\theta\phi_0}\varepsilon^{\mu jk}\ {}_aD^{\alpha}_{x_j}A_\mu\,. \tag{31}$$

The substitution of ${}_aD^{\alpha}_{\sigma}F^{\sigma\beta} = {}_aD^{\alpha}_{t}F^{0\beta} + {}_aD^{\alpha}_{j}F^{j0} + {}_aD^{\alpha}_{j}F^{jk}$ into Eq. (31) gives

$$-\left(\frac{e\pi\, v^2{}_{eff}}{2\theta\phi_0}\varepsilon^{i\mu}\right)^2 A_\mu - \frac{e\pi\, v^2{}_{eff}}{2\theta\phi_0}\varepsilon^{k0\mu}\left(-\pi_\mu + {}_aD^{\alpha}_{x_\mu}A_0\right) - \frac{e\pi\, v^2{}_{eff}}{2\theta\phi_0}\varepsilon^{\mu i\rho}\ {}_aD^{\alpha}_{x_j}A_\rho + \left(1+v_{eff}\right)e\overline{\psi}\,\gamma^\mu\psi = \frac{e\pi\, v^2{}_{eff}}{2\theta\phi_0}\varepsilon^{i\mu 0}\ {}_aD^{\alpha}_{t}A_\mu + -\frac{e\pi\, v^2{}_{eff}}{2\theta\phi_0}\varepsilon^{\mu jk}\ {}_aD^{\alpha}_{x_j}A_\mu + {}_aD^{\alpha}_{\sigma}F^{\sigma\beta}. \tag{32}$$

By substituting Eq. (28c) into Eq. (32) and undergoing mathematical manipulation, the following equation is obtained:

$$\frac{e\pi\, v^2{}_{eff}}{\theta\phi_0}\varepsilon^{\beta\mu\sigma}\ {}_aD^{\alpha}_{x_\sigma}A_\mu - \left(1+v_{eff}\right)e\overline{\psi}\,\gamma^\beta\psi\ -\ {}_aD^{\alpha}_{x_\sigma}F^{\sigma\beta} = 0. \tag{33}$$

While the equation of motion for ψ reads

$$\frac{\partial\mathcal{H}}{\partial\psi} = -\ {}_aD^{\alpha}_{t}\pi - {}_aD^{\alpha}_{x_j}\left(\frac{\partial\mathcal{L}}{\partial\left({}_aD^{\alpha}_{x_j}\psi\right)}\right)$$

$$m\,\overline{\psi} + \left(1+v_{eff}\right)e\,\gamma^\mu\overline{\psi}\,A_\mu = -i\gamma^0\ {}_aD^{\alpha}_{t}\,\overline{\psi} - {}_aD^{\alpha}_{x_j}\left(\overline{\psi}\,i\gamma^j\right), \tag{34}$$

but

$$i\gamma^0\ {}_aD^{\alpha}_{t}\,\overline{\psi} + i\gamma^j\ {}_aD^{\alpha}_{x_j}\,\overline{\psi} = i\gamma^\sigma\ {}_aD^{\alpha}_{x_\sigma}\overline{\psi}$$

Thus, Eq. (34) becomes

$$m\,\overline{\psi} + \left(1+v_{eff}\right)e\,\gamma^\mu\overline{\psi}\,A_\mu = -i\gamma^\sigma\ {}_aD^{\alpha}_{x_\sigma}\overline{\psi}. \tag{35}$$

Similarly, the equation of motion for $\overline{\psi}$ is

$$\frac{\partial\mathcal{H}}{\partial\overline{\psi}} = -\ {}_aD^{\alpha}_{t}(\bar{\pi}) - {}_aD^{\alpha}_{x_j}\left(\frac{\partial\mathcal{L}}{\partial\left({}_aD^{\alpha}_{x_j}\overline{\psi}\right)}\right)$$

or

$$\left(i\gamma^j\ {}_aD^{\alpha}_{x_j} - m\right)\psi - \left(1+v_{eff}\right)e\,\gamma^\mu\psi\,A_\mu = 0. \tag{36}$$

The results from Eqs. (33), (35), and (36) are in full accordance with those derived from the fractional EL method.

6. CONCLUSION

The Riemann-Liouville fractional derivative were employed to reformulate the composite Fermions QED Lagrangian density. It was observed that the fractional Euler-Lagrange equations and the fractional Hamilton's equations of motion, both derived from the same Lagrangian density, produced the same outcomes. The fractional formulation was demonstrated to encompass the classical results as a specific case.

ORCID ID

Amer D. Al-Oqali, https://orcid.org/0000-0003-2254-0019

REFERENCES

[1] Y.L. Wang, and C.T. Xu, "Dirac Canonical Quantization of Composite Fermions QED", International Journal of Theoretical Physics, **49**, 421 (2010). https://doi.org/10.1007/s10773-009-0211-y
[2] Z. Li, "Quantum field theory for a system of interacting photons, electrons, and phonons", International Journal of Theoretical Physics, **35**(7), 1353 (1996). https://doi:10.1007/bf02084945
[3] M. Kossow, "Quantum field theory and composite fermions in the fractional quantum Hall effect", Annalen Der Physik, **18**(5), 285(2009). https://doi.org/10.1002/andp.200910350
[4] R.R. Du, A.S. Yeh, H.L. Stormer, D.C. Tsui, L.N. Pfeiffer, and K.W. West, "Fractional Quantum Hall Effect around *ν=3/2* : Composite Fermions with a Spin", Physical Review Letters, **75**(21), 3926 (1995). https://doi.org/10.1103/physrevlett.75.3926
[5] J.K. Jain, "Composite-fermion approach for the fractional quantum Hall effect", Physical Review Letters, **63**(2), 199(1989). https://doi.org/10.1103/physrevlett.63.199
[6] A. Lopez, and E. Fradkin, "Universal structure of the edge states of the fractional quantum Hall states", Physical Review B, **59**(23), 15323 (1999). https://doi.org/10.1103/physrevb.59.15323
[7] V. Kalmeyer, and S.C. Zhang, "Metallic phase of the quantum Hall system at even-denominator filling fractions", Physical Review B, **46**(15), 9889 (1992). https://doi.org/10.1103/physrevb.46.9889
[8] D. Baleanu, and S. I. Muslih, "Fractional Euler-Lagrange and Fractional Hamilton Equations for super Symmetric Classical", Fractals, **15**(04), 379 (2007). https://doi.org/10.1142/s0218348x07003642
[9] D. Baleanu, and O.P. Agrawal, "Fractional Hamilton Formalism Within Caputo's Derivative", Czechoslovak Journal of Physics **56**, 1087 (2006). https://doi.org/10.1007/s10582-006-0406-x
[10] R. Hilfer, Applications of Fractional Calculus in Physics, (World Scientific Publishing Company, Singapore, New Jersey, London and Hong Kong, 2000). https://doi.org/10.1142/3779
[11] M.A.E. Herzallah, and D. Baleanu, "Fractional-order Euler–Lagrange equations and formulation of Hamiltonian equations", Nonlinear Dynamics, **58**, 385 (2009). https://doi.org/10.1007/s11071-009-9486-z
[12] A.A. Diab, R.S. Hijjawi, J.H. Asad, and J.M. Khalifeh, "Hamiltonian formulation of classical fields with fractional derivatives: revisited", Meccanica, **48**, 323–330 (2013). https://doi.org/10.1007/s11012-012-9603-9
[13] A.D. Al-Oqali, "Fractional formulation of Podolsky Lagrangian density", International Journal of Advanced and Applied Sciences, **9**(2) 136 (2022). https://doi.org/10.21833/ijaas.2022.02.015
[14] A.D. Al-Oqali, B.M. Al-Khamiseh, E.K. Jaradat, and R.S. Hijjawi, "The Linear Sigma Model Lagrangian Density: Fractional Formulation", Canadian Journal of Pure and Applied Sciences, **10**, 3803 (2016).
[15] R.E. Gutiérrez, J.M. Rosário, and J.T. Machado, "Fractional Order Calculus: Basic Concepts and Engineering Applications", Mathematical Problems in Engineering, **2010**, 1 (2010). https://doi.org/10.1155/2010/375858
[16] F. Riewe, "Nonconservative Lagrangian and Hamiltonian mechanics", Physical Review E, **53**(2), 1890 (1996). https://doi.org/10.1103/physreve.53.1890
[17] E.K. Jaradat, R.S. Hijjawi, and J.M. Khalifeh, "Maxwell's equations and electromagnetic Lagrangian density in fractional form", Journal of Mathematical Physics, **53**(3), 033505 (2012). https://doi.org/10.1063/1.3670375
[18] V.E. Tarasov, "Fractional vector calculus and fractional Maxwell's equations", Annals of Physics, **323**(11), 2756 (2008). https://doi.org/10.1016/j.aop.2008.04.005
[19] T.P. Stefański, and J. Gulgowski, "Fundamental properties of solutions to fractional-order Maxwell's equations", Journal of Electromagnetic Waves and Applications, **34**(15), 1955 (2020). https://doi.org/10.1080/09205071.2020.1801520
[20] S.I. Muslih, O.P. Agrawal, and D. Baleanu, "A Fractional Schrödinger Equation and Its Solution", International Journal of Theoretical Physics, **49**(8), 1746 (2010). https://doi.org/10.1007/s10773-010-0354-x
[21] N. Laskin, "Fractional Schrödinger equation", Physical Review E, **66**(5), (2002). https://doi.org/10.1103/physreve.66.056108
[22] S.I. Muslih, O.P. Agrawal, and D. Baleanu, "A fractional Dirac equation and its solution", Journal of Physics A: Mathematical and Theoretical, **43**(5), 055203 (2010). https://doi.org/10.1088/1751-8113/43/5/055203
[23] O.P. Agrawal, "Formulation of Euler–Lagrange equations for fractional variational problems", Journal of Mathematical Analysis and Applications, **272**(1), 368 (2002). https://doi.org/10.1016/s0022-247x(02)00180-4

ЩІЛЬНІСТЬ ЛАГРАНЖІАНА КОМПОЗИЦІЙНИХ ФЕРМІОНІВ QED У ДРОБОВОМУ ФОРМУЛЮВАННІ

Амер Д. Аль-Окалі
Департамент фізики, Університет Мута, Аль-Карак, Йорданія

Квантова електродинаміка (КЕД) – точна й успішна теорія, яка описує взаємодію між електрично зарядженими частинками та електромагнітним випромінюванням. Вона є невід'ємною частиною Стандартної моделі фізики елементарних частинок і забезпечує теоретичну основу для пояснення широкого спектру фізичних явищ, у тому числі поведінки атомів, молекул і матеріалів. У цій роботі щільність Лагранжіана композитних ферміонів у КЕД була виражена у дробовій формі за допомогою дробової похідної Рімана-Ліувіля. Були також отримані дробове рівняння Ейлера-Лагранжа і дробове рівняння Гамільтона, виведені з дробової форми лагранжіана густини. Коли α встановлено на 1, відновлювались звичайні математичні рівняння.

Ключові слова: *квантова електродинаміка; композитні ферміони; дробова похідна; щільність лагранжіана; рівняння Ейлера-Лагранжа*

East European Journal of Physics. 2. 69-75 (2023)
DOI:10.26565/2312-4334-2023-2-04 ISSN 2312-4334

THEORETICAL DESCRIPTION OF EVEN-EVEN PLATINUM Pt-186 NUCLEUS USING IBM AND (VMI) MODELS[†]

Ali K. Aobaid
College of Education for Pure Science, Department of Physics, University of Anbar, Anbar, Iraq
E-mail: esp.alik.obaid@uoanbar.edu.iq
Received March 8, 2023; revised March 28, 2023; accepted March 28, 2023

The aim of this study, is to investigate, in a phenomenological way, the backbending effect in platinum Pt-186 nucleus, in order to get a good description of the bends by using new parameters. VMI model and interacting boson model IBM-1 have been used to perform this research for a heavy mass nucleus (Z = 78). Energy ratios and arrangement of the bands show that the platinum Pt-186 have O(6)-SU(3) dynamical symmetry. Our current calculations gave results that are reasonably consistent with the most recent experimental data, especially the results calculated according to the VMI-model. Variable moment of inertia has been applied to describe successfully the effect of backbending in deformed even-even Pt-186 nucleus. Backbending was observed in the ground and β-bands, due to the change of the moment of inertia but not for (γ_1, γ_2) bands, because no changing in the moment of inertia.
Keywords: *Nuclear structure; IBM; nuclear physics; VMI model; back-bending*
PACS: 21.45.+v, 21.60.gx

1. INTRODUCTION

There are two nuclear collections particles: protons, and neutrons so called nucleons, separately divided over certain energy level subjected to the restrictions of the Pauli exclusion principle. All nuclei have ground and excited states, and the nucleons in excited states can be removed from, or added to, nuclei. The nuclear structure gained by studying these phenomena [1]. The IBM-1 was used to description the nuclear collective motion suggested firstly, by Iachello and Arima in order to study the collective states in e-e positive parity nuclei. This model does not distinguish between neutron bosons and proton bosons [2,3]. This research, aims to calculate energy levels, gamma transition and study the backbending phenomena, using the IBM-1 and VMI models.

Backbending has been observed experimentally in the band of the ground state [4,5] or in the rotational band of some deformed nuclei. The effect occurs because, the moment of inertia ($\mathcal{J}$) rapidly increases with the rotational frequency (ω) towards the solid value [6]. When the rotational energy ħω is greater than the energy needed to separate a pair of protons or neutrons S_{2por2n}, the separated proton or neutron moves to another orbit, which result in change of the moment of inertia [7]. An explanation of this effect is attributed to a disappearance of the pairing by band crossing of two rotational energy and Corielis force effect [8,9], this effect of Corielis force increases with rotational frequency at high angular momentum for some bands, leads to depairing nucleon pairs, the first pair depairing called "two quasi particles". the case where the depairing of two quasi particles, which may couple with the collective rotation to produce a new band, this effect leads to back-bending phenomena [10]. Many researchers have been interested in studying the phenomenon of backbending using different methods, including Regan(2003) [10] who used the E-Gos method by drawing the relation between the transitional energy E_γ over spin ($\frac{E_\gamma}{j}$) for two successive levels and the spin (J).Some theoretical researchers have recently focused on studying the nuclear properties of platinum isotopes, including N. Ashok and A.Joseph(2019)[11] studied the ground state properties of Pt isotopes with the help of Skyrme-Hartree-Fock-Bogoliutov (HFB)theory by using harmonic oscillator H.O. and transformed harmonic oscillator T.H.O. to calculate S_{2n} (separation energy of 2-neutrons) and r.m.s radii of proton and neutron. The results obtained are in good agreement with the practical data.

M. Khalil et al (2019) [12] studied the platinum isotopes properties using particle rotor model VMI and IBM to calculate the energies of single particle spectrum and investigated the phenomena of the back-bending. S.H. Al-Fahdawi, A.K. Aobaid (2021) [13] used the first model of interacting bosons and the generalized moment of inertia model to study some of the nuclear properties of deformed heavy nuclei and obtained acceptable results compared to the experimental values and concluded the success of these two models for the study of heavy nuclei. E.A. Al-Kubaisi, A.K. Aobaid (2021) [14] also used the first model of the interacting bosons and vibrator moment of inertia (VAVM) model to calculate the energy levels, the quadrupole moment for even-even Dy-162 nucleus and showed that the (VAVM) model are better than the results calculated by (IBM-1).

2. THEORETICAL ASPECT

2.1. IBM-1 Basis

The interacting b3oson model-1 is an important model used to study the low-lying collective states structure in deformed e-e nuclei, and has been considered as systems composed of interacting (s –d) bosons, which described in terms of monopole boson with $s_{\ell=0}$ and quadrupole boson with $d_{\ell=2}$ [15]. The formula of the Hamiltonian operator can be written by [16]:

[†] ***Cite as:*** A.K. Aobaid, East Eur. J. Phys. **2**, 69 (2023), https://doi.org/10.26565/2312-4334-2023-2-04

$$\widehat{H}=\sum_{i=1}^{N}\varepsilon_i+\sum_{i<j}^{N}V_{ij}. \tag{1}$$

Where ε_i is the energy of bosons i, V_{ij} is the potential energy between the bosons i and j.

General formula for Hamiltonian operator in Eq. 1 assumed by Iachello and Arima can be written as [16,17]:

$$\begin{aligned}\widehat{H}&=\varepsilon_s(s^{\dagger}.\tilde{s})+\varepsilon_d(d^{\dagger}.\tilde{d})+\sum_{\ell=0,2,4}\frac{1}{2}(2\ell+1)^{\frac{1}{2}}C_\ell\left[(d^{\dagger}\times d^{\dagger})^{(\ell)}\otimes(\tilde{d}\otimes\tilde{d})^{(\ell)}\right]^{(0)}\\&+\frac{1}{\sqrt{2}}U_2[(d^{\dagger}\otimes d^{\dagger})^{(2)}\times(\tilde{d}\otimes\tilde{s})^{(2)}+(d^{\dagger}\otimes s^{\dagger})^{(2)}\otimes(\tilde{d}\otimes\tilde{d})^{(2)}]^{(0)}\\&+\frac{1}{2}U_0[(d^{\dagger}\otimes d^{\dagger})^{(0)}\otimes(\tilde{s}\otimes\tilde{s})^{(0)}+(s^{\dagger}\otimes s^{\dagger})^{(0)}\times(\tilde{d}\otimes\tilde{d})^{(0)}]^{(0)}\\&+V_2\,[(d^{\dagger}\otimes s^{\dagger})^{(2)}\otimes(\tilde{d}\otimes\tilde{s})^{(2)}]^{0}+\tfrac{1}{2}V_0[(s^{\dagger}\otimes s^{\dagger})^{(0)}\otimes(\tilde{s}\otimes\tilde{s})^{(0)}]^{(0)}.\end{aligned} \tag{2}$$

Where: $(s^{\dagger},d^{\dagger})$, $(\hat{s},\hat{d})$ are creation and annihilation operators respectively, $C_{\ell=0,2,4}$, $U_{\ell=0,2}$, $V_{\ell=0,2}$ describes the bosons interactions with each other, $\varepsilon=\varepsilon_d-\varepsilon_S$ represent the bosons energy. The energy of the boson s (ε_S) was considered to be zero, therefore: $\varepsilon=\varepsilon_d$. The other formulas of Hamiltonian operator in equation (2) can be written as multipole expansion mutual into equation of various boson-boson interactions [18]:

$$\widehat{H}=\varepsilon\hat{n}_d+\alpha_0\hat{P}\hat{P}+\alpha_1\hat{L}\hat{L}+\alpha_2\hat{Q}\hat{Q}+\alpha_3\widehat{T_3}\widehat{T_3}+\alpha_4\widehat{T_4}\widehat{T_4}. \tag{3}$$

Where the parameters($\alpha_0,\alpha_1,\alpha_2,\alpha_3,\alpha_4$) represents the strength of the pairing, angular momentum,quadrupole, octupole and hexadecapole interactions between bosons respectively.

2.2. VMI Model Basis

The (VMI) model proposed firstly, by M. Mariscotti et al. 1969 [19] to calculate the energy states values for any band as:

$$E_J(\mathcal{J})=\tfrac{1}{2}C(\mathcal{J}-\mathcal{J}_0)^2+\tfrac{1}{2}\,[\mathrm{J(J+1)}]/\mathcal{J} \tag{4}$$

Moment of inertia can be determined from equilibrium condition [19,20]:

$$\frac{\partial E(\mathcal{J})}{\partial\mathcal{J}}=0 \tag{5}$$

Determines $\mathcal{J}_J$ (in $\hbar^2$ unit) as a function of (J).

The parameter C is the hardness coefficient and $\mathcal{J}_0$ is the moment of inertia of the ground state (for $\mathcal{J}_0>0$).

From equations (4,5) can obtained:

$$\mathcal{J}_J^3-\mathcal{J}_0\mathcal{J}_J^2=[\mathrm{J(J+1)}]/2\mathrm{C} \tag{6}$$

Eq. 6 contains one real root for any value when ($\mathcal{J}_0$,C) finite and positive.

The lest fit-to-square (l.s.f.) procedure has been applied to all measured E_J values for any state.

The energy of the J-level according to the rotational model is given by the relation [21]:

$$E_J=\tfrac{\hbar^2}{2\mathcal{J}}J(J+1) \tag{7}$$

As for the transition energy between levels J → J-2 is given by the relationship [22,23]:

$$\Delta\mathrm{E}_\gamma=\mathrm{E_J}-\mathrm{E_{J-2}}=\tfrac{\hbar^2}{2\mathcal{J}}(4\mathrm{J}-2)\ \text{ for (g, β) band} \tag{8}$$

$$\Delta\mathrm{E}_\gamma=\tfrac{E2_1^+}{4}(\mathrm{J+2})\qquad\text{for }\gamma\text{ –unstable O(6)} \tag{9}$$

In order to study the phenomenon of backbending, the moment of inertia ($2\mathcal{J}/\hbar\hat{}2$) must be calculated from the Eq. 8 and the square of the rotational energy $(\hbar\omega)^2$ as:

$$\frac{2\mathcal{J}}{\hbar^2}=\frac{4J-2}{\Delta\mathrm{E}_\gamma}\qquad\text{for (g, β) band} \tag{10}$$

Where $\Delta\mathrm{E}_\gamma=\mathrm{E_J}-\mathrm{E_{J-2}}$

$$\frac{2\mathcal{J}}{\hbar^2}=\frac{2J}{\Delta\mathrm{E}_\gamma}\qquad\text{for gamma band} \tag{11}$$

Equation (8) can be written for harmonic oscillator as:

$$\mathrm{E}_\gamma(\mathrm{J}\rightarrow\mathrm{J\text{-}2})=\hbar\omega \tag{12}$$

While the rotational energy squared $(\hbar\omega)^2$ can be written as [22,23]:

$$(\hbar\omega)^2=(J^2-J+1)\left[\frac{\Delta\mathrm{E}_\gamma}{2J-1}\right]^2 \tag{13}$$

The nuclear stiffness parameter σ was introduced, which measures the initial variation of moment of inertia w.r.t. angular momentum, can be calculated from equation (6) as [19,24]:

$$\sigma = \left[\frac{1}{\mathcal{J}}\frac{d\mathcal{J}}{dJ}\right]_{J=0} = \frac{1}{2C\mathcal{J}_0^3} \tag{14}$$

3. HAMILTONIAN INTERACTION PARAMERERS

The Hamiltonian parameters in the IBM computer program "PHINT COD" [25] was used to make the Hamiltonian diagonal. The equivalent program for PHINT code is (IBM1.For) and the input file called "Bos.inp.". All parameters can be changed indepently fitting with the experimentally energy spectrum for the nucleuos, and from these calculations, we find the nuclear structure of the Pt-186 spectra by the Hamiltonian interaction paramerers values, These coefficients that have reasonable agreement with the experimental data were shown in Table 1. These chosen parameters depended on number of proton bosons N_π and neutron bosons number N_ν were calculated from the nearst closed shell, and the number of total bosons N = $N_\pi + N_\nu$. The nucleuos of even-even Pt-186 have atomic number equel 78 protons ,so there are 4 holes (2 protons bosons) to fill the shell Z = 82, and neutrons number equel 108, so there are 18 holes to fill the shell N = 126 or 9 neutrons bosons. The total numbers of bosons N=11.

While the results of VMI model were calculated using VMI. For program from file "Par.input" this file depends on ($\frac{\mathcal{J}_0}{\hbar^2}$, C, E_k) parameters, where: $\frac{\mathcal{J}_0}{\hbar^2}$ moment of inertia for ground state, C is constant parameter fitted with experimental data, E_k is the head of the band energy.

The other files called "Enr. out" and "Enr1.out" these files calculated the following:

1 – Theoretical energy $E_{cal.}$

2 – Rotational energy square $(\hbar\omega)^2$ and $(\frac{2\mathcal{J}}{\hbar^2})$.

3 – Nuclear softness (σ)from equation (12)

4 – Deviation (Δ) [26,27] which determined the deviation between calculate energy states $E_{cal.}$ and experimental values $E_{exp.}$ from equation:

$$\Delta = [\tfrac{1}{k}\textstyle\sum_{i=1}^{k}(E_{cal.} - E_{exp.})^2\,]^{1/2}, \tag{15}$$

where k is the number of levels.

5 – Chi-squared (χ^2) from equation [19]:

$$\chi^2 = \left(\frac{E_{cal.}-E_{exp.}}{E_{exp.}}\right)^2 \tag{16}$$

Where all calculations for VMI model were chosen from the smallest (χ^2) as in Table.1.

Table 1. Best fitted interaction parameters for the energies of IBM-1 and VMI model

The parameters used for IBM-1 in MeV units except CHI and SO6 unless units								
N	ε	α_0	α_1	α_2	α_3	α_4	CHI	SO6
11	0.0000	0.0399	0.0041	0.0000	0.1206	0.0010	0.0000	1.0000
The parameters used for VMI model parameters σ, Δ and χ^2 unless units								
Band		$\frac{\mathcal{J}_0}{\hbar^2}$ (MeV)$^{-1}$	C (MeV)^3	E_k (MeV)		σ	Δ	χ^2
g-band		10.881000	0.0010200	0.001020		0.380508	0.039794	0.006069
β-band		8.8810008	0.000820	0.471000		0.870504	0.114324	0.071045
γ_1- band		34.000000	0.011100	1.000000		0.001146	0.130298	0.130763
γ_2- band		7.832500	90.500500	0.770000		0.000011	0.095356	0.015812

The ratios of the excitation energies 4_1^+, 6_1^+ and 8_1^+ dividing on the energy level of the first exited 2_1^+ for Pt-186 nucleus using IBM-1 and VMI have been calculated and compared with the identical values for the three limits, SU(5),SU(3) and O(6) as in Table 2, these calculations shows that the platinum-186 has Gamma unstable O(6) dynamical symmetry, but the arrangement of the bands according to their appearance (g, β, γ_1, γ_2) bands shows that the nucleus under study belong to rotational dynamic SU(3)limit.

Table 2. Ideal energy ratios of three chains [18] compared with experiment [28,29] and theoretical (IBM-1 and VMI) values

Energy Ratios R	**$E4_1^+/E2_1^+$**	**$E6_1^+/E2_1^+$**	**$E8_1^+/E2_1^+$**	**Dynamical symmetry**
Identical values [18]	2.0	3.0	4.0	SU(5)
	3.33	7	12	SU(3)
	2.500	4.500	7	O(6)
Experimental data [28,29]	2.565	4.592	7.026	O(6)
IBM-1 Model	2,290	3.881	5.761	O(6)
VMI Model	2,623	4.623	6.916	O(6)

4. RESULTS AND DISCUSSION

4.1. Energy levels

The ideal, practical, and theoretically calculated energy ratios in Table 2 show that the platinum nucleus belongs to gamma unstable O(6) limit, while the arrangement of the band (g, β, γ) indicates that it belongs to rotational SU(3) limit, because the level (0_2^+) appeared before (2_2^+) level this means that a beta band (β) had appeared and therefore the nucleus understudy had O(6)-SU(3) dynamical symmetry.

The calculated of energy levels values for IBM-1 and VMI are compared with the experimental values [28,29] for all bands are shown in Table 3.

Table 3. Comparision of experimental and calculated results for IBM-1 and VMI model

$^{186}_{78}Pt$		E_J (MeV)			E_γ (MeV) $J \rightarrow J-2$			$\frac{2\vartheta}{\hbar^2}(MeV)^2$	$(\hbar\omega)^2 exp.(MeV)^2$
band	J_i^+	Exp. [28,29]	IBM-1	VMI	Exp. [28,29]	IBM-1	VMI		
G--band	0_1^+	0.000	0.000	0.000	----	----	-----	-----	-----
	2_1^+	0.191	0.193	0.191	0.191	0.193	0.191	20.942	0.034
	4_1^+	0.490	0.442	0.501	0.299	0.249	0.310	26.755	0.088
	6_1^+	0.877	0.749	0.883	0.367	0.307	0.382	31.007	0.149
	8_1^+	1.342	1.112	1.321	0.465	0.363	0.438	34.408	0.215
	10_1^+	1.858	1.532	1.803	0.516	0.420	0.482	38.759	0.265
	12_1^+	2.336	2.008	2.324	0.478	0.476	0.521	50.209	0.228
	(14_1^+)	2.825	2.542	2.879	0.489	0.534	0.555	57.259	0.238
	(16_1^+)	3.394	3.133	3.465	0.569	0.591	0.586	56.239	0.323
	(18_1^+)	4.051	3.782	4.079	0.657	0.649	0.614	54.794	0.431
	(20_1^+)	4.788	4.488	4.719	0.737	0.706	0.640	54.274	0.542
$\beta 1$ - band	0_2^+	0.471	0.482	0.471	---	---	---	---	---
	2_2^+	0.607	0.555	0.670	0.136	0.073	0.199	5.012	0.017
	4_2^+	0.991	0.925	0.976	0.384	0.370	0.306	37.974	0.145
	(6_2^+)	1.470	1.233	1.346	0.479	0.308	0.370	30.075	0.227
	(8_2^+)	2.004	1.597	1.766	0.534	0.364	0.420	71.428	0.284
	(10_2^+)	2.108	2.018	2.226	0.104	0.421	0.460	50.420	0.010
	(12_2^+)	2.611	2.498	2.722	0.503	0.480	0.496	69.651	0.252
	(14_2^+)	3.192	3.035	3.249	0.581	0.537	0.527	49.689	0.337
	(16_2^+)	3.664	3.630	3.805	0.472	0.595	0.556	114.64	0.222
	(18_2^+)	4.258	4.285	4.385	0.594	0.655	0.580	75.757	0.352
	(20_2^+)	4.956	5.943	4.990	0.698	0.605	0.605	---	---
$\gamma 1$- band	2_3^+	0.798	0.675	0.954	---	---	---	---	---
	3_1^+	0.956	0.909	1.047	0.158	0.234	0.093	---	---
	4_3^+	1.222	0.926	1.172	0.266	0.017	0.125	---	---
	(5_1^+)	1.362	1.349	1.328	0.140	0.423	0.156	---	---
	(6_3^+)	1.600	1.353	1.604	0.238	0.004	0.276	---	---
	(7_1^+)	1.801	1.765	1.735	0.201	0.412	0.131	---	---
	(8_3^+)	2.123	1.837	1.984	0.322	0.072	0.249	---	---
	(9_1^+)	2.280	2.038	2.266	0.157	0.201	0.282	---	---
	(10_3^+)	2.544	2.378	2.578	0.264	0.340	0.312	---	---
	11_1^+	---	2.669	2.922	---	0.291	0.344	---	---
	(12_3^+)	2.864	2.916	3.296	---	0.247	0.374	---	---
$\gamma 2$- band	2_4^+	1.175	1.038	1.153	---	---	---	---	---
	3_2^+	1.417	1.474	1.535	0.242	0.436	0.382	---	---
	4_4^+	2.159	1.632	2.046	0.742	0.158	0.511	---	---
	5_2^+	---	1.934	2.684	---	0.302	0.638	---	---
	6_4^+	---	1.963	3.450	---	0.029	0.766	---	---
	7_2^+	---	2.452	4.343	---	0.489	0.893	---	---

In Table 3 The values of the energy levels are calculated theoreticaly for the spins ($11_1^+, 5_2^+, 6_4^+, 7_2^+$) respectively which are not determined experimentally, especially in γ_2 –band. Theoretical calculations also showed that the value of the uncertain practical energy, which is equal to (2.825MeV)for the spin{(14_1^+)}, is more probable to the confirmed value, especially for VMI model (2.879 MeV) also at the spin {(16_1^+),(18_1^+), (20_1^+),(14_2^+), (20_2^+),(5_1^+), (6_3^+), (9_1^+), (10_3^+)}.

The energy spectram of platinum Pt-186 for (g, $\beta, \gamma_1, \gamma_2$) bands as a comparison of IBM-1 and VMI calculations with experimental data were plotted in Figure 1.

The experimental data and calculated of energy bands for the ground and β-bands were plotted in Figure 2. Good agreements from the comparison of the IBM-1 and VMI model calculations (energies, spin and parity) with the

experimental data. But in γ_1 − band, the agreements were acceptable in the low-lying states, while it is deviated in the high spin (energies)of the experimental data because, the calculations of IBM-1 have been performed with no distinction made between neutron and proton bosons.

In γ_2 − band VMI calculations were in agreements with experimental data while, the calculations of IBM-1 were not good with experimental data because the interacting boson model does not distinguish between neutron and proton bosons, there were no experimental values for the energy states for band.

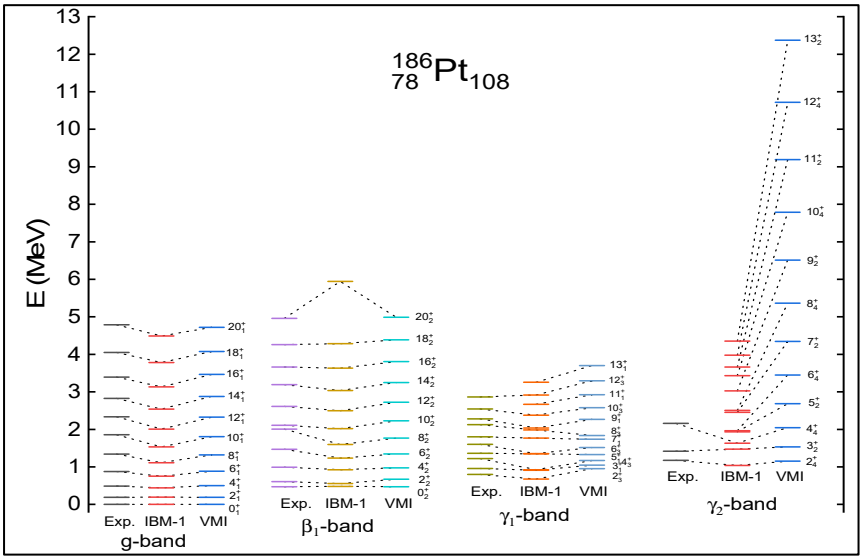

Figure 1. The energy spectra for Pt-186 nucleus as a comparison of IBM-1 and VMI calculations with the available experimental data [28,29]

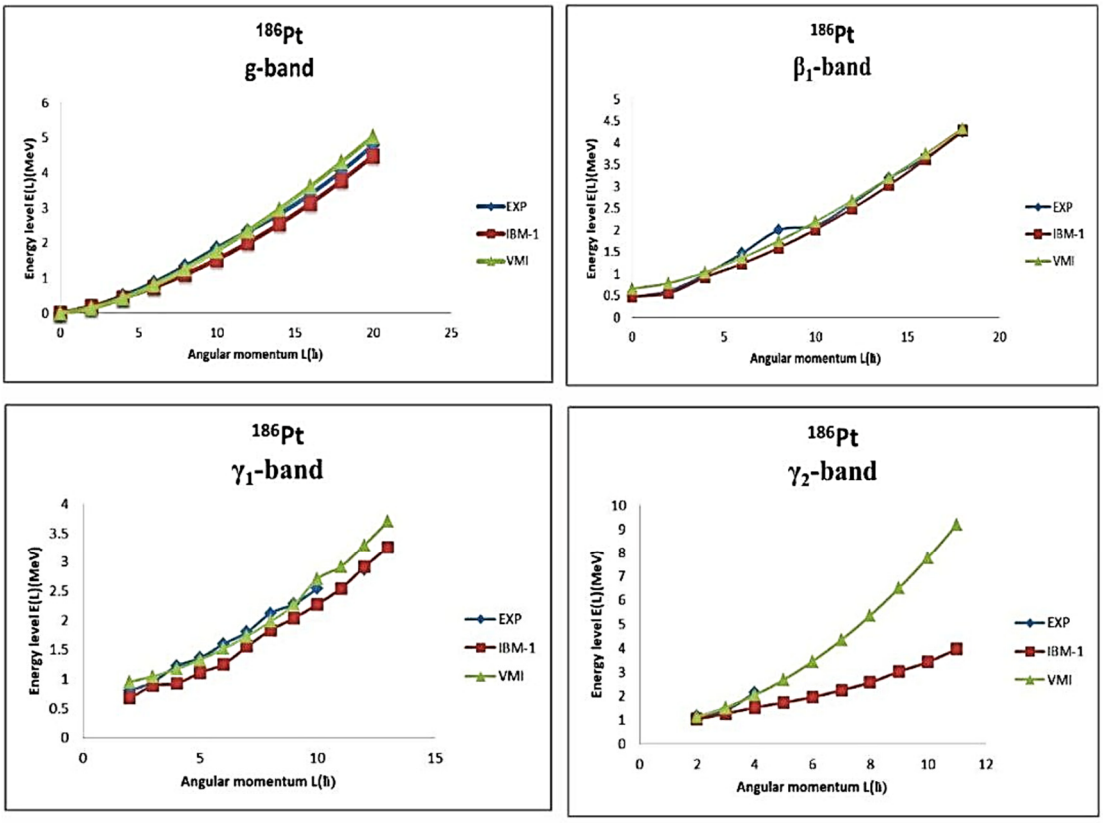

Figure 2. The experimental [28,29] and theoretical results IBM-1, VMI, E(L) versus L for g, β, γ,-bands

4.2. Backbending phenomena

For the purpose of identifying the properties of the nuclei and studying the possibility of backbending in them, the moment of inertia ($\frac{2\mathcal{J}}{\hbar^2}$) and Rotational energy squared$(\hbar\omega)^2$ were calculated using equations (10 and 12) respectively,

these values are shown in Table 3. The relation between $(\frac{2\mathcal{J}}{\hbar^2})$ and $(\hbar\omega)^2$ was drawn for the ground and beta bands in which a backbending appeared in it, and shown in Figures 3 and 4. The backbending of these bands occur, due to the change in the moment of inertia and β-band lies in SU(3) limit, and no backbending was observed in the (γ_1,γ_2) bands, because the moment of inertia does not change ,also these bands belonging to γ-unstable limit.

The drawing of the ground state band Figure 3 had a backbending between the levels 12_1^+, and (18_1^+), due to the deformation of these levels, also, the backbending occurs due to the rapid increase in the moment of inertia at relatively high spin than the expected value according to the rotational motion model of some nuclei, which causes a decrease in the expected energy value at these cases result in a backbending in the moment of inertia curve as a result of the disengagement of one or two pairs of nucleons and their re-engagement, which reduces the expected energy value that causes the backbending.

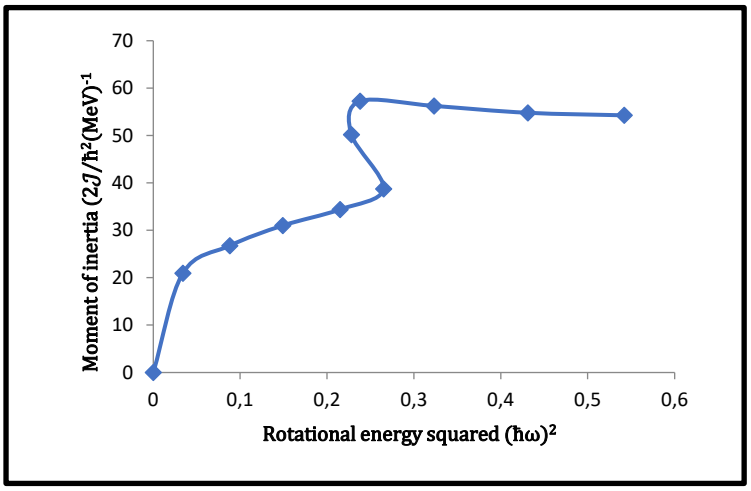

Figure 3. Moment of inertia (2ℐ/ħ^2) as a function of Rotational energy squared $(\hbar\omega)^2$ for g-band experimental

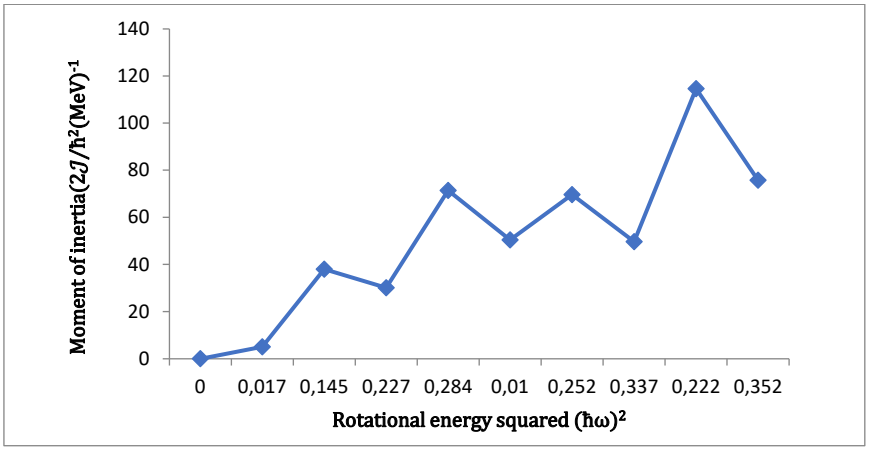

Figure 4. Moment of inertia (2ϑ/ħ^2) as a function of Rotational energy squared $(\hbar\omega)^2$ for β-band experimental

5. CONCLUSIONS

In the present work, the IBM-1and VMI model have been applied successfully in description deformed e-e Pt-186 nucleus and I got:

1. The results of state bands show reasonable agreement with empirically but had been found a little difference in high states, due to the interacting boson model do not distinguish between proton and neutron bosons.

2. The IBM-1 calculations show that the currently results of the energy states were in good agreement with practical calculations for the g-band and in reasonable agreement with the beta band and high in (γ_1, γ_2) band, also some of the energy states calculated in my current research did not calculate empirically, especially in γ_2 – band.

3. The results of VMI successfully investigated energy bands in low and high spin levels, and the predictions of this model gave a good description of the occurrence of backbending in the ground and beta bands due to the small rotational frequency (ω) of nucleons, and thus, the nucleon pair behavior at high angular momentum appears to be crucial for this an effect, and either the lack of backbending in the gamma bands may be attributed to the presence the deformation of an octupole or a hexadecabol in these bands.

4. From the curves of the backbending of the energy bands is clear that the β-band lies in SU(3) limit, and this is confirmed by the arrangement of the energy bands and the appearance of the backbending in them. while the energy ratios shows that the platinum Pt-186 has Gamma unstable O(6) limit.

ORCID ID

Ali K. Aobaid, https://orcid.org/0000-0002-1135-3675

REFERENCES

[1] W. Meyerhof, *Elements of Nuclear Physics*, (McGraw-Hill, New York, 1967). pp. 288.
[2] A. Arima, and F. Iachello, Phys. Rev. Lett. **35**, 1069 (1975). https://doi.org/10.1103/PhysRevLett.35.1069
[3] A. Arima, and F. Iachello, Ann. Phys. **111**, 201 (1978). https://doi.org/10.1016/0003-4916(78)90228-2
[4] M. Ploszajczak et al, J. Phys. G: Nucl. Phys. **8**, 709 (1982). https://doi.org/10.1088/0305-4616/8/5/012
[5] E. Grosse, F.S. Stephens, and R.M. Diamond, Phys. Rev. Lett. **31**, 840 (1973). https://doi.org/10.1103/PhysRevLett.31.840
[6] W.E. Burcham, *Elements of Nuclear Physics*, (Longman Inc., New York, 1989).
[7] K. Krane, *Introductory Nuclear Physics*, (John Wiley and Sons, New York, 1987).
[8] B.R. Mottelson, and J.G. Valatin, Phys. Rev. Lett. **5**, 511 (1960). https://doi.org/10.1103/PhysRevLett.5.511
[9] A. Faessler, Collective description of deformed and transitional nuclei, in: *Nuclear Spectroscopy. Lecture Notes in Physics*, vol. 119, edited by G.F. Bertsch, and D. Kurath, (Springer, Berlin, Heidelberg, 1980). pp. 97–139. https://doi.org/10.1007/3-540-09970-0_4
[10] P.H. Regan, C.W. Beausang, R.F. Zamfir, R.F. Casten, J. Zhang, A.D. Yamamoto, M.A. Caprio, et al., Phys. Rev. Letters, **90**, 1525021-4 (2003). https://doi.org/10.1103/PhysRevLett.90.152502
[11] N. Ashok, and A. Joseph, "A systematic study of the ground state properties of W, Os and Pt isotopes using HFB theory," International Journal of Modern Physics E, **28**(10), 1950093 (2019). https://doi.org/10.1142/S0218301319500939
[12] M. Khalil, A.M. Khalaf, M. Kotb, and M.D. Okasha, "Properties of platinum isotopes in framework of particle rotor model and IBM," Nuclear Physics A, **991**, 121610 (2019). https://doi.org/10.1016/j.nuclphysa.2019.121610
[13] S.H. Al-Fahdawi, and A.K. Aobaid, "Studying the Nuclear Structure of the (Yb-172) Deformed Nucleus using (IBM-1) and (GVMI) Models," Journal of Physics: Conference Series, IOP Conference Series Materials Science and Engineering, **1095**, 012012 (2021). https://doi.org/10.1088/1757-899X/1095/1/012012
[14] E.A. Al-Kubaisi, and A.K. Aobaid, "Studying the nuclear structure of the ($\boldsymbol{Dy}$-**162**) deformed nucleus by using (IBM-1) and (VAVM) Models," Journal of Physics: Conference Series, **1879**, 032104 (2021). https://doi.org/10.1088/1742-6596/1879/3/032104
[15] F. Iachello, *Nuclear Structure*, edited by K. Abrahms, K. Allaart, and A.E.L. Dieperink, (Plemum Press, New York, 1981).
[16] W. Greiner, and J.A. Maruhn, *Nuclear Models*, (Spring-Verlag, Berlin Heidelberg, NewYork, 1996).
[17] F. Iachello, "An Introduction to the Interacting Boson Model," in: *Nuclear structure*, edited by K. Abrahams, K. Allaart, and A.E.L. Dieperink, (Plenum press, 1980). pp. 53-87.
[18] R.F. Casten, and D.D. Warner, "Interacting Boson Approximation," Rev. Mod. Phys. **60**(2), 389-465 (1988). https://doi.org/10.1103/RevModPhys.60.389
[19] M.A.J. Mariscotti, G. Scharff-Goldhaber, and B. Buck, Phys. Rev. **178**, 1864-1887 (1969). https://doi.org/10.1103/PhysRev.178.1864
[20] T.V. Alenicheva, P. Kabina, I.A. Mitropolsky, and T.M. Tyukavina, *Atlas of Rotational Bands in ODD-MASS Nuclei*, (International Atomic Energy Agency, Vienna, Austria, 2004), pp. 439. https://www-nds.iaea.org/publications/indc/indc-ccp-0439.pdf
[21] M.A. Deleplanque, S. Frauenderf, V.V. Pashkevich, S.Y. Chu, and A. Unzhakova, *Gross shell structure of moments of inertia*, Vol. 52316, (Lawrence Berkeley National Laboratory, University of California, 2002).
[22] S.U. El Kameesy, H.H. Alharbi, H.A. Alhendi, "Backbending phenomena in light nuclei at A~60 mass region," (2005). https://arxiv.org/pdf/nucl-th/0509015
[23] M.E. Kelabi, "Backbending Effect in Deformed e-e Nuclei," (2005). https://arxiv.org/abs/nucl-th/0503021
[24] D. Bonatsos, *Interaction boson model of nuclear structure*, (Oxford university press, New York, 1988).
[25] O. Scholton, *The program package "PHINT",* (Kerrfysisch Verseneller Comiger, KNI-63, 1997).
[26] F.X. Xu, C.S. Wu, and J.Y. Zeng, Phys. Rev. C, **40**, 2337 (1989). https://doi.org/10.1103/PhysRevC.40.2337
[27] R.M. Spiegel, and L.J. Stephens, *Schaum's outlines statistics*, (McGraw-Hill, New York, 1999.).
[28] C.M. Baglin, Nuclear Data Sheets, **99**, 1-196 (2003). https://doi.org/10.1006/ndsh.2003.0007
[29] J.C. Batchelder, A.M. Hurst, and M.S. Basunia, "Nuclear Data Sheets for A=186", **183**, 1-346 (2022). https://doi.org/10.1016/j.nds.2022.06.001

ТЕОРЕТИЧНИЙ ОПИС ПАРНО-ПАРНОГО ЯДРА ПЛАТИНИ Pt-186 З ВИКОРИСТАННЯ МОДЕЛЕЙ IBM ТА (VMI)

Алі К. Аобейд
Освітній коледж чистої науки, факультет фізики, Анбарський університет, Анбар, Ірак

Метою цього дослідження є феноменологічне дослідження backbending ефекту в ядрі платини Pt-186, з метою отримати покращений опис вигинів за допомогою нових параметрів. Модель VMI та модель взаємодіючого бозона IBM-1 використовувалися для виконання цього дослідження для ядра важкої маси (Z = 78). Енергетичні співвідношення та розташування смуг показують, що платина Pt-186 має O(6)-SU(3) динамічну симетрію. Наші поточні розрахунки дали результати, які досить узгоджуються з останніми експериментальними даними, особливо тими, що розраховані відповідно до VMI-моделі. Змінний момент інерції був застосований для успішного опису back-bending ефекту в деформованому парно-парному ядрі Pt-186. Backbending спостерігався в основному та β-смугах через зміну моменту інерції, але не для (γ_1, γ_2) смуг, оскільки не змінювався момент інерції.

Ключові слова: *структура ядра; IBM; ядерна фізика; модель VMI; backbending*

East European Journal of Physics. **2.** 76-84 (2023)
DOI:10.26565/2312-4334-2023-2-05 ISSN 2312-4334

A STUDY OF THE WEAKLY BOUND STRUCTURE OF NUCLEI AROUND THE MAGIC NUMBER N = 50[†]

Ruwaida S. Obaid, Ali A. Alzubadi*
Department of physics, College of Science, University of Baghdad, Baghdad, Iraq
**Corresponding Author e-mail: ali.kareem@sc.uobaghdad.edu.iq*
Received February 16, 2023; revised March 22, 2023; accepted March 24, 2023

An investigation of the quadrupole deformation of Kr, Sr, Zr, and Mo isotopes has been conducted using the HFB method and SLy4 Skyrme parameterization. The primary role of occupancy of single particle state $2d_{5/2}$ in the existence of the weakly bound structure around N = 50 is probed. Shell gaps are performed using a few other calculations for the doubly magic number ^{100}Sn using different Skyrme parameterizations. We explore the interplays among neutron pairing strength and neutron density profile in two dimensions, along with the deformations of ^{100}Sn.
Keywords: *weakly bound structure; quadrupole deformation; pairing strength*
PACS: 21.10.−k, 21.60.Cs, 21.60.Ev

1. INTRODUCTION

The mass region around neutron number $N = 50$ is a fascinating region characterized by many phenomena. Unlike other shape phenomena, nuclear deformation leads to the bound structure of a quantum state characterized by different equilibrium contributions. Many theories and experiments have been performed to study these contributions. One of the most influential theories widely used to study nuclear deformation and structure is the Skyrme-Hartree-Fock (SHF) theory. The nuclear system is a self-bound system consisting of nucleons that move in a mean field (MF). The nucleons occupy single-particle states according to the Pauli exclusion principle. HF theory is a fundamental MF theory that was studied using Skyrme parameterizations to describe the nuclear interaction with different terms in the framework of the Slater determinant.

The Hartree-Fock-Bogoliubov (HFB) method is formulated for the Hamiltonian. It is expressible in the second quantization, which includes two phenomena: the HFMF and the pairing correlations, considering the relationship between them. This method will be used in the present work to investigate the deformed shape of nuclear systems with SLy4 Skyrme parameterization using the HFBTHO (v1.66p) code [1]. This code uses the axially transformed harmonic oscillator (THO) on a single-particle basis to expand quasiparticle wave functions. It iteratively diagonalizes the HFB Hamiltonian based on the Skyrme forces and zero-range pairing interaction until a self-consistent solution is found. In addition, the single-particle energy of ^{100}Sn will be investigated using the shell model with different Skyrme parameterizations as single particle potential via the shell model code NuShellX@MSU [2], which used data files for different model spaces, mixing configurations, and Hamiltonians to generate input for NuShellX. As well as the quadrupole deformation, Fermi level, pairing strength, and density profile of ^{100}Sn with Skyrme tensor parameterization are studied using the code [3], which is a highly optimized two-dimensional HF+ Bardeen-Cooper-Schrieffer (BCS) code used for computing ground states and deformation energy surfaces for axially symmetric deformed nuclei.

2. HARTREE-FOCK-BOGOLIUBOV METHOD

In the HFB method, the Hamiltonian is essentially reduced to two potentials: the self-consistent average potential (Γ) from HF method, and an additional pairing field (Δ), known from the BCS, the BCS theory states basically that the pairing strength is constant for the matrix elements.

In the following section we will introduce the general quasiparticle picture in the standard HFB formalism. The basic idea in the most general quasiparticle concept is to define the HFB approximate ground state of the many-body system as a vacuum with respect to quasiparticles. The many-body Hamiltonian of a system of fermions can be expressed in terms of a set of annihilation and creation operators [4]:

$$\hat{H} = \sum_{ij} t_{ij} \hat{a}_i^{\dagger} \hat{a}_j + \frac{1}{4} \sum_{ijkl} \bar{v}_{ijkl} \hat{a}_i^{\dagger} \hat{a}_j^{\dagger} \hat{a}_l \hat{a}_k \tag{1}$$

where the first term corresponding to the kinetic energy and the second term $\bar{v}_{ijkl}=<ij|V|kl>$ is anti-symmetrized two-body interaction matrix elements of the effective nucleon-nucleon interaction. An eigenstate of this Hamiltonian can be expanded as a sum over states which all have the same total number of nucleons, but with the nucleons occupying the available single-particle states in all possible combinations. The Skyrme interaction for nuclear structure calculations was developed from the idea that the energy functional could be expressed in terms of a zero-range expansion, leading to a simple derivation of the HF equations, in which the exchange terms have the same mathematical structure as the direct terms. This approximation greatly reduces the number of integrations over single-particle states when solving the equations.

[†] ***Cite as:*** R.S. Obaid, and A.A. Alzubadi, East Eur. J. Phys. **2**, 76 (2023), https://doi.org/10.26565/2312-4334-2023-2-05

The Skyrme effective interaction is a two-body density-dependent interaction that models the strong force in the particle-hole channel and contains a central and spin-orbit, given by Ref [5]:

$$\begin{aligned} V_{Sky}\left(\vec{r}_i,\vec{r}_j\right) &= t_\circ\left(1+x_\circ\hat{P}_\sigma\right)\delta\left(\vec{r}_i-\vec{r}_j\right)+\frac{1}{2}t_1\left(1+x_1\hat{P}_\sigma\right)\left\{\hat{k}'^2\delta\left(\vec{r}_i-\vec{r}_j\right)+\delta\left(\vec{r}_i-\vec{r}_j\right)\hat{k}^2\right\}+ \\ &+\mathrm{t}_2\left(1+x_2\hat{P}_\sigma\right)\hat{k}'\cdot\delta\left(\vec{r}_i-\vec{r}_j\right)\hat{k}+\frac{1}{6}t_3\left(1+x_3\hat{P}_\sigma\right)\rho^\alpha\left(\frac{\vec{r}_i+\vec{r}_j}{2}\right)\delta\left(\vec{r}_i-\vec{r}_j\right)+\mathrm{iW}_\circ\,\hat{k}'\left(\vec{\hat{\sigma}}_i+\vec{\hat{\sigma}}_j\right)\times\hat{k}\,\delta\left(\vec{r}_i-\vec{r}_j\right) \end{aligned} \tag{2}$$

where $V_{Sky}\left(\vec{r}_i,\vec{r}_j\right)$ is the Skyrme effective interaction and $\hat{k}$, $\hat{k}'$ are the relative momentum operators, which operate on the wave functions to the right and to the left, given by:

$$\hat{k}=\frac{1}{2i}\left(\vec{\nabla}_1-\vec{\nabla}_2\right)\ ,\ \hat{k}'=-\frac{1}{2i}\left(\vec{\nabla}'_1-\vec{\nabla}'_2\right) \tag{3}$$

The terms $t_\circ$, t_1, t_2, t_3, $x_\circ$, x_1, x_2, x_3, α and $W_\circ$ are the free parameters describing the strengths of the different interaction terms which are fitted to the nuclear structure data. The $t_\circ$ parameter represents the central term, the parameters (t_1, t_2) are the momentum dependent term, the t_3 parameter represents the effective density-dependence term, the $W_\circ$ parameter represents a two-body spin-orbit term and $\hat{p}_\sigma$ being the spin exchange operator:

$$\hat{P}_\sigma=\frac{1}{2}\left(1+\hat{\sigma}_1\cdot\hat{\sigma}_2\right) \tag{4}$$

To obtain HF equations, we have to evaluate the expectation value of the Hamiltonian in a Slater determinant $\left|HF\right\rangle$. It is given by:

$$E=\left\langle\phi_{HF}\left|\,\hat{H}\right|\phi_{HF}\right\rangle=\sum_{i=1}^{A}\left\langle\phi_i\left|\,\hat{T}\right|\phi_i\right\rangle+\frac{1}{2}\sum_{ij}^{A}\left\langle\phi_{ij}\left|\,V\left(i,j\right)\right|\phi_{ij}\right\rangle \tag{5}$$

The expectation value of the HF Hamiltonian or energy of the Skyrme can be rewritten as a spatial integral over a Hamiltonian density:

$$E=\int d^3\vec{r}\,\hat{H}\left(\vec{r}\right) \tag{6}$$

By substituting the Skyrme interaction terms into the full energy expression, the form of the density function, H can be derived. Where $V(i,j)$ contains all parts of the nucleon-nucleon force, including the coulomb interaction. The full expression for the expectation value of the HF equations with the Skyrme force is then:

$$\begin{aligned} E_{Sky} &= \int d^3r\left\{\frac{\hbar^2}{2m}\tau+\frac{1}{2}t_\circ\left[\rho\left(r\right)^2\left(1+\frac{1}{2}x_\circ\right)-\left(x_\circ+\frac{1}{2}\right)\left(\rho_n\left(r\right)^2+\rho_p\left(r\right)^2\right)\right]\right. \\ &+\frac{1}{12}t_3\left[\rho\left(r\right)^{\alpha+2}\left(1+\frac{1}{2}x_3\right)-\left(x_3+\frac{1}{2}\right)\rho\left(r\right)^\alpha\left(\rho_n\left(r\right)^2+\rho_p\left(r\right)^2\right)\right] \\ &+\frac{1}{4}\left(t_1+t_2\right)\rho\,\tau+\frac{1}{8}\left(t_2-t_1\right)\left(\rho_n\tau_n+\rho_p\,\tau_p\right)+\frac{1}{16}\left(t_2-3t_1\right)\rho\,\nabla^2\rho \\ &\left.+\frac{1}{32}\left(3t_1+t_2\right)\left(\rho_n\,\nabla^2\rho_n+\rho_p\nabla^2\rho_p\right)+\frac{1}{16}\left(t_1-t_2\right)\left(J_n^2+J_p^2\right)-\frac{1}{2}W_\circ\left(\vec{\nabla}\rho\cdot J+\vec{\nabla}\rho_n\cdot J_n+\vec{\nabla}\rho_p\cdot J_p\right)\right\} \end{aligned} \tag{7}$$

In the HFB method, the ground state wave function is defined as the quasiparticle vacuum, where the quasiparticle operators ($\hat{\beta}$, $\hat{\beta}^\dagger$) are connected to the original particle operators ($\hat{a}$, $\hat{a}^\dagger$) via a linear Bogoliubov transformation [4]

$$\hat{\beta}_i^\dagger=\sum_{k=1}^{A}\left(U_{ki}^*\hat{a}_k+V_{ki}^*\hat{a}_k^\dagger\right)=\sum_{k=1}^{A}\left(U_{ik}^\dagger\hat{a}_k+V_{ik}^\dagger\hat{a}_k^\dagger\right) \tag{8}$$

$$\hat{\beta}_i=\sum_{k=1}^{A}\left(U_{ki}\hat{a}_k^\dagger+V_{ki}\hat{a}_k^\dagger\right)=\sum_{k=1}^{A}\left(U_{ki}^T\hat{a}_k+V_{ki}^T\hat{a}_k^\dagger\right) \tag{9}$$

where k and i run over the whole configuration space (k = 1, ..., A) and U and V are transformation matrices.

The Hermitian conjugation of these equations gives the quasiparticle operators. Therefore, we have unitary transformation is a transformation from the system of single particle operators to the system of quasiparticle operators),

$$\hat{a}=\left(\hat{a}_1,...,\hat{a}_m;\hat{a}_1^\dagger,...,\hat{a}_K^\dagger\right)\rightarrow\hat{\beta}=\left(\hat{\beta}_1,...,\hat{\beta}_m;\hat{\beta}_1^\dagger,...,\hat{\beta}_K^\dagger\right) \tag{10}$$

which it can be written in the matrix form [4]:

$$\begin{pmatrix}\hat{\beta}\\ \hat{\beta}^\dagger\end{pmatrix}=\begin{pmatrix}U^\dagger V^\dagger\\ V^T U^T\end{pmatrix}\begin{pmatrix}\hat{a}\\ \hat{a}^\dagger\end{pmatrix}=W^\dagger\begin{pmatrix}\hat{a}\\ \hat{a}^\dagger\end{pmatrix} \tag{11}$$

The matrices U and V satisfy the relations:

$$\begin{aligned} U^{\dagger}U + V^{\dagger}V = 1, \quad UU^{\dagger} + V^{*}V^{T} = 1 \\ U^{T}V + V^{T}U = 0, \quad UV^{\dagger} + V^{*}U^{T} = 0 \end{aligned} \tag{12}$$

and allows us to invert Eqs. (8) and (9),

$$\hat{a}_l = \sum_{i=1}^{A} \left(U_{li}^{*} \hat{\beta}_i + V_{li}^{*} \hat{\beta}_i^{\dagger} \right) \tag{13}$$

$$\hat{a}_l^{\dagger} = \sum_{i=1}^{A} \left(V_{li} \hat{\beta}_i + U_{li} \hat{\beta}_i^{\dagger} \right) \tag{14}$$

which means that the Bogoliubov transformation of Eq. (11) is unitary and it can be easily inverted,

$$\begin{pmatrix} \hat{a} \\ \hat{a}^{\dagger} \end{pmatrix} = \begin{pmatrix} U & V^{*} \\ V & U^{*} \end{pmatrix} \begin{pmatrix} \hat{\beta} \\ \hat{\beta}^{\dagger} \end{pmatrix} = W^{\dagger} \begin{pmatrix} \hat{\beta} \\ \hat{\beta}^{\dagger} \end{pmatrix} \tag{15}$$

Using the inverse Bogoliubov transformation Eqs. (13) and (14), the Hamiltonian in Eq. (1) can be expressed in terms of the generalized quasiparticle operators

$$\begin{aligned} \hat{H} = H^{\circ} + \sum_{k_1 k_2} H_{k_1 k_2}^{11} \beta_{k_1}^{\dagger} \beta_{k_2} + \frac{1}{2} \sum_{k_1 k_2} \left(H_{k_1 k_2}^{20} \beta_{k_1}^{\dagger} \beta_{k_2} + h.c. \right) + \sum_{k_1 k_2 k_3 k_4} \left(H_{k_1 k_2 k_3 k_4}^{40} \beta_{k_1}^{\dagger} \beta_{k_2}^{\dagger} \beta_{k_3}^{\dagger} \beta_{k_4}^{\dagger} + h.c. \right) \\ + \sum_{k_1 k_2 k_3 k_4} \left(H_{k_1 k_2 k_3 k_4}^{31} \beta_{k_1}^{\dagger} \beta_{k_2}^{\dagger} \beta_{k_3}^{\dagger} \beta_{k_4} + h.c. \right) + \frac{1}{4} \sum_{k_1 k_2 k_3 k_4} \left(H_{k_1 k_2 k_3 k_4}^{22} \beta_{k_1}^{\dagger} \beta_{k_2}^{\dagger} \beta_{k_3} \beta_{k_4} + h.c. \right) \end{aligned} \tag{16}$$

the last three terms in Eq. (16) are usually involved in so called residual interaction term $\hat{\mathrm{H}}_{\mathrm{int}}$. So, the expression of Eq. (16) is written as:

$$\hat{H} = H^{\circ} + \sum_{k_1 k_2} H_{k_1 k_2}^{11} \beta_{k_1}^{\dagger} \beta_{k_2} + \sum_{k_1 k_2} \left(H_{k_1 k_2}^{20} \beta_{k_1}^{\dagger} \beta_{k_2} + h.c. \right) + \hat{\mathrm{H}}_{\mathrm{int}} \tag{17}$$

The HFB is a variational theory that treats in a unified fashion MF and pairing correlations. The HFB equations can be written in matrix form as:

$$\begin{pmatrix} h - \lambda & \Delta \\ -\Delta^{*} & -h^{*} + \lambda \end{pmatrix} \begin{pmatrix} U_k \\ V_k \end{pmatrix} = E_k \begin{pmatrix} U_k \\ V_k \end{pmatrix} \tag{18}$$

where E_k are the quasiparticle energies, λ is the chemical potential, h and Δ are the HF Hamiltonian and the pairing potential, respectively, and the U_k and V_k are the upper and lower components of the quasiparticle wave functions.

These equations are solved subject to constraints on the average numbers of neutrons and protons in the system, which determine the two corresponding chemical potentials, λ_n and λ_p. Pairing is important as one moves away from spherical closed shell nuclei and therefore becomes a necessary ingredient within MF models for describing properties that vary strongly with shell effects. Pairing correlations are accounted for within the HF framework by generalizing the MF concept to include a pairing field, which is calculated through the HFB equations [6].

As we move away from close shells, pairing correlations play an important role and should be taken into account. If one were dealing with a fundamental many-body Hamiltonian, where one of the proceed to apply HFB formalism to it, and dealing with Skyrme force that have been simplified with the aim of reproducing average, one would have to include additional parameterization in order to warranty that sensible pairing matrix elements are obtained [4].

3. SKYRME TENSOR INTERACTION

The Skyrme tensor interaction is the sum of the triplet-even and triplet-odd tensor zero range tensor parts, has the following form [7]:

$$\begin{aligned} \upsilon_T = \; & \frac{1}{2} T \left\{ \left[\left(\vec{\sigma}_1 \cdot \vec{k}' \right) \left(\vec{\sigma}_2 \cdot \vec{k}' \right) - \frac{1}{3} k'^2 \left(\vec{\sigma}_1 \cdot \vec{\sigma}_2 \right) \right] \delta \left(\vec{r}_1 - \vec{r}_2 \right) \right. \\ & \left. + \delta \left(\vec{r}_1 - \vec{r}_2 \right) \left[\left(\vec{\sigma}_1 \cdot \vec{k} \right) \left(\vec{\sigma}_2 \cdot \vec{k} \right) - \frac{1}{3} k^2 \left(\vec{\sigma}_1 \cdot \vec{\sigma}_2 \right) \right] \right\} \\ & + U \left\{ \left(\vec{\sigma}_1 \cdot \vec{k}' \right) \delta \left(\vec{r}_1 - \vec{r}_2 \right) \left(\vec{\sigma}_2 \cdot \vec{k} \right) \right. \\ & \left. - \frac{1}{3} \left(\vec{\sigma}_1 \cdot \vec{\sigma}_2 \right) \left[k' \cdot \delta \left(\vec{r}_1 - \vec{r}_2 \right) k \right] \right\} \end{aligned} \tag{19}$$

where the coupling constant T and U measure the strength of the tensor forces in even and odd states of relative motion.

The combined effect of central exchange interactions α plus tensor contribution β give extra terms to the energy density

$$\Delta H(\vec{r}) = \frac{1}{2}\alpha\left[J_n^2(\vec{r}) + J_p^2(\vec{r})\right] + \beta\, J_n(\vec{r}) J_p(\vec{r}) \tag{20}$$

where $J_n(\vec{r})$ and $J_p(\vec{r})$ are the spin-orbit densities for neutrons and protons, respectively, defined by [8]

$$J_q(\vec{r}) = \frac{1}{4\pi r^3}\sum_{i=n,l,j} \upsilon_i^2 (2j_i+1)\left[j_i(j_i+1) - l_i(l_i+1) - \frac{3}{4}\right] R_i^2(\vec{r}) \tag{21}$$

where i runs over all occupied states having the given q: the isospin quantum number $q = (1\text{-}t_z)/2$ for neutrons and protons (q = 0,1), respectively. υ_i^2 is refers to the occupation probability determined by the BCS theory. The spin-orbital potential is given by [9]

$$V_{S.O.}(\vec{r}) = U_{S.O.}^{q}(\vec{r})\, l.s \tag{22}$$

with $U_{S.O.}^{q}(\vec{r})$ defined by [10]

$$U_{S.O.}^{q}(\vec{r}) = \frac{W_0}{2r}\left(2\frac{d\rho_q}{dr} + \frac{d\rho_{q'}}{dr}\right) + \left(\alpha\frac{J_q}{r} + \beta\frac{J_{q'}}{r}\right) \tag{23}$$

Interactions between like, and unlike particles are presented by q (q') where the first term comes from the Skyrme two body spin-orbit interaction. The second term with $\alpha = \alpha_T + \alpha_c$ and $\beta = \beta_T + \beta_c$ where α_c, β_c are the parameters of the central exchange part [11,7]

$$\begin{aligned} \alpha_c &= \frac{1}{8}(t_1 - t_2) - \frac{1}{8}(t_1 x_1 + t_2 x_2), \\ \beta_c &= -\frac{1}{8}(t_1 x_1 + t_2 x_2) \end{aligned} \tag{24}$$

and in terms of the tensor parameters

$$\begin{aligned} \alpha_T &= \frac{5}{12}U, \\ \beta_T &= \frac{5}{24}(T+U) \end{aligned} \tag{25}$$

4. DENSITY PROFILE, PAIRING STRENGTH AND NUCLEAR DEFORMATION

Nuclei is a quantum many-body system exhibiting the quadrupole collectivity associated with the shape of the mean field. The collective degree of freedom is associated with the measure of the operator $\hat{Q}$.
The local nucleon density is defined as [3]

$$\rho_q(\vec{r}) = \sum_{\alpha\in q}\sum_{S} \upsilon_\alpha^2 \left|\psi_\alpha(\vec{r},s)\right|^2 \tag{26}$$

The total energy is composed as

$$E_{tot} = T + E_{Skyrme} + E_{Coulomb} + E_{pair} + E_{cm} \tag{27}$$

where E_{Culomb} is the Coulomb energy

$$E_C = \frac{e^2}{2}\int dV dV' \frac{\rho_p(\vec{r})\rho_p(\vec{r}')}{|\vec{r}-\vec{r}'|} - \int dV \frac{3e^2}{4}\left(\frac{3}{\pi}\right)^{\frac{1}{3}} \rho_p^{\frac{4}{3}} \tag{28}$$

and the pairing energy is

$$E_{pair} = \frac{1}{4}\sum_{q\in\{p,n\}} V_{pair,q}\int dV \left|\xi_q\right|^2 \left[1 - \frac{\rho}{\rho_{0,pair}}\right] \tag{29}$$

where dV stands for the volume element in full three-dimensional space, e is the elementary charge with e^2=1.43989 MeV.fm, and ξ_q is the pairing density

$$\xi_q(\vec{r}) = \sum_{\alpha \in q} \sum_{S} w_\alpha u_\alpha v_\alpha \psi_{\bar{\alpha}}(\vec{r}, s) \psi_\alpha(\vec{r}, s) \tag{30}$$

where w_α stands for a soft cut-off of pairing space. The $s \in \pm 1$ variables indicate the spinor component of the wave functions.

The pairing energy contains the parameter $\rho_{0,pair}$ which regulates the balance between volume and surface pairing [12]. Nuclear deformation is defined as the deviation from the spherical symmetry about center of mass (c.m.) which expressed by the electric quadrupole moment. Thus, the most important moments are the center of mass moments [3]

$$\vec{R}_{type} = \frac{\int dV\, \vec{r}\, \rho_{type}(\vec{r})}{\int dV\, \rho_{type}(\vec{r})} \tag{31}$$

where "*type*" can refer to proton from ρ_p neutron from ρ_n isoscalar or total from the total density $\rho_= \rho_p+\rho_n$ or isovector moment from the isovector density $\rho_{T=1} = (N/A)\, \rho_p - (Z/A)\, \rho_n$. The anisotropic combinations can be quantified in terms of the spherical quadrupole moments

$$Q_{2m,type} = \int dV r^2 Y_{2m} \rho_{type}\left(\vec{r} - \vec{R}_{type}\right) \tag{32}$$

The axial symmetry allows non-vanishing quadrupole moments only for m=0. It is often convenient to express them as a dimensionless quadrupole moment (quadrupole deformation parameter)

$$\beta_{20} = \frac{4\pi}{3} \frac{Q_{20}}{AR^2}, \quad R = R_0 A^{1/3}, \quad R_0 = 1.2 \text{ fm} \tag{33}$$

We briefly outline the formalisms used in our calculations. Further details can be found in the cited references.

5. RESULTS AND DISCUSSIONS

The calculated quadrupole deformation parameter (β_2) for Kr, Sr, Zr, and Mo isotopes from N = 52 to 58 neutron numbers are shown in Fig. 1. Results were calculated using the HFB method with SLy4 parameterization and listed in Table 1.

Table 1. SkX, Skxta, Skxtb, Skxcsb, SkM, and SLy4 Skyrme parameterizations [2]

Parameters	SkX	Skxta	Skxtb	Skxcsb	SkM	SLy4
α	0.5	0.5	0.5	0.5	0.5	0.167
X_w	0	0	0	0	0	0
X_c	0	0	0	0	0	0
X	0.72	-	-	-	0.91	-
X_a	-	-	-	0.014±0.002	-	-
t_0	-1445.3	-1443.180	-1446.8	-1437.353	-1803.1	-2488.91
t_1	246.9	257.229	250.9	238.390	273.8	486.82
t_2	-131.8	-137.843	-133.0	-111.766	-95.9	-546.39
t_3	12103.9	12139.420	12127.6	12157.747	12755.1	13777.0
X_0	0.340	0.341	0.329	0.348	0.306	0.834
X_1	0.580	0.580	0.518	-0.845	0.225	-0.344
X_2	0.127	0.167	0.139	0.407	0.698	-1.000
X_3	0.030	0.000	0.018	0.373	0.116	1.354
W_0	148.6	180.441	153.1	149.779	155.9	123.0
α	-	93.6	-83.9	-	-	-
β	-	94.2	96.1	-	-	-

One can see different equilibrium distributions around β_2=0 with two minima for ^{88,90,92}Kr, ^{90,92,94}Sr, and ^{98}Mo, but these two minima are arranged symmetric about β_2=0, then the breaking symmetry for $\beta_2 \neq 0$ removed in a symmetry point [13] and the nuclei will as a spherical shape with weakly bound structure. For ^{92,94,96}Zr and ^{94,96}Mo have a spherical shape. The curve for ^{94}Kr has prolate and oblate quadrupole deformations corresponding to the two close-lying energy minima; this indicates that their ground states have shape coexistence. All the isotopes with N=58, ^{96}Sr, ^{98}Zr, and ^{199}Mo, have an oblate shape (corresponding to the significant negative deformations).

The weakly bound structure of these nuclei is observed due to their occupancy in the $2d_{5/2}$ neutron single particle state; when it is completely filled, this state causes deformation of nuclei shapes. The pairing correlations and collective motion of the nucleons result in an oblate shape for all isotopes with neutron number N = 58. Many Skyrme parameterizations are fitted to the properties of the nuclei: Skxta and Skxtb with the tensor term, SkX, SkM, SLy4 without tensor term, and Skxcsb with consideration of the effect of charge symmetry breaking (CSB), which is tabulated in Table 1. Based on the Skyrme parameterizations, Figs 2 and 3 show the neutron and proton shell gaps for ^{100}Sn, as compared to the experimental data [14] shown in Tables 2 and 3.

Skxcsb parameterization includes CSB in the *s*- wave part of Skyrme interaction together with the usual direct and exchange Coulomb terms. The CSB modification of the Skyrme is expressed as a change to proton-proton and neutron-neutron *s*- wave interaction [15]:

$$V_{Skyrme}^{pp} = t_0\left(1-x_0\right)\left(1+x_a\right)\delta \tag{34}$$

$$V_{Skyrme}^{nn} = t_0\left(1-x_0\right)\left(1-x_a\right)\delta \tag{35}$$

where $x_a = -0.014 \pm 0.002$ [14]. Charge symmetry assumption is based on the equality of *p-p* and *n-n* interactions.

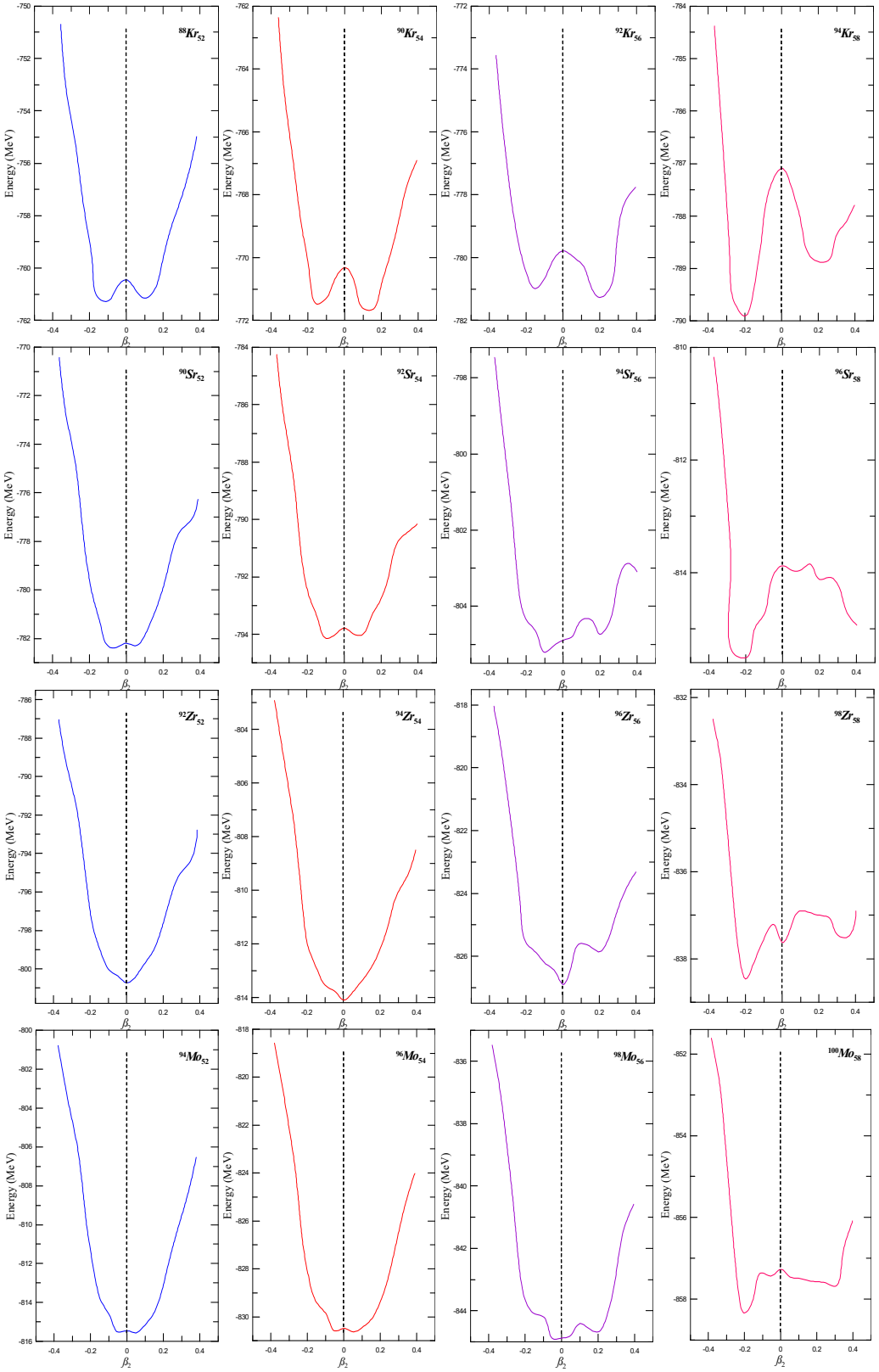

Figure 1. The quadrupole deformation parameter as a function of binding energy of the *Kr*, *Sr*, *Zr*, *and Mo* isotopes

According to SLy4 parameterization, the gaps between the states are too large compared to experimental data. This parameterization fails to describe the spin-orbit splitting between the states, whereas using the SkX, SkM, and Skxtb parameterizations, the state ordering of single-particle energies is nearly identical and gives good results compared with the experimental data. The Skxta fails to give acceptable results. The interaction with the Skxcsb gives outstanding results where the symmetry-breaking effects on the nuclear structure are associated with Coulomb interaction between nucleons.

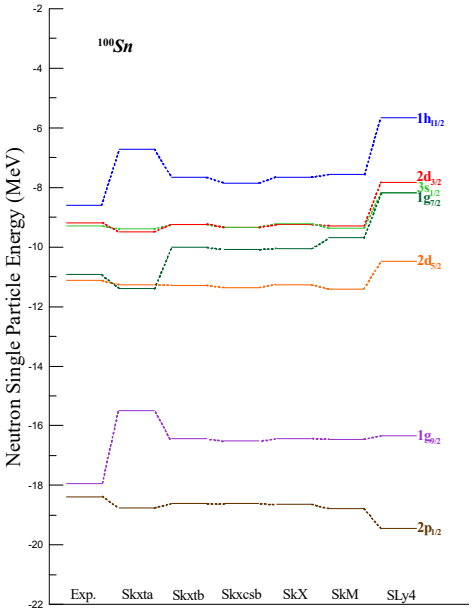

Figure 2. The neutron particle states for ^{100}Sn with different Skyrme parameterizations

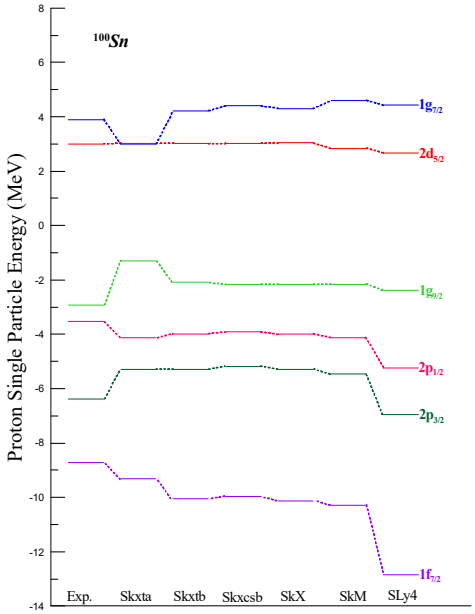

Figure 3. The proton particle states for ^{100}Sn with different Skyrme parameterizations

Table 2. Experimental and calculated neutron single particle energy for ^{100}Sn in MeV by using different Skyrme parameterizations Skxta, Skxtb, Skxcsb, SkX, SkM, and SLy4

nlj	ε_{exp} [13]	ε_{Skxta}	ε_{Skxtb}	ε_{Skxcsb}	ε_{SkX}	ε_{SkM}	ε_{SLy4}
v1$h_{11/2}$	-8.60	-6.73	-7.67	-7.85	-7.66	-7.57	-5.67
v2$d_{3/2}$	-9.20	-9.49	-9.24	-9.34	-9.25	-9.29	-7.83
v3$s_{1/2}$	-9.30	-9.40	-9.25	-9.33	-9.23	-9.37	-8.18
v1$g_{7/2}$	-10.93	-11.39	-10.02	-10.09	-10.06	-9.70	-8.19
v2$d_{5/2}$	-11.13	-11.27	-11.29	-11.36	-11.27	-11.41	-10.47
v1$g_{9/2}$	-17.93	-15.50	-16.44	-16.52	-16.44	-16.46	-16.34
v2$p_{1/2}$	-18.38	-18.75	-18.62	-18.62	-18.64	-18.78	-19.45

Table 3. Experimental and calculated proton single particle energy for ^{100}Sn in MeV by using different Skyrme parameterizations Skxta, Skxtb, Skxcsb, SkX, SkM, and SLy4

nlj	ε_{exp} [13]	ε_{Skxta}	ε_{Skxtb}	ε_{Skxcsb}	ε_{SkX}	ε_{SkM}	ε_{SLy4}
π1$g_{7/2}$	3.90	3.00	4.22	4.40	4.31	4.60	4.44
π2$d_{5/2}$	3.00	3.03	3.02	3.03	3.04	2.84	2.67
π1$g_{9/2}$	-2.92	-1.29	-2.10	-2.16	-2.16	-2.16	-2.39
π2$p_{1/2}$	-3.53	-4.13	-3.98	-3.91	-4.00	-4.12	-5.23
π2$p_{3/2}$	-6.38	-5.30	-5.30	-5.18	-5.29	-5.47	-6.94
π1$f_{7/2}$	-8.71	-9.33	-10.05	-9.96	-10.12	-10.29	-12.84

Proton and neutron Fermi energies for ^{100}Sn as a function of the quadrupole deformation parameter β_2 are shown in Fig. 4 (a and b) (on the left). Fermi energy correlates with the potential energy surface (on the right) in terms of binding energy. Interestingly, the ground state of the potential energy surface at β_2=0 reflected with large proton and neutron Fermi energies. In contrast, the appearance of minima around β_2=0 (transition between prolate and oblate shape) decreased the binding of the single-particle energies, which affected the nucleus's stability. As a result, one can conclude that the collective motion and the pairing correlations between the protons and neutrons caused a slight distortion in the energy curve. However, the symmetry in the number of protons and neutrons filling the same orbit enhances the stability of ^{100}Sn.

Fig. 5 depicts the corresponding neutron pairing strength and neutron density profile in two dimensions (on the right) and the deformation for ^{100}Sn (on the left). The pairing strength effect is found as the nucleons are concentrated. No pairing strength for β_2=0 (region a) with a large concentration of nucleons in the central region as compared with β_2=0.252 (region b), where there is a small concentration of nucleons on the exterior surface, leads to the slight distortion.

Furthermore, the red and blue colors correspond to the high density (0.08 fm^{-3}) and low density (0.02 fm^{-3}) of the neutron density profile. The central density of $\beta_2 = 0$ is very high compared to the central density of $\beta_2 = 0.252$.

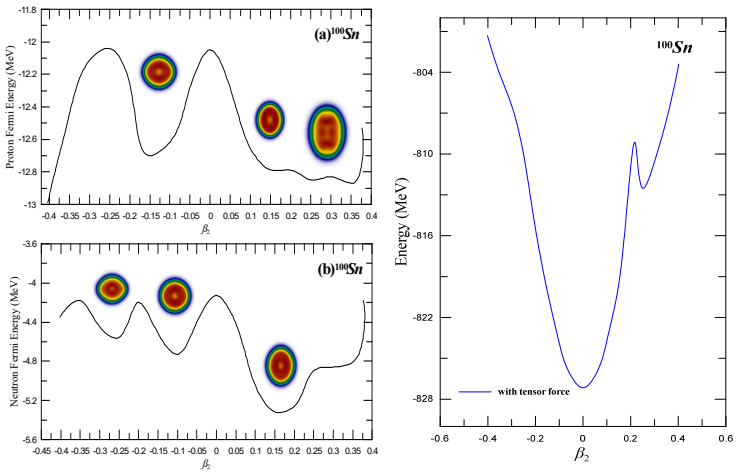

Figure 4. Left: The Fermi energy curve of ^{100}Sn of (a) protons and (b) neutrons and Right: the potential energy curve, with tensor force term as a function of the quadrupole deformation parameter

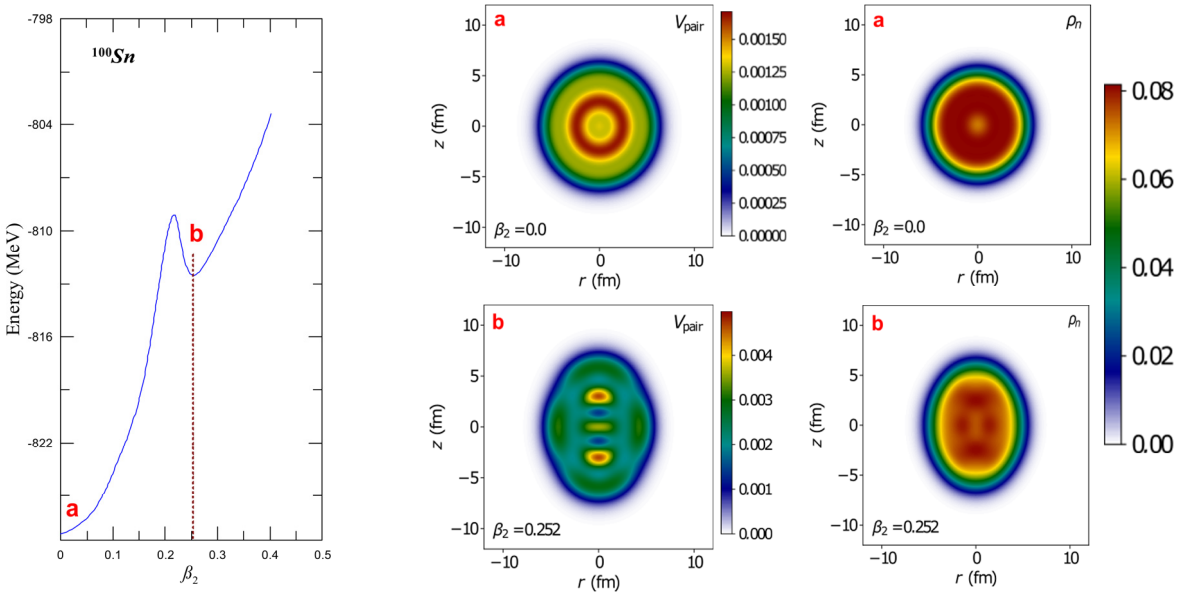

Figure 5. Left: The Potential energy curve of ^{100}Sn with tensor force term as a function of the quadrupole deformation parameter. The pairing strength and density profile of neutrons for ^{100}Sn corresponding to the two regions, marked a and b, are shown in the Right panel

In Fig. 6 the corresponding pairing energies for ^{100}Sn is plotted along with quadrupole deformation. It is found that there is a great correlation between the *n-p* pairings leads to a small distortion in the region $\beta_2 = 0.252$.

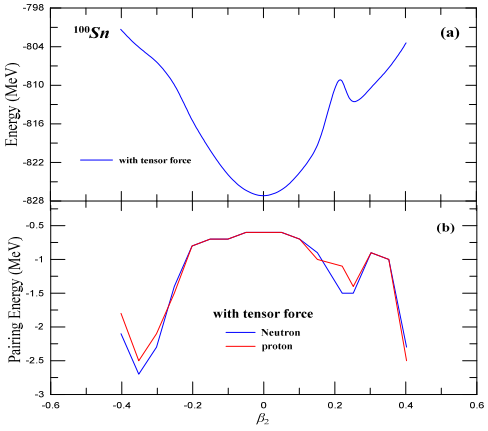

Figure 6. The potential energy curve (a) and (b) the corresponding neutrons and protons pairing energies for ^{100}Sn

6. CONCLUSIONS

In summary, we have used the SHFB method to estimate the quadrupole deformation and examine the bound structure of nuclei around the magic number N=50. We find that while the neutrons in the $2d_{5/2}$ state increase, nuclei have a weakly bound structure, the deformed shape developed, and then the nuclei with filled $2d_{5/2}$ state (N=58) have total deformation in their ground state (0^+); ^{94}Kr,^{96}Sr,^{98}Zr, and ^{100}Mo. Shell gaps of doubly magic number ^{100}Sn with different Skyrme parameterizations are giving rise that SLy4 and Skxta falling in describing the spin-orbit splitting between the states. In contrast, Skxtb and Skxcsb in both calculations give acceptable results with the experimental data. More results have been performed by using a few other calculations of neutron pairing strength and neutron density profile in two dimensions using Skyrme tensor parameterization and the deformations of ^{100}Sn. The energy curve gives rise to a weakly bound structure leading to a slight distortion. However, the symmetry in the number of protons and neutrons filling the same orbit enhances the stability.

We find that the equilibrium contribution is deformed for the isotopes with a small number of nucleons outside the closed shell (N=50) might be attributed to the pairing correlations that lead to raising the collective motion between the nucleons, and this fact changes the bound structure of these nuclei around N=50.

ORCID IDs

Ali A. Alzubadi, https://orcid.org/0000-0002-7226-1141

REFERENCES

[1] M.V. Stoistsov, J. Dobaczewski, W. Nazarewicz, and P. Ring, Comp. Phys. Comm. **167** 43 (2005). https://doi.org/10.1016/j.cpc.2005.01.001
[2] B.A. Brown, and W.D.M. Rae, Nucl. Data Sheets, **120**, 115 (2014). https://doi.org/10.1016/j.nds.2014.07.022
[3] P.G. Reinhard, B. Schuetrumpf, and J.A. Maruhn, Comp. Phys. Comm. **258**, 107603 (2021). https://doi.org/10.1016/j.cpc.2020.107603
[4] P. Ring, and P. Schuck, *The Nuclear Many Body Problem*, (Springer, Berlin-Heidelberg, 1980).
[5] A.A. Alzubadi, Indian J. Phys. **89**, 619 (2015). https://doi.org/10.1007/s12648-014-0614-3
[6] A.I. Goodman, Adv. Nucl. Phys. **11**, 263 (1975).
[7] Fl. Stancu, D.M. Brink, and H. Flocard, Phys. Lett. B, **68**, 108 (1977). https://doi.org/10.1016/0370-2693(77)90178-2
[8] D. Vautherin, and D.M. Brink, Phys. Rev. C, **5**, 626 (1972). https://doi.org/10.1103/PhysRevC.5.626
[9] P.J. Brussaard, and P.W.M. Glademans, *Shell Model Application in Nuclear Spectroscopy*, (North-Holland Publishing Company, Amsterdam, 1977).
[10] G. Colò, H. Sagawa, S. Fracasso, and P.F. Bortignon, Phys. Lett. B, **646**, 227 (2007). https://doi.org/10.1016/j.physletb.2007.01.033
[11] M. Beiner, H. Flocard, N. Van Giai, and P. Quentin, Nucl. Phys. A, **238**, 29 (1975). https://doi.org/10.1016/0375-9474(75)90338-3
[12] P. Klupfel, P.-G. Reinhard, T.J. Bürvenich, and J.A. Maruhnet, Phys. Rev. C, **79**, 034310 (2009). https://doi.org/10.1103/PhysRevC.79.034310
[13] A.A. Alzubadi, and R.S. Obaid, Indian J. Phys. **93**, 75 (2019). https://doi.org/10.1007/s12648-018-1269-2
[14] V.I. Isakov, Phys. Part. Nuclei, **38**, 269 (2007). https://doi.org/10.1134/S1063779607020062
[15] B.A. Brown, W.A. Richter, and R. Lindsay, Phys. Lett. B, **483**, 49 (2000). https://doi.org/10.1016/S0370-2693(00)00589-X

ДОСЛІДЖЕННЯ СЛАБКОЗВ'ЯЗАНОЇ СТРУКТУРИ ЯДЕР НАВКОЛО МАГІЧНОГО ЧИСЛА N = 50

Рувайда С. Обейд, Алі А. Алзубаді
Департамент фізики, Науковий коледж, Багдадський університет, Багдад, Ірак

Досліджено квадрупольну деформацію ізотопів Kr, Sr, Zr і Mo за допомогою методу HFB та параметризації SLy4 Skyrme. Досліджено першочергову роль зайнятості одночастинкового стану $2d_{5/2}$ у слабкозв'язаній структурі навколо N = 50. Щілини в оболонці розраховуються за допомогою кількох інших розрахунків для подвійного магічного числа ^{100}Sn з використанням різних параметрів Скірма. Досліджено взаємодію між силою сполучення нейтронів і профілем густини нейтронів у двох вимірах у напрямку деформацій в ^{100}Sn.

Ключові слова: *слабозв'язана структура; квадрупольна деформація; сила сполучення*

East European Journal of Physics. 2. 85-90 (2023)
DOI:10.26565/2312-4334-2023-2-06 ISSN 2312-4334

DESCRIBE OF NUCLEAR STRUCTURE OF GERMANIUM ($^{66}_{32}Ge_{34}$) NUCLEUS USING NUCLEAR IBM-1, GVMI AND VMI MODELS[†]

Imad A. Hamdi*, Ali K. Aobaid[§]
Department of Physics, Faculty of Education for Pure Science, University of Anbar, Anbar, Iraq
**Corresponding Author e-mail: ema21u3002@uoanbar.edu.iq, [§]e-mail: esp.alik.obaid@uoanbar.edu.iq*
Received March 9, 2023; revised April 6, 2023; accepted April 9, 2023

In this paper, the interacting bosons model-1 (IBM-1), a variable moment of inertia (VMI) and generalized moment of inertia (GVMI) models were used to calculate the energy levels of the positive parity and its gamma transitions as a function of the angular momentum of even-even ($^{66}_{32}Ge_{34}$) nucleus. To determine the dynamic symmetry of this nucleus, the ratios of the energy levels E_4^+/E_2^+, E_6^+/E_2^+, *and* E_8^+/E_2^+) were evaluated and compared with experimental energy values and the ideal scheme of the three dynamic symmetries SU(5), SU(3), and O(6). The current study showed that the dynamic symmetry of this nucleus is determined to be O(6) - SU(5). The intersection of the energy band and the phenomenon of back bending were also studied using the (VMI) and (GVMI) models. These consequences were compared with the experimental results, and the results obtained have been in good agreement.
Keywords: *Nuclear structure, $^{66}_{32}Ge_{34}$, (IBM-1, GVMI and VMI) Models*
PACS: 21.45.-v, 21.60.Fw, 14.20.Dh.

INTRODUCTION

The importance of the nuclear models lies in studying and explaining many nuclear properties. One of these models is the Interacting Bosons Model (IBM), as it is considered one of the important nuclear models that succeeded in finding most of the nuclear properties. It gives good theoretical values that are compared to practical values and its ability to explain the decay of excited nuclear levels that lead to the emission of gamma rays [1].

The first interacting boson model (IBM-1) treated the movement of nucleons inside the nucleus as the movement of a group of paired particles called bosons, which represent either pair of protons or neutrons or proton-neutrons nearest outside the outermost closed shell [2].

The simplest concept of the first model of interacting bosons, developed by Arima and Iachello, (1974) [3], assumed that the low-lying collective energy levels in even-even medium and heavy nuclei are far from closed shells, with magic numbers 2, 8, 20, 28, 50, 82 and 126 are the ones in which only valence protons and neutrons prevail, while the core of the shell is inactive, in addition to that, it is assumed that similar particles are interacting together in pairs with an angular momentum of $\boldsymbol{L = 0}$ called s-boson and $\boldsymbol{L = 2}$ are called d-boson[4]. This model can describe the nuclear levels with positive parity only, which have medium and heavy mass numbers, except for those with closed shells, because the number of bosons equals zero. This model depends on "Unitary group theory" in six components called U(6), that then produces three subsection symmetries; vibrational U(5), rotational SU(3), and γ-unstable O(6) [1,5]. Determining dynamic symmetry depends on the ground energy levels, as it explains many nuclear properties [6].

Several models were introduced for associating a large number of experimental data for energy levels bands of even-even nuclei, in particular, the variable moment of inertia (VMI) model [7]. This model proposes that moment of inertia is mutable, the energy of a level with angular momentum (L) comprises in addition to the usual rotational term, a potential energy term which depends on the change of the moment of inertia ($\boldsymbol{\vartheta}_L$) from that of the ground state ($\boldsymbol{\vartheta}_o$). It can be said that this model succeeded in describing the energy levels of the rotational and, to some extent, vibrational nuclei.

The (GMI) [8] model is easier and more comprehensive than the (VMI) model, although it consists of the basic building blocks upon which the (VMI) model is built. The energy levels, which are a function of spin (L), are reduced to two limits in the new model. This model gave results that are highly consistent with the experimental findings of nuclei that have limitations within the SU(3) and SU(5) regions [9].

The phenomenon of back bending was demonstrated using both the VMI model and the GVMI model. This phenomenon can be explained by using band crossing and Coriolis force effect. The phenomenon of back bending was discovered by Johnson and his group in 1971. This phenomenon is one of the characteristics of the moment of inertia of deformed nuclei [10].

BAND CROSSING

The phenomenon of bands crossing states that if an energy band, such as $(\gamma - band)$ with a moment of inertia ϑ_2 and the ground state band $(g - band)$ with a moment of inertia ϑ_1 so that $(\vartheta_2 > \vartheta_1)$, an intersection between the two bands at a certain angular momentum (L_{cross}) L_c will be occurred. what is meant by this intersection is that the high

[†] ***Cite as:*** I.A. Hamdi, and A.K. Aobaid, East Eur. J. Phys. **2**, 85 (2023), https://doi.org/10.26565/2312-4334-2023-2-06

moment energy band will substitute energy by a low moment of inertia when the angular momentum is increased from L_c. At the intersection of two bands, all nucleons have a spin equal to zero under the influence of the pairing correlation interaction. In this case, the nucleus is considered super-soft and its self-energy is less than the double-bonding energy, and the nucleus has a small moment of inertia. The phenomenon of band crossing is an important characteristic of the moment of inertia [11].

CORIOLIS FORCE EFFECT

The force or effect of Coriolis is a physical term given to the visible and exposed deformation in the movement of objects when observed from a rotational frame of reference, and it was named after the French scientist Gustave Coriolis who described this deformation during 1835 AD. The Coriolis effect occurs due to the Coriolis force that appears in the equation of motion for a specific body in a rotational reference frame [12].

When the angular momentum of the nucleons is high, the effect of the Coriolis force begins to increase. This leads the boson located outside the closed shells to decoupling into two neutrons, where a new band called a *Two-quasiparticle* (2QP) band appears. While if the boson splits into a proton-neutron, here a *four-quasiparticle* (4QP) band appears. The intersection of the bands that appeared with $(g-band)$ at a certain angular momentum leads to the occurrence of the phenomenon of back bending [13].

SUMMARY OF THE FIRST INTERACTING BOSON MODEL (IBM-1)

The Hamiltonian operator for IBM-1 is given [14],

$$\hat{\mathrm{H}} = \sum_{i=1}^{N} \varepsilon_i + \sum_{i<j}^{N} U_{ij} \,. \tag{1}$$

Where ε_i: represents the energy of the boson.

U_{ij}: The energy of interacting bosons.

N: It is the sum of the number of bosons of nucleons.

Thus

$$\hat{\mathrm{H}} = \varepsilon_s(\hat{s}^{+}\hat{s}) + \varepsilon_d \sum_{\mu} \hat{d}^{+}_{\mu}\hat{\tilde{d}}_{\mu} + U \quad (\mu = 0, \pm 1, \pm 2, ...) \,. \tag{2}$$

Where

ε_s: The energy of *s*-type bosons.

ε_d: The energy of *d*-type bosons.

However, it is more mutual to write the Hamiltonian of the IBM-1 as a multipole extension, grouped into different boson-boson interactions [15]:

$$\hat{\mathrm{H}} = \varepsilon(\hat{n}_d) + \alpha_0\left(\hat{P}.\hat{P}\right) + \alpha_1\left(\hat{L}.\hat{L}\right) + \alpha_2\left(\hat{Q}.\hat{Q}\right) + \alpha_3\left(\hat{T}_3.\hat{T}_3\right) + \alpha_4\left(\hat{T}_4.\hat{T}_4\right) \,. \tag{3}$$

Where, $\varepsilon = \varepsilon_d - \varepsilon_s$ is the energy of the bosons. And $(\hat{n}_d)$ is the boson number operator and the pairing bosons operator isoctupole operator, and the hexadecapole . The angular momentum operator, the quadruple operator, the $(\hat{P})$ operator are $(\hat{L})\ (\hat{Q})\ (\hat{T}_3)\ (\hat{T}_4)$, respectively. And $\alpha_0, \alpha_1, \alpha_2, \alpha_3, \alpha_4$ are the phenomenological parameters.

Thus,

$$\left.\begin{aligned}
&\hat{n}_d = (\hat{d}^{\dagger}.\hat{\tilde{d}}) \\
&\hat{P} = 1/2(\hat{\tilde{d}}.\hat{\tilde{d}}) - 1/2(\hat{\tilde{S}}.\hat{\tilde{S}}) = \frac{1}{2}(\hat{\tilde{d}}^2 - \hat{\tilde{s}}^2) \\
&\hat{L} = \sqrt{10}[\hat{d}^{\dagger} \times \hat{\tilde{d}}]^{(1)} \\
&\hat{Q} = [(\hat{d}^{\dagger} \times \hat{\tilde{S}}) + (\hat{S}^{\dagger} \times d)]^{(2)} - CHI[\hat{d}^{\dagger} \times \hat{\tilde{d}}]^{(2)} \\
&\hat{T}_3 = [\hat{d}^{\dagger} \times \hat{\tilde{d}}]^{(3)} \\
&\hat{T}_4 = [\hat{d}^{\dagger} \times \hat{\tilde{d}}]^{(4)}
\end{aligned}\right\} \tag{4}$$

$CHI = -\frac{\sqrt{7}}{2}$ is for the rotational limitation and it equals zero for vibrational and γ-soft limitations.

The interacting boson model can be divided into three chains or three analytic solutions according to the eigenvalues problem of IBM-1 Hamiltonian. And these chains are [16],

$$U(6) \supset SU(5) \supset O(5) \supset O(3) \supset O(2) \tag{5}$$

Eq. 5 means anharmonic spherical vibrator.

$$U(6) \supset SU(3) \supset O(3) \supset O(2). \tag{6}$$

Eq. 6 means axially−deformed rotovibrator

$$U(6) \supset O(6) \supset O(5) \supset O(3) \supset O(2). \tag{7}$$

Finally, Eq. 7 represents γ-unstable deformed rotovibrator.

The region of the transition $O(6) - SU(5)$

The region is meant to represent the joint characteristics of two dynamical symmetries $O(6) - SU(5)$. The Hamiltonian operator's function can be expressed as [17].

$$\hat{H} = \varepsilon(\hat{n}_d) + \alpha_0(\hat{P}.\hat{P}) + \alpha_1(\hat{L}.\hat{L}). \tag{8}$$

The ratio (ε/α) was necessary for solving the equation (8). When the ratio is high, the vibration dynamical symmetry SU(5) is under the control. While the gamma-unstable dynamical symmetry O(6) is in charge while the ratio is low.

Summary of the variable moment of inertia (VMI) model

In the VMI model, the energy of level E(L) with Angular momentum (L) can be written as [18],

$$E(L) = \frac{1}{2\vartheta(L)} L(L+1) + \frac{C}{2}[\vartheta(L) - \vartheta_o]^2. \tag{9}$$

Where, $\vartheta(L)$: the moment of inertia with angular momentum L, ϑ_o: the moment of inertia with ground state, C: the restoring force constant

According to the variable moment of inertia model, the nuclear softness coefficient δ can be written in the following form [7],

$$\delta = \frac{1}{2C\vartheta_o^3}. \tag{10}$$

The back bending phenomenon occurs due to an increase in the moment of inertia, which is accompanied by a decrease in the rotational energy at a certain angular momentum in some nuclei. The total angular momentum $L(L+1)$ can be separated into two parts $L(L+1)$ and $(L-2)(L-1)$. The square of the rotational energy $(\omega\hbar)^2$ and the moment of inertia $\frac{2\vartheta}{\hbar^2}$ can be written for $(g\text{-}band)$ as [19],

$$(\omega\hbar)^2 = \left[\frac{E(L\to L-2)}{\sqrt{L(L+1)}-\sqrt{(L-2)(L-2+1)}}\right]^2 \tag{11}$$

$$\frac{2\vartheta}{\hbar^2} = \frac{4L-2}{E(L_i)-E(L_f)} = \frac{4L-2}{E_\gamma}. \tag{12}$$

For $\gamma - band$ as [18],

$$(\omega\hbar)^2 = \left[\frac{E(L\to L-1)}{\sqrt{L(L+1)}-\sqrt{(L-1)}}\right]^2. \tag{13}$$

$$\frac{2\vartheta}{\hbar^2} = \frac{L(L+1)-L(L-1)}{E(L\to L-1)} = \frac{2L}{E_\gamma}. \tag{14}$$

The transition energy E_γ of $g\text{-}band$ and any other band are the difference between the energy of the initial angular momentum $E(L_i)$ and the energy of the final momentum $E(L_f)$. Meaning that E_γ equals to $E(L) - E(L-2)$ regarding to $g\text{-}band$, while E_γ equals to $E(L) - E(L-1)$ following to $\gamma\text{-}band$.

Chi-square represents the suitability of VMI and GVMI models is given [20],

$$\chi^2 = \frac{(E_{cal}-E_{exp})^2}{(E_{exp})^2}. \tag{15}$$

Where, (E_{cal}) theoretically calculated energy and (E_{exp}) is the experimental error in the excitation energy.

The root mean square of the standard deviation was calculated from the following equation [20],

$$Standard\ Deviation = \sqrt{\left[\frac{1}{N}\sum_{i=1}^{N}(E_{cal} - E_{exp})^2\right]}. \tag{16}$$

where, N is the number of data points entering the fitting procedure.

CALCULATION PROCEDURES

Calculation of energy levels

- The energy levels of the nucleus under study were calculated using the IBM model by programming Equation 3 in the FN95-Plato program and through the *IBM program* code.
- The energy levels for the same core were calculated using the VMI model by programming Equation 9 in the same computer program through the code *VMI.For*.
- The energy levels of the studied nuclei were calculated using the GVMI model through the code *GVMI.For*.

The principle of matching between the values of the energy levels theoretically calculated in the IBM-1 model and its experimentally measured values is the first criterion adopted in our study. Table (1) shows the values of the parameters of the Hamiltonian function represented in Equation (3) were appropriated and adjusted.

Table 1. The parameters for which the best fit is chosen, which represent Equation 3. These parameters are the energies operator measured in (MeV).

Nuclei	N_π	N_υ	N	EPS (MeV)	$\hat{P}.\hat{P}$ (MeV)	$\hat{L}.\hat{L}$ (MeV)	$\hat{Q}.\hat{Q}$ (MeV)	$\hat{T}_3.\hat{T}_3$ (MeV)	$\hat{T}_4.\hat{T}_4$ (MeV)	CHI (MeV)	SO6 (MeV)
$^{66}_{32}Ge_{34}$	2	3	5	0.5532	0.0269	0.0444	0.0365	0.0184	0.0071	0.0001	0.0001

While the energy levels were theoretically calculated using the (IVM) and (GVMI) models by applying Equation (9). These parameters were selected and fitted to obtain the smallest value of the chi-square (χ^2).

According to the best selected parameters: moment of inertia ($\vartheta_\circ/\hbar$), recovery force (C), band head energy (E_k), for the VMI model. As for the (GVMI) model, it depends on the three parameters in addition to the parameter (Y) is the constant parameter fitted with experimental data as shown in Table (2). The last three columns contain, respectively, the values of the nuclear ductility coefficient δ, standard deviation, and chi-squared χ^2.

Table 2. The consistent parameters of (VMI) and (GVMI) models for $^{66}_{32}Ge_{34}$ nucleus

Isotope	Band	Model	$\vartheta_\circ/\hbar$ $(MeV)^{-1}$	C $(MeV)^3$	E_k (MeV)	Y (MeV)	δ	Standard deviation	χ^2
$^{66}_{32}Ge_{34}$	g	VMI	0.516370	0.036550	0.000000	-------	99.357262	0.203520	0.036356
		GVMI	2.034200	3.999000	0.000000	0.085224	0.024644	0.248871	0.052858
	γ	VMI	4.178000	0.040400	1.300000	-------	0.169701	0.182449	0.061080
		GVMI	1.000000	2.112000	0.100000	0.004224	0.469485	0.152464	0.038602

The values of the energy levels of the nucleus under study are shown in Figure (1). These results were compared according to the applied programs and the experimental values [22], and there was a good agreement between the experimental values and the theoretical values for these levels.

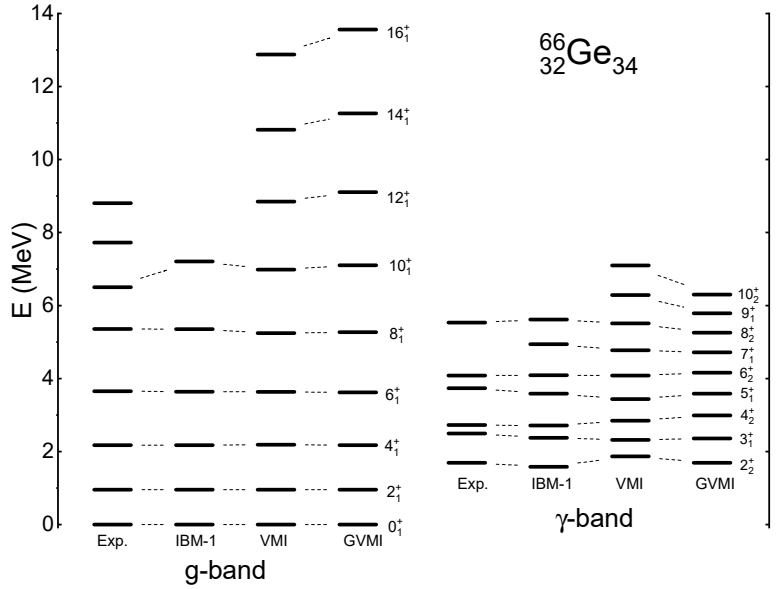

Figure 1. Experimental [22] and theoretical energy levels studied by (IBM-1) and (VMI) and (GVMI) models.

It is possible to identify and know the type of dynamic symmetry, which is considered one of the important nuclear properties to describe the behavior of the nucleus, and it can be reached by relying on the ratios for energy values calculated experimentally [23] and the theoretically calculated values of the nucleus under study and comparing them with the ideal values shown in Table (3), where practical and theoretical calculations indicate that this nucleus belongs to the two determinations $O(6) - SU(5)$ and according to the appearance of energy bands (g, γ). The presence of the $(\gamma - band)$ immediately after the $(g - band)$ confirms that the nucleus under study has O(6) dynamic symmetry.

Table 3. Perfect energy ratios for the three main limitations [23] compared with experimental [22] and theoretical values

Limit	$E4_1^+/E2_1^+$	$E6_1^+/E2_1^+$	$E8_1^+/E2_1^+$	Dynamicl symmetry
	2	3	4	SU(5)
Identical values [23]	3.33	7	12	SU(3)
	2.5	4.5	7	O(6)
Exp[22].	2.2712	3.8186	5.5997	O(6)-SU(5)
IBM-1	2.2735	3.8065	5.5999	O(6)-SU(5)
VMI	2.2905	3.7999	5.4801	O(6)-SU(5)
GVMI	2.2714	3.7823	5.5071	O(6)-SU(5)

The Energy Band Crossing

The importance of the energy band crossing phenomenon lies in explaining the back bending of deformed nuclei. Fig. (2) shows the band crossing of the nucleus under study using the (VMI) and (GVMI) models, depending on the energy equation (4). In both models, the (g-$band$) and (γ-$band$) intersect approximately at ($L_c = 6$).

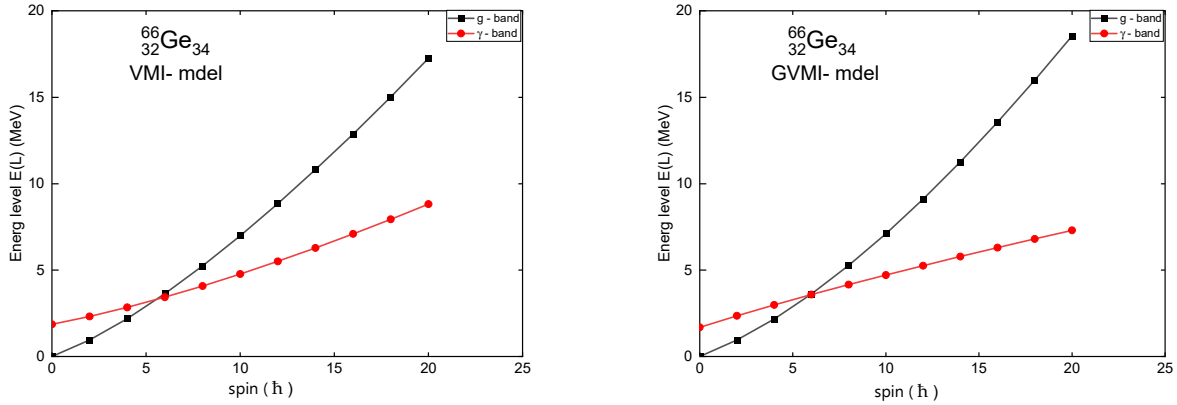

Figure 2. The energy levels calculated theoretically by means of a) the VMI model and b) the GVMI model for the nucleus under study.

The back bending phenomenon

In nuclear physics, the effect of the moment of inertia is an important topic in order to identify and study the phenomenon of back bending. To get acquainted with this phenomenon, both ($2\vartheta_\circ/\hbar$) and $(\hbar\omega)^2$ were calculated by computing the equations (11, 12,13, and 14) using a computer simulation programs (*VMI.For*) and (*GVMI.Model*). Fig. (3) shows the relationship between the moment of inertia ($2\vartheta_\circ/\hbar$) as a function of the rotational energy squared $(\hbar\omega)^2$ of the nucleus under study using the (VMI) and (GVMI) models. It was observed that there are backbends in the ground state band (g-$band$) and the (γ-$band$).

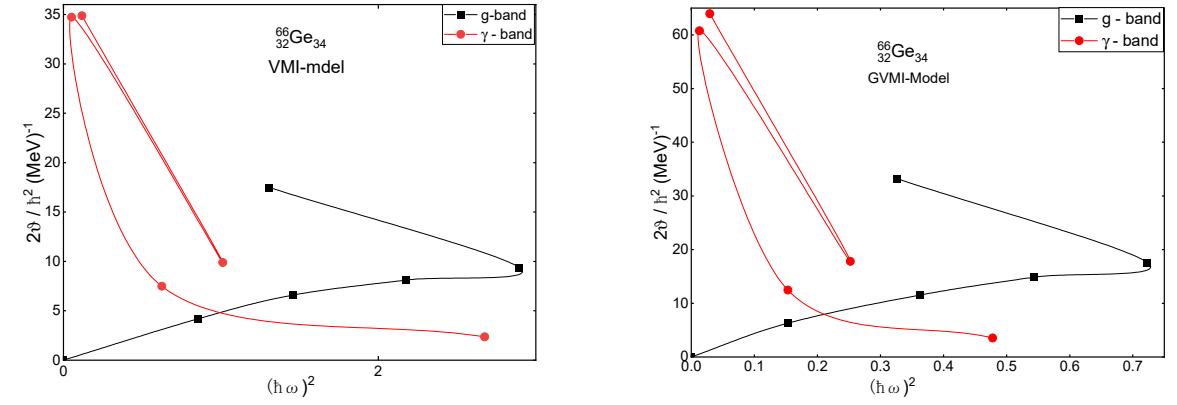

Figure 3. The relationship between moment of inertia $(2\vartheta/\hbar 2)$ and rotational energy $(\hbar\omega)^2$ of the nucleus under study within the scope of a) the (GVMI) model and b) the (VMI) model.

CONCLUSIONS

The three models (IBM-1, VMI and GVMI) achieved acceptable success in this study. In this study, it was found that the models used gave a good agreement in calculating the energy levels and excited energies as a function of angular momentum, compared with the experimental calculations.

It was concluded that the determination of dynamic symmetry by calculating the energy ratios for each of the three models and comparing them with the ideal values with the nucleus under study develops the determination of O(6) -SU(5).

With regard to the intersection of bands, it was found that each of the $g-band\ and\ the\ \gamma-band$, which were calculated through the VMI and GVMI models, intersect at angular momentum $L_c = 6$. This leads to the occurrence of the back bending phenomenon.

Through the theoretical results obtained, it was found that the models can give many explanations in the nuclear structure.

ORCID IDs

Ali K. Aobaid, https://orcid.org/0000-0002-1135-3675

REFERENCES

[1] A.M. Al-Nuaimi, R.B. Alkhayat, and M.A. Al-Jubbori, "Investigating the Nuclear Properties of 162-172 Er Isotopes using IBM-1, SEF, and NEE," Karbala International Journal of Modern Science, **8**, 391-396 (2022). https://doi.org/10.33640/2405-609X.3249

[2] S.S. Hummadi, O.A.M. Safauldeen, A.M. Hadee, and R.H. Honi, "Calculate Energy Levels, Energy Ratios and Electric Quadrupole Transition Probability B (E2), of the Even-Even Yb-164 Isotopes Using IBM-1," Al-Mustansiriyah Journal of Science, **31**, 71-75 (2020). https://doi.org/10.23851/mjs.v31i1.606

[3] F. Iachello, and A. Arima, "Boson Symmetries in Vibrational nuclei," Phys. Lett. B, **53**, 309-312 (1974). https://doi.org/10.1016/0370-2693(74)90389-X

[4] H.N. Hady, and M.K. Muttalb, "Investigation of transition symmetry shapes of $^{160\text{-}168}$Yb nuclei using IBM," Iraqi Journal of Science, **62**, 1135-1143 (2021). https://doi.org/10.24996/ijs.2021.62.4.10

[5] T. Otsuka, A. Arima and F. Iachello, "Shell model description of interacting bosons," Phys. Lett. B, **76**, 139-143 (1978). https://doi.org/10.1016/0370-2693(78)90260-5

[6] Y.Y. Kassim, M.A. Al-Jubbori, I.M. Ahmed, H.Y. Abdullah, and F.I. Sharrad, "Microscopic description of ^{170}Er, ^{172}Yb, ^{174}Hf, ^{176}W isotones," in: *IOP Conference Series: Materials Science and Engineering*. (IOP Publishing, 2020), pp. 072124.

[7] G. Scharf-Goldhaber, C.B. Dover, and A.I. Goodman, "The Variable Moment of Inertia (VMI) Model and Theories of Nuclear Collective Motion," Annu. Rev. Nucl. Sci. **26**, 239-317 (1976). https://doi.org/10.1146/annurev.ns.26.120176.001323

[8] D. Bonatsos, and A. Klein, "Generalized phenomenological models of the yrast band," Phys. Rev. C, **29**, 1879-1886 (1984). https://doi.org/10.1103/PhysRevC.29.1879

[9] I.T. Al-Alawy, K.S. Ibraheim, and A.K. Aobaid, "The effect of the VMI, VAVM and GVMI moment of inertia and rotational motion on the nuclear structure of $^{56}_{26}Fe_{30}$ nucleus," J. Coll. Edu. **1**, 233-252 (2016).

[10] A. Johnson, H. Ryde, and J. Sztarkier, "Evidence for a "singularity" in the nuclear rotational band structure," Phys. Let. B, **34**, 605-608 (1971). https://doi.org/10.1016/0370-2693(71)90150-X

[11] D. Ward, R.L. Graham, J.S. Geiger, and H. R. Andrews, "Anomalous Moments of Inertia for High-spin Levels in The Beta Vibration Band of ^{154}Gd," Phys. Lett. B, **44**, 39-40 (1973). https://doi.org/10.1016/0370-2693(73)90294-3

[12] V. Apostolyuk, *Coriolis Vibratory Gyroscopes Theory and Design*, editor, (Springer International Pub. Switzerland, 2016).

[13] B.L. Birbrair, "Influence of the nuclear Meissner - effect on the ground - state rotational bands of deformed nuclei," Phys. Let. B, **39**, 489-491 (1972). https://doi.org/10.1016/0370-2693(72)90326-7

[14] G.A.H. Jaber, and M. K. Muttaleb, "Studying The Breaking Symmetry for O(6) Even Hg Isotopes in Interacting Boson Model (1 and 2)," in AIP Conference Proceedings, **2144**, (AIP Publishing LLC, 2019), pp. 030014. https://doi.org/10.1063/1.5123084

[15] H.N. Hady, and M.K. Muttalb, "Geometric structure features in $^{72\text{-}80}Se$ isotopes," J. Rad. Nucl. Appl. **5**, 147-152 (2020). https://www.naturalspublishing.com/download.asp?ArtcID=21429

[16] A. Frank, J. Jolie, and P.V. Isacker, "Symmetry in Nuclear Physics: The Interacting Boson Model," in: *Symmetries in Atomic Nuclei*, (Springer Nature, Switzerland AG, 2019), pp. 71-102.

[17] K.S. Ibrahim, I.T. Al-Alawy, and N.M. Umran, "The Potential Energy Surface (P.E.S.) of $^{114}_{48}Cd_{64}$ and $^{146}_{60}Nd_{86}$ of U(5)–O(6) Dynamical symmetries," J. Coll. Edu. **1**, 281-298 (2018). https://www.iasj.net/iasj/pdf/210cac021a430477

[18] A.M. Khalaf, M.D. Okasha, G.S.M. Ahmed, and A. Abdelsalam, "Identical bands in doubly even nuclei in framework of variable moment of inertia (VMI) and interacting boson models," Nucl. Phys. A, **997**, 121719 (2020). https://doi.org/10.1016/j.nuclphysa.2020.121719

[19] R. Nojarov, and E. Nodjakov, "Band Coupling and Crossing in Nuclei," Nucl. Phys. A, **397**, 29-60 (1983). https://doi.org/10.1016/0375-9474(83)90077-5

[20] M.R. Spiegel, and L.J. Stephens, "The Standard Deviation and Other Measures of Dispersion," in: *Schaum's Outlines Statistics*, 6th ed., (Mc Graw Hill Education, 2018), pp. 100-105.

[21] M. Sakai, "Quasi-Bands in Even–Even Nuclei," Atomic data and nuclear data tables, **31**, 399-432 (1984). https://doi.org/10.1016/0092-640X(84)90010-X

[22] E. Browne, and J.K. Tuli, "Nuclear Data Sheet for A=66," **111**(4), 1093-1209 (2010). https://doi.org/10.1016/j.nds.2010.03.004

[23] A.M. Ali, Y.Y. Kassim, and M.M. Yosuf, "Study of Nuclear Structure of Even–Even Dy Isotopes," J. Edu. and Sci. **30**, 94-105 (2021). http://dx.doi.org/10.33899/edusj.2021.129809.1151

ОПИС СТРУКТУРИ ЯДРА ГЕРМАНІЮ $^{66}_{32}Ge_{34}$ З ВИКОРИСТАННЯМ ЯДЕРНИХ МОДЕЛЕЙ IBM-1, GVMI ТА VMI

Імад А. Хамді, Алі К. Аобейд

Кафедра фізики, Факультет освіти для чистої науки, Анбарський університет, Анбар, Ірак

У цій статті для розрахунку рівнів енергії позитивної парності та її гамма-переходів як функція кутового моменту парно-парного ($^{66}_{32}Ge_{34}$) ядра використовувалися модель взаємодіючих бозонів (IBM-1), модель змінного моменту інерції (VMI) і узагальненого моменту інерції (GVMI). Також були оцінені співвідношення рівнів енергій E_4^+/E_2^+, $E_6^+/E_2^+, and\ E_8^+/E_2^+$) та порівняні з експериментальними значеннями енергії та ідеальною схемою для трьох динамічних симетрій SU(5), SU(3) та O(6), щоб визначити динамічну симетрію цього ядра поточне дослідження показало, що при динамічна симетрія визначення O(6)-SU(5). Перетин енергетичної зони та явище вигину назад також вивчали за допомогою моделей (VMI) та (GVMI). Ці наслідки порівнювали з експериментальними результатами, і отримані результати добре узгоджувалися.

Ключові слова: *структура ядра;* $^{66}_{32}Ge_{34}$*; моделі (IBM-1, GVMI та VMI)*

EAST EUROPEAN JOURNAL OF PHYSICS. **2.** 91-97 (2023)
DOI:10.26565/2312-4334-2023-2-07 ISSN 2312-4334

SHELL MODEL INVESTIGATION OF SOME *p* AND *sd*-SHELL NUCLEI WITH HARMONIC OSCILLATOR AND SKYRME INTERACTIONS[†]

Sarah M. Obaid[a], Shaimaa A. Abbas[b], Aeshah Ali Hussein[b], Noor Adil Mohammed[c], Fouad A. Majeed[d]*

[a]*Department of Engineering Health Physics Techniques and Radiotherapy, Technical Engineering College of Al-Najaf, Al-Furat Al-Awsat Technical University, Al-Najaf, Iraq*
[b]*Department of Physics, College of Education for Pure Science (Ibn-Alhaitham), University of Baghdad, Baghdad, Iraq*
[c]*Ministry of Education, Directorate General of Education Rusafa3, Baghdad, Iraq*
[d]*Department of Physics, College of Education for Pure Sciences, University of Babylon, Babylon, Iraq*
**Corresponding Author e-mail: fmajeed@uobabylon.edu.iq*
Received November 3, 2022; revised December 14, 2022; accepted March 7, 2023

In this study, the longitudinal charge $|F_{ch}(q)|^2$ and $|F(C2,q)|^2$form factors for the nuclei ^{9}Be and ^{28}Si lying in the *p* and *sd* shells are studied by employing the Harmonic Oscillator potential (HO) and Skyrme effective interaction (Sk35−Skzs*). The C0 and C2 from factors calculated for the ground state 3/2$^-$, the 5/2$^-$ (2.429 MeV) and 7/2$^-$ (6.380 MeV) for ^{9}Be, while the ground state 0^+ and 2^+ (1.779 MeV) state for ^{28}Si nucleus. Calculations of microscopic perturbations that involve intermediate one-particle, one-hole excitation from the core and MS orbits into all upper orbits with $n\hbar\omega$excitations are utilized to generate the effective charges necessary to account for the "core polarization effect". The shell model calculations are utilized on the extended model space to include all 1s, 1p, 2s–1d, 2p-1f orbits with $(0+2)\hbar\omega$ truncation. Bohr-Mottelson collective model and Tassie model with properly estimated effective neutron and proton charges are taken into account to consider the effect of the core contribution. The estimated form factors were compared with the measured available data and they were in good agreement for most of the studied states. A conclusion can be drawn that $(0+2)\hbar\omega$ truncation is very good choice to study the longitudinal form factors.

- The choice of Harmonic Oscillator potential (HO) and Skyrme effective interaction (Sk35−Skzs*) is adequate for form estimation of longitudinal form factors.
- The estimation of the effective charges based on microscopic perturbations that involve intermediate one-particle, one-hole excitation from the core and MS orbits into all upper orbits with $n\hbar\omega$ excitations is adequate.
- The $(0+2)\hbar\omega$ truncation proves to be very successful to perform the study.

Keywords: *Shell Model; Charge form factor; Longitudinal Form Factors; Harmonic Oscillator; Skyrme Interactions*
PACS: 21.60.Cs, 13.40.Gp, 25.30.Dh, 03.65.−w, 21.30.Fe

INTRODUCTION

The investigation of nuclei has more access neutrons, than what is known as "neutron-rich nuclei" far from the line of stability is important for understanding nuclear structure. Exotic features differ from those of stable nuclei and deserve experimental and theoretical exploration. One of the most striking characteristics of neutron-rich nuclei is nuclear deformation, which may be studied both theoretically and empirically using electromagnetic properties like electric quadrupole (Q) moments and magnetic dipole (μ) moments. Using a microscopic particle vibration model, Sagawa and Asahi [1] investigated the N/Z dependence of the quadrupole polarization charges of C isotopes. The single-particle wave functions and gigantic quadrupole resonances are approximated using the Hartree-Fock and random-phase approximations. The polarization charges of nuclei with a high N/Z ratio experienced a significant quenching. Cohen and Kurath [2] model properly explain the features of low energy p shell nuclei, but it fails to represent the form factors of higher momentum transfer. Radhi et al. [3-6] have previously stated that the CP effects must be taken into account for nuclei in the *p* shell and *sd* shell to improve form factor calculations. Taihua Heng et al. [7] used the ab initio no-core full configuration NCFC technique to explore the characteristics of ^{7}Li with the NNLO$_{opt}$ chiral nucleon-nucleon and JISP16 interactions, as well as ^{7}Be with the JISP16 interaction. They calculated observables like energy spectra, proton point radii at the root mean value, transitions, and electromagnetic moments. Zheng et al. performed calculations based on large-basis shell model without core calculations for *p-shell* nuclei using six main shells (from 1s to 3p-2f-1h) [8, 9]. All nucleons are active in these calculations, according to Zheng et al., If computer resources are restricted, we have to adopt a truncated calculation without core with some freezing orbits, in which only a few $\hbar\omega$ excitations of the lowest unperturbed configurations are evaluated can be used. The result will converge and approximate that of the full no-core calculations as the number of $\hbar\omega$ increases. In the work of Navratil *et al.* [10] it is found that the predicted rate of the E2 transition with $4\hbar\omega$ space for ^{6}Li is weaker than $6\hbar\omega$ space prediction. Majeed *et al.* [11-13] revealing that the form factor calculation on a large basis of the shell model was used to analyze nuclei in the *p*, *sd*, and *Fp* shells, including the contribution of high-energy configurations beyond the *p*, *sd*, and *Fp* shell space model space is essential to be considered to consider the effect of the core polarization contribution arises from the closed core.

[†] ***Cite as:*** S.M. Obaid, S.A. Abbas, A.A. Hussein, N.A. Mohammed, and F.A. Majeed, East Eur. J. Phys. **2**, 91 (2023), https://doi.org/10.26565/2312-4334-2023-2-07

In this study, the longitudinal charge and C2 form factors for ^{9}Be and ^{28}S exotic nuclei utilizing the shell model calculations by considering the major shells 1s, 1p, 2s–1d, 2p–1f, with partially inert core using the model space *spsdpf* with *wbt* effective interaction using the code NushellX@MSU [14]. Since the space configuration is a very large dimension, the shell model calculations in the whole *spsdpf* space are not possible, therefore a truncation is required in the valence space. We will consider the $(0+2)\hbar\omega$ truncated *spsdpf* model space (ms) calculation. The form factors will be calculated by considering the residual interactions, between harmonic oscillator (HO) and Skyrme effective interaction (Sk35−Skzs*) [15] with using the Tassie and Bohr-Mottelson collective models. The core polarization (CP) will be considered by evaluating the suitable effective charges at zero photon point. Theoretical results of C0 and C2 were compared with the available measured data for each studied case for the studied nuclei.

METHOD DETAILS

Tassie and Bohr-Mottelson models were adopted along with Harmonic Oscillator potential and Skyrme effective interaction (Sk35−Skzs*) with suitable parametrization were adopted. As mentioned in Ref. [16], the neutron and proton effective charges for the model of Tassie are predicted by using microscopic perturbation calculations that include intermediate (1p-1h) excitations from the orbit contribution MS and core to include higher orbits with $n\hbar\omega$ excitations. The effective proton and neutron charges for Bohr-Mottelson were estimated using the equations [17]

$$e^{eff}(t_z) = e(t_z) + e\delta e(t_z)$$

$$e\delta e(t_z) = Z/A - 0.32(N-Z)/A - 2t_z[0.32 - 0.3(N-Z)/A], \quad (1)$$

where $t_z(p) = 1/2$ and $t_z(n) = -1/2$

In terms of transition charge density, the element matrix of Coulomb can be represented as the sum of the MS and CP elements [18]

$$O(C\lambda, q) = q\int_0^\infty drr^2 j_\lambda(qr)\rho_{\lambda,p}^{MS}(r) + \int_0^\infty drr^2 j_\lambda(qr)\Delta\rho_\lambda(r) \quad (2)$$

where the momentum transfer is q and $j_\lambda(qr)$ is spherical Bessel function. For the initial (i) and final (f) nuclear states, the nucleons charge density *F* of the transition is described using the one-body density matrix [18]

$$\rho_{\lambda,u}^{MS}(r) = \sum_{k_a,k_b}^{MS} F(i,f,k_a,k_b,\lambda,u)\langle j_a||Y_\lambda||j_b\rangle R_{n_a l_a}(r)R_{n_b l_b}(r), \quad (3)$$

where k stands for $(n\ l\ j)$ the s.p. states and (u) is the index which refers to either neutrons or protons.

The transition density for the CP valence model is given by [18]

$$\Delta\rho_\lambda^V(r) = \delta e_p\rho_{\lambda,p}^{MS}(r) + \delta e_n\rho_{\lambda,n}^{MS}(r) \quad (4)$$

δe_p , δe_n are the charges associated with the neutron and protons to account for polarization.

The CP for Tassie model transition density is provided by

$$\Delta\rho_{\lambda,p}^T(r) \propto r^{\lambda-1}\frac{d\rho_{0,p}^{core+MS}(r)}{dr} = Nr^{\lambda-1}\frac{d\rho_{0,p}^{core+MS}(r)}{dr} \quad (5)$$

The charge density of the ground state is [18]

$$d\rho_{0,p}^{core+MS}(r) = \sum_{k_a,k_b}^{Core+MS} F(i,f,k_a,k_b,0,p)\langle j_a||Y_0||j_b\rangle R_{n_a l_a}(r)R_{n_b l_b}(r) \quad (6)$$

At the photon point, the proportionality constant N is given by the matrix elements of gamma transitions $M(E\lambda)$, $q = E_\gamma/\hbar c$, where E_γ is the energy due to excitation [18]

$$M(E\lambda) = \left\{e\int_0^\infty drr^2\, r^\lambda(qr)\rho_{\lambda,p}^{MS}(r) + N\int_0^\infty drr^2 r^{2\lambda+1}\frac{d\rho_{0,p}^{core+MS}(r)}{dr}\right\} \quad (7)$$

The matrix of gamma transition elements can be described as MS matrix elements with effective charges.

$$M(E\lambda) = e_p^{eff}\int_0^\infty drr^2\, r^\lambda(qr)\rho_{\lambda,p}^{MS}(r) + e_n^{eff}\int_0^\infty drr^2\, r^\lambda(qr)\rho_{\lambda,n}^{MS}(r) \quad (8)$$

Equating Eq. (7) with Eq. (8) yields the constant of proportionality *N* by means of the effective charges. A detailed discussion of these above-mentioned models for effective neutrons and protons [18]

$$|F_{L\lambda}(q)|^2 = \frac{4\pi}{Z^2}\frac{1}{2j_i+1}|O(C\lambda,q)|^2\left|F_{cm}(q)F_{fs}(q)\right|^2 \quad (9)$$

Skyrme energy is produced through Skyrme interaction. According to E_{Skyrme} is a two-body density-dependent interaction that represents central spin-orbit and tensor components in coordinate space and replicates the strong force in the particle-hole channel [19]

$$v_{12} = t_0\left(1 + x_0\hat{P}_\sigma\right)\delta(\vec{r}_1 - \vec{r}_2) + \frac{t_1}{2}\left(1 + x_1\hat{P}_\sigma\right)\left(\hat{k}^2\delta(\vec{r}_1 - \vec{r}_2) + \delta(\vec{r}_1 - \vec{r}_2)\hat{k}^2\right) + t_2\left(1 + x_2\hat{P}_\sigma\right)\hat{k}.\delta(\vec{r}_1 - \vec{r}_2)\hat{k} + \frac{t_3}{6}\left(1 + x_3\hat{P}_\sigma\right)\rho^\alpha\left(\vec{R}\right)\delta(\vec{r}_1 - \vec{r}_2) + iW_0\hat{k}(\hat{\sigma}_1 + \hat{\sigma}_2) \times \hat{k}\delta(\vec{r}_1 - \vec{r}_2) \quad (10)$$

here $\vec{R} = \frac{\vec{r}_1 + \vec{r}_2}{2}$ and α is the force of Skyrme parameters. The operators $\hat{k} = \left(\vec{\nabla}_1 - \vec{\nabla}_2\right)/2i$ and $\hat{\acute{k}} = -\left(\overleftarrow{\nabla}_1 - \overleftarrow{\nabla}_2\right)/2i$ are the relative momentum wavevectors for the two nucleons acting to the right and left, with coordinate $\acute{r}$ respectively. When the nuclear structure data is fitted, the variables t_0, t_1, t_2, t_3, x_1, x_2, x_3, and W_0 are free parameters taken to describe the components of various interactions. The Pauli matrices ($\hat{\sigma}$), the spin-exchange operator, and the delta function of Dirac $\delta(\vec{r}_1 + \vec{r}_2)$ are all mathematical terms. The energy of the total density of the nucleus is expressed as follows in the (SHF) model [19]:

$$E = E_{kin} + E_{Sky}\left(\rho_u + \tau_u + \vec{s}_u + \vec{j}_u + \vec{\mathfrak{H}}_u\right) + E_{Coul} + E_{pair} - E_{cm} \quad (11)$$

Here E_{kin} refers to energy of kinetic motion, E_{Sky} refers to Skyrme energy which include time even (nucleon ρ_u, kinetic energy τ_u and orbital–spin $\vec{\mathfrak{H}}_u$ and the odd-time (current $\vec{j}_u$, spin $\vec{s}_u$, and the vector of the kinetic energy $\vec{T}_u$) both densities and the pairing energy E_{pair} and the mass at the center E_{cm}. The u label refers to neutrons or protons. The Skyrme type of parametrization is taken to perform the calculations is (Sk35−Skzs*) [16].

The "mean square charge radius" is expressed by the formula [16]

$$\langle r_c^2\rangle = \langle r_p^2\rangle + \langle R_p^2\rangle + \frac{N}{Z}\langle r_n^2\rangle + \frac{3}{4}\left(\frac{\hbar}{M_p c}\right)^2 \quad (12)$$

$$\langle r_c^2\rangle = \langle r_p^2\rangle + 0.769 - \frac{N}{Z}0.1161 \; + \; 0.033 \quad (13)$$

Here r_p is the radius comes from the distribution of the proton point of the nucleus, R_p and r_n are the charge radii of the free proton and neutron, and the final term is known as the Darwin-Foldy term (0.033 fm^2).

RESULTS AND DISCUSSION

The longitudinal Coulomb charge $|F_{ch}(q)|^2$ and $|F(C2,q)|^2$ form factors for the ^{9}Be and ^{28}Si nuclei have been calculated by considering a truncated *spsdpf* model space with *wbt* effective interaction [20] with $(0+2)\hbar\omega$. The C0 and C2 from factors calculated for the ground state 3/2$^-$, the 5/2$^-$ (2.429 MeV) and 7/2$^-$ (6.380 MeV) for ^{9}Be, while the ground state 0^+ and 2^+ (1.779 MeV) state for ^{28}Si nucleus. In all proceeding figures (see Fig.1, panels a, b, c, and d), the dotted grass green and magenta curves display the results of the calculations of the Tassie and Bohr-Mottelson models using the valence model (MS) calculations only, while the solid red and blue curves show the calculations of Tassie and Bohr-Mottelson models including the core polarization effect by means of effective charge of protons and neutrons.

^{9}Be nucleus

The nucleus ^{9}Be is a neutron-halo with 4 protons and 5 neutrons considered as (4α+n) and it is stable with the ground state is 3/2$^-$. The effective charge at the zero-photon point considered in this work is taken from Ref. [21]. The longitudinal Coulomb charge $|F_{ch}(q)|^2$ and $|F(C2,q)|^2$ Form factors for the ground state have been calculated $\left(J_f^\pi = 3/2^-, T = 1/2\right)$ of the ^{9}Be as displayed in Figure 1 panels (a, b, c and d) by utilizing the Tassie and Bohr-Mottelson collective models. Due to large number of dimensions to be used in the model space *spsdpf,* a truncation has to be used, therefore the truncation is taken as $(0+2)\hbar\omega$ following the restriction adopted in Ref. [16].

The state (3/2$^-$ 1/2) at 0.000 MeV (g.s)

The C0 and C2 form factors and their sum (C0+C2) for the ground state 3/2$^-$ are depicted in Fig.1 , b, c, and d. The calculations were performed by using harmonic oscillator (HO) and Skyrme effective interactions (Sk35−Skzs*) for both Tassie and Bohr-Mottelson models. Panels a and b represent the Tassie model with the Harmonic Oscillator potential (HO) and Skyrme effective interaction (Sk35−Skzs*), while in c and d in Fig.1, represent Bohr-Mottelson model Tassie model with the Harmonic Oscillator potential (HO) and Skyrme effective interaction (Sk35−Skzs*). The effective charges for neutron and proton are 0.70e and 1.075e, respectively [21], while for Bohr-Mottelson estimated using Eq.1 as 0.17 and 0.4 for the proton and neutron respectively. The observed data from Ref. [22] for this state form factor. The data could not be reproduced in all regions of the momentum transfer using bare model space computations. Introducing the effective charge in both Tassie and Bohr Mottelson with account for the core polarization effect makes

a remarkable improvement especially for Bohr Mottelson calculations shown in panel (a) where the solid bule line which is (C0+C2) form factor matches the measured data in all momentum transfer regions using HO as the residual effective interaction.

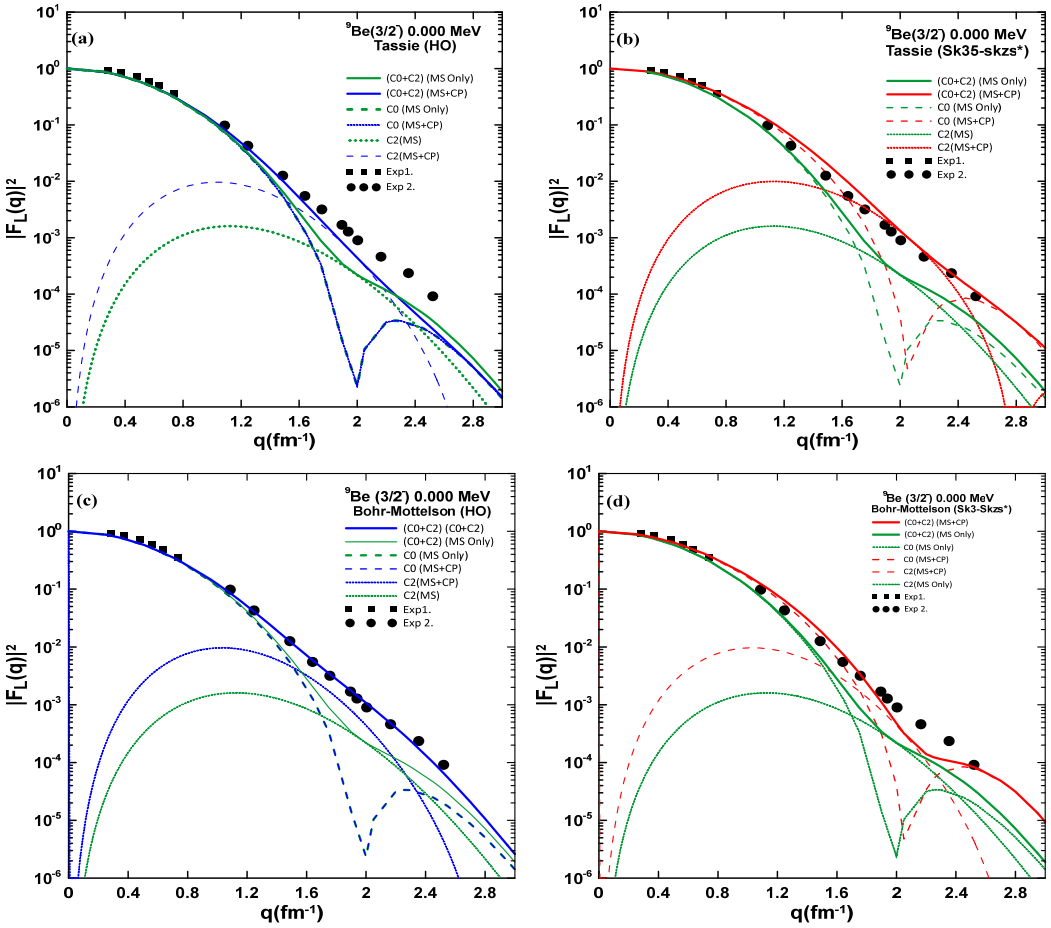

Figure 1. Longitudinal C0 and C2 form factors and their sum C0+C2 for the Tassie and Bohr-Mottelson models by using the Harmonic Oscillator potential (HO) and Skyrme effective interaction (Sk35−Skzs*) in comparison to the measured data [22].

The state (5/2$^-$ 1/2) 2.429 MeV

Figure 2 shows the calculation of the form factor for C2 for the state (5/2$^-$ 1/2) at E_x=2.429 MeV. The bare model space calculation for both Bohr-Mottelson collective model and Tassie model by using the Harmonic Oscillator potential (HO) and Skyrme effective interaction (Sk35−Skzs*) underestimates the measured data in all momentum transfer regions. The measured data for this state are taken from [22-24]. The form factor of Bohr-Mottelson model reproduces the high q values of the effective charge to consider the CP effects, explains the data up $q \geq 1.5 fm^{-2}$.

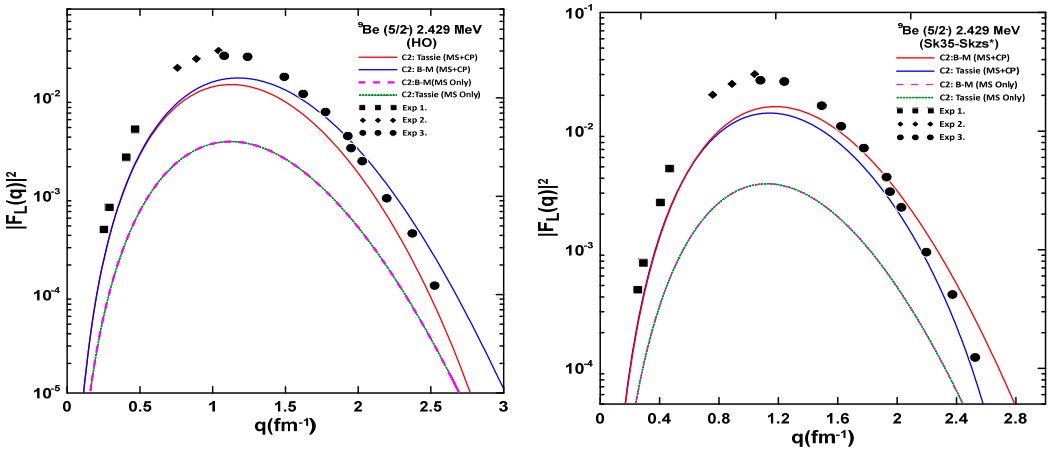

Figure 2. The C2 longitudinal form factors for the Tassie and Bohr-Mottelson models by using the Harmonic Oscillator potential (HO) and Skyrme effective interaction (Sk35−Skzs*) in comparison to the measured data [23, 24].

The state ($7/2^-$ 1/2) 2.429 MeV

The longitudinal C2 form factor for ($7/2^-$ 1/2) at E_x=6.380 MeV. The calculation of the model space for the Tassie and Bohr-Mottelson models at the peak value, it underpredicts the data by nearly a factor of three. The measured data are scattered therefore Introducing the effective charge in both Tassie and Bohr Mottelson to account for the core polarization effect aren't able to reproduce the measured data for these states. The measured data are taken from [22] (Fig. 3).

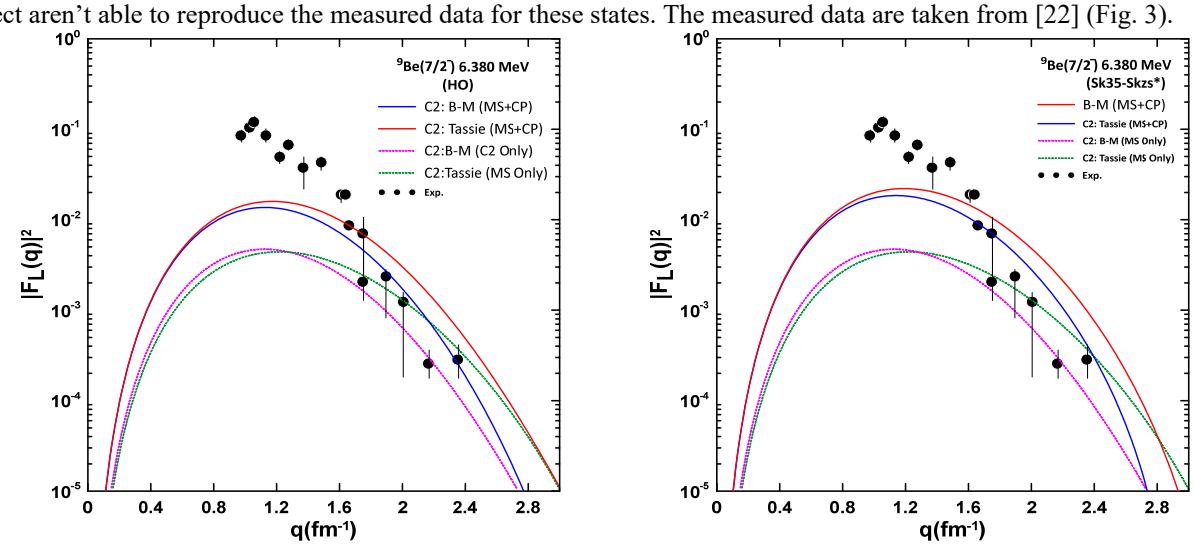

Figure 3. The C2 longitudinal form factors for the Tassie and Bohr-Mottelson models by using the Harmonic Oscillator potential (HO) and Skyrme effective interaction (Sk35−Skzs*) in comparison to the measured data [23, 24].

^{28}Si nucleus

The nucleus ^{28}Si is even-even nucleus with 14 protons and 14 neutrons and it is stable with the ground state is 0^+. The longitudinal Coulomb charge $|F_{ch}(q)|^2$ and $|F(C2,q)|^2$ form factors are calculated for the transitions to the ground state $\left(J_f^\pi = 0^+, T = 0\right)$ of the ^{28}Si as demonstrated in Figure 4 by utilizing the Tassie and Bohr-Mottelson collective models. Due to large number of dimensions to be used in the model space *spsdpf,* a truncation has to be used, therefore the truncation is taken as $(0+2)\hbar\omega$ following the restriction model from Ref. [16].

The state (0^+ 0) 0.000 MeV (g.s)

The C0 form factor for the ground state $0^+$is displayed in Fig.4. The calculations were performed by using Harmonic oscillator (HO) and Skyrme effective interactions (Sk35−Skzs*) for both Bohr-Mottelson collective model and Tassie model. In both Tassie and Bohr Mottelson models, the effective charge is included to account for the core polarization effect. The measured data is taken from [25]. The theoretical calculations of the model space only don't reproduce the measured data for all q values. The inclusion of the core polarization in the Bohr Mottelson model harmonic oscillator (HO) describes the experimental data very well up to momentum transfer $q \geq 1.5 fm^{-2}$ and is able to reproduce the measured data very well and agrees with previous theoretical work in Ref. [6].

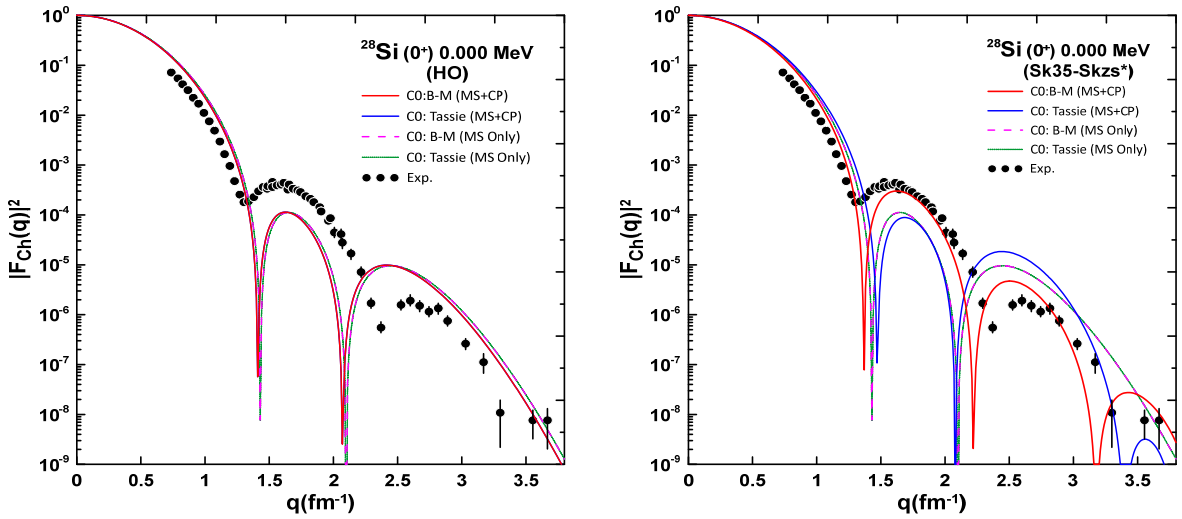

Figure 4. Longitudinal C0 form factors for the Tassie and Bohr-Mottelson models by using the Harmonic Oscillator potential (HO) and Skyrme effective interaction (Sk35−Skzs*) in comparison to the measured data [25].

The state (2^+ 0) 1.779 MeV

Figure 5 displays the longitudinal C2 calculations with their comparison to the measured data for the state (2^+ 0) at 1.779 MeV to the ground state (0^+ 0). The measured data is taken from [25] The model space $(0+2)$ only with Harmonic oscillator (HO) and Skyrme effective interactions (Sk35−Skzs*) for Bohr-Mottelson collective model and Tassie model underestimate the experimental data in the first maxima and second maxima. The inclusion of the core polarization in the Bohr Mottelson model harmonic oscillator (HO) and Skyrme effective interactions (Sk35−Skzs*) describe the experimental data very well up to momentum transfer $q \geq 1\ fm^{-2}$. The effects of core polarization enhance the C2 form factors at the first and second maximums, bringing the calculated values extremely near to the experimental data.

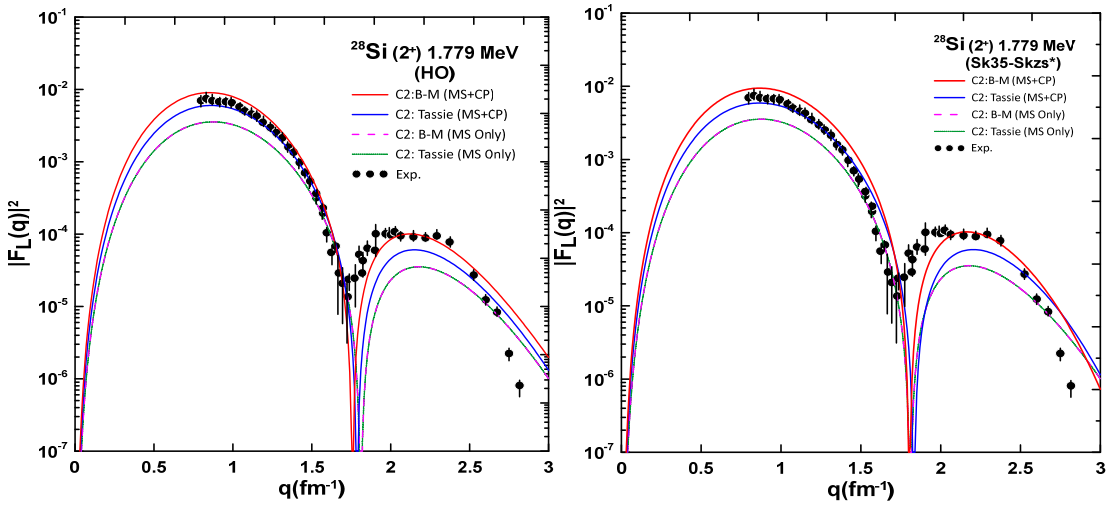

Figure 4. Longitudinal C2 form factors for the Tassie and Bohr-Mottelson models by using the Harmonic Oscillator potential (HO) and Skyrme effective interaction (Sk35−Skzs*) in comparison to the measured data [25].

CONCLUSION

The longitudinal charge $|F_{ch}(q)|^2$ and $|F(C2,q)|^2$ form factors the nuclei (^{9}Be and ^{28}Si) in the *p*-and *sd*-shells by utilizing the shell model calculations by considering the major shells 1s, 1p, 2s–1d, 2p–1f, including a partially inert core using the model space *spsdpf* with *wbt* effective interaction using the code NushellX@MSU were conducted. The residual interactions used in the calculation of the form factors are harmonic oscillator (HO) and Skyrme effective interaction (Sk35−Skzs*) by employing Tassie and Bohr-Mottelson collective models. The result of the form factors with $(0+2)\hbar\omega$ shell is not able to reproduce the data for all momentum transfer regions for both nuclei under study. Introducing the effective charges in both Tassie and Bohr Mottelson to account for the core polarization effect makes a remarkable improvement especially for Bohr Mottelson calculations.

Acknowledgments

The author S.M. Obaid would like to thank Al-Mustaqbal University College for the financial help.

Conflicts of Interest. The Authors confirm that there are no conflicts of interest.

ORCID IDs

Sarah M. Obaid, https://orcid.org/0000-0001-7534-9125; **Shaimaa A. Abbas**, https://orcid.org/0000-0002-5580-233X
Aeshah Ali Hussein, https://orcid.org/0000-0002-2408-4347; **Noor Adil Mohammed**, https://orcid.org/0000-0002-3647-0384
Fouad A. Majeed, https://orcid.org/0000-0002-0701-9084

REFERENCES

[1] H. Sagawa, and K. Asahi, "N/Z dependence of core polarization charges and quadrupole moments of B isotopes," Phys. Rev. C, **63**(6), 064310, (2001). https://doi.org/10.1103/PhysRevC.63.064310
[2] S. Cohen, and D. Kurath, "Effective interactions for the 1p shell," Nucl. Phys. **73**(1), 1-24, (1965). https://doi.org/10.1016/0029-5582(65)90148-3
[3] R.A. Radhi, A.A. Abdullah, Z.A. Dakhil, and N.M. Adeeb, "Core-polarization effects on C2 form factors of *p*-shell nuclei," Nucl. Phys. A, **696**(3-4), 442-452 (2001). https://doi.org/10.1016/S0375-9474(01)01218-0
[4] R.A. Radhi, "Nuclear structure study with inelastic electron scattering from ^{27}Al," Nuclear Physics A, **707**(1-2), 56-64 (2002). https://doi.org/10.1016/S0375-9474(02)00794-7
[5] R.A. Radhi, "Core polarization effects on C4 form factors of sd-shell nuclei," Eur. Phys. J. A, 16(3), 381-385 (2003). https://doi.org/10.1140/epja/i2002-10065-1
[6] R.A. Radhi, and A. Bouchebak, "Microscopic calculations of C2 and C4 form factors in sd shell nuclei," Nucl. Phys. A, **716**, 87-99 (2003). https://doi.org/10.1016/S0375-9474(02)01335-0
[7] T. Heng, J.P. Vary, and P. Maris, "Ab initio no-core properties of ^{7}Li and ^{7}Be with the JISP16 and chiral NNLO$_{opt}$ interactions," Phys. Rev. C, **95**(1), 014306 (2017). https://doi.org/10.1103/PhysRevC.95.014306

[8] D.C. Zheng, J. Vary, and B.R. Barrett, "Large-space shell-model calculations for light nuclei," Phys. Rev. C, **50**(6), 2841 (1994). https://doi.org/10.1103/PhysRevC.50.2841
[9] D.C. Zheng, B.R. Barrett, J.P. Vary, W.C. Haxton, and C. Song, "Large-basis shell model studies of light nuclei with a multivalued G-matrix effective interaction," Phys. Rev C, **52**(5), 2488-2498 (1995). https://doi.org/10.1103/physrevc.52.2488
[10] P. Navratil, M.B. Thoresen, and R. Barrett, "Microscopic origins of effective charges in the shell model," Phys. Rev. C, **55**(2), R573-R576 (1997). https://doi.org/10.1103/PhysRevC.55.R573
[11] F.A. Majeed, "The effect of core polarization on longitudinal form factors in ^{10}B," Phys. Scr, **85**(6), 065201 (2012). https://doi.org/10.1088/0031-8949/85/06/065201
[12] F.A. Majeed, and F.M. Hussain, "The Role of the core polarization on C2 and C4 form factor", Rom. Jour. Phys, **59**(1-2), 95-105 (2014). https://rjp.nipne.ro/2014_59_1-2/RomJPhys.59.p95.pdf
[13] F.A. Majeed, S.M. Obaid, "Nuclear structure study of ^{22,} ^{24}Ne and ^{24}Mg nuclei," Rev. Mex. Fis. **65**(1-2), 159-167 (2019). https://www.scielo.org.mx/pdf/rmf/v65n2/0035-001X-rmf-65-02-159.pdf
[14] B.A. Brown, and W.D.M. Rae. "The Shell-Model Code NuShellX@MSU," Nucl. Data. Sheets, **120**, 115-118 (2014). https://doi.org/10.1016/j.nds.2014.07.022
[15] J. Friedrich, and P.-G. Reinhard, "Skyrme-force parametrization: Least-squares fit to nuclear ground-state properties," Phys. Rev. C, **33**, 335 (1986). https://doi.org/10.1103/PhysRevC.33.335
[16] R.A. Radhi, Z.A. Dakhil, and N.S. Manie, "Microscopic calculations of quadrupole moments in Li and B isotope," Euro. Phys. J. A, **50**(7), 1-9 (2014). https://doi.org/10.1140/epja/i2014-14115-9
[17] A. Bohr, and B.R. Mottelson, *Nuclear Structure*, vol. 2, (Benjamin, New York, 1975).
[18] B.A. Brown, R. Radhi, and B.H. Wildenthal, "Electric quadrupole and hexadecupole nuclear excitations from the perspectives of electron scattering and modern shell-model theory," Phys. Rep. **101**(5), 313-358 (1983). https://doi.org/10.1016/0370-1573(83)90001-7
[19] D.E.J. Skyrme, "The effective nuclear potential," Nucl. Phys. A, **9**(4), 615-634 (1958). https://doi.org/10.1016/0029-5582(58)90345-6
[20] E.K. Warburton, and B.A. Brown, "Effective interactions for the 0p1s0d nuclear shell-model space," Phys. Rev. C, **46**(3), 923-944 (1992). https://doi.org/10.1103/PhysRevC.46.923
[21] R.A. Radhi, N.M. Adeeb, and A.K. Hashim, "Electro excitations of ^{9}Be using large-basis shell model wavefunctions with higher energy configurations", J. Phys. G: Nucl. Part. Phys. **36**(10), 105102 (2009). https://doi.org/10.1088/0954-3899/36/10/105102
[22] J.P. Glickman, W. Bertozzi, T.N. Buti, S. Dixit, F.W. Hersman, C.E. Hyde-Wright, M.V. Hynes, et al, "Electron scattering from ^{9}Be," Phys. Rev. C, **43**(4), 1740-1757 (1990). https://doi.org/10.1103/PhysRevC.43.1740
[23] J.A. Jensen, R.Th. Preedeman and C. de Vries, "Nuclear charge radii of ^{12}C and ^{9}Be", Nucl. Phys. A, **188**(2), 337-352 (1972). https://doi.org/10.1016/0375-9474(72)90062-0
[24] N. Ensslin, W. Bertozzi, S. Kawalski, C.P. Sargent, W. Turchintz, C.F. Williamson, S.P. Fivozinsky, J.W. Lightbody, and S. Penner, "Electron scattering from excited states in ^{14}N and ^{9}Be," Phys. Rev. C, **9**(5), 1705-1717 (1974). https://doi.org/10.1103/PhysRevC.9.1705
[25] B. Pritychenko, M. Birch, B. Singh, and M. Horoi, "Tables of E2 transition probabilities from the first 2^+ states in even–even nuclei," At. Data Nucl. Tables, **107**, 1-139 (2016). https://arxiv.org/pdf/1312.5975.pdf

ДОСЛІДЖЕННЯ ОБОЛОНКОВОЇ МОДЕЛІ ДЕЯКИХ p-ТА sd-ОБОЛОНКОВИХ ЯДЕР З ГАРМОНІЧНИМ ОСЦИЛЯТОРОМ ТА SKYRME ВЗАЄМОДІЯМИ

Сара М. Обейд[a], Шайма А. Аббас[b], Айша Алі Хусейн[b], Нур Аділь Мохаммед[c], Фуад А. Маджід[d]
[a]Департамент інженерної медичної фізики та радіотерапії, Інженерно-технічний коледж Аль-Наджаф, Технічний університет Аль-Фурат Аль-Аусат, Аль-Наджаф, Ірак
[b]Департамент фізики, Освітній коледж чистої науки (Ібн-Альхайтам), Багдадський університет, Багдад, Ірак
[c]Міністерство освіти, Генеральний директорат освіти Rusafa3, Багдад, Ірак
[d]Департамент фізики, Освітній коледж чистих наук, Вавилонський університет, Вавилон, Ірак

У цьому дослідженні поздовжній заряд $|F_{ch}(q)|^2$ і $|F(C2,q)|^2$формфактори для ядер ^{9}Be і ^{28}Si, що лежать в *p* і *sd* оболонках, вивчаються за допомогою потенціалу гармонічного осцилятора (HO) та ефективна *Skyrme* взаємодії (Sk35−Skzs∗). C0 і C2 з факторів, розрахованих для основного стану 3/2-, 5/2- (2,429 MeB) і 7/2- (6,380 MeB) для ^{9}Be, водночас як основний стан 0+ і 2+ (1,779 MeB) для ядра ^{28}Si. Розрахунки мікроскопічних збурень, які передбачають проміжне збудження однієї частинки, однієї дірки з орбіт ядра та MS на всі верхні орбіти з збудженнями nħω, використовуються для створення ефективних зарядів, необхідних для врахування «ефекту поляризації ядра». Розрахунки моделі оболонки використовуються в розширеному просторі моделі для включення всіх орбіт 1s, 1p, 2s–1d, 2p 1f з усіканням (0 +2)ħω. Колективна модель Бора-Моттельсона та модель Тассі з правильно оціненими ефективними нейтронними та протонними зарядами враховуються для врахування ефекту внеску ядра. Оцінені форм-фактори порівнювали з наявними виміряними даними, і вони добре збігалися для більшості досліджуваних станів. Можна зробити висновок, що (0 +2)ħω скорочення є дуже хорошим вибором для вивчення поздовжніх форм-факторів.

- Вибір потенціалу гармонійного осцилятора (HO) та ефективної Skyrme взаємодії (Sk35−Skzs∗) є адекватним для оцінки форми поздовжніх формфакторів.
- Оцінка ефективних зарядів на основі мікроскопічних збурень, які включають проміжні одночастинкові, однодіркові збудження від орбіт ядра та MS до всіх верхніх орбіт зі збудженнями nħω, є адекватною.
- Скорочення (0 +2)ħω виявляється дуже успішним для виконання дослідження.

Ключові слова: *модель оболонки; форм-фактор заряду; поздовжні форм-фактори; гармонічний осцилятор; Skyrme взаємодії*

East European Journal of Physics. **2.** 98-106 (2023)
DOI:10.26565/2312-4334-2023-2-08 ISSN 2312-4334

DUAL SOLUTIONS OF HYBRID NANOFLUID FLOW OVER A CONE WITH THE INFLUENCE OF THERMAL RADIATION AND CHEMICAL REACTION AND ITS STABILITY ANALYSIS[†]

Debasish Dey[a,§], Rupjyoti Borah[a,*], Ashim Jyoti Baruah[b,‡]
[a]*Department of Mathematics, Dibrugarh University, Dibrugarh-786004, Assam, India*
[b]*Department of Mathematics, Namrup College, Dibrugarh-786623, Assam, India*
[§]*E-mail: debasishdey1@dibru.ac.in;*[‡]*e-mail: ashimjyotibaruah1@gmail.com*
**Corresponding Author e-mail: rs_rupjyotiborah@dibru.ac.in*
Received March 3, 2023; revised March 17, 2023; accepted March 20, 2023

The main intention of this study is to differentiate the stable and realisable solutions between the dual solutions of the water-based hybrid nanofluid flow driven by a solid cone along with energy transfer in the form of heat and mass by employing a new approach called stability analysis. The deviation of thermal radiation, chemical responses and heat absorption/generation are reserved into account. The leading equations which support the mathematical representation of this study are renovated by utilizing a set of similarity variables and solved by the MATLAB built-in bvp4c solver scheme. The outcomes of this study are presented both graphically and numerically. From this study, two kind of flow solutions have been achieved where one of them is related to the time-independent solutions and stable in nature. Also, the speed of the hybrid nanofluid can be controlled by applying magnetic field, but we should keep in mind that excessive amount of magnetic parameter may damage the system by burning.
Keywords: *Hybrid nanofluid; Solid cone; Thermal radiation; Chemical reaction; Dual solutions; Stability Analysis*
PACS: 44.10.+i; 44.30.+v; 44.40.+a; 44.20.+b; 47.11.+j

INTRODUCTION

In recent times, physics of nanofluid flow has achieved important significance due to their various significance in diverse areas such as medicine, electronics and heat transfer devices etc. Nanofluids have better performance in different thermo-physical properties compared to the base fluids like water and oil etc. The mixture of nanoparticles with base fluids are termed as "Nanofluid" which was first coined by Choi [1].

The nanoparticles with different oxidation stages such as metallic or non-metallic particles like Cu, Al, Ag, Fe, Al_2O_3 and CuO etc that are typically used in a base fluid like water, ethylene glycol, Kerosene and different bio-fluids to form nanofluids. Due to the vast applications of nanofluids, researchers have motivated to study the importance of nanofluids and interpreted different kind of results associated with nanofluids and their properties. Recently, Mishra *et al.* [2] have investigated the water based nanofluid containing Ag-nanoparticle under different slip effects. Chanie *et al.* [3] have explored the flow behaviour of water-based nanofluid containing Cu and Ag particles and found that the motion of the fluid containing Cu is more effective than the $Ag - H_2O$.

Hybrid nanofluids are new kind of fluids that are made up of two or more different nanoparticles with traditional base fluids. This kind of fluid has advance features than the general nanofluids. An individual matter can never has all the required characteristic that is the material may be omitted or deficient some properties. The hybrid nanoparticles can be customized in such a way that it can process better significant than the other nanofluids. $Al_2O_3 + Cu$, $Al_2O_3 + Ni, MgO + Fe\&Al_2O_3 + SiO_2$ etc are some examples of hybrid nanomaterials. Turcu *et al.* [4] and Jana *et al.* [5] were the foremost authors who have studied hybrid nanofluid experimentally. They have examined that the rate of heat transfer of the hybrid nanofluids is noticeably superior than the general nanofluids. This kind of fluids have better significant thermo-physical properties than the nanofluids.

In this study, we have investigated the water-based hybrid nanofluid containing Cu and Al_2O_3 nanoparticles by considering a solid cone with the influence of both thermal and mass transmissions. This type of hybrid nanoparticles is used for oxygen storage, production and many other industrial applications [6]. There are many applications of fluid flow due to a solid cone in different industrial and engineering sciences such as the solder tip, the conical heater and the continuous variable transmission (CVT) in modern car [7]. Recently, many authors [2,7,8,9,10,11] have investigated the nanofluid and hybrid nanofluid flow caused due to a solid cone and given different importance outcomes and characteristics of cone.

Different physical areas recognise the importance of the synchronised effects of heat and mass transmissions on the flow of magnetised fluid under various flow geometries. Many industrial and engineering processes such as annealing and thickening of copper wire, paper production, MHD pump and MHD generators etc need both heat and mass transfers phenomenon with magnetic field effects. Dey and Borah [12] and Dey *et al.* [13,14 15] have investigated the boundary-layer fluid flow under the influence of both heat and mass transfers by considering different geometries. Alzahrani *et al.* [16] have examined the flow behaviour of hybrid nanofluid over a flat plate with the effects of both heat and mass transfers. Devi and Anjali Devi [17] and Khashi'ie *et al.* [18] have looked towards improving thermal transmission of $Cu - Al_2O_3$ hybrid nanofluid flow over a extending surface. Researchers [2,7,19] have investigated the hybrid nanofluid flow due to a solid and

[†] ***Cite as:*** D. Dey, R. Borah, and A.J. Baruah, East Eur. J. Phys. **2**, 98 (2023), https://doi.org/10.26565/2312-4334-2023-2-08

rotating cone under different flow factors such as heat and mass transfers etc. Abdullah *et al.* [20] have analysed the convective heat transfer characteristics of hybrid nanofluid driven by square enclosure.

Also, the thermal radiation and chemical reaction effects on the fluid flow problems have played an important role in different physical fields. From the several decades, many researchers have given attention on these two flow factors as because of their multifarious application in different industrial, engineering and medical applications. Chamkha *et al.* [21] have examined the effects of radiation on mixed convection fluid flow by suspending nanoparticles. Sulochana *et al.* [22] have explored the influence of both thermal radiation and chemical reaction on magnetohydrodynamics nanofluid flow due to moving surface. Recently, Sharma *et al.* [23] have explored the effects of radiation parameter on the hybrid nanofluid flow over an extending surface with Joule heating. Dey *et al.* [24] have analyzed the stability analysis of magnetized fluid flow with the effects of chemical reaction. Saleem *et al*. [25] have investigated the MHD nanofluid flow over a rotating cone under the influence thermal radiation.

Due to the lack of information about the smoothness of the surface of the considering geometry and mathematical tools with assumptions, some initial complexity in the flow is observed which may develop non-uniqueness flow solutions. This initial complexity in the flow classifies the flow solutions into two categories, one solution is stable and physically tractable. Markin [26] was the first author who has explored the idea of dual solutions and their stability. Recently, Ghosh and Mukhopadhyay [27], Dey and Borah [12], Dey *et al.* [14], Dey *et al.* [24], Waini *et al.* [28] and Dey *et al.* [29] have explored the nature of non-uniqueness solutions and their stability behaviour by considering different fluids model.

The present work is all inspired by the above literatures and its immense relevance in different physical fields. We were able to ascertain via the literature review that this study has novelty like effects of thermal radiation, considering nanoparticles to form hybrid nanofluid, dual solutions and its stability analysis and will have a significant influence on other experts in the field. To the authors' awareness, this type of fluid model obtained by inserting the nanoparticles $Cu + Al_2O_3$ with water which is driven by a solid cone along with energy transfers has not yet been taken into account while analysing dual solutions and their stability.

The intention of this work is to analyze the dual solutions and their stability of the water-based hybrid nanofluid driven by a solid cone which is sited in a porous medium under the influence of thermal radiation and chemical reaction with different slip flow effects such as velocity, thermal and concentration slips. Here, we have initially suspended the Cu solid nanoparticle of volume fraction $\phi_2 = 0.06$ into the water base fluid to form $Cu/water$ nanofluid. Again, Al_2O_3 solid nanoparticle of volume fraction $\phi_1 = 0.1$ is added into $Cu/water$ nanofluid and achieved the $Al_2O_3 - Cu/water$ hybrid nanofluid. Also, a harmonized magnetic field is applied in the normal direction of the conical surface which plays an important role to enhance the thermal properties of the fluid. The leading equations which support the mathematical model of this problem are renovated by utilizing a set of similarity variables and solved by the MATLAB built-in bvp4c solver technique. Stability analysis is executed between the flow solutions to characterise the stable and physically achievable solution. Also, for the verification of our numerical codes, we established a reasonable uniformity when we compared our findings to the previously published article Mishra *et al.* [2].

FORMULATION OF THE PROBLEM

We have constructed a mathematical model of this study by considering a permeable cone of radius $r(x)$ which is immersed in a steady, incompressible and two-dimensional hybrid nanofluid. The flow diagram and its coordinate system are shown in Fig. 1. Where, the x- axis is measured along the surface of the cone and y- axis is taken in the normal direction of the conical surface such that vertex of the cone is taken as the origin of the system. In this study, we have considered the influence of both heat and mass transfers such that T_w and C_w prescribe the constant wall temperature and concentration respectively and T_∞&C_∞ the temperature and concentration at free stream region. A uniform magnetic field of strength B_0 is applied in the normal direction of the conical surface. Here, we have considered the hybrid nanofluid which is formed by adding Al_2O_3 nanoparticles into the Cu/H_2O nanofluid and hence $Al_2O_3 - Cu/H_2O$ hybrid nanofluid is found. Table 1 discusses the thermo-physical characteristics of the base fluid and solid particles.

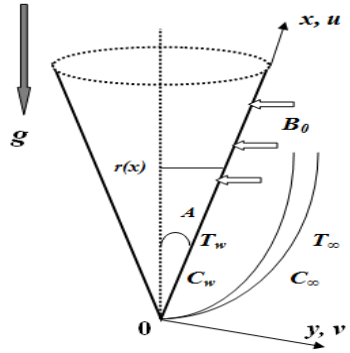

Figure 1. Flow diagram and its coordinate system.

Table 1. Thermo-physical properties of base fluid and solid particles (Mohmed *et al*. [7]).

Property	H_2O	Cu	Al_2O_3
$\rho\ (Kg\cdot m^{-3})$	997.1	8933	3970
$C_p\ [J(Kg\cdot K)^{-1}]$	4179	385	765
$k\ [W(mK)^{-1}]$	0.613	400	40
$\sigma\ (Sm^{-1})$	5.5×10^{-6}	59.6×10^{6}	35×10^{6}

Under the aforesaid assumptions and boundary-layer approximations, we have considered the following leading equations which govern the present problem ([7] and [2]).

$$\frac{\partial(ru)}{\partial x}+\frac{\partial(rv)}{\partial y}=0, \tag{1}$$

$$u\frac{\partial u}{\partial x}+v\frac{\partial u}{\partial y}=\nu_{hnf}\frac{\partial^2 u}{\partial y^2}+g\beta(T-T_\infty)CosA-g\beta^*(C-C_\infty)CosA-\frac{\mu_{hnf}}{\rho_{hnf}}\frac{1}{k_p}u-\frac{\sigma_{hnf}}{\rho_{hnf}}B_0^2u=0, \tag{2}$$

$$u\frac{\partial T}{\partial x}+v\frac{\partial T}{\partial y}=\frac{k_{hnf}}{(\rho C_P)_{hnf}}\frac{\partial^2 T}{\partial y^2}+\frac{\mu_{hnf}}{(\rho C_P)_{hnf}}\left(\frac{\partial u}{\partial y}\right)^2+\frac{Q_0}{(\rho C_P)_{hnf}}(T-T_\infty)+\frac{\sigma_{hnf}}{(\rho C_P)_{hnf}}B_0^2u^2-\frac{1}{(\rho C_P)_{hnf}}\frac{\partial q_r}{\partial y}, \tag{3}$$

$$u\frac{\partial C}{\partial x}+v\frac{\partial C}{\partial y}=D_m\frac{\partial^2 C}{\partial y^2}-Kr(C-C_\infty). \tag{4}$$

Here, we have initially suspended the Cu solid nanoparticle of volume fraction $\phi_2=0.06$ into the water base fluid to form Cu/H_2O nanofluid. Again, Al_2O_3 solid nanoparticle of volume fraction $\phi_1=0.1$ is added into Cu/H_2O nanofluid and achieved the Al_2O_3-Cu/H_2O hybrid nanofluid. The properties of hybrid nanofluidis given below such that the base fluid and the nanoparticles are denoted with the subscript $f, s_1 \& s_2$ [7].

$$\mu_{hnf}=\frac{\mu_f}{(1-\phi_1)^{2.5}(1-\phi_2)^{2.5}},\rho_{hnf}=(1-\phi_2)\left[(1-\phi_1)\rho_f+\phi_1\rho_{s_1}\right]+\phi_2\rho_{s_2},$$

$$(\rho C_P)_{hnf}=(1-\phi_2)\left[(1-\phi_1)(\rho C_P)_f+\phi_1(\rho C_P)_{s_1}\right]+\phi_2(\rho C_P)_{s_2},$$

$$\frac{k_{hnf}}{k_{bf}}=\frac{\left(k_{s_2}+2k_{bf}-2\phi_2\left(k_{bf}-k_{s_2}\right)\right)}{\left(k_{s_2}+2k_{bf}+\phi_2\left(k_{bf}-k_{s_2}\right)\right)},\frac{k_{bf}}{k_f}=\frac{\left(k_{s_1}+2k_f-2\phi_1\left(k_f-k_{s_1}\right)\right)}{\left(k_{s_1}+2k_f+\phi_1\left(k_f-k_{s_1}\right)\right)},$$

$$\frac{\sigma_{hnf}}{\sigma_{bf}}=1+\frac{3\left(\frac{\sigma_{s_2}}{\sigma_{bf}}-1\right)\phi_2}{\left(\frac{\sigma_{s_2}}{\sigma_{bf}}+2\right)-\left(\frac{\sigma_{s_2}}{\sigma_{bf}}-1\right)\phi_2},\frac{\sigma_{bf}}{\sigma_f}=1+\frac{3\left(\frac{\sigma_{s_1}}{\sigma_f}-1\right)\phi_1}{\left(\frac{\sigma_{s_1}}{\sigma_f}+2\right)-\left(\frac{\sigma_{s_1}}{\sigma_f}-1\right)\phi_1}.$$

The related boundary conditions are:

$$y=0: u=u_w+l_1\frac{\partial u}{\partial x}, v=v_w, T=T_w+l_2\frac{\partial T}{\partial y}, C=C_w+l_3\frac{\partial C}{\partial y}, \tag{5}$$

$$y\to\infty: u\to 0, T\to T_\infty, C\to C_\infty.$$

Where, $l_1, l_2 \& l_3$ are the slip factors and vanishing of $l_1, l_2 \& l_3$ implies the no slip flow in the system. To alter the nature of equations (1)-(4), we have adopted the following set of variables [2].

$$\eta=\sqrt{a/\upsilon_f}\,y,\psi=\sqrt{a\upsilon_f}\,xrf(\eta),r=x\sin A,\theta(\eta)=\frac{T-T_\infty}{T_w-T_\infty},\phi(\eta)=\frac{C-C_\infty}{C_w-C_\infty},$$
$$u=\frac{1}{r}\frac{\partial\psi}{\partial y}=axf'(\eta),v=-\frac{1}{r}\frac{\partial\psi}{\partial x}=-2\sqrt{a\upsilon_f}\,f(\eta). \tag{6}$$

From the Roseland approximation (following Prameela *et al.* [30]), the local radiative heat flux term for optically thick gray fluid is given by

$$q_r=-\frac{4\sigma_0}{3k_2}\frac{\partial T^4}{\partial y}\approx-\frac{16\sigma_0T_\infty^3}{3k_2}\frac{\partial T}{\partial y}, \tag{7}$$

where $T^4\approx 4T_\infty^3T-3T_\infty^4$ (by Taylor series approximation). As a result,

$$\frac{\partial q_r}{\partial y}\approx-\frac{16\sigma_0T_\infty^3}{3k_2}\frac{\partial^2 T}{\partial y^2}. \tag{8}$$

After utilizing the equations (6) and (8) into the equations (1)-(4), we have achieved the following set of equations and the equation (1) which represents the conservation of mass identically satisfies the similarity variables (6).

$$A_1f'''+Gr\theta-Gm\phi-A_1k_1f'-A_2A_3Mf'-f'^2+2ff''=0, \tag{9}$$

$$A_4\frac{1}{\Pr}(1+Nr)\theta''+A_5Ecf''^2+A_6Q\theta+A_7MEcf'^2+2f\theta'=0, \tag{10}$$

$$\phi''+Scf\phi'-ScCr\phi=0. \tag{11}$$

The boundary restrictions become in the following form:

$$f(0)=S, f'(0)=1+L_vf''(0), \theta(0)=1+L_T\theta'(0), \phi(0)=1+L_m\phi'(0), \tag{12}$$

$$f'(\infty)\to 0, \theta(\infty)\to 0, \phi(\infty)\to 0.$$

Where, $A_i(i=1,2,3,4,5,6,7)$'s are defined in the following way:

$$A_1=\frac{\upsilon_{hnf}}{\upsilon_f}, A_2=\frac{\sigma_{hnf}}{\sigma_f}, A_3=\frac{\rho_f}{\rho_{hnf}}, A_4=\frac{k_{hnf}/k_f}{(\rho C_P)_{hnf}/(\rho C_P)_f}, A_5=\frac{\mu_{hnf}/\mu_f}{(\rho C_P)_{hnf}/(\rho C_P)_f},$$

$$A_6=(\rho C_P)_f/(\rho C_P)_{hnf}, A_7=\frac{\sigma_{hnf}/\sigma_f}{(\rho C_P)_{hnf}/(\rho C_P)_f}.$$

The dimensionless parameters are:

$$Gr=\frac{g\beta(T_w-T_\infty)}{a^2x}, Gm=\frac{g\beta^*(C_w-C_\infty)}{a^2x}, k_1=\frac{\upsilon_f}{ka}, M=\frac{\sigma_fB_0^{\,2}}{\rho_fa}, \Pr=\frac{(\rho C_P)_f\upsilon_f}{k_f}, Q=\frac{Q_0}{a(\rho C_P)_f},$$

$$Ec=\frac{(ax)^2\rho_f}{(\rho C_P)_f(T_w-T_\infty)}, Nr=\frac{16\sigma_0T_\infty^{\,3}}{3k_2k_f}, Sc=\frac{\upsilon_f}{D_m}, Cr=\frac{k_r}{a}, L_v=\frac{l_1}{\sqrt{\upsilon_f/a}}, L_T=\frac{l_2}{\sqrt{\upsilon_f/a}}, L_m=\frac{l_3}{\sqrt{\upsilon_f/a}}.$$

During this study, we have observed three types of physical quantities which play an important role in different physical fields by computing shear stress, rate of heat transfer and rate of mass development at the surface. These physical quantities are defined in the following way [2], [7]:

$$C_f=2\frac{\mu_{hnf}}{\rho_fU_w^2}\left(\frac{\partial u}{\partial y}\right)_{y=0}, Nu_x=-\frac{xk_{hnf}}{k_f(T_w-T_\infty)}\left(\frac{\partial T}{\partial y}\right)_{y=0}, Sh_x=-\frac{x}{(C_w-C_\infty)}\left(\frac{\partial C}{\partial y}\right)_{y=0}. \tag{13}$$

Now, using the equation (6) into the equation (13), we have achieved the following normalize form of the above quantities as:

$$C_f=2\frac{\mu_{hnf}}{\mu_f}\left(\mathrm{Re}_x\right)^{-\frac{1}{2}}f''(0), Nu_x=-\frac{k_{hnf}}{k_f}\left(\mathrm{Re}_x\right)^{\frac{1}{2}}\theta'(0), Sh_x=-\left(\mathrm{Re}_x\right)^{\frac{1}{2}}\phi'(0), \tag{14}$$

where, the local Reynolds number, $Re_x=\frac{xU_w}{\nu_f}$.

FLOW STABILITY

Due to the considering geometry and lack of mathematical tools and assumptions, some initial disturbances in the flow have been occurred which are decay or growth with time. These disturbances classify the flow solutions into two categories, one of them converges to its time-independent flow solutions as the initial complexity in the flow decay with time. The flow stability is needed to characterize the stable and unstable solutions between the dual solutions. To implement the stability analysis of this problem, the unsteady governing equations are essential which are obtained by adding the terms $\frac{\partial u}{\partial t}, \frac{\partial T}{\partial t}$ & $\frac{\partial C}{\partial t}$ into the equations (2), (3) & (4) respectively. Due to the presence of time variable, equation (6) takes a modified form as given below:

$$\eta=\sqrt{\frac{a}{\nu_f}}y, \psi=\sqrt{a\nu_f}xrf(\eta,\tau), r=xsinA, \theta(\eta,\tau)=\frac{T-T_\infty}{T_w-T_\infty}, \phi(\eta,\tau)=\frac{C-C_\infty}{C_w-C_\infty}, \tau=at \tag{15}$$

The time-dependent governing equations after using equation (15) become:

$$A_1\frac{\partial^3f}{\partial\eta^3}+Gr\theta-Gm\phi-A_1k_1\frac{\partial f}{\partial\eta}-A_2A_3M\frac{\partial f}{\partial\eta}-\left(\frac{\partial f}{\partial\eta}\right)^2+2f\frac{\partial^2f}{\partial\eta^2}-\frac{\partial^2f}{\partial\eta\partial\tau}=0, \tag{16}$$

$$\frac{A_4}{Pr}(1+Nr)\frac{\partial^2\theta}{\partial\eta^2}+A_5Ec\left(\frac{\partial^2f}{\partial\eta^2}\right)^2+A_6Q\theta+A_7MEc\left(\frac{\partial f}{\partial\eta}\right)^2+2f\frac{\partial\theta}{\partial\eta}-\frac{\partial\theta}{\partial\tau}=0, \tag{17}$$

$$\frac{\partial^2\phi}{\partial\eta^2}+Scf\frac{\partial\phi}{\partial\eta}-ScCr\phi-Sc\frac{\partial\phi}{\partial\tau}=0. \tag{18}$$

The surface restrictions become:

$$f(0,\tau)=S, \frac{\partial f(0,\tau)}{\partial\eta}=1+L_v\frac{\partial^2f(0,\tau)}{\partial\eta^2}, \frac{\partial f(\infty,\tau)}{\partial\eta}\to 0,$$

$$\theta(0,\tau) = 1 + L_T \frac{\partial\theta(0,\tau)}{\partial\eta}, \theta(\infty,\tau) \to 0, \tag{19}$$

$$\phi(0,\tau) = 1 + L_m \frac{\partial\phi(0,\tau)}{\partial\eta}, \phi(\infty,\tau) \to 0.$$

To test the stability of the steady flow solution $f(\eta) = f_0, \theta(\eta) = \theta_0$ and $\phi(\eta) = \phi_0$ fulfilling the equations (9)-(11), a set of perturb equations is employed for differentiating the variables ([26], [12] and [14, 24]):

$$\begin{aligned} f(\eta) &= f_0(\eta) + e^{-\omega\tau}F(\eta), \\ \theta(\eta) &= \theta_0(\eta) + e^{-\omega\tau}G(\eta), \\ \phi(\eta) &= \phi_0(\eta) + e^{-\omega\tau}H(\eta). \end{aligned} \tag{20}$$

Where, ω is an unknown eigenvalue parameter, $F, G\&H$ the small associated to time-independent solutions. Inserting equation (20) into the equations (16)-(18), fixing $\tau \to 0$ and simplifying the equations, we have achieved the following linearized eigenvalue problems.

$$A_1F''' + GrG - GmH - A_1k_1F' - A_2A_3MF' - 2f_0'F' + 2(f_0F'' + Ff_0'') + \omega F' = 0, \tag{21}$$

$$\frac{A_4}{Pr}(1+Nr)G'' + 2A_5Ecf_0''F'' + A_6QG + 2A_7MEcf_0'F' + 2(f_0G' + F\theta_0') + \omega G = 0, \tag{22}$$

$$H'' + Sc(f_0H' + F\phi_0') - ScCrH + Sc\omega H = 0. \tag{23}$$

Relevant boundary conditions are:

$$\begin{aligned} F(0) = 0, F'(0) = 0, G(0) = 0, H(0) = 0, \\ F'(\infty) \to 0, G(\infty) \to 0, H(\infty) \to 0. \end{aligned} \tag{24}$$

Following Mishra *et al.* [31] and Dey and Borah [12], the equations (21)-(23) are solved together with adjusted boundary conditions (referring Wahid *et al.* [28] and Dey and Borah [32]). It is noticed that this eigenvalue problem gives an infinite number of eigenvalues $\omega_1 < \omega_2 < \omega_3 < \cdots$, where ω_1 signifies the smallest eigenvalue. The flow stability can be examined with the help of this smallest eigenvalue. If $\omega_1 > 0$, then the initial complexity in the flow decay with time and the flow solution becomes stable. Otherwise, the flow solution to be unstable due to the escalation of complexity in the flow with time.

RESULT AND DISCUSSION

The set of equations (9)-(11) and (21)-(23) along with their two-point boundary conditions have been solved numerically by utilizing the MATLAB built-in bvp4c solver scheme. This technique performs the three-stage Lobatto IIIa formula and executes the finite difference method. It controls and adjusts the error upto 10^{-6} by its residuals.

The numerical explanations of this study have been achieved for the velocity $f'(\eta)$, thermal fraction$\theta(\eta)$and mass fraction $\phi(\eta)$ profiles of the hybrid nanofluid as an outcomes of different novel flow parameters and have been displayed in figures (2)-(9). In this problem, we have achieved two types of solutions, first solution is represented by the solid line and it is related to the time-independent solution. The dashed line signifies the second solution which is converged slowly to its free stream region due to the presence of flow disturbance.

Before conferring the numerical results, we afford confirmation of our numerical code by solving the model presented in [2] and comparing the present numerical results (first solution) with the results reported in [2]. Mishra *et al.* [2] have analysed the water based nanofluid flow containing the Ag nanoparticle over a solid cone with the influence of heat and mass transfers. In the non-appearance of thermal radiation and hybrid nanofluid, our leading equations during steady case of this study are matched with Mishra *et al.* [2] works. Table 2 reflects the comparison of the numerical code in terms of local Nusselt number and gives a good conformity for our results.

Table 3 is developed to check the flow stability between the dual solutions with the help of evaluated smallest eigenvalues for different values of suction parameter (S). From this table, it is noticed that the smallest eigenvalues are positive and negative for first solution and second solution respectively. Due to the positive values of least eigenvalues, the initial disturbances in the flow lie down as time evolves and the flow solution converges quickly to its time-independent solution. Hence, the first solution becomes stable and physically achievable. But, negative values of least eigenvalues develop the initial disturbances in the flow and hence the flow solution (second solution) is being as unstable behaviour and slowly converges to its free stream region.

Table 4 is inserted to show the skin friction coefficient numerically during time-dependent and time-independent cases for developing values of the Prandtl, Schmidt and Eckert numbers. These quantities help to evaluate the effects of shear stress at the surface of the cone. It appears from this data that the skin friction coefficient has been experienced a reduction from the noble gas ($Pr = 0.015$) to sea-water ($Pr = 13.5$). Again, the effects of shear stress at the surface have been enhanced from the hydrogen ($Sc = 0.22$) to water vapour ($Sc = 0.60$). It is also seen from this table is that increasing values of the Eckert number (Ec) raises the influence of shear stress during both the solutions at the surface

of the cone. It is also observed that the effects of shear stress of the fluid at the surface of the cone during time-dependent case (second solution) is fewer than the first solution. Table 5 is inserted to show the heat transfer rate of the fluid at the surface of the cone for developing values of Prandtl and Eckert numbers. From this table, it is achieved that the Prandtl number develops the rate of heat transfer of the fluid during both the cases. But the Eckert number reduces the rate of heat transfer at the surface of the cone.

Table 2. Numerical presentation of Nusselt number $\left(-\theta'(0)\right)$ of Ag/H_2O nanofluid for different values of M when $Pr = 0.7, Sc = 1,\ L_v = 0.1, L_T = 0.1, L_m = 0.1, Ec = 0.05, Q = 0.1, S = 0.4, \phi_1 = 0.1, Gr = Gm = 0.1, k_1 = 0.5, Nr = 0.$

	Mishra *et al*. [2] works	Present Results
M	$-\theta'(0)$	$-\theta'(0)$
0.5	2.279557	2.265545
0.7	2.259399	2.251232
1	2.231499	2.221432

Table 3. Numerical presentation of smallest eigenvalue for different values of S when $M = 0.5, Gr = 1, Gm = 2, Q = 0.1, Nr = 0.2, k_1 = 0.5, L_v = 0.2, L_T = 0.1, L_m = 0.2, Sc = 0.22, Pr = 0.71, Ec = 0.3.$

	Smallest Eigenvalue (ω_1)	
S	**First Solution**	**Second Solution**
0.25	0.20209420	-1.220506212
0.63	1.20955422	-3.02148542
0.82	2.26992567	-4.00797213

Table 4. Numerical presentation of skin friction coefficient for different values of $Pr, Sc\&Ec$ when $M = 0.5, Gr = 1, Gm = 2, Q = 0.1, Nr = 0.2, k_1 = 0.5, L_v = 0.2, L_T = 0.1, L_m = 0.2.$

Pr	Sc	Ec	Skin friction coefficient (C_f)	
			First Solution	**Second Solution**
0.015	0.22	0.005	-1.88491462	-2.35204790
7			-1.91532212	-2.41139078
13.5			-1.92660748	-2.40977806
0.71	0.22		-1.88406043	-2.35823329
	0.30		-1.88286201	-2.35613715
	0.60		-1.87858313	-2.34883267
	0.22	0.0	-1.88408938	-2.35828831
		0.3	-1.88235554	-2.35499662
		1	-1.87833480	-2.34738988

Table 5. Numerical presentation of local Nusselt number for different values of $Pr\&Ec$ when $M = 0.5, Gr = 1, Gm = 2, Q = 0.1, Nr = 0.2, k_1 = 0.5, L_v = 0.2, L_T = 0.1, L_m = 0.2, Sc = 0.22.$

Pr	Ec	Local Nusselt Number (Nu_x)	
		First Solution	**Second Solution**
0.015	0.005	0.24259499	0.264506742
7		1.26955410	3.12148393
13.5		2.29992551	4.32797261
0.71	0.0	0.18628192	0.35992906
	0.3	0.07307090	0.11873327
	1.0	-0.18963456	-0.43981793

The effect of M on the hybrid nanofluid's velocity and thermal fraction is shown in Figs. (2) and (3).

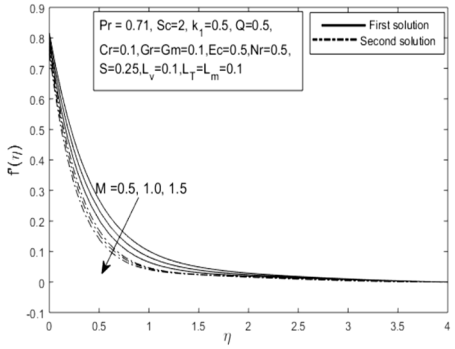

Figure 2. Velocity profile for incremental amount of M

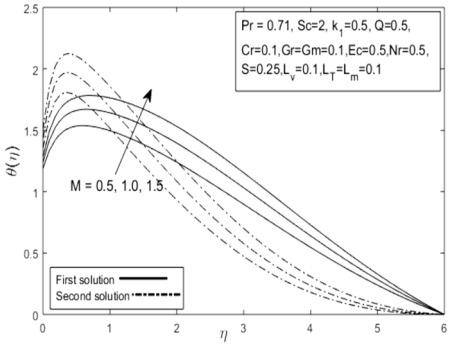

Figure 3. Sketch of thermal fraction for incremental amount of M

From these figures, it is believed that the hybrid nanofluid's velocity has been decelerated with the increasing amount of Mduring both the cases, whereas the thermal fraction of the fluid has been developed with M. A resistive type force known as the "Lorentz force" is produced as a result of the application of a magnetic field and has the power to control fluid motion. As a result, the hybrid nanofluid's velocity is decreased with increased values of M. Again, due to the effects of magnetic field, the velocity of the fluid has been decelerated and a frictional force is developed between the fluid and surface of the cone which generates additional energy in terms of heat at the surface of the cone and hence the thermal fraction of the hybrid nanofluid is enhanced with$M$. From Figure (2), it appears that the hybrid nanofluid moves more slowly in the time-dependent (second solution) situation than in the time-independent (first solution) case. Due to this reason, fluid's temperature during second solution superiors than the first solution in the vicinity of the surface of the cone. Figures (4)-(6) are depicted to show the effects of porosity of the porous medium on the velocity, thermal fraction and mass fraction of the hybrid nanofluid.

From Figure (4), it is noticed that the speed of the fluid has been enhanced with the increasing values of k_1 during both the cases. As a result, the overall pressure of the hybrid nanofluid reduces and the thermal fraction and mass fraction of the fluid are directly proportional to the pressure and hence the thermal fraction and mass fraction are experienced reduction with k_1 (see Fig. 5 and Fig. 6). Also, the second solution of the velocity distribution and mass fraction of the fluid are comparatively fewer than the first solution.

Figure (7) shows how Nr affects the thermal fraction of the hybrid nanofluid. It can be seen from this figure that when Nr increases, the thermal portion of the hybrid nanofluid decreases in both cases.

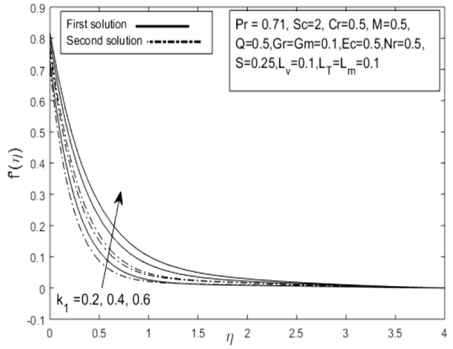

Figure 4. Velocity profile for incremental amount of k_1

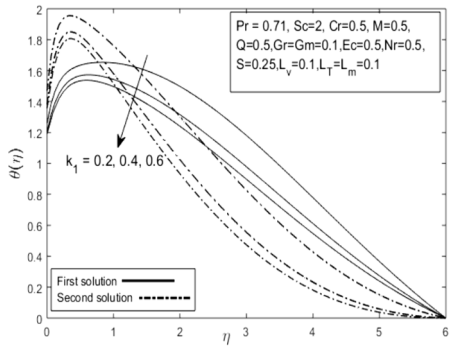

Figure 5. Sketch of thermal fraction for incremental amount of k_1

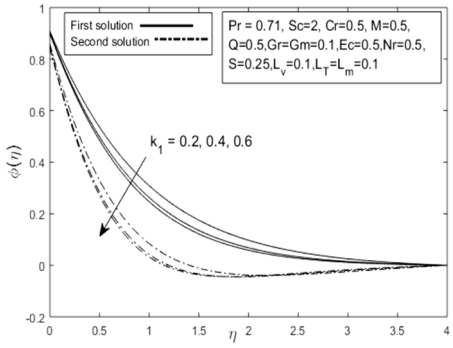

Figure 6. Sketch of mass fraction for incremental amount of k_1

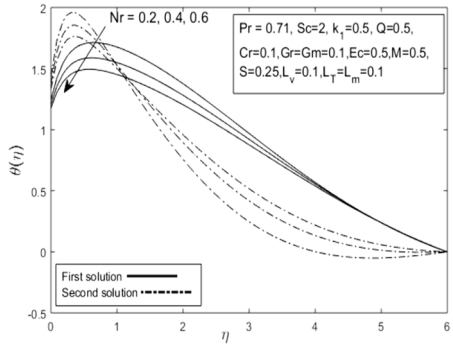

Figure 7. Sketch of thermal fraction for incremental amount of Nr

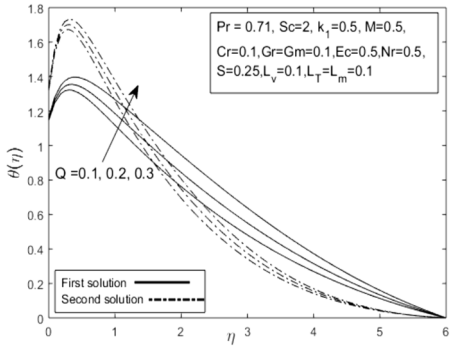

Figure 8. Sketch of thermal fraction for incremental amount of Q

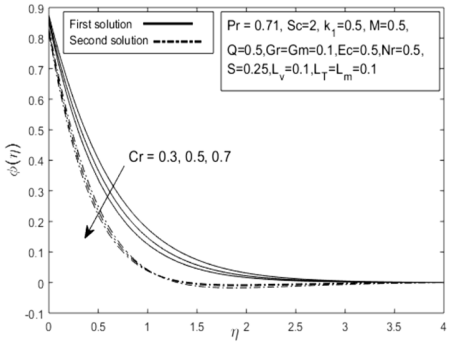

Figure 9. Sketch of mass fraction for incremental amount of Cr.

The cause of this occurrence is that the thermal radiation parameter (Nr) is directly proportional to the third power of the temperature of fluid at free stream region. Therefore, as Nr increases, the hybrid nanofluid's thermal fraction over the cone decreases. Also, it is seen that the thermal fraction of the fluid during the second solution is larger than the first

solution near the surface of the cone. Figure (8) reflects the impact of heat generation parameter (Q) on the thermal fraction of the fluid. From this figure, it is perceived that the thermal fraction of the hybrid nanofluid has been increased with Q. Influence of Cr on the mass fraction of the hybrid nanofluid is presented in Fig. 9. The chemical reaction is occurred mainly due to the effects of suction/injection of the fluid flow and presence of flow slips effects. The chemical reaction parameter has the capacity to fall down the mass fraction of the considering fluid. It can also be observed that the concentration level of the hybrid nanofluid during the second solution is fewer and slowly conversed to its free stream region over the first solution.

We have found from this study that all flow profiles display dual solutions up to a specific area of the similarity variable (η) and asymptotically meet the far-field boundary conditions.

CONCLUSION

This paper analyzes $Cu - Al_2O_3$/water hybrid nanofluid flow driven by a solid cone which sited in a porous medium. The energy transfer in terms of heat and mass is encountered with the effects of magnetic field, thermal radiation and chemical reaction. The leading equations are solved through numerical method called "three-stage Lobatto IIIa formula" by using MATLAB built in bvp4c solver scheme. Major results have been obtained as follows:

1) The velocity of the hybrid nanofluid has been decelerated with the improving amount of M, but it has enhanced the thermal fraction of the fluid during both the cases.
2) Due to the increasing amount of k_1, the velocity of the fluid has accelerated. Whereas, thermal and mass fractions of the hybrid nanofluid have been controlled by employing k_1.
3) Thermal fraction of the hybrid nanofluid flow is a decreasing function of the thermal radiation (Nr) and an increasing function of the heat generation (Q) parameters.
4) Mass fraction of the hybrid nanofluid during the second solution is fewer than the first solution with the increasing amount of Cr.
5) Effects of shear stress is dropped down for incremental values of the Prandtl number. But we should keep in mind that the excessive amount of the Prandtl number may damage the system by developing the rate of heat transfer at the surface of the cone.
6) "According to the stability point of view, the first solution, which converges to the steady flow solution more quickly, is stable, whereas the second solution is unstable and impractical.

ORCID IDs

Debasish Dey, https://orcid.org/0000-0003-4215-6735; **Rupjyoti Borah**, https://orcid.org/0000-0001-7765-7877
Ashim Jyoti Baruah, https://orcid.org/0009-0000-3107-2005

REFERENCES

[1] S.U.S. Choim, "Enhancing thermal conductivity of uids with nanoparticles," in *Proceedings of the 1995 ASME Int. Mech. Eng. Cong. and Exposition, (San Francisco, USA, ASME FED 231/MD*, 1995). pp. 99-105
[2] A. Mishra, A.K. Pandey, and M. Kumar, "Velocity, thermal and concentration slip effects on MHD silver-water nanofluid flow past a permeable cone with suction/injection and viscous-ohmic dissipation," Heat Trans. Res. **50**(14), 1351–1367 (2019). https://doi.org/10.1615/HeatTransRes.2018020420
[3] A.G. Chanie, B. Shankar, and M.M. Nandeppanavar, "MHD flow of nanofluids through a porous media due to a permeable stretching sheet," J. Nanofluids, **7**(3), 488–498 (2018). https://doi.org/10.1166/jon.2018.1480
[4] R. Turcu, Al. Darabont, A. Nan, N. Aldea, D. Macovei, D. Bica, L. Vekas, et al., "New polypyrrolemultiwall carbon nanotubes hybrid materials," J. Optoelectron. Adv. Mater. **8**(2), 643–647 (2006).
[5] S. Jana, A. Salehi-Khojin, and W.H. Zhong, "Enhancement of fluid thermal conductivity by the addition of single and hybrid nano-additives," Thermochim. Acta, **462**, 45–55 (2007). https://doi.org/10.1016/j.tca.2007.06.009
[6] W. Hu, F. Donat, S.A. Scott, and J.S. Dennis, "The interaction between CuO and Al2O3 and the reactivity of copper aluminates below 1000c and thier implication on the use of the Cu-Al-O system for oxygen storage and production," RSC Adv. **6**(114), 113016 (2016). https://doi.org/10.1039/C6RA22712K
[7] M.K.A. Mohamed, A. Ishak, I. Pop, N.F. Mohammad, and S.K. Soid, "Free Convection Boundary Layer Flow from a Vertical Truncated Cone in a Hybrid Nanofluid," Malaysian J. Fundam. Appl. Sci. **18**(2), 257–270 (2022). https://doi.org/10.11113/mjfas.v18n2.2410
[8] A. Khan, M. Ashraf, A.M. Rashad, and H.A. Nabwey, "Impact of heat generation on magneto-nanofluid free convection flow about sphere in the plume region," Mathematics, **8**(11), 1–18 (2020). https://doi.org/10.3390/math8112010
[9] V. Buddakkagari, and M. Kumar, "Transient Boundary Layer Laminar Free Convective Flow of a Nanofluid Over a Vertical Cone/Plate," Int. J. Appl. Comput. Math. **1**(3), 427–448 (2015). https://doi.org/10.1007/s40819-015-0027-9
[10] S.E. Ahmed, and A. Mahdy, "Natural Convection Flow and Heat Transfer Enhancement of a Nanofluid past a Truncated Cone with Magnetic Field Effect," World J. Mech. **02**(05), 272–279 (2012). http://dx.doi.org/10.4236/wjm.2012.25033
[11] O.P. Meena, P. Janapatla, and D. Srinivasacharya, "Mixed Convection Fluid Flow Over a Vertical Cone Saturated Porous Media with Double Dispersion and Injection/Suction Effects," Int. J. Appl. Comput. Math, **7**, 59 (2021). https://doi.org/10.1007/s40819-021-00990-y
[12] D. Dey, and R. Borah, "Dual Solutions of Boundary Layer Flow with Heat and Mass Transfers over An Exponentially Shrinking Cylinder: Stability Analysis," Lat. Am. Appl. Res. **50**(4), 247–253 (2020). https://doi.org/10.52292/j.laar.2020.535
[13] D. Dey, M. Hazarika, and R. Borah, "Entropy Generation Analysis of Magnetized Micropolar Fluid Streaming above An Exponentially Extending Plane," Lat. Am. Appl. Res. **51**(4), 255-260 (2021). https://doi.org/10.52292/j.laar.2021.716

[14] D. Dey, O.D. Makinde, and R. Borah, "Analysis of Dual Solutions in MHD Fluid Flow with Heat and Mass Transfer Past an Exponentially Shrinking/Stretching Surface in a Porous Medium," Int. J. Appl. Comput. Math. **8**, 66 (2022). https://doi.org/10.1007/s40819-022-01268-7
[15] A.S. Khound, D. Dey, and R. Borah, "Analysis of Entropy Generation of Casson Fluid Flow Over a Stretching Surface with Second-Order Velocity Slip in Presence of Radiation and Chemical Reaction," Int. J. Appl. Comput. Math. **8**(2), (2022). https://doi.org/10.1007/s40819-022-01243-2
[16] A.K. Alzahrani, M.Z. Ullah, A.S. Alshomrani, and T. Gul, "Hybrid nanofluid flow in a Darcy-Forchheimer permeable medium over a flat plate due to solar radiation," Case Stud. Therm. Eng. **26**, 100955 (2021). https://doi.org/10.1016/j.csite.2021.100955
[17] S.U. Devi, and S.P.A. Devi, "Heat Tansfer Enhancement of Cu-Al2O3/Water Hybrid Nanofluid Flow over a Stretching Sheet," J. Niger. Math. Soc. **36**(2), 419–433 (2017). https://ojs.ictp.it/jnms/index.php/jnms/article/view/147/47
[18] N.S. Khashi'ie, N.M. Arifin, I. Pop, and N.S. Wahid, "Flow and heat transfer of hybrid nanofluid over a permeable shrinking cylinder with Joule heating: A comparative analysis," Alexandria Eng. J. **59**, 1787–1798 (2020). https://doi.org/10.1016/j.aej.2020.04.048
[19] N. Ahmed, and K. Choudhury, "Heat and mass transfer in three-dimensional flow through a porous medium with periodic permeability," Heat Transf. - Asian Res. **48**(2), 644-662 (2019). https://doi.org/10.1002/htj.21399
[20] D. Abdullah, G. Engin, K. Ali, P.H. Kadir, A. Kamil, and A. Ammar, "Effect of Al2O3-SiO2/water Hybrid Nanofluid filled in a square Enclosure on the Natural Convective heat Transfer Characteristics: A numerical Study," J. Nanofluids, **11**, 772–781 (2022). https://doi.org/10.1166/jon.2022.1881
[21] A.J. Chamkha, S. Abbasbandy, A.M. Rashad, and K. Vajravelu, "Radiation Effects on Mixed Convection over a Wedge Embedded in a Porous Medium Filled with a Nanofluid," Transp. Porous Media, **91**(1), 261–279 (2012). https://doi.org/10.1007/s11242-011-9843-5
[22] C. Sulochana, M.K.K. Kumar, and N. Sandeep, "Radiation and Chemical Reaction Effects on MHD Nanofluid Flow over a Continously Moving Surface in Porous Medium with Non-Uniform Heat Source/Sink," Chem. Process Eng. Res. **33**, 1-13 (2015). https://www.iiste.org/Journals/index.php/CPER/article/view/22208/22650
[23] R.P. Sharma, S.R. Mishra, S. Tinker, and B.K. Kulshretha, "Radiative Heat Transfer of Hybrid Nanofluid Flow over an Expanding surface with the interaction of Joule Effect," J. Nanofluids, **11**, 745–753 (2022). https://doi.org/10.1166/jon.2022.1872
[24] D. Dey, R. Borah, and A. S. Khound, "Stability analysis on dual solutions of MHD Casson fluid flow with thermal and chemical reaction over a permeable elongating sheet," Heat Transf. **51**(4), 3401-3417 (2022). https://doi.org/10.1002/htj.22456
[25] A. Saleem,W. Sabih, S. Nadeem, and M. Ghalambaz, "Theoretical aspects of micropolar nanofluid flow past a deformable rotating cone," Math. Methods Appl. Sci. 1–19 (2020). https://doi.org/10.1002/mma.6777
[26] J.H. Merkin, "On dual solutions occuring in mixed convection in a porous medium," J. Eng. Math, **20**(2), 171-179 (1986). https://doi.org/10.1007/BF00042775
[27] S. Ghosh, and S. Mukhopadhyay, "Flow and heat transfer of nanofluid over an exponentially shrinking porous sheet with heat and mass fluxes," Propuls. Power Res. **7**(3), 268-275 (2018). https://doi.org/10.1016/j.jppr.2018.07.004
[28] I. Waini, A. Ishak, and I. Pop, "Hiemanz flow over a shrinking sheet in a hybrid nanofluid," Results Phys. **19**(8), 103351 (2020). https://doi.org/10.1016/j.rinp.2020.103351
[29] D. Dey, R. Borah and B. Mahanta, "Boundary Layer flow and Its Dual Solutions over a Stretching Cylinder: Stability Analysis," In: Hassanien, A.E., Bhattacharyya, S., Chakrabati, S., Bhattacharya, A., Dutta, S. (eds) Emerging Technologies in Data Mining and Information Security. Advances in Intelligent Systems and Computing, vol 1286. Springer, Singapore. https://doi.org/10.1007/978-981-15-9927-9_3
[30] M. Prameela, D. V. Lakshmi, https://doi.org/10.34049/bcc.52.2.5168and J. R. Gurejala, "Influence of thermal radiation on mhd fluid flow over a sphere," Biointerface Res. Appl. Chem. **12**(5), 6978–6990 (2022). https://doi.org/10.33263/BRIAC125.69786990
[31] G.S. Mishra, M.R. Hussain, O.D. Makinde, and S.M. Seth, "Stability analysis and dual multiple solutions of a hydromagnetic dissipative flow over a stretching/shrinking sheet," Bulg. Chem. Commun. **52**(2), 259-271 (2020). https://doi.org/10.34049/bcc.52.2.5168
[32] D. Dey, and R. Borah, "Stability analysis on dual solutions of second-grade fluid flow with heat and mass transfers over a stretching sheet," International Journal of Thermofluid Science and Technology, **8**(2), 080203 (2021). https://doi.org/10.36963/IJTST.2021080203

ДУАЛЬНІ РІШЕННЯ ДЛЯ ГІБРИДНОЇ ТЕЧІЇ НАНОРІДИНИ ПО КОНУСУ З ВПЛИВОМ ТЕПЛОВОГО ВИПРОМІНЮВАННЯ І ХІМІЧНОЇ РЕАКЦІЇ ТА АНАЛІЗ ЇЇ СТАБІЛЬНОСТІ

Дебасіш Дей[a], Рупджоті Борах[a], Ашим Джйоті Баруах[b]
[a]*Департамент математики, Університет Дібругарх, Дібругарх-786004, Ассам, Індія*
[b]*Департамент математики, Намруп коледж, Дібругарх -786623, Ассам, Індія*

Основна мета цього дослідження полягає в тому, щоб розрізнити стабільні та реалізовані рішення між подвійними рішеннями потоку гібридної нанофлюїди на водній основі, що рухається по твердому конусу, разом із передачею енергії у формі тепла та маси, використовуючи новий підхід, який називається аналізом стабільності. Враховано відхилення теплового випромінювання, хімічних реакцій і поглинання/утворення тепла. Провідні рівняння, які підтримують математичне представлення цього дослідження, оновлені за допомогою набору змінних подібності та розв'язані за допомогою вбудованої схеми рішення рівнянь MATLAB bvp4c. Представлені графічні та чисельні результати цього дослідження. У результаті цього дослідження було отримано два типи потокових рішень, де один із них пов'язаний із незалежними від часу рішеннями та є стабільним за своєю природою. Крім того, швидкість течії гібридного нанофлюїду можна контролювати, застосовуючи магнітне поле, але треба мати на увазі, що надмірна кількість магнітного параметра може пошкодити систему шляхом окислення.

Ключові слова: *гібридний нанофлюїд; твердий конус; теплове випромінювання; хімічна реакція; подвійні рішення; аналіз стабільності*

East European Journal of Physics. 2. 107-116 (2023)
DOI:10.26565/2312-4334-2023-2-09 ISSN 2312-4334

NUMERICAL SOLUTION OF RADIATIVE BOUNDARY LAYER FLOW IN POROUS MEDIUM DUE TO EXPONENTIALLY SHRINKING PERMEABLE SHEET UNDER FUZZY ENVIRONMENT†

Amir Barhoi[a,*], G.C. Hazarika[b,§], Hrishikesh Baruah[a,‡], Pranjal Borah[c,&]
[a]*Duliajan College, Duliajan, Assam, India*
[b]*Dibrugarh University, Dibrugarh, Assam, India*
[c]*D.R. College, Golaghat, Assam, India*
**Corresponding Author e-mail: barhoiamir@gmail.com, [§]e-mail: gchazarika@gmail.com*
[‡]e-mail: h.baruah07@gmail.com,[&]e-mail: pranjalborah.drc@gmail.com
Received March 18, 2023; revised March 21, 2023; accepted March 28, 2023

In this paper we are considering a fluid flows problem that contains two equation of motions and more than two parameters in the governing equation of motion. Which is namely *Radiative Boundary Layer Flow in Porous Medium due to Exponentially Shrinking Permeable Sheet*. The parameters are $K = \frac{ck_0}{L\vartheta}$, $Pr = \frac{\mu c_p}{k_\infty}$, $N = \frac{4\sigma_1 T_\infty^{\ 3}}{3k_1 k_\infty}$ and ε denote the permeability parameter, Prandtl number, and radiation parameter and is the thermal conductivity variation parameter respectively. The governing differential equation can be obtained by using similarity variable technique and then the governing equation of motion can be Fuzzified by the help of Zadeh extension theorem. The $\alpha - cut$ technique is used for the validation of the uncertainty of the equation of the motion. The effect of the K, Pr, N and ε are discussed with the fuzzified governing equation of motion under fuzzy environment. It is observed none of the parameters are directly involved in the occurrence of the uncertainty of the solutions. The uncertainty occurs in the problem is due to the assumption and the numerical computation. Finally, the solution is being carried out under fuzzy environment. It is found that the increasing values of permeability parameter, the values of both the numbers Skin friction coefficient as well as Nusselt number are increases.
Keywords: *Shrinking sheet; Fuzzified; computer codes;* $\alpha - cut$
PACS: 44.05 +e, 44.30 +v, 47.10 A-

1. INTRODUCTION

Flow and heat Transfer in boundary layer flow of viscous fluid due to deforming surface is pivotal in many industrial processes cutting across different realms. Specially radiative thermal regime in porous medium has drawn much attention recently due to large application in gasification of oil shale waste heat storage in aquifer and many more.

Vast application of radioactive thermal in porous medium we need to study this class of problems in different ways. Due to involvement of nonlinear differential equation, there is no direct process available to solve exactly. Here we consider such a mechanical problem for our discussion in which the governing equations of motion can have two non-linear differential equations of motion (One for velocity profile and another one is for temperature profile) and four parameters in the governing equation of motion and one parameter in the boundary conditions. The specific problem is *Radiative Boundary Layer Flow in Porous Medium due to Exponentially Shrinking permeable Sheet.*

A few relevant research has been presented in recent years (2010 to cont.). Radiative flow of Jeffery fluid with variable thermal conductivity in a porous medium was discussed by Elbashbeshy and Emam (2011), Hayat et al. (2012) about the effects of radiation and heat transfer over an unsteady stretching surface embedded in a porous medium. Paresh Vyas and Nupur Srivastava studied (2016) about the flow past and exponentially shrinking placed at the bottom of fluid saturated porous medium taking variable thermal conductivity and radiation using fourth order Runge-kutta scheme together with shooting method.

Here we introduce a new approach of solving of the said problem using fuzzy set theory. In this chapter our objective is to find is there any kind of uncertainty involved in the specific problem i.e. Radiative Boundary Layer Flow in Porous Medium due to Exponentially Shrinking permeable Sheet using fuzzy environment. For the graphical interpretation we developed computer codes for the said problem and represent the parameter's effect on the uncertainty involved in the flow of motion. On the basic concept of fuzzy differential equations Chakraverty et al., (2016) proposed some numerical methods for fuzzy fractional differential equations. Hazarika and Bora (2017, 2018) studied about the fuzzification of some numerical problems. J. Bora et al (2020) discussed some fluids problems using fuzzy set theory.

2. FORMULATION OF THE PROBLEM

2.1. Derivation of The Basic Equation

Let us consider the steady 2D boundary layer flow of optical thick viscous Newtonian fluid and associated heat transfer over a permeable sheet placed at bottom of the fluid saturated porous medium having permeability of specific form. A Cartesian coordinate system is chosen where the *x*-axis is taken along the sheet and *y*-axis is normal to it. The flow is caused by the sheet shrinking in an exponential fashion. A suction is applied normal to sheet to contain the

† ***Cite as:*** A. Barhoi, G.C. Hazarika, H. Baruah, and P. Borah, East Eur. J. Phys. 2, 107 (2023), https://doi.org/10.26565/2312-4334-2023-2-09

vorticity. The fluid considered here is without phase change, optically dense, absorbing-emitting radiation but a nonscattering medium. The thermal conductivity of the fluid is assumed to vary linearly with temperature. The radiation flux in the energy equation is presumed to follow Rosseland approximation. The boundary layer equations for the considered setup are

$$\frac{\partial u}{\partial x}+\frac{\partial u}{\partial y}=0, \tag{1}$$

$$u\frac{\partial u}{\partial x}+v\frac{\partial u}{\partial y}=\vartheta\left(\frac{\partial^2 u}{\partial y^2}\right)-\vartheta\frac{u}{k} \tag{2}$$

$$\rho c_p\left(u\frac{\partial T}{\partial x}+v\frac{\partial T}{\partial y}\right)=\frac{\partial}{\partial y}\left(k\frac{\partial T}{\partial y}\right)-\frac{\partial q_r}{\partial y} \tag{3}$$

With the boundary condition

At $y=0,\quad u=U_w(x)=-ce^{\frac{x}{l}},\quad v=V_w(x)=-v_0e^{\frac{x}{2l}},\quad T=T_w(x)=T_\infty+T_0e^{\frac{x}{2l}}$

and at

$$y\to\infty, u\to 0,\ T\to T_\infty \tag{4}$$

where u, v are the velocity components along x and y directions, respectively, k is the permeability, $c_p$is the specific heat at constant pressure, υ is the kinematic viscosity, ρ is the density, and T, μ, and κ are the temperature, viscosity and thermal conductivity of the fluid, respectively. Further, L is the characteristic length, $T_w$is the variable temperature at the sheet, T_0 is the constant reference temperature, and T_∞ is the constant free stream temperature. U_w and V_w are the shrinking velocity of the sheet and mass transfer velocity, respectively, where $c > 0$ is the shrinking constant and v_0 is a constant (where $v_0 < 0$ corresponds to mass suction).
Let us introduce the stream function $\psi(x,y)$ as

$$u=\frac{\partial\psi}{\partial y}=-\frac{\partial\psi}{\partial x} \tag{5}$$

Thus equation (5.1) is identically satisfied and the similarity transformation can be written as

$$\psi=\sqrt{2\upsilon Lc}f(\eta)e^{\frac{x}{2l}}\ \eta=y\sqrt{\frac{c}{2\upsilon L}}e^{\frac{x}{2l}},\text{ and }\theta(x)=\frac{T-T_\infty}{T_w-T_\infty} \tag{6}$$

On using (5.5) and (6.5) we obtain the expression for velocity component in non-dimensional form as

$$u=cf'(\eta)\ e^{\frac{x}{2l}}\text{ and }v=-\sqrt{\frac{\upsilon c}{2L}}\left(\eta f'(\eta)+f(\eta)\right)e^{\frac{x}{2l}} \tag{7}$$

In order to obtain the similarity solutions, it is assumed that the permeability k of the porous medium takes the following form

$$k(x)=2k_0e^{-\frac{x}{L}} \tag{8}$$

Where k_0 is the reference permeability.
As in our setup the thermal conductivity of the fluid is assumed to vary with temperature in a linear function as

$$k=k_\infty(1+\in\theta) \tag{9}$$

Where $\in$ is the thermal conductivity variation parameter. In general, $\in > 0$ for fluids such as water and air, while $\in<0$ for fluids such as lubrication oils. The radiative heat flux in the energy equation is presumed to follow Rosseland approximation and is given by

$$q_r=-\frac{4\sigma_1}{3k_1}\frac{\partial T^4}{\partial y} \tag{10}$$

Where σ_1 is the Stephan-Boltzmann constant and k_1 is the mean absorption constant. It is further assumed that the temperature difference within the fluid is sufficiently small sothat T^4 may be expressed as a linear function of temperature T. This is done by expanding T^4 in a Taylor series about $T_\infty$and omitting higher-order terms to yield

$$T^4\cong 4{T_\infty}^3T-3{T_\infty}^4$$

Thus, the equation of momentum (5.2) and energy (5.3) reduces to the following non dimensional form

$$f'''+ff''-2f'^2-\frac{f'}{K}=0 \tag{11}$$

$$\left(1+\frac{4N}{3}\right)\theta''+\epsilon\theta\theta''+\epsilon\theta'^2+\Pr(f\theta'-\theta f')=0 \tag{12}$$

With the boundary conditions

$$\eta \to 0: f'(\eta) = -1, f(\eta) = \frac{-v_0}{\sqrt{vc/2L}} = S, \theta(\eta) = 1, \eta \to \infty: f'(\eta) \to 0, \theta(\eta) \to 0 \tag{13}$$

Where

$$K = \frac{ck_0}{L\vartheta}, \quad Pr = \frac{\mu c_p}{k_\infty}, \; N = \frac{4\sigma_1 {T_\infty}^3}{3k_1 k_\infty}$$

Denote the permeability parameter, Prandtl number, and radiation parameter respectively.

2.2. Conversion of The Basic Equation into Fuzzified Form

Now we Applying Zadeh fuzzy Extension theorem in (5.11-5.12) and (5.13-5.14)

$$\widehat{f'''} + \hat{f}\widehat{f''} - \hat{2}\widehat{f'^2} - \frac{\hat{f'}}{K} = 0 \tag{15}$$

$$(\hat{1} + \frac{\widehat{4N}}{3})\,\widehat{\theta''} + \hat{\epsilon}\hat{\theta}\widehat{\theta''} + \hat{\epsilon}\widehat{\theta'^2} + \widehat{\mathrm{Pr}}\,\left(\hat{f}\hat{\theta'} - \hat{\theta}\hat{f'}\right) = \hat{0} \tag{16}$$

And the boundary condition became as (Fuzzy Environment)

$$\hat{\eta} \to \hat{0} : \hat{f'}(\eta) = \widehat{-1}, \hat{f}(\eta) = \frac{\widehat{-v_0}}{\sqrt{vc/2L}} = \hat{S}, \hat{\theta}(\eta) = \hat{1}, \tag{17}$$

$$\hat{\eta} \to \hat{\infty}: \hat{f'}(\eta) \to \hat{0}, \hat{\theta}(\eta) \to \hat{0} \tag{18}$$

Considering the Fuzzified (5.15) equations as triangular fuzzy number then the Fuzzified equation became the following:

$$[\underline{f'''}, f''', \overline{f'''}] + [\underline{f}, f, \overline{f}]\,[\underline{f''}, f'', \overline{f''}] - 2\left[\underline{f'^2}, f'^2, \overline{f'^2}\right] - \frac{[\underline{f'}, f', \overline{f'}]}{[\underline{K}, \; K, \overline{K}]} = [\underline{0}, 0, \overline{0}]$$

Using fuzzy arithmetic we have,

$$\Rightarrow [\underline{f'''}, f''', \overline{f'''}] + [\min T, \; T_0, \max T] - \left[2\underline{f'^2}, 2f'^2, 2\overline{f'^2}\right] - [\min \boldsymbol{S}, \; \boldsymbol{S}_0, \max \boldsymbol{S}] = [\underline{0}, 0, \overline{0}]$$

$$\Rightarrow [\underline{f'''} + \min T, f''' + T_0, \overline{f'''} + \max T] - \left[2\underline{f'^2} + \min \boldsymbol{S}, 2f'^2 + \boldsymbol{S}_0, 2\overline{f'^2} + \max \boldsymbol{S}\right] = \quad [\underline{0}, 0, \overline{0}]$$

$$\Rightarrow [\underline{f'''} + \min T - (2\overline{f'^2} + \max \boldsymbol{S}), f''' + T_0 - (2f'^2 + \boldsymbol{S}_0), \overline{f'''} + \max T - (2\underline{f'^2} + \min \boldsymbol{S})] = [\underline{0}, 0, \overline{0}]$$

Thus, we have,

$$\underline{f'''} + \min T - \left(2\overline{f'^2} + \max \boldsymbol{S}\right) = \underline{0} \tag{19}$$

$$f''' + T_0 - \left(2f'^2 + S_0\right) = 0. \tag{20}$$

$$\overline{f'''} + \max T - \left(2\underline{f'^2} + \min \boldsymbol{S}\right) = \overline{0} \tag{21}$$

Where $\boldsymbol{S} = \frac{\underline{f'}}{\underline{K}}, \frac{\overline{f'}}{\underline{K}}, \frac{\underline{f'}}{\overline{K}}, \frac{\overline{f'}}{\overline{K}}$ and $\boldsymbol{S}_0 = \frac{f'}{K}$

$$T = \underline{ff''}, \underline{f}\overline{f}^{''}, \overline{f}\underline{f''}, \overline{ff''}, \text{ and } T_0 = ff''$$

Similarly considering the Fuzzified (5.16) equations as triangular fuzzy number then the Fuzzified equation became the following:

$$\left[\underline{1 + \frac{4N}{3}}, 1 + \frac{4N}{3}, \overline{1 + \frac{4N}{3}}\right][\underline{\theta''}, \theta'', \overline{\theta''}] + [\underline{\in}, \in, \overline{\in}][\underline{\theta}, \theta, \overline{\theta}][\underline{\theta''}, \theta'', \overline{\theta''}] + [\underline{\in}, \in, \overline{\in}]\,[\theta'^2, \theta'^2, \theta'^2] + [\underline{Pr}, Pr, \overline{Pr}]$$
$$\{\left[\underline{f}, f, \overline{f}\right]\left[\underline{\theta'}, \theta', \overline{\theta'}\right] - \left[\underline{f'}, f', \overline{f'}\right]\left[\underline{\theta}, \theta, \overline{\theta}\right]\} = [\underline{0}, 0, \overline{0}]$$

$$\Rightarrow [\min X, \tilde{X}, \max X] + [\underline{\in}, \in, \overline{\in}]\,[\min Y, \; \tilde{Y}, \max Y] + [\min Z, \; \tilde{Z}, max\; Z] + [\underline{Pr}, Pr, \overline{Pr}]\,\{[\min A, \tilde{A}, \max A] - [\min B, \tilde{B}, \max B]\} = [\underline{0}, 0, \overline{0}]$$

$$\Rightarrow [\min X, \tilde{X}, \max X] + [\min Y_0, \tilde{Y_0}, \max Y_0] + [\min Z, \; \tilde{Z}, max\; Z] + [\underline{Pr}, Pr, \overline{Pr}]\,[\min A - \max B, \tilde{A} - \tilde{B}, \; \max A - \min B] = [\underline{0}, 0, \overline{0}]$$

$$\Rightarrow [\min X + \min Y_0 + \min Z, \tilde{X} + \tilde{Y_0} + \tilde{Z}, \max X + \max Y_0 + \max Z] + [\min A_0 B_0, \widetilde{A_0 B_0}, \max A_0 B_0] = [\underline{0}, 0, \overline{0}]$$

$$\Rightarrow [\min X + \min Y_0 + \min Z + \min A_0B_0\,, \tilde{X} + \tilde{Y_0} + \tilde{Z} + \widetilde{A_0B_0},\ \max X + \max Y_0 + \max Z + \max A_0B_0] = [\underline{0}, 0, \overline{0}] \quad (22)$$

Where

$$X = \underline{1 + \tfrac{4N}{3}\ \theta''}, \underline{1 + \tfrac{4N}{3}\ \overline{\theta''}}\,, \overline{1 + \tfrac{4N}{3}\ \underline{\theta''}}, \overline{1 + \tfrac{4N}{3}\ \overline{\theta''}} \quad \text{and } \tilde{X} = 1 + \tfrac{4N}{3}\ \theta''$$

$$Y = \underline{\theta}\ \underline{\theta''}, \underline{\theta}\ \overline{\theta'}\,, \overline{\theta}\underline{\theta''}, \overline{\theta}\ \overline{\theta''}, \quad \text{and} \quad \tilde{Y} = \theta\theta''$$

$$Z = \underline{\epsilon}\ \underline{\theta'^2}, \underline{\epsilon}\ \overline{\theta'^2}, \overline{\epsilon}\ \underline{\theta'^2}, \overline{\epsilon}\ \overline{\theta}^{\prime 2} \quad \text{and } \tilde{Z} = \epsilon\theta'^2$$

$$Y_0 = \underline{\in} \min Y\,, \overline{\in} \min Y\,, \underline{\in} \max Y\,, \overline{\in} \max Y, \quad \text{and } \widetilde{Y_0} = \in \tilde{Y}$$

$$A = \underline{f}\ \underline{\theta'}, \underline{f}\ \overline{\theta}^{\prime}, \overline{f}\underline{\theta'}, \overline{f}\ \overline{\theta'}, \quad \text{and } \tilde{A} = f\theta'$$

$$B = \underline{f'}\ \underline{\theta}, \underline{f'\overline{\theta}}, \overline{f'}\ \underline{\theta}, \overline{f'}\ \overline{\theta}, \quad \text{and } B = f'\theta$$

$A_0B_0 = \underline{\Pr}\ (\min A - \max B)$, $\underline{\Pr}\ (\max A - \min B)$, $\overline{\Pr}\ (\min A - \max B)$, $\overline{\Pr}\ (\max A - \min B)$, $\widetilde{A_0B_0} = Pr\ (\tilde{A} - \tilde{B})$,

Now we can re-write the equation (5.22) as follows

$$\min X + \min Y_0 + \min Z + \min A_0B_0 = \underline{0} \quad (23)$$

$$\tilde{X} + \tilde{Y_0} + \tilde{Z} + \widetilde{A_0B_0} = 0, \quad (24)$$

$$\max X + \max Y_0 + \max Z + \max A_0B_0 = \overline{0}, \quad (25)$$

Similarly if we convert the boundary condition into Fuzzified form then a new system of equation will arise as follows

$$\underline{f'''} + \min T - \left(2\overline{f'^2} + \max \boldsymbol{S}\right) = \underline{0}$$

$$\min X + \min Y_0 + \min Z + \min A_0B_0 = \underline{0}$$

With the boundary conditions

$$\underline{\eta} \to \underline{0} : \underline{f'(\eta)} = \underline{-1}, \underline{f(\eta)} = \underline{\frac{-v_0}{\sqrt{vc/2L}}} = \underline{S},\ \underline{\theta(\eta)} = \underline{1}, \underline{\eta} \to \underline{\infty}: \underline{f'(\eta)} \to \underline{0}, \underline{\theta(\eta)} \to \underline{0} \quad (26)$$

$$f''' + T_0 - \left(2f'^2 + S_0\right) = 0$$

$$\tilde{X} + \tilde{Y_0} + \tilde{Z} + \widetilde{A_0B_0} = 0,$$

With the boundary conditions

$$\eta \to 0 : f'(\eta) = -1, f(\eta) = \frac{-v_0}{\sqrt{vc/2L}} = S, \theta(\eta) = 1, \eta \to \infty: f'(\eta) \to 0, \theta(\eta) \to 0 \quad (27)$$

$$\overline{f'''} + \max T - \left(2\underline{f'^2} + \min \boldsymbol{S}\right) = \overline{0} \qquad \max X + \max Y_0 + \max Z + \max A_0B_0 = \overline{0}$$

With the boundary conditions

$$\overline{\eta} \to \overline{0} : \overline{f'(\eta)} = \overline{-1}, \overline{f(\eta)} = \overline{\frac{-v_0}{\sqrt{vc/2L}}} = \overline{S}, \overline{\theta(\eta)} = \overline{1},$$

$$\overline{\eta} \to \overline{\infty}: \overline{f'(\eta)} \to \overline{0}, \overline{\theta(\eta)} \to \overline{0} \quad (28)$$

3. Definition of Skin Friction C_f and Nusselt Number Nu_x

The physical quantities of principal interest are the skin friction coefficient C_f and the local Nusselt number Nu_x, which are defined as

$$Re_x{}^{1/2} C_f = f''(0) \text{ and } \qquad Re_x{}^{-1/2} Nu_x = -\theta'(0)$$

Where $Re_x = \frac{u_x(x)x}{v}$ is the local Reynolds number.

4. Result and Discussion

The system of equations (26-28), the fuzzified equations of motion with fuzzified boundary conditions are solved numerically by using finite difference scheme. The discretized fuzzified equations are solved using an iterative method based on Gauss Seidel iterative method by developing suitable codes in python.

The numerical computations carried out for different sets of values of the parameters entering into the problem have been depicted through graphs and tables. Result is obtained for different values for the parameter $s = 1, K = .25, \in = .1,$ $Pr = 0.7$ and for different $\alpha - cut$ of the fuzzified system of equations (26-28)

In each of the following graphs the blue curve is the solution for the right values of the of the fuzzified velocity profile, green curve is the solution for the mid values of the fuzzified velocity profile which is same as the crisp velocity profile and blue curve is the solution for the right values of the of the Fuzzified velocity profile.

The Figure (1-3) exhibits the Fuzzified temperature profile for $\alpha - cut\ with\ \alpha = 0.3$,0.6,0.9, and $K = 0.25, n = 0.5\ , Pr = 0.7\ , \in = 0.1, s = 1$. It is observed from the graph that there is a deflection on the curve in the right solution of the temperature profile as compare to the left solution of the temperature profile from the mid value solution (i.e. crisp solution). Which is the indication of the uncertainty involved in the temperature profile.

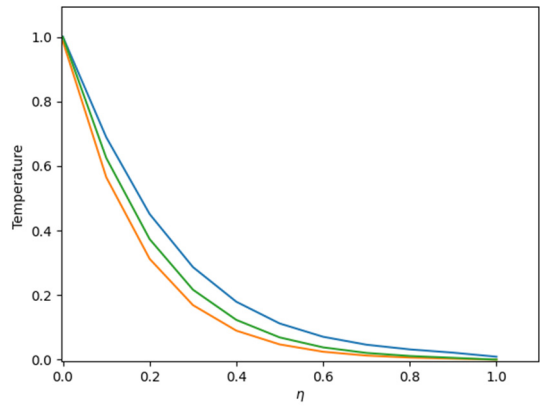

Figure 1. Fuzzified Temperature profile for $\alpha - cut, with\ \alpha = 0.3, s = 1, K = .25, \in = .1, Pr = 0.7$

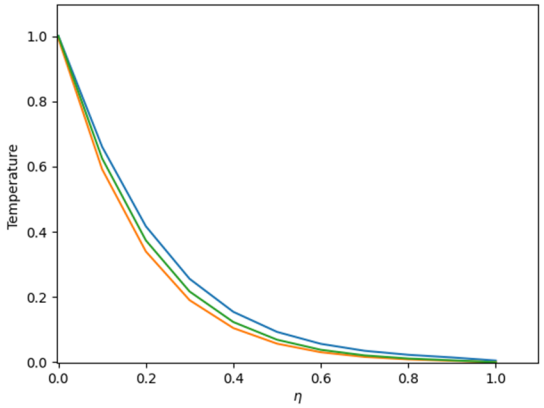

Figure 2. Fuzzified Temperature profile for $\alpha - cut\ with\ \alpha$=0.6, $s = 1, K = .25, \in = .1, Pr = 0.7$

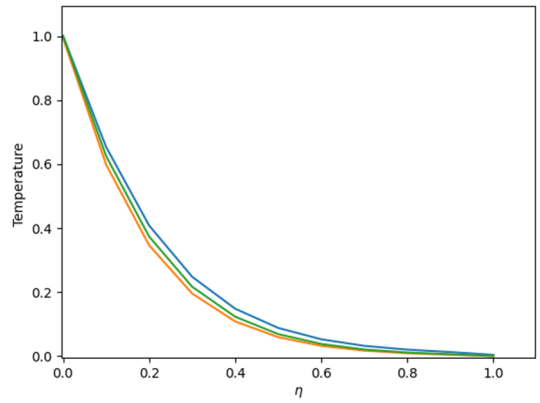

Figure 3. Fuzzified Temperature profile for $\alpha - cut\ with\ \alpha = 0.9, s = 1, K = .25, \in = .1, Pr = 0.7$

Figure (4-7) are the fuzzified temperature profiles for $\alpha - cut\ with\ \alpha = 0.5$ and different values of the parameters $s = 1\ and\ 2, K = 0.25\ and\ 0.5, Pr = 0.7\ and\ 1.1\ , \varepsilon = 0.1\ and\ 0.3.$

It is observed from the Figures that there is no significant deflection of right solution as compare to left solution from the mid value solution (Crisp solution). Which is due to the changes of these parameter are not the cause of the uncertainty involved in the solution of the temperature profile.

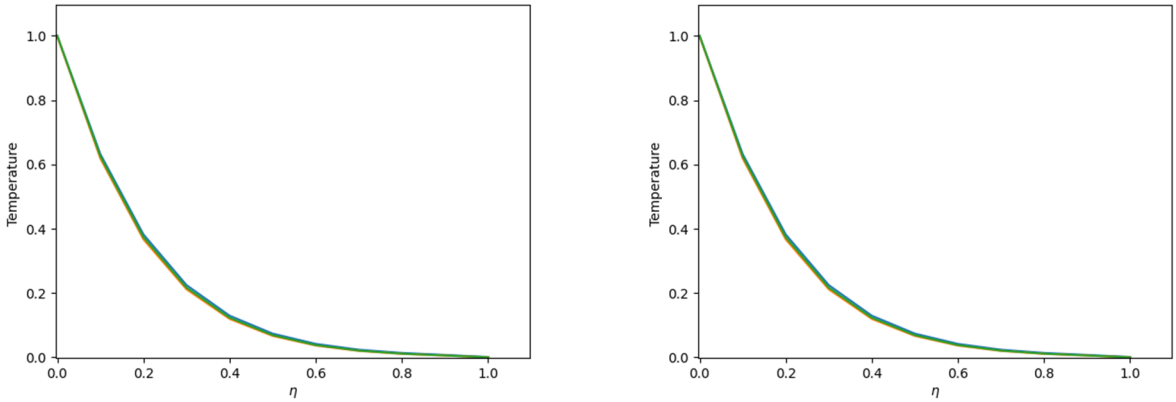

Figure 4. Fuzzified temperature profile for $\alpha - cut\ with\ \alpha$ =0.5, $\boldsymbol{s = 1\ and\ 2}, K = .25, \in = .1, Pr = 0.7$

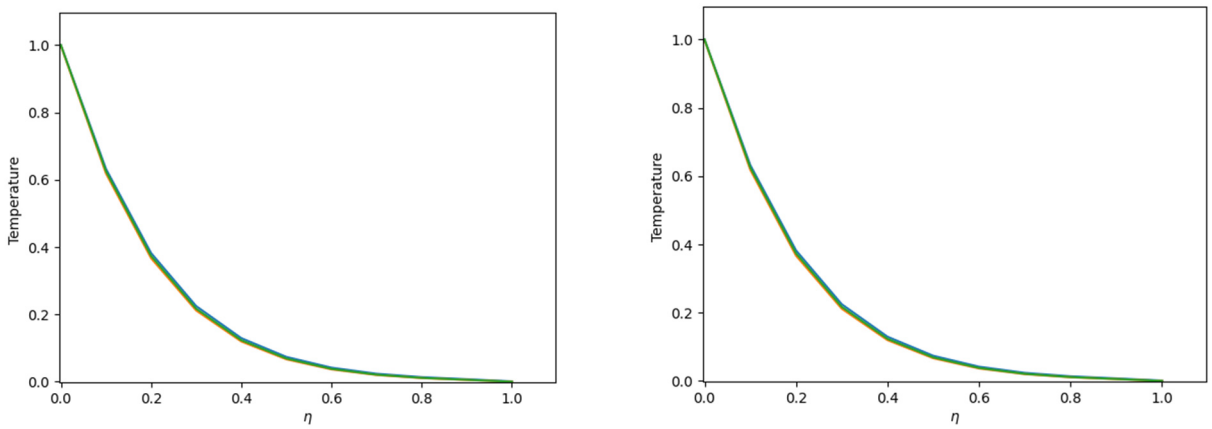

Figure 5. Fuzzified temperature profile for $\alpha - cut\ with\ \alpha$ =0.5, $s = 1, \boldsymbol{K} = \boldsymbol{.25\ and\ 0.5}, \in = .1, Pr = 0.7$

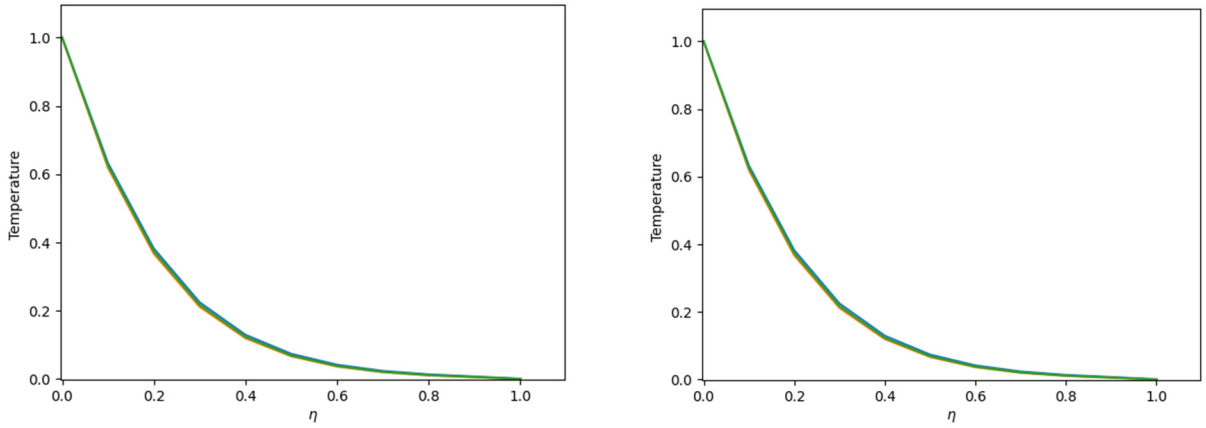

Figure 6. Fuzzified temperature profile for $\alpha - cut\ with\ \alpha$ =0.5, $s = 1, K = .25, \in = \boldsymbol{0.1\ and\ 0.3}, Pr = 0.7$

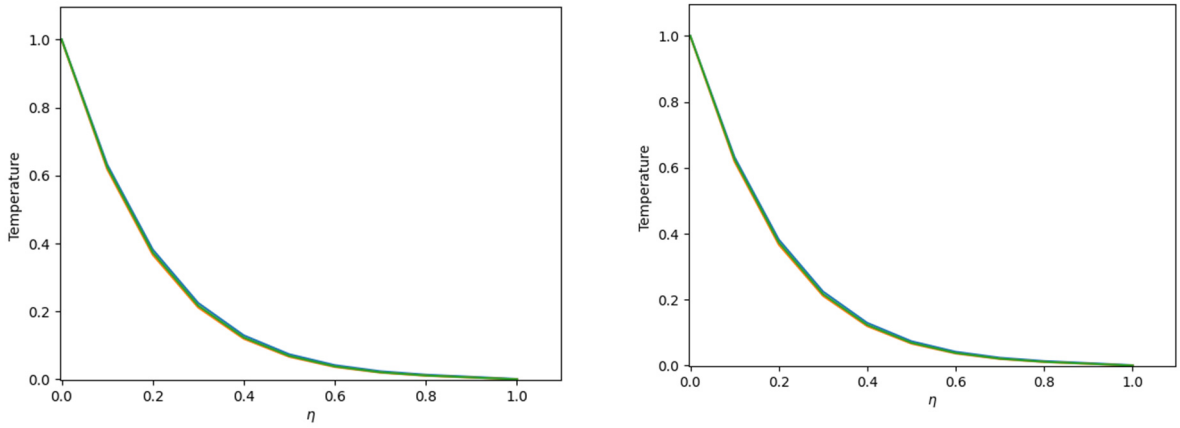

Figure 7. Fuzzified temperature profile for $\alpha - cut\ with\ \alpha$ =0.5, $s = 1, K = .25,\ \in = .1, \boldsymbol{Pr = 0.7 and\ 1.1}$

Figure (7-9) represent the crisp velocity profile for different values of $s, \in and\ Pr$. It is observed in Figure 7 that with the increasing values of suction parameter s the velocity decrease. Whereas velocity decreases with increase of Pr in Figure 8. It is found that the pattern of the flows is almost similar in the temperature profile for the changes of the parameter. Also, we see that $\theta(n)$ decay with the increase of Pr. Whereas $\theta(n)$ increases with increasing value of $\in$ in Figure 9.

As the parameter changes are not affect in the uncertainty of the solution of the temperature profile so we are discussed the effect of the parameter in Crisp Solution i.e., $\alpha - cut = 1$.

Figure (10) is the Fuzzified velocity profile for $\alpha - cut\ \ with\ \alpha = 0.5$, and $K = 0.25,\ n = 0.5\ ,\ Pr = 0.7, \in = 0.1,$ $s = 1$. It is observed from the graph that there is a deflection on the curve in the right solution of the velocity profile (Green curve) as compare to the left solution of the velocity profile (Light yellow curve) from the mid value solution i.e. crisp solution (Violet curve). Which is the indication of the uncertainty involved in the solution of the velocity profile.

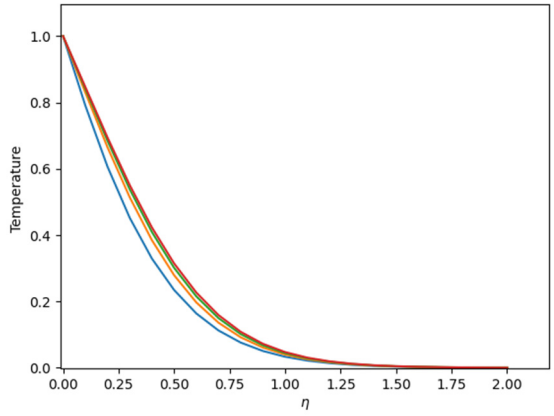

Figure 7. Crips Temperature profile for $\in = 0.1\ (blue), 0.5\ (Orange), 0.9\ (Green), 1.2\ (Brown)$ $and\ \ s = 1, K = .25, Pr = 0.7$

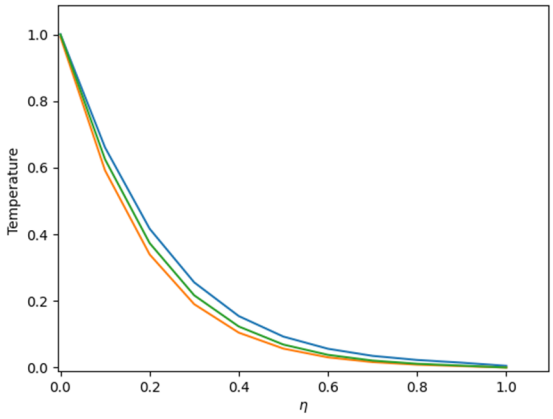

Figure 8. Crips Temperature profile for $\boldsymbol{s} = 1(Blue), 3\ (Green), 5\ (Orange)$ $and\ \ K = .25, \in = .1, Pr = 0.7$

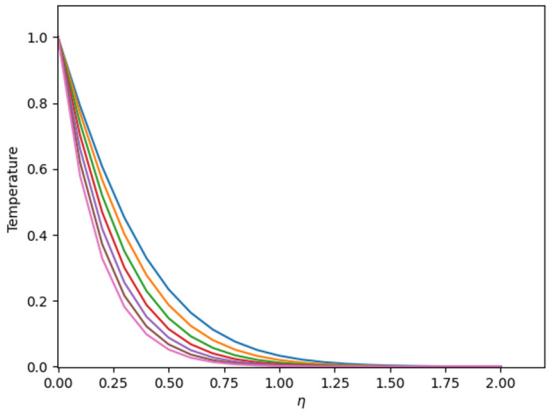

Figure 9. Crips Temperature profile for $\boldsymbol{Pr} = 21.7\ (Light\ Pink), 17(\ dark\ brown), 13.7(Violet), 10.7(brown), .7(Green), 4.7(Orange), 0.7(Blue)$ and $s = 1,\ \ K = .25,\ \ \in = .1$

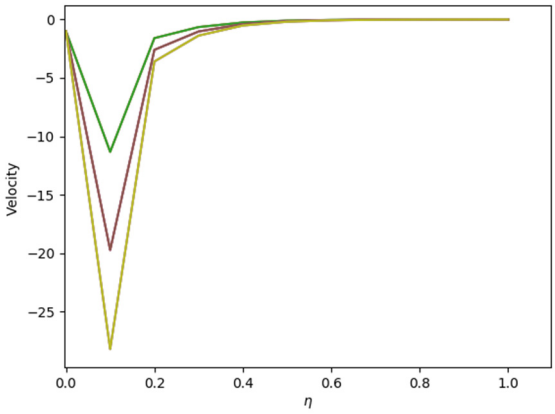

Figure 10. Fuzzified Velocity profile for $\alpha - cut\ with\ \ \alpha = 0.5, s = 1, K = .25, \in = .1, Pr = 0.7$

Fig (11-14) are the fuzzified velocity profiles for $\alpha - cut\ with\ \alpha = 0.5$ and different values of the parameters $s = 1\ and\ \ 2,\ \ K = 0.25\ and\ 0.5, Pr = 0.7\ and\ 1\ , \varepsilon = 0.1\ and\ 0.5$. It is observed from the Figures that there are no significant deflections of right solution as compare to left solution from the mid value solution (Crisp solution). This is due to the changes of these parameter are not the cause of the uncertainty involved in the solution of the velocity profile.

As the parameter changes are not affect in the uncertainty of the solution of the velocity profile so we are discussed the effect of the parameter in Crisp Solution i.e. $\alpha - cut = 1$.

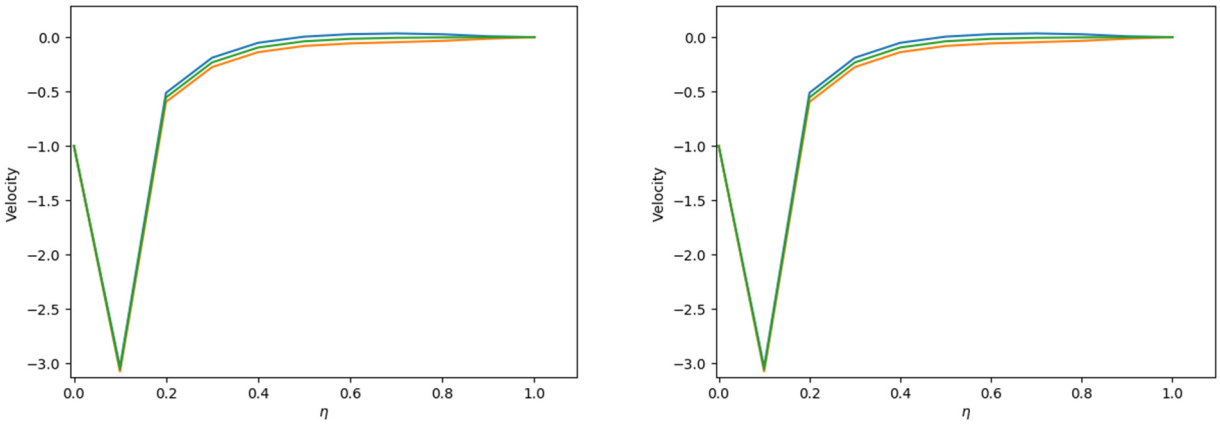

Figure 11. Fuzzified Velocity profile for $\alpha - cut\ with\ \alpha = 0.5, s = \boldsymbol{1\ and\ 2}, K = .25, \in = .1, Pr = 0.7$

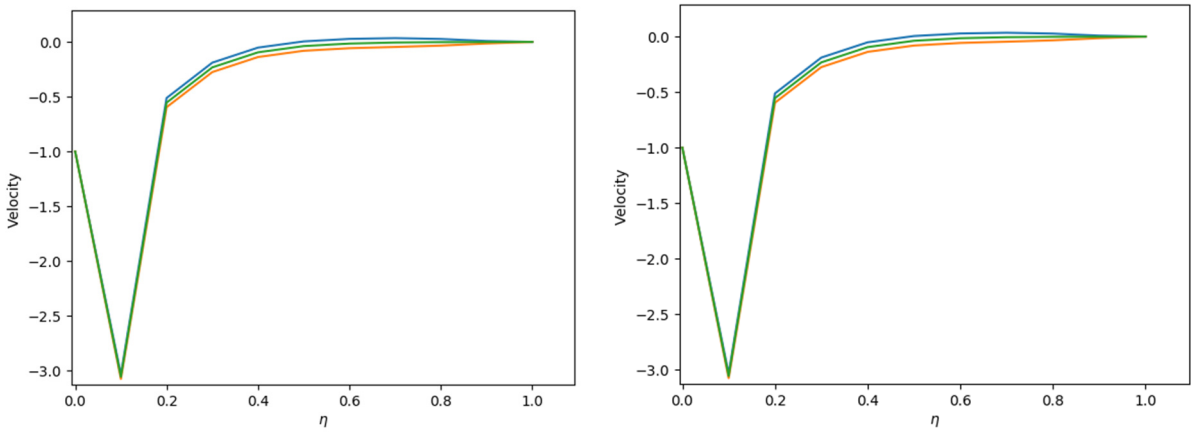

Figure 12. Fuzzified Velocity profile for $\alpha - cut\ with\ \alpha$ =0.5, $s = 1, K = .25\ and\ 0.5, \in = .1, Pr = 0.7$

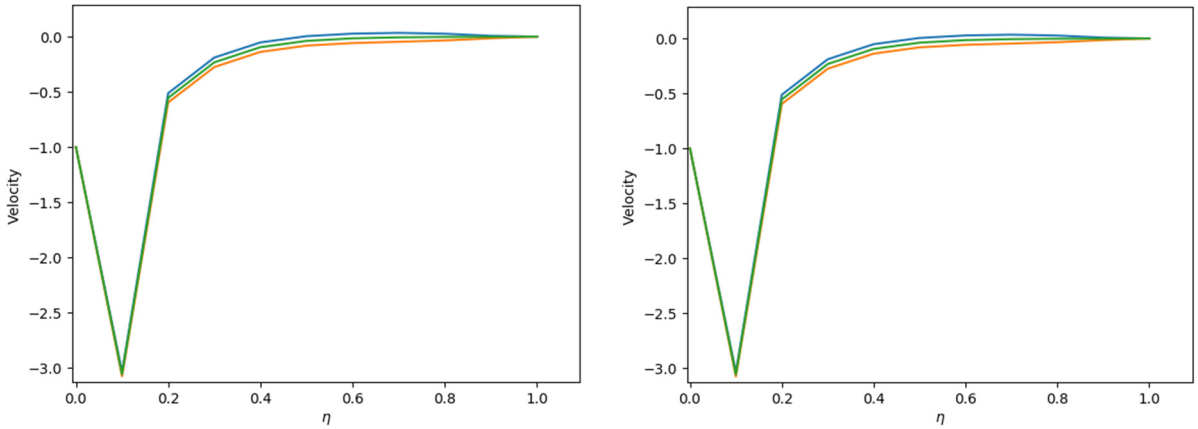

Figure 13. Fuzzified Velocity profile for $\alpha - cut\ with\ \alpha$ =0.5, $s = 1,\ K = 0.25, \in = 0.1\ \ and\ \ 0.5,\ \ Pr = 0.7$

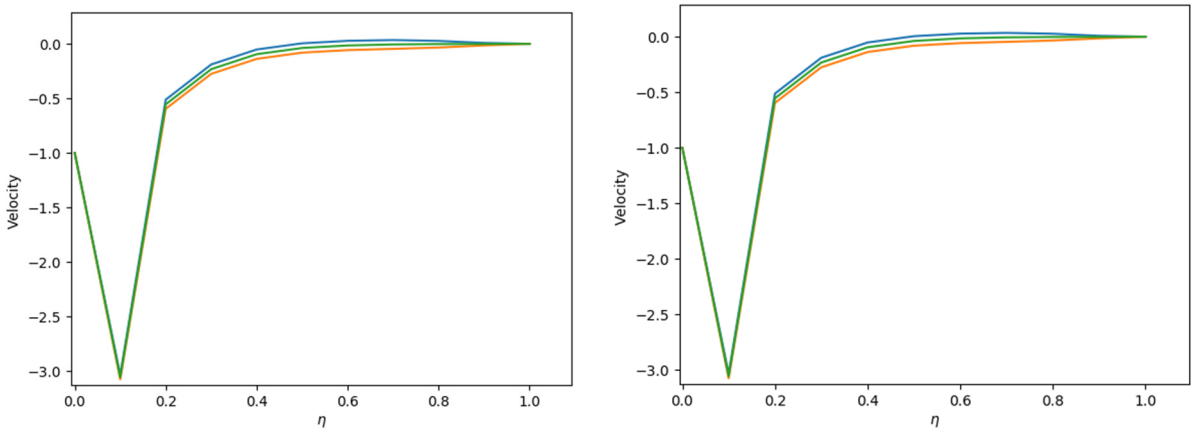

Figure 14. Fuzzified Velocity profile for $\alpha - cut\ with\ \ \alpha = 0.5,\ \ s = 1,\ \ K = 0.25,\ \ \in = .1,\ \ Pr = 0.7\ and\ 1$

Figure (15) represent the crisp velocity profile for the different values of the parameter $\in$ and fix value of the parameter $= 0.25,\ \ s = 1\ and\ \ Pr = 0.7$. It is observed that with the increasing value of $\in$ the velocity profile decreases.

Again Figure (16) represents the crisp velocity profile for the different values of the parameter s and fix value of the parameter $K = 0.25,\ \in = 0.1\ and\ \ Pr = 0.7$ respectively. It is observed that with the increasing value of s the velocity profile also increases.

It is observed from the graphs of the crisp velocity profile in Fig. (15-16) that the solution shows the occurrence of reverse flow. The occurrence of the sharp point in the back flow this is due to the numerical difficulties as the numbers of subdivision are less in number. If we increase the number of divisions to as large extend time complicity arise in the fuzzified solution but the curve would be smooth.

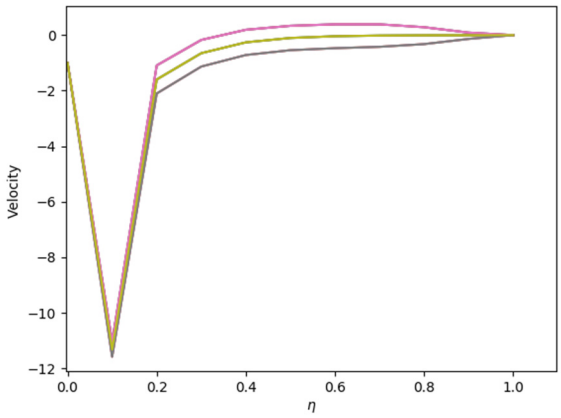

Figure 15. Crips Velocity profile for $\in = 0.1(Violet), 0.5(yellow), 1(pink)\ and\ s = 1, K = .25,$ $Pr = 0.7$

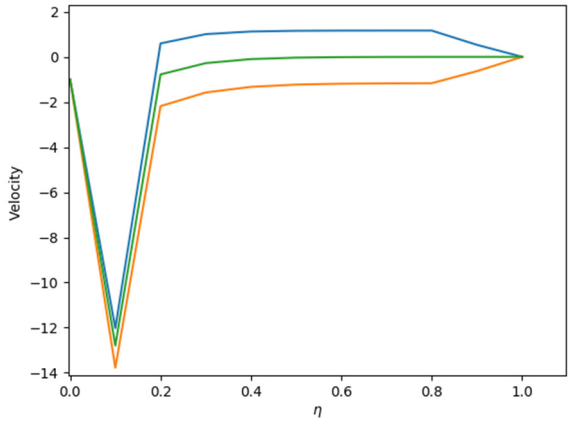

Figure 16. Crips Velocity profile for $s = 9(Blue), 5(Green), 1(Orange)\ and\ K = .25, \in = .1,$ $Pr = 0.7$

5. Comparison of Skin Friction Coefficient C_f and Local Nusselt Number Nu_x

The two important parameters in fluid flow problem are the skin friction coefficient C_f and local nusselt number Nu_x we have computed these two parameters for different values of the Permiability parameter which are given in the following Table.

Table

Permiability Parameter	C_f		Nu_x	
	Crips	**Fuzzified**	**Crisp**	**Fuzzified**
10	0.264853	0.243849	-2.13187057	-2.00200567
20	0.265152	0.244158	-2.13187043	-2.0020055
30	0.265251	0.244261	-2.13187038	-2.00200544
40	0.265301	0.244313	-2.13187036	-2.00200541

It is observed from the table that with the increasing values of permeability parameter the values of the Skin friction coefficient increases. Similarly with the increasing values of permeability parameter the values of Nusselt number also increases. The results are well agreed with those of crisp values. The effect of fuzzification is also observed from the above Table.

6. Conclusion

In this chapter, the Radiative boundary layer flow in Porous medium due to exponentially shrinking steady MHD stagnation point flow due to shrinking permeable sheet has been theoretically considered under fuzzy environment. The effect of suction parameter, velocity ration parameter, Prandlt number on the flow and heat transfer have been studied under fuzzy environment. The numerical results have been obtained by developing computer codes on PYTHON. Thus, we conclude the followings from the above discussion:

(1) The involvement of uncertainty in the equation of motion of this problem.
(2) None of the parameters are directly involved in the occurrence of the uncertainty of the solutions. The uncertainty occurs in the problem is due to the assumption and the numerical computation.
(3) The crisp solution of velocity profile as well as temperature profile and the fuzzified velocity profile as well as temperature profile are in good agreements. The flow pattern for both the case velocity profile as well as Temperature profile are almost similar for different values of parameters.
(4) With the increasing values of permeability parameter, the values of both the numbers Skin friction coefficient as well as Nusselt number are increases.
(5) The effect of fuzzification is observed in the values of the physical quantities of the Skin friction coefficient C_f and local Nusselt number Nu_x.

Funding: Not Applicable
Consent Statement: Not Applicable
Data Applicability: Not Applicable
Conflict of Interested: Here with I declare there is no conflict of interested.

ORCID IDs
Amir Barhoi, https://orcid.org/0000-0003-3533-6000; **G.C. Hazarika,** https://orcid.org/0000-0003-3937-8919
Hrishikesh Baruah, https://orcid.org/0000-0002-0747-6103; **Pranjal Borah,** https://orcid.org/0009-0007-6737-2027

REFERENCES

[1] N.F.M. Noor, S.A. Kechil, and I. Hashim, "Simple non- perturbative solution for MHD viscous flow due to a shrinking sheet," Communications in Nonlinear Science and Numerical Simulation, **15**(2), 144–148 (2010). https://doi.org/10.1016/j.cnsns.2009.03.034
[2] T. Hayat, Z. Abbas, and M. Sajid, "On the analytic solution of magnetohydrodynamic flow of a second grade fluid over a shrinking sheet," Journal of Applied Mechanics, Transactions ASME, **74**(6), 1165-1171 (2007). https://doi.org/10.1115/1.2723820
[3] T. Fang, W. Liang, and C. F. F. Lee, "A new solution branch for the Blasius equation-A shrinking sheet problem," Computers and Mathematics with Applications, **56**(12), 3088-3095 (2008). https://doi.org/10.1016/j.camwa.2008.07.027
[4] N.F. Mohd, and I. Hashim, "MHD flow and heat transfer adjacent to a permeable shrinking sheet embedded in a porous medium," Sains Malaysiana, **38**(4), 559-565 (2009).
[5] D.S. Chauhan, and R. Agrawal, "MHD flow and heat transfer in a channel bounded by a shrinking sheet and a plate with a porous substrate," Journal of Engineering Physics and Thermophysics, **84**(5), 1034-1046 (2011). https://doi.org/10.1007/s10891-011-0564-y
[6] K. Bhattacharyya, "Boundary layer flow and heat transfer over an exponentially shrinking sheet," Chinese Physics Letters, **28**(7), ID 074701 (2011). http://dx.doi.org/10.1088/0256-307X/28/7/074701
[7] B.S. Dandapat, B. Santra, and K. Vajravelu, "The effects of variable fluid properties and thermocapillarity on the flow of a thin film on an unsteady stretching sheet," International Journal of Heat and Mass Transfer, **50**(5-6), 991-996 (2007). https://doi.org/10.1016/j.ijheatmasstransfer.2006.08.007
[8] P. Vyas, and A. Rai, "Radiative flow with variable thermal con- ductivity over a noniIsothermal Stretching sheet in a porous medium, Int," Journal of Contemporary Mathematical Sciences, **5**, 2685-2698 (2010). http://www.m-hikari.com/ijcms-2010/53-56-2010/raiIJCMS53-56-2010.pdf
[9] U. Sarma, and G.C. Hazarika, "Effects of variable viscosity and thermal conductivity on heat and mass transfer flow along a vertical plate in the presence of a magnetic field," Latin-American Journal of Physics Education, **5**, 100-106 (2011). https://dialnet.unirioja.es/descarga/articulo/3699657.pdf
[10] P. Vyas, and N. Srivastava, "Radiative MHD flow over a non- isothermal stretching sheet in a porous medium," Applied Mathematical Sciences, **4**(49-52), 2475-2484 (2010). https://www.m-hikari.com/ams/ams-2010/ams-49-52-2010/srivastavaAMS49-52-2010.pdf
[11] M.L. Puri, and D.A. Ralescu, "Differentials of fuzzy function," Journal of Mathematical Analysis and Application, **91**(2), 552-558 (1983). https://doi.org/10.1016/0022-247X(83)90169-5
[12] O. Kaleva, "Fuzzy differential equation", Fuzzy Sets and System, **24**(3), 301-317 (1987).https://doi.org/10.1016/0165-0114(87)90029-7
[13] O. Kaleva, "The Cauchy problems for fuzzy differentials equations", Fuzzy Sets and System, **35**(3), 389-396 (1990). https://doi.org/10.1016/0165-0114(90)90010-4
[14] Y. Zhang, G. Wang, and S. Liu, "Frequently domain methods for solution of n-order fuzzy differentials equations", Fuzzy Sets and System, **2**, 45-59 (1998).
[15] F. Rabie, F. Ismail, A. Ahmadian, and S. Salahshour, "Numerical solution of fuzzy differentials equation using Improved Runge-Kutta Nystrom Method", Mathematical Problems in Engineering, **2013**, 803462 (2013). http://dx.doi.org/10.1155/2013/803462
[16] M.A. Kermani, and F. Saburi, "Numerical methods for fuzzy differential equations", Applied Mathematical Sciences, (2007).
[17] V.A. Romanov, "Stability of plane-parallel Couette flow", Funct. Anal. Appl. **7**, 137-146 (1973). https://doi.org/10.1007/BF01078886
[18] A. Barhoi, P. Dutta, and G.C. Hazarika, "Numerical solution of MHD viscous flow over a shrinking sheet with second order slip under fuzzy Environment", Adv. Math. Sci. J. **9**(12), 10621-10631 (2020). https://doi.org/10.37418/amsj.9.12.47

ЧИСЛОВЕ РІШЕННЯ ТЕЧІЇ РАДІАЦІЙНОГО ПРИКОРДОННОГО ШАРУ В ПОРИСТОМУ СЕРЕДОВИЩІ ЧЕРЕЗ ЕКСПОНЕНЦІАЛЬНО ЗТИСНУТИЙ ПРОНИКНИЙ ШАР В НЕЧІТКИХ УМОВАХ

Амір Бархой[a], Г.К. Хазаріка[b], Хрішикеш Баруах[a], Пранджал Бора[c]
[a]Коледж Дуліаджана, Дуліаджан, Асам, Індія
[b]Університет Дібругарх, Дібругарх, Ассам, Індія
[c]D.R. Коледж, Гологхат, Асам, Індія

У цій статті розглянуто задачу про течії рідини, яка містить два рівняння руху та більше двох параметрів у визначальному рівнянні руху. Це саме радіаційний потік прикордонного шару в пористому середовищі через проникний лист, що експоненційно стискається. Параметри рівняння $K = \frac{ck_0}{L\vartheta}$, $Pr = \frac{\mu c_p}{k_\infty}$, $N = \frac{4\sigma_1 T_\infty{}^3}{3k_1 k_\infty}$, ε означають відповідно параметр проникності, число Прандтля, параметр випромінювання та параметр варіації теплопровідності. Основне диференціальне рівняння може бути отримане з використанням методу змінних подібності, а потім основне рівняння руху може бути fuzzified за допомогою теореми розширення Заде. Метод α-зрізу використовується для перевірки невизначеності рівняння руху. Обговорюється вплив K, Pr, N та ε з нечітким керуючим рівнянням руху в нечіткому середовищі. Знайдено, що жоден із параметрів не бере безпосередньої участі у виникненні невизначеності рішень. Невизначеність виникає через припущення та чисельний розрахунок. Нарешті, рішення виконано у нечіткому середовищі. Встановлено, що зі збільшенням значення параметра проникності зростають значення обох чисел: коефіцієнта поверхневого тертя, а також числа Нуссельта.

Ключові слова: *термозбіжний лист; нечіткість; комп'ютерні коди; α-зріз*

East European Journal of Physics. 2. 117-123 (2023)
DOI:10.26565/2312-4334-2023-2-10 ISSN 2312-4334

INVOLVING NIKIFOROV-UVAROV METHOD IN SCHRODINGER EQUATION OBTAINING HARTMANN POTENTIAL†

Mahmoud A. Al-Hawamdeh[a], Abdulrahman N. Akour[b,*], Emad K. Jaradat[a], Omar K. Jaradat[c]
[a]*Department of Physics, Mutah University, Jordan*
[b]*Department of Basic scientific Sciences, Al-Huson College, Al-Balqa Applied University, Jordan*
[c]*Department of Mathematic, Mutah University, Jordan*
**Corresponding Author e-mail: abd-akour@bau.edu.jo*
Received February 25, 2023; revised March 14, 2023; accepted March 15, 2023

The total wave function and the bound state energy are investigated by involving Nikiforov-Uvarov method to Schrodinger equation in spherical coordinates employing Hartmann Potential (HP). The HP is considered as non-central potential that is mostly recognized in nuclear field potentials. Every wave function is specified by principal quantum number n, angular momentum number l, and magnetic quantum number m. The radial part of the wave function is obtained in terms of the associated Laguerre polynomial, using the coordinate transformation $x = \cos\theta$ to obtain the angular wave function that depends on inverse associated Legendre polynomials.
Keywords: *Schrödinger equation; Nikiforov-Uvarov method; Hartmann Potential*
PACS: 03.56.-w, 03.65.Fd, 03.65Ge

INTRODUCTION

The Hartmann Potential is a kind of non-central potentials that have been studied in nuclear physics field, which consider as the coulomb potential surrounded by the ring-shaped inverse square potential. Organic molecules such as cyclic polyenes and benzene, handling this potential since 1972 [1-2]. In spherical coordinate the Hartmann potential is coulomb potential adding a one potential proportional to $(r\tan\theta)^{-2}$. So, it defined by [3-4]:

$$V(r,\theta) = -\frac{\alpha}{r} + \frac{\beta\cos^2\theta}{r^2\sin^2\theta}. \tag{1}$$

Where α, β are constants that consider as positive real numbers. Obtaining this HP in Schrodinger equation, assuming $(\mu = \hbar = 1)$ [5]:

$$\left\{\frac{1}{r^2}\frac{\partial}{\partial r}\left(r^2\frac{\partial}{\partial r}\right) + \frac{1}{r^2\sin\theta}\frac{\partial}{\partial\theta}\left(\sin\theta\ \frac{\partial}{\partial\theta}\right) + \frac{1}{r^2\sin^2\theta}\left(\frac{\partial^2}{\partial\phi^2}\right) + \frac{2\alpha}{r} - 2\beta\frac{\cos^2\theta}{r^2\sin^2\theta}\right\}\psi(r,\theta,\varphi) + 2E\psi(r,\theta,\varphi) = 0. \tag{2}$$

The equation (2) depends on the total coordinates in spherical coordinates (r,θ,φ), to find the total wave function we need apply separation of variables method on equation (2). The main object in this work is to determine the bound state energy and the wave function.

SEPARATION OF VARIABLES METHOD

Obviously, in spherical potential, we let [6]:

$$\psi(r,\theta,\varphi) = \frac{U(r)}{r}\,H(\theta)\,\phi(\varphi). \tag{3}$$

Now, by Separating variables in equation (2), we hold that:

The Radial Part

$$\frac{d^2U(r)}{dr^2} + \left[2E + 2\frac{\alpha}{r} - \frac{\lambda}{r^2}\right]U(r) = 0,$$

where λ is separation constant. And, to solve the equation, we let

$$\lambda = l`(l`+1) - 2\beta.$$

$$\beta = \frac{m`^2 - m^2}{2}.$$

Where $l`$ and $m`$ are positive integers or zero.

$$L = \frac{1}{2}\left\{\sqrt{1 + 4\left[\left(k + \sqrt{2\beta + m^2}\right)\left(k + \sqrt{2\beta + m^2} + 1\right) - 2\beta\right]} - 1\right\}. \tag{4}$$

† ***Cite as:*** M.A. Al-Hawamdeh, A.N. Akour, E.K. Jaradat, and O.K. Jaradat, East Eur. J. Phys. **2**, 117 (2023), https://doi.org/10.26565/2312-4334-2023-2-10

So, one can easily show that $\lambda = L(L+1)$ (see Appendix I)

The radial Schrodinger equation can displayed as:

$$\frac{d^2U(r)}{dr^2} + \left[2E + 2\frac{\alpha r}{r} - \frac{L(L+1)}{r^2}\right]U(r) = 0. \tag{5}$$

Where the angular part can displayed as:

The Angular part

Insert a new variable $x = \cos\theta$ and using Chain rules technique, to get the angular Schrodinger equation.

$$\frac{d^2H(x)}{dx^2} - \frac{2x}{1-x^2}\frac{dH(x)}{dx} + \frac{1}{1-x^2}\left(\lambda + 2\beta - \frac{m^2+2\beta}{1-x^2}\right)H(x) = 0. \tag{6}$$

And we let, $\lambda + 2\beta = l`(l` + 1)$, $m`^2 = m^2 + 2\beta$ and $v` = l`(l` + 1)$.

After applying all assumes into equation (6), we get

$$\frac{d^2H(x)}{dx^2} - \frac{2x}{1-x^2}\left\{\frac{dH(x)}{dx}\right\} + \frac{(-v`x^2+v`-m`^2)}{(1-x^2)^2}H(x) = 0\,. \tag{7}$$

The Azimuthal Part

$$\frac{1}{\phi(\varphi)}\left(\frac{d^2}{d\phi^2}\right)\phi(\varphi) = m^2. \tag{8}$$

Where m is the magnetic quantum number.

NIKIFOROV-UVAROV METHOD

The Nikiforov-Uvarov method is a one of the methods used to predict the solutions of generalized second order liner differential equation like Schrodinger equation with particular orthogonal function, we could be obtaining the solution by NU-method when make some transforming to Schrodinger equation to be the same of the below equation [7]

$$u``(z) + \frac{\check{\tau}(z)}{\sigma(z)}u`(z) + \frac{\check{\sigma}(z)}{\sigma^2(z)}u(z) = 0. \tag{9}$$

Where equation (9) is considering the standard form of NU-method. Where, $\sigma(z)$ and $\check{\sigma}(z)$ are polynomials with a maximum degree of 2; $\check{\tau}(z)$is polynomial with a maximum degree of 1; $u(z)$ is a hypergeometric function type, and the primes intending the derivatives respect to z. by supposing that:

$$u(z) = \phi(z)X(z). \tag{10}$$

The equation (9) become as hypergeometric form:

$$\sigma(z)X``(z) + \tau(z)X`(z) + \lambda X(z) = 0. \tag{11}$$

Where

$$\tau(z) = 2\pi(z) + \check{\tau}(z) \qquad , \frac{d}{dz}\tau(z) < 0. \tag{12}$$

Where $\pi(z)$ is a parameter of 1st polynomial degree and introduces by equation (13):

$$\pi(z) = \frac{\sigma`-\check{\tau}}{2} \pm \sqrt{\left(\frac{\sigma`-\check{\tau}}{2}\right)^2 - \hat{\sigma}(z) + k\sigma}. \tag{13}$$

While λ is introduced by equation (14)

$$\lambda = k + \pi`(z). \tag{14}$$

Since $\pi(z)$ is 1st degree polynomial, this implies that second order function under square root must be equal to zero, then the quadratic equation can determine k.

To obtain $\phi(z)$ we can use the integral below equation:

$$\frac{\phi`(z)}{\phi(z)} = \frac{\pi(z)}{\sigma(z)`}. \tag{15}$$

And the parameter λ in equation (14) defined by;

$$\lambda = \lambda_n = -n\tau`(z) - \frac{n(n-1)}{2}\sigma``(z). \tag{16}$$

The weight function $\rho(z)$ is obtained in (Eq. 17).

$$\frac{d}{dz}[\sigma(z)\,\rho(z)] = \tau(z)\;\rho(z). \tag{17}$$

While the Rodrigue relation (Eq. 18) is used to determine $X_n(z)$.

$$X_n(z) = \frac{B_n}{\rho(z)} \frac{d^n}{dz^n}[\sigma^n \rho(z)]. \tag{18}$$

Where $B_n$is normalization constant, now Substitute $X_n(z)$ and $\phi(z)$ into equation (10) to find $u(z)$ [8-12].

DEVELOPING HARTMANN POTENTIAL IN SCHRODINGER EQUATION

The Radial Schrodinger Equation

From equation (5) we can write the radial part by the below form

$$\frac{d^2U(r)}{dr^2} + \frac{1}{r^2}[2Er^2 + 2\alpha r - L(L+1)]U(r) = 0. \tag{19}$$

By comparing equation (9) by equation (19) to obtain the NU-Coefficients, we get

$$\check{\tau}(r) = 0, \tag{20-a}$$

$$\sigma(r) = r, \tag{20-b}$$

$$\check{\sigma}(r) = 2Er^2 + 2\alpha r - L(L+1). \tag{20-c}$$

Using equations (20-a) (20-b) and (20-c) into equation (13) to get the parameter $\pi(r)$

$$\pi(r) = \frac{1}{2} \pm \frac{1}{2}\sqrt{-8Er^2 + 4(k - 2\alpha)r + 4L(L+1) + 1}. \tag{21}$$

Now, taking this quadratic equation's discriminant equal zero, then the value of constant k could be determined.

$$k^2 - 4\alpha k + 4\alpha^2 + 2E\{4L(L+1) + 1\} = 0. \tag{22}$$

The quadratic equation (22) provides two roots for k

$$k_{\pm} = 2\alpha \pm \sqrt{-2E\{4L(L+1) + 1\}}. \tag{23}$$

Substituting equation (23) into equation (21), to get:

$$\pi_1(r) = \pi_{++}(r) = \frac{1}{2} + \left\{\sqrt{-2E}r + \left(L + \frac{1}{2}\right)\right\}, \tag{24-a}$$

$$\pi_2(r) = \pi_{\pm}(r) = \frac{1}{2} + \left\{\sqrt{-2E}r - \left(L + \frac{1}{2}\right)\right\}, \tag{24-b}$$

$$\pi_3(r) = \pi_{\mp}(r) = \frac{1}{2} - \left\{\sqrt{-2E}r + \left(L + \frac{1}{2}\right)\right\}, \tag{24-c}$$

$$\pi_4(r) = \pi_{--}(r) = \frac{1}{2} - \left\{\sqrt{-2E}r - \left(L + \frac{1}{2}\right)\right\}. \tag{24-d}$$

Taking $\pi_4(r)$ where $\tau(r)$ is negative in equation (12) to hold the well value by NU method; so:

$$\tau_4(r) = 1 - 2\left(\sqrt{-2E}r - \left(L + \frac{1}{2}\right)\right). \tag{25}$$

Returning to the equations (14) and (16) respectively, and developing equation (25) we get:

$$\lambda = 2\alpha - (2L + 2)\sqrt{-2E}. \tag{26}$$

$$\lambda_n = 2n\left(\sqrt{-2E}\right). \tag{27}$$

Comparing equations (26) and (27) one can predict bound state energy.

$$E = -\frac{\alpha^2}{2(L+n+1)^2}. \tag{28}$$

Where L is given by equation (4).

Depending on previous result especially equation 25 we can hold the function $\phi(r)$ and the weight function $\rho(r)$ that in equations (15) and (17) in a new form:

$$\phi(r) = r^{(L+1)}e^{-\sqrt{-2E}r} \tag{29}$$

$$\rho(r) = e^{-2\sqrt{-2E}r}r^{(2L+1)} \tag{30}$$

By obtaining equation (18) and (30); one can establish the polynomial $X_n(r)$:

$$X_n(r) = B_n e^{2\sqrt{-2E}r}r^{-(2L+1)} \frac{d^n}{dz^n}\left[e^{-2\sqrt{-2E}r}r^{(2L+1+n)}\right] \tag{31}$$

Also, the wave function $U(r)$ is hold by multiply $X_n(r)$ with $\phi(r)$.

$$U_{nl}(r) = B_n\, r^{(L+1)} e^{-\sqrt{-2E}r} e^{2\sqrt{-2E}r} r^{-(2L+1)}\ \frac{d^n}{dz^n}\left[e^{-2\sqrt{-2E}r} r^{(2L+1+n)}\right].$$

Involving associated Laguerre polynomial in equation [4] then $U_{nl}(r)$ can be defined as:

$$U_{nl}(r) = B_n\, r^{(L+1)} e^{-\sqrt{-2E}r}\ L_n^{2L+1}\left(2\sqrt{-2E}r\right). \tag{32}$$

By substituting $\sqrt{-2E}$ as in equation (28) where $\alpha = ze^2$, then the radial wave function $R(r)$, which defined as $R(r) = \frac{U(r)}{r}$ is obtained as:

$$R_{ln}(r) = B_n r^L e^{-\frac{ze^2}{(L+n+1)}r}\ L_n^{2L+1}\left(\frac{2ze^2}{(L+n+1)}r\right). \tag{33}$$

Where, B_n is the normalized constant for orthogonally associated Laguerre polynomial. So, the normalized constant equal

$$B_n\ = \sqrt{\frac{n!}{\Gamma(2L+n+2)}\ \frac{A^{2L+3}}{\{2n+2L+2\}}} \tag{34}$$

Substituting equation (34) to write the final form of radial Schrodinger equation

$$R_{nl}(r) = \sqrt{\frac{n!}{\Gamma(2L+n+2)}\ \frac{\left(\frac{2ze^2}{(L+n+1)}\right)^{2L+3}}{2\{n+L+1\}}} (r)^L e^{-\frac{\frac{2ze^2}{(L+n+1)}}{2}r}\ L_n^{2L+1}\left(\frac{2ze^2}{(L+n+1)}r\right) \tag{35}$$

The Angular Schrodinger Equation

Now, to determine the angular wave function $H(x)$; compare equation (7) with equation (9) to obtain

$$\check{\tau}\,(x) = -2x \tag{36-a}$$

$$\sigma(x) = 1 - x^2 \tag{36-b}$$

$$\check{\sigma}\,(x) = -v`x^2 + v` - m`^2 \tag{36-c}$$

Substitute equations $(36-a)$, $(36-b)$and $(36-c)$ into (13), then one can conclude $\pi(x)$:

$$\pi(x) = \pm\sqrt{(v`-k)x^2 - v` + m`^2 + k} \tag{37}$$

following the NU-method technic, both values of constant k.

$$k_1 = v` - m`^2\ ,\ k_2 = v` \tag{38}$$

So, the values of parameter $\pi(x)$ giving by;

$$\pi_{11}(x) = \sqrt{(m`^2)x^2} = m`x \tag{39-a}$$

$$\pi_{12}(x) = -\sqrt{(m`^2)x^2} = -m`x \tag{39-b}$$

$$\pi_{21}(x) = \sqrt{m`^2} = m` \tag{39-c}$$

$$\pi_{22}(x) = -\sqrt{m`^2} = -m` \tag{39-d}$$

Substituting the four values of $\pi(x)$ into equation (14) and equation (36-a), we obtain $\tau(z)$; where $\tau`_2(r) < 0$

$$\tau_2(x) = -2x - 2m`x \tag{40}$$

We have obtained the constants λ and λ_n from the equations (14) and (16) respectively.

$$\lambda = v` - m`^2 - m \tag{41}$$

$$\lambda_n = -n(-2 - 2m`) + n(n-1) \tag{42}$$

Comparing equation (41) with equation (42), we get:

$$l` = -\tfrac{1}{2} + \tfrac{1}{2}\sqrt{1 + 4\left\{n + \sqrt{m^2 + 2\beta}\right\}\left(n + \sqrt{m^2 + 2\beta} + 1\right)\Big\}} \tag{43}$$

Now, depending on the upon result we return to use equations (15) and (17) to determine the function $\phi(r)$ and weight function $\rho(r)$

$$\frac{\phi`(x)}{\phi(x)} = \frac{-m`x}{1-x^2}$$

$$\frac{\rho`(r)}{\rho(r)} = \frac{\{-2x(1+m`)+2x\}}{1-x^2}$$

By integration the above equations we get;

$$\phi(x) = (1-x^2)^{\frac{m`}{2}} \tag{44}$$

$$\rho(x) = (1-x^2)^m \tag{45}$$

Now we can determine the polynomial $X_n(r)$ by equation (18) and (45).

$$X_n(x) = B_n(1-x^2)^{-m`} \ \frac{d^n}{dx^n}[(1-x^2)^{m`} \ (1-x^2)^n] \tag{46}$$

And by using $H(x) = X_n(x)\,\phi(x)$ that are defined by equations (46) and (44) and where

$$n + m` = l`$$

$$H_n(x) = (-1)^{l`}B_n\,(1-x^2)^{-\frac{m`}{2}} \ \frac{d^{l`-m`}}{dx^{l`-m`}}[(x^2-1)^{l`}] \tag{47}$$

By use some relations in associated Legendre polynomials

$$p_l^{-m`} = \frac{(-1)^{m`}}{2^l\,l!}(1-x^2)^{-\frac{m`}{2}}\,\frac{d^{l-m`}}{dx^{l-m`}}(x^2-1)^l = (-1)^{m`}\frac{(l-m`)!}{(l+m`)!}\,p_l^{m`}(x)$$

$$\frac{d^{l-m`}}{dx^{l-m`}}(x^2-1)^l = (-1)^{m`}\frac{(l-m`)!}{(l+m`)!}\,(1-x^2)^{m`}\ \frac{d^{l+m`}}{dx^{l+m`}}(x^2-1)^l \tag{48}$$

Now apply the equation (48) into equation (47);

$$H_n(x) = (-1)^{l`}B_n(1-x^2)^{-\frac{m`}{2}}\left\{c_{lm}(1-x^2)^{m`}\ \frac{d^{l+m`}}{dx^{l+m}}(x^2-1)^l\right\} \tag{49}$$

Where:

$$c_{lm`} = (-1)^{m`}\frac{(l-m`)!}{(l+m`)!} \tag{50}$$

Where associated Legendre polynomials is giving by equation [13];
So, equation (49) become:

$$H_n(x) = (-1)^{l`}B_n\,c_{lm`}\,\frac{2^l l!}{(-1)^{m`}}\,p_l^{m`}(x) \tag{51}$$

Where the normalization constant is

$$N_{lm`} = (-1)^{l`}B_n\,c_{lm`}\,\frac{2^l l!}{(-1)^{m`}} \tag{52}$$

So $H_n(x)$become $H_n(x) = N_{lm`}\,p_l^{m`}(x)$.
To find the normalized constant, use the normalized condition $\int_{-1}^{1} H_n^2(x)dx = 1$.
By use associated Legendre polynomials orthogonally [13], we get

$$N_{lm`} = \sqrt{\frac{2l+1}{2}\,\frac{(l`-m`)!}{(l`+m`)!}} \tag{53}$$

So, the angular wave function become:

$$H_n(x) = \sqrt{\frac{2l+1}{2}\,\frac{(l`-m`)!}{(l`+m`)!}}\ p_l^{m`}(x)$$

Where associated Legendre polynomials equal;[14]

$$p_l^{m`}(x) = (1-x^2)^{\frac{m`}{2}}\sum_{v=0}^{\frac{l`-m`}{2}}\frac{(-1)^v\Gamma(2l`-2v+1)}{2^{l`}v!\,(l`-m`-2v)!\,\Gamma(l`-v+1)}\,x^{l`-m`-2v}$$

So, after replacing $x = \cos\theta$ the angular wave function equal;

$$H_n(x) = \sqrt{\frac{2l+1}{2}\frac{(l`-m`)!}{(l`+m`)!}}\,\sin^{m`}\theta \times \sum_{v=0}^{\frac{l`-m`}{2}} \frac{(-1)^v \Gamma(2l`-2v+1)}{2^{l`} v!(l`-m`-2v)!\Gamma(l`-v+1)}\,(\cos\theta)^{l`-m`-2v} \tag{54}$$

The Azimuthal Wave Function

From equation (8) we can easily determine the azimuthal part equation [15]:

$$\phi(\varphi) = \frac{1}{\sqrt{2\pi}} e^{-im\varphi} \tag{55}$$

by including the equations (35), (54) and (55), then the total wave function $\psi(r,\theta,\varphi)$ can be expressed as:

$$\psi(r,\theta,\varphi) = \sqrt{\frac{n!}{\Gamma(2L+n+2)}\frac{\left(\frac{2ze^2}{(L+n+1)}\right)^{2L+3}}{2\{n+L+1\}}}\,(r)^L e^{-\frac{\frac{2ze^2}{(L+n+1)}}{2}r}\, L_n^{2L+1}\left(\frac{2ze^2}{(L+n+1)}r\right) \times$$
$$\sqrt{\frac{2l+1}{2}\frac{(l`-m`)!}{(l`+m`)!}}\,\sin^{m`}\theta \sum_{v=0}^{\frac{l`-m`}{2}} \frac{(-1)^v \Gamma(2l`-2v+1)}{2^{l`} v!(l`-m`-2v)!\Gamma(l`-v+1)}\,(\cos\theta)^{l`-m`-2v} \times \frac{1}{\sqrt{2\pi}} e^{-im\varphi} \tag{56}$$

CONCLUSIONS

The total wave function and bound state energy using Hartmann potential are determined explicitly where they show a great similarity with other studies. The total wave function depends firstly, on associated Laguerre functions in the radial part, secondly, on the value of cosine in the angular part, and lastly, on the exponential function in the azimuthal part. The number of states n and quantum numbers l, m are also appeared and established.

ORCID ID

Abdulrahman N. Akour, https://orcid.org/0000-0002-9026-4098

REFERENCES

[1] G.G. Blado, Theor. Chim. Acta, **94**, 53 (1996). https://doi.org/10.1007/BF00190155
[2] C. Chang-Yuan, L. U. Fa-Lin, and S. Dong-Sheng. Theor. Phys. **45**, 889 (2006).
[3] C. Quesne, J. Phys. A: Math. Gen. **21**, 3093 (1988). https://doi.org/10.1088/0305-4470/21/14/010
[4] C.Y. Chen, and S.H. Dong, Physics Letters, Section A: General, Atomic and Solid-State Physics, **335**(5–6), 374 (2005). https://doi.org/10.1016/j.physleta.2004.12.062
[5] D. Griffiths, and D.F. Schroeter, *Introduction to quantum mechanics*, 3rd ed, (United Kingdom, 2018), pp. 172-175.
[6] S.P. Singh, European J. of Physics Education, **10**(4), 1309 (2019). https://typeset.io/pdf/solving-hydrogen-atom-problem-using-spherical-polar-1ml17d8yfi.pdf
[7] A.F. Nikiforov, and V.B. Uvarov. *Special Functions of Mathematical physics*, (Birkhäuser Verlag, Basel 1988), pp.1-20.
[8] C. Berkdemir, *Application of the Nikiforov-Uvarov Method in Quantum Mechanics: a Unified Introduction with Applications*, edited by M.R. Pahlavani, (Pennsylvania State University, USA, 2012), https://doi.org/10.5772/33510
[9] M. Abusini, M. Serhan, M.F. Al-Jamal, A. Al-Jamel, and E.M. Rabei, Pramana - Journal of Physics. **93**, 93 (2019), https://doi.org/10.1007/s12043-019-1860-x
[10] H. Mansour, and A. Gamal. Advance In High Energy Physics, **2018**, 7269657 (2018). https://doi.org/10.1155/2018/7269657
[11] M. Abu-Shady. International Journal of Modern Physics A, **34** (31), 1950201 (2019), https://doi.org/10.1142/S0217751X19502014
[12] I.B. Okon, O. Popoola, and C.N. Isonguyo, Advances in High Energy Physics, **2017**, Article 9671816 (2017), https://doi.org/10.1155/2017/9671816
[13] M.R. Spiegel, S. Lipschutz, and J. Liu, *Mathematical Handbook of Formulas and Tables*, 3rd ed, (McGraw-Hill, 2008)
[14] C.Y. Chen, F.L. Lu, D.S. Sun, Y. You, and S.H. Dong, Appl Math. Lett. **40**, 90 (2015). https://doi.org/10.1016/j.aml.2014.10.001
[15] A.D. Antia, C.C. Eze, and L.E. Akpabio, Physics & Astronomy International Journal, **2** (3), 187 (2018), https://doi.org/10.15406/paij.2018.02.00084

Appendix (I)

$$\frac{d^2U(r)}{dr^2} + \left[2E + 2\frac{\alpha}{r} - \frac{\lambda}{r^2}\right]U(r) = 0$$

$$\lambda = l`(l` + 1) - 2\beta \tag{1}$$

$$\beta = \frac{m`^2 - m^2}{2} \tag{2}$$

$$L = \frac{1}{2}\left\{\sqrt{1 + 4\left[\left(k + \sqrt{2\beta + m^2}\right)\left(k + \sqrt{2\beta + m^2} + 1\right) - 2\beta\right]} - 1\right\}$$

Substation equation (2) into equation (1):

$$\lambda = l`(l` + 1) - m`^2 + m^2 \tag{3}$$

Let $l` = k + m`$

$$k = l` - m`$$

From equation (2), we get:

$$2\beta + m^2 = m`^2$$

From equation (3), we get:

$$\lambda = k^2 + 2km` + m`^2 + k + m` + l` - m`^2 + m^2$$

$$\lambda = k^2 + 2k\sqrt{2\beta + m^2} + \sqrt{2\beta + m^2} + 2k + \sqrt{2\beta + m^2} + m^2$$

$$\lambda = k^2 + 2k\sqrt{2\beta + m^2} + 2\sqrt{2\beta + m^2} + 2k + m^2$$

To proof $L(L + 1) = \lambda$, we use Some simple calculations.

$$L^2 + L = \lambda$$

$$\frac{1}{4}\left\{\sqrt{1 + 4\left[\left(k + \sqrt{2\beta + m^2}\right)\left(k + \sqrt{2\beta + m^2} + 1\right) - 2\beta\right]} - 1\right\}^2 + \frac{1}{2}\left\{\sqrt{1 + 4\left[\left(k + \sqrt{2\beta + m^2}\right)\left(k + \sqrt{2\beta + m^2} + 1\right) - 2\beta\right]} - 1\right\} = \lambda \tag{4}$$

The value that under square root in equation (4):

$$\left(k + \sqrt{2\beta + m^2}\right)\left(k + \sqrt{2\beta + m^2} + 1\right) = k^2 + 2km` + k + m`^2 + m`$$

Equation (4) become:

$$\frac{1}{4}\left\{\sqrt{1 + 4[k^2 + 2km` + k + m`^2 + m` - 2\beta]} - 1\right\}^2 + \frac{1}{2}\left\{\sqrt{1 + 4[k^2 + 2km` + k + m`^2 + m` - 2\beta]} - 1\right\} = \lambda$$

After use equation (2), we get:

$$\frac{1}{4}\left\{\sqrt{1 + 4[k^2 + 2km` + k + m`^2 + m` - m`^2 + m^2]} - 1\right\}^2 + \frac{1}{2}\left\{\sqrt{1 + 4[k^2 + 2km` + k + m`^2 + m` - m`^2 + m^2]} - 1\right\} = \lambda \tag{5}$$

Substation equation (1) into equation (5), and simple mathematics.

$$\frac{1}{4}\left\{\sqrt{1 + 4[(l` - m`)^2 + 2(l` - m`)m` + l` + m^2]} - 1\right\}^2 + \frac{1}{2}\left\{\sqrt{1 + 4[(l` - m`)^2 + 2(l` - m`)m` + l` + m^2]} - 1\right\} = l`(l` + 1) - m`^2 + m^2$$

by expand the Quadratic Arc, we get:

$$\frac{1}{4} + [(l` - m`)^2 + 2(l` - m`)m` + l` + m^2] - \frac{1}{2}\sqrt{1 + 4[(l` - m`)^2 + 2(l` - m`)m` + l` + m^2]} + \frac{1}{4} + \frac{1}{2}\sqrt{1 + 4[(l` - m`)^2 + 2(l` - m`)m` + l` + m^2]} - \frac{1}{2} = l`(l` + 1) - m`^2 + m^2$$

$$\frac{1}{4} + [(l` - m`)^2 + 2(l` - m`)m` + l` + m^2] - \frac{1}{4} = l`(l` + 1) - m`^2 + m^2$$

$$(l` - m`)^2 + 2(l` - m`)m` + l` + m^2 = l`(l` + 1) - m`^2 + m^2$$

$$l^{2`} - 2m`l` + m`^2 + 2l`m` - 2m`^2 + l` + m^2 = l`(l` + 1) - m`^2 + m^2$$

$$l^{2`} + l` - m`^2 + m^2 = l`(l` + 1) - m`^2 + m^2$$

$$l`(l` + 1) - m`^2 + m^2 = l`(l` + 1) - m`^2 + m^2$$

ЗАСТОСУВАННЯ МЕТОДУ НІКІФОРОВА-УВАРОВА ДО РІВНЯННЯ ШРЕДІНГЕРА, З ВИКОРИСТАННЯМ ПОТЕНЦІАЛУ ГАРТМАНА

Махмуд А. Аль-Хавамде[a], Абдулрахман Н. Акур[b], Емад К. Джарадат[a], Омар К. Джарадат[c]

[a]*Фізичний факультет, Університет Мута, Йорданія*

[b]*Департамент фундаментальних наук, коледж Аль-Хусон, прикладний університет Аль-Балка, Йорданія*

[c]*Факультет математики, Університет Мута, Йорданія*

Повна хвильова функція та енергія зв'язаного стану досліджуються методом Нікіфорова-Уварова до рівняння Шредінгера в сферичних координатах з використанням потенціалу Гартмана (HP). HP вважається нецентральним потенціалом, який в основному визнається в потенціалах ядерного поля. Кожна хвильова функція визначається головним квантовим числом n, числом кутового моменту l і магнітним квантовим числом m. Радіальну частину хвильової функції отримано через асоційований поліном Лагерра за допомогою перетворення координат $x = \cos\theta$ для отримання кутової хвильової функції, яка залежить від обернених асоційованих поліномів Лежандра.

Ключові слова: *рівняння Шредінгера; метод Нікіфорова-Уварова; потенціал Гартмана*

East European Journal of Physics. **2.** 124-131 (2023)
DOI:10.26565/2312-4334-2023-2-11 ISSN 2312-4334

ON ACCOUNTING FOR OWN FIELDS OF EMITTERS WHEN DESCRIBING GENERATION MODES[†]

Volodymyr M. Kuklin*, Eugen V. Poklonskiy
V.N. Karazin Kharkiv National University,
Svobody Sq. 4, Kharkiv, Ukraine, 61022
**Corresponding Author: v.m.kuklin@karazin.ua*
Received March 30, 2023; revised April 1, 2023; accepted April 15, 2023

The paper discusses three different modes of electromagnetic field generation by an ensemble of oscillators placed at the radiation wavelength in the one-dimensional case. The excitation of the resonator field is considered, which, as a rule, is determined by the geometry of the system, with and without taking into account the eigenfields of the emitters. The superradiance regime of the same ensemble of oscillators is also analyzed. In fact, superradiance is formed due to the emitters' own fields even in the absence of a resonator. It is noted that the maximum achievable amplitudes of induced fields both in the superradiance regime and in the regime of excitation of the resonator field are comparable. This makes us think about the role of the self-fields of emitters in electronic devices. It is shown that in describing the resonator excitation mode, in addition to the resonator field, it is also necessary to take into account the sum of the natural fields of the emitters in the active zone. Synchronization of emitters leads not only to an increase in the resonator field, but also, as in the superradiance regime, it significantly increases the amplitude of the sum of the oscillator fields. It is shown that in the practically interesting case of open systems (dissipative generation modes), taking into account the eigenfields of the emitters significantly reduces the characteristic time for the development of the generation process and increases the maximum achievable oscillation amplitude. This account also changes the conditions for achieving the maximum energy flow from the system. This can change the operating point of the generation process, which is determined by the requirement for the maximum rate of energy output from the system.
Keywords*: Ensemble of oscillators; Resonator field; Sum of oscillators eigenfields; Resonator field excitation mode; Superradiance excitation mode*
PACS: 03.65.Sq

Introduction

Field generation in waveguides and resonators. The traditional description of the process of generating or amplifying a high-frequency field in waveguides and resonators of electronic devices in a nonlinear mode actually began with work [1], based on the formalism presented there. A significant increase in interest in describing the excitation of oscillations by beams of charged particles and oscillators in waveguide systems has caused numerous publications. The bibliographies of works [2,3] contain material that is very useful for understanding such a description.

The modes with output or loss of energy. The need to take into account absorption, as well as the output of radiation energy from electronic devices, forced us to consider the so-called dissipative generation modes [4-7]. Such modes of generation and amplification in such open (for energy output) systems were of practical interest to the creators of electronic devices. In addition, the analysis of such regimes makes it possible to take into account the effect of different levels of energy extraction on the generation efficiency.

It was in such devices that it was possible to find operating points that ensure the maximum output of energy from the system, as was, in particular, presented in [6,7]. The considered problems were solved under conditions when oscillators (or emitters) in the active zone of waveguides and resonators interacted only with a waveguide or resonator field, the form of which was determined by the geometry of the system. The induced field of the resonator or waveguide synchronized the oscillators due to phase change (or the emitters due to bunching), which led to a significant self-consistent amplification of the field amplitude. Moreover, the interaction of oscillators (or emitters) with each other was usually neglected, excluding their total field from consideration.

Apparently, at first it was believed that due to the spread of phases emitted by particles and oscillators, the intensity of their integral radiation would remain insignificant. On the other hand, it was believed that if the radiation of particles and oscillators is spontaneous, then their total radiation will also remain spontaneous. In other words, this radiation will be much less than the intensity of the waveguide or resonator field, which is obviously induced field. There was also a point of view that the field of emitters in a waveguide or resonator would rather quickly be rebuilt into a set of eigenmodes of waveguides and resonators. It was believed that under these conditions, the self-field of the emitters can be ignored. The last consideration made sense in the case of a single act of radiation by a particle in a waveguide and resonator. Although in the continuous mode, even under conditions of partial rearrangement of the eigenfields of the emitters into waveguide and resonator modes, their total field does not go anywhere and should be taken into account.

At the same time, it was known that the process of phase synchronization of oscillators (or spatial synchronization of emitters), even in the absence of waveguide and resonator fields, led to the regime of superradiance, with induced fields [8].

[†] ***Cite as:*** V.M. Kuklin, and E.V. Poklonskiy, East Eur. J. Phys. **2**, 124 (2023), https://doi.org/10.26565/2312-4334-2023-2-11

The superradiance field arises as a total field of initially spontaneously emitting oscillators even in the absence of a waveguide and a resonator. Obviously, the own field of each oscillator (or emitter) is spontaneous. However, under the influence of the total ensemble field external to each particle, the phase of radiation of this particle can change. If the amplitude of the external field is large compared to the value of the spontaneous field of a given particle, the phase of its own radiation changes. This is the nature of phase synchronization of oscillators (and spatial synchronization of emitters) and the appearance of superradiance (see, for example, [9]).

Recall that the superradiance regime discovered for a compact bunch of particles [10] manifested itself as the appearance of coherence in the study of most emitters and oscillators. This phenomenon was clearly manifested both in the quantum case and in the classical case. In distributed systems of electronics, due to rather large distances between particles, the interaction between them, as a rule, occurs only due to their own electromagnetic fields.

The mechanism of phase synchronization of radiation of an ensemble of classical oscillators was discussed in [9,11,12]. Let us show that this process of phase synchronization of emitters and oscillators in the volume of the active zone of the waveguide, in addition to generating waveguide and resonator fields, can also excite superradiance fields with an intensity comparable to that of the waveguide or resonator field [13, 14].

Accounting for fields of particles. Let us return to the discussion of the processes of excitation and amplification of oscillations by particles in waveguides and resonators. The development of high-current electronics required taking into account slowly changing currents and fields of charged particles in the active zone of the waveguide, which was first pointed out by Ya.B. Fainberg in his work “Plasma electronics”, published in the “Ukrainian journal of physics” in 1978. This was required at first to search for the stability of charged particle beams and systems of oscillators [15]. Later N.I. Karbusev in the early 1980s drew attention to the high-frequency radiation fields of individual emitters and generators.

The question arose about the role of the radiation of particles in the process of generation and amplification of oscillations in waveguides and resonators. For even in the absence of a waveguide and a resonator, the ensemble of these active elements is capable of generating superradiance fields comparable to waveguide and resonator fields [13]. That is, for a correct description of the process of excitation or amplification in such devices, in addition to the waveguide or resonator field, it is important to take into account these own fields of the particles of the active zone.

The purpose of this work is to compare the fields generated by open systems in the cases of 1) excitation of only the resonator field, 2) excitation of only the self-radiation fields of active oscillators, that is, the superradiance field, and 3) joint excitation of the resonator field, taking into account the intrinsic fields of oscillators. Let us show that, in addition to the resonator field, it is necessary to take into account the self-radiation field of oscillators, because it qualitatively affects all characteristics of the oscillation generation mode.

1. The Excitation of the Fields of Oscillators

We discuss the nature of the excitation of the field with a system of oscillators. Consider an oscillator whose charge (electron) moves along the *OX* axis, that is $\vec{r} = (x(t), 0, z_0)$, where $x(t) = i \cdot a \cdot \exp\{-i\omega t + i\psi\}$, at the same time whose speed (electron) $dx/dt = a \cdot \omega_0 \cdot \exp\{-i\omega t + i\psi\}$ is along the *OX* axis, $\mathrm{Re}\, x = a \cdot \sin(\omega_0 t - \psi)$. The current can be recorded as $J_x = -edx/dt = -e \cdot a \cdot \omega_0 \cdot \exp\{-i\omega t + i\psi\}$. The equation describing the excitation of the field with the current of the oscillator

$$\frac{\partial^2 E_x}{\partial z^2} - \frac{1}{c^2}\frac{\partial^2 D_x}{\partial t^2} = \frac{4\pi}{c^2}\frac{\partial J_x}{\partial t} = \frac{4\pi}{c^2} \cdot e \cdot a \cdot \omega_0^2 \cdot i \cdot \exp\{-i\omega t + i\psi\} \cdot \delta(z - z_0), \tag{1}$$

The dielectric permittivity of the medium in the absence of oscillators is taken as equal to one $\varepsilon_0 = 1$. We will look for a solution for the electric field amplitude in the form $\vec{E} = (E \cdot \exp\{-i\omega t + ikz\}, 0, 0)$, i.e. $E_x = E\exp\{-i\omega t + ikz\}$, assuming a slow change of the complex amplitude $E_x(t,z)$:

$$\left|\frac{1}{E_x(t,z)}\frac{\partial}{\partial t}E_x(t,z)\right| << \omega, \quad \left|\frac{1}{E_x(t,z)}\frac{\partial}{\partial z}E_x(t,z)\right| << k\ . \tag{2}$$

Below we consider the excitation of the field of the resonators ensemble, which in our one -dimensional case are evenly distributed in the active zone at the interval equal to the length of the radiation wave. We will discuss three generation regimes of fields by the oscillator ensemble.

The first mode of excitation of the resonator field (or waveguide) meets the traditional description of the generation (or amplification) in electronics devices, when all oscillators (emitters) interact only with the resonator field, which houses an active zone. The interaction of the oscillators in this case will exclude. That is, we do not take into account the own fields of emitters in the active zone. The conclusion of the equations describing this process is given in Appendix 1.

The second mode of excitation of the field with the emitters ensemble takes into account only the own fields of emitters located in the same interval of the active zone, and there is no resonator field in this case. It is not difficult to

see that this process meets the superradiation regime. By the way, at the same time, a resonator or waveguide in this case may be completely absent. The withdrawal of equations to describe such a process is considered in Appendix 2.

And the third regime of excitation of oscillations with oscillators takes into account both the resonator (waveguide) field and the amount of its own fields of particles. It is this case that meets the correct description of the excitation of oscillations in resonators and waveguides.

In further calculations, the number of oscillators is chosen $N = 1000$. The initial amplitude of the external field in expressions (6) and (11) is equal 0.01, accounting for non -linearity (relativism) is determined by a coefficient $\alpha = 1$.

2. The Excitation of The Resonator Field with The Exclusion of The Interaction of The Oscillators To Each Other

In the traditional description of generation, all oscillators interact only with the resonator field, in which an active zone is located. Oscillators do not interact with each other. We use equations in a dimensionless form (see Appendix 1) that describe this process. The resonator field in this case can be represented in the form of the sum of two waves that spread in opposite directions

$$\mathrm{E}_{wg}(Z,\tau) = \mathrm{E}_{+}(\tau)e^{i2\pi Z} + \mathrm{E}_{-}(\tau)e^{-i2\pi Z}, \tag{3}$$

Moreover, the components of radiation in different directions can be recorded

$$\frac{\partial \mathrm{E}_{+}}{\partial \tau} + \Theta \mathrm{E}_{+} = \frac{1}{N}\sum_{s} \mathrm{A}_{s} \cdot e^{-i2\pi Z_{s}}, \tag{4}$$

$$\frac{\partial \mathrm{E}_{-}}{\partial \tau} + \Theta \mathrm{E}_{-} = \frac{1}{N}\sum_{s} \mathrm{A}_{s} \cdot e^{i2\pi Z_{s}}, \tag{5}$$

At the initial moment we should set their value

$$\mathrm{E}_{+}(0) = \mathrm{E}_{0+} \text{ and } \mathrm{E}_{-}(0) = \mathrm{E}_{0-}. \tag{6}$$

Movement equations for oscillators take the form

$$\frac{d\,\mathrm{A}_{j}}{dt} = \frac{i\alpha}{2} \cdot \left|\mathrm{A}_{j}\right|^{2} \mathrm{A}_{j} - \mathrm{E}_{wg}(Z_{j},\tau). \tag{7}$$

For this case of excitation of the resonator field, excluding the fields of the oscillators, the field intensity $\propto |E|^2$ (continuous line), the reverse time (increment) $\gamma = \left(\frac{1}{|E|^2}\frac{d|E|^2}{d\tau}\right)_{\max}$ of the process (stroke-dashed), and the rate of energy output $\Theta |E|^2$ (dashed) are presented in Fig. 1 (a). If you focus on the excitation regime of the resonator field without taking into account its fields of the oscillators, then the most effective output of energy would occur in the area of about $\Theta = 3$ (see also [6]).

3. The Excitation of The Same Oscillators Ensemble

In this section, we take into account only the own fields of oscillators located in the same interval of the active zone. The resonator field is absent, like the resonator itself. The dimensionless system of equations in this case (see Appendix 2) takes the following form. For fields are fair the form

$$\mathrm{E}_{sr}(Z,\tau) = \frac{1}{\Theta N}\sum_{s=1}^{N} \mathrm{A}_{s} \cdot e^{i2\pi|Z-Z_{s}|}, \tag{8}$$

And the equations of movement describing the dynamics of the oscillators can be recorded as

$$\frac{d\,\mathrm{A}_{j}}{dt} = \frac{i\alpha}{2} \cdot \left|\mathrm{A}_{j}\right|^{2} \mathrm{A}_{j} - \mathrm{E}(Z_{j},\tau), \tag{9}$$

where for a common field the expression is true

$$\mathrm{E}(Z,\tau) = \mathrm{E}_{sr}(Z,\tau) + \mathrm{E}_{ex}(Z,\tau), \tag{10}$$

Moreover, the second term in (10) is an external field that is usually used to accelerate the process in the form.

$$\mathrm{E}_{ex}(Z,\tau)=\mathrm{E}_{0+}\,e^{i2\pi Z}+\mathrm{E}_{0-}\,e^{-i2\pi Z}\,. \tag{11}$$

For the field intensity $\propto|E|^2$ (continuous line), the reverse time $\gamma=\left(\frac{1}{|E|^2}\frac{d|E|^2}{d\tau}\right)_{\max}$ (increment) of the process (strokh- dashed), energy withdrawal $\Theta|E|^2$ (dashed) are presented in Fig. 1 (b). The most effective output of energy would be near the values Θ = 2.5-3, and with an output one and a half times larger than in the case of an excitation only the resonator field.

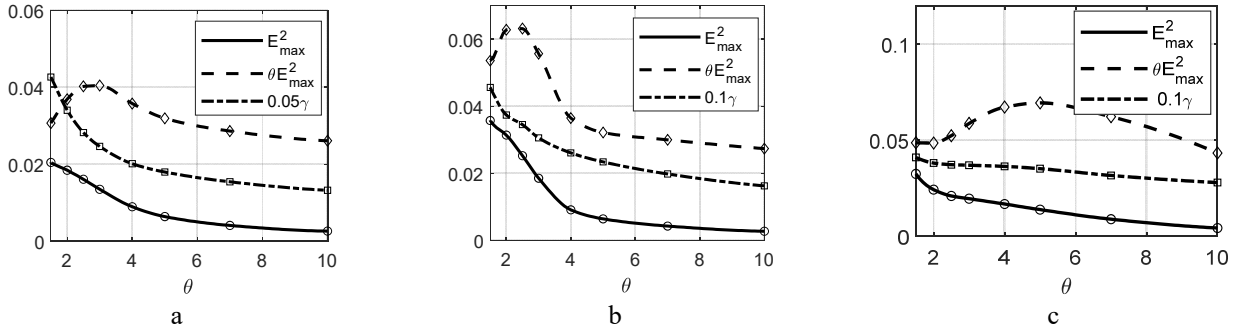

Figure 1. Field intensity $\propto|E|^2$ (continuous line), the reverse time (incremental) of the process γ (stroke-dashed), the rate of energy output $\Theta|E|^2$ (dashed) as function of energy loss Θ for cases: (a) of the generation of the resonator field, excluding the oscillator radiation field, (b) of the supperradiation mode, (c) the generation of the resonator field together with the radiation field of the oscillators.

4. The Excitation of the Resonator Field When Taking into Account the Interaction of Oscillators to Each Other

Using the entered variables and the expressions obtained in the applications for the fields, you can represent the system of equations for the excitation of the resonator, and we will additionally take into account the total field of oscillators. It is clear that thereby it is possible to take into account the direct interaction of the oscillators with each other. Here you cannot take into account the external initial field (11), the role of which will be assumed by the resonator field (4)-(5). The equation of motion for oscillators can be written in the form

$$\frac{d\,\mathrm{A}_j}{dt}=\frac{i\alpha}{2}\cdot\left|\mathrm{A}_j\right|^2\mathrm{A}_j-\mathrm{E}(Z_j,\tau)\,. \tag{12}$$

Here, the resonator field and the total field of radiation of the oscillators are simultaneously taken into account $\mathrm{E}(Z,\tau)=\mathrm{E}_{sr}(Z,\tau)+\mathrm{E}_{wg}(Z,\tau)$, where $\mathrm{E}_{wg}(Z,\tau)$ it is described by expressions (3-5), and $\mathrm{E}_{sr}(Z,\tau)$ by expression (8). The initial conditions for the fields of the resonator will choose the same (6). The nature of the excitation of the resonator field, taking into account the own fields of the oscillators, the field intensity $\propto|E|^2$ (continuous line), the reverse time (increment) of the process $\gamma=\left(\frac{1}{|E|^2}\frac{d|E|^2}{d\tau}\right)_{\max}$ (stroke-dashed), the rate of energy output $\Theta|E|^2$ (dashed) are represented in Fig. 1 (c).

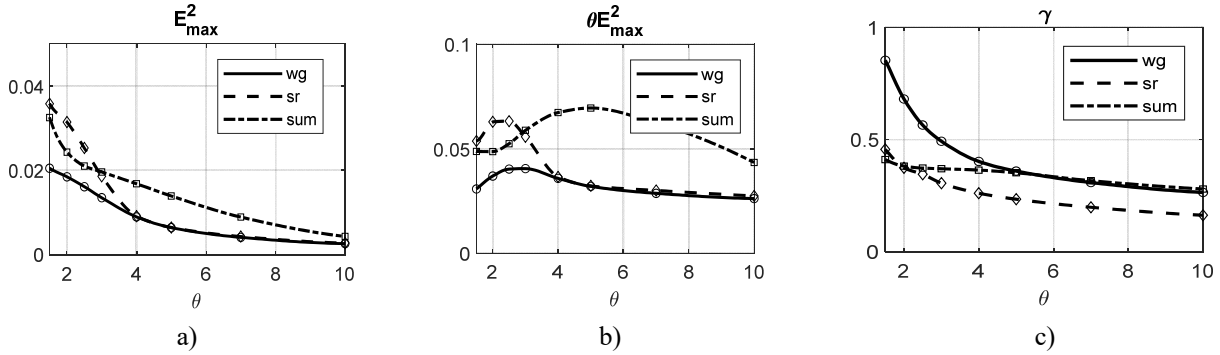

Figure 2. Dependence on the level of energy loss Θ : (a) - the square of the field amplitude $\propto|E|^2$, (b) - the rate of energy output $\Theta|E|^2$, (c) - the inverse time (increment) of the process $\propto\left(\frac{1}{|E|^2}\frac{d|E|^2}{dt}\right)$. Here are cases: the generation of the resonator field, excluding the oscillator radiation field (continuous line), the superradiation mode (stroke-dashed), and the generation of the resonator field together with the radiation field of the oscillators (dashed).

It can be seen here that joint accounting for the excitation of the resonator field and the oscillator field leads to a noticeable increase in energy selection, and for large values about $\Theta = 5$.

5. Comparison of Three Modes

Consider three modes. A solid line on the graphs marks the resonator regime without taking into account the impact on the process of generating oscillators fields, The superradiation mode is represented by dashed lines on the graphs, and the strokh- dashed line on the graphs is responsible for the case of excitation of the resonator, taking into account the influence of the fields of the oscillators.

In the mode of excitation of the resonator, taking into account fields of emitters, the field intensity and output of energy are the highest. A slightly inferior to him is the superradiation mode. The working points (the rate of energy output from the system that meets the maximum), are realized for different values Θ. But the working point, for resonators, where we taking into account fields of oscillators is shifted in the large values of Θ .The characteristic times of the process near the highest energy output is half as much as for resonator which don't taking into account the of the own fields of the oscillators.

6. Conclusion

Three different generation modes of the electromagnetic field are discussed for the oscillators ensemble, placed on the length of the radiation wave. The consideration is carried out for an open system, which is characterized by the output of energy from the system. The parameter of the degree of openness is a value that is determined by the ratio of the attenuation to the value of the reverse characteristic time of the process (increment) in the absence of losses. The following generation modes are considered.

1. The generation of an open resonator, excluding own fields of oscillators - emitters.
2. The superradiation mode - the generation of the field in the open system of the same ensemble of the oscillators without resonator.
3. The excitation of an open resonator, taking into account the own fields of oscillators emitters.

The superradiation regime, which is of independent interest, demonstrates the nature of the synchronization of emitters (see Appendix 2). The superradiation, as you know, arises due to its own fields of emitters even in the absence of a resonator. As a result of the phase synchronization of fixed oscillators, an integral field is formed, which is not spontaneous, but induced field. It is this field that synchronizes the noticeable part of the emitters. It is important that the total field intensity of the is exceeds the intensity of the own field of emitter. Although the distributed system does not allow synchronizing all the oscillators, especially in areas where the total field of the ensemble is small.

Accounting for own radiation of the oscillators significantly reduces the characteristic time of the development of the generation process in resonators and waveguide, increases the most achievable amplitude of oscillations. At the same time, the conditions for achieving the maximum energy flow from the system also change. This is able to significantly shift the work point of the generation process, determined, for example, by the requirement of the maximum pace of energy output from the system.

In conclusion, the authors express gratitude to V.A. Buts, V.V. Yanovsky and A.V. Kirichok for a constructive discussion of the results of the work.

Appendix 1. The Field of Resonator

In the resonator (or waveguide), the field can be formed in such a way that the type of field will not depend on the radiation of individual oscillators. Note that such a field generally speaking should consist of running waves in two directions

$$E_x = E_+ \cdot \exp\{-i\omega t + ikz\} + E_- \cdot \exp\{-i\omega t - ikz\}, \tag{A1}$$

where the slowly changing complex amplitude of the waves has the form $E_\pm = | E_\pm | \cdot \exp\{i\varphi_\pm\}$.

The interaction of oscillators with these fields can be described by the equation [9,13]

$$2i\omega_0 \left(\frac{\partial E_\pm}{\partial t} + \delta_D \right) = -e\omega^2{}_0 \frac{4\pi n_0}{N \cdot 2i} \int a_s dz \cdot \exp\{i\psi_s \mp ikz\} \cdot \delta(z - z_s), \tag{A2}$$

where added δ_D - the decrement of the absorption of the wave in the absence of sources, $A_j = a_j \exp(i\psi_j)$.

The equations of the movement will present in the form

$$\frac{d}{dt} \frac{v_i}{\sqrt{1 - \frac{|v_i|^2}{c^2}}} + \omega_0{}^2 x_i = -\frac{e}{m} E_x(z_i, t) \tag{A3}$$

where $x_i(t) = i \cdot a_i \cdot \exp\{-i\omega t + i\psi\} = iA \cdot \exp\{-i\omega t\}$, $v_i = \omega \cdot a_i \cdot \exp\{-i\omega t + i\psi\} = \omega A \cdot \exp\{-i\omega t\}$.

We further assume that the resonator has size *b*, equal to wavelength (without loss of generality the results are generalized to the case of several wavelengths), group velocity of radiation *c*, effective decrement of field damping equals $\delta_D = c/b$, number of oscillators equal to $M = b \cdot n_0$.

Equation (A2) for slowly varying amplitudes then takes the form

$$\frac{\partial E_{\pm}(t)}{\partial t} + \delta_D E_{\pm}(t) = \frac{2\pi \cdot e \cdot \omega \cdot M}{b} \frac{1}{N} \sum_s A_s \cdot \exp(\mp ikz_s) = 2\pi \cdot e \cdot \omega \cdot n_0 \cdot \frac{1}{N} \sum_s A_s \cdot \exp(\mp ikz_s)\,. \tag{A4}$$

The equation of motion (A3) can be represented as

$$\frac{dA_j}{dt} = \frac{i\omega\alpha_1}{2} \cdot A_j(t) - \frac{e \cdot E_{wg}(t, z_j)}{2 \cdot \omega \cdot m}, \tag{A5}$$

$$E_{wg}(t,z) = E_+ \cdot \exp(ikz) + E_- \cdot \exp(-ikz)\,. \tag{A6}$$

Here $E_{wg}(t,z)$ is the resonator field, the parameter $\alpha_1 = 3|A|^2 k^2 / 4$ takes into account the weak dependence of the relativistic mass of the particle on speed.

Choosing dimensionless variables and parameters

$$\mathrm{A} = A / a_0, \quad kz = 2\pi Z, \quad \gamma_0 = \omega_{pe}/2, \quad \gamma_0^2 = \omega_{pe}^2/4 = \frac{\pi n e^2}{m}, \quad \gamma_0 t = \tau, \quad \beta = m/m_1, \quad kb = 2\pi\bar{b},$$

$$\delta = \frac{c}{b}, \quad \Theta = \delta/\gamma_0, \quad E_{01} = \frac{2m \cdot \gamma_0 \cdot \omega \cdot a_0}{e}, \quad \mathrm{E} = E/E_{01}, \qquad \alpha = \frac{3\omega}{4\gamma_0}(ka_0)^2,$$

we get an expression for the resonator field an expression

$$\mathrm{E}_{wg}(Z,\tau) = \mathrm{E}_+(\tau) e^{i2\pi Z} + \mathrm{E}_-(\tau) e^{-i2\pi Z}\,. \tag{A7}$$

where the components corresponding to spreading of radiation in different directions can be written as

$$\frac{\partial \mathrm{E}_+}{\partial \tau} + \Theta \mathrm{E}_+ = \frac{1}{N} \sum_s \mathrm{A}_s \cdot e^{-i2\pi Z_s}, \tag{A8}$$

$$\frac{\partial \mathrm{E}_-}{\partial \tau} + \Theta \mathrm{E}_- = \frac{1}{N} \sum_s \mathrm{A}_s \cdot e^{i2\pi Z_s}, \tag{A9}$$

moreover, at the initial moment you should set their values

$$\mathrm{E}_+(0) = \mathrm{E}_{0+} \text{ and } \mathrm{E}_-(0) = \mathrm{E}_{0-}\,. \tag{A10}$$

Movement equations for oscillators take the form

$$\frac{d\,\mathrm{A}_j}{dt} = \frac{i\alpha}{2} \cdot \left|\mathrm{A}_j\right|^2 \mathrm{A}_j - \mathrm{E}_{wg}\left(Z_j, \tau\right). \tag{A11}$$

We can get the law of conservation of energy in the form

$$\left(\frac{\partial}{\partial \tau} + 2\theta\right)\left\{|\,\mathrm{E}_+\,|^2 + |\,\mathrm{E}_-\,|^2\right\} = 2\frac{\partial}{\partial \tau} \sum_{j=1}^{N} |\,\mathrm{A}_j\,|^2 \tag{A12}$$

Appendix 2. Description of the Superraiation Mode

Generally speaking, the field excited in the system of oscillators consists of the sum of all fields of individual oscillators. Consider the superradiation mode when the resonator field or a waveguid field is absent. It is also possible to determine the total field of radiation of oscillators in the same volume, as presented in Appendix 1. An important circumstance is the conditions for synchronization of the oscillators. It turns out, as noted, for example, in the work of Yu.A. Il'inskii, and N.S. Maslova, “Classical analog of superradiance in a system of interacting nonlinear oscillators” published in 1988, that only when the nonlinearity of oscillators is taken into account in this case, it becomes possible to ensure phase synchronization of the field and the oscillator (see also [11]).

The field of one oscillator. For the amplitude of the radiation field slowly changing in the space, the equation is fair

$$\frac{\partial E}{\partial z} = 2ea\omega^2 \frac{\pi}{c^2 k} \cdot \exp\{i\psi + ikz\} \cdot \delta(z - z_0) = \lambda \cdot \delta(z - z_0)\,. \tag{A13}$$

Chose solution is form of $E = C + \lambda \cdot \theta(z - z_0)$ where $\theta(\mathrm{z} < 0) = 0, \quad \theta(\mathrm{z} \geq 0) = 1$. Since for the wave radiated by the oscillator the equation $D(\omega, k) \equiv (\omega^2 \varepsilon_0 - k^2) = 0$, the roots of which $k_{1,2} = \pm(\omega_0 \operatorname{Re}\varepsilon_0 / c)(1 + i \operatorname{Im}\varepsilon_0 / \operatorname{Re}\varepsilon_0) \approx$ $\approx \pm(\omega_0 / c\varepsilon_0)(1 + i0)$, for the wave, which propagates in the direction $Z > Z_0$, the wave number is equal $k = k_1 > 0$ and the value of the constant C should be selected equal to zero in order to avoid unlimited growth of the field at infinity. For a wave which propagates in the direction $Z < Z_0$, the wave number is equal $k = k_2 < 0$, the value of constant C in the same reasons should be selected equal $-\lambda$. The amplitude of the electric field while

$$E_x = 2\pi e a \omega_0 M \cdot c^{-1} \exp\{-i\omega t + i\psi\}[\exp\{ik_0(z - z_0) \cdot \theta(z - z_0) + \\ + \exp\{-ik(z - z_0) \cdot \theta(z - z_0)\} \tag{A14}$$

For one particle in such a volume of a single section and the length of the resonator *b*, *M* it is numerically equal to one. The equation of motion for the oscillating electron has the form (A3).

The particle ensemble field. Using these designations, we will write particle ensemble field in the form

$$\frac{dA_j}{dt} - i\frac{|3A_j|^2 \cdot \omega^3}{4c^2} A_j + i\frac{|3A_{j0}|^2 \cdot \omega^3}{4c^2} A_{j0} = \\ = -\frac{\pi \cdot e^2 \cdot M}{mc} \cdot \frac{1}{N} \sum_{s=1}^{N} A_s \left(e^{ik(z_j - z_s)} \cdot \theta(\mathrm{z}_j - \mathrm{z}_s) + e^{-ik(z_j - z_s)} \cdot \theta(\mathrm{z}_s - \mathrm{z}_j) \right) . \tag{A15}$$

Let choose dimensionless variables and parameters

$$\mathrm{A} = A / a_0, \quad kz = 2\pi Z, \quad \gamma_0 = \omega_{pe} / 2, \quad \gamma_0^2 = \omega_{pe}^2 / 4 = \frac{\pi n e^2}{m}, \quad \gamma_0 t = \tau, \quad \beta = m / m_1, \quad kb = 2\pi \bar{b},$$

$$\delta = \frac{c}{b}, \quad \Theta = \delta / \gamma_0, \quad E_{01} = \frac{2m \cdot \gamma_0 \cdot \omega \cdot a_0}{e}, \quad \mathrm{E} = E / E_{01}, \quad \alpha = \frac{3\omega}{4\gamma_0} (ka_0)^2 .$$

Let consider the excitation of the field in the resonator, the size of which b, equal to the wavelength (without losing community, the results are generalized in case of several wavelengths) group radiation speed *c*, and the effective decrement of the fading of the field is equal $\delta = \frac{c}{b}$. If you take into account radiation from the system (which, due to the small size of the system, can be considered distributed), then the increment of the process $\gamma \approx \gamma_0^2 / \delta = \gamma_0 / \Theta$, and $\delta > \gamma_0$. It should be noted that in all cases under discussion, due to the selected placement of the ensemble of the oscillators, the the increment of the regime without energy loss $\Theta = 0$ is equal γ_0 [13]. One gets the expression for the superradiation field

$$\mathrm{E}_{sr}(Z, \tau) = \frac{1}{\Theta N} \sum_{s=1}^{N} \mathrm{A}_s \cdot e^{i2\pi |Z - Z_s|} , \tag{A16}$$

moreover, the equation of movement describing the dynamics of the oscillators takes the form

$$\frac{d\,\mathrm{A}_j}{d\tau} = \frac{i\alpha}{2} \cdot |\mathrm{A}_j|^2 \mathrm{A}_j - \mathrm{E}(Z_j, \tau) \tag{A17}$$

where for a common field the expression is true

$$\mathrm{E}(Z, \tau) = \mathrm{E}_{sr}(Z, \tau) + \mathrm{E}_{ex}(Z, \tau) . \tag{A18}$$

The second term in (A18) is an external stimulation field that is often necessary to accelerate the process can be recorded as

$$\mathrm{E}_{ex}(Z, \tau) = \mathrm{E}_{0+} e^{i2\pi Z} + \mathrm{E}_{0-} e^{-i2\pi Z} . \tag{A19}$$

The nature of the synchronization of the oscillators in this and other regimes is quite obvious [13]. Let return back to equation (A17), which can be recorded differently

$$\frac{d\left[|\mathrm{A}_j| \exp(i\psi_j) \right]}{dt} = \frac{i\alpha}{2} \cdot |\mathrm{A}_j|^2 |\mathrm{A}_j| \cdot \exp(i\psi_j) - |\mathrm{E}(Z_j, \tau)| \cdot \exp(i\varphi) . \tag{A20}$$

Then the equation for the oscillator phase, which follows from (A20), takes the form

$$\frac{d\psi_j}{dt}-\frac{\alpha}{2}\cdot\left|\mathrm{A}_j\right|^2=-\left\{\left|\mathrm{E}\left(Z_j,\tau\right)\right|\Big/\left|\mathrm{A}_j\right|\right\}\cdot\sin\left(\varphi-\psi_j\right). \tag{A21}$$

You can pay attention to the fact that the right part of the last equation is quite large $\left|\mathrm{E}\left(Z_j,\tau\right)\Big/\mathrm{A}_j\right|\gg 1$. This forces the phase of a separate oscillator to synchronize with the phase of the total field of the ensemble $\psi_j\to\varphi$. The value $0.5\cdot i\alpha\cdot\left|\mathrm{A}_j\right|^2$ gives regularisation, i.e. a certain spread of phase values.

ORCID IDs

Volodymyr Kuklin, https://orcid.org/0000-0002-0310-1582; **Eugen Poklonskiy,** https://orcid.org/0000-0001-5682-6694

References

[1] A. NordSieck, "Theory of large Signal Behavior of Travelingwave amplifiers," Proc. IRE, **41**(5), 630-631 (1953). https://doi.org/10.1109/JRPROC.1953.274404

[2] V.D. Shapiro, and V.I. Shevchenko, "Interaction of a wave-part in nonequilibrium media," Radiophysics and Quantum Electronics, **19**, 543-560 (1976). https://link.springer.com/article/10.1007/BF01034470

[3] A.N. Kondratenko, and V.M. Kuklin, *Fundamentals of plasma electronics*, (Energoatomizdat, Moscow, 1988). https://www.researchgate.net/publication/367500092_Osnovy_Plazmennoj_Elektroniki

[4] R.J. Briggs, *Electron-Stream Intection with Plasmas*, (MIT Press, Cambridge, 1964).

[5] V.U. Abramovich, and V.I. Shevchenko, "Nonlinear Theory of Dissipative Instability of a Relativistic Beam in a Plasma" Soviet physics JETP, **35**(4), 730-732 (1972). http://www.jetp.ras.ru/cgi-bin/dn/e_035_04_0730.pdf

[6] A.N. Kondratenko, V.M. Kuklin, and V.I. Tkachenko, "Nonlinear theory of fuel instability in the collision plasma," Izv. Universities. Radiophysics, **21**(10), 1535-1537 (1978). https://radiophysics.unn.ru/sites/default/files/papers/1978_10_1535.pdf

[7] A.G. Zagorodniy, A.V. Kirichok, V.M. Kuklin, and A.V. Priymak, "Modulation of the integral field of multi-muddy beams in plasma," East Eur. J. Phys. **1**(2), 53-66 (2014). https://periodicals.karazin.ua/eejp/article/view/129/40. (in Russian)

[8] V.L. Ginzburg, "Radiation of evenly moving sources (Vavilov-Cherenkov effect, transitional radiation and some other phenomena)," UFN, **166**(10), 1033-1042 (1996). http://elibrary.lt/resursai/Uzsienio%20leidiniai/Uspechi_Fiz_Nauk/1996/10/r9610a.pdf. (in Russian)

[9] V.M. Kuklin, "On the Nature of Coherens in the System of Oscillators," PAST, **4**, 91-95 (2019). https://vant.kipt.kharkov.ua/ARTICLE/VANT_2019_4/article_2019_4_91.pdf

[10] R.N. Dicke, "Coherence in Spontaneous Radiation Processes," Physical Review, **93**(1), 99-110 (1954). https://doi.org/10.1103/PhysRev.93.99

[11] V.M. Kuklin, D.N. Litvinov, S.M. Sevidov, and V.E. Sporov, "Simulation of Synchronization of Nonlinear Oscillators by the External Field," East Eur. J. Phys. 4(1), 75-84 (2017). https://periodicals.karazin.ua/eejp/article/view/8561

[12] Kuklin V.M., D.N. Litvinov, and V.E. Sporov, "Superradiance of Stationary Oscillators," PAST, **4**(116), 217-220 (2018). https://vant.kipt.kharkov.ua/ARTICLE/VANT_2018_4/article_2018_4_217.pdf

[13] V.M. Kuklin, and E.V. Poklonskiy, "Dissipative Instabilites and Superradiation Regimes (Classic Models)," PAST, **4**(134), 138-143 (2021). https://vant.kipt.kharkov.ua/ARTICLE/VANT_2021_4/article_2021_4_138.pdf

[14] V.M. Kuklin, *Selected Chapters (Theoretical Physics)*, (V.N. Karazin Kharkiv National University publishing, Kharkiv, 2021). http://dspace.univer.kharkov.ua/handle/123456789/16359

[15] A.N. Didenko, V.P. Grigoryev, and Yu.P. Usov, *Powerful electronic beams and their use*, (Atomizdat, Moscow, 1977). (in Russian)

[16] M.V. Kuzelev, and A.A. Rukhadze, *Electrodynamics of dense electron beams in plasma*, (Nauka, Moscow, 1990).

ПРО НЕОБХІДНІСТЬ ОБЛІКУ ВЛАСНИХ ПОЛІВ ВИПРОМІНЮВАЧІВ ПРИ ОПИСІ РЕЖИМІВ ГЕНЕРАЦІЇ

Володимир М. Куклін, Євген В. Поклонський

Харківський національний університет імені В. Н. Каразіна, Харків, Україна

У роботі обговорюються три різні режими генерації електромагнітного поля ансамблем осциляторів, розміщених на довжині хвилі випромінювання в одновимірному випадку. Розглянуто збудження резонаторного поля, яке, як правило, визначається геометрією системи, з урахуванням та без урахування власних полів випромінювачів. Аналізується також режим надвипромінювання такого ж ансамблю осциляторів. Фактично надвипромінювання формується за рахунок власних полів випромінювачів навіть без резонатора. Зазначається, що максимально можливі амплітуди індукованих полів як у режимі надвипромінювання, так і в режимі генерації поля резонатора можна порівняти. Це змушує подумати про роль власних полів випромінювачів у приладах електроніки. Наголошується на помилковості традиційного підходу до опису збудження резонаторів і хвилеводів, де облік суми власних полів випромінювачів не проводився. Показано, що при коректному описі режиму збудження резонатора, крім поля резонатора, необхідно враховувати також суму власних полів випромінювачів в активній зоні. Синхронізація випромінювачів також, як і в режимі надвипромінювання, приводить до появи значної амплітуди індукованого поля системи осциляторів. Показано, що в практично цікавому випадку відкритих систем (дисипативні режими генерації) цей облік помітно зменшує характерний час розвитку генерації, збільшує максимально можливу амплітуду коливань. Облік власних полів випромінювачів також змінює умови досягнення максимального потоку енергії із системи. Це здатне змінювати робочу точку процесу генерації, що визначається вимогою максимального темпу виведення енергії із системи.

Ключові слова: *ансамбль осциляторів; поле резонатора; сума власних полів випромінювачів; режим збудження поля в резонаторі; збудження поля в режимі надвипромінювання*

East European Journal of Physics. **2.** 132-137 (2023)
DOI:10.26565/2312-4334-2023-2-12 ISSN 2312-4334

DETERMINATION OF BAND STRUCTURE AND COMPTON PROFILES FOR ALUMINUM-ARSENIDE USING DENSITY FUNCTIONAL THEORY[†]

Sameen F. Mohammed[a], Salah M.A. Ridha[b], Abdulhadi Mirdan Ghaleb[b,*], Zahraa Talib Ghaleb[c], Yamina Benkrima[d], Mahran Abdulrhman Abdullah[e]

[a]*Department of Mechanical Techniques, Technical institute Kirkuk, Northern Technical University, Iraq*
[b]*Department of Physics, College of Science, University of Kirkuk, Iraq*
[c]*Department Chemistry, College of Science, University of Kirkuk, Kirkuk, Iraq*
[d]*Department of Exact Sciences, ENS Ouargla, Algeria*
[e]*Ministry of Education, Kirkuk Education Directorate, Iraq*
**Corresponding author e-mail: abdlhadig4@gmail.com*
Received March 21, 2023; revised April 14, 2023; accepted April 15, 2023

First-principles computations of the electronic structure of AlAs have been carried out using the density functional theory (DFT) within Local Density Approximation-LDA and Generalized Gradient Approximation - GGA. We utilized the CASTEP's plane wave basis set implementation for the total energy computation (originally from Cambridge Serial Total Energy Package). We have used to examine structure parameter in structure of AlAs The electronic structure calculation using the two approximations show that the LDA and the GGA methods underestimated the band gap while the band gap predicted by the GGA is closer to the experimental result. according to the electronic structure calculation utilizing the two approximations. The GGA calculation shows a direct band-gap semiconductor of 2.5 eV. The energy band diagram is used to calculate the total and partial densities of AlAs states. Multiple configurations of the ionic model were calculated for $Al^{+x}As^{-x}$ $(0.0 \leq x \leq 1)$ also performed utilizing free-atom profiles. According to the ionic model, 0.75 electrons would be transferred from the valence 5p state of aluminium to the 3p state of Arsenide.
Keywords: *generalized gradient approximation; localized density approximation; Density functional theory; energy band gap; density of states; Ionic model; Compton profiles*
PACS:02.70.-c, 71.15.Ap, 71.15.Mb, 17.20.-b, 71.15.Dx , 73.20.At

1. INTRODUCTION

Groups III–V have been the focus of a great deal of research during the past few decades. LEDs, lasers, photo detectors, integrated circuits, modulators, and filters are only some of the electronic and optoelectronic devices that benefit from the AlAs compound [1]. These compounds often crystallize into the zincblende (ZB) form under standard circumstances [2]. AlAs's band structure has only been fully calculated using a SCOPW model by Stukel and Euwema [3]. There is a several theoretical calculations of the electrical structures of AlAs over the past two decades [4-6]. But to our knowledge, only fitting methods like the tight-binding model [7,8,9] exist. Almost all theoretical analyses of the AlAs band structure have produced band gaps that differ to variable degrees from the actual values [4-6,10-13]. Density-functional-theory (DFT) [14,15] was used to conduct first-principles calculations [16], and the open-source software package Quantum ESPRESSO was used to approximate the exchange-correlation functional using the local density approximation. Existing theories and experiments are linked to the outcomes achieved. They have come to a satisfactory accord. The electrical, optical, and structural characteristics of AlAs are the subject of a variety of theoretical investigations [3,17–25]. However, because to its high hygroscopicity [26-29], very few experimental experiments are conducted on bulk AlAs. Stukel and Euwema [3] presented energy band calculations for cubic AlAs using a first-principles plane-wave approach self-consistent orthogonalized. Using the pseudo potential approach in the local density approximation, Cohen and Froyen [17] investigated the structural properties of various III-V semiconductor compounds and the static, including Aluminum-Arsenide (LDA). Many researchers [19-21] have published AlAs's electrical characteristics, total energy, effective mass, lattice constants, etc. Using the empirical pseudo potential technique, Joshi and Sharma [22] reported a few years ago on the theoretical directional Compton profiles of AlP and Aluminum-Arsenide. (EPM). This paper is structured as follows: in Section 2, presented the paper's theoretical framework and computational details. Section 3 contains the discussion and results in the final section have been provided a conclusion.

2. METHODOLOGY DETAILS

2.1. Computation Method

The ion-electron interactions in the electronic structure computations have been performed using the non-local ultra soft pseudo potential developed by Vanderbilt [30]. The computations employed the LDA with the Ceperley Alder PerdewZunger [31] and the GGA with the Perdew-Burke Ernzerh of Solid [32] exchange correlation potentials. Al $3s^2$ $3p^1$ and As $4s^2$ 4p3 are studied by pseudo-atom computations. Total energy converges to 0.5E-05 eV/atom, which is self-consistent. Our estimates' convergence is verified through in-depth exploration of the interplay between the k-point

[†] ***Cite as:*** S.F. Mohammed, S.M.A. Ridha, A.M. Ghaleb, Z.T. Ghaleb, Y. Benkrima, and M.A. Abdullah, East Eur. J. Phys. **2**, 132 (2023), https://doi.org/10.26565/2312-4334-2023-2-12

and the cut-off energy set mesh on the Monk horst-Pack grid. For the computational expense, we use a Monk horst-Pack mesh with 16×16×16 k-points for the Brillouin zone sample and a plane wave basis set with an energy cutoff of 800 eV. In addition, Vanderbilt's [30] non-local ultra soft pseudo potential is used. Kramer's-Kronig transform accuracy and the energy range that can be accounted for are both sensitive to the number of conduction bands that are included in the calculation. The electrical structure is investigated here by employing the Cambridge Serial Total Energy Package (CASTEP) [33,34], which takes into account not only the occupied bands but also the 16 unoccupied ones.

2.2. Ionic model

The free atom profiles-FA of Aluminum and Arsenide, the data were taken from a table Biggs [35], were used to produce the theoretical Compton profiles of Aluminum-Arsenide for various ionic configurations. We were able to identify the valence profiles of a wide variety of Al^{+x} As^{-x} (x ranges from 0 to 1) combinations by transferring an electron from Al's 3p or 3s shell into As's 4p shell. The valence profiles were combined to the core contributions to generate the entire profiles [36], which were then normalized to ($19.966e^{-}$) in the range of 0 to 7 a.u. in order to give a direct comparison with other studied in the same experimental data [37].

3. RESULTS AND DISCUSSION

3.1. Electronic properties

Herein, density functional theory (using LDA and GGA) was used to examine the electrical characteristics of the binary compound AlAs in the zinc mix structure. Researchers have found that AlAs exhibits a direct band gap (G-G). You can see the outcomes in Fig. 1 (a and b).

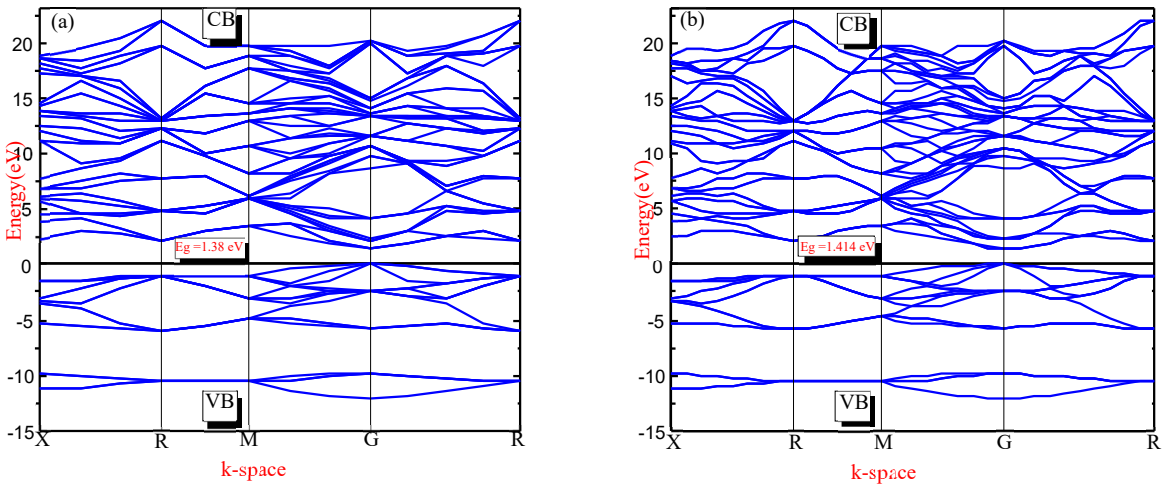

Figure 1. Band gap structure of AlAs applying (a) LDA and (b) GGA approximation

The band gap values generated by GGA are more in line with the known experimental results than the LDA values. The LDA is known to consistently understate the energy gap [38]. The GGA technique can provide a more stable band structure because it is based on potential optimization. Band gap values computed using the GGA approach fare far better in comparison to experiment than those produced using the LDA method. Our recent calculations indicate that the GGA approximation performs a decent job of characterizing the band features, and that the GGA results may be compared to those produced using more expensive approaches, such as GW and hybrid functional for band gaps. It can be used to simulate the electronic characteristics of semiconductors. It has a direct band gap of 1.38 eV (LDA) and 1.415 eV (GGA), with the valence and conduction band minimums both located at the G point. The measured findings are roughly in agreement with our calculated band gap size [39]. Using the data shown in Fig. 1, we can see that the Fermi energy of aluminum arsenide (AlAs) is 0.699eV (LDA) and 0.689eV (GGA), and that the G-point symmetry point is where the valence bad-VB is at its maximum and the conduction band-CB is at its minimum. As the valence band maximum and conduction band minimum are positioned on distinct symmetry points, AlAs is a direct band gap semiconductor with an energy gap value of 1.38eV (LDA) and 1.414 eV. The Al 3p-like and 3s-like electrons and the As 4p-like electrons are responsible for the 3 bands found below the Fermi level. Because of the presence of Al 3p-like states and as 4p-like ones, the conduction bands-CB above the Fermi level are empty. The theoretical values for Aluminum-Arsenide [40] correspond with the calculated energy gaps. The higher ionic nature of AlAs causes it to exhibit a wider optical band gap and a higher rate of charge transfer. These similarities in structure also explain why it exhibits metallic and covalent characteristics. AlAs is commonly used in applications that need higher temperature operation due to its broad band gap, which pointing to the ability of Aluminum-Arsenide for higher photon energy in reflectivity measurements. As a result of their direct band gap and large band gap, they are a prospective option for use in semiconductor technology. Because of this, it is also used as an active material in the production of LEDs and other optoelectronic devices. Applications in the technology of

higher power and higher frequency electronic devices in the short wave length region have also gained traction. Light-emitting diodes, blue and ultraviolet lasers, photo detectors, optical pumping devices, and hetero structures all rely on AlAs as a fundamental material [41,42].

3.2. Density of State

According to the Density of State Diagram for AlAs, the 4p states of As and 3p states of Al are responsible for the small peaks in Fig. 2(a and b) above its Fermi energy. The p-like and s-like electrons of as are what give rise to the longer peaks near the Fermi energy. The third zone is composed of the top (2) valence bands, which are mostly p-like. The anion state, which is comparable to that of the alkali halides, displays both the density of states and the band structure [43,44].

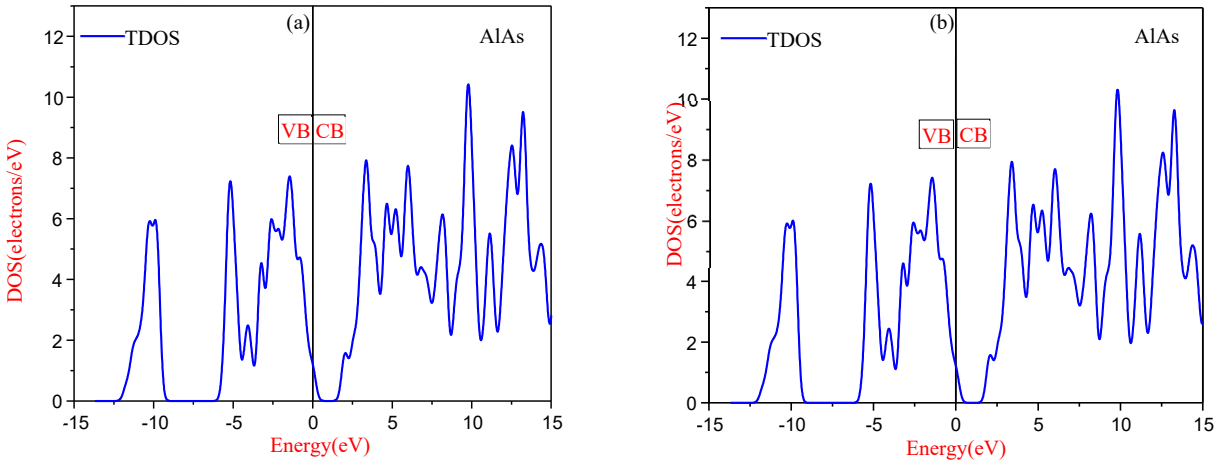

Figure 2. The total density of states of compounds binary AlAs using the LDA and GGA approaches

3.3. Charge Transfer

Particularly, Figure (3) illustrates. The current study uses theoretical approaches as opposed to earlier research, which relied on experimental valence Compton profiles of the elemental solids [37].

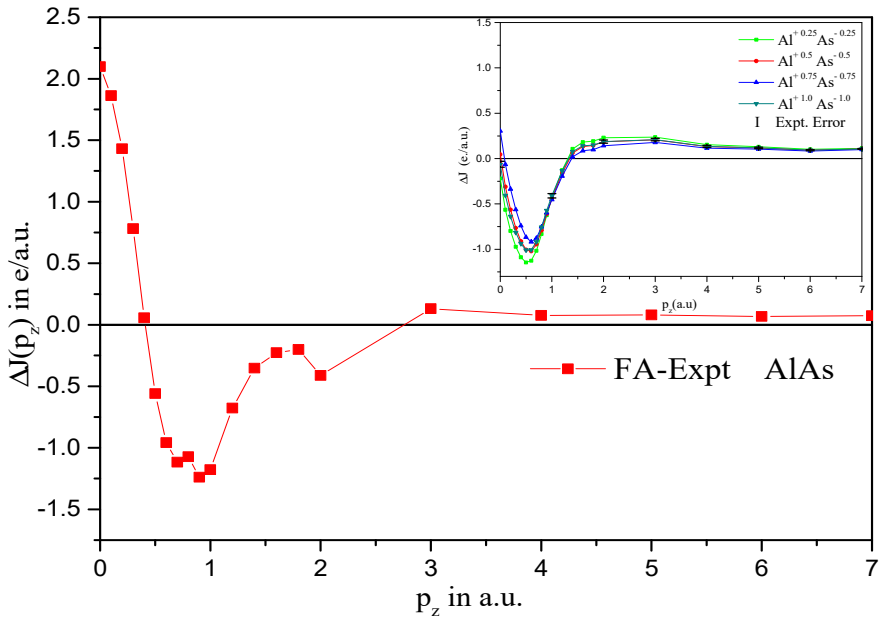

Figure 3. Comparison of the theoretical and experimental Compton profiles of AlAs.
The measuring of the differences between various ionic configurations [37].

We have also included free atom valence profiles in the current charge transfer analysis. The 4s 4p states of As and the 3s 3p states of Al are included in these profiles. In the inset, we see the matching difference profiles (convoluted

ionic - experiment) shown. Importantly, it is necessary to convolute the ionic profiles with the resolution function of the instrument and to normalize them to the free atom area, which is equal to 19.967 electrons. for 0 to 7 a.u. before a comparison of ionic values with experimental data can be made [37]. From the inset, it is clear that the effect of changing charges on As and Al is not noticeable until the charge reaches 1.5 au. All ionic configurations behave identically and overlap at distances greater than 1.5 a.u. We have calculated χ^2 as follows, which allows us to test the global concordance of all ionic configurations with the experiment:

$$\chi^2 = \sum_{p_z=0}^{7} \left| \frac{\Delta J(p_z)}{\sigma(p_z)} \right|^2 \quad (1)$$

where $\sigma(p_z)$ represents a random error in the experiment [37]. According to X^2 tests, the best agreement among the ionic structures is found in the $Al^{3.0}As^{-3.0}$state.

According to the basic ionic model, the charge in this molecule must flow from Aluminum to Arsenide. The same explanations are also given in the ref [36]. However, this process requires three electrons to be transferred from Al$3s^2 3p^1$ state to As$4s^2 4p^3$state, indicating that AlAs bonds primarily through ionic interactions. There is a clear limitation of the ionic model in the low momentum area, where the discrepancies between the convoluted ionic and experimental profiles are quite large. It is worth noting that the ionic model's predicted charge transfer is greater than the value derived by a different technique [37].

4. CONCLUSIONS

The present research summarizes the results of a density functional theory (DFT) analysis of electronic AlAs Compound in the LDA and GGA approximations. Following is a brief synopsis of the key findings: The direct gap at G is the only exception; otherwise, our calculated band gaps agree quite well with the experimental findings. The intrinsic property of LDA pseudo potentials means that the estimated band gap values are smaller than the experimental values. The reason for this is the reduced complexity of the exchange correlation functional. The estimated electronic band structure reveals that AlAs is a Semiconductors with a direct band gap of 1.38 eV (LDA) and 1.414 eV (GGA), respectively. When compared to other theoretical calculations obtained, this shows a significant improvement. Semiconductors have conducting properties, as indicated by the fact that the DOS energy level within them reveals a particularly high situation of electron occupation and that the DOS seen near the Fermi level for semiconductors is zero. For the spherically averaged electron momentum density (EMD), there is good agreement between the measured and estimated values. Calculations using the ionic model for a variety of (Al^{+x}) (As^{-x}) (x varies from 0 to 1), combinations result in a 0.75 electron transfer from the $3s^2$ $3p^1$Aluminum valence state to the $4s^2$ $4p^3$Arsenide valence state.

ORCID IDs

Salah M.A. Ridha, https://orcid.org/0000-0003-0569-3849; **Abdulhadi Mirdan Ghaleb**, https://orcid.org/0000-0002-2202-8827; **Zahraa Talib Ghaleb**, https://orcid.org/0000-0003-0569-3849, **Yamina Benkrima,** https://orcid.org/0000-0001-8005-4065

REFERENCES

[1] R. Ahmed, S.J. Hashemifar, H. Akbarzadeh, and M. Ahmed, "Ab initio study of structural and electronic properties of III-arsenide binary compounds," Computational materials science, **39**(3), 580-586 (2007). https://doi.org/10.1016/j.commatsci.2006.08.014

[2] A. Mujica, A. Rubio, A. Munoz, and R.J. Needs, "High-pressure phases of group-IV, III–V, and II–VI compounds," Reviews of modern physics, **75**(3), 863(2003). https://doi.org/10.1103/RevModPhys.75.863

[3] D.J. Stukel, and R.N. Euwema, "Energy-band structure of aluminum arsenide," Physical Review, **188**(3), 1193 (1969). https://doi.org/10.1103/PhysRev.188.1193

[4] B.I. Min, S. Massidda, and A.J. Freeman, "Structural and electronic properties of bulk GaAs, bulk AlAs, and the $(GaAs)_1$ $(AlAs)_1$ superlattice," Physical Review B**,** **38**(3), 1970 (1988). https://doi.org/10.1103/PhysRevB.38.1970

[5] M.Z. Huang, and W.Y. Ching, "Calculation of optical excitations in cubic semiconductors. I. Electronic structure and linear response," Physical Review B, **47**(15), 9449 (1993). https://doi.org/10.1103/PhysRevB.47.9449

[6] S. Lebègue, B. Arnaud, M. Alouani, and P.E. Bloechl, "Implementation of an all-electron GW approximation based on the projector augmented wave method without plasmon pole approximation: Application to Si, SiC, AlAs, InAs, NaH, and KH," Physical Review B, **67**(15), 155208 (2003). https://doi.org/10.1103/PhysRevB.67.155208

[7] T.B. Boykin, "Generalized eigenproblem method for surface and interface states: The complex bands of GaAs and AlAs," Physical Review B, **54**(11), 8107 (1996). https://doi.org/10.1103/PhysRevB.54.8107

[8] J.P. Loehr, and D.N. Talwar, "Exact parameter relations and effective masses within sp 3 szinc-blende tight-binding models," Physical Review B, **55**(7), 4353 (1997). https://doi.org/10.1103/PhysRevB.55.4353

[9] A.B. Chen, and A. Sher, "Electronic structure of III-V semiconductors and alloys using simple orbitals," Physical Review B, **22**(8), 3886 (1980). https://doi.org/10.1103/PhysRevB.22.3886

[10] R.W. Godby, M. Schlüter, and L.J. Sham, "Quasiparticle energies in GaAs and AlAs," Physical Review B, **35**(8), 4170 (1987). https://doi.org/10.1103/PhysRevB.35.4170

[11] P. Boguslawski, and I. Gorczyca, "Influence of chemistry on the energy band structure: AlAs versus GaAs," Acta Physica Polonica, A, **80**(3), 433-436 (1991). http://dx.doi.org/10.12693/APhysPolA.80.433

[12] B.K. Agrawal, and S. Agrawal, "Ab initio calculation of the electronic, structural, and dynamical properties of AlAs and CdTe," Physical Review B, **45**(15), 8321 (1992). https://doi.org/10.1103/PhysRevB.45.8321

[13] Q. Guo, C.K. Ong, H.C. Poon, and Y.P. Feng, "Calculation of electron effective masses in AlAs," Physica Status Solidi (b), **197**(1), 111-117 (1996). https://doi.org/10.1002/pssb.2221970117

[14] P. Hohenberg, and W. Kohn, "Inhomogeneous electron gas," Physical review, **136**(3B), B864 (1964). https://doi.org/10.1103/PhysRev.136.B864
[15] W. Kohn, and L.J. Sham, "Self-consistent equations including exchange and correlation effects," Physical review, **140**(4A), A1133 (1965). https://doi.org/10.1103/PhysRev.140.A1133
[16] P. Giannozzi, S. Baroni, N. Bonini, M. Calandra, R. Car, C. Cavazzoni, D. Ceresoli, et al., "QUANTUM ESPRESSO: a modular and open-source software project for quantum simulations of materials," Journal of physics: Condensed matter, **21**(39), 395502 (2009). https://doi.org/10.1088/0953-8984/21/39/395502
[17] S. Froyen, and M.L. Cohen, "Structural properties of III-V zinc-blende semiconductors under pressure," Physical Review B, **28**(6), 3258 (1983). https://doi.org/10.1103/PhysRevB.28.3258
[18] A. Mujica, R.J. Needs, and A. Munoz, "First-principles pseudopotential study of the phase stability of the III-V semiconductors GaAs and AlAs," Physical Review B, **52**(12), 8881 (1995). https://doi.org/10.1103/PhysRevB.52.8881
[19] M. Städele, M. Moukara, J.A. Majewski, P. Vogl, and A. Görling, "Exact exchange Kohn-Sham formalism applied to semiconductors," Physical Review B, **59**(15), 10031 (1999). https://doi.org/10.1103/PhysRevB.59.10031
[20] A.R. Jivani, H.J. Trivedi, P.N. Gajjar, and A.R. Jani, "Total energy, equation of state and bulk modulus of AlP, AlAs and AlSb semiconductors," Pramana, **64**(1), 153-158 (2005). https://doi.org/10.1007/BF02704540
[21] H. Jin, G.L. Zhao, and D. Bagayoko, "Density functional band gaps of AlAs," Physical Review B, **73**(24), 245214 (2006). https://doi.org/10.1103/PhysRevB.73.245214
[22] K.B. Joshi, and B.K. Sharma, "Compton profile study of AlAs and AlP by empirical pseudopotential method," Proceedings-national academy of sciences India, Section A, **76**(1), 79 (2006). http://nasi.nic.in/76_a_I_14.htm
[23] J. Cai, and N. Chen, "Theoretical study of pressure-induced phase transition in AlAs: From zinc-blende to NiAs structure," Physical Review B, **75**(17), 174116 (2007). https://doi.org/10.1103/PhysRevB.75.174116
[24] N. Fraj, I. Saïdi, S.B. Radhia, and K. Boujdaria, "Band structures of AlAs, GaP, and SiGe alloys: A 30 k×p model," Journal of Applied Physics, **102**(5), 053703 (2007). https://doi.org/10.1063/1.2773532
[25] H. Arabshahi, M.R. Khalvati, and M.R. Rokn-Abadi, "Temperature and doping dependencies of electron mobility in InAs, AlAs and AlGaAs at high electric field application," Brazilian Journal of Physics, **38**, 293-296 (2008). https://doi.org/10.1590/S0103-97332008000300001
[26] B. Monemar, "Optical Dispersion and Ionicity of AlP and AlAs," Physica Scripta, **3**(3-4), 193 (1971). https://doi.org/10.1088/0031-8949/3/3-4/015
[27] B. Monemar, "Fundamental energy gaps of AlAs and AlP from photoluminescence excitation spectra," Physical Review B, **8**(12), 5711-5718 (1973). https://doi.org/10.1103/PhysRevB.8.5711
[28] A. Onton, and R.J. Chicotka, "Free-exciton-impurity interaction in AlAs," Physical Review B, **10**(2), 591 (1974). https://doi.org/10.1103/PhysRevB.10.591
[29] R.G. Greene, H. Luo, T. Li, and A.L. Ruoff, "Phase transformation of AlAs to NiAs structure at high pressure," Physical review letters, **72**(13), 2045 (1994). https://doi.org/10.1103/PhysRevLett.72.2045
[30] D. Vanderbilt, "Soft self-consistent pseudopotentials in a generalized eigenvalue formalism," Physical review B, **41**(11), 7892 (1990). https://doi.org/10.1103/PhysRevB.41.7892
[31] J.P. Perdew, A. Ruzsinszky, G.I. Csonka, O.A. Vydrov, G.E. Scuseria, L.A. Constantin, X. Zhou, and K. Burke, "Restoring the density-gradient expansion for exchange in solids and surfaces," Physical review letters, **100**(13), 136406 (2008). https://doi.org/10.1103/PhysRevLett.100.136406
[32] S.H. Vosko, L. Wilk, and M. Nusair, "Accurate spin-dependent electron liquid correlation energies for local spin density calculations: a critical analysis," Canadian Journal of physics, **58**(8), 1200-1211 (1980). https://doi.org/10.1139/p80-159
[33] V. Milman, B. Winkler, J.A. White, C.J. Pickard, M.C. Payne, E.V. Akhmatskaya, and R.H. Nobes, "Electronic structure, properties, and phase stability of inorganic crystals: A pseudopotential plane-wave study," International Journal of Quantum Chemistry, **77**(5), 895-910 (2000). https://doi.org/10.1002/(SICI)1097-461X(2000)77:5%3C895::AID-QUA10%3E3.0.CO;2-C
[34] M.C. Payne, M.P. Teter, D.C. Allan, T.A. Arias, and A.J. Joannopoulos, "Iterative minimization techniques for ab initio total-energy calculations: molecular dynamics and conjugate gradients," Reviews of modern physics, **64**(4), 1045 (1992). https://doi.org/10.1103/RevModPhys.64.1045
[35] F. Biggs, L.B. Mendelsohn, and J.B. Mann, "Hartree-Fock Compton profiles for the elements," Atomic data and nuclear data tables, **16**(3), 201-309 (1975). https://doi.org/10.1016/0092-640X(75)90030-3
[36] S.F. Mohammed, A.M. Ghaleb, and E.S. Ali, "Electron Momentum Density of Nan particles ZrO2: A Compton Profile Study," International Journal of Nanoscience, **20**(02), 2150018 (2021). https://doi.org/10.1142/S0219581X21500186
[37] G. Sharma, K.B. Joshi, M.C. Mishra, R.K. Kothari, Y.C. Sharma, V. Vyas, and B.K. Sharma, "Electronic structure of AlAs: a Compton profile study," Journal of alloys and compounds, **485**(1-2), 682-686 (2009). http://dx.doi.org/10.1016%2Fj.jallcom.2009.06.043
[38] A.M. Ghaleb, A.T. Shihatha, and Z.T. Ghaleb, "Investigation of the physical properties and Mulliken charge distribution of the cube perovskite $BiGaO_3$ is calculated by GGA-PBE," Digest Journal of Nanomaterials and Biostructures (DJNB), **17**(4), (2022). https://doi.org/10.15251/DJNB.2022.174.1181
[39] M.P. Thompson, G.W. Auner, T.S. Zheleva, K.A. Jones, S.J. Simko, and J.N. Hilfiker, "Deposition factors and band gap of zinc-blende AlN," Journal of Applied Physics, **89**(6), 3331-3336 (2001). https://doi.org/10.1063/1.1346999
[40] K. Boubendira, H. Meradji, S. Ghemid, and F.E.H. Hassan, "Theoretical prediction of the structural, electronic, and thermal properties of $Al_{1-x}B_xAs$ ternary alloys," Materials science in semiconductor processing, **16**(6), 2063-2069 (2013). https://doi.org/10.1016/j.mssp.2013.07.022
[41] D. Kirin, and I. Lukačević, "Stability of high-pressure phases in II-VI semiconductors by a density functional lattice dynamics approach," Physical Review B, **75**(17), 172103 (2007). https://doi.org/10.1103/PhysRevB.75.172103
[42] A.M. Ghaleb, and A.Q. Ahmed, "Structural, electronic, and optical properties of sphalerite ZnS compounds calculated using density functional theory (DFT)," Chalcogenide Letters, **19**(5), 309-318 (2022). https://doi.org/10.15251/CL.2022.195.309

[43] C.N. Louis, and K. Iyakutti, "Electronic phase transition and superconductivity of vanadium under high pressure," Physical Review B, **67**(9), 094509 (2003). https://doi.org/10.1103/PhysRevB.67.094509
[44] A.T. Shihatha, A.M. Ghaleb, and R.A. Munfi, "Theoretical study of electronic structure and optical properties for ZnO thin film," AIP Conference Proceedings, **2398**(1), 020023 (2022). https://doi.org/10.1063/5.0094037

ВИЗНАЧЕННЯ ЗОННОЇ СТРУКТУРИ ТА КОМПТОН ПРОФІЛІВ ДЛЯ АРСЕНІДУ АЛЮМІНІЮ З ВИКОРИСТАННЯМ ФУНКЦІОНАЛУ ГУСТИНИ

Самін Ф. Мохаммед[a], Салах М.А. Рідха[b], Абдулхаді Мірдан Галеб[b], Захра Таліб Галеб[c], Яміна Бенкріма[d], Махран Абдулрхман Абдулла[e]

[a]Кафедра механічних технологій, Технічний інститут Кіркук, Північний технічний університет, Ірак
[b]Факультет фізики, Науковий коледж, Університет Кіркука, Ірак
[c]Кафедра хімії Наукового коледжу Кіркукського університету, Кіркук, Ірак
[d]Департамент точних наук, ENS Уаргла, Алжир
[e]Міністерство освіти, Директорат освіти Кіркука, Ірак

Основні розрахунки електричних характеристик AlAs були проведені з використанням теорії функціоналу щільності (DFT) і локальної щільності (LDA), методів (DFT) і узагальненої градієнтної апроксимації (GGA). Ми використали реалізацію базового набору плоских хвиль CASTEP для обчислення загальної енергії (спочатку з Cambridge Serial Total Energy Package). Раніше ми дивилися на структурний параметр структури AlAs. Ширина забороненої зони була переоцінена за допомогою узагальненої градієнтної апроксимації та методів LDA, хоча ширина забороненої зони, передбачена GGA, більше відповідає експериментальним висновкам, згідно з розрахунком електронної структури з використанням двох наближень. За допомогою GGA розрахунку виявлено напівпровідник із шириною забороненої зони 2,5 еВ. Енергетична зонна діаграма була використана для розрахунку повної та часткової густини станів AlAs. Було розраховано кілька конфігурацій іонної моделі. $Al^{+x}As^{-x}$ $(0.0 \leq x \leq 1)$ також виконуються з використанням профілів вільних атомів. Відповідно до іонної моделі, 0,75 електрона буде перенесено з валентного 5p-стану алюмінію в 3p-стан арсеніду.

Ключові слова: *узагальнена градієнтна апроксимація; апроксимація локалізованої щільності; теорія функціонала густини; енергетична заборонена зона; щільність станів; іонна модель; Комптон-профілі*

EAST EUROPEAN JOURNAL OF PHYSICS. 2. 138-149 (2023)
DOI:10.26565/2312-4334-2023-2-13 ISSN 2312-4334

ELECTROEXCITATION FORM FACTORS AND DEFORMATION OF ^{20,22}NE ISOTOPES BASED ON THE SHELL MODEL AND HARTREE-FOCK PLUS BCS CALCULATIONS[†]

Omar A. Alswaidawi, Ali A. Alzubadi
Department of Physics, College of Science, University of Baghdad, Baghdad, Iraq
Corresponding Author e-mail: ali.kareem@sc.uobaghdad.edu.iq
Received March 22, 2023; revised April 10, 2023; accepted April 11, 2023

Nuclear structure of ^{20,22}Ne isotopes has been studied via the shell model with Skyrme-Hartree-Fock calculations. In particular, the transitions to the low-lying positive and negative parity excited states have been investigated within three shell model spaces; *sd* for positive parity states, *spsdpf* large-basis (no-core), and *zbme* model spaces for negative parity states. Excitation energies, reduced transition probabilities, and elastic and inelastic form factors were estimated and compared to the available experimental data. Skyrme interaction was used to generate a one-body potential in the Hartree-Fock calculations for each selected excited state, which is then used to calculate the single-particle matrix elements. Skyrme interaction was used to calculate the radial wave functions of the single-particle matrix elements, from which a one-body potential in Hartree-Fock theory with SLy4 parametrization can be generated. Furthermore, we have explored the interplays among neutron and proton density profiles in two dimensions, along with the deformations of ^{20,22}Ne using Hartree-Fock plus BCS calculations.
Keywords: *Sd model space; negative parity state; elastic and inelastic form factor; density distribution*
PACS: 21.60.−n, 21.60.Cs, 21.10.−k

I. INTRODUCTION

For a microscopic description of the nucleus, different nuclear models have been utilized [1]. The most efficient one is the Shell Model (SM) [2], based on the idea of an independent nucleon freely orbiting in a spherically symmetrical core potential generated by all the other nucleons within the nucleus. In actual SM calculations, nuclear states are linear combinations of states rather than pure states [3]. Always, SM computations are performed in a configuration space with a limited number of single-particle states outside of an inert core, which is typically a doubly-magical nucleus. As a result of this truncation, the residual interactions must be regarded as effective interactions, and choosing the proper N-N interaction is not simple [4, 5]. The ground states of nuclei are created when nucleons fill shells to the Fermi level. Fermi's level is the same for protons and neutrons in stable nuclei, but the Coulomb repulsion between protons [6] explains why the line of stability and the N = Z line on the chart of the nuclides do not correspond for heavier nuclei. The laws of quantum mechanics govern the location and characteristics of the nucleus' discrete energy levels, just like they do for the atom. The positions of excited states vary from nucleus to nucleus. Excitation energy (E_x) is influenced by each nucleus's internal structure. Quantum numbers denote each excited state's angular momentum, parity, and isospin, in addition to its electromagnetic and strong properties. Positive-parity spectra can be generated by considering only the $1d_{5/2}$, $2s_{1/2}$, and $1d_{3/2}$ orbits in the *sd*-shell configuration space. Any realistic negative parity calculation must account for both $1p$ and $2p$-$1f$ active shells. In the absence of such theoretical work, approaches to comprehending the structure of negative-parity states typically rely on more generalized descriptions [7]. In a system of identical Fermions, the Pauli exclusion principle dictates that the properties of a nucleus with a given number of protons and neutrons are defined by the filling of the lowest energy single-particle levels (the nucleons in this case). The Pauli Exclusion Principle states that a particular set of quantum numbers can only be occupied by a single proton or neutron. The average nuclear potential is determined by the shape of the nuclear density distribution and the attractive short-range nucleon-nucleon interaction [8].

II. THEORETICAL FRAMEWORK

(a) Shell model calculations

The reduced matrix elements of the electron scattering $\hat{X}(\lambda)_{t_z}$ operator between the final f and initial i states can be expressed as the sum of the one-body density matrix (OBDM) times the reduced single-particle matrix elements [9];

$$\left\langle f \parallel \hat{X}(\lambda)_{t_z} \parallel i \right\rangle = \sum_{k_a k_b} \mathrm{OBDM}(fik_a k_b \lambda) \left\langle k_a \parallel \hat{X}(\lambda)_{t_z} \parallel k_b \right\rangle \tag{1}$$

The OBDM of multipolarity (λ) can be expressed in term of the second quantization notation as;

$$\mathrm{OBDM}(fik_{a,t_z} k_{b,t_z} \lambda) = \frac{\left\langle f \left\| \left[a^{+}_{k_a t_z} \otimes \tilde{a}_{k_b t_z} \right]^{\lambda} \right\| i \right\rangle}{\sqrt{2\lambda+1}} \tag{2}$$

[†] ***Cite as:*** O.A. Alswaidawi, and A.A. Alzubadi, East Eur. J. Phys. **2**, 138 (2023), https://doi.org/10.26565/2312-4334-2023-2-13

where the single-partical state (k), and t_z =1/2 and -1/2 for proton and neutron, respectively and i and f contain all the quantum numbers needed to separate the states.

M1 operator is used to define the nuclear magnetic dipole moment as [10]

$$\mu = \sqrt{\frac{4\pi}{3}} \begin{pmatrix} J_i & 1 & J_f \\ -J_i & 0 & J_f \end{pmatrix} \sum_{t_z} \left\langle f \left\| \hat{O}(M1)_{t_z} \right\| i \right\rangle \mu_N \tag{3}$$

where the nuclear magneton $\mu_N = \frac{e\hbar}{2m_p c} = 0.1051$ efm. While, in terms of the E2 operator, the electric quadrupole moment is defined as

$$Q = \sqrt{\frac{16\pi}{5}} \begin{pmatrix} J_i & 2 & J_f \\ -J_i & 0 & J_f \end{pmatrix} \sum_{t_z} \left\langle f \left\| \hat{O}(\mathrm{E2})_{t_z} \right\| i \right\rangle e_{t_z} \tag{4}$$

where the initial and final nuclear states |J> contain all the quantum numbers necessary to differentiate the nuclear states.

The reduced of transition probability given as [11].

$$B(X\lambda) = \frac{1}{4\pi} \left[Z \frac{(2\lambda+1)!!}{k^{\lambda}} \right]^2 \; |F(X\lambda,k)|^2 \tag{5}$$

where $k = E_X/\hbar c$, $B(E\lambda)$ is in unit of $e^2fm^{2\lambda}$ and $B(M\lambda)$ is in the unit of $\mu_N{}^2\, fm^{2\lambda-2}$.

With the realization that the energy functional could be written as a zero-range expansion, the Skyrme interaction was developed for nuclear structure computations, resulting in a straightforward derivation of the Hartree-Fock (HF) equations in which exchange terms have the same mathematical structure as direct terms. This approach decreases significantly the number of single-particle state integrations necessary to solve the equations. The Skyrme energy (E_{Sky}) reflects the strong force in the particle-hole channel in coordinate space and consists of central, spin-orbit, and tensor contributions [6]. Central potential is represented by Skyrme potential. It is a one-body potential as a mean-field potential.It is designed to approach the realistic nucleon–nucleon forces by providing the average field owing to all of the nucleons constituting the nucleus. VSky equals the combination of two and three bodily components. [12] as:

$$\hat{V}_{Sky} = \sum_{i<j} V_{ij}^{(2)} + \sum_{i<j<k} V_{ijk}^{(3)} \tag{6}$$

The two-body part is given by:

$$\begin{aligned} \hat{V}_{Sky}^{(2)}(i,j) = \; & t_0(1+x_0\hat{P}_\sigma)\delta_{12} + \frac{t_1}{2}(1+x_1\hat{P}_\sigma)\left[\vec{k}'^2\delta_{12} + \delta_{12}\vec{k}^2\right] \\ & + t_2(1+x_2\hat{P}_\sigma)\vec{k}'\delta_{12}\vec{k} + \frac{t_3}{6}(1+x_3\hat{P}_\sigma)\rho\left(\frac{\vec{r}_1+\vec{r}_2}{2}\right)^{\alpha}\delta_{12} + \; iW_0 \; \vec{k}'\delta_{12}(\vec{\hat{\sigma}}_1+\vec{\hat{\sigma}}_2)\times\vec{k} \\ & + \frac{t_e}{2}\left(\left[3\,(\vec{\hat{\sigma}}_1\cdot\vec{k}')\,(\vec{\hat{\sigma}}_2\cdot\vec{k}') - (\vec{\hat{\sigma}}_1\cdot\vec{\hat{\sigma}}_2)\vec{k}'^2\right]\delta_{12} + \delta_{12}\left[3(\vec{\hat{\sigma}}_1\cdot\vec{k})\,(\vec{\hat{\sigma}}_2\cdot\vec{k}) - (\vec{\hat{\sigma}}_1\cdot\vec{\hat{\sigma}}_2)\vec{k}^2\right]\right) \\ & + t_0\left[3(\vec{\hat{\sigma}}_1\cdot\vec{k})\delta_{12}(\vec{\hat{\sigma}}_2\cdot\vec{k}) - (\vec{\hat{\sigma}}_1\cdot\vec{\hat{\sigma}}_2)\vec{k}'\delta_{12}\vec{k}\right] \end{aligned} \tag{7}$$

where $\delta_{12} = \delta(\vec{r}_1 - \vec{r}_2)$, The $\hat{k}$ and $\hat{k}'$ operators represent the relative wave vectors of two nucleons acting to the right and left, respectively (i.e., complex conjugate wave functions with coordinate r'), They possess the shape;

$$\hat{K} = \frac{1}{2i}(\vec{\nabla}_1 - \vec{\nabla}_2) \;\; \text{and} \;\; \hat{K}' = -\frac{1}{2i}(\vec{\nabla}_1 - \vec{\nabla}_2) \tag{8}$$

Also

$$\hat{P}_\sigma = \frac{1}{2}(1 + \hat{\sigma}_1.\hat{\sigma}_2) \tag{9}$$

Electron scattering form factor between final and initial nuclear shell model states, including angular momentum λ and momentum transfer q, is given by [13].

$$\left|F_\lambda^\chi(q)\right|^2 = \left(\frac{4\pi}{Z^2}\right)\frac{1}{(2J_i+1)}\left|\sum_{t_z} e(t_z)\left\langle J_f \left\| \hat{T}_{\lambda,t_z}^{\chi}(q) \right\| J_i \right\rangle F_{cm}(q)F_{fs}(q)\right|^2 \tag{10}$$

where J_f and J_i are the total angular momentum λ of final and initial state, $F_{cm}\,(q)$ is the correction (center- of-mass) and $F_{fs}(q)$ is the finite size of the nucleon, with χ involving the transverse (T) and longitudinal (C) form factors. The nuclear

structure enters into the electron scattering through the longitudinal F^C form factor and the transverse F^T form factors (F^E and F^M) are the electric and magnetic transverse form factor, respectively). The total longitudinal and transverse form factors for electron scattering are given by:

$$\left|F^C(q)\right|^2 = \sum_{J\geq 0}\left|F_\lambda^C(q)\right|^2 \tag{11}$$

$$\left|F^T(q)\right|^2 = \sum_{J>0}\left[\left|F_\lambda^E(q)\right|^2 + \left|F_\lambda^M(q)\right|^2\right] \tag{12}$$

These form factors are functions of the momentum transfer q only.

$$\left|F_\lambda^C(q)\right|^2 = \frac{4\pi}{Z^2(2J_i+1)}\left|\left\langle Jf\left\|M_\lambda^C\right\|J_i\right\rangle\right|^2 \tag{13}$$

$$\left|F_\lambda^E(q)\right|^2 = \frac{4\pi}{Z^2(2J_i+1)}\left|\left\langle Jf\left\|T_\lambda^e\right\|J_i\right\rangle\right|^2 \tag{14}$$

$$\left|F_\lambda^M(q)\right|^2 = \frac{4\pi}{Z^2(2J_i+1)}\left|\left\langle Jf\left\|T_\lambda^m\right\|J_i\right\rangle\right|^2 \tag{15}$$

The related to the electromagnetic transition operators as

$$(M_\lambda^C,\ T_\lambda^e,\ T_\lambda^m)$$

$$M_{\lambda_\mu}^C(q) = \int d^3r\, j_\lambda(qr)Y_{\lambda_\mu}\hat{\rho}(r) \tag{16}$$

$$T_{\lambda_\mu}^e(q) = \frac{1}{q}\int d^3r\left\{\nabla\times j_\lambda(qr)Y_{\lambda\lambda 1}^\mu\right\}.\hat{J}(r) + q^2\int d^3r\left\{j_\lambda(qr)Y_{\lambda\lambda 1}^\mu\right\}.\hat{\mu}(r) \tag{17}$$

$$T_{\lambda_\mu}^m(q) = \int d^3r\left\{j_\lambda(qr)Y_{\lambda\lambda 1}^\mu\right\}.\hat{J}(r) + \int d^3r\left\{\nabla\times j_\lambda(qr)Y_{\lambda\lambda 1}^\mu\right\}.\hat{\mu}(r) \tag{18}$$

where $\hat{\rho}(r)$, $\hat{J}(r)$, and $\hat{\mu}(r)$, are the nuclear charge, the magnetization current density operators is $j_\lambda(qr)$, Bessel function of order λ, $Y_{\lambda\mu}$ is the spherical harmonic. The total form factor is equal to the addition of the longitudinal and transverse relations:

$$\left|F(q)\right|^2 = \left|F_\lambda^C(q,f,i)\right|^2 + \left(\frac{1}{2}+\tan^2(\frac{\theta}{2})\right)\left|F_\lambda^T(q,f,i)\right|^2 \tag{19}$$

(b) Hartree-Fock plus BCS calculations

The self-consistent mean field based on HF plus BCS calculations are designed to describe the structure of nuclei and study the evolution shapes, using the Skyrme forces performed to study the transitional in density shape where the pairing correlation have been taken into account. HF method is probably the best method for anticipating the total binding energies and single particle energies of closed shell nuclei [14]. Also SHF is a useful tool because this force is central and has zero-range interactions [15]. Nuclei is a quantum many-body system exhibiting the quadrupole collectivity associated with the shape of the mean field. The collective degree of freedom is associated with the measure of the operator $\hat{Q}$.

From these single-particle wave functions and fractional occupation amplitudes, a mean-field theory can be built υ_α, i.e., [16]

$$\{\psi_\alpha, \upsilon_\alpha, \alpha = 1,...,\Omega\} \tag{20}$$

where Ω denotes the size of the active single particle space.

The formula for the resulting BCS many-body state is [16].

$$\left|\phi\right\rangle = \prod_{\alpha>0}\left(u_\alpha + \upsilon_\alpha\hat{a}_\alpha^+\hat{a}_{\bar{\alpha}}^+\right)\left|0\right\rangle \tag{21}$$

Where $\left|0\right\rangle$ is the particle-vacuum state, is the Fermion production operator $\hat{a}_\alpha^+$ in state ψ_α, and is the time-reversed partner to state α. The local density of nucleons is defined as [16]

$$\rho_q(\vec{r}) = \sum_{\alpha\in q}\sum_s \upsilon_\alpha^2\left|\psi_\alpha(\vec{r},s)\right|^2 \tag{22}$$

The local nucleon density is defined as [16]

$$\rho_q(\vec{r}) = \sum_{\alpha \in q} \sum_{s} \upsilon_\alpha^2 \left|\psi_\alpha(\vec{r},s)\right|^2 \tag{23}$$

The total energy consists of

$$E_{tot} = T + E_{Skyrme} + E_{Coulomb} + E_{pair} + E_{cm} \tag{24}$$

$$E_C = \frac{e^2}{2}\int dV dV' \frac{\rho_p(\vec{r})\rho_p(\vec{r}')}{|\vec{r}-\vec{r}'|} - \int dV \frac{3e^2}{4}\left(\frac{3}{\pi}\right)^{\frac{1}{3}} \rho_p^{4/3} \tag{25}$$

where E_{Culomb} is the Coulomb energy

$$E_{pair} = \frac{1}{4} \sum_{q \in \{p,n\}} V_{pair,q} \int dV \left|\xi_q\right|^2 \left[1 - \frac{\rho}{\rho_{0,pair}}\right] \tag{26}$$

the pairing energy is

$$\xi_q(\vec{r}) = \sum_{\alpha \in q} \sum_{s} w_\alpha u_\alpha \upsilon_\alpha \psi_{\bar{\alpha}}(\vec{r},s)\psi_\alpha(\vec{r},s) \tag{27}$$

where dV represents the volume element in whole three-dimensional space and is the fundamental charge e. with e^2=1.43989 MeV.fm, and ξ_q is the pairing density, w_α is a soft pairing space cut-off. The variables $s \in \pm 1$ represent the spinor component of the wave functions.

The pairing energy includes the parameter $\rho_{0,pair}$ that controls the equilibrium between volume and surface pairing. Deformation of the nucleus is defined as the departure from spherical symmetry about the center of mass (c.m), which is quantified by the electric quadrupole moment. Hence, the most significant moments are center-of-mass moments [16]

$$\vec{R}_{type} = \frac{\int dV\, \vec{r}\, \rho_{type}(\vec{r})}{\int dV\, \rho_{type}(\vec{r})} \tag{28}$$

In terms of the spherical quadrupole moments, the anisotropic combinations can be quantified

$$Q_{2m,type} = \int dV\, r^2\, Y_{2m}\, \rho_{type}\left(\vec{r} - \vec{R}_{type}\right) \tag{29}$$

the quadrupole deformation parameter

$$\beta_{20} = \frac{4\pi}{3}\frac{Q_{20}}{AR^2}\ ,\ R = R_0\, A^{1/3}\ \ ,\ R_0 = 1.2\ \text{fm} \tag{30}$$

III. RESULTS AND DISCUSSION

In this study, the OBDM elements for low-lying positive parity J^+ states were calculated using the *sd*-shell model space. For negative parity J^- states, the *spsdpf* no core with (0, 1) ħω restriction and the *zbme* shell model spaces have been employed. Using the NuShellX@MSU code [17], all calculations were performed. As we mentioned previously, the Skyrme interaction was used to calculate the radial wave functions of the single-particle matrix elements, from which a one-body potential in HF theory with SLy4, parametrization can be generated in addition to the harmonic oscillator (HO) and Wood-Saxson potentials. For ^{20,22}Ne isotopes, using USDC [18] two-body effective interaction in the calculation of the OBDM and SLy4 parameterization yields root mean square (rms) charge radii of 2.954 and 2.9525 *fm*, which are in good agreement with the experimental values 3.005 and 2.9525 *fm* [19]. The calculated binding energies are 150.15 and 168.84 MeV, which are in reasonable agreement with the experimental values of 160.64 and 177.76 MeV [20]. The nuclear magnetic dipole moment is (1.076 and 0.780) *nm*, in good agreement with experimental values of +1.08 and +0.65 *nm* [19], and the electric quadrupole moment (Q2) is -14.31, and -14.03 $e^2.fm^2$, the experimental -23(3), -19(4) $e^2.fm^2$ [19]. All these results together match the experimental value.

Also, we have used the code SkyAx [16] is a highly optimized two-dimensional HF+ Bardeen-Cooper-Schrieffer (BCS) code is using for computing ground states and deformation energy surfaces for axially symmetric deformed nuclei. The calculated results will be discussed in three sections. The first will focus on the Excitation Energies and reduce transition probability, the second on electroexcitation Form Factor, and the third on structure densities in two dimensions (Contour Lines), which will be given.

1. Excitation Energies and reduce transition probability

The excitation energies and reduced transition probabilities for low-lying positive and negative parity states in ^{20,22}Ne isotopes are calculated and tabulated in Table 1 and compared with the corresponding experimental data. The OBDM

elements for positive parity states were calculated using *sd* MS with the last updated two-body effective interactions USDE [21] and USDC [18]. In contrast, for negative ones, we have used the *spsdpf* (no core with one ħω restriction) and *zbme* model spaces with WBP and REWILE effective interactions, respectively.

The majority of estimated excitation energies in all model spaces closely match experimental data. [19], except for a few levels. Those levels with deviations exceeding 1.5 MeV include 2_3^+ at 7.833 MeV for ^{20}Ne and 4_2^+ at 6.345 MeV for ^{22}Ne. The negative-parity energy levels are accurately predicted using *zbme* MS. However, for *spsdpf* MS, the excitation energy state 1_1^- at 7.119 MeV is overestimated by the experimental data. The coupling between the states, such as the $1p_{1/2}$ holes coupled to the $1d_{5/2}$ neutron ($1p$-$1h$), may account for these discrepancies. The additional pairing correlation and a change in the proton–neutron interaction, which results in a more considerable quadrupole deformation energy, reduce the energy of the $1p$–$1h$ state [8]. Fig.1 illustrates the extent of convergence between theoretical calculations and experimental data.

The calculated reduced transition probabilities $B(EL)$ for the low-lying positive and negative parity states in ^{20}Ne and ^{22}Ne isotopes are presented in Table 2. The discrepancies with experimental data regarding the energy of transitions from these states might be due to the possible admixture of states involving neutron and proton excitations. From a general point of view, the $B(EL)$ values for the transitions of low excitation energies agree reasonably well with experimental data [20,22-24]. The $B(E2)$ transition rates are slightly larger than the experimental data except for 2_1^+, where the agreement is quite good for 2_3^+ in ^{22}Ne using the USDE interaction. The slight difference between the experimental data and the theory could be because the quadrupole vibration was not taken into account. Regarding $B(E3)$ and $B(E1)$ transition probabilities in ^{22}Ne, the calculated results are in poor agreement with the experimental results.

Table 1. Excitation energies in MeV for a different transition to excited states using two-body interactions USDE, USDC, WBP, and REWILE. The experimental data taken from Ref. [19]

Nucleus	J^π	E_x(Exp.)	Model Space			
			sd		*spsdpf*	*zbme*
			USDE	USDC	WBP	REWILE
^{20}Ne	2_1^+	1.633(15)	1.736	1.735	---	---
	2_2^+	7.421(12)	7.548	7.532	---	---
	2_3^+	7.833(15)	9.598	9.992	---	---
	4_1^+	4.247(11)	4.192	4.146	---	---
	4_2^+	9.031(7)	9.974	9.956	---	---
	3_1^-	5.787(26)	---	---	7.119	6.099
	1_1^-	5.621(17)	---	---	5.448	5.436
^{22}Ne	2_1^+	1.274(7)	1.350	1.345	---	---
	2_2^+	4.456(9)	4.301	4.321	---	---
	2_3^+	5.363(11)	5.160	5.130	---	---
	4_1^+	3.357(5)	3.370	3.335	---	---
	4_2^+	6.345(10)	5.380	5.404	---	---
	3_1^-	5.910(9)	---	---	5.372	5.386
	1_1^-	6.689(11)	---	---	6.671	5.720

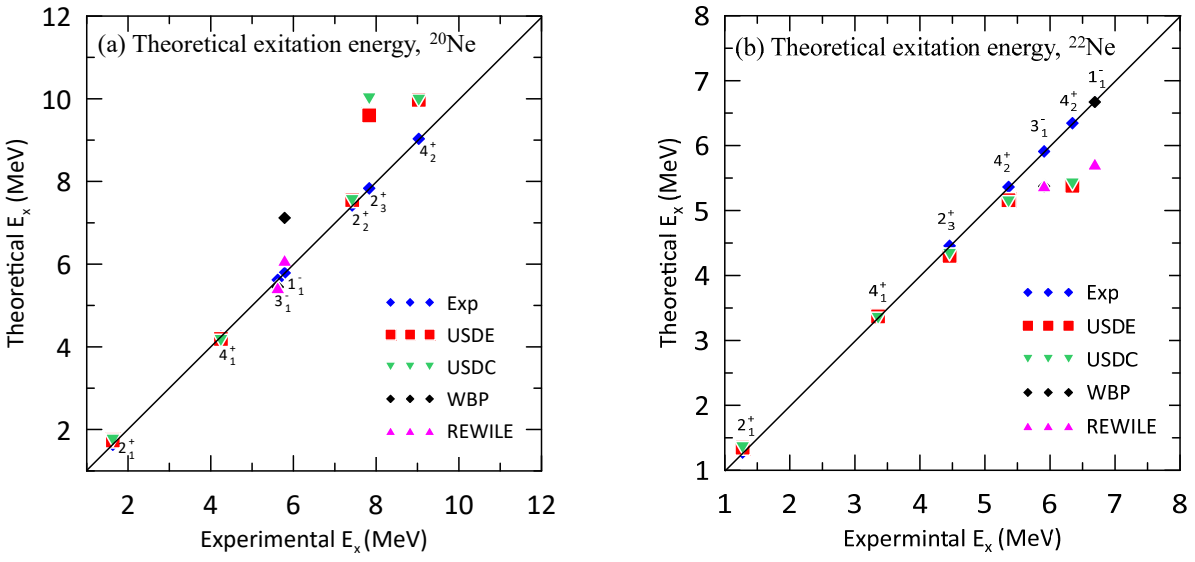

Figure 1. Theoretical excitation energies in MeV states vs. experimental for the different transition to low-lying excited states using USDE, WBP, and REWILE two-body effective interactions. The experimental data are taken from Ref. [19].

Table 2. The reduced transition probabilities B(EL) in e^2fm^{2L} for the different transition to excited states using two-body interactions USDE, USDC, WBP, and REWILE. The experimental data taken from Ref. [20, 22-24]

Nucleus	J^π	E_x(Exp.)	B (EL)Exp	B(EL)Theo.	
				USDE	USDC
^{20}Ne	2_1^+	1.633(*15*)	340(30)	462	247.1
	2_2^+	7.421(12)	0.13(0.03)	0.185	0.112
	2_3^+	7.833(15)	0.83(0.13)	2.901	2.474
	4_1^+	4.247(11)	---	0.6257E+05	0.6408E+05
	4_2^+	9.031(7)	---	0.3418E+04	0.3548E+04
				WBP	**REWILE**
	3_1^-	5.787(26)	1763	2172	1528
	1_1^-	5.621(17)	---	0.187E-03	0.252E-07
				USDE	**USDC**
^{22}Ne	2_1^+	1.274(7)	271(36)	384	393
	2_2^+	4.456(9)	13(2)	31.1	29.5
	2_3^+	5.363(11)	3.2(1.5)	3.802	2.48
	4_1^+	3.357(5)	17000(4000)	20500	21930
	4_2^+	6.345(10)	---	7076	6904
				WBP	**REWILE**
	3_1^-	5.910(9)	870(250)	407.7	1278
	1_1^-	6.689(11)	0.08(0.04)	0.914 E-05	0.349 E-03

2. Electroexcitation form factor

The nuclear structure can only enter the cross-section through longitudinal (FC), transverse (FE), and magnetic (FM). These form factors are functions of the momentum transfer q only. The FC and FT form factors correspond to fields parallel and perpendicular to the direction of momentum transfer, respectively [25]. $|F_T(q)|^2$, is influenced by both magnetic and electric currents, whereas $|F_L(q)|^2$ is caused solely by the electric Coulomb field.

A. Elastic electron scattering form factor ($J^\pi = 0^+$)

Fig. 2 (a) and (b) depicts the calculated elastic longitudinal C0 electroexcitation form factors for the ground state (GS) of ^{20,22}Ne isotopes in the *sd*-shell MS wave functions employing SLy4, HO, and WS parameterization compared with experimental data from Ref. [22,26]. Observable agreement exists in the momentum transfer region of q (0-1.3) fm^{-1}, based on experimental data.

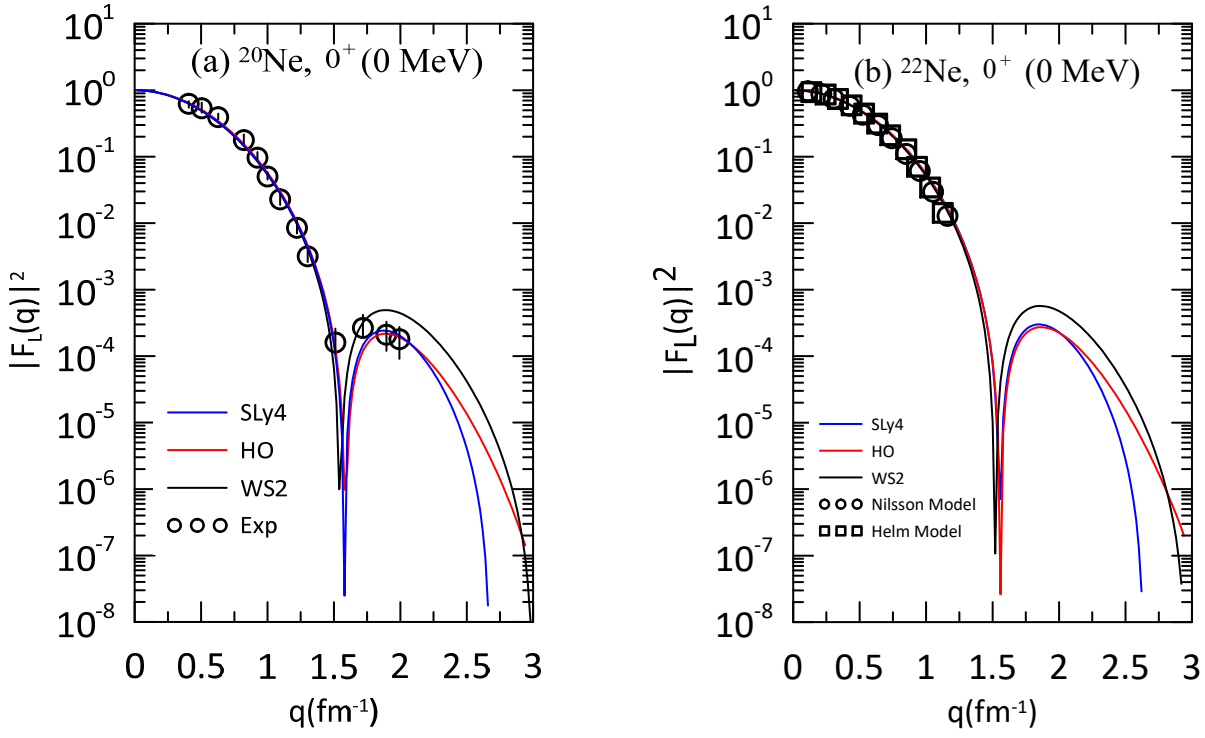

Figure 2. Theoretical longitudinal C0 form factors (a) for ^{20}Ne isotope 0^+, (0 MeV) (b) for ^{22}Ne isotope 0^+, (0 MeV) using SLy4 parameterization, HO and WS compared with experimental data taken from Ref [22, 23]

B. Inelastic scattering form factor

1. Positive parity states

The calculated inelastic longitudinal C2 electroexcition form factors of transition at positive parity states 2^+ in ^{20}Ne isotope are shown in Fig. 3; (a) 2_1^+(1.633 MeV), (b) 2_2^+(7.422 MeV), and (c) 2_3^+(7.833 MeV), and for ^{22}Ne isotope Fig.4 (a) 2_1^+(1.274 MeV), (b) 2_2^+(4.456 MeV), and (c) 2_3^+(5.363 MeV). Inspection of these figures reveals that the longitudinal form factors are all dominated by the electric quadrupole transition C2 components and are in reasonable agreement with available experimental data [22,23] using all the single particle potentials. Although we have not been changing parameters, they were altered to accommodate the experimental electron scattering data. The WS potential agrees satisfactorily with experimental data, except 2_2^+, at (7.422MeV) higher than experimental data at all momentum transfer points.

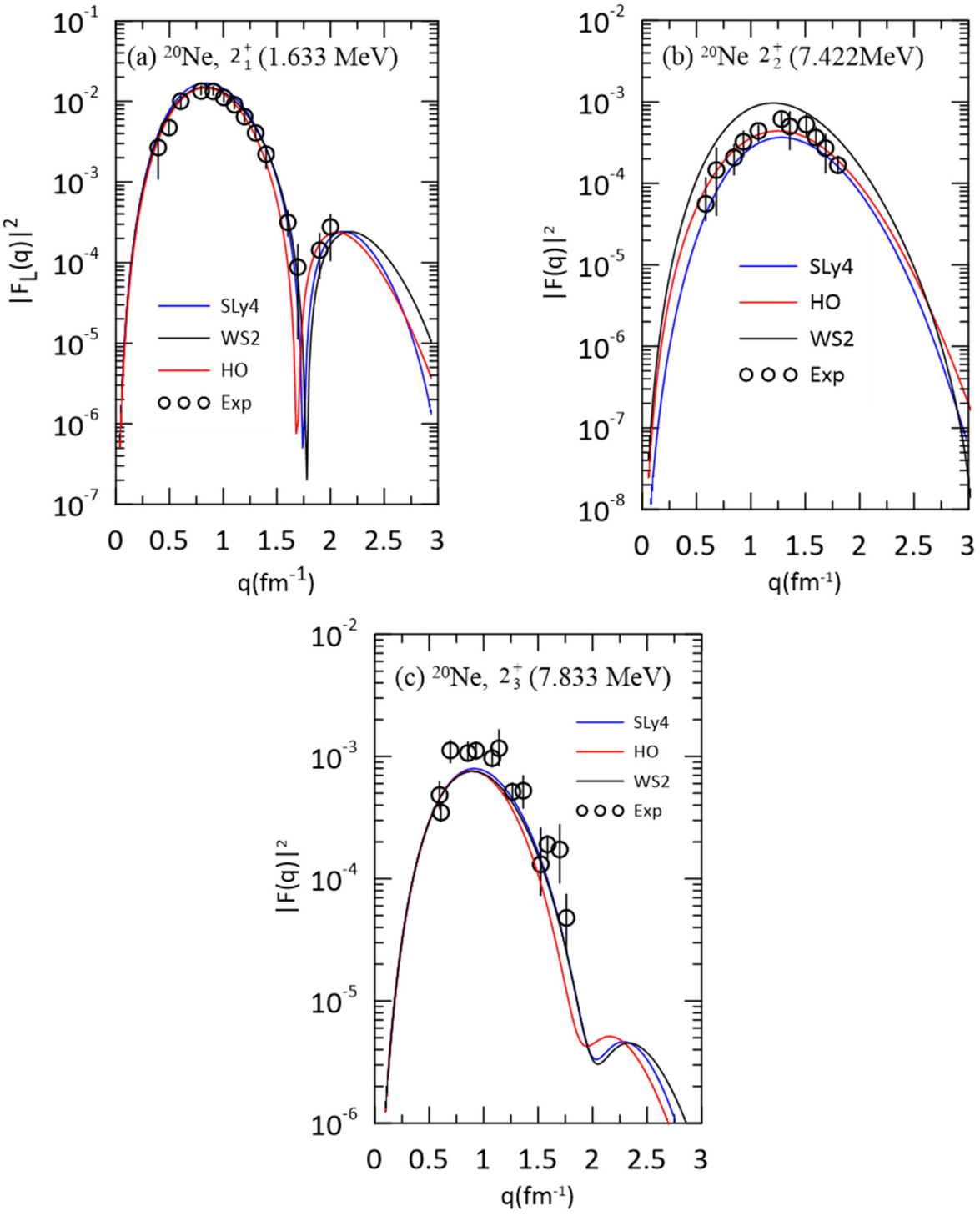

Figure 3. longitudinal C2 form factor for ^{20}Ne using SLy4, HO, and WS parametrizations vs with the experimental value taken from Ref. [22,23]

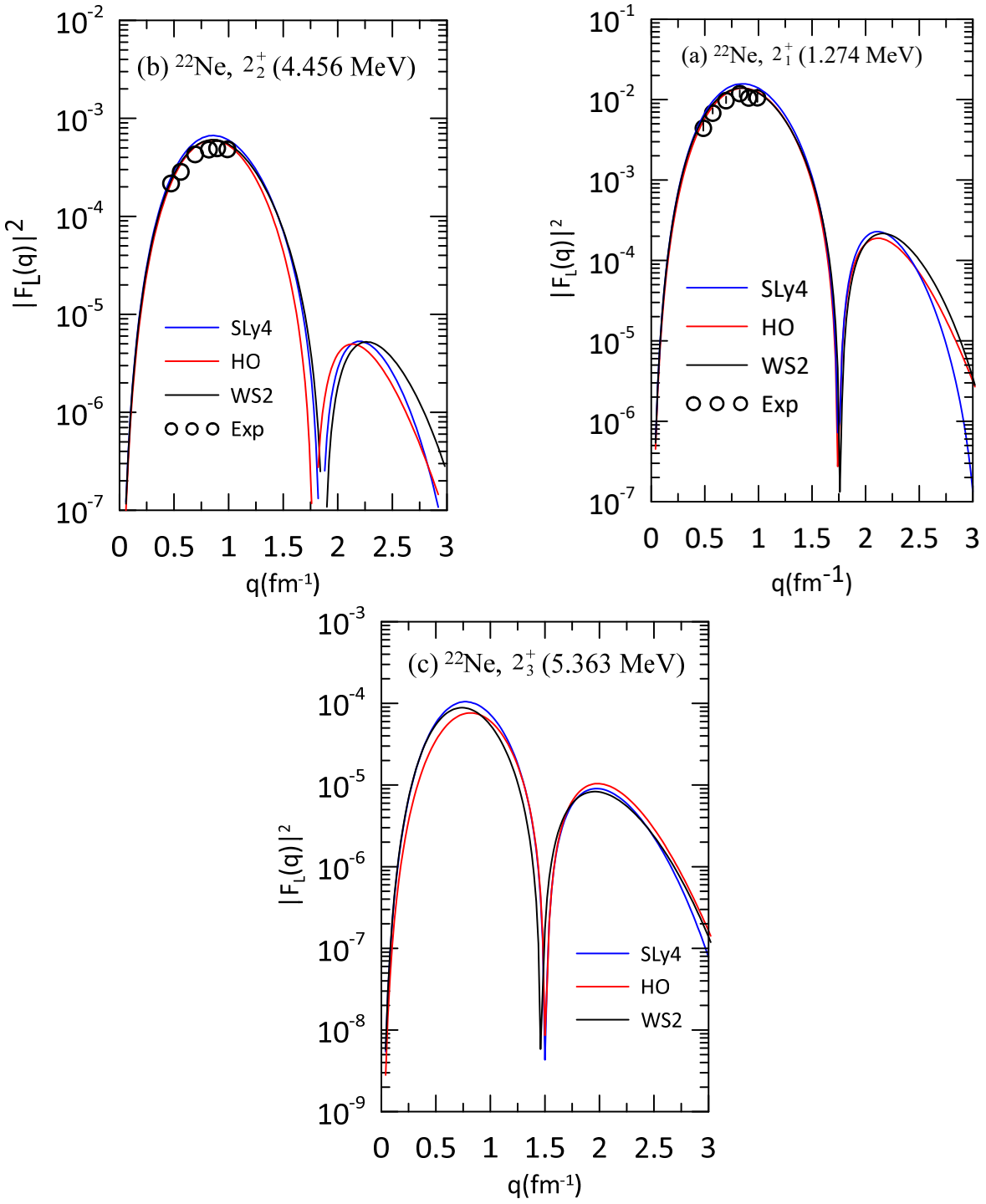

Figure 4. longitudinal C2 form factor for ^{22}Ne calculate by SLy4, HO, and WS parametrizations vs the experimental data taken from Ref. [22,23].

Fig. 5 (a) and (b) show the calculated inelastic longitudinal C4 electroexcitation form factor of the transition to the 4^+ state in ^{20}Ne at (4.2477MeV) and in ^{22}Ne at (3.357 MeV). It is obvious that the longitudinal form factor is dominated by electric hexa transition C4 components and in reasonable agreement with experimental data in light of the fact that parameters were not changed to fit the experimental electron scattering data [23,24].

2. Negative parity states

Based on the results obtained in showing the sensitivity of the effect of changing the single particle potentials. The longitudinal form factors were calculated, considering the effect of the two-particle interactions in improving the convergence with the practical values. Fig. 6 shows the calculated total form factors for the transition to the negative-parity state1_1^-, (5.787 MeV) and 3_1^-, (5.624 MeV) for ^{20}Ne isotope compared with experimental data [23], which refer to the total sum of (1_1^- ,3_1^-) states together. The WBP interaction predicts a rapid increase in low-lying C3 concentration.

While C1 form factor result under the experimental data. On the contrary, the REWILE result is in reasonable agreement with experimental results for the C3 form factor, in contrast to the C1 result, which was based on experimental data.

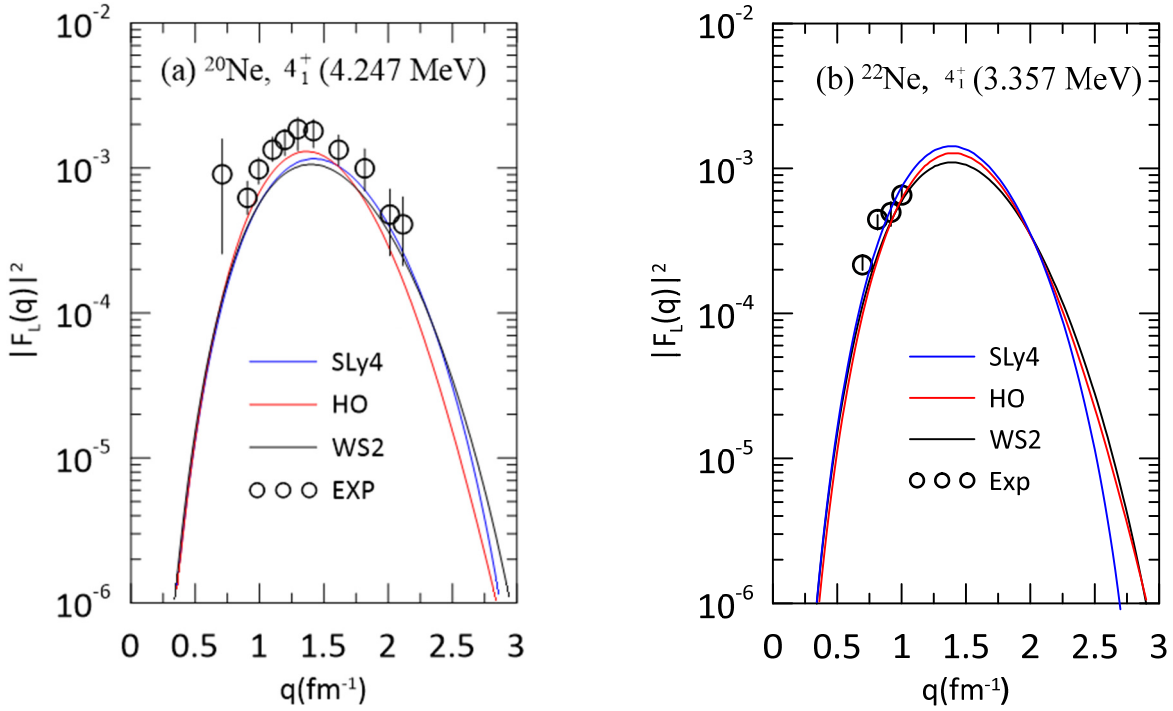

Figure 5. Theoretical longitudinal C4 form factor for ^{20}Ne and ^{22}Ne isotope, using SLy4 parameterization in comparison with experimental data taken from Ref. [23, 24].

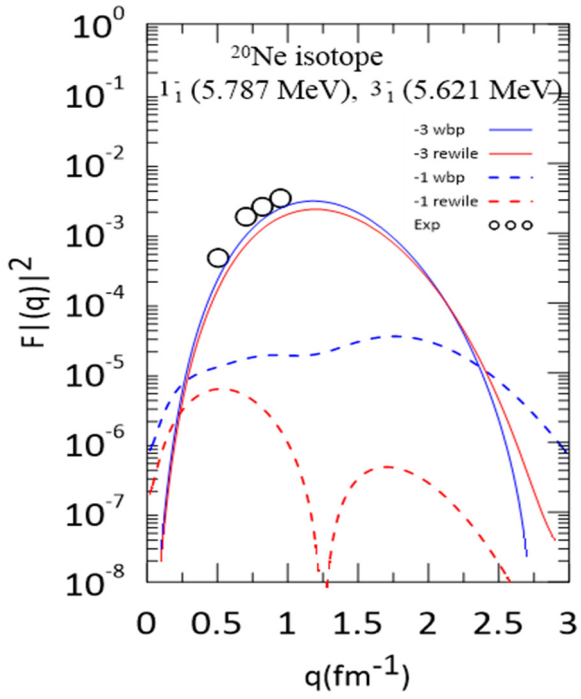

Figure 6. Total form factor for the transition $^{-}1_1$(5.578) and $^{-}3_1$(5.621MeV) using SLy4 parameterization in comparison with experimental data taken from Ref [26]

Fig. 7 (a), and (b) show the calculated longitudinal C1, C3 form factors in ^{22}Ne isotope for the transitions 1_1^-, (6.689 MeV) and 3_1^-, (5.910 MeV) states. The WBP prediction agrees qualitatively with experimental data in all momentum transfer regions of these data. Also, it can be observed that the REWILE prediction for the longitudinal C1 form factors under estimate the experimental result. The longitudinal C1 experimental data reveals an additional maximum form factor. The theoretical C1 contribution does not include this maximum. From the our previous calculates

we noted that WBP is the best in approximation with experimental data, thus means the contribution valance nucleon in $1p_{3/2}$ state is accountable for the substantial C1, C3 strength.

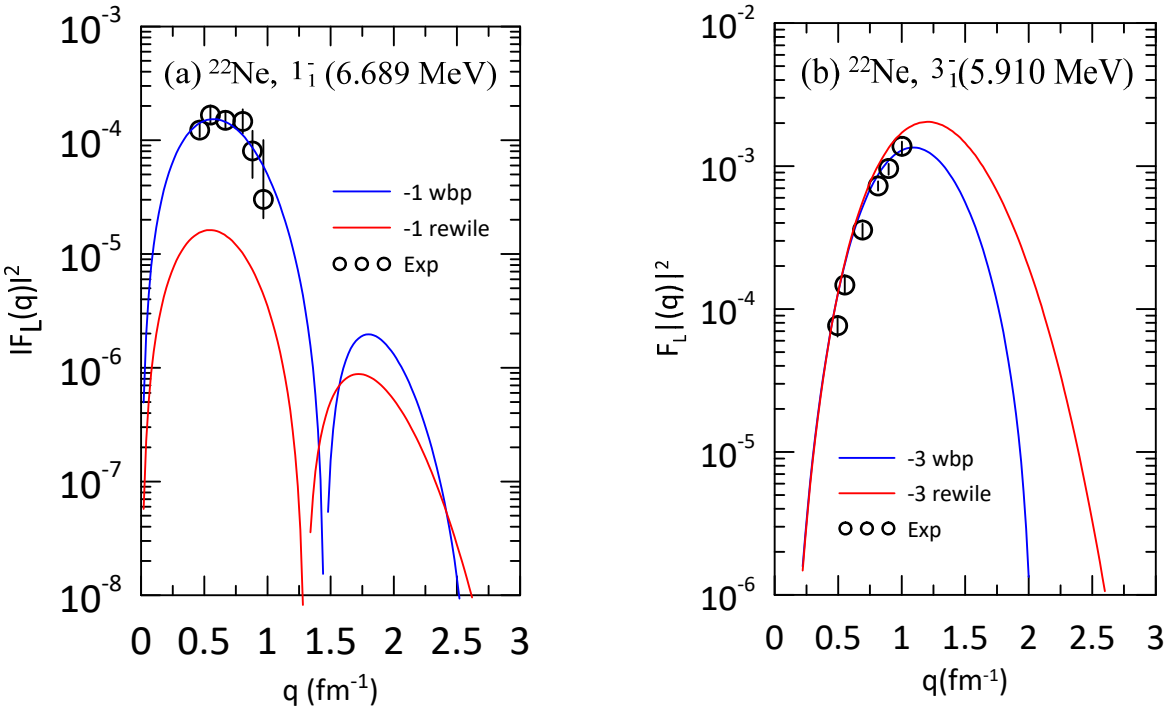

Figure 7. Theoretical longitudinal C1 and C3 form factor (a) for1^-_1, 6.689 MeV. (b) For 3^-_1, 5.910 MeV using SLy4 parameterization in comparison with experimental data taken from Ref. [23]

3. The Quadrupole Deformation using BCS Calculation

Fig. 8 and 9 shows the potential energy curve of $^{20,\ 22}$Ne isotopes (on the left) as a function of the quadrupole deformation parameter $\beta 2$. The corresponding neutron and proton structure densities are also displayed (on the right). Following the color code, the red and blue colors correspond to the high density (~0.08 fm^{-3}) and low density (~0.02 fm^{-3}), respectively. The two local minima in Fig. 8 are predicted as (a) β_2=-0.154 and (b) β_2=0.406. ^{20}*Ne* have a stable quadrupole deformation where the high neutron and proton density distribution is in the center for the two regions (a) and (b), as expected (^{20}Ne have the same numbers of protons and neutrons), where there is no effect of *n-p* pairing. For the ^{22}Ne isotope, the two local minima in Fig. 9 are predicted as (a) β_2=-0.204 and (b) β_2=0.404. We can notice that the stability decreases with decreasing central proton density because of the two neutrons added to the last state, which increases the effect of *n-p* pairing.

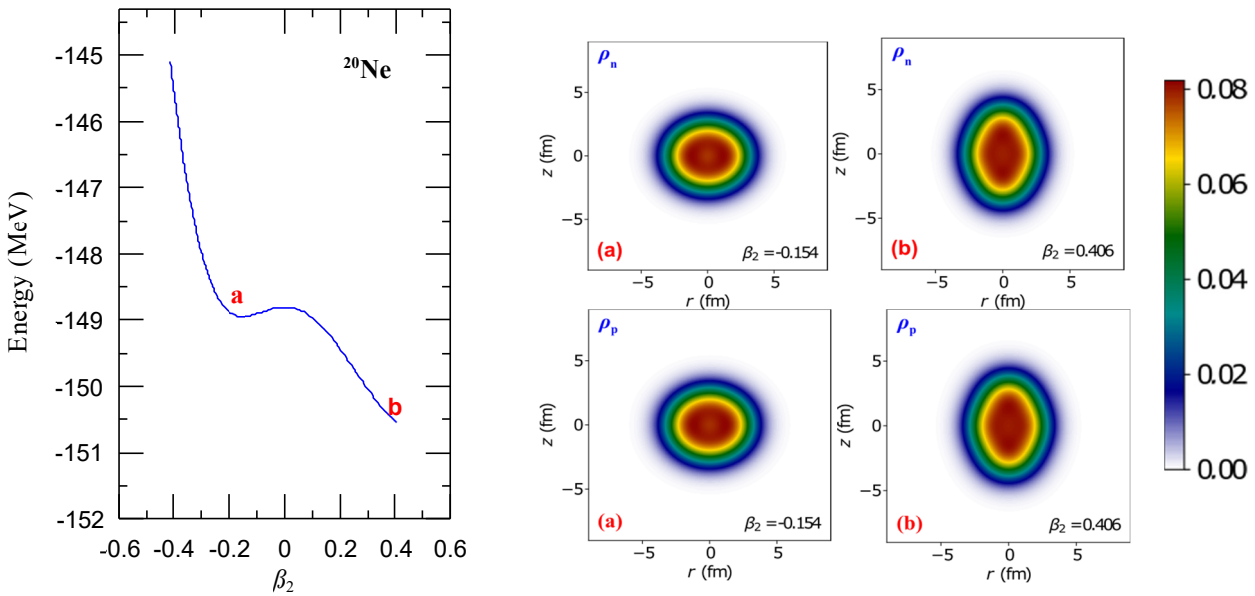

Figure 8. Left, the potential energy curve of ^{20}*Ne* as a function of the quadrupole deformation parameter. The neutron and proton structure densities corresponding to the two local minima, marked a, and b are shown in the right panel

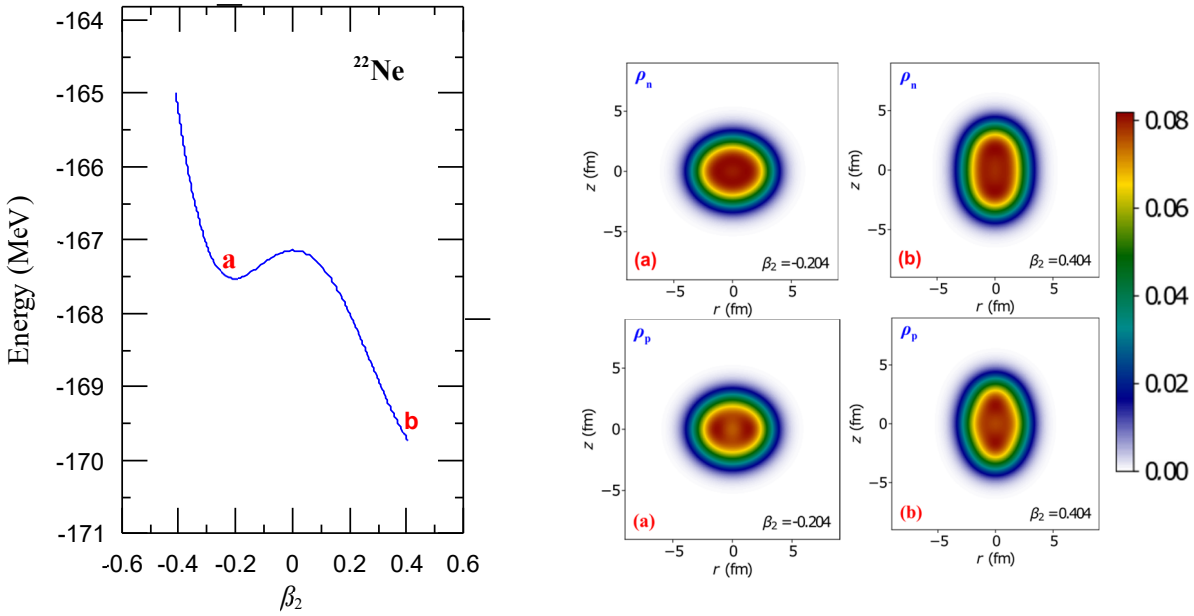

Figure 9. Left, the potential energy curve of ^{22}Ne as a function of the quadrupole deformation parameter. The neutron and proton structure densities corresponding to the two local minima, marked a, and b are shown in the right panel

IV. CONCLUSION

In this study, the nuclear structure of ^{20,22}Ne isotopes was investigated in the framework of the shell model and BCS calculation with Skyrme parametrization. In this context, excitation energies and the corresponding reduced transition probabilities, the elastic and inelastic electroexcitation form factors for positive and negative parity states in the momentum-transfer range 0.0 <q< 3.0 fm^{-1}, and quadrupole deformation parameter are discussed. Additionally, the work inspects the effect of three single-particle potentials; in particular, HO, WS and SLy4 parameterizations. It can be concluded that, on the whole, the impression of using different model spaces has fairly well reproduced the experimental data for positive and negative parity states and is not sensitive for changing the single particle potentials rather than the two-body effective interactions. The most important limitation lies in the fact that the strong collective feature of the nuclei in this mass region and internally consistent interaction formulation.

ORCID IDs

Ali A. Alzubadi, https://orcid.org/0000-0002-7226-1141

REFERENCES

[1] R. Stock, *Encyclopedia of Nuclear Physics, and its Applications*, 1st edition, (Wiley-VCH, 2013).
[2] O. Sorlin, and M.G. Porquet, "Nuclear magic numbers: new features far from stability," Prog. Part. Nucl. Phys, **61**, 602-673 (2008). https://doi.org/10.1016/j.ppnp.2008.05.001
[3] R.F. Casten, *Nuclear Structure from a Simple Perspective*, 2nd edition, (Oxford Univ. Press, New York, 2000).
[4] P. Ring, and P. Schuck, *The Nuclear Many-Body Problem*, (Springer Verlag, Berlin Heidelberg, 1980).
[5] E. Caurier, G. Martinez-Pinedo, F. Nowacki, A. Poves, and A.P. Zuker, Rev. Mod. Phys. **77**, 427 (2005). https://dx.doi.org/10.1103/RevModPhys.77.427
[6] W. Greiner, and J.A. Maruhn, *Nuclear Models*, (Springer, 1996).
[7] J.B. Mc.Grory, and B.H. Wildenthal, Phys. Rev. C, **7**, 974 (1973). https://doi.org/10.1103/PhysRevC.7.974
[8] J.E. Garcia-Ramos, M.V. Andrés, J.A.L. Valera, and A.M. Moro, editors, *Basic Concepts in Nuclear Physics: Theory, Experiments and Applications*, (Springer, Span, 2018). https://doi.org/10.1007/978-3-030-22204-8
[9] R.A. Radhi, A.A. Alzubadi and A.H. Ali, Phys. Rev. C, **97**, 064312 (2018). https://doi.org/10.1103/PhysRevC.97.064312
[10] P.J. Brussaard, and P.W.M. Glaudemans, *Shell Model Appli ations in Nuclear Spectroscopy*, (North Holand, Amsterdam, 1977).
[11] R.A. Radhi, A.A. Alzubadi, and N.S. Manie, Phys. Rev. C, **97**, 1 (2018). https://doi.org/10.1103/PhysRevC.97.024316
[12] D. Vautherin, and D.M. Brink, Phys. Rev. C, **5**, 626 (1972). https://doi.org/10.1103/PhysRevC.5.626
[13] T. de Forest, and J.D. Walecka, Adv. Phys. **15**, 1 (1966). https://doi.org/10.1080/00018736600101254
[14] A.A. Alzubadi, and R.A. Allawi, Indian J. Phys. **96**, 1205 (2022). https://doi.org/10.1007/s12648-021-02052-x
[15] A.A. Alzubadi, Indian J. Phys. **89**, 619 (2015). https://doi.org/10.1007/s12648-014-0614-3
[16] P.-G Reinhard, B. Schuetrumpf, J.A. Maruhn, "The Axial Hartree–Fock + BCS Code SkyAx," Comp. Phys. Comm. **258**, 107603 (2021). https://doi.org/10.1016/j.cpc.2020.107603
[17] B.A. Brown, and W.D.M. Rae, Nucl. Data Sheets, **120**, 115 (2014). https://doi.org/10.1016/j.nds.2014.07.022
[18] A. Magilligan, and B.A. Brown, "New isospin-breaking "USD" Hamiltonians for the sd shell," Phys. Rev. C, **101**, 064312 (2020). https://doi.org/10.1103/PhysRevC.101.064312
[19] National Nuclear Data Center (NNDC), Brookhaven National Laboratory, Upton, NY, 11973-5000, http://www.nndc.bnl.gov/
[20] B. Pritychenko. M. Birch, B. Singh, and M. Horoi, Atom. Data Nucl. Data Tab. **107**, 1 (2016). https://doi.org/10.1016/j.adt.2015.10.001

[21] W.A. Richter, S. Mkhize, and B.A. Brown, Phys. Rev. C, **78**, 064302 (2008). https://doi.org/10.1103/PhysRevC.78.064302
[22] S. Mitsunobu, and Y. Torizuka, Phys. Rev. Lett. **28**, 920 (1972). https://doi.org/10.1103/PhysRevLett.28.920
[23] X.K. Maruyama, F.J. Kline, J.W. Lightbody, Jr., S. Penner, W.J. Briscoe, M. Lunnon, and H. Crannell, Phys. Rev. C, **19**, 1624 (1979). https://doi.org/10.1103/PhysRevC.19.1624
[24] A.I. Steshenko, Nucl. Phys. A, **445,** 462 (1985). https://doi.org/10.1016/0375-9474(85)90452-X
[25] A. Obertelli, and H. Sagawa, *Modern Nuclear Physics from Fundamentals to Frontiers*, (Springer Nature, Singapore, 2021).
[26] R.P Singhal, H.S. Caplan, J.R. Moreira, and T.E. Drake, Can. J. Phys. **51,** 2125 (1973). https://doi.org/10.1139/p73-278

ФОРМ-ФАКТОРИ ЕЛЕКТРОЗБУДЖЕННЯ ТА ДЕФОРМАЦІЯ ІЗОТОПІВ ^{20,22}NE НА ОСНОВІ МОДЕЛІ ОБОЛОНКИ ТА РОЗРАХУНКІВ HARTREE-FOCK PLUS BCS

Омар А. Алсвайдаві, Алі А. Альзубаді
Факультет фізики, Науковий коледж, Багдадський університет, Багдад, Ірак

За допомогою оболонкової моделі з розрахунками Скірма-Хартрі-Фока досліджено ядерну структуру ізотопів ^{20,22}Ne. Зокрема, були досліджені переходи до збуджених станів низького рівня позитивної та негативної парності в трьох моделях оболонок; sd для позитивних станів парності, *spsdpf* з великим базисом (без ядра) та простори моделі *zbme* для станів з негативною парністю. Оцінено енергії збудження, зменшені ймовірності переходу, пружні та непружні форм-фактори та порівняно з наявними експериментальними даними. Взаємодія Скірма була використана для створення потенціалу одного тіла в розрахунках Хартрі-Фока для кожного вибраного збудженого стану, який потім використовується для розрахунку одночастинкових матричних елементів. Взаємодія Скірма була використана для розрахунку радіальних хвильових функцій одночастинкових матричних елементів, з яких може бути згенерований потенціал одного тіла в теорії Хартрі-Фока з параметризацією SLy4. Крім того, ми дослідили взаємодію між профілями густини нейтронів і протонів у двох вимірах разом із деформаціями ^{20,22}Ne за допомогою розрахунків Хартрі-Фока та BCS.

Ключові слова: *Sd модельний простір; стан негативного паритету; пружний і нееластичний форм-фактор; розподіл щільності*

East European Journal of Physics. 2. 150-156 (2023)
DOI:10.26565/2312-4334-2023-2-14 ISSN 2312-4334

PHYSICOCHEMICAL CHARACTERISTICS FOR Fe_n (n = 2–10) CLUSTER BY DENSITY FUNCTIONAL THEORY[†]

Yamina Benkrima[a], Djamel Belfennache[b], Radhia Yekhlef[b], Mohammed Elbar Soudani[c], Abdelkader Souigat[a], Yahia Achour[d,e]

[a]*Ecole normale supérieure de Ouargla, 30000 Ouargla, Algeria*
[b]*Research Center in Industrial Technologies CRTI, P.O. Box 64, Cheraga, 16014 Algiers, Algeria*
[c]*Laboratory for the Development of New and Renewable Energies in Arid and Saharan Zones, Faculty of Mathematics and Materials Science, Kasdi Merbah Ouargla University, Ouargla 30000 Algeria*
[d]*Laboratoire de Physique Des Matériaux (LPM), Université Amar Telidji de Laghouat, BP37G, Route de Ghardaïa,03000 Laghouat, Algeria*
[e]*Ecole Normale Supérieure de Laghouat, BP 4033 Rue des martyrs, La gare, 03000, Laghoat, Algeria*
**Correspondence Author e-mail: b-amina1@hotmail.fr*
Received March 14, 2022; revised April 5, 2023; accepted April 6, 2023

In this work, we present a theoretical study on the equilibrium geometry and the energetic, electronic and magnetic properties of Fe_n (n = 2–10) based on the use of density functional theory (DFT). The results are obtained using Both Generalized Gradient Approximation according to the scheme described by Perdew-Burke-Ernzerhof (GGA-PBE). More stable structures obtained compared to other isomers have not been previously found. It is shown by the results calculated as the calculated fragmentation energy, and the second-order energy difference that Fe_n (n = 7,8,9) clusters are more stable than the other cluster sizes. The calculated magnetic properties of the most stable clusters display varying magnetic torque between values 3.00 μ_B and 3.35 μ_B, except for the Fe_{10} cluster, which takes the upper value of 3.38 μ_B. These results are very important for experimental experts who are active in designing new nanocatalysis systems in the physical and chemical fields.
Keywords: *Iron clusters; Relative stabilities; Density functional theory DFT; Binding energies;Magnetic properties*
PACS: 36.40.Cg

1. INTRODUCTION

Iron is one of the most important materials due to its physical and magnetic properties among the first transition (TM) metals. It also has high magnetism and in addition to the high value of transverse relaxation, iron metal and its oxides make it a suitable component in magnetic nanoparticles (MNPs). The high values of transverse relaxation result from the external magnetic field, and thus the detection of signals is facilitated through the transverse relaxation of iron as well. The uses of compounds based on MNP materials fall into several fields, the most important of which are in biosensing applications using magnetic resonance [1], as well as the detection of tuberculosis bacteria [2], As for magnetic enrichment, it is used to detect the in vivo circulation of cancer cells [3].

Cluster physicists admit, according to their opinion, the difficulty of conducting accurate studies of iron clusters at experimental levels [4,5]; however, applications have been made using density functional theory (DFT), which has been successful and has become widely used in calculating TM properties during the past years [6]. Among the most important advantages of the DFT theory is the ability to look for the correct and accurate electronic structure among many other possible cases that has lower energy [5], this is what makes us obtain the accurate and correct magnetic and structural properties. Thus, the presence of a strong correlation in partially filled d orbitals leads to the highest magnetic moments. In previous theoretical studies of small iron, clusters [7-10] showed a close correlation between their size and the value of their magnetic moment. The experimental study of clusters containing more than 500 atoms was also addressed. Whereas, the obtained iron cluster structures were in deformed geometries and completely different from the bcc crystal structure of iron, this was predicted by Jahn-Teller [11].

In this work we confirm the value of the quality of the calculations of all electrons within the DFT framework and find the most stable Fe_n clusters compared to other isomers.

In addition, we also calculate the important electronic properties of these clusters such as homo–lumo energy, second-order energy difference, vertical ionization potential (VIP) and vertical electronic affinity (VEA), this is for a deeper understanding of the stability of the clusters and the differences between them. The next section reviews the theoretical methodology used in the calculation briefly, while the third section presents the results of our calculations and their analysis, while this work concludes with a general summary.

2. MATERIALS AND METHODS

Our calculations were performed in order to determine the ground-state structures within the framework of spin-polarized density functional theory [12] with the use of the generalized gradient approximation (GGA) defined by Perdew,

[†] ***Cite as:*** Y. Benkrima, D. Belfennache, R. Yekhlef, M.E. Soudani, A. Souigat, and Y. Achour, East Eur. J. Phys. **2**, 150 (2023), https://doi.org/10.26565/2312-4334-2023-2-14

Burke, and Ernzerhof (PBE) [13,14] functional has been used for the exchange correlation energy as implemented in the SIESTA package [15]. Among the features of this program is that it can be used for all kinds of non-local pseudo-standards preservation method for Troullier-Martins [16]. The geometries were optimized without any symmetry constraints by self-consistent field (SCF) solving of the Kohn–Sham equations with a convergence criterion of 10^{-4}a.u. on the electron density and energy.

In order to avoid interaction between neighboring clusters, we used the cubic supercell of 20 Å void, and also used the conjugate gradient (CG) algorithm. Using the Γ point approximation, the k grid integration was carried out. Geometrical optimizations were considered as converged when the residual forces were smaller than 10^{-3} eV/Å.

We employed the double polarizer ξ (DZ) basis with polarization function for all iron atoms. We have performed a relaxation for a large number of possible initial structures for iron clusters in the size (n= 2–10) atom-sized iron clusters in a very recent and previously unpublished work. In this work we could find the most appropriate structures of Fe_n clusters by searching the various possible isomers.

We studied the various properties of iron Fe_n clusters by determining their relative stability, which is represented by the binding energy E_b, fragmentation energy E_f, second-order energy difference Δ_2E. The electronic properties represented by the vertical ionization potential (VIP), vertical electronic affinity (VEA) and Chemical hardness η, were also investigated. All these quantities were calculated according to the following formulas:

The binding energy E_b/atom.

$$E_b\,(Fe_n) = [nE\,(Fe) - E\,(Fe_n)]/(n). \quad (1)$$

Fragmentation energy E_f

$$E_f\,(Fe_n) = E\,(Fe_{n-1}) + E\,(Fe) - E\,(Fe_n). \quad (2)$$

Second-order energy difference Δ_2E

$$\Delta_2E\,(Fe_n) = E\,(Fe_{n+1}) + E\,(Fe_{n-1}) - 2E\,(Fe_n). \quad (3)$$

The HOMO–LUMO energy ΔE

$$\Delta E = E\,(LUMO) - E\,(HOMO). \quad (4)$$

Vertical ionization potential (VIP)

$$VIP = E\,(Fe_n^{+}) - E\,(Fe_n). \quad (5)$$

Vertical electronic affinity VEA

$$VEA = E\,(Fe_n^{-}) - E\,(Fe_n). \quad (6)$$

Chemical hardness η

$$\eta = VIP - VEA. \quad (7)$$

Where E is the total energy of the given system.

3. RESULTS AND DISCUSSION

3.1. Structural Properties

We found a large number of isomers and determined the ground state structure of all Fe_n clusters (n = 2–10) using the above calculation scheme. The most stable structures were selected for each size among the lower energy isomers, as shown in Figure 1.

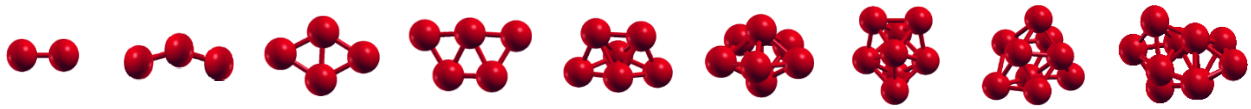

Figure 1. The lowest energy structures of Fe_n (n = 2–10) clusters

In the Table we calculated bond length for Fe-Fe dimer is 1.98 Å and its binding energy per atom of 1.40 eV. In Figure 1 shows the most stable structures in this study, using SIESTA program based on DFT. Actually, this result is close to theoretical results of B.V. Reddy et al. and S. Dhar et al. and J.L. Chen et al. [17-19] and experimental results of the average bond length in the work of P.A. Montano et al. and H. Purdum et al. [20,21].

Table 1. Bond lengths of dimer Fe_2(Å).

This work	Other calculations	Experimental
1.98	2.02 [17] 1.96 [18] 1.98 [19]	1.87 [20] 2.02 [21]

Various values of the average bond length of clusters Fe_n where (n= 2–10) are shown in Figure 2. For the clusters of Fe_n where (n=2–6), they are either linear or closed Chains in the plane, with an average bond length estimated as 1.98 Å, 2.11 Å, 2.28 Å, 2.37 Å, 2.53 Å, respectively. Generally, it is observed that the average bond length increases with the cluster size.

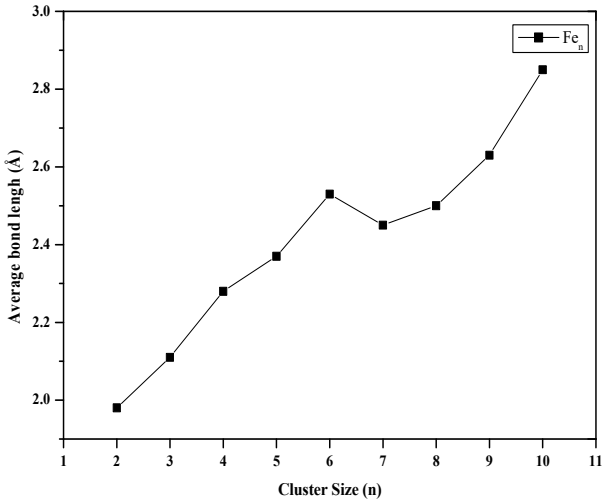

Figure 2. Average bond lengths for Fe_n(n=2–10) clusters

Based on the results shown in Figure 2, we conclude that the values of the average bond length increase in parallel with the increase in the cluster size. This is due to the fact that the ratio of atoms on the surface of the cluster is greater than the ratio of atoms in the core of it. In fact, because they are less compact, they cause the increase in the bond length.

3.2. Relative Stability

One of the most important physical factors that must be studied in the physics of materials and clusters is:

Binding Energy (cohesion)

It shows the stability of clusters obtained by comparing the result of their binding energy to other previous results for the same metal clusters. We report the calculated binding energies of Fe_n (n = 2 –10) clusters their growth with cluster size is plotted for the lowest-energy of each cluster in Figure 3. Through the general form, we notice a direct relationship, as the increase in the binding energy corresponds to the increase in the mass size. This behavior means that the clusters can obtain energy continuously during the growth process.

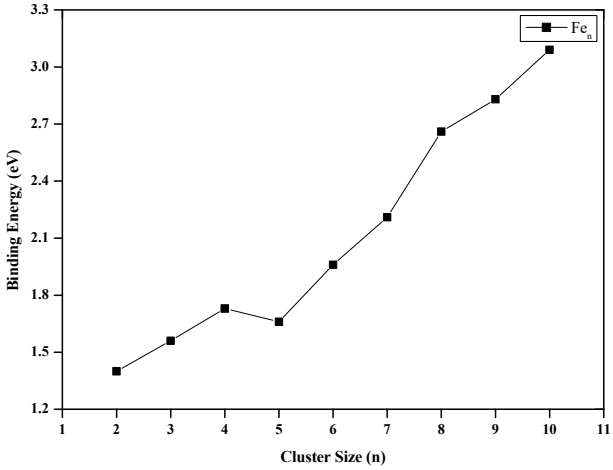

Figure 3. Binding energies per atom for the Fe_n (n = 2–10) clusters

Fragmentation energy

The fragmentation energy can also be considered as an indicator for forecasting the relative stability of the clusters. In Figure 4 we feature the growth of E_f as a function of the size clusters n. Overall through the general shape, fluctuating behavior in the values was detected. The results obtained indicate that the Fe_7, Fe_8 and Fe_9 clusters have bigger values compared to the rest of the neighboring clusters and therefore, so the clusters are relatively more powerful in terms of thermodynamic stability.

Second-order energy difference

In addition to both the fragmentation energy and the binding energy, we can use another amount that has a great indication of the stability of the clusters, which is second-order energy difference. In Figure 5, we show the growth of Δ_2E in terms of changing cluster size. Through the positive values reached at the following clusters for (n = 3,7 and 9) clusters, indicating that these clusters may have special stability compared to the rest of the clusters.

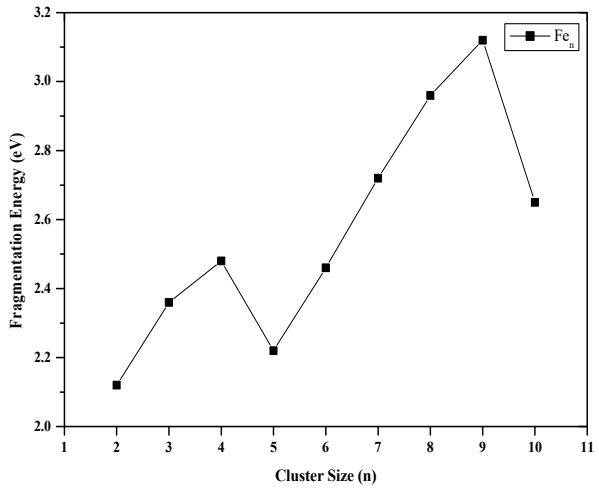

Figure 4. Fragmentation energy per atom for the Fe_n (n = 2-10) clusters

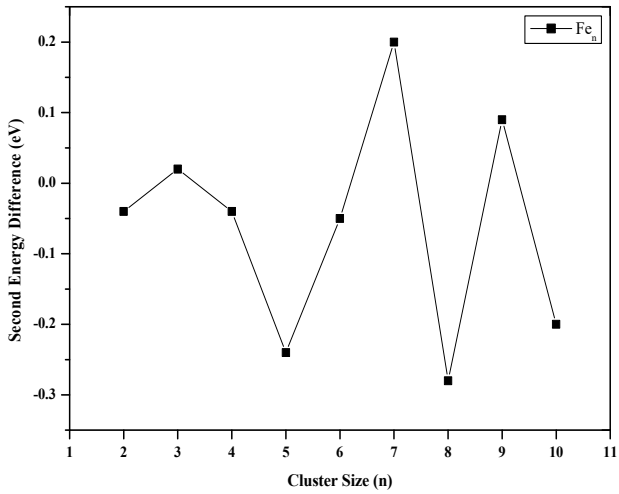

Figure 5. The Second energy difference for the Fe_n (n = 2-10) clusters

3.3. Electronic Properties

HOMO–LUMO energy

When the value of the energy gap HOMO–LUMO (ΔE) is small, the chemical reactivity is high, whereas a considerable value is ascribed to an even higher chemical stability, for this reason, the HOMO-LUMO energy gap is considered as a milestone and an important criterion for the chemical stability of small clusters. The ΔE change in terms of the cluster size variation, for the most suitable structures, is shown in Figure 6.

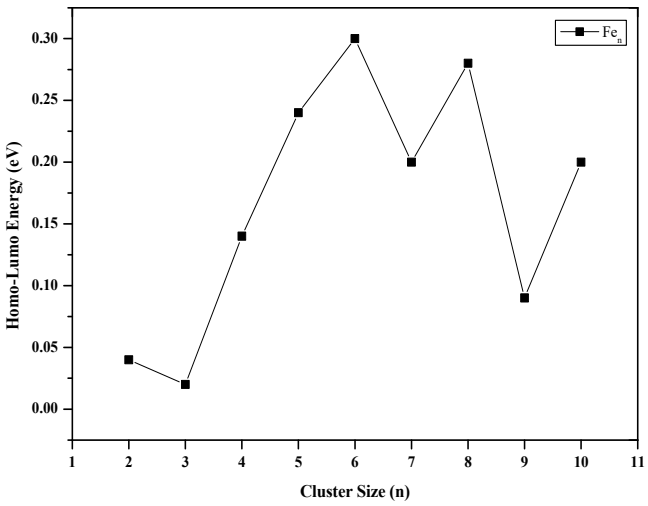

Figure 6. HOMO–LUMO energy for the Fe_n (n = 2–10) clusters

An oscillatory behavior has been recorded in the growth of ΔE values when the volume of clusters is increased. Generally, we note that ΔE of Fe_n (n = 2,3) clusters are smaller than the rest of the existing iron clusters. This means that these clusters come with a greater stability and a low reactivity compared to their neighbors and could be suitable to be utilized as an essential element in developing new materials.

Vertical ionization potential (VIP) and vertical electronic affinity (VEA)

We calculate the vertical electronic affinity and vertical ionization potential for the Fe_n (n = 2–10) ground state, they are plotted in Figures 7 and 8 as a function of the cluster size.

The vertical ionization potential (VIP) is used to determine the chemical stability of small clusters as the proportion between the size of the cluster and its stability is inverse, meaning that the greater the size of the cluster, the less its

chemical activity, and thus its stability. Through Figure 6, we observe a non-monotonic oscillating behavior in the evolution of VIP values of Fe_n clusters. We found the highest values for Fe_6 worth an estimated 5.82 eV, followed by the same value recorded for the Fe_2 and Fe_7 clusters with values of 5.73 eV. The results obtained are close to the theoretical works of Keitel Cervantes-Salguero et al. and Gong and Zheng et al. [22,23].

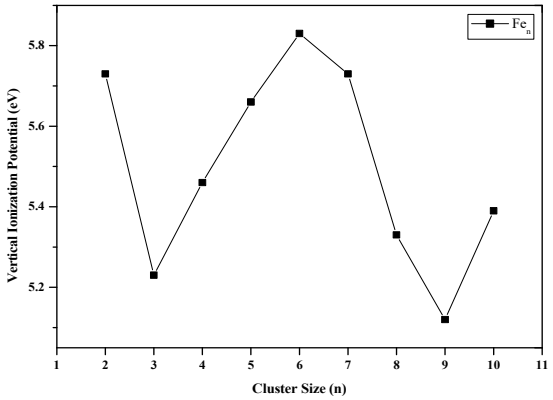

Figure 7. Vertical ionization potential (VIP) for the Fe_n (n = 2-10) clusters

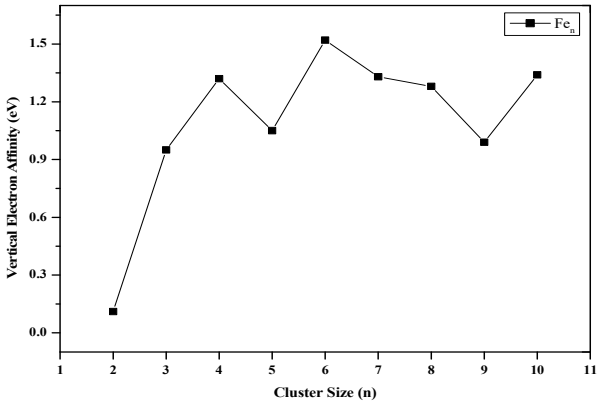

Figure 8. Vertical Electron Affinity for the Fe_n (n = 2-10) clusters

Also, what is recorded for vertical electronic affinity (VEA) values, where a non-monotonic increase with cluster size is observed, this is what the Figure 8 shows. Also, VEA in mass physics shows how stable and coherent a structure is; it is seen that the small clusters approach the metallic state, the VEA values increase with the size of the cluster. Where the following clusters recorded the smallest values of Fe_2 and Fe_9, with values estimated at 0.11 eV and 0.99 eV, respectively. Our results are very close to what has been reached in the theoretical work of Keitel Cervantes-Salguero et al., Chrétien and Salahub, and Castro and Salahub [22,24,25].

Chemical hardness η

Pearson [26] proposed the principle of maximum hardness (PMH) in order to distinguish between the relative stability of the clusters; In general, if the clusters have less interaction, is more stability, the value of their chemical hardness is greater. In Figure 9, we report the growth of η for the lowest-energy structures as a function of the cluster size. The chemical hardness of the Fe_2 and Fe_7 clusters seems to be the largest values recorded compared to all other clusters, this makes these two clusters very inert and they can be considered as good candidates for the fabrication of cluster materials applicable to nanotechnologies and nanoelectronics.

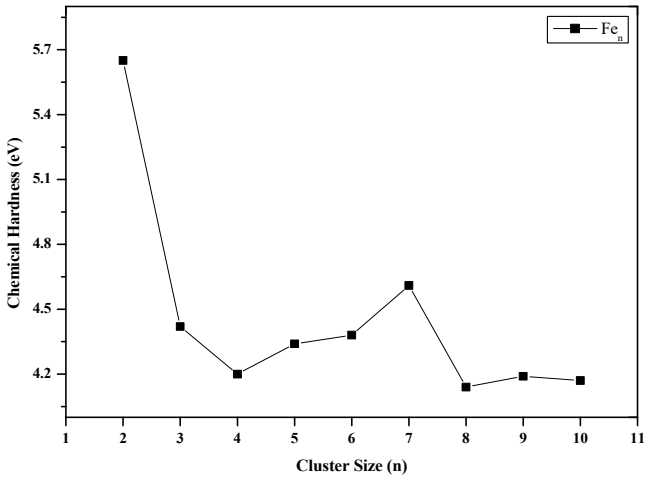

Figure 9. Chemical hardness η for the Fe_n (n = 2–10) clusters

3.3. Magnetic Characteristics

Magnetic behavior can also be considered an important marker for small clusters. In fact, we can find small clusters with specific magnetic moments that qualify them to be used in many important applications in nanotechnology. It is clear from the obtained results that the magnetic torque value of the Fe_{10} cluster takes the largest value and is estimated at 3.38 μ_B which makes it available for use in designing new Nanocatalytic systems, while the rest of the clusters recorded a value of magnetic moment ranging between 3.00 μ_B and 3.354 μ_B values. Our results regarding magnetic moment are close to those reported in the works [27-29]. The magnetic moment results are shown in Figure 10.

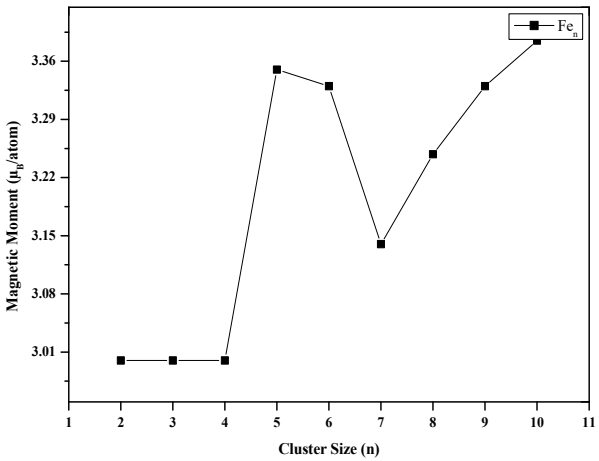

Figure 10. Magnetic moments for the Fe_n (n = 2–10) clusters

4. CONCLUSION

The equilibrium geometries, energetic, electronic and magnetic characteristics of Fe_n (n = 2–10) clusters have been performed by using DFT calculations, with the use of generalized gradient approximation GGA. The geometric structures of the clusters are in good agreement with previous computational studies; the reported binding energy for the dimer is closest to the experimental and theoretical value available. Furthermore, we find that the decay behavior of the binding energy curve indicates that the obtained cluster structures are the ground states.

The calculated fragmentation energy, second-order energy difference, and HOMO-LUMO energy gap revealed that the Fe_7, Fe_8 and Fe_9 clusters are more stable than other cluster sizes.

Compared to experimental and theoretical data, all of our VIP and VEA results are sometimes underestimated and sometimes overstated. The Fe_2 cluster corresponds to the most stable structure in the chemical hardness analysis.

The calculated magnetic properties of the lowest energy Fe_n clusters exhibited a total magnetic torque of (3.00 - 3.354) μ_B, except for the Fe_{10} cluster, which takes the value 3.385 μ_B. To our knowledge, the physicochemical properties of iron groups have not yet been calculated with the SIESTA code. Therefore, the results obtained from this fundamental work will be useful to guide future experiments, particularly in the fabrication of new nanocatalysts.

ORCID IDs

Yamina Benkrima, https://orcid.org/0000-0001-8005-4065; **Djamel Belfennache,** https://orcid.org/0000-0002-4908-6058

REFERENCES

[1] J.B. Haun, T-J. Yoon, H. Lee, and R. Weissleder, "Magnetic nanoparticle biosensors,"WIREs Nanomedicine and Nanobiotechnology. **2**(3), 291-304 (2010). https://doi.org/10.1002/wnan.84

[2] H. Lee, T-J. Yoon, and R. Weissleder, "Ultrasensitive detection of bacteria using core-shell nanoparticles and an NMR-filter system," Angew. Chem. Int. Ed.**48**(31), 5657-5660 (2009). https://doi.org/10.1002/anie.200901791

[3] E.I. Galanzha, E.V. Shashkov, T. Kelly, J-W. Kim, L. Yang, and V.P. Zharov, "In vivo magnetic enrichment and multiplex photoacoustic detection of circulating tumor cells," Nat. Nano. **4**(12), 855-860 (2009). https://doi.org/10.1038/nnano.2009.333

[4] M.D. Morse, "Clusters of transition-metal atoms," Chem. Rev. **86**(6), 1049-1109 (1986). https://doi.org/10.1021/cr00076a005

[5] J.N. Harvey, "DFT computation of relative spin-state energetic of transition metal compounds," Struct. Bond. **112**, 151-184 (2004). https://doi.org/10.1007/b97939

[6] C.J. Cramer, and D.G. Thrular, "Density functional theory for transition metals and transition metal chemistry," Phys. Chem. Chem.Phys. **11**, 10757-10816 (2009). https://doi.org/10.1039/b907148b

[7] M. Castro, "The role of the Jahn-Teller distortions on the structural, binding, and magnetic properties of small Fe_n clusters n≤7," International J. Quantum. Chem. **64**(2), 223-230 (1997). https://doi.org/10.1002/(SICI)1097-461X(1997)64:2<223::AID-QUA9>3.0.CO;2-Y

[8] Ž. Šljivančanin, and A. Pasquarello, "Supported Fe nanoclusters: evolution of magnetic properties with cluster size," Phys. Rev. Lett. **90**(24), 247202-247204 (2003). https://doi.org/10.1103/PhysRevLett.90.247202

[9] T. Oda, A. Pasquarello, and R. Car, "Fully unconstrained approach to noncollinear magnetism: application to small Fe clusters," Phys.Rev. Lett. **80**(16), 3622-2625 (1998). https://doi.org/10.1007/s00894-012-1395-2

[10] C. Köhler, G. Seifert, and T. Frauenheim, "Density functional based calculations for Fen (n≤32)," Chem. Phys. **309**(1), 23-31 (2005). https://doi.org/10.1016/J.CHEMPHYS.2004.03.034

[11] F.S. Ham, "The Jahn-Teller effect: a retrospective view," J. Luminescence, **85**(4), 193-197 (2000). https://doi.org/10.1016/S0022-2313(99)00187-8

[12] P. Ordejón, E. Artacho, and J.M. Soler, "Self-consistent order-N density-functional calculations for very large systems," Physical Review B, **53**(16), 10441 (1996). https://doi.org/10.1103/PhysRevB.53.R10441

[13] J.P. Perdew, and A. Zunger, "Self-interaction correction to density-functional approximations for many-electron systems," Physical. Review B, **23**(10)**,** 5048 (1981). https://doi.org/10.1103/PhysRevB.23.5048

[14] J.P. Perdew, K. Burke, and M. Ernzerhof, "Generalized gradient approximation made simple," Physical review letters. **77**(18), 3865 (1996). https://doi.org/10.1103/PhysRevLett.77.3865

[15] J.M. Soler, "The SIESTA method for ab initio order-N materials simulation," Journal of Physics. Condensed Matter. **14**(11), 2745 (2002). https://doi.org/10.1088/0953-8984/14/11/302
[16] N. Troullier, and J.L. Martins, "Efficient pseudopotentials for plane-wave calculations," Physical Review B, **43**(3), 1993 (1991). https://doi.org/10.1103/PhysRevB.43.1993
[17] B.V. Reddy, S.N. Khanna, and S.C. Deevi, "Electronic structure and magnetism in (FeAl)n(n⩽6) clusters," Chem. Phys. Lett. **333**, 465-470 (2001). https://doi.org/10.1016/S0009-2614(00)01393-2
[18] S. Dhar, and N.R. Kestner,"Electronic structure of the Fe2 molecule in the local-spin-density approximation," Phys. Rev. A, **38**, 1111-1119 (1988). https://doi.org/10.1103/physreva.38.1111
[19] J.L. Chen, C.S. Wang, K.A. Jackson, and M.R. Pederson, "Theory of magnetic and structural ordering in iron clusters," Phys. Rev. B, **44**, 6558-6561 (1991). https://doi.org/10.1103/PhysRevB.44.6558
[20] P.A. Montano, and G.K. Shenoy, "EXAFS study of iron monomers and dimers isolated in solid argon," Solid State Commun. **35**, 53-56 (1980). https://doi.org/10.1016/0038-1098(80)90769-3
[21] H. Purdum, P.A. Montano, G.K. Shenoy, and T. Morrison," Extended-x-ray-absorption-fine-structure study of small Fe molecules isolated in solid neon," Phys. Rev B, **25**, 4412-4417 (1982). https://doi.org/10.1103/PhysRevB.25.4412
[22] C-S. Keitel, and M.J. Seminario," Structure and energetics of small iron clusters," J. Mol. Model. **18**(9), 4043-4045 (2012). https://doi.org/10.1007/s00894-012-1395-2
[23] X.G. Gong, and Q.Q. Zheng, "Local spin-density electronic structures and magnetic properties of small iron clusters," J. Phys. Condensed. Matter. **7**(12), 2421-2428 (1995). https://doi.org/10.1088/0953-8984/7/12/006
[24] S. Chrétien, and D.R. Salahub, "Kohn-Sham density-functional study of low-lying states of the iron clusters Fen +/Fen/Fen - (n01−4)," Phys Rev. B, **66** (15), 155401-155412 (2002). https://doi.org/10.1103/PhysRevB.66.155425
[25] M. Castro, and D.R. Salahub, "Density-functional calculations for small iron clusters: Fen, Fen +, and Fen - for n≤5," Phys. Rev. B, **49**(17), 11842-11852 (1994). https://doi.org/10.1103/PhysRevB.49.11842
[26] R. G. Pearson, *Chemical hardness*, (Wiley-VCH Verlag GmbH, Weinheim, 1997).
[27] O. Diéguez, M.M.G. Alemany, C. Rey, P. Ordejón, and L.J. Gallego, "Density-functional calculations of the structures, binding energies, and magnetic moments of Fe clusters with 2 to 17 atoms," Phys Rev. B, **63**(20), 205407-205406 (2001). https://doi.org/10.1103/PhysRevB.63.205407
[28] G. Rollmann, P. Entel, and S. Sahoo, "Competing structural and magnetic effects in small iron clusters," Comput. Mater. Sci. **35**(3), 275-278 (2006). https://doi.org/10.1016/j.commatsci.2004.09.059
[29] C. Köhler, G. Seifert, and T. Frauenheim, "Density functional based calculations for Fen (n≤32)," Chem. Phys. **309**(1), 23-31 (2005). https://doi.org/10.1016/J.CHEMPHYS.2004.03.034

ФІЗИКО-ХІМІЧНІ ХАРАКТЕРИСТИКИ КЛАСТЕРА Fe_n (n = 2–10) ЗА ТЕОРІЄЮ ФУНКЦІОНАЛУ ГУСТИНИ

Яміна Бенкріма[a], Джамель Белфеннаше[b], Радхіа Єклеф[b], Мохаммед Ельбар Судані[c], Абделькадер Сугат[a], Ях'я Акур[d,e]

[a]Вища нормальна школа Уаргла, 30000 Уаргла, Алжир
[b]Науково-дослідний центр промислових технологій, Черага, 16014, Алжир
[c]Лабораторія з розробки нових і відновлюваних джерел енергії в посушливих зонах і зонах Сахари, Факультет математики та матеріалознавства, Університет Касді Мерба Уаргла, Уаргла 30000, Алжир
[d]Лабораторія фізики матеріалів, Університет Амара Теліджі, Лагуат, Алжир
[e]Вища нормальна школа Лагуата, Лагуат, Алжир

У цій роботі ми представляємо теоретичне дослідження геометрії рівноваги та енергетичних, електронних і магнітних властивостей Fen (n = 2–10) на основі теорії функціоналу густини (DFT). Результати отримані з використанням обох узагальнених градієнтних наближень відповідно до схеми, описаної Perdew-Burke-Ernzerhof (GGA-PBE). Більш стабільні отримані структури порівняно з іншими ізомерами раніше не були знайдені. Результати, розраховані як розрахована енергія фрагментації та різниця енергій другого порядку, показують, що кластери Fen(n = 7,8,9) більш стабільні, ніж кластери інших розмірів. Крім того, розраховані магнітні властивості найбільш стабільних кластерів демонструють різний магнітний момент між значеннями 3,00 мкБ і 3,35 мкБ, за винятком кластера Fe10, який приймає верхнє значення 3,38 мкБ. Ці результати важливі для експертів-експериментаторів, які активно розробляють нові системи нанокаталізу у фізичній та хімічній областях.

Ключові слова: *кластери заліза; відносна стабільність; теорія функціоналу густини; енергія зв'язку; магнітні властивості*

East European Journal of Physics. 2. 157-164 (2023)
DOI:10.26565/2312-4334-2023-2-15 ISSN 2312-4334

EFFECT OF SI_3N_4/TaC NANOMATERIALS ON THE STRUCTURAL AND ELECTRICAL CHARACTERISTICS OF POLY METHYL METHACRYLATE FOR ELECTRICAL AND ELECTRONICS APPLICATIONS[†]

Alaa Abass Mohammed[§], Majeed Ali Habeeb*
University of Babylon, College of Education for Pure Sciences, Department of Physics, Iraq
**Correspondence Author e-mail: pure.majeed.ali@uobabylon.edu.iq, [§]e-mail: alaa.mohammed.pure405@student.uobabylon.edu.iq*
Received January 27, 2023; revised April 6, 2023; accepted April 8, 2023

This study used the casting method to prepared PMMA/Si_3N_4/TaC nanocomposites with variant content (0,2,4,6,8) % wt of Si_3N_4/TaC nanoparticles. The structural and electrical properties have been investigated. Scanning electron microscope (SEM) indicates the homogenous, smooth and dispersed of Si_3N_4 and TaC NPs inside the PMMA matrix due to strong covalent interaction between the Si_3N_4 and TaC NPs in the PMMA matrix, which means a good method for prepared films. Optical microscope images explained that increasing nanoparticle content forms network paths inside the polymeric matrix that act as charge carriers. FTIR spectra indicate a physical interference between the polymer matrix and nanoparticles. The AC electrical properties of nanocomposites obtained that the dielectric constant and dielectric loss rise with rising content of nanoparticles and decrease with increasing frequency of applied electric field. While the A.C. electrical conductivity rises with the rising frequency and weight content of Si_3N_4/TaC nanoparticles. These results indicated that the PMMA/Si_3N_4/TaC nanostructures could be considered promising materials for electronics and electrical nanodevices.
Keywords: *Nanocomposites; PMMA; Si_3N_4; TaC; AC electrical properties*
PACS: 68.37.Hk,77.22.Gm,77.84.Lf

1. INTRODUCTION

Polymers hold the potential to revolutionize industrial thought by replacing the majority of materials with plastic ones and enabling a wide range of applications. Additionally, it entered all sectors of the economy, including the medical sector, and a variety of optical, electronic, and applications, including photovoltaic cells and optoelectronics [1]. Last year, there was a lot of interest in innovative materials called nanocomposites polymers, composed of organic and inorganic polymers and nanoparticles in a nanoscale region. These composite materials differ from pure polymers regarding their chemical and physical characteristics. Impurity polymers' effects on the properties of polymers provide them with more significant advantages and enable them to improve desirable features. In many different types of applications, that might be highly significant and helpful [2,3].

A good thermoplastic polymer known as poly (methyl methacrylate, or PMMA) has papers describing how it can be used as a gate insulator in organic transistors with thin films (OTFTs). PMMA is a great choice as a dielectric layer in organic electronics due to its excellent mechanical and thermal durability, excellent electrical resistivity (>21015.cm), appropriate dielectric characteristics, and thin film processability on vast regions by spin coating. We explore the optical, electrical, and microgravimetric properties of PMMA thin sheets to assess their chemical sensing potential. This tactility-dependent thermoplastic material is made of volatile organic compounds with high stiffness, transparency, outstanding insulating qualities, excellent planarity, and thermal stability [4,5].

Polymers' chemical and physical composition and structure influence the size of their dielectric. The unique characteristics of the molecular mobility of polymers, and consequently their chemical and physical structure, affect the parameters that describe the dielectric loss and losing tangential. Due to their low conductivity, most polymers are insulators in general. The inclusion of the proper dopants as well as thermally and electrically produced carriers affect the conductivity [6,7]. Due to its excellent oxidation resistance and strong thermal conductivity, silicon nitride (Si_3N_4) is a possible alternative to silica supports that are more frequently utilized in reactions where efficient heat transmission is required. Because it still contains NH_2 and NH groups, amorphous silicon nitride made from sol-gel is especially intriguing for solid base catalysis [8,9]. Silicon nitride is a good contender for use in material science, the microelectronics industry, solar technology, and other fields due to its physical features. Due to the silicon nitride film's exceptionally high transparent in the spectral range of 300-1200 nm, it is employed in solar cell technology as an antireflective coating and to passivate silicon surfaces [10,11].

Tantalum Carbide (TaC), which is also a very promising ultra-high temperature material, has been found to be wear-resistant as well as to have biocompatible qualities that make it suitable for biomedical applications [12,13]. TaC has drawn investigation, but thorough comprehension has eluded researchers because, like other transition-metal carbides, it appears in a broad variety of compositions, and as a result, its physical characteristics vary. Additionally, impurities can affect characteristics, and well-characterized TaC materials, particularly single crystals, are typically hard to come by. TaC's lattice dynamics and band structure, as well as its mechanical, thermal, and electrical characteristics, have all been studied [14,15]. This paper aims to preparation of the PMMA/Si_3N_4/TaC nanocomposite and study the structural and AC electrical properties.

[†] ***Cite as:*** A.A. Mohammed, and M.A. Habeeb, East Eur. J. Phys. **2**, 157 (2023), https://doi.org/10.26565/2312-4334-2023-2-15

2. MATERIALS AND METHOD

The casting method was used to create films of poly methyl methacrylate (PMMA) doped with silicon nitride nanoparticles (Si_3N_4 NPs) and tantalum carbide nanoparticles (TaC NPs). PMMA pure film was created by dissolving 1.5 gm of this polymer in 30 ml of chloroform at room temperature with magnetic stirrer for half an hour. The nanocomposites films were created by adding Si_3N_4 and TaC NPs to a PMMA solution with concentrations of (2, 4, 6, and 8) % wt. The structural characteristics of ($PS/SiC/Sb_2O_3$) nanocomposites examined by the scanning electron microscopic (SEM) using a Hitachi SU6600 variable, Optical microscope (OM) provided by Olympus (Top View, type Nikon-73346) and the Fourier Transformation Infrared Spectroscopy (FTIR) (Bruker company type vertex-70, German origin) with variety wavenumber (500-4000) cm^{-1}. The dielectric characteristics were studied at range (f=100 Hz to 5×10^6 Hz) by LCR meter (HIOKI 3532-50 LCR HI TESTER).
The dielectric constant (έ) is given by [16,17]

$$\acute{\varepsilon} = \frac{C_p}{C_o}, \tag{1}$$

where, Cp is capacitance and C_o is a vacuum capacitance
Dielectric loss (ε'') is calculated by [18,19]:

$$\varepsilon'' = \acute{\varepsilon} D. \tag{2}$$

Where, D: is displacement
The A.C. electrical conductivity is determined by [20,21]

$$\sigma_{AC} = \omega \acute{\varepsilon}\, \varepsilon_o, \tag{3}$$

where w angular frequency

3. RESULTS AND DISCUSSION

The scanning electron microscope (SEM) is used to study the morphological of PMMA/Si_3N_4/TaC nanocomposites. The SEM images of pure PMMA and PMMA/Si_3N_4/TaC nanocomposites are revealed in Fig. (1) with various concentration 0, 2, 4, 6 and 8 wt.% of Si_3N_4 and TaC NPs with a magnification 50 KX and scale 200 nm. From this figure in image A, it is observed that the pure PMMA was homogenous and smooth this indicates a good method for prepared films. Also, it is observed that in images (B, C, D and E) the homogeneous dispersed of Si_3N_4 and TaC NPs inside the PMMA matrix respectively primarily due to strong covalent interaction between the Si_3N_4 and TaC NPs in the PMMA matrix [22,23].

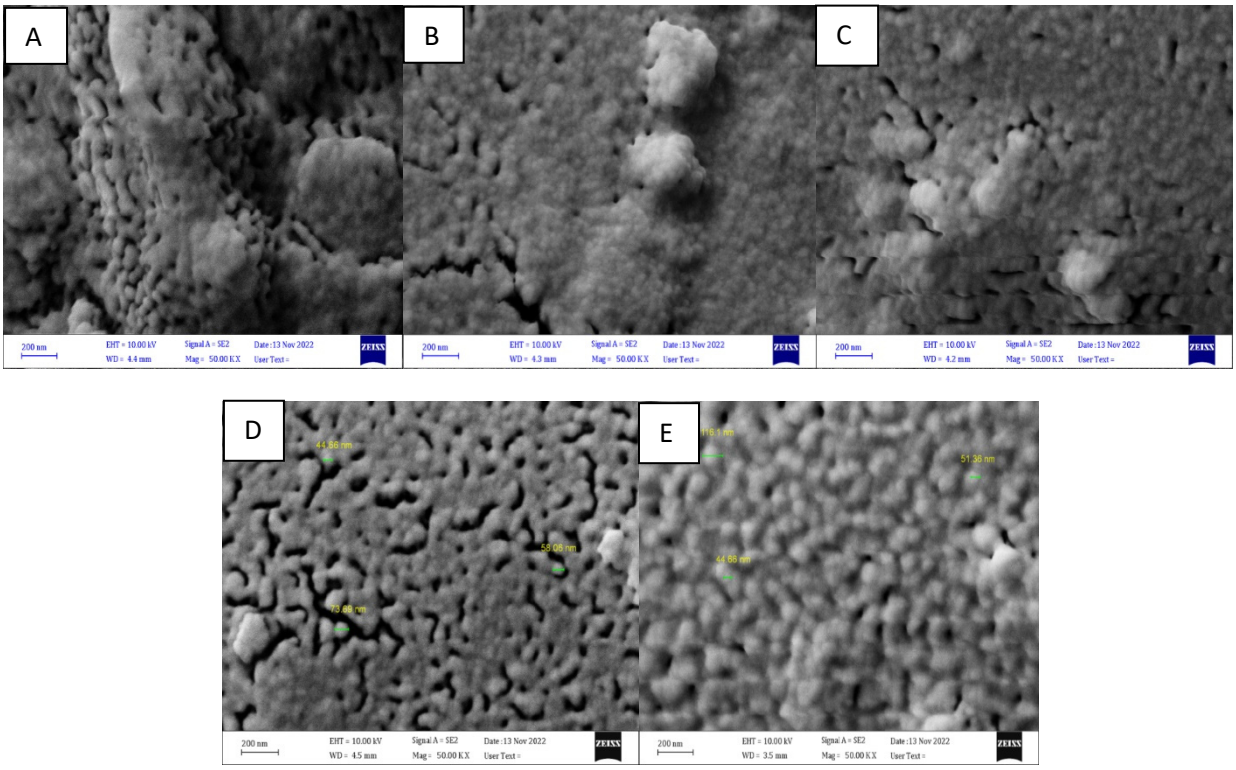

Figure 1. SEM images of (PMMA/Si_3N_4/TaC) nanocomposites, (A) for (PMMA), (B) 2 wt.% Si_3N_4 / TaC NPs, (C) 4 wt.% Si_3N_4 / TaC NPs, (D) 6 wt.% Si_3N_4 / TaC NPs, (E) 8 wt.% Si_3N_4 / TaC NPs

The optical microscope gives the change of surface morphology of PMMA/Si_3N_4/TaC nanocomposites. Figure (2) displays the PMMA/Si_3N_4/TaC nanocomposites optical microscope (OM) at magnification power (10x) for all specimens. The polymer blend film surface image(A) shows an uniform phase without phase separation; in the other hand, it has a finer morphology and smooth surface, demonstrating at this successful polymer ratio of PMMA. While image (B-E), it can be seen, that Si_3N_4/TaC NPs are well dispersed on the surface of the PMMA polymer films and this apparent more evident with the increase in the wt.% of Si_3N_4/TaC. The nanocomposite shows nearly elliptical structure of particles of uniform shape. This is because the NPs have a large surface area while the polymeric solution containing different polar groups has a high affinity for Si_3N_4/TaC which leads to the orientation of the nanoparticles within the polymer chain and thus the Si_3N_4/TaC structure becomes more compact and thus the consistency of the material increases. This provided a suitable preparation method for preparing nanocomposite films [24-26].

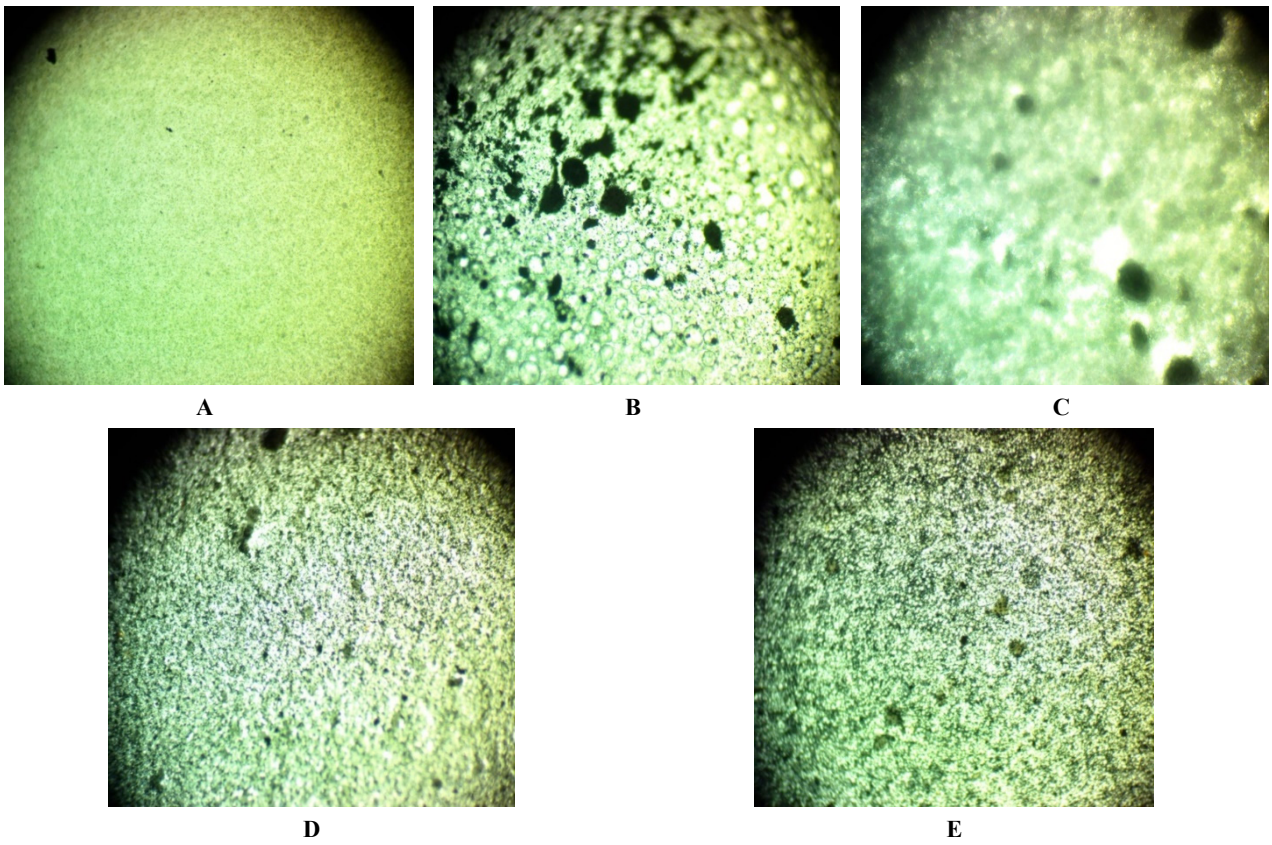

Figure 2. OM images (10×) for (PMMA/Si_3N_4/TaC) nanocomposites A. pure polymer, B. 2 wt.% of Si_3N_4/TaC NPs, C. 4 wt.% of Si_3N_4/TaC NPs, D. 6 wt.% of Si_3N_4/TaC NPs and E. 8 wt.% of Si_3N_4/TaC NPs

FTIR spectra provide information on the vibration and rotation of molecular groups in a material. Figure (3) displays the FTIR spectra of (PMMA/Si_3N_4/TaC) nanocomposites in the range wave number (500–4000) cm^{-1}. In the image (A), FTIR spectra of (PMMA) polymer reveal an absorption band at 2950.45 cm^{-1} corresponding to the CH_3 bending vibration and the band 1723.22 cm-1 attributed to the C=O stretching vibration. CH_3 stretching vibration indicate to the band 1434.60 cm^{-1}. The absorption band at 1142.95 attribute to the symmetric stretching vibration of C-O. The bands 985.57 cm^{-1}, 698.13 cm^{-1} and 750.29 cm^{-1} corresponding to the C−C bending and stretching vibration respectively. The spectra of PMMA with variant concentration of Si_3N_4 and TaC NPs in images B, C, D and E respectively. In image B where the additive 2 wt.% Si_3N_4 and TaC NPs caused change shift in some bands and intensities at low wavenumber (1434.63, 1142.83) cm^{-1} and high wave number at bands (1723.30, 995.01, 750.01) cm^{-1}but bands 2950.45 cm^{-1} and 698.13 cm^{1} there is not affected on this band while, the image C which additive concentration of 4 wt.% from Si_3N_4 and TaC NPs, affected change shift in some bands and intensities at low wavenumber (995.34, 750.45) cm^{-1} and high wave number at bands (1723.45, 1434, 1143) cm^{-1}but bands 2950.45 cm^{-1} and 698.13 cm^{1} there is not affected on this band. the image D which additive concentration of 6 wt.% from Si_3N_4 and TaC NPs, shifted and changed several bands' intensity at low wavenumber (995.42, 750.02) cm^{-1} and high wave number at bands (1723.54, 1434.64, 1143) cm^{-1}but bands 2950.45 cm^{-1} and 698.13 cm^{1} has not been impacted and added concentration of 8 wt.% from Si_3N_4 and TaC NPs in image E, caused shifts in certain bands and intensities at low wavenumber (994.90, 749.93) cm^{-1} and high wave number at bands (1724.04, 1434.68, 1143) cm^{-1}but bands 2950.45 cm^{-1} and 698.13 cm^{1} has not been impacted. The FTIR studies show that adding different concentration of Si_3N_4/TaC in images B, C,D and E leads to the displacement of some of the bonds and not emergence of new peaks therefore, there is no chemical interaction between Si_3N_4/TaC nanoparticle and the PMMA polymer matrix [27-29].

Equation (1) was used to calculate the dielectric constant (ε') of (PMMA/Si_3N_4/TaC) nanocomposites. Figure (4) explain the dielectric constant of (PMMA/Si_3N_4/TaC) nanocomposites with frequency. It is note that dielectric constant decrease with rising of frequency for all the sample prepare which, as a result of the capabilities of dipoles in nano-composites samples to transform in the direction of the applying electric current and the reduction of space charge polarization [30-32]. Figure (5) explain the dielectric constant of (PMMA/Si_3N_4/TaC) nanocomposite with the content of nanoparticle at 100 Hz. It is observed that dielectric constant rise with rising of concentration nanoparticle for all illustrations of nano-composites. Interfacial polarization in the nanocomposites' internal alternating electric field and an increase in the charge carriers are responsible for these processes of (PMMA/Si_3N_4/TaC) nanocomposite [33-35].

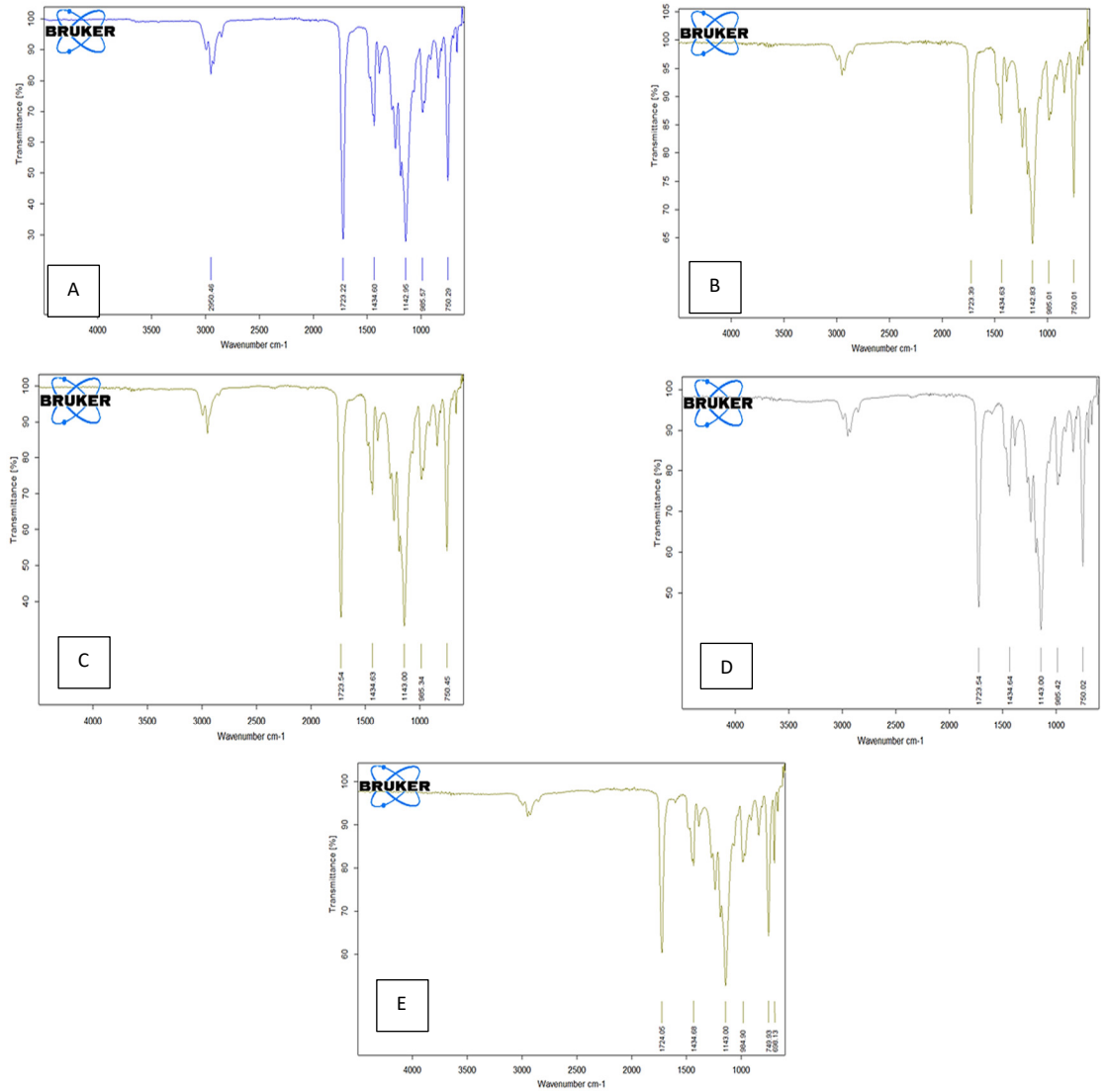

Figure 3. FTIR spectra of PMMA/Si_3N_4/TaC nanocomposites A. pure polymer, B. 2 wt.% of Si_3N_4/TaC NPs, C. 4 wt.% of Si_3N_4/TaC NPs, D. 6 wt.% of Si_3N_4/TaC NPs and E. 8 wt.% of Si_3N_4/TaC NPs

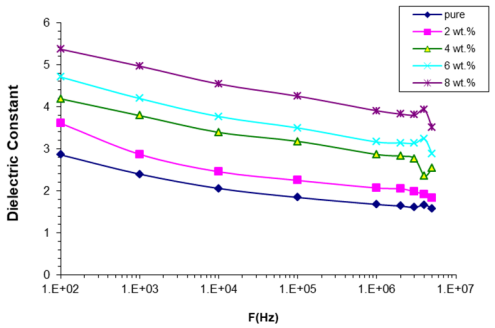

Figure 4. Variation of dielectric constant with frequency of PMMA/Si3N4/TaC nanocomposite

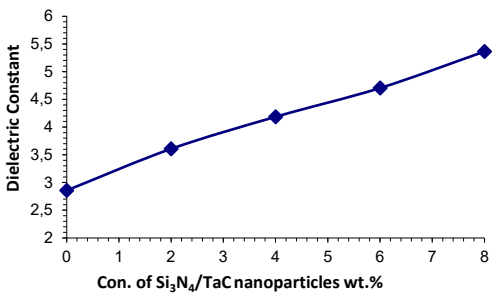

Figure 5. Effect of Si_3N_4/TaC nanoparticles concentrations on dielectric constant for PMMA/ Si_3N_4/TaC nanocomposite at 100 Hz

Equation (2) was used to calculate the dielectric loss (ε″) of the nanocompsites. Figure (6) shows the relation between dielectric loss of PMMA/Si_3N_4/TaC nanocomposites and frequency. The dielectric losses for nanocomposites reduce as the frequency increases for all samples. This phenomenon was linked to a reduction in the contributions of polarization of space charges. According to the data, nanocomposites have a substantial dielectric loss at low frequencies. Due to the reduced time available for the dipoles to align at high frequencies, the dielectric loss decreases [36-38]. The dielectric loss of PMMA/Si_3N_4/TaC nanocomposites as a function of Si_3N_4/TaC NPs are shown in Figure (7). From this figure, it is note that the dielectric loss rises with rising content of the Si_3N_4/TaC nanoparticle. This result attributed to increased charge on the dipole [39-41].

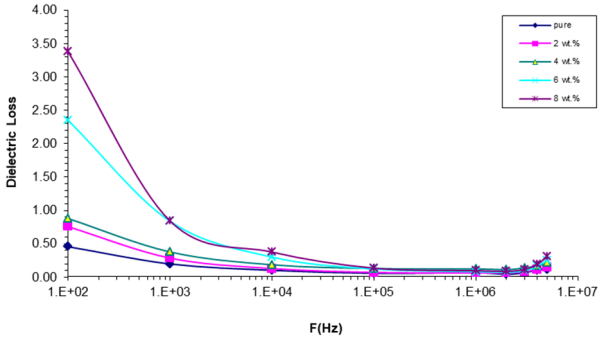

Figure 6. Variation of dielectric loss with frequency of PMMA/Si3N4/TaC nanocomposite

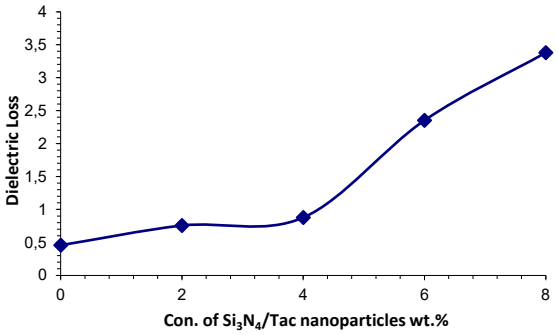

Figure 7. Influence of Si_3N_4/TaC NPs concentrations on dielectric loss for (PMMA/ Si_3N_4/TaC) nanocomposite at 100 Hz

Equation (3) was used to calculate the A.C electrical conductivity. Figure (8) shows the relationship between A.C. electrical conductivity of PMMA/Si3N4/TaC nanocomposites and frequency. The mobility of charge carriers and the hopping of ions from the cluster cause the A.C electrical conductivity of all specimens to increase as the frequency of the electric field increases. At low frequencies, the amount of mobile ions and electrical conductivity decreased due to increased charge accumulation at the electrode and electrolyte interface [42-44]. Because charge carriers moved more easily at high frequencies, the electrical conductivity of PMMA/Si_3N_4/TaC nanocomposites increases with frequency [45-47]. Figure (9) reveals that the electrical conductivity of nanocomposites rises with the rising of Si_3N_4/TaC nanoparticle content due to rise in the ionic charge carriers and the formation of a continuous network of Si_3N_4/TaC nanoparticles inside polymer matrix [48-50]. The results of the ε', ε″, and A.C. conductivity are shown in Table (1).

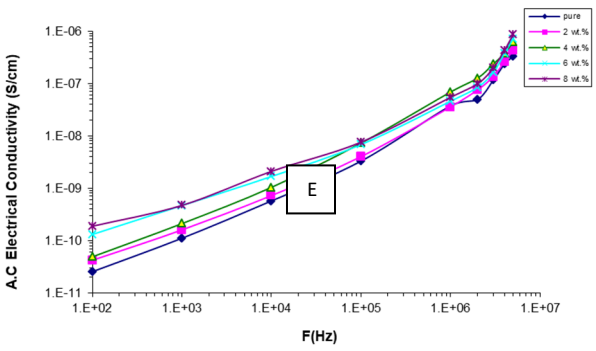

Figure 8. Variation of AC electrical conductivity with frequency of PMMA/Si3N4/TaC nanocomposite

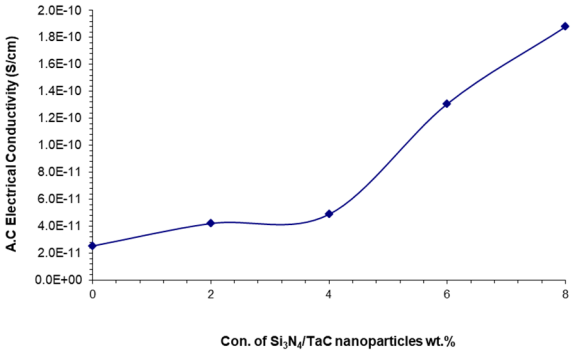

Figure 9. Effect of Si_3N_4/TaC NPs content on AC electrical conductivity for PMMA/Si_3N_4/TaC nanocomposite at 100Hz

Table 1. The values of the Dielectric constant, Dielectric loss and AC electrical conductivity at 100 Hz of (PMMA/Si_3N_4TaC) nanocomposites

Concentration of Si_3N_4/TaC (wt.%)	Dielectric constant	Dielectric loss	A.C. Conductivity (S/cm)
0	2.86	0.46	2.54E-11
2	3.61	0.76	4.21E-11
4	4.19	0.88	4.89E-11
6	4.71	2.35	1.31E-10
8	5.37	3.38	1.88E-10

4. CONCLUSION

This work summaries that the scanning electron microscope (SEM) indicate that the homogenous, smooth and dispersed of Si_3N_4 and TaC NPs inside the PMMA matrix due to strong covalent interaction between the Si_3N_4 and TaC NPs in the PMMA matrix which mean a good method for prepared films. Optical microscope (OM) images explained

that when increasing in content of nanoparticles that forming network paths inside the polymeric matrix that act as charge carriers. FTIR exhibited that when combined, the polymer and the nanoparticles exist in a physical superposition. at the concentrations of Si_3N_4 and TaC nanoparticles rise, the (PMMA/Si_3N_4/TaC) nanocomposites ε', ε″, and A.C conductivity also rise. When the frequency is raised, the A.C. electrical conductivity raised while the ε' and ε″ of nanocomposites decreased. This behavior make it may be considered as excellent electronics materials for electrical applications.

ORCID IDs

Majeed Ali Habeeb, https://orcid.org/0000-0001-5064-2835

REFERENCE

[1] S.S. Al-Abbas, R.A. Ghazi, A.K. Al-shammari, N.R. Aldulaimi, A.R. Abdulridha, S.H. Al-Nesrawy, and E. Al-Bermany, "Influence of the polymer molecular weights on the electrical properties of Poly (vinyl alcohol)–Poly(ethylene glycols)/Graphene oxide nanocomposites," Materials Today: Proceedings, **42**, 2469-2474 (2021). https://doi.org/10.1016/j.matpr.2020.12.565

[2] D.R. Paul, and L.M. Robeso, "Polymer nanotechnology: nanocomposites," Polymer, **49**(15), 3187-3204 (2008). https://doi.org/10.1016/j.polymer.2008.04.017

[3] M.A. Habeeb, "Effect of rate of deposition on the optical parameters of GaAs films," European Journal of Scientific Research, **57** (3), 478-484 (2011)

[4] [4] G. Aras, E.L. Orhan, I.F. Selçuk, S.B. Ocak, and M. Ertuğrul, "Dielectric Properties of Al/Poly (methylmethacrylate) (PMMA)/p-Si Structures at Temperatures Below 300 K", Procedia-Social and Behavioral Sciences, **95**, 1740-1745 (2015). https://doi.org/10.1016/j.sbspro.2015.06.295

[5] M.A. Habeeb, and W.K. Kadhim, "Study the optical properties of (PVA-PVAC-Ti) nanocomposites," Journal of Engineering and Applied Sciences, **9**(4), 109-113 (2014). https://doi.org/10.36478/jeasci.2014.109.113

[6] K. Sardar, R. Bounds, M. Carravetta, G. Cutts, J.S. Hargreaves, A.L. Hector, and F. Wilson, "Sol–gel preparation of low oxygen content, high surface area silicon nitride and imidonitride materials," Dalton Transactions, **45**(13), 5765-5774 (2016). https://doi.org/10.1039/C5DT04961J

[7] S.M. Mahdi, M.A. Habeeb, "Synthesis and augmented optical characteristics of PEO–PVA–SrTiO3–NiO hybrid nanocomposites for optoelectronics and antibacterial applications," Optical and Quantum Electronics, **54**(12), 854 (2022). https://doi.org/10.1007/s11082-022-04267-6

[8] N. Manavizadeh, A. Khodayari, and E. Asl-Soleimani, "An Investigation of the Properties of Silicon Nitride (SiNx) Thin Films Prepared by RF Sputtering for Application in Solar Cell Technology," edited by D.Y. Goswami, and Y. Zhao, in: *Proceedings of ISES World Congress 2007*, (Vol. I - Vol. V), (Springer, Berlin, Heidelberg, 2008). pp. 1120-1122. https://doi.org/10.1007/978-3-540-75997-3_220

[9] S.M. Mahdi, and M.A. Habeeb, "Low-cost piezoelectric sensors and gamma ray attenuation fabricated from novel polymeric nanocomposites," AIMS Materials Science, **10**(2), 288-300 (2023). https://doi.org/10.3934/matersci.2023015

[10] A.R. Farhadizadeh, and H. Ghomi, "Mechanical, structural, and thermodynamic properties of TaC-ZrC ultra-high temperature ceramics using first principle methods," Materials Research Express, **7**(3), 036502 (2020). https://doi.org/10.1088/2053-1591/ab79d2

[11] M.A. Habeeb, and W.H. Rahdi, "Titanium carbide nanoparticles filled PVA-PAAm nanocomposites, structural and electrical characteristics for application in energy storage," Optical and Quantum Electronics, **55**(4), 334 (2023). https://doi.org/10.1007/s11082-023-04639-6

[12] F.A. Modine, R.W. Major, T.W. Haywood, G.R. Gruzalski, and D.Y. Smith, "Optical properties of tantalum carbide from the infrared to the near ultraviolet," Physical Review B, **29**(2), 836 (1984). https://doi.org/10.1103/PhysRevB.29.836

[13] M.H. Dwech, M.A. Habeeb, and A.H. Mohammed, "Fabrication and Evaluation of Optical Characteristics of (PVA-MnO_2–ZrO_2) Nanocomposites for Nanodevices in Optics and Photonics," Ukr. J. Phys. **67**, (10), 757-762 (2022). https://doi.org/10.15407/ujpe67.10.757

[14] O.E. Gouda, S.F. Mahmoud, A.A. El-Gendy, and A.S. Haiba, "Improving the Dielectric Properties of High Density Polyethylene by Incorporating Clay-Nano Filler," Indonesian Journal of Electrical Engineering, **12**(12), 7987-7995 (2014). https://ijeecs.iaescore.com/index.php/IJEECS/article/download/3909/2449

[15] A.H. Hadi, and M.A. Habeeb, "Effect of CdS nanoparticles on the optical properties of (PVA-PVP) blends," Journal of Mechanical Engineering Research and Developments," **44**(3), 265-274 (2021).

[16] H. Shivashankar, A.M. Kevin, P.R. Sondar, M.H. Shrishail, and S.M. Kulkarni, "Study on low-frequency dielectric behavior of the carbon black/polymer nanocomposite", J. Mater. Sci.: Mater Electron, **32**, 28674–28686 (2021). https://doi.org/10.1007/s10854-021-07242-1

[17] N. Hayder, M.A. Habeeb, and A. Hashim, "Structural, optical and dielectric properties of (PS-In_2O_3/$ZnCoFe_2O_4$) nanocomposites," Egyptian Journal of Chemistry, **63**, 577-592 (2020). https://doi.org/10.21608/ejchem.2019.14646.1887

[18] T.S. Praveenkumar, T. Sankarappa, J.S. Ashwajeet, and R. Ramanna, "Dielectric and AC Conductivity Studies in PPy-Ag Nanocomposites" Journal of Polymers, **2015**, 893148 (2015). https://doi.org/10.1155/2015/893148

[19] Q.M. Jebur, A. Hashim, and M.A. Habeeb, "Structural, A.C electrical and optical properties of (polyvinyl alcohol-polyethylene oxide-aluminum oxide) nanocomposites for piezoelectric devices," Egyptian Journal of Chemistry, **63**, 719-734 (2020). https://dx.doi.org/10.21608/ejchem.2019.14847.1900

[20] M. Rezvanpour, M. Hasanzadeh, D. Azizi, A. Rezvanpour, and M. Alizadeh, "Synthesis and characterization of micronanoencapsulated n-eicosane with PMMA shell as novel phase change materials for thermal energy storage," Mater. Chem. Phys. **215**, 299-304 (2018). https://doi.org/10.1016/j.matchemphys.2018.05.044

[21] M.A. Habeeb, A. Hashim, and N. Hayder, "Fabrication of (PS-Cr2O3/ZnCoFe2O4) nanocomposites and studying their dielectric and fluorescence properties for IR sensors," Egyptian Journal of Chemistry, **63**, 709-717 (2020). https://dx.doi.org/10.21608/ejchem.2019.13333.1832

[22] J.B. Ramesh, and K.K. Vijaya, "Studies on structural and electrical properties of NaHCO3 doped PVA films for electrochemical cell applications", Chemtech, **7**, 171–180 (2014). https://sphinxsai.com/2015/ch_vol7_no1/2/(171-180)%20014.pdf

[23] S.M. Mahdi, and M.A. Habeeb, "Evaluation of the influence of SrTiO3 and CoO nanofillers on the structural and electrical polymer blend characteristics for electronic devices," Digest Journal of Nanomaterials and Biostructures, **17**(3), 941-948 (2022). https://doi.org/10.15251/DJNB.2022.173.941
[24] A. Paydayesh, A.A. Azar, and A.J. Arani, "Investigation the effect of Graphene on The Morphology, Mechanical and Thermal properties of PLA/PMMA Blends," Ciência e Natura, **37**, 15-22 (2015). https://doi.org/10.5902/2179460X20823
[25] A.A. Mohammed, M.A. Habeeb, "Modification and Development of the Structural, Optical and Antibacterial Characteristics of PMMA/Si3N4/TaC Nanostructures," Silicon, (2023). https://doi.org/10.1007/s12633-023-02426-2
[26] S. Ahmad, and S.A. Agnihotry, "Synthesis and characterization of in situ prepared poly (methyl methacrylate) nanocomposites," Bull. Mater. Sci. **30**(1), 31-35 (2007). https://doi.org/10.1007/s12034-007-0006-9
[27] N.K. Al-Sharifi, and M.A. Habeeb, Synthesis and Exploring Structural and Optical Properties of Ternary PS/SiC/Sb_2O^3 Nanocomposites for Optoelectronic and Antimicrobial Applications, Silicon, (2023). https://doi.org/10.1007/s12633-023-02418-2
[28] S. Ramesh, and L.C. Wen, "Investigation on the effects of addition of SiO2 nanoparticles on ionic conductivity, FTIR, and thermal properties of nanocomposite PMMA–LiCF3SO3–SiO2," Ionics (Kiel), **16**, 255-262 (2010). https://doi.org/10.1007/s11581-009-0388-3
[29] A. Hashim, M.A. Habeeb, and Q.M. Jebur, "Structural, dielectric and optical properties for (Polyvinyl alcohol-polyethylene oxide manganese oxide) nanocomposites," Egyptian Journal of Chemistry, **63**, 735-749 (2020). https://dx.doi.org/10.21608/ejchem.2019.14849.1901
[30] M. Haghighi-Yazdi, and P. Lee-Sullivan, "FTIR analysis of a polycarbonate blend after hygrothermal aging," Journal of Applied Polymer Science, **132**(3), (2015). https://doi.org/10.1002/app.41316
[31] Q.M. Jebur, A. Hashim, and M.A. Habeeb, "Fabrication, structural and optical properties for (Polyvinyl alcohol-polyethylene oxide iron oxide) nanocomposites," Egyptian Jour of Chemistry, **63**(2), 611-623 (2020). https://dx.doi.org/10.21608/ejchem.2019.10197.1669
[32] A. Goswami, A.K. Bajpai, and B.K. Sinha, "Designing vanadium pentoxide-carboxymethyl cellulose/polyvinyl alcohol-based bionanocomposite films and study of their structure, topography, mechanical, electrical and optical behavior," Polym. Bull. **75**(2), 781-807 (2018). https://doi.org/10.1007/s00289-017-2067-2
[33] M.A. Habeeb, and W.S. Mahdi, "Characterization of (CMC-PVP-Fe2O3) nanocomposites for gamma shielding application," International Journal of Emerging Trends in Engineering Research, **7**(9), 247-255 (2019). https://doi.org/10.30534/ijeter/2019/06792019
[34] K. Rajesh, V. Crasta, K.N.B. Rithin, G. Shetty, and P.D. Rekha, "Structural, optical, mechanical and dielectric properties of titanium dioxide doped PVA/PVP nanocomposite," J. Polym. Res. **26**(4), 1-10 (2019). https://doi.org/10.1007/s10965-019-1762-0
[35] M.A. Habeeb, R.S.A. Hamza, "Synthesis of (polymer blend –MgO) nanocomposites and studying electrical properties for piezoelectric application", Indonesian Journal of Electrical Engineering and Informatics, **6** (4), 428-435 (2018). https://doi.org/10.11591/ijeei.v6i1.511
[36] G. Chakraborty, K. Gupta, D. Rana, and A.M. Kumar, "Dielectric relaxation in polyvinyl alcohol–polypyrrole–multiwall carbon nanotube composites below room temperature," Advances in Natural Sciences, **4**, 1-4 (2014).
[37] M.A. Habeeb, R.S. Abdul Hamza, "Novel of (biopolymer blend-MgO) nanocomposites: Fabrication and characterization for humidity sensors," Journal of Bionanoscience, **12** (3), 328-335 (2018). https://doi.org/10.1166/jbns.2018.1535
[38] S. Ju, M. Chen, H. Zhang, and Z. Zhang, "Dielectric properties of nanosilica/low-density polyethylene composites: The surface chemistry of nanoparticles and deep traps induced nanoparticles," Journal of express Polymer Letters, **8**(9), 682-691 (2014). https://doi.org/10.3144/expresspolymlett.2014.71
[39] M.A. Habeeb, A. Hashim, and N. Hayder, "Structural and optical properties of novel (PS-Cr2O3/ZnCoFe2O4) nanocomposites for UV and microwave shielding," Egyptian Journal of Chemistry, **63**, 697-708 (2020). https://dx.doi.org/10.21608/ejchem.2019.12439.1774
[40] O. Abdullah, G.M. Jamal, D.A. Tahir, and S.R. Saeed, "Electrical Characterization of Polyester Reinforced by Carbon Black Particles," International Journal of Applied Physics and Mathematics, **1**(2), 101-105 (2011). https://doi.org/10.7763/IJAPM.2011.V1.20
[41] M.A. Habeeb, "Dielectric and optical properties of (PVAc-PEG-Ber) biocomposites," Journal of Engineering and Applied Sciences, **9**(4), 102-108 (2014). https://doi.org/10.36478/jeasci.2014.102.108
[42] R.N. Bhagat, and V.S. Sangawar, "Synthesis and Structural Properties of Polystyrene Complexed with Cadmium Sulfide," Int. J. Sci. Res. **6**, 361-365 (2017). https://www.ijsr.net/get_abstract.php?paper_id=ART20177794
[43] A.H. Hadi, M.A. Habeeb, "The dielectric properties of (PVA-PVP-CdS) nanocomposites for gamma shielding applications," Journal of Physics: Conference Series, **1973**(1), 012063 (2021). https://doi.org/10.1088/1742-6596/1973/1/012063
[44] L. Kungumadevi, R. Sathyamoorthy, and A. Subbarayan, "AC conductivity and dielectric properties of thermally evaporated PbTe thin films," Solid. State. Electron. **54**(1), 58-62 (2010). https://doi.org/10.1016/j.sse.2009.09.023
[45] M.A. Habeeb, and Z.S. Jaber, "Enhancement of Structural and Optical Properties of CMC/PAA Blend by Addition of Zirconium Carbide Nanoparticles for Optics and Photonics Applications," East European Journal of Physics, **4**, 176-182 (2022). https://doi.org/10.26565/2312-4334-2022-4-18
[46] R. Dalven, and R. Gill, "Electrical properties of β-Ag2Te and β-Ag 2Se from 4.2°k to 300°K," J. Appl. Phys. **38**(2), 753-756 (1967). https://doi.org/10.1063/1.1709406
[47] S.M. Mahdi, and M.A. Habeeb, "Fabrication and Tailored Structural and Dielectric characteristics of ($SrTiO_3$/NiO) Nanostructure Doped (PEO/PVA) polymeric Blend for Electronics Fields," Physics and Chemistry of Solid State, **23**(4), 785-792 (2022). https://doi.org/10.15330/pcss.23.4.785-792
[48] Y. Li, H. Porwal, Z. Huang, H. Zhang, E. Bilotti, and T. Peijs, "Enhanced Thermal and Electrical Properties of Polystyrene-Graphene Nanofibers via Electrospinning," J. Nanomater. **2016**, 4624976 (2016). https://doi.org/10.1155/2016/4624976
[49] S.M. Mahdi, and M.A. Habeeb, "Tailoring the structural and optical features of (PEO–PVA)/(SrTiO3–CoO) polymeric nanocomposites for optical and biological applications," Polymer Bulletin, (2023). https://doi.org/10.1007/s00289-023-04676-x
[50] C.M. Mathew, K. Kesavan, and S. Rajendran, "Structural and Electrochemical Analysis of PMMA Based Gel Electrolyte Membranes," Int. J. Electrochem. **2015**, 1-7 (2015). https://doi.org/10.1155/2015/494308

ВПЛИВ НАНОМАТЕРІАЛІВ Si_3N_4/TaC НА СТРУКТУРНІ ТА ЕЛЕКТРИЧНІ ХАРАКТЕРИСТИКИ ПОЛІМЕТИЛМЕТАКРИЛАТУ ДЛЯ ЕЛЕКТРОТЕХНІКИ ТА ЕЛЕКТРОНІКИ

Алаа Абас Мохаммед, Маджід Алі Хабіб

Вавилонський університет, Освітній коледж чистих наук, Фізичний факультет, Ірак

У цьому дослідженні використовувався метод лиття для отримання нанокомпозитів PMMA/ Si_3N_4/TaC з різним вмістом (0,2,4,6,8) % мас. наночастинок (НЧ) Si_3N_4/TaC. Досліджено структурні та електричні властивості. Дослідження на скануючому електронному мікроскопі (SEM) вказують на однорідність, гладкість і дисперсію НЧ Si_3N_4 і TaC всередині матриці ПММА через сильну ковалентну взаємодію між НЧ Si_3N_4 і TaC в матриці ПММА, що означає хороший метод для підготовлених плівок. Зображення з оптичного мікроскопа пояснюють, що збільшення вмісту наночастинок утворює мережеві шляхи всередині полімерної матриці, які діють як носії заряду. Спектри FTIR вказують на фізичну інтерференцію між полімерною матрицею та наночастинками. Електричні властивості змінного струму нанокомпозитів показали, що діелектрична проникність і діелектричні втрати зростають зі збільшенням вмісту наночастинок і зменшуються зі збільшенням частоти прикладеного електричного поля. Тоді як електропровідність змінного струму зростає зі збільшенням частоти та ваги наночастинок Si_3N_4/TaC. Ці результати показали, що наноструктури PMMA/Si_3N_4/TaC можна вважати перспективними матеріалами для електроніки та електричних нанопристроїв.

Ключові слова: *нанокомпозити; ПММА; Si_3N_4; TaC; електричні властивості змінного струму*

East European Journal of Physics. **2.** 165-172 (2023)
DOI:10.26565/2312-4334-2023-2-16 ISSN 2312-4334

COMPUTATION OF CHARACTERISTICS OF C IV TRANSITIONS[†]

Muhammad Saeed[a], Shafiq Ur Rehman[a], Mahwish Mobeen Khan[b], Zaheer Uddin[a]*
[a]*Department of Physics, University of Karachi, Pakistan*
[b]*Department of Applied Chemistry & Chemical Technology, University of Karachi, Pakistan*
**Corresponding Author e-mail: zuddin@uok.edu.pk*
Received February 10, 2023; revised April 2, 2023; in final form May 17, 2023; accepted May 18, 2023

In this research, we computed transition probabilities, line strength, and oscillator strengths of more than 5000 transitions in C IV. Very few values of these spectroscopic characteristics were previously known and reported. The calculation method, based on a combination of the weakest bound electron model and numerical approximation, shows reliable values because the correlation between known and calculated values is high. The transition probabilities calculated in this work are compared with known values of the NIST database and those found in literature, and a reasonably good agreement has been observed. The lifetime of Rydberg levels ns, np, nd, nf, ng has been reported up to n = 25. A general sixth-degree polynomial was developed, generating C IV lifetimes with reasonable accuracy. Most of the results presented are new.
Keywords: *carbon atom; transition probability; oscillator strength; Rydberg atom; quantum defects*
PACS: 31.10, +z, 31.15.−p, 31.15.Ct, 31.90.+s

INTRODUCTION

The star's atmosphere or other astronomical objects like interstellar nebula have various chemical elements. The chemical composition varies from object to object; astronomers can identify it by recording and measuring the relative amount of electromagnetic radiation emitted by each. Understanding stellar evolution requires precise abundances of various elements, including carbon. The chemical abundance is also vital to understand the complex picture of stars. The study of Excited states of atoms is the foundation of quantum mechanics and has grabbed the focus of scientists for many decades. Many research papers and articles have been published with the application of the transition state of carbon atoms in molecular physics, nanochemistry, medicinal chemistry, environmental chemistry, and material science [1-7]. In 1970, Martinson measured the Mean lives of 16 excited levels in C II - C V with the beam-foil technique and found good agreement for the C III $2s3d\,^3D$ - $2s4f\,^3F^0$ (1923 Å) transition and the C IV $2s^2S$ - $2p^2p^0$ (1548 Å) transition [8]. In 1971, Poulizac also used the beam-foil excitation method to study the carbon spectra between 1100 Å and 7000 Å for C I, C II, C III, C IV, and C V energy ranging from 0.18 to 2.0 MeV [9]. In 1979, Ganas used a semiempirical approach with Optical oscillator strengths for excitations from the valence subshell of C (IV) and N (V) and obtained good agreement with experimental data [10]. In 1989, Baudinet-Robinet et al. applied the beam-foil-laser method to determine the lifetimes of two levels in multiply ionized carbon atoms and found the results for C Ill $2s3d^1$ D, 0.15±0.01 ns and C IV $3s^2$ S, 0.21±0.02 ns. These values are in good agreement with the theoretical predictions. They also determined these lifetimes using the classical (nonselective) beam-foil method and reported ≈ 20% longer than the beam-foil-laser values. These factors limit the accuracy of the lifetime determinations by the beam-foil-laser method [11]. In 1996, Gou used the multichannel saddle-point and saddle-point complex-rotation methods for Seven triply excited states of lithium-like beryllium and carbon, using first-order perturbation theory [12]. In 1997, Cheng improved the energy levels in neutral carbon using high-resolution infrared solar spectra. The main source is the ATMOS spectrum measured by the Fourier transform spectroscopy technique from 600 to 4800 cm^{-1}, supplemented by the MARK IV balloon data, covering 4700 to 5700 cm^{-1} [13]. P. Quinet, in 1998, by using the Ritz and the polarization methods, calculated the term energies up to $n = 30$ and $l \geq 3$ in C II, C III, and C IV. His article also reported the predicted wavelengths for these lines of high-*nl* term energies and the related oscillator strengths [14]. Nengwu Zheng et al., in 2001, by employing the WBEPM, computed transition probabilities of C I, C II, C III, and C IV. They calculated the required parameters for the calculation of transition probabilities through a proposed coupled equation which relates the energy and radial expectation value $\langle r \rangle_{nl}$ of the Weakest Bound Electron [15]. In 2004, Agarwal investigated Energy levels and radiative rates for transitions among the lowest 24 fine structure levels belonging to the $1s^2\,nl$ ($n \leq 5$) configurations of C IV using the fully relativistic GRASP code. Additionally, collision strengths for transitions among these levels have been computed over a wide energy range below 28 Ry using the Dirac Atomic R-matrix Code [16]. In 2002, Nengwu Zheng and Tao Wang computed the radiative lifetimes, transition probabilities, and oscillator strengths for individual lines of different transitions for atomic carbon and oxygen. In their article, WBEPM theory has been employed for calculations [17]. Zheng et al., in 2004, developed a unified WBEPM theory in which they presented the relativistic form of the theory and combined it with the non-relativistic form they proposed earlier. They have employed the newly proposed theory for calculating transition probabilities and F II oscillator strength, carbon atom energy levels, and Ionization potential for oxygen-like ions [18]. In 2018, Lischka introduced the progress in time-resolved spectroscopy to explain the characteristic features of excited states accurately. At the same time, the stable molecule's electronic ground state problems

[†] ***Cite as***: M. Saeed, S.U. Rehman, M.M. Khan, and Z. Uddin, East Eur. J. Phys. **2**, 165 (2023), https://doi.org/10.26565/2312-4334-2023-2-16

can efficiently solve with the implementation of quantum chemical methodology [19]. In 2020, Li et al. worked with the multiconfiguration Dirac-Hartree-Fock and Relativistic Configuration Interaction methods for the General-purpose Relativistic Atomic Structure Package GRASP2K to compute the Landé g-factors for states in C I−IV and other atoms. Further, they compared the accuracy of the wave functions for the states and the resulting Landé g-factors' accuracy with the computed excitation energies and energy separations with the National Institute of Standards and Technology (NIST) recommended data [20]. In 2022, Whang et al. employed a neural network machine learning method to simulate interatomic potentials for the structural properties of several carbon structures. First-principles Density Functional Theory (DFT) calculations are used to train the potential with a database of crystalline and liquid structures. The excellent accuracy and transferability of the NNP provide a promising tool for accurate atomistic simulations of various carbon materials with faster speed and much lower cost [21].

THEORY

Due to its complex nature, the Schrodinger equation for atoms and ions having many electrons is difficult to solve. However, an approximate solution for the hydrogen atom exists, with only one electron in its outermost shell. Like the hydrogen atom, some atoms have only one electron in the outermost shells; thus, the interaction terms are no longer required in the equation for the hydrogen-like atom. Hence Schrodinger equation for hydrogen atoms can be used for such atoms and ions with the approximation that all other electrons in the inner shells together with the nucleus form the core, like the hydrogen atom, e.g., hydrogen-like atoms and ions are Li I, Be II, B III, C IV, N V, and O VI. The theory used in this work is the same as in [22]. The Schrodinger equation for hydrogen-like atoms and ions is given by,

$$\left(\frac{d^2}{dr^2} - 2V(r) - \frac{l^*(l^*+1)}{r^2} + 2E\right)P(r) = o, \tag{1}$$

Here $P(r) = rR(r)$, and $R(r)$ is the radial wavefunction,

$$\frac{l^*(l^*+1)}{r^2} + V(r) = \frac{l(l+1)}{r^2} + \frac{B}{r^2} + \frac{A}{r} \tag{2}$$

The first term on the right side $\left(\frac{l(l+1)}{r^2}\right)$ is the same as for hydrogen atom, the second term $\left(\frac{B}{r^2} + \frac{A}{r}\right)$ is the total potential felt by the weakest bound electron. The energy of hydrogen-like atoms and ions is given by,

$$E = \frac{Z^{*2}}{2n^{*2}} \tag{3}$$

$n^* = n - \delta_n$ and $l^* = l - \delta_l$ are effective principal and orbital quantum numbers for hydrogen-like atoms and ions. δ is a quantum defect in principal and orbital quantum numbers (n, l). The quantum defect can be expressed as a polynomial in x, where x is $1/(n - \delta_o)$, the δ_o is the lowest value of quantum defect. The radial function can be defined as $R(r) = \frac{P(r)}{r}$, and can be expressed in terms of associated Laguerre polynomials.

The transition probability A_{fi} of a transition for spontaneous emission between levels (n_f, l_f) & (n_i, l_i) is given as,

$$A_{fi} = 2.0261 \times 10^{-6} \frac{(E_f - E_i)^3}{2l_i+1} S \tag{4}$$

$E_f > E_i$ and are energies of upper and lower levels, S is the electric dipole line strength; it is proportional to the dipole matrix element $P^{(1)}_{l_i l_f}$ which is given as,

$$P^{(1)}_{l_i l_f} = l_> < n_i, l_i|r|n_f, l_f > = l_> \int_0^\infty r^3 R_{n_i l_i} R_{n_f l_f} dr \tag{5}$$

The lifetime (τ) of Rydberg levels can be found by the following equation;

$$\tau_i = \frac{1}{\sum_f A_{fi}} \tag{6}$$

RESULT AND DISCUSSION

The Martin formula was used to calculate energies and quantum defects of the Rydberg lithium levels like C IV. These results calculated transition probabilities, oscillator strength, and line strength of five thousand two hundred and fifty transitions. The transition probability mainly depends on the energy difference of the levels involved in the transition and the line strength of the transition. Due to the unavailability of the wavefunction for the atoms and ions, it isn't easy to calculate line strength which depends on the dipole matrix element. However, the Weakest Bound Electron Potential Model (WBEPM) suggests hydrogen-like wavefunction for lithium-like atoms and ions. This wavefunction for C IV was used, and dipole integral was evaluated using the wavefunction of WBEPM; consequently, line strength was evaluated, which was further used in calculating transition probability. The energy levels of ns, np, nd, nf, and ng up to $n = 30$ have been calculated; using selection rules, more than 5250 transitions in C IV were studied. In Table I, the first column gives the configuration of the upper and lower levels of the transition (nlj). The first letter represents the principal quantum number, the second is the sub-orbital corresponding to the orbital quantum number, and the term in the bracket is the total angular momentum of the

level. The second column gives the transition probabilities determined in this work, NIST values, and Zheng's work. The third and fourth columns give oscillator strengths & line strengths determined in this work and NIST values.

Out of these 5250, only 225 transition probabilities are given on the NIST site, the comparison of these transition probabilities with those calculated in this work has a percentage error of less than 1% in most cases, and in a few cases, it is up to 7%. Similar is the case upon comparing the transition probabilities of Zheng's work and this study. However, there is one transition in each comparison with NIST data and Zheng's work, where a large deviation is seen from this work, as mentioned below.

The Transition $1s^2 8s - 1s^2 2p$

The transition probabilities for the transitions $1s^2 8s_{3/2} - 1s^2 2p_{1/2}$ and $1s^2 8s_{1/2} - 1s^2 2p_{3/2}$ determined in this work are 5.75×10^7 and 1.15×10^8, the corresponding values in the NIST data are 1.66×10^9, and 3.22×10^9, respectively. A difference of 99% between them can be seen. NIST data classifies these transitions in accuracy code B, which means it has 10% or fewer errors. As mentioned below, Zheng did not measure this transition where a large deviation is seen from this work.

The Transition $1s^2 3d$-$1s^2 2p$

The transition probabilities for the transitions $1s^2 3d_{3/2} - 1s^2 2p_{1/2}$ determined in this work are 1.52×10^{10}, and the corresponding value in Zheng's work is 1.47×10^6. A big difference is observed between the two, whereas the reported value in the NIST database is close to the value determined in this work (1.46×10^{10}). NIST data classifies it in accuracy code B, which means it has a 10% or less error. The maximum probability is found for the transition $1s^2 3d - 1s^2 2p$.

Fig. 1 compares transition probabilities calculated in this work and listed in the NIST database. An approximate straight-line graph among transition probabilities between this work and NIST values indicates a good agreement between both. The correlation coefficient between these probabilities is 0.999.

Since many transition probabilities are known, all possible transition probabilities from each level are known; hence equation (6) can be used to find the lifetime of the levels. The lifetimes of Rydberg levels $1s^2$ ns, $1s^2$ np, $1s^2$ nd, $1s^2$ nf, and $1s^2$ ng up to n = 25 have also been determined. Table II gives the values of the lifetime of the corresponding level.

Table I. List of transition calculated transition probabilities, oscillator strengths, and line strength compared with corresponding values in the NIST database.

Configurations	Transition Probability			Oscillator Strength		Line Strength	
Lower level - Upper level	This Work	NIST	Zheng ($\times10^8$)	This Work	NIST	NIST	This Work
$2p_{1/2} \rightarrow 3d_{3/2}$	1.516E+10	1.460E+10	0.0147	0.6690	0.6460	1.6913	1.6300
$3p_{1/2} \rightarrow 3d_{3/2}$	4.872E+05	4.890E+05	0.0049	0.0625	0.0629	8.5221	8.5700
$2p_{3/2} \rightarrow 3d_{3/2}$	3.030E+09	2.920E+09	29.3400	0.0669	0.0646	0.3385	0.3270
$3p_{3/2} \rightarrow 3d_{3/2}$	9.553E+04	9.580E+04	0.0010	0.0062	0.0062	1.7043	1.7100
$2p_{1/2} \rightarrow 4d_{3/2}$	5.045E+09	4.900E+09	49.7400	0.1262	0.1230	0.2402	0.2340
$3p_{1/2} \rightarrow 4d_{3/2}$	1.508E+09	1.470E+09	14.5600	0.5537	0.5410	4.0374	3.9400
$4p_{1/2} \rightarrow 4d_{3/2}$	1.527E+05	1.530E+05	0.0015	0.1115	0.1120	36.2447	36.4000
$2p_{3/2} \rightarrow 4d_{3/2}$	1.008E+09	9.780E+08	9.9400	0.0126	0.0123	0.0480	0.0467
$3p_{3/2} \rightarrow 4d_{3/2}$	3.016E+08	2.940E+08	2.9130	0.0554	0.0541	0.8084	0.7890
$4p_{3/2} \rightarrow 4d_{3/2}$	2.995E+04	3.000E+04	0.0003	0.0111	0.0111	7.2487	7.2700
$2p_{1/2} \rightarrow 5d_{3/2}$	2.340E+09	2.280E+09	23.2400	0.0471	0.0460	0.0805	0.0786
$3p_{1/2} \rightarrow 5d_{3/2}$	7.614E+08	7.430E+08	7.4390	0.1352	0.1320	0.6854	0.6700
$4p_{1/2} \rightarrow 5d_{3/2}$	3.026E+08	2.970E+08	2.9330	0.5239	0.5150	8.2970	8.1600
$5p_{1/2} \rightarrow 5d_{3/2}$	5.523E+04	5.520E+04	0.0006	0.1551	0.1550	98.9188	99.0000
$2p_{3/2} \rightarrow 5d_{3/2}$	4.676E+08	4.550E+08	4.6440	0.0047	0.0046	0.0161	0.0157
$3p_{3/2} \rightarrow 5d_{3/2}$	1.522E+08	1.480E+08	1.4880	0.0135	0.0132	0.1371	0.1340
$4p_{3/2} \rightarrow 5d_{3/2}$	6.054E+07	5.930E+07	0.5869	0.0524	0.0515	1.6616	1.6300
$5p_{3/2} \rightarrow 5d_{3/2}$	1.082E+04	1.080E+04	0.0001	0.0154	0.0154	19.7832	19.8000
$2p_{1/2} \rightarrow 6d_{3/2}$	1.287E+09	1.250E+09	12.8200	0.0233	0.0226	0.0376	0.0366
$3p_{1/2} \rightarrow 6d_{3/2}$	4.293E+08	4.190E+08	4.2150	0.0561	0.0549	0.2441	0.2390
$4p_{1/2} \rightarrow 6d_{3/2}$	1.842E+08	1.800E+08	1.8000	0.1386	0.1360	1.4475	1.4200
$5p_{1/2} \rightarrow 6d_{3/2}$	8.861E+07	8.720E+07	0.8621	0.5232	0.5160	15.3016	15.1000
$6p_{1/2} \rightarrow 6d_{3/2}$	2.325E+04	2.180E+04		0.1961	0.1840	216.7812	204.0000
$2p_{3/2} \rightarrow 6d_{3/2}$	2.571E+08	2.500E+08	2.5630	0.0023	0.0023	0.0075	0.0073
$3p_{3/2} \rightarrow 6d_{3/2}$	8.582E+07	8.380E+07	0.8428	0.0056	0.0055	0.0488	0.0478
$4p_{3/2} \rightarrow 6d_{3/2}$	3.684E+07	3.600E+07	0.3601	0.0139	0.0136	0.2897	0.2840
$5p_{3/2} \rightarrow 6d_{3/2}$	1.773E+07	1.740E+07		0.0524	0.0515	3.0652	3.0100
$6p_{3/2} \rightarrow 6d_{3/2}$	4.550E+03	4.280E+03		0.0195	0.0183	43.3555	40.9000
$2p_{3/2} \rightarrow 3d_{5/2}$	1.818E+10	1.750E+10	176.0300	0.6022	0.5810	3.0462	2.9400
$3p_{3/2} \rightarrow 3d_{5/2}$	5.770E+05	5.790E+05	0.0058	0.0560	0.0563	15.3405	15.4000
$2p_{3/2} \rightarrow 4d_{5/2}$	6.050E+09	5.870E+09		0.1136	0.1100	0.4324	0.4210
$3p_{3/2} \rightarrow 4d_{5/2}$	1.809E+09	1.760E+09	17.4700	0.4986	0.4860	7.2736	7.0900
$4p_{3/2} \rightarrow 4d_{5/2}$	1.808E+05	1.810E+05	0.0018	0.0999	0.1000	65.2427	65.4000
$2p_{3/2} \rightarrow 5d_{5/2}$	2.806E+09	2.730E+09	27.8700	0.0424	0.0414	0.1449	0.1410
$3p_{3/2} \rightarrow 5d_{5/2}$	9.135E+08	8.910E+08	8.9260	0.1217	0.1190	1.2343	1.2100

Configurations	Transition Probability			Oscillator Strength		Line Strength	
Lower level - Upper level	This Work	NIST	Zheng ($\times 10^8$)	This Work	NIST	NIST	This Work
$4p_{3/2} \rightarrow 5d_{5/2}$	3.632E+08	3.560E+08	3.5210	0.4719	0.4630	14.9503	14.7000
$5p_{3/2} \rightarrow 5d_{5/2}$	6.524E+04	6.520E+04	0.0007	0.1389	0.1390	178.0578	178.0000
$2p_{3/2} \rightarrow 6d_{5/2}$	1.543E+09	1.500E+09	15.3800	0.0209	0.0204	0.0677	0.0660
$3p_{3/2} \rightarrow 6d_{5/2}$	5.149E+08	5.030E+08	5.0570	0.0505	0.0494	0.4395	0.4300
$4p_{3/2} \rightarrow 6d_{5/2}$	2.210E+08	2.160E+08	2.1600	0.1248	0.1220	2.6069	2.5500
$5p_{3/2} \rightarrow 6d_{5/2}$	1.064E+08	1.050E+08	1.0350	0.4713	0.4660	27.5757	27.3000
$6p_{3/2} \rightarrow 6d_{5/2}$	2.747E+04	2.580E+04		0.1756	0.1650	390.2184	367.0000
$2s_{1/2} \rightarrow 2p_{1/2}$	2.726E+08	2.640E+08	2.6490	0.0981	0.0952	1.0017	0.9720
$2s_{1/2} \rightarrow 3p_{1/2}$	4.598E+09	4.630E+09	43.5200	0.0671	0.0678	0.1381	0.1390
$3s_{1/2} \rightarrow 3p_{1/2}$	3.186E+07	3.160E+07	0.3140	0.1612	0.1600	6.1694	6.1300
$3d_{3/2} \rightarrow 4p_{1/2}$	1.238E+08	1.280E+08		0.0266	0.0138	0.2100	0.2180
$2s_{1/2} \rightarrow 4p_{1/2}$	2.258E+09	2.270E+09	21.0900	0.0203	0.0204	0.0327	0.0329
$3s_{1/2} \rightarrow 4p_{1/2}$	5.054E+08	5.030E+08	4.9210	0.0680	0.0678	0.4245	0.4230
$4s_{1/2} \rightarrow 4p_{1/2}$	7.144E+06	7.110E+06	0.0709	0.2205	0.2200	20.8530	20.8000
$3d_{3/2} \rightarrow 5p_{1/2}$	5.230E+07	5.470E+07		0.0051	0.0027	0.0270	0.0283
$4d_{3/2} \rightarrow 5p_{1/2}$	6.511E+07	6.670E+07		0.0657	0.0337	1.1224	1.1500
$2s_{1/2} \rightarrow 5p_{1/2}$	1.207E+09	1.210E+09	11.2100	0.0090	0.0090	0.0131	0.0132
$3s_{1/2} \rightarrow 5p_{1/2}$	3.117E+08	3.110E+08	3.0070	0.0219	0.0219	0.0987	0.0986
$4s_{1/2} \rightarrow 5p_{1/2}$	1.083E+08	1.080E+08	1.0650	0.0718	0.0717	0.9954	0.9940
$5s_{1/2} \rightarrow 5p_{1/2}$	2.263E+06	2.260E+06	0.0225	0.2785	0.2790	52.5840	52.6000
$3d_{3/2} \rightarrow 6p_{1/2}$	2.722E+07	2.860E+07		0.0019	0.0010	0.0086	0.0091
$4d_{3/2} \rightarrow 6p_{1/2}$	3.191E+07	3.290E+07		0.0131	0.0068	0.1424	0.1470
$5d_{3/2} \rightarrow 6p_{1/2}$	3.251E+07	3.310E+07		0.1115	0.0569	3.5159	3.5900
$2s_{1/2} \rightarrow 6p_{1/2}$	7.113E+08	7.150E+08		0.0048	0.0048	0.0067	0.0068
$3s_{1/2} \rightarrow 6p_{1/2}$	1.914E+08	1.910E+08		0.0102	0.0102	0.0398	0.0398
$4s_{1/2} \rightarrow 6p_{1/2}$	7.601E+07	7.560E+07		0.0236	0.0235	0.2238	0.2230
$5s_{1/2} \rightarrow 6p_{1/2}$	3.319E+07	3.300E+07		0.0770	0.0766	1.9943	1.9900
$6s_{1/2} \rightarrow 6p_{1/2}$	8.893E+05	8.940E+05		0.3358	0.3380	111.0743	112.0000
$3d_{3/2} \rightarrow 7p_{1/2}$	1.609E+07	1.700E+07		0.0010	0.0005	0.0039	0.0042
$4d_{3/2} \rightarrow 7p_{1/2}$	1.817E+07	1.880E+07		0.0050	0.0026	0.0449	0.0465
$5d_{3/2} \rightarrow 7p_{1/2}$	1.763E+07	1.810E+07		0.0227	0.0117	0.4396	0.4520
$6d_{3/2} \rightarrow 7p_{1/2}$	1.707E+07	1.730E+07		0.1615	0.0820	8.4548	8.5800
$2s_{1/2} \rightarrow 7p_{1/2}$	4.521E+08	4.550E+08		0.0029	0.0029	0.0039	0.0040
$3s_{1/2} \rightarrow 7p_{1/2}$	1.239E+08	1.240E+08		0.0057	0.0057	0.0206	0.0206
$4s_{1/2} \rightarrow 7p_{1/2}$	5.102E+07	5.080E+07		0.0112	0.0112	0.0892	0.0890
$5s_{1/2} \rightarrow 7p_{1/2}$	2.529E+07	2.520E+07		0.0254	0.0254	0.4340	0.4330
$6s_{1/2} \rightarrow 7p_{1/2}$	1.271E+07	1.260E+07		0.0827	0.0821	3.5929	3.5700
$7s_{1/2} \rightarrow 7p_{1/2}$	4.049E+05	4.080E+05		0.3928	0.3960	208.2167	210.0000
$3d_{3/2} \rightarrow 8p_{1/2}$	1.034E+07	1.100E+07		0.0006	0.0003	0.0022	0.0023
$4d_{3/2} \rightarrow 8p_{1/2}$	1.142E+07	1.180E+07		0.0025	0.0013	0.0203	0.0210
$5d_{3/2} \rightarrow 8p_{1/2}$	1.072E+07	1.100E+07		0.0088	0.0046	0.1367	0.1410
$6d_{3/2} \rightarrow 8p_{1/2}$	9.956E+06	1.010E+07		0.0334	0.0170	1.0434	1.0600
$2s_{1/2} \rightarrow 8p_{1/2}$	3.044E+08	3.070E+08		0.0019	0.0019	0.0025	0.0025
$3s_{1/2} \rightarrow 8p_{1/2}$	8.427E+07	8.400E+07		0.0035	0.0035	0.0122	0.0122
$4s_{1/2} \rightarrow 8p_{1/2}$	3.524E+07	3.510E+07		0.0063	0.0063	0.0459	0.0458
$5s_{1/2} \rightarrow 8p_{1/2}$	1.805E+07	1.800E+07		0.0122	0.0122	0.1701	0.1700
$6s_{1/2} \rightarrow 8p_{1/2}$	1.025E+07	1.020E+07		0.0273	0.0272	0.7597	0.7570
$7s_{1/2} \rightarrow 8p_{1/2}$	5.673E+06	5.570E+06		0.0889	0.0875	5.9918	5.8900
$8s_{1/2} \rightarrow 8p_{1/2}$	2.052E+05	2.070E+05		0.4495	0.4540	358.0851	361.0000
$3d_{3/2} \rightarrow 9p_{1/2}$	7.064E+06	7.580E+06		0.0004	0.0002	0.0013	0.0014
$4d_{3/2} \rightarrow 9p_{1/2}$	7.680E+06	7.780E+06		0.0015	0.0008	0.0111	0.0113
$5d_{3/2} \rightarrow 9p_{1/2}$	7.060E+06	7.280E+06		0.0045	0.0023	0.0613	0.0633
$6d_{3/2} \rightarrow 9p_{1/2}$	6.365E+06	6.650E+06		0.0131	0.0069	0.3207	0.3360
$2s_{1/2} \rightarrow 9p_{1/2}$	2.145E+08	2.110E+08		0.0013	0.0013	0.0017	0.0017
$3s_{1/2} \rightarrow 9p_{1/2}$	5.973E+07	5.940E+07		0.0023	0.0023	0.0079	0.0079
$4s_{1/2} \rightarrow 9p_{1/2}$	2.518E+07	2.460E+07		0.0040	0.0039	0.0272	0.0266
$5s_{1/2} \rightarrow 9p_{1/2}$	1.307E+07	1.290E+07		0.0070	0.0069	0.0868	0.0858
$6s_{1/2} \rightarrow 9p_{1/2}$	7.656E+06	7.700E+06		0.0131	0.0132	0.2930	0.2950
$7s_{1/2} \rightarrow 9p_{1/2}$	4.770E+06	4.700E+06		0.0293	0.0289	1.2363	1.2200
$8s_{1/2} \rightarrow 9p_{1/2}$	2.828E+06	2.850E+06		0.0953	0.0962	9.4203	9.5100
$9s_{1/2} \rightarrow 9p_{1/2}$	1.128E+05	1.130E+05		0.5061	0.5070	576.9346	578.0000
$2s_{1/2} \rightarrow 2p_{3/2}$	2.741E+08	2.650E+08	2.6630	0.1966	0.1900	2.0040	1.9400
$2s_{1/2} \rightarrow 3p_{3/2}$	4.593E+09	4.630E+09	43.4500	0.1341	0.1360	0.2758	0.2790
$3s_{1/2} \rightarrow 3p_{3/2}$	3.205E+07	3.170E+07	0.3160	0.3230	0.3200	12.3406	12.2000
$3d_{3/2} \rightarrow 4p_{3/2}$	1.235E+07	1.280E+07		0.0053	0.0028	0.0419	0.0435
$3d_{5/2} \rightarrow 4p_{3/2}$	1.112E+08	1.150E+08		0.0319	0.0165	0.3774	0.3910
$2s_{1/2} \rightarrow 4p_{3/2}$	2.256E+09	2.270E+09	21.0700	0.0405	0.0408	0.0653	0.0658
$3s_{1/2} \rightarrow 4p_{3/2}$	5.047E+08	5.040E+08	4.9120	0.1358	0.1360	0.8474	0.8480
$4s_{1/2} \rightarrow 4p_{3/2}$	7.185E+06	7.150E+06	0.0713	0.4419	0.4410	41.7094	41.6000
$3d_{3/2} \rightarrow 5p_{3/2}$	5.220E+06	5.470E+06		0.0010	0.0005	0.0054	0.0057

Configurations	Transition Probability			Oscillator Strength		Line Strength	
Lower level - Upper level	This Work	NIST	Zheng ($\times 10^8$)	This Work	NIST	NIST	This Work
$4d_{3/2} \rightarrow 5p_{3/2}$	6.499E+06	6.680E+06		0.0131	0.0068	0.2240	0.2310
$3d_{5/2} \rightarrow 5p_{3/2}$	4.700E+07	4.920E+07		0.0061	0.0032	0.0486	0.0510
$4d_{5/2} \rightarrow 5p_{3/2}$	5.851E+07	6.010E+07		0.0787	0.0405	2.0170	2.0800
$2s_{1/2} \rightarrow 5p_{3/2}$	1.206E+09	1.210E+09	11.2000	0.0179	0.0180	0.0263	0.0264
$3s_{1/2} \rightarrow 5p_{3/2}$	3.114E+08	3.110E+08	3.0020	0.0437	0.0437	0.1971	0.1970
$4s_{1/2} \rightarrow 5p_{3/2}$	1.081E+08	1.080E+08	1.0630	0.1433	0.1430	1.9863	1.9900
$5s_{1/2} \rightarrow 5p_{3/2}$	2.277E+06	2.270E+06	0.0227	0.5582	0.5570	105.1729	105.0000
$3d_{3/2} \rightarrow 6p_{3/2}$	2.717E+06	2.860E+06		0.0004	0.0002	0.0017	0.0018
$4d_{3/2} \rightarrow 6p_{3/2}$	3.186E+06	3.290E+06		0.0026	0.0014	0.0284	0.0294
$5d_{3/2} \rightarrow 6p_{3/2}$	3.245E+06	3.310E+06		0.0223	0.0114	0.7015	0.7170
$3d_{5/2} \rightarrow 6p_{3/2}$	2.446E+07	2.580E+07		0.0023	0.0012	0.0155	0.0164
$4d_{5/2} \rightarrow 6p_{3/2}$	2.868E+07	2.960E+07		0.0157	0.0081	0.2560	0.2650
$5d_{5/2} \rightarrow 6p_{3/2}$	2.922E+07	2.980E+07		0.1336	0.0683	6.3171	6.4500
$2s_{1/2} \rightarrow 6p_{3/2}$	7.108E+08	7.150E+08		0.0096	0.0097	0.0134	0.0135
$3s_{1/2} \rightarrow 6p_{3/2}$	1.912E+08	1.910E+08		0.0203	0.0203	0.0796	0.0796
$4s_{1/2} \rightarrow 6p_{3/2}$	7.589E+07	7.560E+07		0.0471	0.0470	0.4468	0.4460
$5s_{1/2} \rightarrow 6p_{3/2}$	3.312E+07	3.300E+07		0.1535	0.1530	3.9781	3.9700
$6s_{1/2} \rightarrow 6p_{3/2}$	8.951E+05	9.000E+05		0.6731	0.6780	222.1530	224.0000
$3d_{3/2} \rightarrow 7p_{3/2}$	1.605E+06	1.700E+06		0.0002	0.0001	0.0008	0.0008
$4d_{3/2} \rightarrow 7p_{3/2}$	1.814E+06	1.880E+06		0.0010	0.0005	0.0090	0.0093
$5d_{3/2} \rightarrow 7p_{3/2}$	1.760E+06	1.810E+06		0.0045	0.0023	0.0877	0.0904
$6d_{3/2} \rightarrow 7p_{3/2}$	1.704E+06	1.730E+06		0.0322	0.0164	1.6868	1.7200
$3d_{5/2} \rightarrow 7p_{3/2}$	1.445E+07	1.530E+07		0.0011	0.0006	0.0071	0.0075
$4d_{5/2} \rightarrow 7p_{3/2}$	1.633E+07	1.690E+07		0.0060	0.0031	0.0807	0.0836
$5d_{5/2} \rightarrow 7p_{3/2}$	1.584E+07	1.620E+07		0.0272	0.0140	0.7901	0.8090
$6d_{5/2} \rightarrow 7p_{3/2}$	1.534E+07	1.560E+07		0.1935	0.0985	15.1918	15.5000
$2s_{1/2} \rightarrow 7p_{3/2}$	4.517E+08	4.550E+08		0.0058	0.0058	0.0078	0.0079
$3s_{1/2} \rightarrow 7p_{3/2}$	1.238E+08	1.240E+08		0.0113	0.0113	0.0411	0.0412
$4s_{1/2} \rightarrow 7p_{3/2}$	5.095E+07	5.080E+07		0.0223	0.0223	0.1781	0.1780
$5s_{1/2} \rightarrow 7p_{3/2}$	2.524E+07	2.520E+07		0.0508	0.0508	0.8662	0.8660
$6s_{1/2} \rightarrow 7p_{3/2}$	1.268E+07	1.260E+07		0.1650	0.1640	7.1649	7.1300
$7s_{1/2} \rightarrow 7p_{3/2}$	4.077E+05	4.100E+05		0.7874	0.7930	416.4325	420.0000
$3d_{3/2} \rightarrow 8p_{3/2}$	1.032E+06	1.100E+06		0.0001	0.0001	0.0004	0.0005
$4d_{3/2} \rightarrow 8p_{3/2}$	1.140E+06	1.180E+06		0.0005	0.0003	0.0041	0.0042
$5d_{3/2} \rightarrow 8p_{3/2}$	1.070E+06	1.100E+06		0.0018	0.0009	0.0273	0.0281
$6d_{3/2} \rightarrow 8p_{3/2}$	9.939E+05	1.010E+06		0.0067	0.0034	0.2083	0.2120
$3d_{5/2} \rightarrow 8p_{3/2}$	9.294E+06	9.870E+06		0.0007	0.0004	0.0039	0.0041
$4d_{5/2} \rightarrow 8p_{3/2}$	1.026E+07	1.070E+07		0.0030	0.0016	0.0365	0.0381
$5d_{5/2} \rightarrow 8p_{3/2}$	9.633E+06	9.910E+06		0.0106	0.0055	0.2457	0.2530
$6d_{5/2} \rightarrow 8p_{3/2}$	8.948E+06	9.130E+06		0.0401	0.0205	1.8754	1.9200
$2s_{1/2} \rightarrow 8p_{3/2}$	3.042E+08	3.070E+08		0.0038	0.0038	0.0050	0.0051
$3s_{1/2} \rightarrow 8p_{3/2}$	8.418E+07	8.400E+07		0.0070	0.0070	0.0243	0.0243
$4s_{1/2} \rightarrow 8p_{3/2}$	3.519E+07	3.510E+07		0.0127	0.0127	0.0916	0.0916
$5s_{1/2} \rightarrow 8p_{3/2}$	1.802E+07	1.800E+07		0.0243	0.0243	0.3397	0.3400
$6s_{1/2} \rightarrow 8p_{3/2}$	1.023E+07	1.020E+07		0.0546	0.0545	1.5162	1.5100
$7s_{1/2} \rightarrow 8p_{3/2}$	5.658E+06	5.570E+06		0.1773	0.1750	11.9461	11.8000
$8s_{1/2} \rightarrow 8p_{3/2}$	2.067E+05	2.080E+05		0.9012	0.9090	716.1562	722.0000
$3d_{3/2} \rightarrow 9p_{3/2}$	7.049E+05	7.580E+05		0.0001	0.0000	0.0003	0.0003
$4d_{3/2} \rightarrow 9p_{3/2}$	7.666E+05	7.780E+05		0.0003	0.0002	0.0022	0.0023
$5d_{3/2} \rightarrow 9p_{3/2}$	7.048E+05	7.280E+05		0.0009	0.0005	0.0122	0.0127
$6d_{3/2} \rightarrow 9p_{3/2}$	6.355E+05	6.650E+05		0.0026	0.0014	0.0640	0.0671
$3d_{5/2} \rightarrow 9p_{3/2}$	6.347E+06	6.820E+06		0.0004	0.0002	0.0024	0.0026
$4d_{5/2} \rightarrow 9p_{3/2}$	6.902E+06	7.010E+06		0.0018	0.0009	0.0200	0.0203
$5d_{5/2} \rightarrow 9p_{3/2}$	6.345E+06	6.550E+06		0.0054	0.0028	0.1101	0.1140
$6d_{5/2} \rightarrow 9p_{3/2}$	5.721E+06	5.980E+06		0.0157	0.0082	0.5765	0.6040
$2s_{1/2} \rightarrow 9p_{3/2}$	2.144E+08	2.110E+08		0.0026	0.0026	0.0034	0.0034
$3s_{1/2} \rightarrow 9p_{3/2}$	5.967E+07	5.940E+07		0.0047	0.0047	0.0157	0.0157
$4s_{1/2} \rightarrow 9p_{3/2}$	2.515E+07	2.460E+07		0.0080	0.0078	0.0543	0.0533
$5s_{1/2} \rightarrow 9p_{3/2}$	1.305E+07	1.290E+07		0.0139	0.0138	0.1733	0.1720
$6s_{1/2} \rightarrow 9p_{3/2}$	7.642E+06	7.700E+06		0.0262	0.0265	0.5848	0.5900
$7s_{1/2} \rightarrow 9p_{3/2}$	4.760E+06	4.700E+06		0.0585	0.0578	2.4668	2.4400
$8s_{1/2} \rightarrow 9p_{3/2}$	2.821E+06	2.850E+06		0.1901	0.1920	18.7786	19.0000
$9s_{1/2} \rightarrow 9p_{3/2}$	1.136E+05	1.130E+05		1.0146	1.0100	1153.8298	1150.0000
$2p_{1/2} \rightarrow 3s_{1/2}$	1.415E+09	1.420E+09		0.0372	0.0375	0.1029	0.1030
$2p_{3/2} \rightarrow 3s_{1/2}$	2.831E+09	2.850E+09		0.0373	0.0376	0.2061	0.2080
$2p_{1/2} \rightarrow 4s_{1/2}$	5.260E+08	5.320E+08		0.0069	0.0070	0.0136	0.0137
$3p_{1/2} \rightarrow 4s_{1/2}$	3.574E+08	3.590E+08		0.0809	0.0814	0.6554	0.6600
$2p_{3/2} \rightarrow 4s_{1/2}$	1.052E+09	1.060E+09		0.0069	0.0070	0.0271	0.0274
$3p_{3/2} \rightarrow 4s_{1/2}$	7.153E+08	7.180E+08		0.0810	0.0815	1.3131	1.3200
$2p_{1/2} \rightarrow 5s_{1/2}$	2.535E+08	2.570E+08		0.0026	0.0027	0.0045	0.0046

Configurations	Transition Probability			Oscillator Strength		Line Strength	
Lower level - Upper level	This Work	NIST	Zheng ($\times 10^8$)	This Work	NIST	NIST	This Work
$3p_{1/2} \rightarrow 5s_{1/2}$	1.623E+08	1.630E+08		0.0155	0.0156	0.0812	0.0818
$4p_{1/2} \rightarrow 5s_{1/2}$	1.165E+08	1.170E+08		0.1270	0.1280	2.2562	2.2700
$2p_{3/2} \rightarrow 5s_{1/2}$	5.072E+08	5.150E+08		0.0026	0.0027	0.0090	0.0092
$3p_{3/2} \rightarrow 5s_{1/2}$	3.247E+08	3.260E+08		0.0155	0.0156	0.1626	0.1640
$4p_{3/2} \rightarrow 5s_{1/2}$	2.332E+08	2.340E+08		0.1272	0.1280	4.5199	4.5400
$2p_{1/2} \rightarrow 6s_{1/2}$	1.416E+08	1.430E+08		0.0013	0.0013	0.0021	0.0021
$3p_{1/2} \rightarrow 6s_{1/2}$	8.824E+07	8.880E+07		0.0060	0.0060	0.0264	0.0266
$4p_{1/2} \rightarrow 6s_{1/2}$	5.977E+07	6.000E+07		0.0245	0.0246	0.2663	0.2680
$5p_{1/2} \rightarrow 6s_{1/2}$	4.621E+07	4.640E+07		0.1741	0.1750	5.7538	5.7900
$2p_{3/2} \rightarrow 6s_{1/2}$	2.834E+08	2.850E+08		0.0013	0.0013	0.0042	0.0043
$3p_{3/2} \rightarrow 6s_{1/2}$	1.765E+08	1.770E+08		0.0060	0.0060	0.0529	0.0531
$4p_{3/2} \rightarrow 6s_{1/2}$	1.196E+08	1.200E+08		0.0245	0.0246	0.5332	0.5360
$5p_{3/2} \rightarrow 6s_{1/2}$	9.249E+07	9.270E+07		0.1744	0.1750	11.5276	11.6000
$2p_{1/2} \rightarrow 7s_{1/2}$	8.720E+07	8.660E+07		0.0007	0.0007	0.0012	0.0012
$3p_{1/2} \rightarrow 7s_{1/2}$	5.351E+07	5.390E+07		0.0030	0.0031	0.0122	0.0124
$4p_{1/2} \rightarrow 7s_{1/2}$	3.527E+07	3.540E+07		0.0095	0.0096	0.0844	0.0849
$5p_{1/2} \rightarrow 7s_{1/2}$	2.575E+07	2.580E+07		0.0336	0.0338	0.6541	0.6570
$6p_{1/2} \rightarrow 7s_{1/2}$	2.111E+07	2.120E+07		0.2219	0.2230	12.2465	12.3000
$2p_{3/2} \rightarrow 7s_{1/2}$	1.745E+08	1.730E+08		0.0007	0.0007	0.0024	0.0023
$3p_{3/2} \rightarrow 7s_{1/2}$	1.071E+08	1.080E+08		0.0030	0.0031	0.0245	0.0248
$4p_{3/2} \rightarrow 7s_{1/2}$	7.057E+07	7.080E+07		0.0095	0.0096	0.1689	0.1700
$5p_{3/2} \rightarrow 7s_{1/2}$	5.152E+07	5.170E+07		0.0337	0.0338	1.3098	1.3200
$6p_{3/2} \rightarrow 7s_{1/2}$	4.224E+07	4.230E+07		0.2222	0.2230	24.5370	24.6000
$2p_{1/2} \rightarrow 8s_{1/2}$	5.751E+07	1.610E+09		0.0005	0.0132	0.0007	0.0204
$3p_{1/2} \rightarrow 8s_{1/2}$	3.497E+07	3.520E+07		0.0018	0.0018	0.0068	0.0069
$4p_{1/2} \rightarrow 8s_{1/2}$	2.269E+07	2.280E+07		0.0049	0.0049	0.0386	0.0389
$5p_{1/2} \rightarrow 8s_{1/2}$	1.612E+07	1.620E+07		0.0132	0.0133	0.2026	0.2040
$6p_{1/2} \rightarrow 8s_{1/2}$	1.248E+07	1.250E+07		0.0429	0.0430	1.3523	1.3600
$7p_{1/2} \rightarrow 8s_{1/2}$	1.070E+07	1.080E+07		0.2700	0.2730	23.0822	23.3000
$2p_{3/2} \rightarrow 8s_{1/2}$	1.151E+08	3.220E+09		0.0005	0.0132	0.0015	0.0408
$3p_{3/2} \rightarrow 8s_{1/2}$	6.996E+07	7.030E+07		0.0018	0.0018	0.0136	0.0137
$4p_{3/2} \rightarrow 8s_{1/2}$	4.539E+07	4.550E+07		0.0049	0.0049	0.0773	0.0776
$5p_{3/2} \rightarrow 8s_{1/2}$	3.225E+07	3.230E+07		0.0132	0.0132	0.4056	0.4070
$6p_{3/2} \rightarrow 8s_{1/2}$	2.498E+07	2.500E+07		0.0429	0.0430	2.7077	2.7100
$7p_{3/2} \rightarrow 8s_{1/2}$	2.142E+07	2.160E+07		0.2704	0.2730	46.2496	46.7000
$2p_{1/2} \rightarrow 9s_{1/2}$	3.993E+07	3.900E+07		0.0003	0.0003	0.0005	0.0005
$3p_{1/2} \rightarrow 9s_{1/2}$	2.413E+07	2.420E+07		0.0011	0.0012	0.0042	0.0043
$4p_{1/2} \rightarrow 9s_{1/2}$	1.550E+07	1.520E+07		0.0029	0.0029	0.0214	0.0210
$5p_{1/2} \rightarrow 9s_{1/2}$	1.084E+07	1.080E+07		0.0068	0.0068	0.0914	0.0913
$6p_{1/2} \rightarrow 9s_{1/2}$	8.170E+06	8.230E+06		0.0168	0.0170	0.4108	0.4140
$7p_{1/2} \rightarrow 9s_{1/2}$	6.625E+06	6.600E+06		0.0522	0.0520	2.4905	2.4900
$8p_{1/2} \rightarrow 9s_{1/2}$	5.884E+06	5.930E+06		0.3184	0.3210	39.8587	40.2000
$2p_{3/2} \rightarrow 9s_{1/2}$	7.989E+07	7.800E+07		0.0003	0.0003	0.0010	0.0009
$3p_{3/2} \rightarrow 9s_{1/2}$	4.828E+07	4.840E+07		0.0011	0.0012	0.0085	0.0085
$4p_{3/2} \rightarrow 9s_{1/2}$	3.101E+07	3.030E+07		0.0029	0.0028	0.0427	0.0418
$5p_{3/2} \rightarrow 9s_{1/2}$	2.168E+07	2.170E+07		0.0068	0.0068	0.1830	0.1830
$6p_{3/2} \rightarrow 9s_{1/2}$	1.635E+07	1.650E+07		0.0168	0.0170	0.8224	0.8310
$7p_{3/2} \rightarrow 9s_{1/2}$	1.326E+07	1.320E+07		0.0522	0.0521	4.9868	4.9700
$8p_{3/2} \rightarrow 9s_{1/2}$	1.178E+07	1.180E+07		0.3188	0.3200	79.8675	80.2000

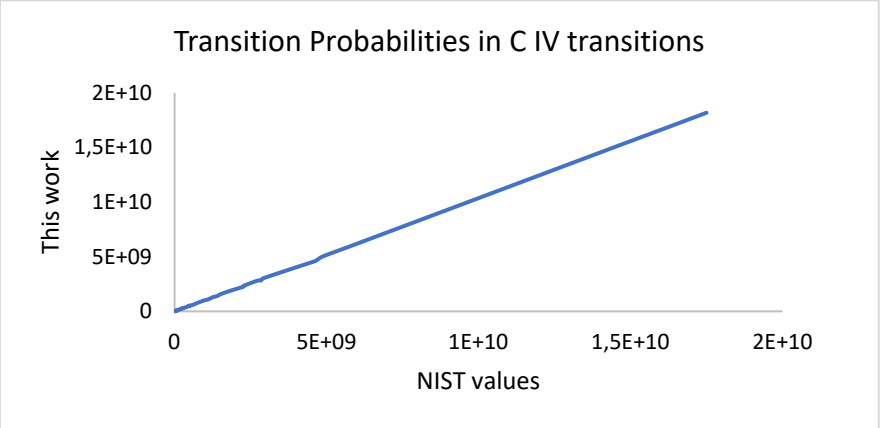

Figure 1. Plot of transition probabilities listed in the NIST database and corresponding calculated values

Table II. Lifetimes of Rydberg levels of C IV

State	Lifetime (ns)	State	Lifetime (ns)	State	Lifetime (ns)	State	Lifetime (ns)	State	Lifetime (ns)
3s	0.236	2p	3.658	4d	0.127	4f	0.281	5g	0.918
4s	0.377	3p	0.216	5d	0.244	5f	0.544	6g	1.571
5s	0.626	4p	0.346	6d	0.416	6f	0.932	7g	2.479
6s	0.992	5p	0.573	7d	0.655	7f	1.467	8g	3.681
7s	1.495	6p	0.906	8d	0.971	8f	2.175	9g	5.216
8s	2.157	7p	1.362	9d	1.374	9f	3.080	10g	7.126
9s	3.000	8p	1.961	10d	1.877	10f	4.206	11g	9.452
10s	4.046	9p	2.723	11d	2.489	11f	5.577	12g	12.235
11s	5.317	10p	3.665	12d	3.222	12f	7.218	13g	15.516
12s	6.837	11p	4.810	13d	4.086	13f	9.152	14g	19.337
13s	8.627	12p	6.176	14d	5.093	14f	11.404	15g	23.739
14s	10.711	13p	7.784	15d	6.253	15f	13.998	16g	28.763
15s	13.111	14p	9.653	16d	7.577	16f	16.960	17g	34.450
16s	15.849	15p	11.804	17d	9.077	17f	20.311	18g	40.841
17s	18.948	16p	14.256	18d	10.763	18f	24.079	19g	47.978
18s	22.432	17p	17.030	19d	12.646	19f	28.285	20g	55.902
19s	26.322	18p	20.145	20d	14.737	20f	32.956	21g	64.654
20s	30.641	19p	23.622	21d	17.046	21f	38.115	22g	74.275
21s	35.412	20p	27.481	22d	19.586	22f	43.786	23g	84.807
22s	40.658	21p	31.742	23d	22.366	23f	49.994	24g	96.292
23s	46.401	22p	36.424	24d	25.398	24f	56.764	25g	108.769
24s	52.665	23p	41.548	25d	28.692	25f	64.119		
25s	59.471	24p	47.134						
		25p	53.202						

A locally developed python program was used to fit a polynomial for each of the known values of lifetimes of Rydberg series. The lifetime for the series ns, np, nd, nf, and ng can be given a function of principal quantum number (n) in the form of a sixth-degree polynomial; the coefficients for the respective series are given in Table III

$$\tau_n = a_o + a_1 n + a_2 n^2 + a_3 n^3 + a_4 n^4 + a_5 n^5 + a_6 n^6$$

Table III. Coefficients of the sixth-degree polynomial for calculation of lifetimes of C IV series

Series	a_0	a_1	a_2	a_3	a_4	a_5	a_6	'n' value
ng	-8.26E-04	-8.90E-03	5.07E-03	6.63E-03	9.77E-06	-2.11E-07	1.93E-09	$5 \leq n$
nf	-7.74E-03	-2.88E-04	2.22E-03	3.97E-03	2.90E-06	-5.50E-08	4.56E-10	$4 \leq n$
nd	-1.73E-03	3.33E-04	8.48E-04	1.77E-03	1.91E-06	-4.40E-08	4.28E-10	$4 \leq n$
np	2.15E-01	-7.53E-02	1.98E-02	1.49E-03	9.59E-05	-2.56E-06	2.75E-08	$3 \leq n$
ns	2.30E-01	-7.87E-02	2.05E-02	1.75E-03	1.05E-04	-2.79E-06	2.99E-08	$3 \leq n$

CONCLUSION

An extended work has been carried out to determine the transition probabilities, oscillator strengths, and line strength for the transition in Rydberg levels of C IV. Total of 5250 transitions were studied. The calculated values were compared with the reported and NIST database values. The NIST database only contains 224 out of 5250 transitions (see Table I). That is, most of the values are reported for the first time. The maximum value of transition probabilities does not occur between the two lowest-lying levels, as is the case of the Li atom; instead, it occurs for the transition $1s^2 3d_{3/2} - 1s^2 2p_{1/2}$. Most transition probabilities are close to the reported values; a difference up to 7% has been observed in a few cases. A 99.9% correlation is found between calculated and known values of Transition probabilities (see Fig. 1). The comparison of calculated values of oscillator strengths and lines strengths with those listed in NIST shows a good agreement. Only 224 values of transition probabilities, oscillator strengths, and line strengths have been presented in this manuscript; a separate supplementary file contains all the 5250 values. The lifetimes of the first 25 levels of the Rydberg Series ns, np, nd, nf, and ng have also been calculated. A function of principal quantum number can calculate the lifetime; a sixth-degree polynomial gives this function for each Rydberg series for C IV.

ORCID IDs

Zaheer Uddin, https://orcid.org/0000-0002-8807-6186

REFERENCES

[1] X. Jiang, Y. Chen, X. Meng, W. Cao, C. Liu, Q. Huang, N. Naik, et al., A review, Carbon, **191**, 448 (2022). https://doi.org/10.1016/j.carbon.2022.02.011
[2] S. Rawat, R.K. Mishra, and T. Bhaskar, Chemosphere, **286**, 131961 (2022). https://doi.org/10.1016/j.chemosphere.2021.131961
[3] J. Xiao, J. Han, C. Zhang, G. Ling, F. Kang, and Q.H. Yang, Advanced Energy Materials, **12**(4), 2100775 (2022). https://doi.org/10.1002/aenm.202100775
[4] Y.Y. Feng, Y.Q. Chen, Z. Wang, and J. Wei, New Carbon Materials. **37**(1), 196 (2022). https://doi.org/10.1016/S1872-5805(22)60577-8

[5] M. Karimi, M. Shirzad, J.A. Silva, and A.E. Rodrigues, Journal of CO_2 Utilization. **57**, 101890 (2022). https://doi.org/10.1016/j.jcou.2022.101890
[6] M. Islam, A.D. Lantada, D. Mager, and J.G. Korvink, Advanced Healthcare Materials, **11(1)**, 2101834 (2022). https://doi.org/10.1002/adhm.202101834
[7] J. Choi, I. Yang, S.S. Kim, S.Y. Cho, and S. Lee, Macromolecular Rapid Communications, **43**(1), 2100467 (2022). https://doi.org/10.1002/marc.202100467
[8] I. Martinson, and W.S. Bickel, Physics Letters A, **31**(1), 25 (1970). https://doi.org/10.1016/0375-9601(70)90566-9
[9] M.C. Poulizac, M. Druetta, and P. Ceyzeriat, Journal of Quantitative Spectroscopy and Radiative Transfer, **11**(7), 1087 (1971). https://doi.org/10.1016/0022-4073(71)90128-2
[10] P.S. Ganas, Physics Letters A, **73**(3), 161 (1979). https://doi.org/10.1016/0375-9601(79)90695-9
[11] Y. Baudinet-Robinet, P.D. Dumont, H.P. Garnir, and A. El Himdy, Physical Review A, **40**(11), 6321 (1989). https://doi.org/10.1103/PhysRevA.40.6321
[12] B. Gou, and K.T. Chung, Journal of Physics B: Atomic, Molecular and Optical Physics, **29**(24), 6103 (1996). https://doi.org/10.1088/0953-4075/29/24/016
[13] E.S. Chang, and M. Geller, Phys. Scr. **58**, 326 (1998). https://doi.org/10.1088/0031-8949/58/4/008
[14] P. Quinet, Astronomy and Astrophysics Supplement Series, **129**(3), 603 (1998). https://doi.org/10.1051/aas:1998208
[15] N. Zheng, T. Wang, D. Ma, and T. Zhou, JOSA B, **18**(10), 1395 (2001). https://doi.org/10.1364/JOSAB.18.001395
[16] K.M. Aggarwal, and F.P. Keenan, Physica Scripta, **69**(5), 385 (2004). https://doi.org/10.1238/Physica.Regular.069a00385
[17] N. Zheng, and T. Wang, The Astrophysical Journal Supplement Series, **143**(1), 231 (2002). https://doi.org/10.1086/342421
[18] N.-W. Zheng, T. Wang, D.-X. Ma, T. Zhou, and J. Fan, International Journal of Quantum Chemistry, **98**, 281 (2004). https://doi.org/10.1002/QUA.20021
[19] H. Lischka, D. Nachtigallova, A.J. Aquino, P.G. Szalay, F. Plasser, F.B. Machado, and M. Barbatti, Chemical reviews, **118**(15), 7293 (2018). https://doi.org/10.1021/acs.chemrev.8b00244
[20] W. Li, P. Rynkun, L. Radžiūtė, G. Gaigalas, B. Atalay, A. Papoulia, K. Wang, et al., Astronomy & Astrophysics, **639**, A25 (2020). https://doi.org/10.1051/0004-6361/202037794
[21] J. Wang, H. Shen, R. Yang, K. Xie, C., Zhang, L. Chen, K.-M. Ho, et al., Carbon, **186,** 1 (2022). https://doi.org/10.1016/j.carbon.2021.09.062
[22] R. Siddiq, M.N. Hameed, M.H. Zaheer, M.B. Khan, and Z. Uddin, Beni-Suef Univ. J. Basic. Appl. Sci. **11**, 42 (2022). https://doi.org/10.1186/s43088-022-00224-0

РОЗРАХУНОК ХАРАКТЕРИСТИК C IV ПЕРЕХОДІВ

Мухаммад Саід[a], Шафік Ур Рехман[a], Махвіш Мобін Хан[b], Захір Уддін[a]
[a]*Департамент фізики, Університет Карачі, Пакистан*
[b]*Департамент прикладної хімії та хімічної технології Університету Карачі, Пакистан*

У цьому дослідженні ми обчислили ймовірності переходів, потужність лінії та потужність осцилятора понад 5000 переходів у C IV. Дуже небагато значень цих спектроскопічних характеристик були раніше відомі та повідомлені. На основі поєднання моделі найслабшого зв'язку електрона та чисельної апроксимації метод розрахунку показує надійні значення, оскільки кореляція між відомими та обчисленими значеннями висока. Імовірності переходу, розраховані в цій роботі, порівнюються з доступними значеннями бази даних NIST і тими, що містяться в літературі, і спостерігається досить хороша згода. Тривалість життя рівнів Рідберга ns, np, nd, nf, ng була повідомлена до n = 25. Було розроблено загальний поліном шостого ступеня, який генерує час життя C IV із достатньою точністю. Більшість представлених результатів є новими.

Ключові слова: *атом вуглецю; ймовірність переходу; сила осцилятора; атом Рідберга; квантові дефекти*